

**VALIDATION OF IONOSPHERIC MODELS**

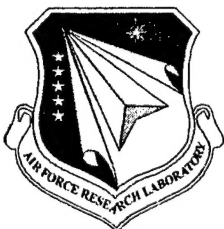
**Patricia H. Doherty  
Leo F. McNamara  
Susan H. Delay  
Neil J. Grossbard**

**Boston College  
140 Commonwealth Avenue  
Chestnut Hill, MA 02467-3682**

**18 September 2003**

**Final Report**

**APPROVED FOR PUBLIC RELEASE; DISTRIBUTION UNLIMITED**



**AIR FORCE RESEARCH LABORATORY  
Space Vehicles Directorate  
29 Randolph Rd  
AIR FORCE MATERIEL COMMAND  
Hanscom AFB, MA 01731-3010**

---

**20040319 089**

This technical report has been reviewed and is approved for publication.

/Signed/  
JOHN A. RETTERER  
Contract Manager

/Signed/  
JAMES HUNTER, Major, USAF  
Branch Chief

This document has been reviewed by the ESC Public Affairs Office and has been approved for release to the National Technical Information Service.

Qualified requestors may obtain additional copies from the Defense Technical Information Center (DTIC). All others should apply to the National Technical Information Service.

If your address has changed, if you wish to be removed from the mailing list, or if the addressee is no longer employed by your organization, please notify AFRL/VSIM, 29 Randolph Rd., Hanscom AFB, MA 01731-3010. This will assist us in maintaining a current mailing list.

Do not return copies of this report unless contractual obligations or notices on a specific document require that it be returned.



REPORT DOCUMENTATION PAGE				Form Approved OMB No. 0704-0188	
<p>The public reporting burden for this collection of information is estimated to average 1 hour per response, including the time for reviewing instructions, searching existing data sources, gathering and maintaining the data needed, and completing and reviewing the collection of information. Send comments regarding this burden estimate or any other aspect of this collection of information, including suggestions for reducing the burden, to Department of Defense, Washington Headquarters Services, Directorate for Information Operations and Reports (0704-0188), 1215 Jefferson Davis Highway, Suite 1204, Arlington, VA 22202-4302. Respondents should be aware that notwithstanding any other provision of law, no person shall be subject to any penalty for failing to comply with a collection of information if it does not display a currently valid OMB control number.</p> <p><b>PLEASE DO NOT RETURN YOUR FORM TO THE ABOVE ADDRESS.</b></p>					
1. REPORT DATE (DD-MM-YYYY) 18-09-2003		2. REPORT TYPE Final Report		3. DATES COVERED (From - To) 1 April 1996 - 31 August 2003	
4. TITLE AND SUBTITLE  VALIDATION OF IONOSPHERIC MODELS			5a. CONTRACT NUMBER F19628-96-C-0039		
			5b. GRANT NUMBER		
			5c. PROGRAM ELEMENT NUMBER 61102F		
6. AUTHOR(S)  Patricia H. Doherty Leo F. McNamara Susan H. Delay Neil J. Grossbard			5d. PROJECT NUMBER 1010		
			5e. TASK NUMBER IM		
			5f. WORK UNIT NUMBER AC		
7. PERFORMING ORGANIZATION NAME(S) AND ADDRESS(ES) Boston College / Institute for Scientific Research 140 Commonwealth Avenue Chestnut Hill, MA 02467-3862			8. PERFORMING ORGANIZATION REPORT NUMBER		
9. SPONSORING/MONITORING AGENCY NAME(S) AND ADDRESS(ES) Air Force Research Laboratory 29 Randolph Road Hanscom AFB, MA 01731-3010			10. SPONSOR/MONITOR'S ACRONYM(S) VSBP		
			11. SPONSOR/MONITOR'S REPORT NUMBER(S) AFRL-VS-TR-2003-1610		
12. DISTRIBUTION/AVAILABILITY STATEMENT Approved for public release; distribution unlimited.					
13. SUPPLEMENTARY NOTES					
14. ABSTRACT  This document represents the final report for work performed under the Boston College contract F19628-96C-0039. This contract was entitled Validation of Ionospheric Models. The objective of this contract was to obtain satellite and ground-based ionospheric measurements from a wide range of geographic locations and to utilize the resulting databases to validate the theoretical ionospheric models that are the basis of the Parameterized Real-time Ionospheric Specification Model (PRISM) and the Ionospheric Forecast Model (IFM). Thus our various efforts can be categorized as either observational databases or modeling studies.					
15. SUBJECT TERMS Ionosphere, Total Electron Content (TEC), Scintillation, Electron density, Parameterized Real-time Ionospheric Specification Model (PRISM), Ionospheric Forecast Model (IFM), Parameterized Ionosphere Model (PIM), Global Positioning System (GPS)					
16. SECURITY CLASSIFICATION OF:			17. LIMITATION OF ABSTRACT  SAR	18. NUMBER OF PAGES	19a. NAME OF RESPONSIBLE PERSON John Retterer
a. REPORT U	b. ABSTRACT U	c. THIS PAGE U			19b. TELEPHONE NUMBER (Include area code) 781-377-3891

## CONTENTS

Section 1.	INTRODUCTION.....	1
Section 2.	JOURNAL PUBLICATIONS.....	2
	Modeling the Formation of Polar Cap Patches Using Large Plasma Flows .....	4
	Collisional Degradation of the Proton-H Atom Fluxes in the Atmosphere: A Comparison of Theoretical Techniques .....	25
	Total Electron Content Over the Pan American Longitudes: March – April 1994 .....	39
	Description and Assessment of Real-Time Algorithms to Estimate the Ionospheric Error Bounds for WAAS .....	48
	Improving IRI-90 Low Latitude Electron Density Specification ..	59
	Comparisons of TOPEX and Global Positioning System Total Electron Content Measurements at Equatorial Anomaly Latitudes .	76
	Intercomparison of Physical Models and Observations of the Ionosphere .....	88
	Formation of Polar Cap Patches Associated with North-to-South Transitions of the Interplanetary Magnetic Field .....	102
	Characteristics of Plasma Structuring in the Cusp/Cleft Region at Svalbard .....	116
	A Comparison of TEC fluctuations and scintillations at Ascension Island .....	131
	Longitude Structure of Ionospheric TEC at Low Latitude Measured by the TOPEX/Poseidon Satellite .....	139
	The Alfven-Falthammer Formula for the Parallel E-Field and its Analogue in Downward Auroral-Current Regions .....	161
	Ionospheric Effects of Major Magnetic Storms during the International Space Weather Period of September and October 1999: GPS Observations, VHF/UHF Scintillations and in-situ Density Structures at Middle and Equatorial Latitudes ...	175
Section 3.	OTHER PUBLICATIONS .....	200
Section 4.	PRESENTATIONS .....	202

## **ACKNOWLEDGEMENTS**

The researchers of this contract would like to thank Dr. John Retterer of AFRL for his dedication as manager of this contract. His continued support, interest and administration of our efforts are gratefully acknowledged. We would also like to thank Dr. Dwight Decker of AFRL for his contributions in the early years of this contract and for his continued collaboration on various efforts throughout the duration of the contract period. We similarly thank Mr. Gregory Bishop, Dr. William Borer, Dr. Odile de la Beaujardiere, Dr. Terence Bullett for their financial and scientific support and interest.

Gratitude is also expressed to Ms. Daneille Berzinis and Dr. M. Patricia Hagan of the Institute for Scientific Research at Boston College for expert and efficient support and administration. Finally, we express our sincerest appreciation to Mr. Leo Power of the Institute for Scientific Research at Boston College for his continued direction and support of our efforts.

## 1. INTRODUCTION

This document represents the final report for work performed under the Boston College contract F19628-96C-0039. This contract was entitled Validation of Ionospheric Models. The objective of this contract was to obtain satellite and ground-based ionospheric measurements from a wide range of geographic locations and to utilize the resulting databases to validate the theoretical ionospheric models that are the basis of the Parameterized Real-time Ionospheric Specification Model (PRISM) and the Ionospheric Forecast Model (IFM). Thus our various efforts can be categorized as either observational databases or modeling studies.

Over the course of this contract, we have accomplished significant work on the collection and analysis of numerous databases to be used in our modeling studies. These databases included Total Electron Content (TEC) from the Global Positioning Satellite (GPS) System, the Navy Navigation Satellite System (NNSS), the TOPEX/POSEIDON satellite and the Low Earth Orbit (LEO) satellite instrumented with a GPS receiver to perform radio occultation measurements of the GPS satellites. Other data types include scintillation data from GPS measurements and VHF/UHF sources. In addition to measured data, we have simulated electron density and TEC measurements of the GPS/MET satellite and the ultraviolet imaging systems proposed for launch on future Defense Meteorological Satellite Program satellites. All of these databases were carefully processed for use in our ionospheric modeling studies. In the process, we have contributed knowledge in our field of ionospheric expertise. Some of our studies were devoted to characterization of ionospheric TEC and scintillation behavior using these databases. This information is critical to ionospheric model development and validation.

Our modeling studies have also been noteworthy. They have covered ionospheric modeling development, validation and improvement at low, middle and high latitude regions. These efforts include theoretical modeling efforts of the polar cap, the middle latitude ionospheric storm effects and the dynamic behavior of the equatorial anomaly regions. We have also developed a model of positioning errors experienced by single-frequency GPS users. We have performed numerous model validations on the PRISM model, the IFM model, the International Reference Ionosphere (IRI) model and others. Our results often resulted in model improvements.

Within the context of this contract we have published 13 papers in refereed journals. We have also published 14 papers in the Proceedings of various scientific meetings and have made 55 presentations. Full copies of the papers published in refereed journals are included in this report together with references to the papers published in meeting proceedings. Finally, we have included a list of the presentations made under the context of this contract.

In assembling this final report, we conclude that our work has addressed and exceeded the objectives of the contract to validate ionospheric models.

## 2. JOURNAL PUBLICATIONS

This section contains the following publications that resulted from our validation of ionospheric models:

Valladares, C.E., Decker, D.T., Sheehan, R. and Anderson, D.N., "Modeling the formation of polar cap patches using large plasma flows", *Radio Science*, 31, 573-593, May-June 1996.

Decker, D.T., Kozelov, B.V., Basu, B., Jasperse, J.R. and Ivanov, V.E., "Collisional Degradation of the Proton-H Atom Fluxes in the Atmosphere: A Comparison of Theoretical Techniques", *J. Geophys. Res.*, 101, 26947-26960, 1996.

Doherty, P.H., Anderson, D.N. and Klobuchar, J.A., "Total Electron Content Over the Pan American Longitudes: March-April 1994", *Radio Science*, 32, no. 4.

Conker, R.S., El-Arini, M.B., Albertson, T.W., Klobuchar, J.A. and Doherty, P.H., "Description and Assessment of Real-Time Algorithms to Estimate the Ionospheric Error Bounds for WAAS", *Navigation, Journal of The Institute of Navigation*, 44(1), Spring 1997.

Decker, D.T., Anderson, D.N. and Preble, A.J., "Improving IRI-90 Low Latitude Electron Density Specification", *Radio Sci.*, 32, 2003-2019, 1997.

Vladimer, J.A., Lee, M.C., Doherty, P.H., Decker, D.T. and Anderson, D.N., "Comparisons of TOPEX and Global Positioning System Total Electron Content Measurements at Equatorial Anomaly Latitudes", *Radio Sci.*, 32, 2209-2220, 1997.

Anderson, D.N., Buonsanto, M.J., Codrescu, M., Decker, D., Fesen, C.G., Fuller-Rowell, T.J., Reinisch, B.W., Richards, P.G., Roble, R.G., Schunk, R.W. and Sojka, J.J., "Intercomparison of Physical Models and Observations of the Ionosphere", *J. Geophys. Res.*, 103, 2179-2192, 1998.

Basu, S., Weber, E.J., Bullett, T.W., Keskinen, M.J., MacKenzie, E., Doherty, P., Sheehan, R., Kuenzler, H., Ning, P. and Bongiolatti, J., "Characteristics of plasma structuring in the cusp/cleft region at Svalbard", *Radio Science*, Vol. 33, Number 6, pp 188-1899, November-December 1998.

Valladares, C.E., Anderson, D.N., Bullett, T., Reinisch, B.W., "Formation of polar cap patches associated with north-to-south transitions of the interplanetary magnetic field.", *J. Geophys. Res.*, 103, 14,657-14,670, 1998.

Basu, S., Groves, K.M., Quinn, J.M., Doherty, P. "A comparison of TEC fluctuations and scintillations at Ascension Island", *JASTP* 61, 1999, 1219-1226, 1999.

Vladimer, J.A., Jastrzebski, P., Lee, M.C., Doherty, P.H., Decker, D.T. and Anderson, D.N., "Longitude Structure of Ionospheric TEC at Low Latitude Measured by the TOPEX/Poseidon Satellite", *Radio Science*, Vol. 34, #5, pp 1239-1260, Sept-Oct 1999.

Jasperse, J.R. and Grossbard, N.J., "The Alfven-Falthammer Formula for the Parallel E Field and its Analogue in Downward Auroral-Current Regions", *IEEE Transactions on Plasma Science*, Vol. 28, No. 6, December 2000.

Basu, Su. Basu, S., Valladares, C.E., Yeh, H.C., Su, S.Y., MacKenzie, E., Sultan, P.J., Aarons, J., Rich, F.J., Doherty, P.H., Grove, K.M. and Bullet, T.W., "Ionospheric effects of major magnetic storms during the international space weather period of September and October 1999: GPS observations, VHF/UHF scintillations and in-situ density structures at middle and equatorial latitudes", *Journal of Geophysical Research*, Vol. 106, No. A12, Pages 30,389-30,413, December 2001.

## Modeling the formation of polar cap patches using large plasma flows

C. E. Valladares, D. T. Decker, and R. Sheehan

Institute for Space Research, Boston College, Newton Center, Massachusetts

D. N. Anderson

Phillips Laboratory, Geophysics Directorate, Hanscom Air Force Base, Massachusetts

**Abstract.** Recent measurements made with the Sondrestrom incoherent scatter radar have indicated that the formation of polar cap patches can be closely associated with the flow of a large plasma jet. In this paper, we report the results of a numerical study to investigate the role of plasma jets on patch formation, to determine the temporal evolution of the density structure, and to assess the importance of  $O^+$  loss rate and transport mechanisms. We have used a time-dependent model of the high-latitude  $F$  region ionosphere and model inputs guided by data collected by radar and ground-based magnetometers. We have studied several different scenarios of patch formation. Rather than mix the effects of a complex of variations that could occur during a transient event, we limit ourselves here to simulations of three types to focus on a few key elements. The first attempt employed a Heelis-type pattern to represent the global convection and two stationary vortices to characterize the localized velocity structure. No discrete isolated patches were evident in this simulation. The second modeling study allowed the vortices to travel according to the background convection. Discrete density patches were seen in the polar cap for this case. The third case involved the use of a Heppner and Maynard pattern of polar cap potential. Like the second case, patches were seen only when traveling vortices were used in the simulation. The shapes of the patches in the two cases of moving vortices were defined by the geometrical aspect of the vortices, i.e. elliptical vortices generated elongated patches. When we "artificially" removed the Joule frictional heating, and hence any enhanced  $O^+$  loss rate, it was found that transport of low density plasma from earlier local times can contribute to ~60% of the depletion. We also found that patches can be created only when the vortices are located in a narrow local time sector, between 1000 and 1200 LT and at latitudes close to the tongue of ionization.

### 1. Introduction

Large-scale density structures are commonly observed in the polar cap. When the interplanetary magnetic field (IMF) is directed southward mesoscale (100 to 1000 km), density enhancements, named polar cap "patches", drift across the polar cap in the antisunward direction [Buchau *et al.*, 1983; Weber *et al.*, 1984, 1986; Fukui *et al.*, 1994]. When the IMF is directed northward, elongated streaks of precipitation-enhanced  $F$  region

plasma extend aligned to the noon-midnight meridian and move toward dawn or dusk [Buchau *et al.*, 1983; Carlson *et al.*, 1984; Valladares *et al.*, 1994a]. Both types of structures can be associated with intense levels of scintillation [Weber *et al.*, 1984; Buchau *et al.*, 1985; Basu *et al.*, 1985, 1989] and disrupt radio satellite communication systems. In this paper, we investigate theoretically the formation of plasma density enhancements that occur during  $B_z$  south conditions. To conduct this study, we have used a three-dimensional time-dependent model of the high-latitude  $F$  region ionosphere developed by Anderson *et al.* [1988, 1996] and Decker *et al.* [1994]. Differing from previous attempts, we have incorporated into the model analytical expressions of localized electric field structures and their

Copyright 1996 by the American Geophysical Union.

Paper number 96RS00481.  
0048-6604/96/96RS-00481\$11.00



time-dependence. We checked the validity of the model results by conducting a detailed comparison with data gathered from the Sondrestrom incoherent scatter radar (ISR) during patch formation events.

The source of the plasma and the physical processes that form the polar cap patches have been under investigation for over 10 years. *Buchau et al.* [1985] and *de la Beaujardiere et al.* [1985] were the first researchers to address the question of the origin of the density inside the patches. *Buchau et al.* [1985] measured values of  $f_oF_2$  at Thule, Greenland (86° magnetic latitude), showing large fluctuations. The minimum  $f_oF_2$  values were equal to densities produced locally by the sun EUV radiation, but the maximum values were similar to the densities that were produced at locations equatorward of the auroral oval. These observations suggested that the plasma density inside the patches was produced by solar radiation in the sunlit ionosphere, probably at subcusp latitudes, and then carried into and across the polar cap by the global convection pattern. In fact, *Weber et al.* [1984] and *Foster and Doupnik* [1984] confirmed the presence of a large eastward electric field near midday, likely directing the subauroral plasma poleward. *Buchau et al.* [1985] found also that the occurrence of patches displayed a strong diurnal UT control. The patches were seen at Thule almost exclusively between 1200 and 0000 UT. This UT control of the polar cap  $F$  layer ionization was interpreted in terms of the displacement of the convection pattern with respect to the geographic pole. It is because of this displacement that the polar convection is able to embrace higher-density plasma only at certain UT hours [*Sojka et al.*, 1993, 1994]. However, the mechanism (or mechanisms) by which the auroral plasma can break up into discrete entities is still a matter of debate.

*Tsunoda* [1988] summarized the role of different mechanisms conducive for patch generation. He suggested that changes in the  $B_y$  and/or  $B_z$  components of the IMF could originate temporal variations in the global flow pattern, drastically disturbing the density distribution within the polar cap. In the mid 1980s, several theoretical studies were designed to study the production, lifetime, and decay of large-scale structures inside the polar ionosphere [*Sojka and Schunk*, 1986; *Schunk and Sojka*, 1987]. These authors indicated that hard precipitation could produce plasma enhancements similar to the patches and blobs found in the auroral oval. They argued that in the absence of solar radiation, although the particle-produced  $E$  region will rapidly recombine, the longer lifetime enhanced  $F$  region ionization could build up and persist for several hours. *Sojka and Schunk*

[1988] theoretically demonstrated that large electric fields could create regions of density depleted by a factor of 4. *Anderson et al.* [1988] presented a model of the high-latitude  $F$  region that was used to investigate the effect of sudden changes in the size of the polar cap upon density enhancements transiting the polar cap. While these model studies were able to form structures, most of the success in patch modeling has been attained only after the first High Latitude Plasma Structures meeting was convened at Peaceful Valley, Colorado, in June 1992. *Sojka et al.* [1993] conducted numerical simulations of the effect of temporal changes of the global pattern. The latter two studies were successful in producing density structures at polar cap latitudes. *Decker et al.* [1994] used six different global convection patterns and localized velocity structures to reproduce the digisonde measurements of  $f_oF_2$  values at Sondrestrom. *Lockwood and Carlson* [1992] used the formulation of transient reconnection [*Cowley et al.*, 1991] to suggest that a transient burst of reconnection together with the equatorward motion of the ionospheric projection of the  $X$  line could extract a region of the high density subauroral plasma, divert the subauroral density poleward, and finally "pinch off" the newly formed patch. More recently, *Valladares et al.* [1994b] has shown a case study where a fast plasma jet containing eastward directed velocities in excess of  $2.5 \text{ km s}^{-1}$  was able to increase the  $O^+$  recombination rate and yield an east-west aligned region of reduced densities across a poleward moving tongue of ionization (TOI). *Rodger et al.* [1994] presented data from the Halley Polar Anglo-American Conjugate Experiment radar in Antarctica, suggesting that a region of depleted densities can be carved out by increased  $O^+$  recombination due to large plasma jets.

This paper presents a detailed modeling of the mechanism of patch formation presented by *Valladares et al.* [1994b] and *Rodger et al.* [1994]. The mechanism described here operates in conjunction with a background poleward convection to produce mesoscale polar structures from subauroral plasma. This process may also have an essential role in determining the size and the shape of the polar cap patches. The basic elements of this mechanism are (1) a fast plasma jet, observed near the midday auroral oval, (2) enhanced ion temperature due to Joule frictional heating, (3) enhanced recombination rates of  $O^+$ , and, (4) transit of low density plasma from earlier local times.

The paper has been organized in the following manner.

Section 2 succinctly describes our model of the high-latitude ionosphere [*Anderson et al.*, 1988; *Decker et al.*, 1994] and the calculations of the localized electric fields



incorporated into the model. Section 3 presents results of a computer model of a patch formation mechanism using convection patterns for typical IMF  $B_y$  positive and negative values. An assessment of the ability of enhanced recombination loss to erode parts of the TOI and to disconnect regions from the oval is also discussed in this section. Section 4 presents model calculations for vortices located at several different local times. The paper concludes with the discussion and conclusions section.

## 2. Model Description

The Global Theoretical Ionospheric Model (GTIM) calculates the density altitude profile of a single ion ( $O^+$ ) along a flux tube. It solves the coupled continuity and momentum equations for ions and electrons. The solution of the differential equations is simplified by selecting a coordinate system in which one dimension is defined parallel to the local magnetic field. The model attains three-dimensionality by repeating the profile calculations along many (a few thousand) flux tubes. The locations of the flux tubes are selected to cover the range of latitudes and local times desired for the simulation. The mathematical foundation of the GTIM model was introduced by Anderson [1971, 1973]. Although initially used to study the low-latitude ionosphere, it has been extended to include physical processes of the high-latitude ionosphere, such as the effects of large electric fields and particle precipitation [Anderson et al., 1988; Decker et al., 1994]. Recently, Decker et al. [1994] have described how the inputs to the GTIM model can easily accommodate a time-dependent convection pattern and spatially localized regions containing high flows to represent highly variable situations, such as those existing in the cusp region. Other geophysical input parameters, such as the neutral density and wind, along with several initial conditions, such as the plasma density, can be freely defined to simulate different scenarios. In this paper, we have adjusted the global convection pattern and included a local electric field to reproduce the velocities measured on February 19, 1990, by the Sondrestrom ISR.

The radar and magnetometer measurements used to define the model inputs were discussed by Valladares et al. [1994b]. These authors observed a large channel oriented in the east-west direction containing jet-type eastward velocities of order  $2 \text{ km s}^{-1}$ . In this channel, the ion temperature ( $T_i$ ) was enhanced and the density ( $N_e$ ) was depleted. These signatures in the  $T_i$  and  $N_e$

values implied a likely increase in the  $O^+$  recombination rate. Successive radar scans indicated that the plasma jet was continuously moving poleward. This motion was also confirmed by the large negative deflection seen at later times by magnetometers located at latitudes poleward of Sondrestrom. The large negative deviation of the  $H$  component due to Hall currents appeared at Qaanaaq 29 min after being observed at Sondrestrom. This implied an average poleward displacement of  $620 \text{ m s}^{-1}$  for the plasma jet. Valladares et al. [1994b] also presented equivalent velocity vectors deduced from the magnetometers located along the east coast of Greenland, implying a flow vorticity. Similar vorticity was seen in the resolved radar velocity vectors. The radar line-of-sight velocity also indicated that adjacent to and both northward and southward of the large plasma jet there existed regions of westward flows. In summary, the radar and magnetometer data suggested the presence of two adjacent vortices of opposite vorticity with the common region in the middle comprising the plasma jet. The GTIM model also requires other geophysical parameters, such as the neutral density, wind and temperature, the ionization, and chemical loss rates, and the diffusion coefficients. These latter atmospheric parameters were selected as described by Decker et al. [1994]. The neutral densities and winds were calculated using the mass spectrometer/incoherent scatter 1986 (MSIS-86) model [Hedin, 1987] and Hedin's wind model [Hedin et al., 1991]. The ion loss rate was computed as a function of an effective temperature. This parameter is derived using the following equation of Schunk et al. [1975]:

$$T_{\text{eff}} = T_n + 0.329E^2$$

where  $E$  is the magnetospheric electric field in millivolts per meter.

Plate 1 displays the  $N_m F_2$  values of the high latitude ionosphere as a function of magnetic latitude and local time. These values were obtained with the GTIM model after following 7200 flux tubes during 8 hours of simulation time. During this time, the global convection pattern and other relevant ionospheric parameters were kept constant. The purpose here was to obtain the initial ionospheric densities to be used as a convenient starting point for simulating the ionospheric effects of a plasma jet. The actual ionosphere rarely has 8 hours of such steady conditions. However, this allows us to single out individual effects that can be produced by various ionospheric processes. The real ionosphere may be a superposition of several of these plasma jet

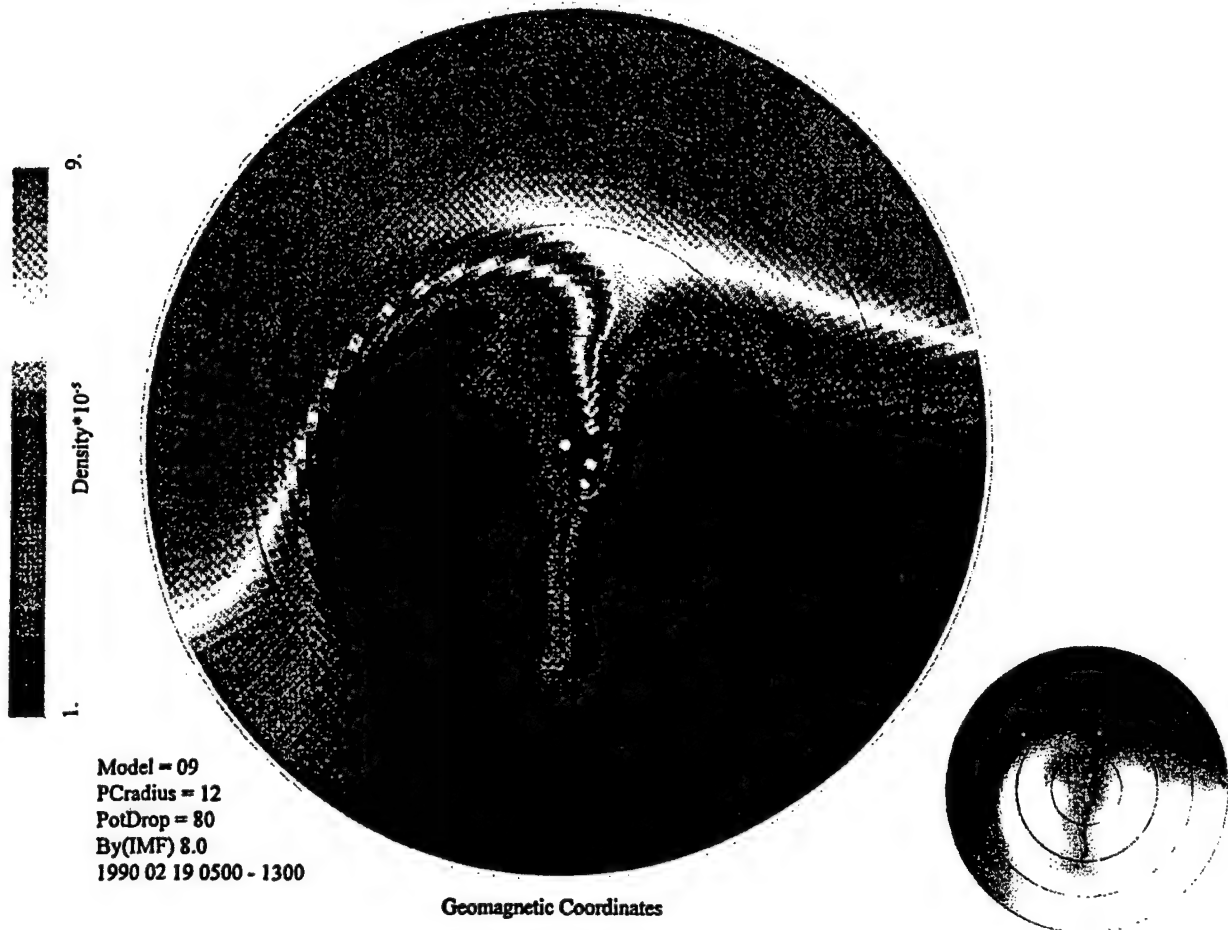


**Plate 1.** Polar plot of the NmF2 (peak F region density) of the high-latitude ionosphere at 1300 UT. This density plot corresponds to the initial values used in the simulations of sections 3.1, 3.2, 3.4, and 4. The values in this plot were obtained by running the model for 8 hours and using steady state inputs. We include in the lower right corner the black and white version of this plot in a format that will be shown in subsequent plots. The black dots correspond to the locations of the Sondrestrom and Qaanaaq stations, and the white dot indicates the location of the European Incoherent Scatter station. The latitudinal circles are in steps of  $10^\circ$ .

and density break-off events. A prominent feature of Plate 1 is the presence of the TOI. At 1300 UT it extends from longitudes close to European Incoherent Scatter EISCAT ( $19^\circ\text{E}$ ) up to  $51^\circ\text{W}$ , where it turns poleward. The TOI is bounded at the equatorward edge by a region of densities reduced by 30% and poleward by densities almost an order of magnitude smaller. The larger densities in the TOI are due mainly to two factors, a small westward flow in the dusk cell and an upward lift of the F region. The longer transit time and the relatively smaller solar zenith angle permit the solar radiation to build up much higher densities in this

confined region. Similar steady structures have been presented by *Crain et al.* [1993] in their total electron content maps of the high-latitude region.

The vorticity suggested by the radar and magnetometer data and other theoretical implications of solar wind - magnetosphere interactions [*Newell and Sibeck*, 1993] led us to infer that the plasma jet may actually consist of a system of two vortices superimposed on the background convection. With this as a guide, we searched for a system of two ellipsoidal potential vortices added to a global convection pattern. The search was carried out by varying the cross polar

**Table 1.** Global and Local Velocity Patterns

Global pattern	$B_y$	Polar Cap Potential, kV	Number of Vortices	Major Axis, deg	Minor axis, deg	Vortex Potential, kV	Latitude of Vortices, deg	Local Time of Vortices, deg
Heelis 12° radius	+	80	2	10, 10	2.4, 1	20, -5	74, 71.5	11, 11
Heppner-Maynard	-	76	2	10, 10	2.4, 1	20, -5	74, 71.5	11, 11

cap potential, the global pattern, the radius of the polar cap and other geometrical parameters of the two-vortex system. The size, peak-to-peak voltage, location, orientation and aspect of the vortices were systematically changed iteratively to obtain the best fit to the radar velocities. We tried over 10 million combinations. Table 1 presents the general parameters of the vortices and the global pattern that provided the best fit to the Sondrestrom velocity data. A Heelis-type pattern gave the smallest error. However, a Heppner and Maynard  $B_y < 0$  pattern provided errors almost as small as the Heelis-type pattern. Because the radar azimuthal scan covers a small region of the total pattern, this method is not very sensitive in discriminating the

convection pattern. Figures 1a and 1b show the Heelis-type global convection pattern and the system of the two vortices of Table 1. Figure 1c depicts the result of adding the velocity patterns of Figures 1a and 1b. Figure 1d represents the simulated line-of-sight velocities which would have been measured at Sondrestrom if the pattern in Figure 1c had been in effect. The agreement between Figure 1d and Figure 6a of Valladares *et al.* [1994b], reproduced here as Figure 1e, is very good. Figure 1f shows the total vector velocity that was obtained using the convection pattern of Figure 1c.

Figure 2 shows the plasma density measured by the Sondrestrom ISR on February 19, 1990, during four

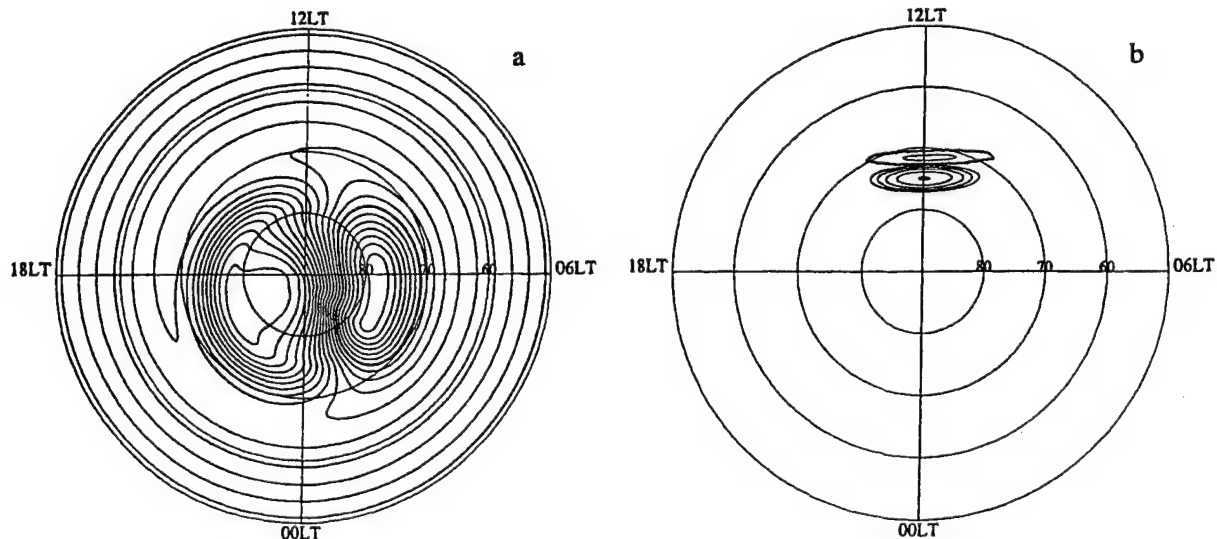


**Figure 1.** Series of polar plots. (a) High-latitude potential corresponding to a Heelis-type pattern for  $B_y = +8$  nT. The cross polar cap potential is 80 kV, and the radius of the polar cap is 12°. (b) the potential of the convective vortices. (c) Addition of the potentials in Figures 1a and 1b. (d) Simulated Sondrestrom line-of-sight velocities considering that the potentials of Figure 1c were in effect. (e) Line-of-sight velocities measured by the Sondrestrom radar on February 19, 1990 [Valladares *et al.*, 1994b, Figure 6a]. (f) Simulated vector velocities using the potential of Figure 1c.

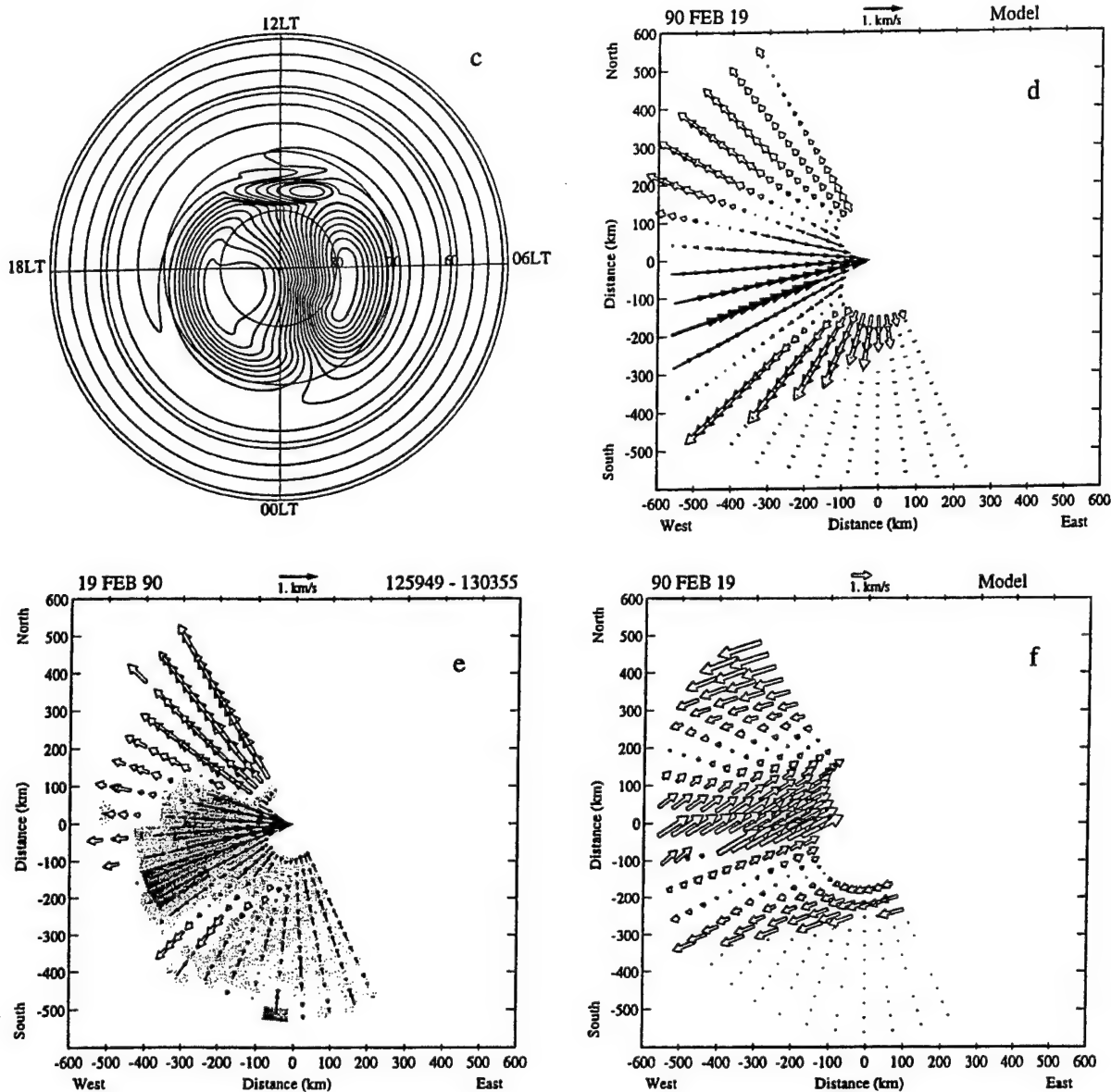


Figure 1. (continued)

consecutive elevation scans. Figure 2a, obtained between 1251 and 1254 UT and before the appearance of the plasma jet, shows a density value above  $3 \times 10^5 \text{ cm}^{-3}$  to the south of the radar. Overhead and to the north, the density is structured and peaks at  $5.5 \times 10^5 \text{ cm}^{-3}$ . These values are in good qualitative agreement with the modeled densities of Plate 1. The maximum modeled peak densities are  $5 \times 10^5 \text{ cm}^{-3}$  and  $9 \times 10^5 \text{ cm}^{-3}$  for the south and north locations respectively.

### 3. Patch Modeling Using Mesoscale Velocity Structures

During the last decade, a large array of transient events have been measured in the high-latitude ionosphere. Convective vortices, double vortices, east-west elongated ellipses, and vortices moving poleward, equatorward, downward and duskward have all been observed. While the magnetic response of these events have been studied

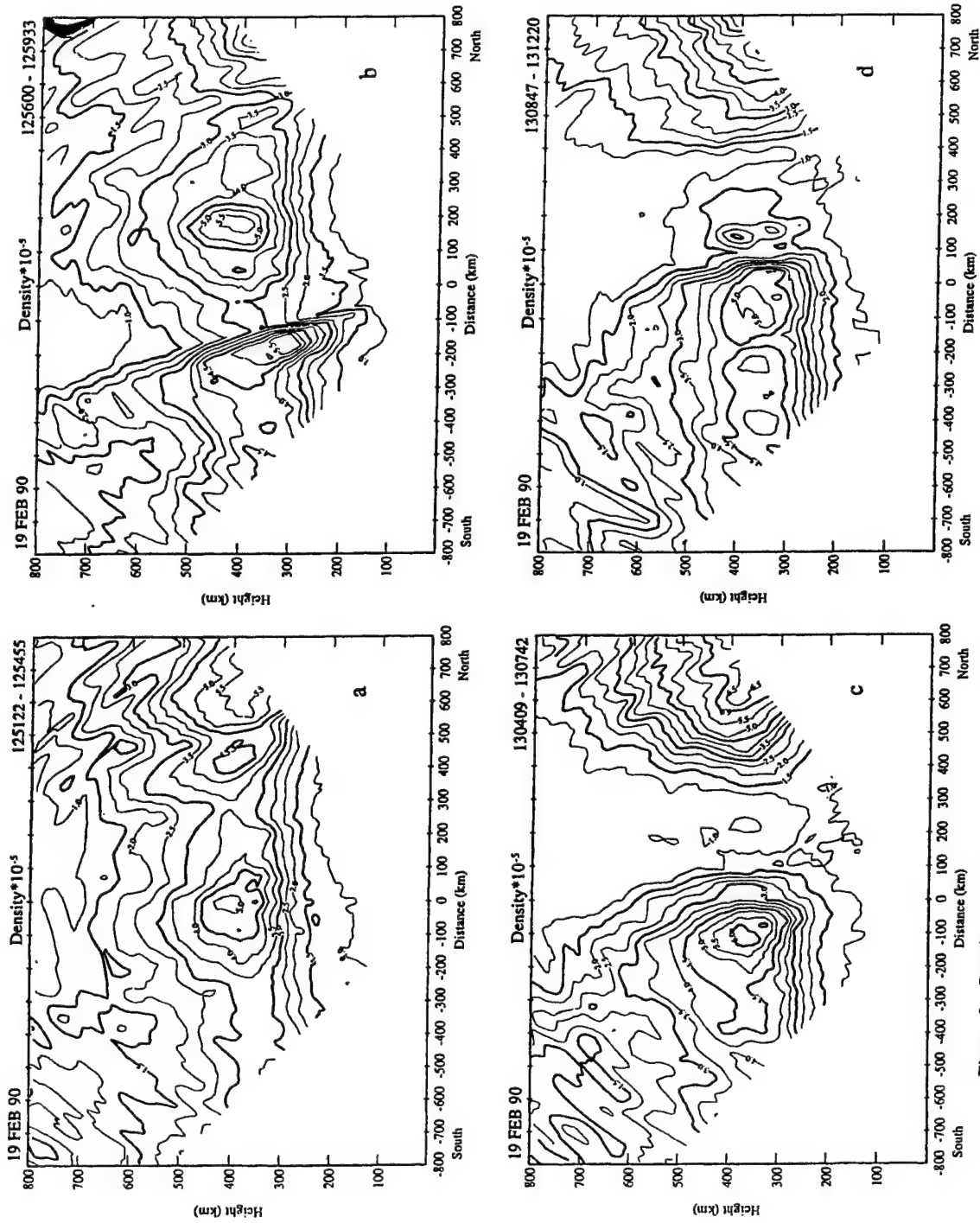


Figure 2. Density contours corresponding to four elevation scans of the Sondrestrom Incoherent Scatter Radar. The spacing between the contours is  $.5 \times 10^5 \text{ cm}^{-3}$ . The antenna azimuth angle was kept fixed at  $-27^\circ$  (magnetic meridian), and the elevation varied from  $30^\circ$  south to  $30^\circ$  north. The number density is displayed as a function of height and distance along the magnetic meridian.

in some detail [Goertz *et al.*, 1985; Heikkila *et al.*, 1989; Ma *et al.*, 1991], very little is known about their effect upon the ionospheric densities. Furthermore, transient events have been observed to have a fairly complex temporal behavior that is not well understood. As a result, rather than attempting a simulation that tries to include all of the observed behavior of a transient event, we have performed four numerical simulations that focus on just a few key elements of the event. The four scenarios modeled were chosen to help us learn how the density evolves under different conditions of the local and global patterns and to give us some insight as to how sensitive our results are to the various properties of these events. In the next four subsections, we report on the results from these simulations. First, we describe a case study in which a pair of transient vortices are kept fixed in a corrected geomagnetic coordinate system. In the next case, we include the observation that these transient vortices move by allowing the vortices to drift according to the background polar cap flow. We continue with a model case study that uses a Heppner-Maynard-type convection pattern as the global convection. This allows us to assess the sensitivity of our previous results to the global pattern that is chosen. Finally, in the fourth simulation, we establish the importance of the enhancement of the recombination rate in producing regions of depleted density across the TOI.

### 3.1. Stationary Vortices

The first modeling effort was implemented using two vortices which were maintained stationary in a local time versus latitude frame of reference. The vortices' potential is set equal to the predetermined value at 1300 UT; 15 min later the potential is turned off. Figure 3 and successive figures present a limited region of the northern hemisphere high latitude ionosphere. Here we show a series of snapshots of the  $N_m F_2$  corresponding to nine different times during the formation of the density structure. The area covered in each panel is about  $3500 \times 3500 \text{ km}^2$ . Figures 3a through 3f are 3 min apart. Figures 3g - 3i display the density in steps of 10 min. Figure 3a displays the initial density at the time of the potential vortices onset. This plot corresponds to a view looking down from a satellite that is traveling from the pole toward the equator. Lower latitudes are at the top of the figure, and poleward latitudes are at the bottom. The magnetic pole is at the center of the bottom edge of each panel. The locations of the Sondrestrom and Qaanaaq facilities are indicated by white dots.

The TOI is clearly depicted in Figure 3a; it extends nearly aligned with the equipotential lines and turns poleward near Sondrestrom. We remind the reader that the  $N_m F_2$  pattern of Figure 3a was calculated for February 19 at 1300 UT using the actual magnetic and solar flux conditions measured on that day and the inferred size of the polar cap, as defined in section 2. A weaker TOI may be obtained for other days of the year, different UT, or even different parameters of the convection pattern. Figure 3b displays the peak density 3 min after the vortex potential has been activated. Even at this time, the TOI is already drastically distorted. A section of the TOI has rotated anticlockwise; simultaneously, three parallel channels containing depleted densities have been created, two equatorward and one poleward of the fragmented TOI segment. All three elongated traces of low density are coincidental with the equatorward, center, and poleward walls of the vortices, which is where the high speed flows and the enhanced temperatures are. Three minutes later at 1306 (Figure 3c), all three low-density channels are further elongated in the east-west direction. A region of low density starts propagating poleward at the poleward edge of the vortex system. The following three panels (Figures 3d to 3f) show further elongation and deeper depletions in all three density channels. Clearly, the presence of the vortices has produced density structures. However, the density structure aligned in the east-west direction (Figure 3f) is still attached to what remains of the TOI. After the localized potential is turned off at 1315 UT, the density structures lose their east-west alignment. Figures 3g to 3i show that the density enhancement acquires instead a more north-south alignment. This additional change in the shape of the density structure is due to a nonuniform velocity near the center of the polar cap of the Heelis-type pattern in Figure 1a. If the flow were uniform, then the equipotential lines should have been parallel lines in the polar plot.

Figure 4 presents simulated radar elevation scans through the modeled ionospheric volume. Each of the panels shows an equivalent elevation scan in the meridian plane that would have been measured at Sondrestrom if the modeled densities were the real densities around the station. This scheme allows us to perform a one-to-one comparison with the data presented by Valladares *et al.* [1994b]. It help us to better understand the radar data when only elevation scans are conducted during the experiment. Each of the scans of Figure 4 are constructed from the density data displayed in the corresponding panels of Figure 3. The orientation of the scans is shown by the white lines in each panel of Figure 3. The larger



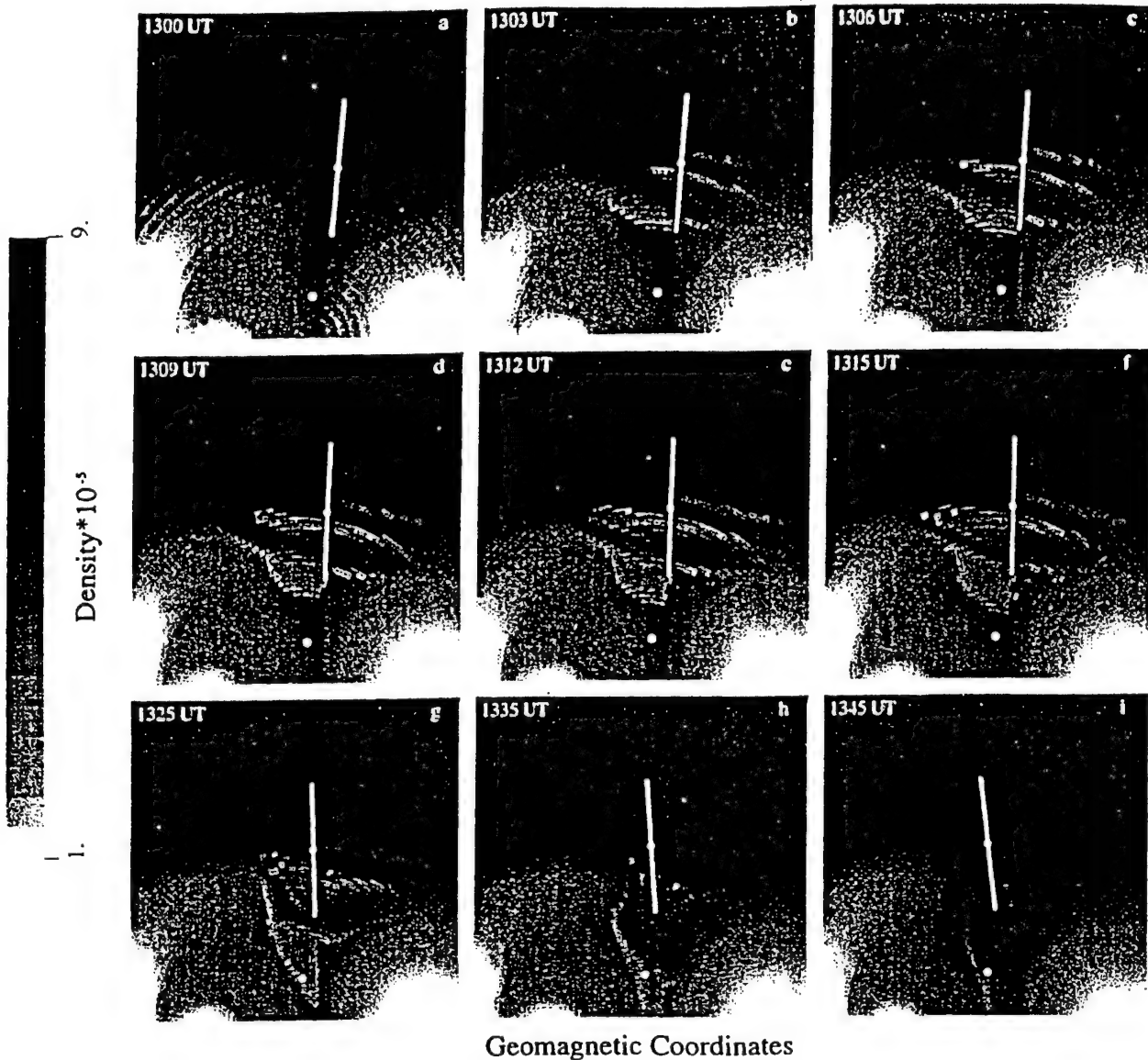


**Figure 3.** Each panel presents NmF2 values of a section of the high-latitude ionosphere at different times during the modeling that uses stationary vortices as input. See section 3.1 for more details. The white dots correspond to the locations of the Sondrestrom and Qaanaaq stations. The white line that crosses the Sondrestrom site indicates the extension of the elevation scans of Figure 2.

density at the northern part of the scan of Figure 4a is due to the passage of the TOI. Figure 4b, corresponding to 3 min along the simulation, shows mesoscale structuring coincident with the vortices. Two deep depletions are evident, one overhead and the other 500 km north of the station. The density of the northern depletion is  $3 \times 10^5 \text{ cm}^{-3}$ . The density remains unperturbed at the northern and southern extremes of the scan, no vortices are located

there. At 1309 UT, 9 min after the beginning of the simulation, both depletions reach a minimum value of  $2 \times 10^5 \text{ cm}^{-3}$ . The  $N_e$  depletion located almost overhead coincides with the center of the vortex, where the plasma flow is maximum. Figure 4e presents the modeled densities 12 min after the onset of the potential vortices. These contours can be closely compared with Figure 2c which shows the density measured by the Sondrestrom

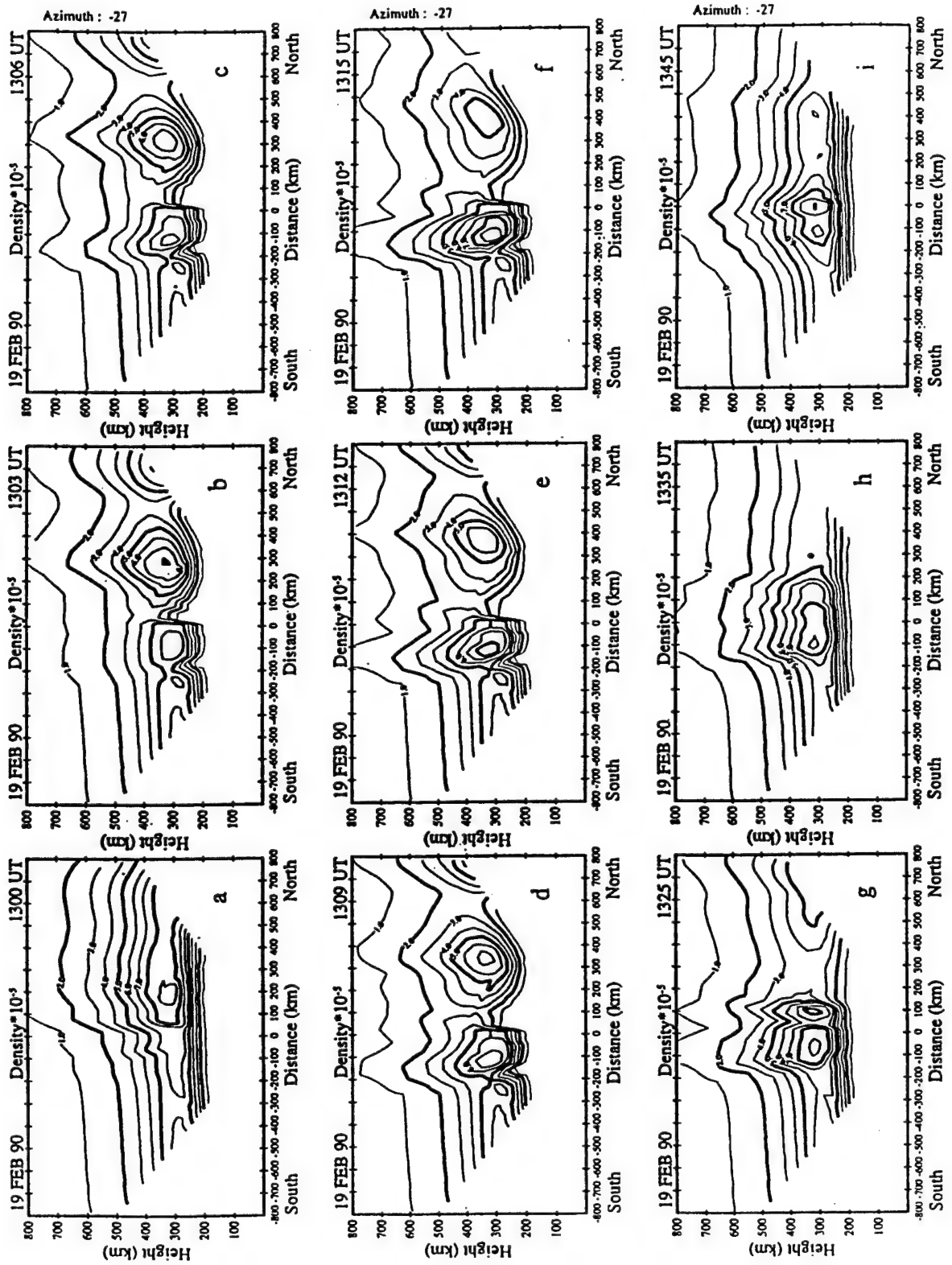


Figure 4. Simulated radar elevation scans through the simulated volume of section 3.1. (a) The large-scale density structure corresponds to the TOI. (b) - (i) The fragmentation of the TOI and formation of smaller-scale structures.



radar ~12 min after the start of the break-off event. Each figure displays two density structures separated by a channel of low density located almost overhead. The peak density in each of the structures shows a good agreement between modeled and measured values. However, the minimum density situated between structures is much more depleted in the experimental data. It is below  $10^5 \text{ cm}^{-3}$  in the radar data but above  $2 \times 10^5 \text{ cm}^{-3}$  in the model. Other differences between the measured and modeled densities are (1) the larger north-south extension of the density depleted region of the measured data, and (2) the noticeable higher bottomside *F* layer density of the experimental data.

While the stationary vortices scheme increases the amount of density structures transiting within the polar cap, it fails to produce isolated islands of enhanced density structures detached from the auroral oval. A camera located within the polar cap will be able to indicate this effect. Moreover, our definition of polar cap patches postulates that less dense plasma should surround the higher density plasma in all directions in order to qualify as a patch. Thus we conclude that stationary vortices do not reproduce all the characteristics of polar cap patches.

### 3.2. Traveling Vortices

The second modeling effort was carried out using a set of two traveling vortices moving with the background plasma flow. To generate the motion of the vortices, the two-vortex system was displaced in the antisunward direction as a whole entity. The displacement was set by the velocity of the plasma at the center of the line joining the vortices' centers. Similar to the previous case, the vortices potential was introduced at 1300 UT. The potential was then reduced by half 15 min later. The location of the vortices in the polar cap was updated every 30 s; this interval was equal to the step time of the simulation. Figure 5a repeats the initial density of Plate 1. During the first 9 min of the simulation (Figures 5b - 5d), the TOI is drastically distorted in a fashion similar to the nonconvective case. However, the width of the depletion channel and the depth of the density decrease are larger for the convecting vortices case. The dawn-dusk extension of the density structure is smaller in this convective scenario. We call this structure a region of enhanced density, because  $N_e$  is higher inside the structure than in the rest of the polar cap. Figures 5d through 5f show that both density structures develop an east-west or dawn-dusk alignment. They are also well collocated with the corresponding vortices. In contrast to

the nonconvecting vortices case, we see (Figure 5f) that the more northern density structure has no attachment to the oval or subauroral plasma. The last three panels at the bottom of Figure 5 show that as two patches travel antisunward across the polar cap, they suffer little distortion. This feature is also different from the previous case, where only one structure was fully formed. The prominent characteristic continues to be that both structures are individual entities with no attachment to the oval or subauroral plasma. The polar cap patches, as described here, are very similar in shape to the "cigar" patches, elongated in the east-west direction, described by Fukui *et al.* [1994].

A more quantitative view of the formation of the density enhancement and depletion is displayed in Figure 6. Figures 6b and 6c show the cross section in the magnetic meridian plane of two structures that were formed by the convective vortices. The structure located at 100 km south of the station was formed from plasma located at subauroral latitudes (south of the TOI). The  $N_e$  structure located at 300 km north is formed from the TOI. The particular location of the vortex causes plasma from the fragmented TOI to intrude into the southern velocity structure and reach values near  $9 \times 10^5 \text{ cm}^{-3}$ . The minimum density between patches is  $10^5 \text{ cm}^{-3}$ , as seen at 100 km north in Figure 6e. This depletion is replenished partially by solar radiation and reaches values near  $3 \times 10^5 \text{ cm}^{-3}$  in Figure 6h. Comparison of Figures 6e and 2c indicates a good qualitative agreement. The modeled densities of Figure 6e show a slightly higher density value and a narrower width in the region of depleted densities. In this region, the modeled density are  $< 10^5 \text{ cm}^{-3}$  at 300 km altitude, similar to the experimental values.

The traveling vortices scenario brought only a qualitative agreement with the density of Figure 2c. However, it was able to produce islands of high density transiting the polar cap. Thus we conclude that the convecting vortices are able to form patches of enhanced densities when they are located near the boundary between the polar cap and the auroral oval.

### 3.3. Heppner-Maynard-Type $B_z$ Negative Global Pattern

As mentioned in section 2.1, the radar data is not effective at discriminating between different global patterns. Thus it is of interest to see how our results might change if a different global pattern is used with the vortices. For this purpose, we repeated the calculations of the previous section to determine the effect on patch formation using a Heppner-Maynard-type pattern. Figure

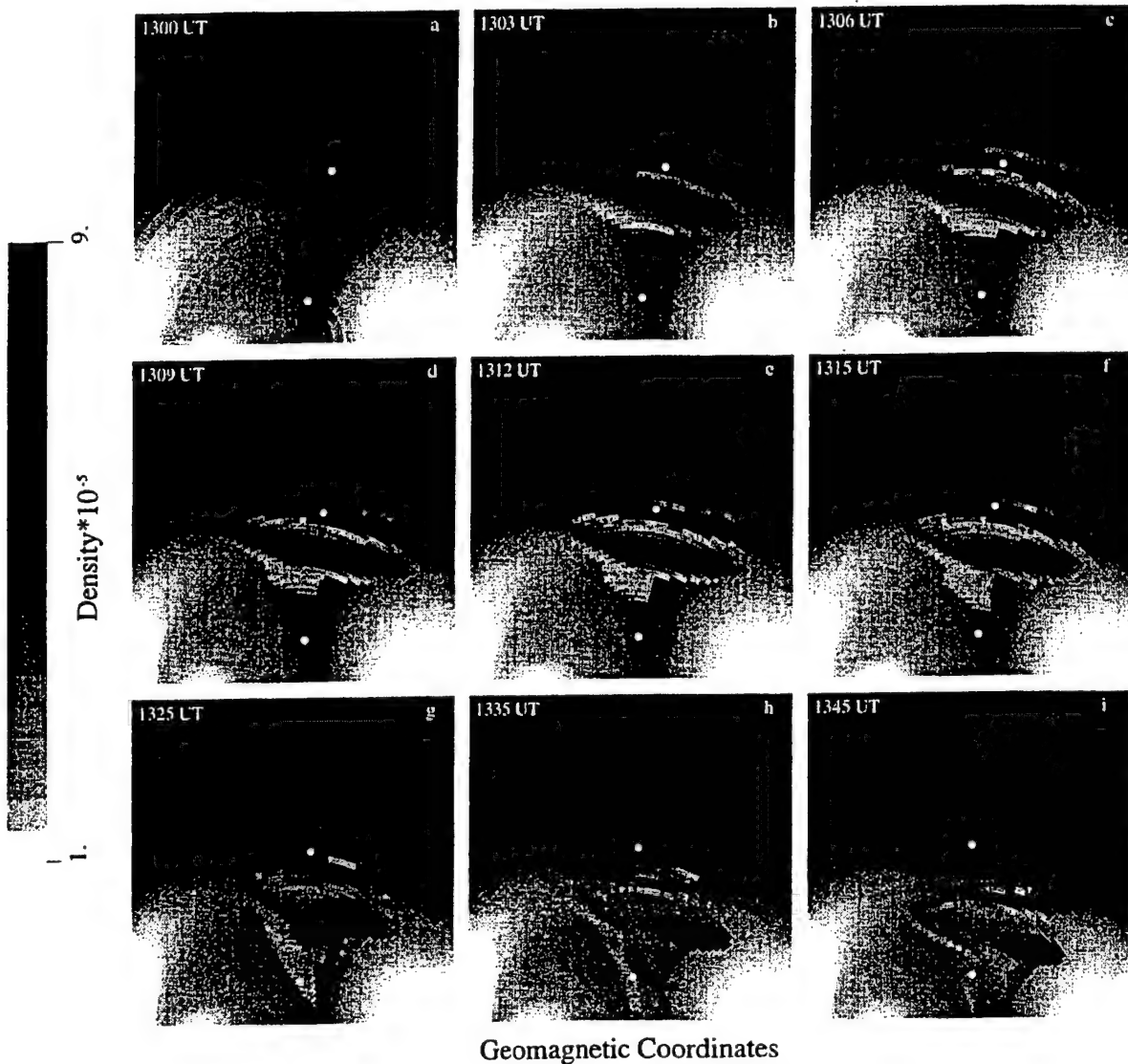


Figure 5. Same as Figure 3 but for the modeling study of traveling convective vortices (section 3.2)

7a displays the initial conditions of the  $N_m F_2$  values before the start of the simulation. The TOI shows a few peculiar differences with respect to the Heelis-type convection pattern of section 3.1. The maximum density is slightly higher, and the TOI is a much wider before it turns poleward. These differences are attributed to a slower flow velocity (stagnation region) near the dayside region in the Heppner-Maynard global convection patterns. The initial location of the vortices and the amplitude of each vortex potential are similar to the case described in section 3.2.

Figures 7b and 7c show that the vortices are able to bisect a region of the TOI and orient the major axis of the density structure in the dawn-dusk direction. A second region of depleted densities is seen at the lower latitudes in Figures 7c through 7f; however, this structure is not completely isolated from the TOI. Moreover, it joins the new TOI that is being formed during the last stages of the simulation. The patch located at higher latitudes retains its alignment for several minutes after the potential was reduced by 50% (Figures 7g - 7h). Figure 8 shows that the patch is bounded on the equatorward side by plasma

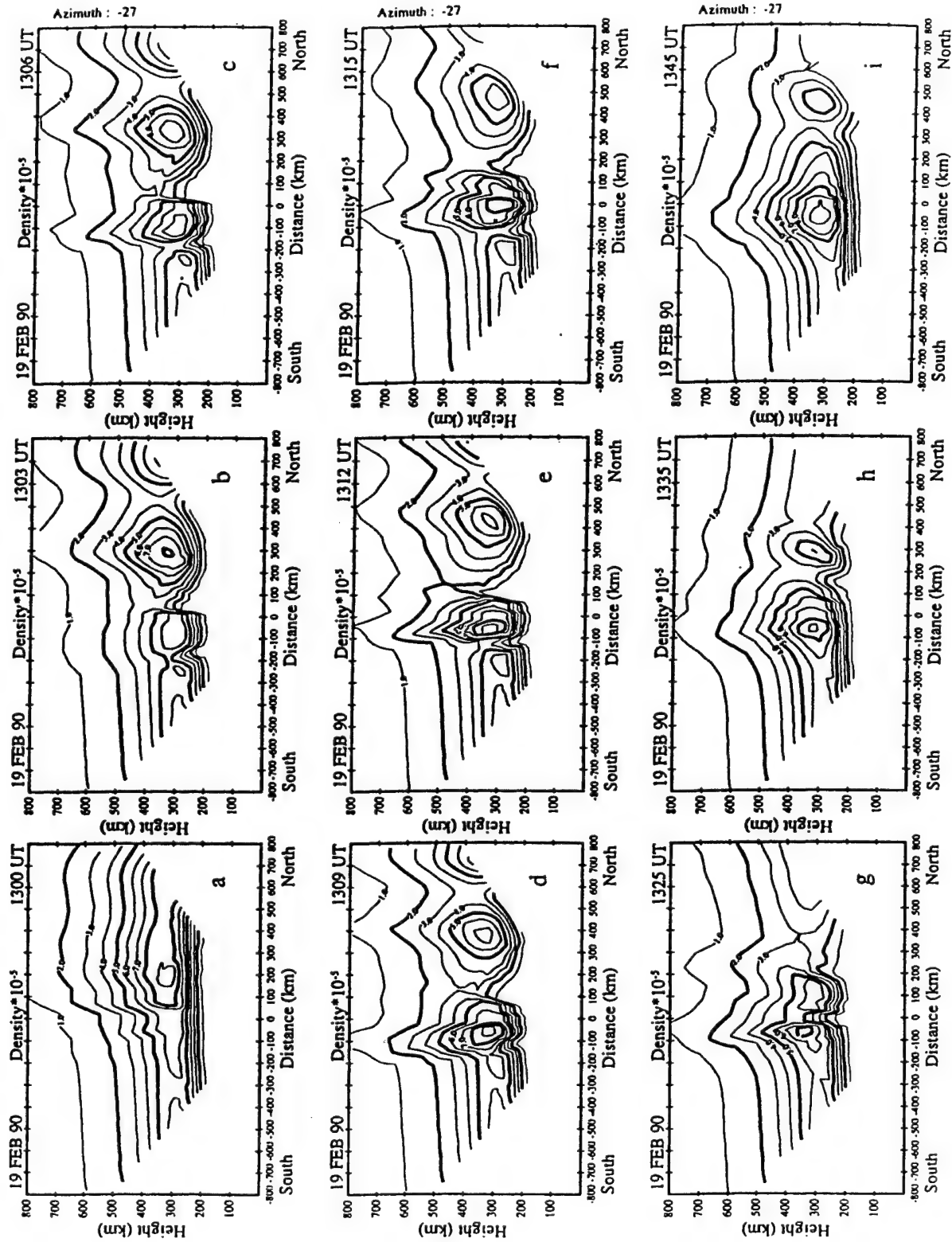


Figure 6. Same as Figure 4 but for the modeling study of traveling convective vortices (section 3.2).

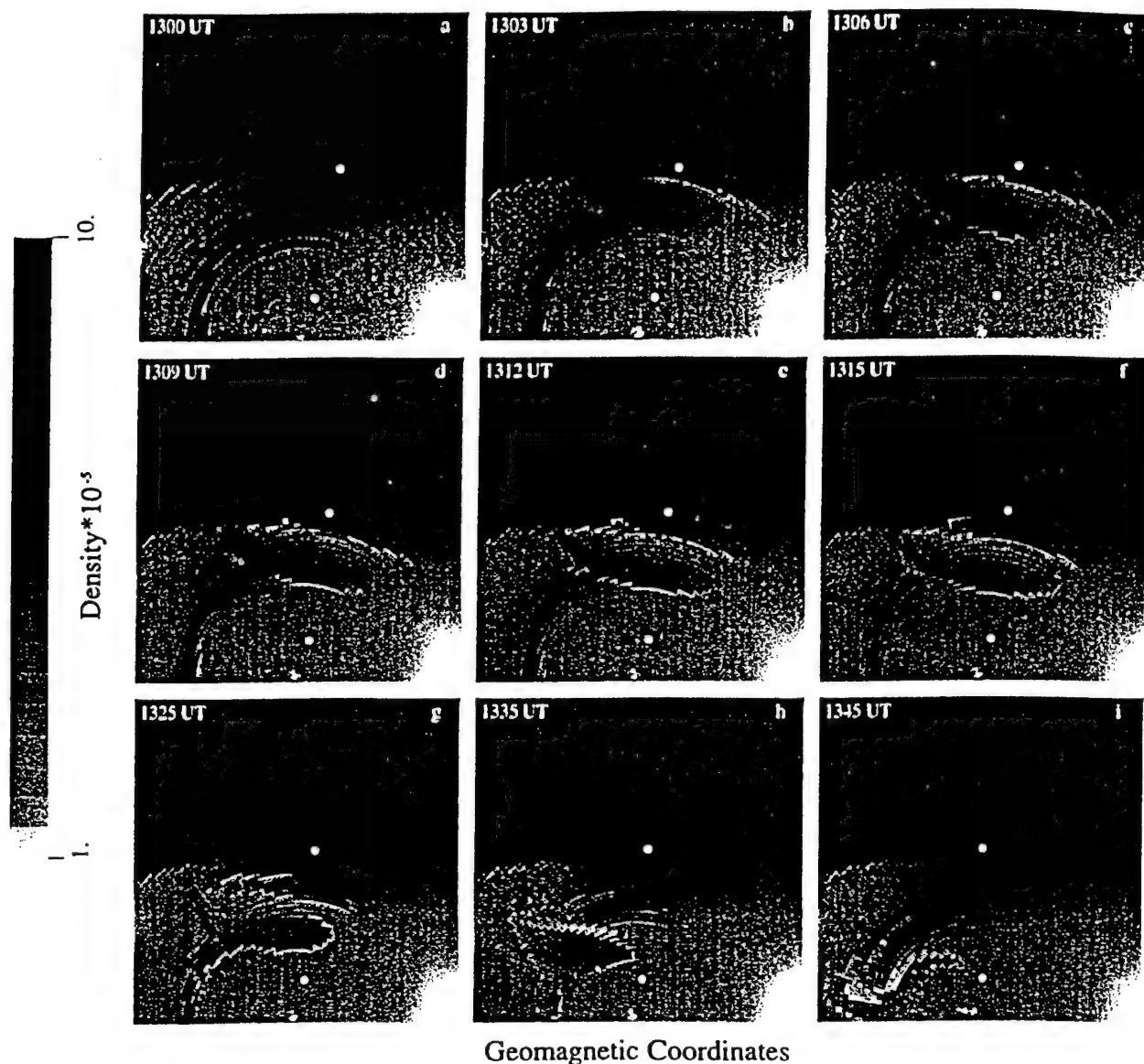


Figure 7. Same as Figure 3 but for the Heppner-Maynard convection pattern (section 3.3)

as low as  $10^5 \text{ cm}^{-3}$ . It also demonstrates that the patch moves toward the pole and subsequently breaks from the TOI. When the patch is circulating across the polar cap, the peak density inside the patch is  $8 \times 10^5 \text{ cm}^{-3}$ , a value much higher than the typical  $1\text{--}2 \times 10^5 \text{ cm}^{-3}$  seen in the polar cap and outside the TOI. Figures 8e and 8f show a more pronounced depletion between the density structures as compared to the Heelis/traveling vortices scenario. When compared to the experimental values of Figure 2c, we notice that several features are well

reproduced. The altitude extension of both structures are very similar.  $N_e = 7 \times 10^5 \text{ cm}^{-3}$  at 700 km is observed in both experimental and modeled data. The region of depleted density is wider than in the previous case. The poleward motion of the structures also resembles more closely the movement of the structures seen in the experimental data. The Heppner-Maynard pattern successfully produced a density structure with all the characteristics of a polar cap patch. In contrast to the Heelis convection pattern, it creates a single structure

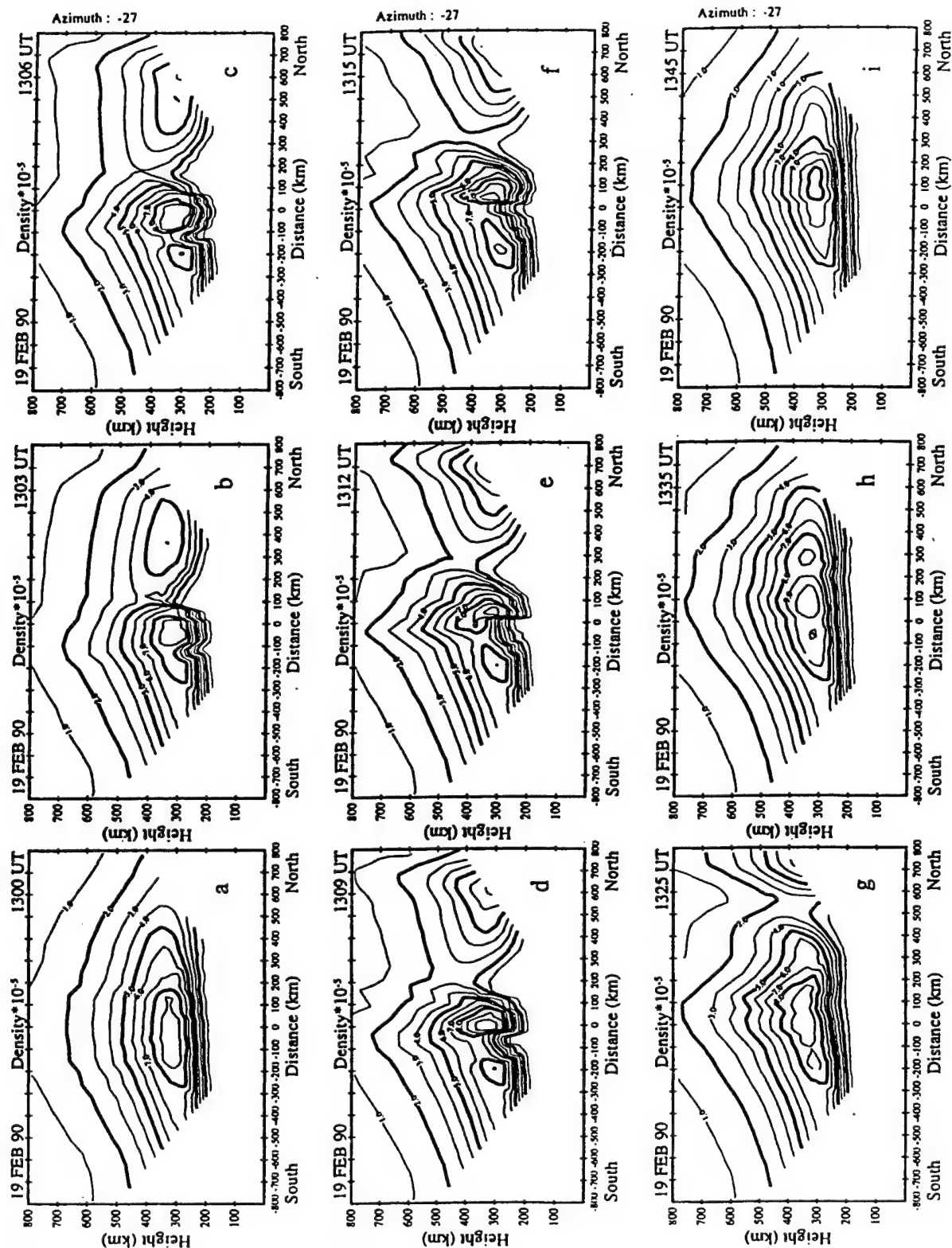


Figure 8. Same as Figure 4 but for the Heppner-Maynard convection pattern (section 3.3).

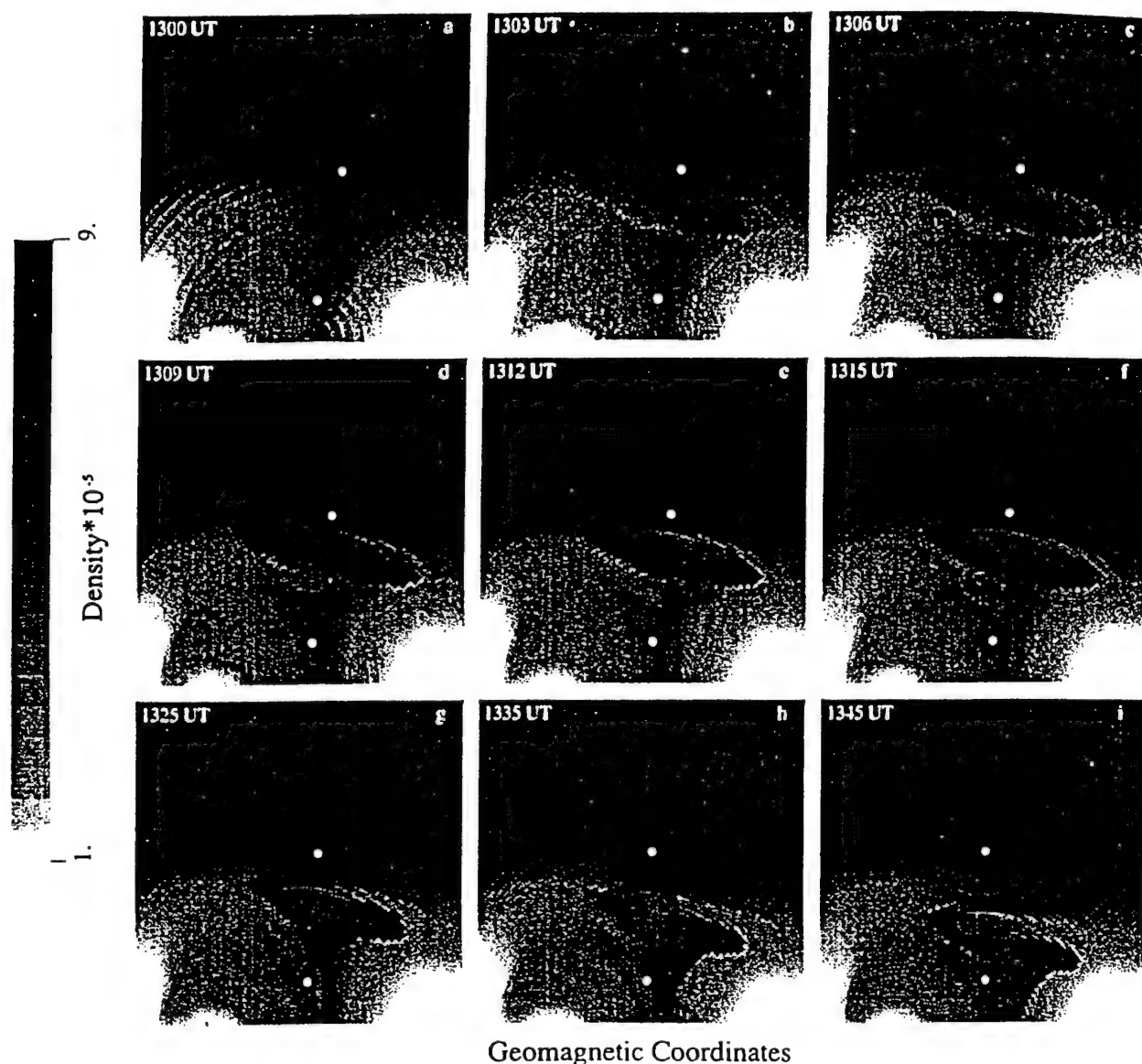


Figure 9. Same as Figure 3 but after eliminating the dependence of the ion temperature on the magnetospheric electric field (section 3.4)

#### 3.4. Assessment of the Temperature Effect on Patch Formation

The fourth case study was performed to quantify the importance of the  $O^+$  recombination rate in producing channels of low density. The results of this study are presented in Figure 9. In this series of simulations, we returned to the Heelis/traveling vortices scenario except we turned off the dependence of  $T_i$  on the magnetospheric electric field and hence turned off any enhanced  $O^+$  loss

rates. The goal in this investigation was to determine quantitatively how much plasma depletion is attributed to erosion by enhancements of the  $O^+$  loss rate and what percentage of the plasma depletion is carried from earlier local times by the vortex flow. Evidently, an eastward flow is needed in order to transport the less dense morning side plasma into the afternoon region. A flow of this type exists at the common region between the vortices.



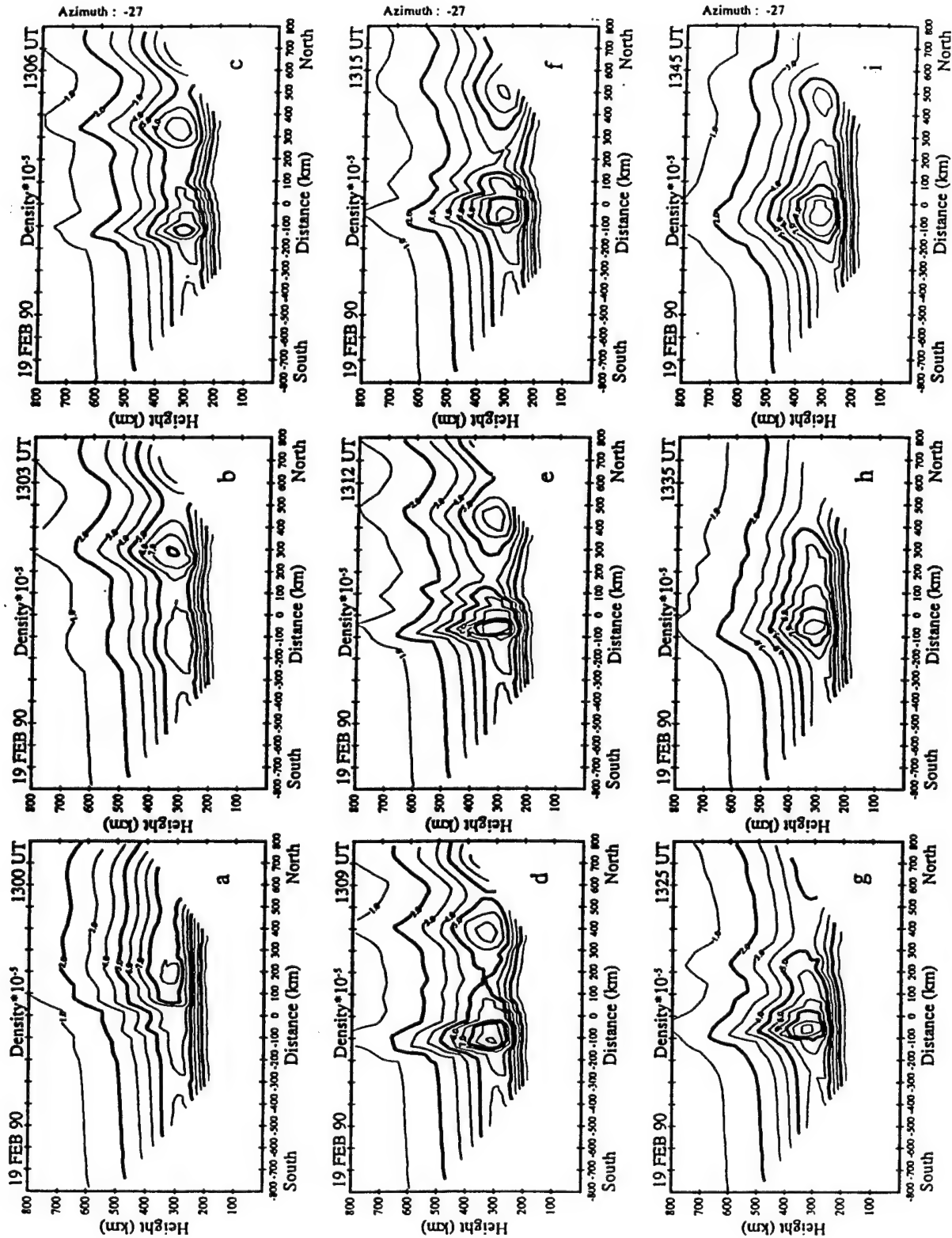


Figure 10. Same as Figure 4 but after eliminating the Ti dependence on the magnetospheric electric field.

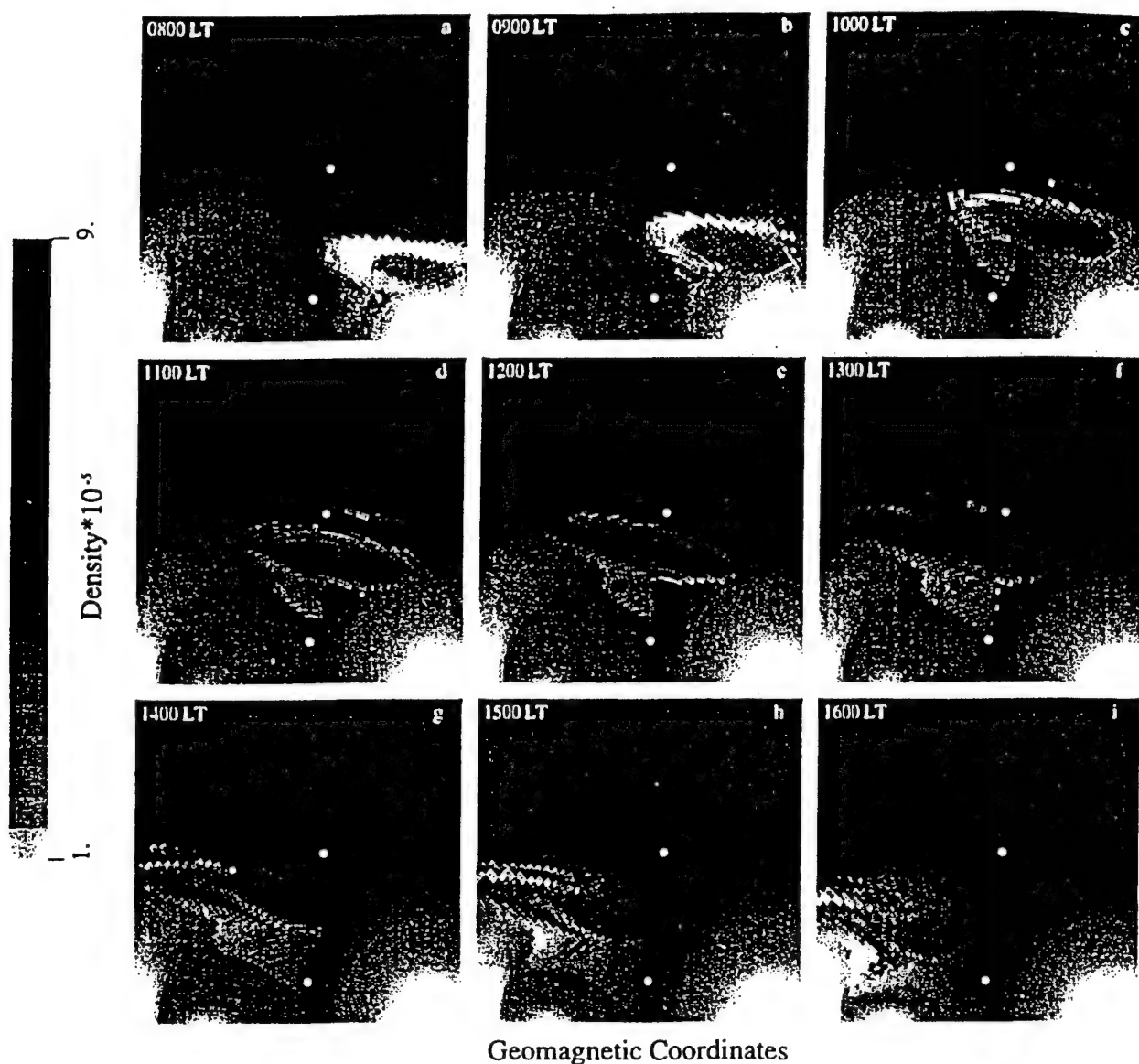


Figure 11. Same as Figure 3, but for nine different initial locations of the traveling vortices

A comparison of Figures 9 and 5 indicates some resemblance between both figures. The structuring is also initiated with a rotation of the TOI toward a dawn-dusk alignment. Plasma from the early morning side also intrudes equatorward of the northern patch. However, there are also some prominent differences. We did not find a full separation between the  $N_i$  structure and the auroral oval, even 15 min into the simulation. There is a channel containing plasma density equal to  $4 \times 10^5 \text{ cm}^{-3}$  in the afternoon side of the structure. The southern  $N_i$

structure is absent, because at this latitude the southern vortex can only bring more dense plasma from the afternoon sector. Figure 10f indicates that the deepest depletion achieved in this simulation is  $4 \times 10^5 \text{ cm}^{-3}$ , while the minimum density value during the full-blown simulation was  $10^5 \text{ cm}^{-3}$  in Figure 5. Considering that the original density was  $9 \times 10^5 \text{ cm}^{-3}$ , then 62% of the depletion is due to convection of low-density plasma and 38% is due to erosion by the temperature-dependent loss rate.



#### 4. Traveling Vortices at Different Local Times

In the previous section, we were concerned with the formation of patches under different patterns of global convection. In this section, we search for the preferred local time at which the vortices are more likely to generate polar cap patches.

Traveling vortices have been observed at a large variety of different local times [Friis-Christensen *et al.*, 1988; Heikkila *et al.*, 1989] using radar and magnetometer data. They have also been predicted on theoretical grounds [Newell and Sibeck, 1993]. They postulated an association between the presence of twin vortices and changes in the high-latitude convection patterns due to pressure pulses in the magnetosphere. In order for the vortices to produce patches, evidently, they have to develop near the TOI and have a lifetime long enough to erode a sector of the TOI. We have carried out eight additional simulations placing the vortices at different local times. The local times that were used varied from 0800 to 1600 LT. The results of this study are compiled in Figure 11. This figure compares  $N_m F_2$  values obtained 15 min along the simulations (at 1315 UT) for the eight new cases and the simulation described in section 3.2. The number on the upper left corner indicates the local times at which the vortices were located at the beginning of the simulation. Only the vortices located at 1000 LT, 1100 LT and 1200 LT (Figures 11c, 11d and 11e) produce distinct patches. Vortices at 0800 LT and 0900 LT (Figures 11a and 11b) only distort the TOI and create isolated regions of low density ( $2 \times 10^5 \text{ cm}^{-3}$ ) plasma. When these structures circulate within the polar cap, they will consist of plasma equally dense to the polar cap plasma. When the vortices were located at 1300 LT (Figure 11f), we obtained dawn-dusk elongated density traces. No detachment from the auroral oval densities was observed. The last three modeling efforts in this subsection were performed using vortices located at 1400 LT, 1500 LT and 1600 LT (Figures 11g-11i). These figures depict the formation of some kind of structuring in the afternoon cell. These structures are connected to the auroral oval and will not penetrate into the polar cap. In fact, we followed all these case simulations for another 30 min and found the structures continuously elongating in the dawn-dusk direction. These structures could certainly appear as isolated structures to digisondes or to low-orbiting satellites, but an all-sky camera properly located could possibly indicate the connection of these structures to the auroral plasma.

#### 5. Discussion and Conclusions

Several researchers have indicated that the TOI is present at longitudes near Sondrestrom when this high-latitude station is near noon [Foster and Doupnik, 1984; Kelly and Vickrey, 1984]. Our simulation during undisturbed conditions has also demonstrated that the TOI is a prominent feature at Sondrestrom when we select a typical  $B_z$  south convection pattern. The mechanism described here requires the existence of an elongated TOI as the basic ingredient to form a patch. It also needs a large plasma jet occurring near and across the TOI. The large plasma velocity will create a region of enhanced  $T_e$ , consequently increase the  $O^+$  recombination rate and then erode the local plasma. We found also that low-density plasma can be brought in by the vortex flow from earlier local times. This patch formation mechanism will create, in this way, sections of depleted and enhanced densities across the TOI.

The elevation scans conducted across our simulated volume demonstrated that the TOI or other structures in the polar cap could be wrongly interpreted as isolated entities (say patches). In reality, they may be connected to the auroral/subauroral plasma. We conclude that it is necessary to conduct antenna azimuthal scans or to use an all-sky camera to properly identify a polar cap patch.

Sojka *et al.* [1993, 1994] have used a scheme of continuous changes of the  $B_y$  component of the IMF to redirect the TOI toward the dawn or dusk sides of the polar cap. In this study, we have employed the appearance of vortices in the polar cap and their subsequent motion across the polar cap to produce polar cap patches. No repetitive changes in any of the components of the IMF were required. The proposed mechanism only needs the existence of vortices moving with the background plasma. Moreover, it was found that the convecting vortices scenario was the most favorable situation to form disconnected plasma structures inside the polar cap.

The modeled densities of Figures 6 and 8 indicated a good qualitative agreement with the data measured by the Sondrestrom ISR. The discrepancies between measured and modeled densities can be understood in terms of the initial inputs that were used in the simulations and a few of the limitations of the GTIM model. The much smaller density, seen in the depleted density region of Figure 2c, can be attributed to a much smaller density in the morning cell from where the vortices grab the low-density plasma. In fact, the Sondrestrom ISR detected values near  $2 \times 10^5 \text{ cm}^{-3}$  at 1100 UT (2 hours before the

measurements reported here) that if unchanged could explain this discrepancy. The radar also measured densities above  $10^3 \text{ cm}^{-3}$  at 200 km altitude; no similar feature was reported in the simulations because of the lack of molecular ions in our simulations. The GTIM model is at the present time essentially a one-ion ( $\text{O}^+$ ) model. Simulations were performed with and without particle precipitation in the auroral oval, and essentially no differences were seen in the  $F$  region. The effects of particle precipitation associated with the vortex located more equatorward where convergent electric fields existed were not included and neither were the effects of soft precipitation that can occur in the cusp/cleft and polar cap. These issues will be topics for future work.

We found that 62% of the density depletion was due to plasma being carried from earlier local times. This fact argues in favor of the ability of smaller potentials associated with the vortices to also create regions of depleted density. However, the vortex potential cannot be too small, otherwise the vortex velocity will also be small, and the time to transport low-density plasma from the morning cell will be considerably longer.

From this study we found the following:

1. Polar cap patches can be generated by traveling vortices independent of the convection pattern being used. We have used a Heelis-type and a Heppner-Maynard-type convection pattern for  $B_y$  positive and for  $B_y$  negative, respectively. An essential condition for forming well-separated patches was to allow the vortices to travel with the background global convection.
2. Enhanced recombination of  $\text{O}^+$  contributes to the creation of a channel of low density. Equally important is the transport of low-density plasma from earlier local times. For the size and potential of the vortices that we used 38% of the depletion was attributed to the  $\text{O}^+$  recombination loss and 62% to transport.
3. There is a preferential local time at which the vortices can generate patches. We found that this local time sector is restricted to between 1000 LT and 1200 LT.
4. The simulation presented here qualitatively agrees with the data collected at Sondrestrom on February 19, 1990 [Valladares et al., 1994b]; both exhibit the same salient features.
5. Our modeling described here postulates that the polar cap patches will intrinsically have the shape of the vortices. Circular vortices will reproduce more circular patches. Elliptical vortices, as presented here, will generate the elongated cigar-shaped patches that have been found in the polar cap [Fukui et al., 1994].

**Acknowledgments.** We would like to thank Ed Weber and Santimay Basu for useful discussions. The work at Boston College was partially supported by Phillips Laboratory contracts F19628-90-K-0007 and F19628-88-K-0008 and by NSF grant ATM-9404088. We thank the Danish Commission for Scientific Research in Greenland for permission to conduct ground experiments at Sondrestrom under continuing project A16-91.

## References

- Anderson, D.N., Daily variation of the ionospheric F2 equatorial anomaly in the American and Asian sectors, cooperative thesis, 24 pp. 1-144, Natl. Cent. Atmos. Res., Boulder, Colo., 1971.
- Anderson, D.N., A theoretical study of the ionospheric F region equatorial anomaly, I, theory, *Planet. Space Sci.*, **21**, 409, 1973.
- Anderson, D.N., J. Buchau, and R.A. Heelis, Origin of density enhancements in the winter polar cap, *Radio Sci.*, **23**, 513, 1988.
- Anderson, D.N., D.T. Decker and C.E. Valladares, Modeling boundary blobs using time varying convection, *Geophys. Res. Lett.*, in press, 1996.
- Basu, Su., S. Basu, E. MacKenzie, and H.E. Whitney, Morphology of phase and intensity scintillations in the auroral oval and polar cap, *Radio Sci.*, **20**, 347, 1985.
- Basu, S., Su. Basu, C.E. Valladares, E.J. Weber, J. Buchau, G.J. Bishop, and B.W. Reinisch, Coordinated observations of high latitude ionospheric turbulence, *Physics of Space Plasma (1988)*, SPI Conf. Proc. Reprint Ser., **8**, 137, 1989.
- Buchau, J., B.W. Reinisch, E.J. Weber, and J.G. Moore, Structure and dynamics of the winter polar cap  $F$  region, *Radio Sci.*, **18**, 995, 1983.
- Buchau, J., E.J. Weber, D.N. Anderson, H.C. Carlson Jr., J.G. Moore, B.W. Reinisch, and R.C. Livingston, Ionospheric structures in the polar cap: their origin and relation to 250-MHz scintillation, *Radio Sci.*, **20**, 325, 1985.
- Carlson, H.C., V.B. Wickwar, E.J. Weber, J. Buchau, J.G. Moore, and W. Whiting, Plasma characteristics of polar cap  $F$  layer arcs, *Geophys. Res. Lett.*, **11**, 895, 1984.
- Cowley, S.W.H., M.P. Freeman, M. Lockwood, and M.F. Smith, The ionospheric signature of flux transfer events, in *CLUSTER - Dayside Polar Cusp*, Eur. Space Agency Spec. Publ. ESA SP-330, 105-112, 1991.
- Crain, D.J., J.J. Sojka, R.W. Schunk, P.H. Doherty and J.A. Klobuchar, A first-principle derivation of the high-latitude total electron content distribution, *Radio Sci.*, **28**, 49, 1993.
- Decker, D.T., C.E. Valladares, R. Sheehan, Su. Basu, D.N. Anderson, and R.A. Heelis, Modeling daytime  $F$  layer patches over Sondrestrom, *Radio Sci.*, **29**, 249, 1994.
- de la Beaujardiere, O., J.D. Craven, V.B. Wickwar, G. Candal, J.M. Holt, L.A. Frank, L.H. Brace, D.S. Evans, and J.D. Winningham, Universal time dependence of nighttime  $F$  region densities at high latitudes, *J. Geophys. Res.*, **90**, 4319, 1985.

- Foster, J.C., and J.R. Doupnik, Plasma convection in the vicinity of the dayside cleft, *J. Geophys. Res.*, **89**, 9107, 1984.
- Friis-Christensen, E., M.A. McHenry, C.R. Clauer, and S. Vennerstrom, Ionospheric traveling convection vortices observed near the polar cleft: A triggered response to sudden changes in the solar wind, *Geophys. Res. Lett.*, **15**, 253, 1988.
- Fukui, K., J. Buchau, and C.E. Valladares, Convection of polar cap patches observed at Qaanaaq, Greenland during the winter of 1989-1990, *Radio Sci.*, **29**, 231, 1994.
- Goertz, C.K., E. Nielsen, A. Korth, K.-H. Glassmeier, C. Haldoupis, P. Hoeg, and D. Hayward, Observations of a possible ground signature of flux transfer events, *J. Geophys. Res.*, **90**, 4069, 1985.
- Hedin, A.E., MSIS-86 thermospheric model, *J. Geophys. Res.*, **92**, 4649, 1987.
- Hedin, A.E., et al., Revised global model of thermosphere winds using satellite and Ground-based observations, *J. Geophys. Res.*, **96**, 7657, 1991.
- Heikkila, W.J., T.S. Jorgensen, L.J. Lanzerotti, and C.G. MacLennan, A transient auroral event on the dayside, *J. Geophys. Res.*, **94**, 15291, 1989.
- Kelly, J.D., and J.F. Vickrey, *F* region ionospheric structure associated with antisunward flow near the dayside cusp, *Geophys. Res. Lett.*, **11**, 907, 1984.
- Lockwood, M., and H.C. Carlson, Production of polar cap density patches by transient magnetopause reconnection, *Geophys. Res. Lett.*, **19**, 1731, 1992.
- Ma, Z.-W., J.G. Hawkins, and L.-C. Lee, A simulation study of impulsive penetration of solar wind irregularities into the magnetosphere at the dayside magnetopause, *J. Geophys. Res.*, **96**, 15751, 1991.
- Newell, P.T., and D.G. Sibeck, *B<sub>y</sub>* fluctuations in the magnetosheath and azimuthal flow velocity transients in the dayside ionosphere, *Geophys. Res. Lett.*, **20**, 1719, 1993.
- Rodger, A.S., M. Pinnock, J.R. Dudeney, K.B. Baker, and R.A. Greenwald, A new mechanism for polar patch formation, *J. Geophys. Res.*, **99**, 6425, 1994.
- Schunk, R.W., and J.J. Sojka, A theoretical study of the lifetime and transport of large ionospheric density structures, *J. Geophys. Res.*, **92**, 12343, 1987.
- Schunk, R.W., W.J. Raitt, and P.M. Banks, Effect of electric fields on the daytime high-latitude *E* and *F* regions, *J. Geophys. Res.*, **80**, 3121, 1975.
- Sojka, J.J., and R.W. Schunk, A theoretical study of the production and decay of localized electron density enhancements in the polar ionosphere, *J. Geophys. Res.*, **91**, 3245, 1986.
- Sojka, J.J., and R.W. Schunk, A model study of how electric field structures affect the polar cap *F* region, *J. Geophys. Res.*, **93**, 884, 1988.
- Sojka, J.J., M.D. Bowline, R.W. Schunk, D.T. Decker, C.E. Valladares, R. Sheehan, D.N. Anderson, and R.A. Heelis, Modeling polar cap *F* region patches using time-varying convection, *Geophys. Res. Lett.*, **20**, 1783, 1993.
- Sojka, J.J., M.D. Bowline, and R.W. Schunk, Patches in the polar ionosphere: UT and seasonal dependence, *J. Geophys. Res.*, **99**, 14959, 1994.
- Tsunoda, R.T., High-latitude *F* region irregularities: a review and synthesis, *Rev. Geophys.*, **26**, 719, 1988.
- Valladares, C.E., H.C. Carlson Jr., and K. Fukui, Interplanetary magnetic field dependency of stable sun-aligned polar cap arcs, *J. Geophys. Res.*, **99**, 6247, 1994a.
- Valladares, C.E., Su. Basu, J. Buchau, and E. Friis-Christensen, Experimental evidence for the formation and entry of patches into the polar cap, *Radio Sci.*, **29**, 167, 1994b.
- Weber, E.J., J. Buchau, J.G. Moore, J.R. Sharber, R.C. Livingston, J.D. Winningham, and B.W. Reinisch, *F* layer ionization patches in the polar cap, *J. Geophys. Res.*, **89**, 1683, 1984.
- Weber, E.J., J.A. Klobuchar, J. Buchau, H.C. Carlson, Jr., R.C. Livingston O. de la Beaujardiere, M. McCready, J.G. Moore, and G.J. Bishop, Polar cap *F* layer patches: structure and dynamics, *J. Geophys. Res.*, **91**, 121, 1986.

D.N. Anderson, Phillips Laboratory, Geophysics Directorate (GPIM), 29 Randolph Rd., Hanscom AFB, MA 01730-3010. (e-mail: danderson@plh.af.mil)

D.T. Decker, R. Sheehan, and C.E. Valladares, Institute for Scientific Research, Boston College, 885 Centre St., Newton, MA 02159. (e-mail: decker@plh.af.mil; sheehan@plh.af.mil; cesar@dlws7.bc.edu)

(Received August 8, 1995; revised February 8, 1996; accepted February 14, 1996.)

# Collisional degradation of the proton-H atom fluxes in the atmosphere: A comparison of theoretical techniques

Dwight T. Decker,<sup>1</sup> Boris V. Kozelov,<sup>2</sup> B. Basu,<sup>3</sup> J. R. Jasperse,<sup>3</sup>  
and V. E. Ivanov<sup>2</sup>

**Abstract.** Three methods for calculating the transport of energetic protons and hydrogen atoms within the Earth's atmosphere are compared. The methods are (1) a Monte Carlo (MC) simulation, (2) a discrete energy loss solution to the linear transport equations, and (3) a continuous slowing-down approximation (CSDA). In the calculations performed, all three models use the same cross sections, three-component ( $N_2$ ,  $O_2$ ,  $O$ ) neutral atmosphere, and incident isotropic Maxwellian proton fluxes of various characteristic energies (1–20 keV). To ensure that all three methods include the same physical processes, the effects of magnetic mirroring and the lateral spreading of particles are "turned off" in the MC simulations as these processes are not included in the present linear transport or CSDA models. A variety of quantities are calculated and compared including energy deposition rates, eV/ion pair, hemispherically averaged differential fluxes of protons and H atoms, energy integrated differential fluxes, and total proton and H atom fluxes. The agreement between all three models is excellent except at the lowest altitudes. Apart from these altitudes, the differences that do exist are small compared to the errors that generally result from poorly known inputs and compared to the typical errors quoted for geophysical observations. The altitudes where the results do differ significantly are where the proton and H atom fluxes are severely attenuated and are below the altitudes where the bulk of the energy deposition and ionization takes place. The success of these comparisons suggests that our ability to model actual observations is presently limited by uncertainties in cross sections and the lack of suitable observations rather than our ability to solve the equations that describe the known physics of proton-H atom transport.

## 1. Introduction

It is well established that an essentially permanent feature of the Earth's high-latitude atmosphere is the presence of auroral particle fluxes. It is also well known that these precipitating fluxes from the magnetosphere consist of mostly electrons and protons with a small admixture of other ions. Early ground-based optical observations [Romick and Elvey, 1958; Galperin, 1959] indicated that electron and proton aurora could have separate latitudinal distributions. Later satellite observations of the precipitating particles established that statistically the electron and protons precipitate within

two ovals that are not colocated [Sharber, 1981; Hardy *et al.*, 1989]. Further, an examination of the Hardy statistical models [Hardy *et al.*, 1987, 1991] reveals that in the afternoon and evening sectors the ions at the lower auroral latitudes can carry a significant portion of the incoming energy flux. Thus, in order to study the dissipation of auroral energy within the Earth's atmosphere, it is necessary to study not just the transport and collisional degradation of energetic electrons but also those of protons.

The transport of energetic protons within matter is a problem that has been studied for a variety of physical situations. In the case of transport of auroral protons within the atmosphere there are several features that add to the difficulty of the problem. Some of those features are (1) auroral proton energies can be less than the energy of the maximum of the ionization cross section, (2) there is a large gradient of the atmospheric density with respect to altitude, and (3) the Earth's magnetic field is present. The first feature requires detailed knowledge of cross sections since simple estimations (Born approximation) of cross sections are not valid. Further, at auroral energies the charge chang-

<sup>1</sup>Institute for Scientific Research, Boston College, Newton, Massachusetts.

<sup>2</sup>Polar Geophysical Institute, Apatity, Russia.

<sup>3</sup>Phillips Laboratory, Hanscom Air Force Base, Massachusetts.

ing processes have to be included and this introduces energetic hydrogen (H) atoms into the problem. The effect of the large gradient in the atmosphere is to create a strong altitude dependence in the mean free path of the protons and H atoms. Hence the behavior of the particle flux is highly dependent on altitude. The presence of the Earth's magnetic field acts to cause the protons to follow field lines into the ionosphere. However, the H atoms are not constrained by the magnetic field. This coupled with the altitude-dependent mean-free path results in a lateral spreading of the p-H flux at high altitudes but essentially no spreading at low altitudes. Finally, a feature that can be a useful simplification in any modeling is that all the collision processes involving protons and H atoms are strongly peaked in the forward direction. However, at very low energies ( $E < 1$  keV) energy loss due to elastic collisions does become significant.

There have been several treatments of p-H transport that have appeared in the literature. They can be generally categorized as range theoretic, continuous slowing down, linear transport theoretic, and Monte Carlo. The range theoretic method is based on laboratory measurements of range energy relations for protons in air or its theoretical approximations and has been used in the works of *Eather and Burrows* [1966], *Eather* [1967, 1970], *Isaev and Pudovkin* [1972], *Henriksen* [1979], and *Rees* [1982]. The continuous slowing-down approximation (CSDA) uses more detailed information about scattering processes and was used for the auroral proton problem by *Edgar et al.* [1973, 1975]. Work on analytic estimations of lateral spreading of p-H flux [*Johnstone*, 1972; *Iglesias and Vondrak*, 1974] also can be classified as using the CSDA.

In more recent years, linear transport (LT) theory has been used to solve for the auroral proton and H atom fluxes. In the work of *Jasperse and Basu* [1982] the coupled transport equations based on the Boltzmann equation were solved analytically, and in a follow-up paper [*Basu et al.*, 1987], theoretically calculated electron density profiles due to incident protons were found in good agreement with Chatanika radar data. This in turn was followed by the development of a fully numerical code for solving the linear transport equations [*Basu et al.*, 1990].

The Monte Carlo (MC) method has been applied to the auroral proton problem by *Davidson* [1965], *Ponomarev* [1976], *Galperin et al.* [1976], and *Kozelov and Ivanov* [1992]. Most recently, *Kozelov* [1993] has implemented the method using a full three species neutral atmosphere and the influence of the Earth's magnetic field. While computationally intensive the Monte Carlo method does have the advantage of including processes, such as beam spreading or mirroring, that are difficult to treat in the other approaches.

Assessing the validity of any approach usually involves either "back of the envelope" estimates of neglected processes, a posteriori calculations of those processes, comparisons to observations, or comparisons to alternative approaches. The difficulty in comparing approaches is that when comparing to results of other

authors there are often differences in cross sections, boundary conditions, and geophysical conditions that confuse the issue of comparing methods. MC and CSDA models with the same input parameters were compared by *Porter and Green* [1975], but the comparison was only for homogeneous molecular nitrogen, and the initial proton flux was taken as isotropic and monoenergetic with initial energy 1 keV. More extensive comparisons for a N<sub>2</sub> atmosphere were made by *Kozelov and Ivanov* [1992]. They considered initial energies from 1 keV to 1 MeV. For initial energies less than 10 keV, differences were found near the high-altitude boundary and at lowest altitudes of penetration.

The purpose of this paper is to compare three methods for calculating the transport and collisional degradation of energetic protons and H atoms in the Earth's ionosphere using identical cross sections, boundary conditions, and geophysical conditions. We will show that for several quantities the differences between the three methods are reasonably small compared to the model uncertainties that arise from uncertainties in the required inputs (cross sections, neutral densities, and boundary conditions) and the uncertainties in the available observations (particle fluxes, optical emissions, and ion densities). The three methods considered are the CSDA, LT, and MC. In section 2 we briefly describe the three models used. A more detailed discussion of the relationship between the CSDA and LT models is given in an appendix. After a discussion in section 3 concerning the physical processes and input parameters included in all three models, we present in section 4 the comparison of the various results from the models. The paper concludes with a discussion and summary in section 5.

## 2. Description of Theoretical Models

### 2.1. Continuous Slowing-Down Approximation

The continuous slowing-down approximation (CSDA) describes the degradation of the energetic particle's energy in terms of loss functions. For a monoenergetic monodirectional p-H flux the equation for energy loss is given by

$$\mu \frac{dE}{dz} = - \sum_{\alpha} n_{\alpha}(z) \times \frac{[L_{\alpha,P}(E)\Phi_P(z, E, \mu) + L_{\alpha,H}(E)\Phi_H(z, E, \mu)]}{\Phi_P(z, E, \mu) + \Phi_H(z, E, \mu)} \quad (1)$$

where  $\Phi$  values are the energetic particle fluxes,  $z$  is the altitude,  $\mu$  is cosine of the pitch angle, and  $n_{\alpha}(z)$  are the densities for neutral specie  $\alpha$ .  $L_{\alpha,P}(E)$  and  $L_{\alpha,H}(E)$  are the loss functions for the protons and H atoms due to collisions with neutral gases and are given by

$$L_{\alpha,P}(E) = \sum_j W_{\alpha,P}^j(E) \sigma_{\alpha,P}^j(E) \quad (2)$$

$$L_{\alpha,H}(E) = \sum_j W_{\alpha,H}^j(E) \sigma_{\alpha,H}^j(E) \quad (3)$$



where  $\sigma_{\alpha,p}^j(E)$  is the cross section for a type  $j$  collision between a proton and a neutral specie  $\alpha$  and  $W_{\alpha,p}^j(E)$  is the corresponding energy loss. Similarly,  $\sigma_{\alpha,H}^j(E)$  and  $W_{\alpha,H}^j(E)$  are the cross sections and the energy loss for collisions involving H atoms.

Usually, the loss function is defined for a charge state equilibrium flux [Porter and Green, 1975]. Here, in an implementation developed by one of us (B.V.K.), the loss function is defined using the nonequilibrium flux that describes the modification of the flux charge state composition. The nonequilibrium flux is calculated using the following equations:

$$\mu \frac{d\Phi_P(z, E, \mu)}{dz} = \Phi_H(z, E, \mu) \sum_{\alpha} n_{\alpha}(z) \sigma_{\alpha}^{01}(E) - \Phi_P(z, E, \mu) \sum_{\alpha} n_{\alpha}(z) \sigma_{\alpha}^{10}(E) \quad (4)$$

$$\frac{d\Phi_H(z, E, \mu)}{dz} = -\frac{d\Phi_P(z, E, \mu)}{dz} \quad (5)$$

where  $\sigma^{10}$  and  $\sigma^{01}$  are the total cross sections for charge exchange and stripping respectively. The calculational procedure consists of solving (1), (4), and (5) on a altitude, energy and pitch angle grid with the incoming flux at the high-altitude boundary being approximated by a set of monoenergetic monodirectional particle streams. A more detailed discussion of the CSDA can be found in the appendix.

## 2.2. Linear Transport Model

The fundamental feature of the linear transport (LT) model is the use of transport theoretic methods to solve two coupled Boltzmann equations for the proton and H atom differential fluxes. In solving these equations, we assume steady state conditions, no electric fields, a uniform geomagnetic field (no magnetic mirroring), and azimuthal symmetry about the geomagnetic field line. The collisional processes included are the various types of collisions between the energetic precipitating particles and the neutral constituents of the ionosphere. The protons and H atoms are coupled to each other by charge-changing collisions with neutrals (charge exchange and stripping). The two transport equations, discussions of the various collision processes, and the numerical methods for solving the equations can be found in the work of Basu *et al.* [1993] and will not be given here. A discussion of the relationship between the linear transport theory and the CSDA can be found in the appendix.

## 2.3. Monte Carlo Model

The Monte Carlo (MC) model uses a "collision-by-collision" algorithm which is based on simulating the individual trajectories of a large number of protons and H atoms. The "history" of each particle is represented as a series of collisions that are separated by segments of free streaming within a magnetic field. The selection of the path length between collisions and the collisional parameters is made by mapping into a random number  $\xi$  generated uniformly in the range 0-1.

The altitude of the particle after the  $(i+1)^{\text{st}}$  path length is determined from the formula

$$-\ln \xi = \int_{z_i}^{z_{i+1}} \frac{dz}{\mu} \sum_{\alpha} n_{\alpha}(z) \sigma_{\alpha,\beta}^{\text{tot}}(E_i), \quad (6)$$

where  $z_i$  is the altitude before the  $(i+1)^{\text{st}}$  path length,  $\sigma_{\alpha,\beta}^{\text{tot}}(E_i)$  is the total cross section of the particle in gas  $\alpha$ ,  $E_i$  is the particle's energy after the  $i$ th collision,  $\beta$  is the charge state of the particle (p or H). The neutral species with which the  $(i+1)^{\text{st}}$  collision occurred are determined by random sampling using the probabilities  $n_{\alpha}(z)/\sum_{\alpha} n_{\alpha}(z)$ , where  $\alpha$  is  $N_2$ ,  $O_2$ , or O. The type of collision is also selected by random sampling using probabilities  $\sigma^j(E_i)/\sigma^{\text{tot}}(E_i)$ , where  $j$  is the type of collision. When a collision occurs, the energy of the particle is decreased based on the type of collision used. In the case of charge exchange or stripping collisions the charge state of the particle is modified. To simulate an initial Maxwellian energy distribution at the high-altitude boundary, we divide the full energy range into 10-12 energy channels and place within each channel 8000 to 24,000 protons. The cosine of the initial pitch angle for each particle is determined from the expression  $\mu = \cos \theta = \sqrt{\xi}$ , where  $\xi$  is a random number generated uniformly in the range 0-1. During the simulation of a particle's trajectory its location is stored along with the various quantities needed for determining such quantities as the particle fluxes, energy deposition, and ionization rates. The results of the simulation are processed by statistical methods. If we have  $N$  realizations of a random variable  $x$ , then the average value is taken as  $\bar{x} = (1/N) \sum_{i=1}^N x_i$ . The statistical error  $\Delta x$  is estimated from expressions

$$\Delta x = C\sqrt{Dx}, \quad Dx \approx \frac{1}{N} \sum_{i=1}^N (x_i - \bar{x})^2,$$

where  $x$  is the random value,  $x_i$  is the  $i$ th realization of the value,  $Dx$  is the dispersion. If  $C \approx 1.4$ , then the probability that the value  $x \in [\bar{x} - \Delta x, \bar{x} + \Delta x]$  is equal to 0.7.

## 3. Inputs

In order to facilitate our comparison, we wanted to make the geophysical inputs, the microscopic parameters, and the physical processes included in the three models as identical as possible. Considering the physical processes, we find that all three models include the transport and degradation of protons and neutral hydrogen atoms as they collide with the neutral species of the ionosphere. On one hand, the CSDA and LT assume a uniform magnetic field (no mirroring) and a plane parallel geometry (no spreading), on the other hand the MC method can handle the effects of magnetic mirroring as well as lateral spreading of the energetic particles. For these comparisons, magnetic mirroring and lateral spreading were turned off in the MC calculations. Similarly, both CSDA and LT assume forward scattering,

while MC can include angular scattering. Again, we simplify the MC model and use the forward scattering approximation in all calculations for this paper.

By microscopic parameter we are referring to the various cross sections and energy losses that are needed by the models. The MC and CSDA use a more extensive set than is used by the LT model. While what cross sections are used can have serious impact when comparing to observations, the critical point here is to have all three models use the same set. We chose to use the simpler LT set as described by *Basu et al.* [1993]. The one exception is that for the average energy of the ejected electron in the stripping process we use the same expression as is used for the ionization process. This was done simply as a convenience for making the comparison between the three models.

Finally, let us turn to what we call the geophysical conditions, that is, the neutral atmosphere and the incoming particle flux. The neutral atmospheric densities ( $N_2$ ,  $O_2$ , and  $O$ ) and the neutral temperature as a function of altitude are obtained from the mass spectrometer/incoherent scatter (MSIS-86) neutral atmosphere model [*Hedin*, 1987]. The MSIS-86 parameters used were an  $F10.7$  and a 81-day averaged  $F10.7$  value of 150, a daily  $A_p$  of 20, a geographic latitude of  $65^\circ N$ , a longitude of  $35^\circ E$ , a local solar time of 24, and a date of December 16, 1993. All calculations have a boundary altitude at 700 km and an incident isotropic proton flux that has a Maxwellian energy distribution.

#### 4. Results

Calculations were made using the models for a range of Maxwellian characteristic energies (1–20 keV) and an incident energy flux of  $0.5 \text{ ergs cm}^{-2} \text{ s}^{-1}$ . The results in all cases were similar so we will present detailed comparisons for just one case: a characteristic energy of 8

keV and a minimum energy of 500 eV. In Figures 1a–1f, we show the hemispherically averaged differential flux for the protons and H atoms at several selected altitudes. In this and in the following figures, the CSDA results are given by the dotted curves, the LT by the dashed curves and the MC by either squares or error bars. The statistical error in the MC results is either indicated by the error bars or is smaller than the size of the square symbols used in the plots. At 550 km, 150 km below the boundary altitude, we see that the proton energy distributions from all three models are in excellent agreement. Likewise, the H atom plot shows excellent agreement, though the MC simulation is a bit "noisy" because of the lack of particles as the H atom flux builds up from a starting value of zero at the boundary. At 250 km (Figure 1b) the agreement remains excellent between all three models. While the shape of the spectra are little changed, the H atom flux has continued to increase at the expense of the proton flux. Descending further to 152 km (Figure 1c), we see that the low-energy part of the spectra have filled in as particles cascade down from higher energies. The MC shows a little more noise at the lowest energies, but the agreement remains fairly good between all models. Dropping to lower altitudes, the low-energy portion of the spectra continue to increase and with the three models still in reasonable agreement reach a maximum around 118 km (Figure 1d). Though we do see a clear separation between the CSDA and LT results at lower energies. At 110 km (Figure 1e), the magnitude of the spectra at all energies have decreased and the CSDA and LT continue to show a clear separation. Finally, just 4 km lower at 106 km (Figure 1f), the CSDA and LT are showing larger differences, and the error in the MC results have grown to the point that it is difficult to decide if it agrees more with the CSDA or the LT model.

Having considered the energy distribution of the par-

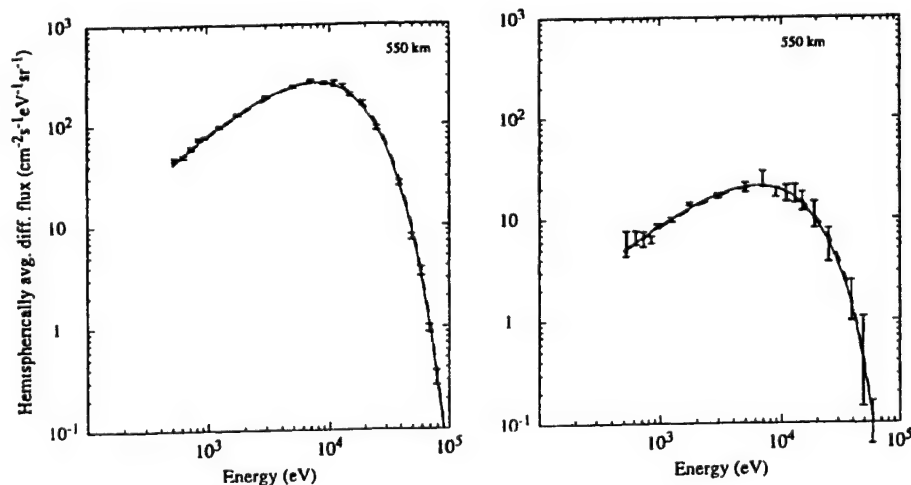


**Figure 1a.** Hemispherically averaged (left) proton and (right) hydrogen atom fluxes versus energy at an altitude of 550 km. The error bars are the Monte Carlo results, the long dashes are the linear transport results, and the dotted curves are the results from the continuous slowing-down approximation. The incident proton flux is a Maxwellian with a characteristic energy of 8 keV and a total incident energy flux of  $0.5 \text{ ergs cm}^{-2} \text{ s}^{-1}$ .

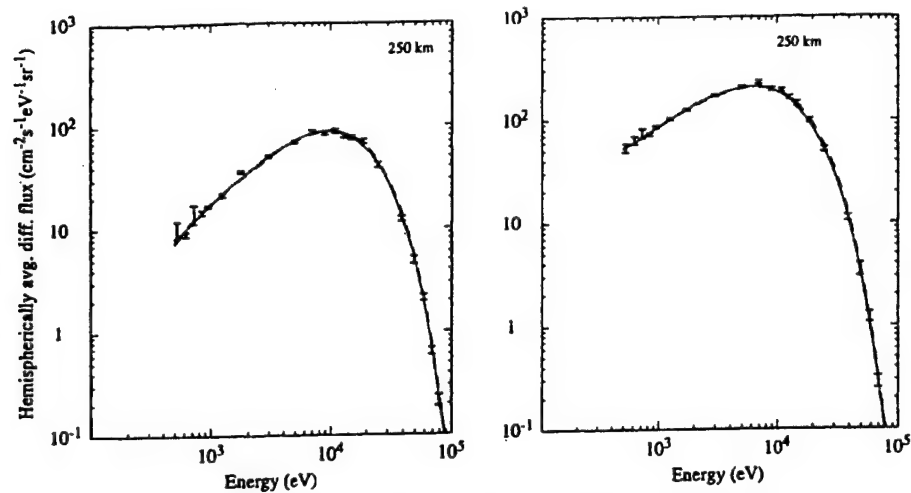


Figure 1b. Same as Figure 1a for an altitude of 250 km.

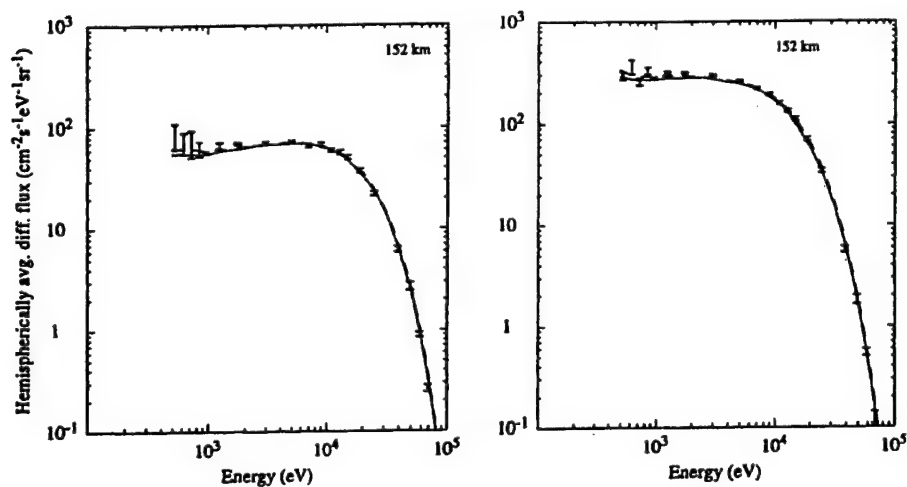


Figure 1c. Same as Figure 1a for an altitude of 152 km.

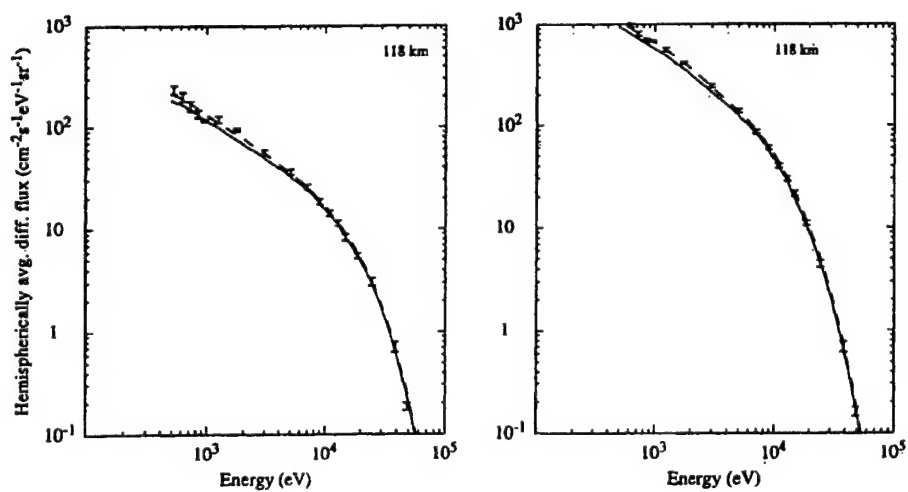


Figure 1d. Same as Figure 1a for an altitude of 118 km.



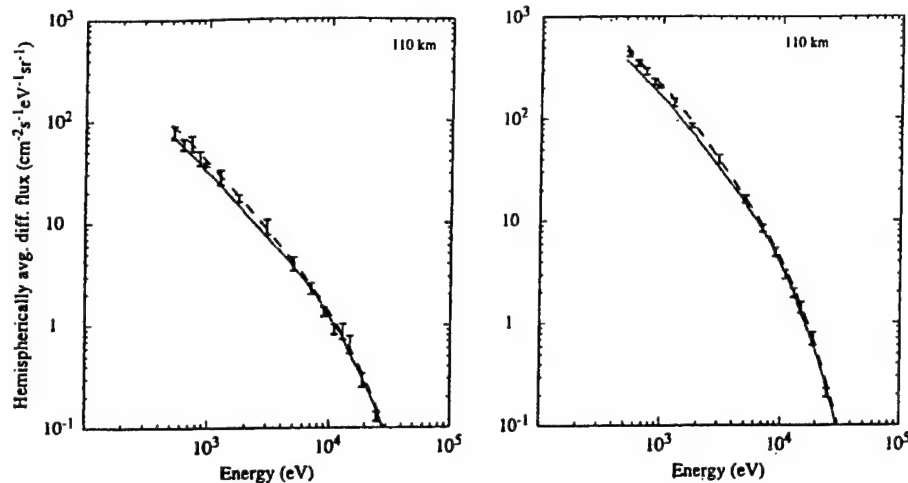


Figure 1e. Same as Figure 1a for an altitude of 110 km.

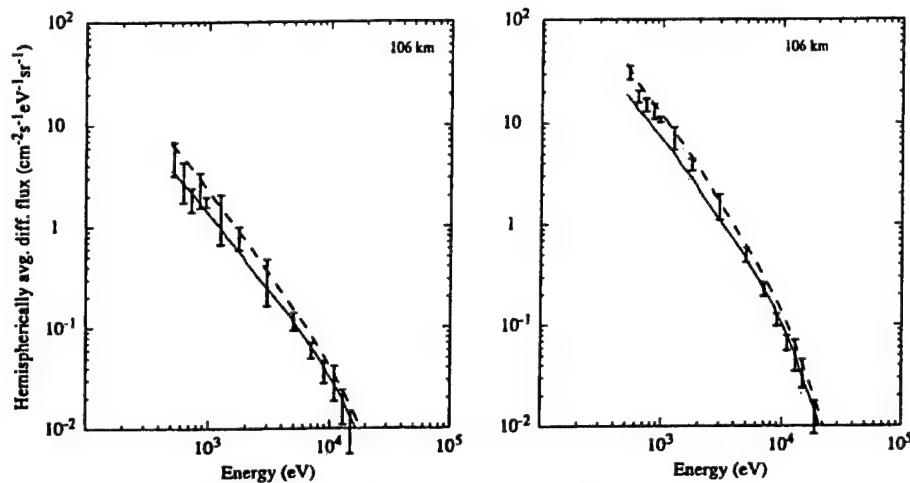
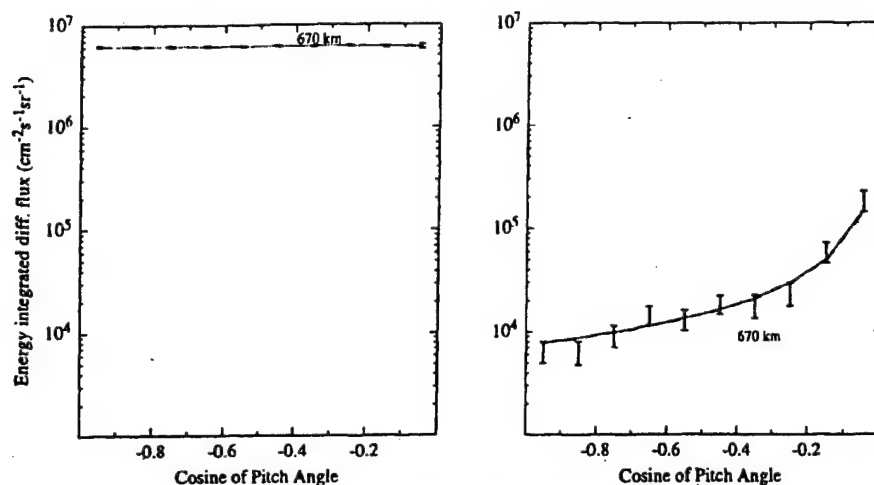


Figure 1f. Same as Figure 1a for an altitude of 106 km.

ticle fluxes averaged over pitch angle, let us now turn to plots (Figures 2a–2g) of the differential flux integrated over energy versus the cosine of the pitch angle. At 670 km (Figure 2a), we see an isotropic proton flux with all three models in excellent agreement and a much smaller H atom flux that has had only 30 km to build up from zero flux at the boundary. The H atom flux is largest near 90° pitch angle where the protons have undergone the greatest number of collisions. Figures 2b and 2c illustrate the buildup of the H atom flux at lower altitudes. At 550 km, we see the buildup is still largest at pitch angles near 90°, though by 250 km the pitch angle distributions for both protons and H atoms are isotropic. Through this range of altitudes the models have remained in excellent agreement. At 250 km the MC proton result is low compared to the CSDA and LT for the pitch angle nearest to 90° (cosine = -0.05). This difference is apparently from a slight numerical oscillation in the altitude dependence of the MC results for this particular pitch angle. Down at 152 km (Figure

2d), the fluxes remain isotropic and the models remain in good agreement except near 90° where significant fall off of the flux is observed. The CSDA shows the largest decrease followed by the LT and then the MC results. By 118 km (Figure 2e), the results at pitch angles closer to 90° are showing large decreases in the fluxes as well as some separation between the models. On the other hand, nearer to 180°, the fluxes are still large and all three models remain in good agreement. As was seen earlier, when there is a significant reduction in the flux, it is the CSDA which shows the greatest decrease. At any particular pitch angle, the LT and MC models remain in reasonable agreement until the flux has decreased about 3 orders of magnitude from what it was at higher altitudes. At 110 km (Figure 2f), some separation between models is occurring at all pitch angles and by 106 km (Figure 2g) both the CSDA and MC results are clearly falling below those of the LT model.

In Figures 3a and 3b, we show the energy integrated differential flux at one pitch angle (cosine = -0.95) as



**Figure 2a.** The differential flux integrated over energy versus the cosine of the pitch angle for (left) protons and (right) hydrogen atoms at an altitude of 670 km. The error bars are the Monte Carlo results, the long dashes are the linear transport results, and the dotted curves are the results from the continuous slowing-down approximation. The incident proton flux is a Maxwellian with a characteristic energy of 8 keV and a total incident energy flux of  $0.5 \text{ ergs cm}^{-2}\text{s}^{-1}$ .

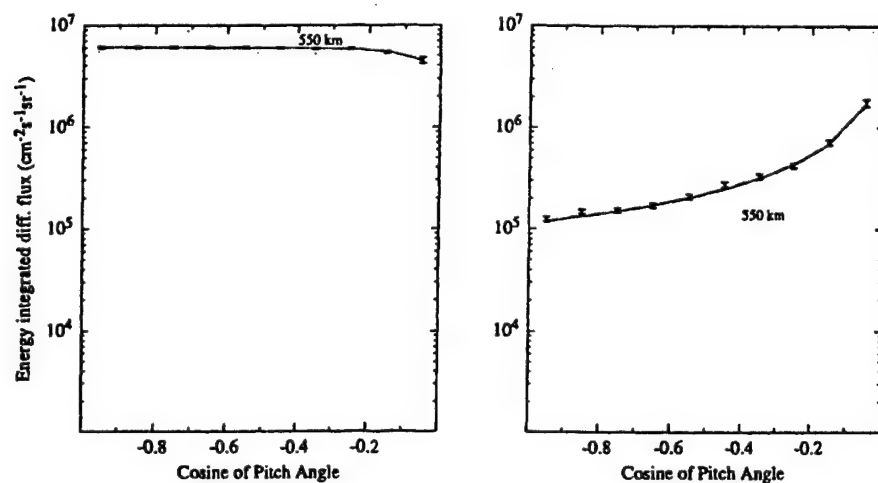


**Figure 2b.** Same as Figure 2a for an altitude of 550 km.

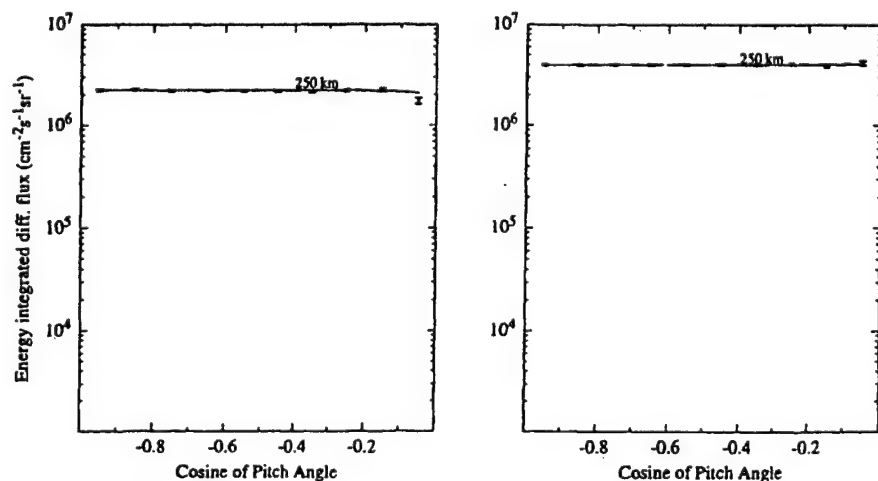


**Figure 2c.** Same as Figure 2a for an altitude of 250 km.

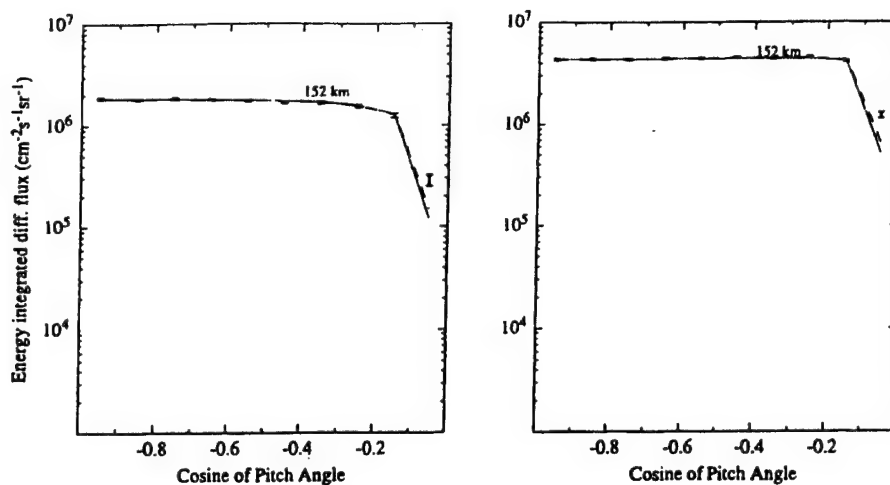


Figure 2d. Same as Figure 2a for an altitude of 152 km.

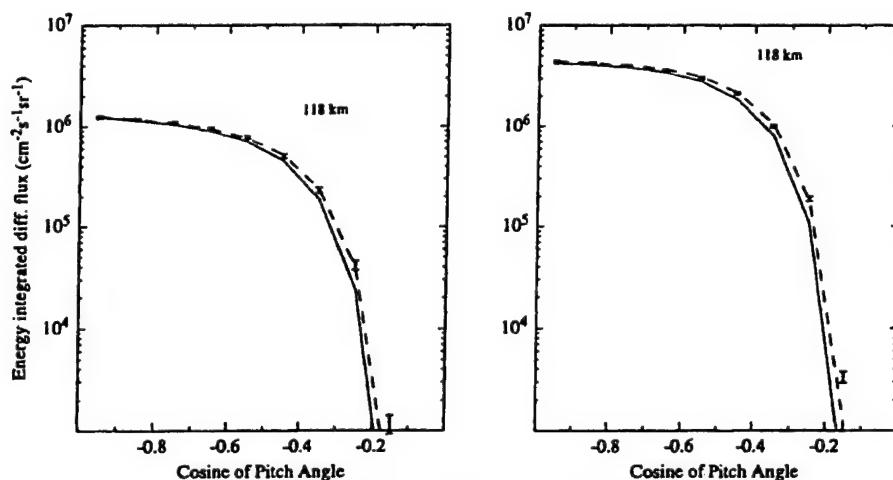


Figure 2e. Same as Figure 2a for an altitude of 118 km.

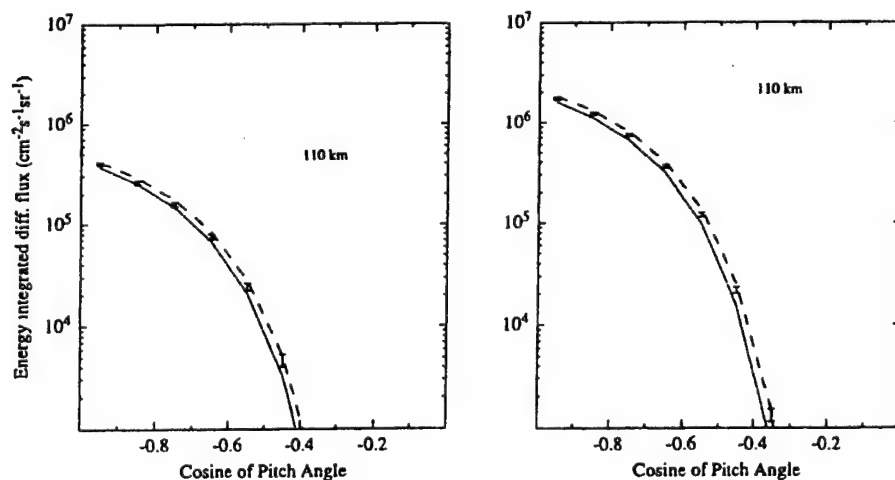


Figure 2f. Same as Figure 2a for an altitude of 110 km.

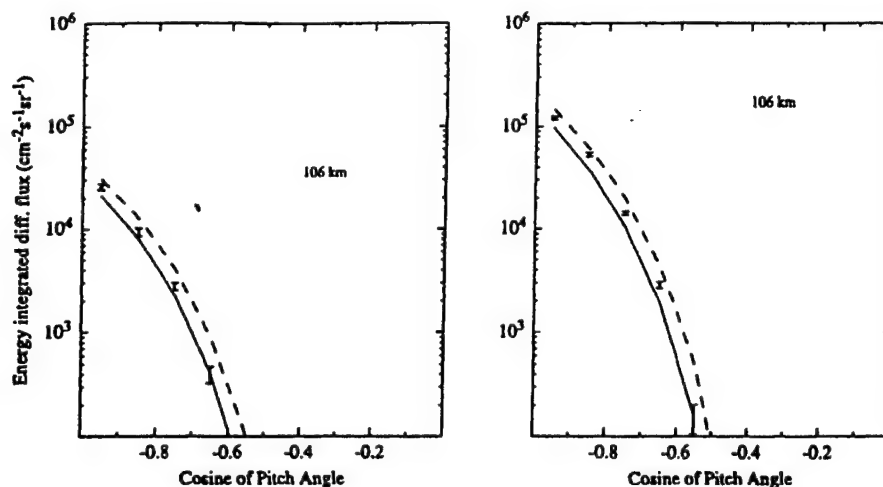


Figure 2g. Same as Figure 2a for an altitude of 106 km.

a function of altitude. As before, we see that all three models are in excellent agreement until they reach the lowest altitudes where the fluxes are severely attenuated. Similar plots for other pitch angles show the same trend with the altitude of severe flux attenuation moving higher as a pitch angle of  $90^\circ$  is approached. As seen above, at all pitch angles except one the LT model penetrates slightly deeper into the atmosphere than the CSDA and MC models. The one exception is the angle nearest  $90^\circ$  (cosine =  $-0.05$ ) where the MC penetrates deeper than the CSDA and LT.

Given the excellent agreement between the differential fluxes, similar agreement is expected between vari-

ous integrals over the fluxes. In Figure 4 we show the hemispherically averaged total flux from all three models and again see excellent agreement. Figures 5a and 5b show the energy deposition rates where the LT and CSDA models agree to within 5% and both generally fall within the MC errors. Again at the lowest altitudes (below the peak of the deposition) we see that the LT model penetrates slightly deeper (less than 1 km) into the atmosphere than does the CSDA or MC model. Finally, in Figure 6, we show the eV/ion pair for various characteristic energies and see excellent agreement (within 1.5%) between all three models.

## 5. Discussion and Summary

We have shown that except at the lowest altitudes three models for proton-H atom transport are in excellent agreement. The differences between the models are generally smaller than the errors that can arise from poorly known cross sections and/or the errors typi-

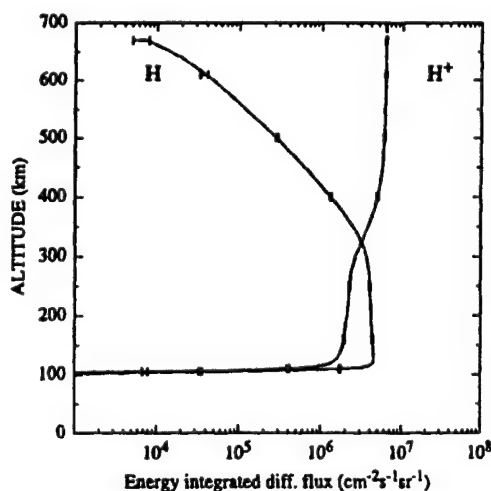


Figure 3a. The differential flux integrated over energy versus altitude for protons ( $H^+$ ) and hydrogen atoms ( $H$ ) at a pitch angle of  $161.8^\circ$  (cosine =  $-0.95$ ). The error bars are the Monte Carlo results, the long dashes are the linear transport results, and the dotted curves are the results from the continuous slowing-down approximation. The incident proton flux is a Maxwellian with a characteristic energy of 8 keV and a total incident energy flux of  $0.5 \text{ ergs cm}^{-2}\text{s}^{-1}$ .

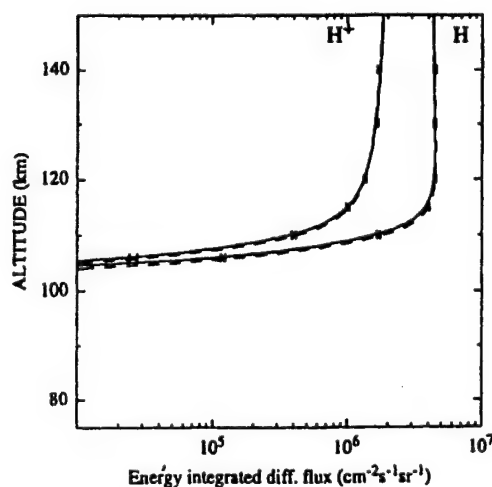
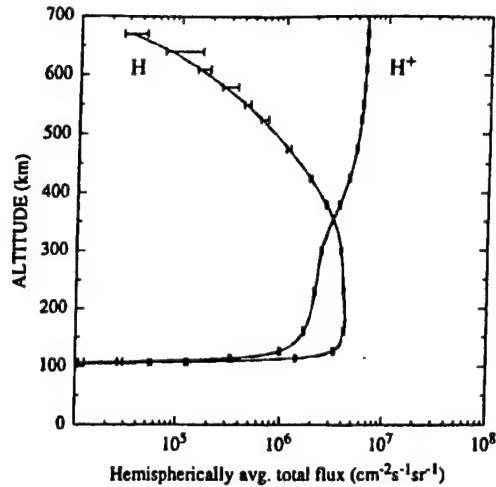
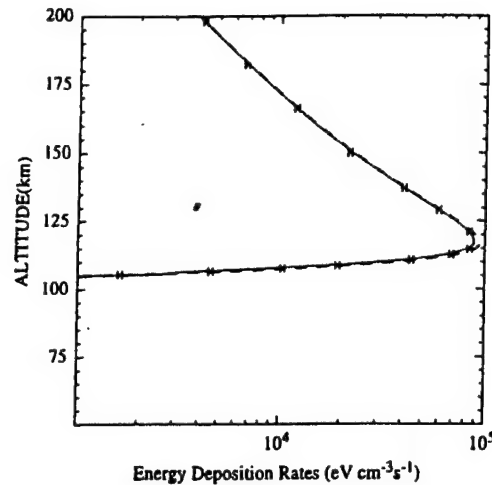


Figure 3b. Same as Figure 3a with expanded scale at lower altitudes.



**Figure 4.** Hemispherically averaged total flux versus altitude for protons ( $H^+$ ) and hydrogen atoms ( $H$ ). The incident proton flux is a Maxwellian with a characteristic energy of 8 keV and a total incident energy flux of  $0.5 \text{ ergs cm}^{-2} \text{ s}^{-1}$ .



**Figure 5b.** Same as Figure 5a with expanded scale at lower altitudes.

cally quoted for geophysical observations. For example, the measured cross sections for proton/ $H$  atom collisions with  $N_2$  and  $O_2$  have quoted accuracies of typically  $\pm 20 - 30\%$ . For most collisions involving atomic oxygen, there are no measurements and one resorts to "estimates" based on other cross sections. One exception is for charge changing collisions for which measurements have been made with quoted accuracies of 25%, but at present there are still factors of 2 disagreement between some of these measurements. Such uncertainties can lead to errors of comparable magnitude in the

model results [Decker *et al.*, 1995]. Likewise, measurements of proton fluxes typically involve low count rates and instrumental errors in the 10 to 30% range. Optical measurements of proton auroras typically quote errors larger than 10%. Thus, for the purposes of comparing to observations all three models are effectively identical. Further, the quality of the agreement between models gives us some confidence that there are no major errors in the three computer codes.

The one exception to the otherwise excellent agreement between the models is at the lowest altitudes

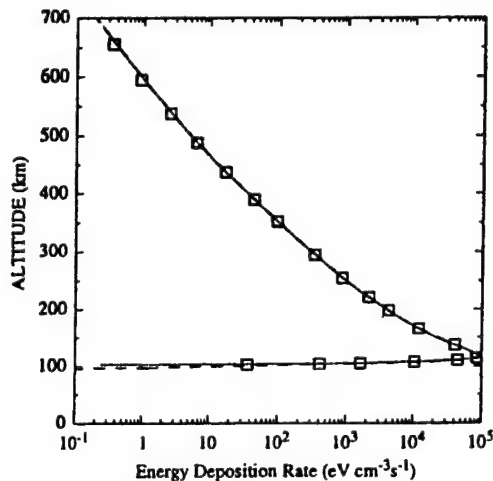


**Figure 5a.** Energy deposition rate versus altitude. The boxes are the Monte Carlo results, the long dashes are the linear transport results, and the dotted curves are the results from the continuous slowing-down approximation. The incident proton flux is a Maxwellian with a characteristic energy of 8 keV and a total incident energy flux of  $0.5 \text{ ergs cm}^{-2} \text{ s}^{-1}$ .

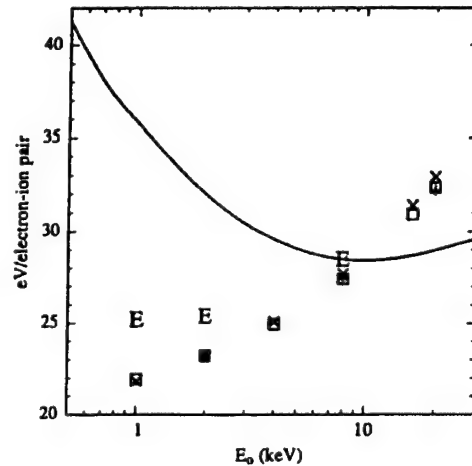


**Figure 6.** The quantity "eV per electron-ion pair" versus characteristic energy of incident protons given by Maxwellian distributions. The boxes are the Monte Carlo results, the pluses are the linear transport results, the crosses are the results from the continuous slowing down approximation, the "E" labels are results from Monte Carlo calculations that include momentum transfer in elastic collisions and have a minimum energy of 100 eV. The solid curve shows results from Monte Carlo calculations that used the original cross-section set of Kozelov and Ivanov.

(see Figures 1f, 2g, and 3b), where the proton and H atom fluxes are severely attenuated. While the differences between the models are apparent in all the altitude-dependent quantities examined, their fundamental source is the differences between the differential fluxes. In Figures 2a–2g it is evident that the altitudes at which these differences occur depend on the pitch angle of the flux. However, if we consider the fluxes not as a function of altitude but rather as a function of a pitch angle dependent collision or scattering depth such as

$$\tau_P(z, E, \mu) = - \sum_{\alpha} \sigma_{\alpha, P}(E) \int_z^{z_b} \frac{dz'}{\mu} n_{\alpha}(z'), \quad (7)$$

we find that the differences between models occur at around the same collision depth essentially independent of the particular pitch angle. It is the dependence of the collision depth on the cosine of the pitch angle that causes the differences between models to appear at different altitudes for different pitch angles. We thus find that the model differences arising at low altitudes occur at large collision depths where the collisional mean free paths are small compared to the scale heights of the neutral constituents and the altitude step sizes that are typically used in transport calculations. One consequence of this is that the algorithms designed to solve the transport problem often have difficulties at these altitudes and can be very sensitive to the details of their numerical implementation. For the LT model, we have found that it is particularly sensitive to the altitude grid used in this region. In our initial calculations of the energy integrated proton differential flux using a nonuniform grid of 77 altitudes, the LT results near a pitch angle of  $180^\circ$  and at 106 km were over a factor of 2 larger than the MC results. The calculations shown here (Figures 2g and 3b) used 353 altitudes, and the LT results are within 20% of the MC results. The general observed tendency was that when too few grid points were used the LT model penetrated deeper into the atmosphere than did the MC model, and as the grid resolution was improved the LT model approached the MC model. Fortunately, these differences have little effect on such issues as where energy is deposited in the atmosphere or where the bulk of the ionization takes place. Likewise, predictions of the typical observables: particle fluxes, ion densities, ion and neutral temperatures, and optical emissions are little affected by these differences. Thus, for most aeronautical purposes these differences deep in the atmosphere are of no consequence.

It is interesting that when the LT calculations were made with a grid of 77 altitudes, the particle and energy conservation was quite good. Over most altitudes, particle and energy conservation was better than 1%, and at the lowest altitudes both particles and energy were conserved to within a few percent. When the calculations were made with 353 altitudes, the conservation properties were little changed. For example, at some lower altitudes the particle conservation was a little better by a couple of percent and at others a little worse by a couple of percent. However, if we examine

the energy integrated differential flux near a pitch angle of  $180^\circ$ , and at 106 km a modest change in particle conservation is accompanied by over an 80% change in the flux. This can be understood by recalling that what is normally done when testing the particle and energy conservation is to first sum the total number of particles and total energy coming into the system at the top of the atmosphere. One then calculates at each altitude the total number of particles and total energy arriving at that altitude along with what has been lost from the system at all higher altitudes. In this way a check is made whether any particles or energy are lost or created as a result of the numerical methods being used. However, once the lowest altitudes have been reached and the fluxes are orders of magnitude below their original values most of the particles and energy have left the system. The number of particles that are left contribute very little to the total conservation, and thus there can be significant errors in the fluxes yet no strong indication of this in the conservation tests. This implies that checking the overall particle and energy conservation is a necessary but not a sufficient test of the accuracy of a particle transport model. On the other hand, one can test particle and energy conservation at a particular altitude relative to an altitude that is fairly close. In that case, it is possible to get some measure of the quality of the solution even when most of the particles have left the system. For example, if we test particle conservation at a particular altitude relative to the altitude one grid point higher, we find for the LT calculation using 77 altitudes that near a pitch angle  $180^\circ$  between 109 and 104 km the conservation degrades from 1% to 26%. Thus we do have some indication that with this particular altitude grid there are problems with the solution at the very low altitudes.

While the models have been brought into good agreement, we should note that differences can be seen between the models as they are used in different studies. This is perhaps most obvious when Monte Carlo runs are made that include mirroring and beam spreading. Kozelov [1993] has shown that these effects have an impact on the albedo, the charge fractions, and the energy deposition. Clearly, when these effects are important for a particular study, neither the CSDA nor the present LT model will be appropriate, and the MC model is needed. In such a case, if the MC is computationally too intensive for the particular study, one could resort to a table lookup of a set of precalculated MC results. Further differences can arise between the models due to differences in the collisional processes, cross sections, and energy losses that are used. To obtain the level of agreement presented in this paper, we had to take great care in making sure that all these factors were the same in all three models. In particular, we found that the eV/ion pair is very sensitive to any such differences. This is consistent with the discussions by Edgar *et al.* [1973] and Strickland *et al.* [1993] where it is pointed out that the shape of the eV/ion pair versus characteristic energy depends on the behavior of the cross sections and energy losses. For example, in Figure

6 we have included some additional calculations of the eV/ion pair. The symbol "E" labels MC calculations that used the cross section set used for this study but also included energy loss due to elastic collisions and extended the minimum energy down to 100 eV. Here we see how including another channel for energy loss (momentum transfer in elastic scattering) leaves less energy available for ionization and hence acts to increase the eV/ion pair. The solid curve gives the results of MC calculations of Kozelov and Ivanov [1994] using their standard cross section set. Here the dramatic difference comes in large part from larger low-energy excitation cross sections in the Kozelov and Ivanov cross-section set. Again, the effect is to raise the eV/ion pair at low energies as other collisional processes compete with ionization to degrade the energy of the protons and H atoms. The differences between cross-section sets arise because of the lack of necessary cross-section measurements and thus the need to make estimates and extrapolations in order to assemble a complete set. The focus of this paper has been on comparing three models and not the issue of what cross sections to use nor how well the models compare to observations. However, the success of the comparisons does suggest that our ability to model actual observations is presently limited by uncertainties in cross sections and the lack of suitable observations rather than our ability to solve the equations that describe the known physics of proton/H atom transport.

## Appendix

The purpose of this appendix is to derive an implementation of the continuous slowing-down approximation (CSDA) from linear transport theory. We begin with the linear transport equations for protons (P) and hydrogen atoms (H) as given by Basu *et al.* [1990]

$$\begin{aligned} & \left[ \mu \frac{\partial}{\partial z} + \sum_{\alpha} n_{\alpha}(z) \sigma_{\alpha,P}(E) \right] \Phi_P(z, E, \mu) \\ &= \sum_{\alpha} n_{\alpha}(z) \int dE' d\mu' \\ & \times \left[ \sum_k \sigma_{\alpha,P}^k(E', \mu' \rightarrow E, \mu) \Phi_P(z, E', \mu') \right. \\ & \left. + \sigma_{\alpha}^{01}(E', \mu' \rightarrow E, \mu) \Phi_H(z, E', \mu') \right] \end{aligned} \quad (A1)$$

$$\begin{aligned} & \left[ \mu \frac{\partial}{\partial z} + \sum_{\alpha} n_{\alpha}(z) \sigma_{\alpha,H}(E) \right] \Phi_H(z, E, \mu) \\ &= \sum_{\alpha} n_{\alpha}(z) \int dE' d\mu' \\ & \times \left[ \sum_k \sigma_{\alpha,H}^k(E', \mu' \rightarrow E, \mu) \Phi_H(z, E', \mu') \right. \\ & \left. + \sigma_{\alpha}^{10}(E', \mu' \rightarrow E, \mu) \Phi_P(z, E', \mu') \right] \end{aligned} \quad (A2)$$

where  $\Phi_{\beta}(z, E, \mu)$  is the differential flux of particles (in units of  $\text{cm}^{-2}\text{s}^{-1}\text{eV}^{-1}\text{sr}^{-1}$ ) of type  $\beta (= P, H)$  as a function of altitude ( $z$ ), energy ( $E$ ), and cosine of the angle between the particle velocity and the  $z$  axis ( $\mu$ ); the  $z$  axis is antiparallel (parallel) to the geomagnetic field line in the northern (southern) hemisphere; and  $n_{\alpha}$  is the concentration of the neutral specie  $\alpha$ . The cross sections for the various collisional processes are  $\sigma_{\alpha,\beta}^j(E)$  (in units of  $\text{cm}^2$ ), where  $j (= k, 10, 01)$  labels the type of collision. The index  $k$  refers only to excitation and ionization type collisions and 10 and 01 refer to charge exchange and stripping collisions, respectively. The total cross section summed over types of collisions is given by  $\sigma_{\alpha,\beta}(E)$ . For the differential cross sections, we make the forward scattering approximation to the angular dependence and assume

$$\begin{aligned} & \sigma_{\alpha,\beta}^j(E', \mu' \rightarrow E, \mu) \\ &= \sigma_{\alpha,\beta}^j(E') \delta(\mu' - \mu) \delta[E' - W_{\alpha,\beta}^j(E') - E] \end{aligned} \quad (A3)$$

where  $E'$  is the incident particle energy,  $E$  is the final energy, and  $W_{\alpha,\beta}^j(E)$  is the energy loss associated with collision type  $j$ .

Our first step in developing a CSDA implementation is to break the calculation into two pieces. On the one hand, we calculate the relative charge state composition of the flux by neglecting energy loss and only considering the conversion of protons into H atoms and H atoms back into protons. This is done by setting  $W_{\alpha,\beta}^j(E) = 0$  and using (A3) in performing the  $\mu'$  and  $E'$  integrations to obtain

$$\begin{aligned} & \left[ \mu \frac{\partial}{\partial z} + \sum_{\alpha} n_{\alpha}(z) \sigma_{\alpha}^{10}(E) \right] \Phi_P(z, E, \mu) \\ &= \sum_{\alpha} n_{\alpha}(z) \sigma_{\alpha}^{01}(E) \Phi_H(z, E, \mu) \end{aligned} \quad (A4)$$

$$\begin{aligned} & \left[ \mu \frac{\partial}{\partial z} + \sum_{\alpha} n_{\alpha}(z) \sigma_{\alpha}^{01}(E) \right] \Phi_H(z, E, \mu) \\ &= \sum_{\alpha} n_{\alpha}(z) \sigma_{\alpha}^{10}(E) \Phi_P(z, E, \mu) \end{aligned} \quad (A5)$$

which are (in a slightly different form) (4) and (5) that are used in calculating the charge state composition of the flux. These equations are identical to (17) and (18) in the work of Basu *et al.* [1990] and were originally derived for use at high altitudes. While the particle fluxes that are predicted from these equations are reasonable only for high altitudes, it was found that the calculated flux fractions are accurate at all altitudes.

On the other hand, we also need a method to calculate the effects of energy degradation on the fluxes. This is done by assuming the flux fractions are known and calculating an "average" energy loss for protons and H atoms together. To develop the needed equation, we multiply (A1) and (A2) by  $E$ , integrate over  $\mu$  and  $E$ , and add the resulting equations to obtain



$$\begin{aligned} & \frac{\partial}{\partial z} \int dE d\mu \mu E \Phi_T(z, E, \mu) \\ &= - \sum_{\alpha} n_{\alpha}(z) \int dE d\mu \left[ L_{\alpha,P}(E) f_P(z, E, \mu) \right. \\ & \quad \left. + L_{\alpha,H}(E) f_H(z, E, \mu) \right] \Phi_T(z, E, \mu) \end{aligned} \quad (A6)$$

where  $\Phi_T = \Phi_P + \Phi_H$ ,  $f_{\beta} = \Phi_{\beta}/\Phi_T$ , and

$$L_{\alpha,\beta}(E) = \sum_j W_{\alpha,\beta}^j(E) \sigma_{\alpha,\beta}^j(E). \quad (A7)$$

Note that these are the loss functions given in section 2 as (2) and (3). At this point, we make the continuous slowing-down approximation. That is, we assume that the energy of a particle is a continuous function of altitude,  $E(z)$ . This means that the stochastic nature of the collisional degradation of the protons and H atoms is neglected, and all particles starting with the same energy will lose the same amount of energy as they pass through the same range of altitudes. Thus, if we divide  $\Phi_T$  into monoenergetic, monodirectional streams at the top of the atmosphere, they will maintain their independent identity as they penetrate down through the atmosphere. Thus the CSDA allows us to write  $\Phi_T$  in the following form:

$$\Phi_T(z, E, \mu) = \sum_S I_S(z) \delta(E - E_S) \delta(\mu - \mu_S). \quad (A8)$$

For each stream, denoted by  $S$ , we can use (A8) in evaluating (A6) giving

$$\begin{aligned} & \frac{\partial}{\partial z} \left[ \mu_S E_S I_S(z) \right] \\ &= - \sum_{\alpha} n_{\alpha}(z) I_S(z) \left[ L_{\alpha,P}(E_S) f_P(z, E_S, \mu_S) \right. \\ & \quad \left. + L_{\alpha,H}(E_S) f_H(z, E_S, \mu_S) \right] \end{aligned} \quad (A9)$$

We next return to (A1) and (A2), integrate over  $\mu$  and  $E$ , add the resulting equations, and obtain the statement of particle conservation that follows from the transport equations, namely,

$$\frac{\partial}{\partial z} \int dE d\mu \mu \Phi_T(z, E, \mu) = 0. \quad (A10)$$

This gives for each stream,

$$\frac{\partial}{\partial z} \left[ \mu_S I_S(z) \right] = 0. \quad (A11)$$

Combining (A9) and (A11) gives

$$\begin{aligned} \frac{dE_S}{dz} = - \frac{1}{\mu_S} \sum_{\alpha} n_{\alpha}(z) \left[ L_{\alpha,P}(E_S) f_P(z, E_S, \mu_S) \right. \\ \left. + L_{\alpha,H}(E_S) f_H(z, E_S, \mu_S) \right] \end{aligned} \quad (A12)$$

which in section 2 is given as (1). This then gives us

an ordinary differential equation to solve for the energy ( $E$ ) as a function of altitude ( $z$ ).

In the implementation used in this paper, we begin with a flux of downgoing protons at some boundary altitude. As mentioned, the energy and pitch angle distribution of the protons is represented by a set of monoenergetic, monodirectional protons stream. The atmosphere is divided into a series of horizontal layers, and (A4), (A5), and (A12) are applied to each stream. The equations are integrated from altitude to altitude using an explicit Euler method with (A4) and (A5) being solved assuming the energy of the stream is unchanged within a layer and (A12) being solved assuming the flux fractions are unchanged within a layer. At each succeeding altitude, the flux fractions and stream energy are updated for use in integrating down to the next altitude. In this way, the energy degradation and changing composition of each stream are calculated as the protons and H atoms penetrate down from the top of the atmosphere.

**Acknowledgments.** The work by D.T.D. at Boston College was supported by Air Force contract F19628-93-K-0001. The work by B.B. and J.R.J. at the Phillips Laboratory was supported by the Air Force Office of Scientific Research (AFOSR). The work of B.V.K. and V.E.I. was supported by the Russian Foundation of Fundamental Investigations (RFFI).

The Editor thanks R. E. Daniell and J. D. Winningham for their assistance in evaluating this paper.

## References

- Basu, B., J.R. Jasperse, R.M. Robinson, R.R. Vondrak, and D.S. Evans, Linear transport theory of auroral proton precipitation. A comparison with observations, *J. Geophys. Res.*, **92**, 5920, 1987.
- Basu, B., J.R. Jasperse, and N.J. Grossbard, A numerical solution of the coupled proton-H atom transport equations for the proton aurora, *J. Geophys. Res.*, **95**, 19069, 1990.
- Basu, B., J.R. Jasperse, D.J. Strickland, and R.E. Daniell Jr., Transport-theoretic model for the electron-proton-hydrogen atom aurora, 1, Theory, *J. Geophys. Res.*, **98**, 21517, 1993.
- Davidson, G.T., Expected spatial distribution of low-energy proton precipitated in the auroral zones, *J. Geophys. Res.*, **70**, 1061, 1965.
- Decker, D. T., B. Basu, J. R. Jasperse, D. J. Strickland, J. R. Sharber, and J. D. Winningham, Upgoing electrons produced in an electron-proton-hydrogen atom aurora, *J. Geophys. Res.*, **100**, 21409, 1995.
- Eather, R.H., Auroral proton precipitation and hydrogen emissions, *Rev. Geophys.*, **5**, 207, 1967.
- Eather, R.H., Ionization produced by auroral proton precipitation, *Ann. Geophys.*, **26**, 609, 1970.
- Eather, R.H., and K.M. Burrows, Excitation and ionization by auroral protons, *Aust. J. Phys.*, **19**, 309, 1966.
- Edgar, B.C., W.T. Miles, and A.E.S. Green, Energy deposition of protons in molecular nitrogen and applications to proton auroral phenomena, *J. Geophys. Res.*, **78**, 6595, 1973.
- Edgar, B.C., H.S. Porter, and A.E.S. Green, Proton energy deposition in molecular and atomic oxygen and applications to the polar cap, *Planet. Space Sci.*, **23**, 787, 1975.

- Galperin, Y.I., Hydrogen emission and two types of auroral spectra, *Planet. Space Sci.*, **1**, 57, 1959.
- Galperin, Y.I., R.A. Kovrazhkin, Y.N. Ponomarev, J. Crasnier, and J.A. Sadaud, Pitch angle distributions of auroral protons, *Ann. Geophys.*, **32**, 109, 1976.
- Hardy, D.A., M.S. Gussenhoven, R. Raistrick, and W.J. McNeil, Statistical and functional representations of the pattern of auroral energy flux, number flux, and conductivity, *J. Geophys. Res.*, **92**, 12275, 1987.
- Hardy, D.A., M.S. Gussenhoven and D. Brautigam, A statistical model of auroral ion precipitation, *J. Geophys. Res.*, **94**, 370, 1989.
- Hardy, D.A., W.J. McNeil, M.S. Gussenhoven, and D. Brautigam, A statistical model of auroral ion precipitation, 2, Functional representation of the average patterns, *J. Geophys. Res.*, **96**, 5539, 1991.
- Hedin, A.E., MSIS-86 thermospheric model, *J. Geophys. Res.*, **92**, 4649, 1987.
- Henriksen, K., Variations of proton energy and pitch angle spectra in the upper atmosphere, *J. Atmos. Terr. Phys.*, **41**, 633, 1979.
- Iglesias, G.E., and R.R. Vondrak, Atmospheric spreading of protons in auroral arcs, *J. Geophys. Res.*, **79**, 280, 1974.
- Isaev, S.I., and M.I. Pudovkin, *Aurora and the Processes in the Earth's Magnetosphere*, Nauka, Moscow, 1972.
- Jasperse, J.R., and B. Basu, Transport theoretic solutions for auroral proton and H atom fluxes and related quantities, *J. Geophys. Res.*, **81**, 811, 1982.
- Johnstone, A.D., The spreading of a proton beam by the atmosphere, *Planet. Space Sci.*, **20**, 292, 1972.
- Kozelov, B.V., Influence of the dipolar magnetic field on transport of proton-H atom fluxes in the atmosphere, *Ann. Geophys.*, **11**, 697, 1993.
- Kozelov, B.V., and V.E. Ivanov, Monte Carlo calculation of proton-hydrogen atom transport in  $N_2$ , *Planet. Space Sci.*, **40**, 1503, 1992.
- Kozelov, B.V., and V.E. Ivanov, Effective energy loss per electron-ion pair in proton aurora, *Ann. Geophys.*, **12**, 1071, 1994.
- Ponomarev, Y.N., Intrusion of the monoenergetic monodirectional beams of protons into the polar high atmosphere, (in Russian), *Kosmi. Issled.*, **14**, 144, 1976.
- Porter, H.S., and A.E.S. Green, Comparison of Monte Carlo and continuous slowing-down approximation treatments of 1-keV proton energy deposition on  $N_2$ , *J. Appl. Phys.*, **46**, 5030, 1975.
- Rees, M.H., On the interaction of auroral protons with the Earth's atmosphere, *Planet. Space Sci.*, **30**, 463, 1982.
- Romick, G.J., and C.T. Elvey, Variations in the intensity of the hydrogen emission line  $H\beta$  during auroral activity, *J. Atmos. Terr. Phys.*, **12**, 283, 1958.
- Sharber, J.R. The continuous (diffuse) aurora and auroral-E ionization. in *Physics of Space Plasmas*, vol. 4, edited by T.S. Chang, B. Coppi and J.R. Jasperse, p. 115, Scientific, Cambridge, Mass., 1981.
- Strickland, D.J., R.E. Daniell Jr., J.R. Jasperse, and B. Basu, Transport-theoretic model for the electron proton-hydrogen atom aurora, 2, Model results, *J. Geophys. Res.*, **98**, 21533, 1993.
- B. Basu and J. R. Jasperse, Phillips Laboratory, 29 Randolph Rd., Hanscom Air Force Base, MA 01731-3010. (e-mail: basub@plh.af.mil)
- D. T. Decker, Institute for Scientific Research, Boston College, 885 Centre St., Newton, MA 02159. (e-mail: decker@plh.af.mil)
- V. E. Ivanov and B. V. Kozelov, Polar Geophysical Institute, 184200, Apatity, Murmansk Region, Russia. (e-mail: kozelov@pgi-ksc.murmansk.su)

(Received April 26, 1996; revised August 28, 1996; accepted August 29, 1996.)

## Total electron content over the Pan-American longitudes: March–April 1994

Patricia H. Doherty

Institute for Scientific Research, Boston College, Chestnut Hill, Massachusetts

David N. Anderson

Phillips Laboratory, Hanscom Air Force Base, Massachusetts

John A. Klobuchar<sup>1</sup>

Total Electronic Concepts, Lincoln, Massachusetts

**Abstract.** An experimental campaign to measure diurnal changes in total electron content (TEC) over the wide latitude range from approximately 50°N to 40°S was carried out from March 28 through April 11, 1994, by monitoring the differential carrier phase from the U.S. Navy Navigation Satellite System using a chain of ground stations aligned along the approximate 70°W longitude meridian. This Pan-American campaign was conducted primarily to study the day-to-day variability of the equatorial anomaly region. The experimental plan included using the received values of TEC from the chain of stations to construct profiles of electron density versus latitude using tomographic reconstruction techniques and, then, to compare these reconstructions against a theoretical model of the low-latitude ionosphere. The diurnal changes in TEC along this latitude chain of stations showed a high degree of variability from day to day, especially during a magnetic storm which occurred near the beginning of the campaign. The equatorial anomaly in TEC showed large changes in character in the two hemispheres, as well as differences in magnitude from day to day. The latitudinal gradients of TEC, especially in the lower midlatitudes, also showed large differences between magnetic storm and quiet conditions. Comparisons of the TEC data with the theoretical model illustrate the sensitivity of the model calculations to changes in magnetic  $E \times B$  drift and serves to validate the strong influence that these drifts have on the formation and the strength of the equatorial anomaly regions.

### Introduction

The equatorial anomaly region is characterized by the highest values of peak electron density and total electron content in the worldwide ionosphere. These large values are primarily due to the daytime upward  $E \times B$  drift at the magnetic equator which drives the ionization to higher altitudes. As the layer is lifted to higher altitudes, it diffuses down magnetic field lines

that connect to the ionosphere north and south of the equator, causing crests at latitudes approximately  $\pm 15^\circ$  from the magnetic equator [Hanson and Moffett, 1966, Anderson, 1973]. This phenomenon has been described as a fountain effect. A discussion on the origin of the terms related to the equatorial fountain effect is presented in the appendix. The day-to-day variability of the equatorial ionosphere can be very large, owing to changes in the strength of the  $E \times B$  drift and from differences in the day-to-day strength of both the meridional and zonal component of neutral winds [Sterling *et al.*, 1969].

While many measurements of the equatorial and low-latitude ionosphere have been made by various techniques, beginning with bottomside ionosondes; then, by incoherent scatter radars at Jicamarca, Peru,

<sup>1</sup>Formerly at Phillips Laboratory, Hanscom Air Force Base, Massachusetts.

Copyright 1997 by the American Geophysical Union.

Paper Number 97RS00840.  
0048-6604/97/97RS-00840\$11.00

and at Kwajalein Island; later, by topside sounders; and finally, by a dual-frequency, dispersive radar on the TOPEX/Poseidon satellite, continuous measurements of the ionosphere over a wide latitude range, in a single longitude sector, have not been generally available. Deshpande *et al.* [1977] first showed the day-to-day variability of the low-latitude total electron content (TEC) and later, Rastogi and Klobuchar [1990] showed examples of the day-to-day variability in TEC over the Indian subcontinent. More recently, Whalen [1993, 1996] used multiple ionospheric sounders to illustrate the variability in latitudinal profiles of maximum  $F_2$  region electron densities through  $\pm 30^\circ$  dip latitude. Model studies by Klobuchar *et al.* [1991] showed that different  $E \times B$  drifts could significantly change the TEC and the electron density at the  $F_2$  region peak over a wide range of latitudes, but little actual diurnal data over a wide range of latitudes have been available to check the validity of this model. This Pan-American campaign was designed to correct this deficiency.

In order to measure the day-to-day variability of the ionosphere over a wide range of latitudes, a chain of stations was set up along the approximate  $70^\circ\text{W}$  longitude meridian to make measurements of TEC using the dual-frequency coherent signals from the U.S. Navy Navigation Satellite System (NNSS). Figure 1 illustrates the station chain. The sites were located at Hanscom Air Force Base, Massachusetts, on the islands of Bermuda and Puerto Rico, as well as at Merida, Venezuela; La Paz, Bolivia, and Tucuman, Argentina. The planned site at Tabatinga, Brazil, was not operated owing to logistical difficulties and resulted in a data gap over the geomagnetic equator. Also shown in Figure 1 are typical NNSS satellite passes, both a northbound and a southbound one, to illustrate that the station chain was nearly ideal for such measurements.

### Ionospheric Measurements

The NNSS satellites transmit coherent radio beacons at 150 and 400 MHz. The space vehicles are placed in near-circular polar orbits at altitudes of approximately 1100 km [Newton, 1967]. Evans and Holt [1973] showed that these satellites are ideally suited to studies of latitudinal variations of ionospheric behavior by using NNSS measurements to observe the location of the midlatitude trough from Millstone Hill, Massachusetts. More recently, tomographic reconstruction studies have utilized NNSS satellite

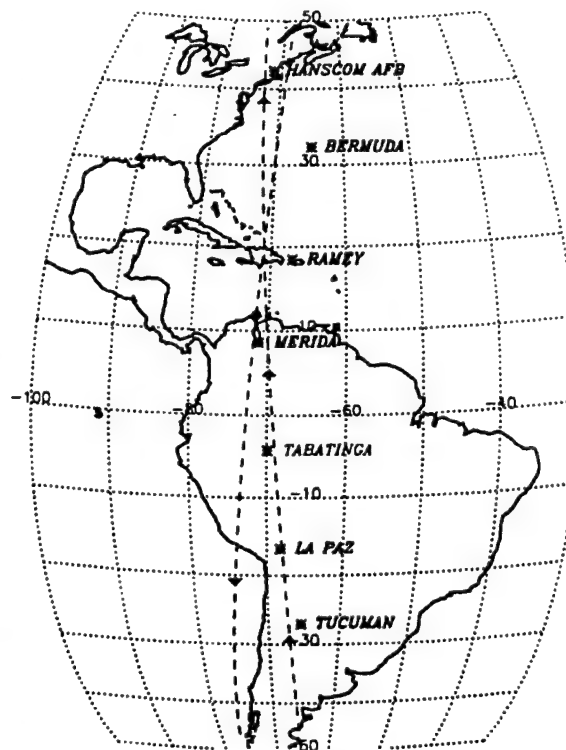


Figure 1. Map of stations along the  $\sim 70^\circ\text{W}$  longitude meridian used in the campaign.

measurements in an effort to construct profiles of electron density versus latitude [Kersley *et al.*, 1993; Pakula *et al.*, 1995]. In this study, there were six NNSS satellites transmitting on the operational navigation frequencies during the approximate 2-week period of the campaign, making it possible to record a high elevation pass from one of the NNSS satellites from the chain of stations approximately every 2 hours. To determine the measurement of TEC along the  $70^\circ\text{W}$  meridian, the relative differential carrier phase recorded at all sites was combined, converted to equivalent vertical TEC, and changed into absolute TEC values using a visual, multistation version of the two-station method developed by Leiting *et al.* [1975].

The campaign data are complemented with simultaneous measurements of TEC from dual-frequency Global Positioning System (GPS) and from vertical TEC measured with the TOPEX/Poseidon satellite. GPS dual-frequency data recorded at Arequipa, Peru; Santiago, Chile, and the island of Bermuda were obtained from the International GPS

Service for Geodynamics network that is managed by the Jet Propulsion Laboratory [International Association of Geodesy, 1995]. For this data set, absolute measurements of TEC were made by combining the differential phase and differential group delay measurements. The slant TEC values then were converted to equivalent vertical TEC at 400 km. In addition, coincident measurements from the TOPEX/Poseidon satellite are also presented in this study. The TOPEX satellite mission is dedicated to the study of ocean topography. The onboard dual-frequency (5.2 and 13.6 GHz) altimeter provides near-global vertical TEC measurements over the ocean areas [Imel, 1994].

The measurements were made near solar minimum in late March and early April 1994. Geomagnetic activity levels were considered quiet in the first few days of the campaign. A major magnetic storm began on April 2, and the remainder of the period of

observations had at least moderate geomagnetic activity. Data recorded during the campaign thus allowed the opportunity to study the latitudinal gradients of the ionosphere during both geomagnetically quiet and disturbed conditions. Figure 2 illustrates the planetary 3-hour  $K_p$  indices recorded during the campaign period.

### Experimental Results

An example of equivalent vertical TEC from the full chain of six stations is shown in Figure 3. In this figure, the TEC is plotted from approximately 50°N to 40°S, a latitude span of 90° encompassing both sides of the equatorial region. At this longitude sector, the magnetic equator is located at approximately 11°S geographic latitude. Figure 3 shows a classic case of two clearly defined anomaly regions spaced approximately 10 to 15° away from the geomagnetic equator in both the northern and southern hemispheres.

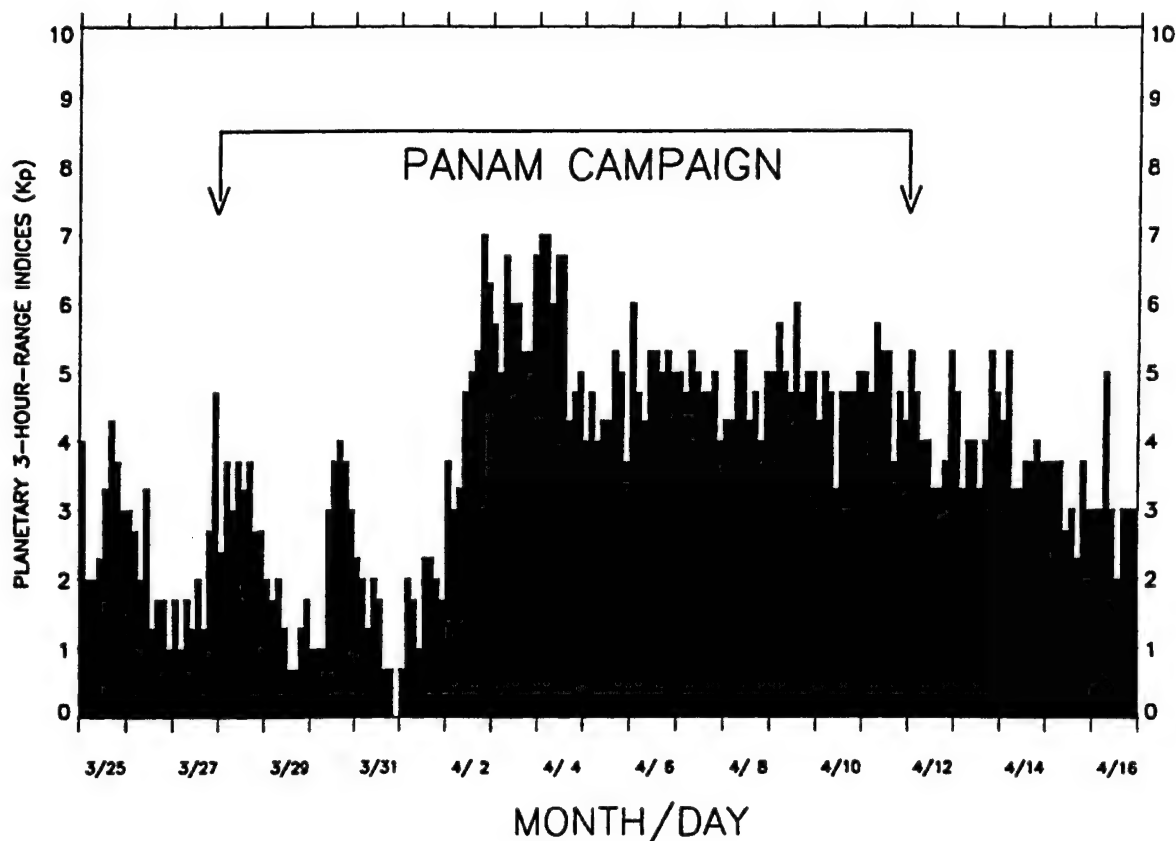


Figure 2. Planetary 3-hour  $K_p$  indices recorded during the campaign period.

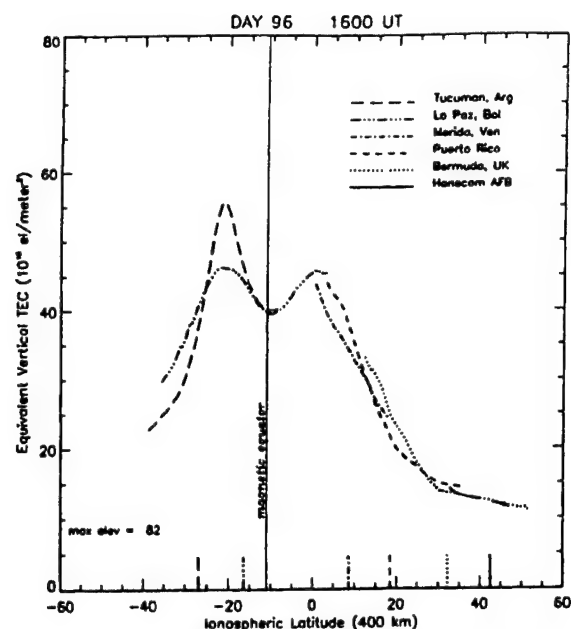


Figure 3. Equivalent vertical total electron content (TEC) from the full chain of six stations at approximately 1600 UT on April 6, 1994.

Note that the two stations from which the southern anomaly peak in equivalent vertical TEC is inferred give somewhat different TEC values, though they both show the peak at the same latitude. This difference in equivalent vertical TEC is due to errors in converting from the measured slant TEC to an equivalent vertical TEC when looking through gradients which are a function of elevation angle. This problem has been discussed by Tsedilina *et al.* [1994].

To assess the accuracy of the TEC measurements made during the campaign, equivalent vertical TEC from GPS receivers located at Santiago, Chile; Arequipa, Peru, and the island of Bermuda, together with vertical TEC measurements made via the TOPEX/Poseidon satellite, were compared with campaign data. Figure 4 illustrates two of these comparisons. The GPS measurements shown in this figure represent simultaneous measurements of equivalent vertical TEC at 400 km. Since GPS satellites are located at an altitude greater than 20,000 km and the NNSS satellites are at approximately 1100 km, simultaneous measurements from the two satellite systems are relatively short in local time. The TOPEX measurements in this illustration are restricted to times when the TOPEX ground track comes within 1 hour

local time of the campaign measurements. The TOPEX satellite is located at approximately 1300 km and provides vertical measurements of TEC to that height. Figure 4 (left) illustrates close agreement between the NNSS and GPS measurements recorded on day 93 (April 3) at approximately 2320 UT. This plot also shows that the TOPEX and NNSS calculations compare favorably in the shape and geographic location of the southern anomaly peak. The differences occur in the slight shift in the anomaly region surrounding the southern anomaly peak and the magnitude at the peak. The TOPEX calculations illustrate a peak that is approximately 6 TEC units smaller than the NNSS measurements. This difference could represent an error in the slant to vertical conversion process used for the NNSS data. In Figure 4 (right), similar measurements of TEC are observed from all three observation types during an NNSS pass occurring near 1030 UT on day 95 (April 5).

The PANAM campaign provided the unique opportunity to observe the full diurnal development and decay of the equatorial anomaly. Figure 5 illustrates measurements from a series of satellite passes for 4 consecutive days during the campaign. Note that the approximate local time of each pass is printed inside the left y axis and that each pass is offset by 15 TEC units for each hour of local time after noon to allow a visual separation between passes. In this figure, a classic response to the  $E \times B$  drift is portrayed, where the anomaly begins to develop by late morning but does not peak until near 2000 hours local time. Not all six stations were operating for these days, but the general behavior of the equatorial anomaly and the differences in the shape of the anomaly among the 4 days can still be seen in Figure 5. Note that the magnitude, width, and symmetry of the latitudinal anomaly peaks in the southern and northern hemisphere exhibit large variation over this 4-day period. In particular, there is little evidence of the northern anomaly peak on day 94 (April 4) at local noon, while there is clear evidence of it on days 95 through 97. Also, the slope on the northern side of the anomaly peak at local noon differs greatly over the 4 days. Finally, the magnitudes of the southern anomaly peaks are much higher on days 94 and 96 than on days 95 and 97. The postmidnight and early morning passes, although not included in Figure 5, show no signs of anomaly features. They are descriptive of the downward motion of the vertical  $E \times B$  drift, where the ionization is driven to lower heights to a region of greater loss. Although this data set is



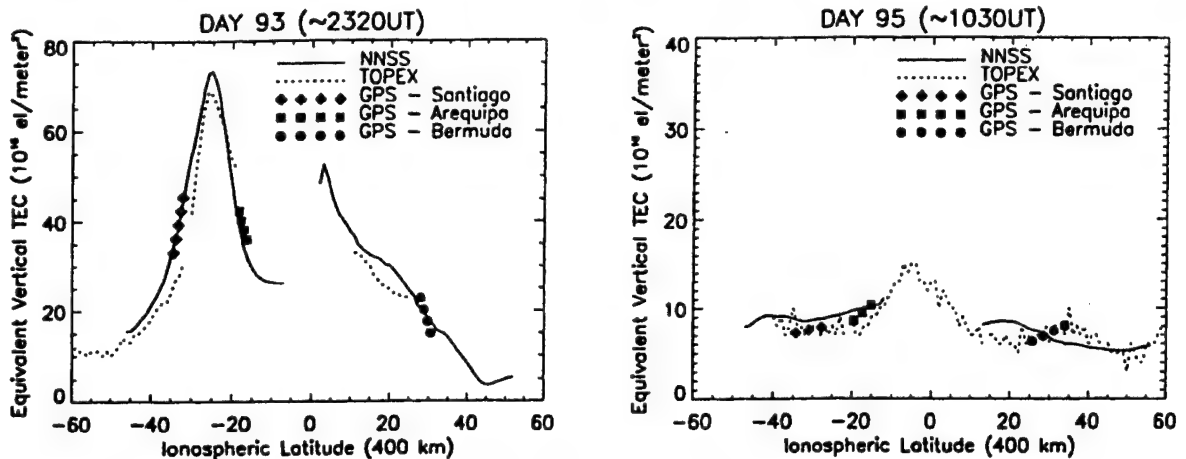


Figure 4. Comparison of TEC measurements from the U.S. Navy Navigation Satellite System (NNSS), TOPEX, and Global Positioning System (GPS) satellite systems at approximately 2320 hours UT on April 3, 1994 (left) and on April 5 at approximately 1030 UT (right).

very informative, the data gaps near the magnetic equator seriously limit our ability to make precise determinations of the location and shape of the anomaly, particularly in the northern hemisphere. These data gaps are due to the lack of a station near the magnetic equator, together with intermittent power difficulties experienced at the La Paz, Bolivia, station.

The dramatic day-to-day variability illustrated in the campaign measurements is consistent with earlier

research. In particular, Whalen [1993, 1996] reconstructed latitudinal profiles of the maximum  $F$  region electron density for 30 consecutive days in September 1958 by combining ionograms from a chain of ionosondes located in the western hemisphere equatorial region. His results illustrate apparent day-to-day differences in the symmetry and magnitude of the equatorial anomaly peaks. He also found asymmetry in the time of the enhancements, where the

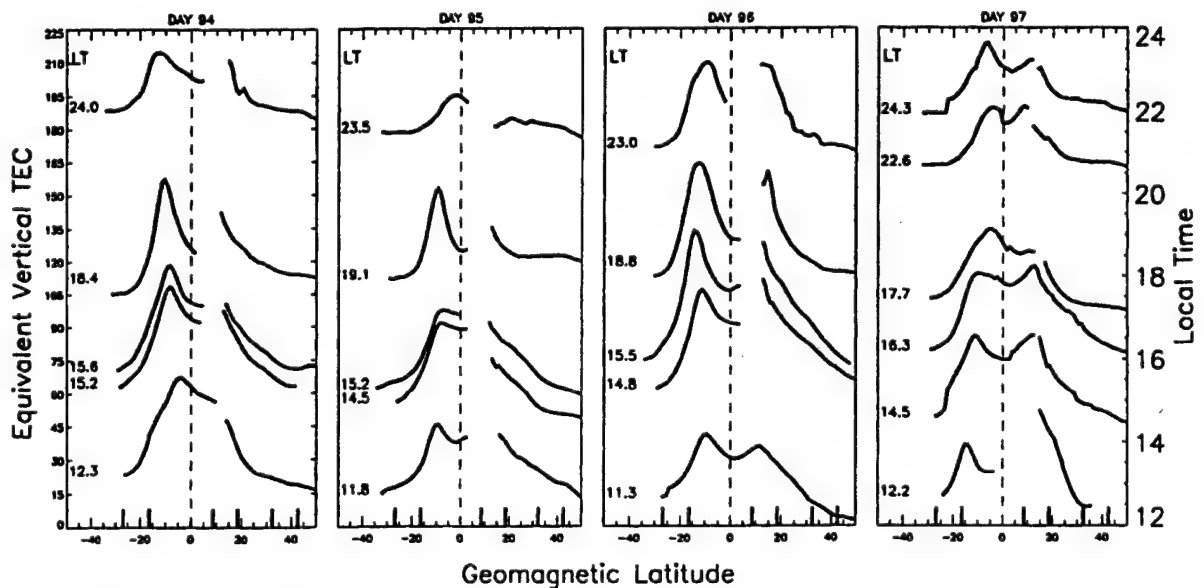


Figure 5. Diurnal development of the equatorial anomaly from 1200 to 2400 hours local time for April 4-7, 1994.

anomaly peak occurred earlier in the north than in the south for most days in the observation period.

The high degree of variation in the development of the equatorial anomaly illustrated in Figure 5 is primarily due to the large differences in the vertical electrodynamic lift at the equator. Drift variations have been shown to have a large impact on the latitudinal location and amplitude of the equatorial anomaly peaks [Klobuchar *et al.*, 1991]. The symmetry of both the amplitude and position of the equatorial anomaly peaks between the northern and southern hemisphere is largely a neutral wind effect. The next section focuses on some of these relationships by comparing campaign data to a theoretical model of the low-latitude ionosphere.

### Model Comparisons

The data recorded during the campaign provides a unique database for model validation. In this section, a comparison of TEC measurements with calculations from the Phillips Laboratory Global Theoretical Ionospheric Model (GTIM) [Anderson *et al.*, 1996], is presented. The *F* region portion of this model numerically solves the  $O^+$  continuity equation to determine  $O^+$  densities as a function of altitude,

latitude, longitude, and local time. The model requires a variety of geophysical inputs that include a neutral atmosphere, neutral winds, ion and electron temperatures, and  $E \times B$  drift velocities. The standard model inputs and calculations used in the low-latitude model are described by Preble *et al.* [1994] and Anderson *et al.* [1996]. The GTIM model is flexible in that the inputs can be modified to test the sensitivity of the ionosphere to any one or more of these parameters.

Figures 6a through 6d illustrate a comparison of the data with a sequence of model calculations. Figure 6a shows the equivalent vertical TEC measurements recorded on April 6. For clarity, the approximate local time is printed near the left y axis and each curve is offset by a factor of 40 TEC units. These data show a well-defined equatorial anomaly at local noon. It peaks near 1900 local time and begins to show signs of decay at 2300 hours. Figures 6b–6d represent model calculations for comparable geomagnetic, seasonal, and solar conditions. The results shown in Figure 6b are based on a climatological vertical  $E \times B$  drift pattern for solar moderate conditions [Fejer, 1981]. Note that the local time development and the dip latitude positions of the peaks are realistic, while the magnitudes of the peaks are much smaller than those exhibited in the data measurements. Initial efforts to increase the magnitude

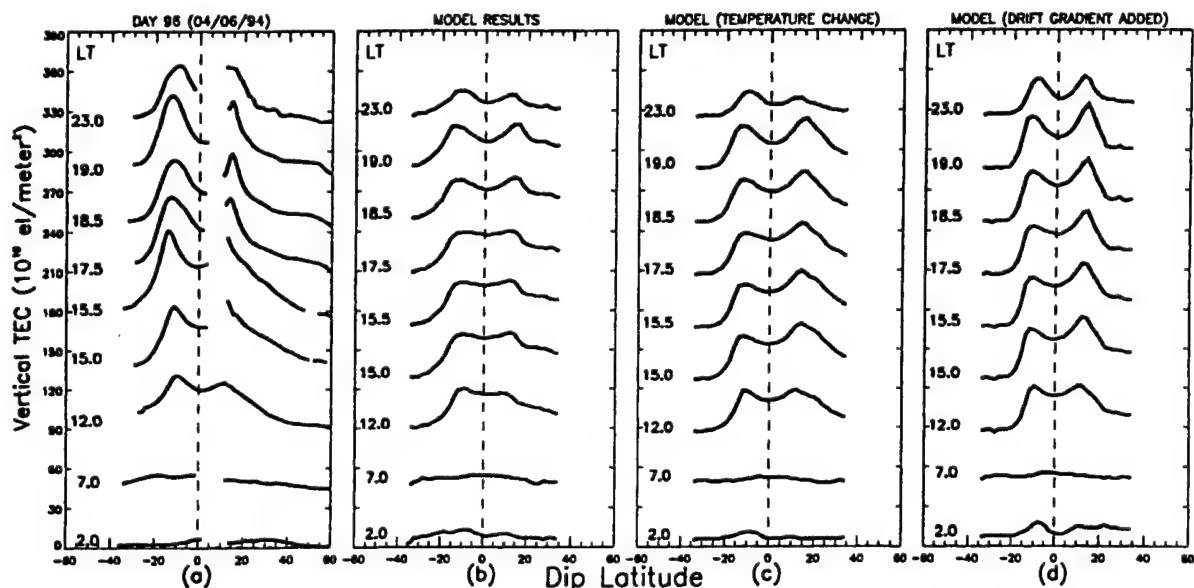


Figure 6. (a) Equivalent vertical TEC measurements of April 6, 1994. (b) Model calculations based on climatological  $E \times B$  drift and original temperature model (see text). (c) Model calculations with a more appropriate low-latitude temperature model. (d) Model calculations with a more appropriate low-latitude temperature model and an  $E \times B$  drift height gradient.

of the equatorial anomaly peaks were made by increasing the  $E \times B$  drift. The results of those efforts (not shown) illustrate larger peaks but with the anomaly pushed out to higher latitudes. The base run of the model shown in Figure 6b used a temperature model that was originally developed for the midlatitude region [Strobel and McElroy, 1970]. Figure 6c represents the model calculations that include a more appropriate low-latitude temperature model [Brace and Theis, 1981]. This modification produces sharper anomaly peaks and more realistic slopes poleward of the anomaly peaks. The dip latitude positions of the anomaly peaks are accurately maintained, but the magnitude of the peaks are still much smaller than the data calculations. The  $E \times B$  vertical drift velocities used in the model are based on drift measurements made at Jicamarca, Peru. In general, they are applied in the GTIM model with no altitude dependence. Work by Pingree and Fejer [1987] and Su *et al.* [1995] indicate that the altitude variations of the vertical drift velocities are important in the development of the equatorial anomaly. Figure 6d illustrates model results when a simple linear height variation in the vertical drift is incorporated into the calculations. This modification produces more accurate peak shapes in both hemispheres and realistic slopes to higher latitudes within  $\pm 20^\circ$  dip latitude. The unrealistic change induced at latitudes greater than  $\pm 20^\circ$  indicates that the drift gradient needs to be refined. Although the magnitudes of the anomaly peaks have been increased, they are still lower than the data measurements. To provide a more quantitative measure of the differences shown in Figure 6, plots of data versus model calculations at 1200, 1900, and 2300 hours local time are provided in Figure 7. In this figure, it is evident that the model calculations that include the linear height variation in the drift velocities best replicate the features shown in the data. This is most apparent at 1900 hours in the northern hemisphere and in the shape of anomaly in the modeled results at 1200 and 2300 hours.

The comparisons illustrated in Figures 6 and 7 illustrate the sensitivity of the equatorial anomaly to ion and electron temperatures and  $E \times B$  drift velocities. Although the data clearly show asymmetries that are likely due to the neutral winds, it is beyond the scope of this paper to replicate this asymmetry with the model. Future modeling studies will include efforts to investigate neutral wind effects and to refine the  $E \times B$  drift gradient applied in the model. In this study,

GTIM has shown the capability to reproduce some of the major features of measured data in the low-latitude region, even under geomagnetically disturbed conditions.

## Conclusions

The first attempt at measuring the day-to-day variability of TEC over a large geographic latitude range has been successful. The database collected illustrates the large day-to-day variability in the occurrence, location, and amplitude of the equatorial anomaly. A surprising feature uncovered by this study is that the TEC values are so low in the latitude range greater than  $\pm 40^\circ$  and that the latitudinal gradients in TEC are steeper on the poleward edge of the southern anomaly peak than on the poleward edge of the northern anomaly peak. The multistation data measurement technique has been validated by simultaneous measurements of TEC from dual-frequency GPS and dual-frequency altimeter measurements from the TOPEX/Poseidon satellite.

Model comparisons with observations have illustrated, for the first time, the sensitivity of the equatorial anomaly to changes in ion and electron temperatures and to vertical  $E \times B$  drift velocities. In particular, the results show that the altitude variations of vertical drift velocities have a significant impact on the development of the equatorial anomaly. Additional modeling work is required to further test variations in drift gradients and to investigate neutral wind effects to determine how closely the model can fit the experimental data over a wide latitude range.

One of the prime purposes of the campaign was to develop an equatorial database to be used in ionospheric tomography reconstructions. The study demonstrates that the absence of a station near the geomagnetic equator significantly hampers the reconstruction of the equatorial ionosphere. Future tomographic campaign organizers, take note!

## Appendix: Origin of the Term "Equatorial Fountain"

Many authors, including Balan and Bailey [1996], have shown that the equatorial fountain greatly increases both peak electron density and TEC throughout the low-latitude ionosphere; but who originated this very apt expression for the source of the largest ionization in the world? The term "fountain effect" was quoted by Hanson and Moffett [1966,

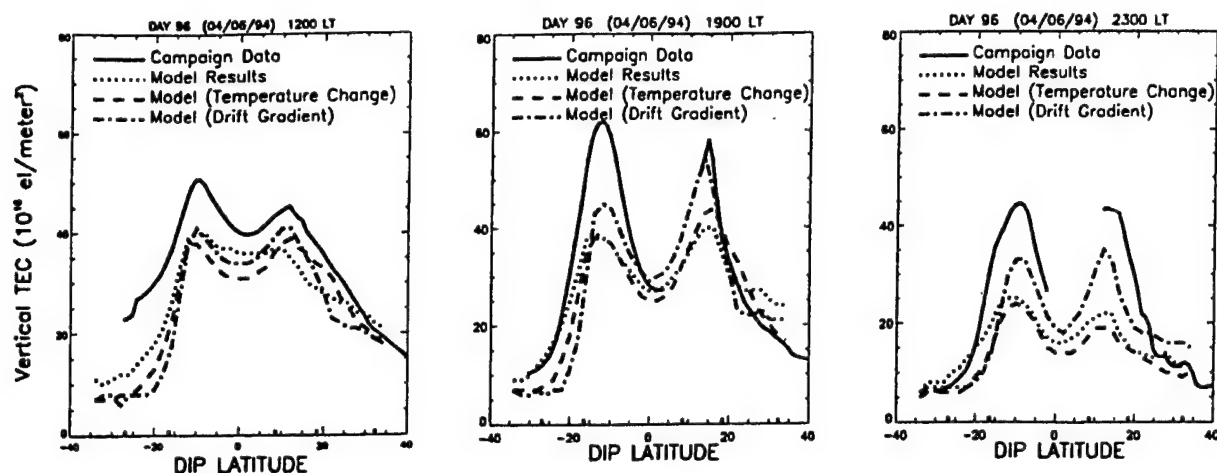


Figure 7. Comparison of data versus model calculations at 1200, 1900, and 2300 hours local time.

p.5560], as "Martyn (1955) envisages a 'fountain effect' in which the ionization is lifted upward at low latitudes and then deposited at higher latitudes by diffusion along the field lines." However, the term "fountain effect" is not found in the work by Martyn [1955].

Rush and Richmond [1973, p. 1171] stated "Duncan (1960) has termed this the 'fountain theory'." However, the term "fountain theory" is not found in the work by Duncan [1960]. After an extensive search, it was discovered that Wright [1962] was the person who coined this term. Wright [1962, p.7], in his discussion of the mechanism producing the equatorial anomaly in *F* region ionization, stated "We propose the term 'Equatorial Fountain' as a concise term for these processes." Thus the historical record is now set straight.

**Acknowledgments.** The authors would like to thank the many members of the Ionospheric Effects Division at Phillips Laboratory who participated in the campaign. Air Force Captain William A. Pakula deserves particular mention for his outstanding role as Operations Manager for the campaign. Additional appreciation is extended to Dwight T. Decker of Boston College for many useful discussions on ionospheric modeling and to Virginia Ewell and Jane Vladimer of the Electrical, Computer, and Systems Engineering Department at Boston University for their assistance in processing the TOPEX measurements used for PANAM data validation. Finally, we would like to thank Jay Spaulding at the U.S. Coast Guard Research and Development Center in Groton, Connecticut, for the loan of the GPS Ashtech receiver that was used in Merida, Venezuela.

## References

- Anderson, D. N., A theoretical study of the ionospheric *F*-region equatorial anomaly, I, Theory, *Planet. Space Sci.*, **21**, 409-419, 1973.
- Anderson, D. N., D. T. Decker, and C. E. Valladares, Global Theoretical Ionospheric Model (GTIM), in *STEP Hand Book*, edited by R. W. Schunk, pp. 133-152, Utah State Univ., Logan, 1996.
- Balan, N., and G. J. Bailey, Modeling studies of the equatorial plasma fountain and equatorial anomaly, *Adv. Space Res.*, **18**(3), 107-116, 1996.
- Brace, L. H., and R. F. Theis, Global empirical models of ionospheric electron temperatures in the upper *F*-region and plasmasphere based on *in situ* measurements for the Atmospheric Explorer-C, ISIS-1 and ISIS-2 satellites, *J. Atmos. Terr. Phys.*, **43**, 1317-1343, 1981.
- Deshpande, M. R., R. G. Rastogi, H. O. Vats, J. A. Klobuchar, and G. Sethia, Effect of the electrojet on the total electron content over the Indian subcontinent, *Nature*, **267**, 599-600, 1977.
- Duncan, R. A., The equatorial *F*-region of the ionosphere, *J. Atmos. Terr. Phys.*, **18**, 89-100, 1960.
- Evans, J. V., and J. M. Holt, The combined use of satellite differential doppler and ground-based measurements for ionospheric studies, *IEEE Trans. Antennas Propag.*, **AP-21**, 685-692, 1973.
- Fejer, B. G., The equatorial ionospheric electric fields, a review, *J. Atmos. Terr. Phys.*, **43**, 377-386, 1981.
- Hanson, W. B., and R. J. Moffett, Ionization transport effects in the equatorial *F* region, *J. Geophys. Res.*, **71** (23), 5559-5572, 1966.
- International Association of Geodesy, *International GPS Service for Geodynamics*, Cent. Bur., Jet Propul. Lab., Pasadena, Calif., 1995.

- Imel, D. A., Evaluation of the TOPEX/POSEIDON dual-frequency ionosphere correction, *J. Geophys. Res.*, 99 (C12), 24,895-24,906, 1994.
- Kersley, L., J. A. T. Heaton, S. E. Pryse, and T. D. Raymund, Experimental ionospheric tomography with ionosonde input and EISCAT verification, *Ann. Geophys.*, 11, 1064-1074, 1993.
- Klobuchar, J. A., D. N. Anderson, and P. H. Doherty, Model studies of the latitudinal extent of the equatorial anomaly during equinoctial conditions, *Radio Sci.*, 26 (4), 1025-1047, 1991.
- Leitinger, R., G. Schmidt, and A. Tauriainen, An evaluation method combining the differential doppler measurements from two stations that enables the calculation of the electron content of the ionosphere, *J. Geophys.*, 41, 201-213, 1975.
- Martyn, D. F., Theory of height and ionization density changes at the maximum of a chapman-like region, taking account of ion production, decay, diffusion, and tidal drift, in *Proceedings of Cambridge Conference*, pp. 254-259, Phys. Soc., London, 1955.
- Newton, R. R., The Navy Navigation Satellite System, *Space Res.*, 7, 735-763, 1967.
- Pakula, W. A., P. F. Fougere, J. A. Klobuchar, H. J. Kuenzler, M. J. Buonsanto, J. M. Roth, J. C. Foster, and R. E. Sheehan, Tomographic reconstruction of the ionosphere over North America with comparisons to ground-based radar, *Radio Sci.*, 30 (1), 89-103, 1995.
- Pingree, J. E., and B. G. Fejer, On the height variation of the equatorial *F*-region vertical plasma drifts, *J. Geophys. Res.*, 92 (A5), 4763-4766, 1987.
- Preble, A. J., D. N. Anderson, B. G. Fejer, and P. H. Doherty, Comparison between calculated and observed *F*-region electron density profiles at Jicamarca, Peru, *Radio Sci.*, 29 (4), 857-866, 1994.
- Rastogi, R. G., and J. A. Klobuchar, Ionospheric electron content within the equatorial *F*<sub>2</sub> layer anomaly belt, *J. Geophys. Res.*, 95 (A11), 19,045-19,052, 1990.
- Rush, C. M., and A. D. Richmond, The relationship between the structure of the equatorial anomaly and the strength of the equatorial electrojet, *J. Atmos. Terr. Phys.*, 35, 1171-1180, 1973.
- Sterling, D. L., W. B. Hanson, R. J. Moffett, and R. G. Baxter, Influence of electrodynamic drifts and neutral air winds on some features of the *F*<sub>2</sub> region, *Radio Sci.*, 4, 1005-1023, 1969.
- Strobel, D. F., and M. B. McElroy, The *F*<sub>2</sub>-layer at mid-latitudes, *Planet. Space Sci.*, 18, 1181-1202, 1970.
- Su, Y. Z., K. I. Oyama, G. J. Bailey, T. Takahashi, and S. Watanabe, Comparison of satellite electron density and temperature measurements at low latitudes with a plasmasphere-ionosphere model, *J. Geophys. Res.*, 100 (A8), 14,591-14,604, 1995.
- Tsedilina, E. E., O. V. Weitsman, and H. Soicher, Time delay of transionospheric radio signals in a horizontally inhomogeneous ionosphere, *Radio Sci.*, 29 (3), 625-630, 1994.
- Whalen, J. A., The equatorial *F* layer:  $\pm 30^\circ$  DIPLAT profiles for a continuous 30 day period (abstract), *Eos Trans AGU*, 74 (43), Fall Meet. Suppl., 457, 1993.
- Whalen, J. A., Mapping a bubble at dip equator and anomaly with oblique ionospheric soundings of range spread *F'*, *J. Geophys. Res.*, 101(A3), 5185-5193, 1996.
- Wright, J. W., Vertical cross sections of the ionosphere across the geomagnetic equator, *NBS Tech. Note* 138, U.S. Dept. of Commer., Washington, D. C., 1962.

D. N. Anderson, Phillips Laboratory/GPSM, 29 Randolph Road, Hanscom Air Force Base, MA 01731. (e-mail: danderson@plh.af.mil)

P. H. Doherty, Institute for Scientific Research, Boston College, St. Clement's Hall, Room 402, 140 Commonwealth Avenue, Chestnut Hill, MA 02167. (e-mail: doherty@plh.af.mil)

John A. Klobuchar, Total Electronic Concepts, 27 Conant Road, Lincoln, MA 01773. (e-mail: tecgps@aol.com)

(Received October 10, 1996; revised March 3, 1997; accepted March 19, 1997.)

# Description and Assessment of Real-Time Algorithms to Estimate the Ionospheric Error Bounds for WAAS\*

ROBERT S. CONKER, M. BAKRY EL-ARINI, and  
THOMAS W. ALBERTSON

The MITRE Corporation, McLean, Virginia

JOHN A. KLOBUCHAR

Innovative Solutions International, Vienna, Virginia

PATRICIA H. DOHERTY

Boston College, Boston, Massachusetts

Received July 1996

Revised December 1996

## ABSTRACT

*The Federal Aviation Administration (FAA) is developing a Wide-Area Augmentation System (WAAS) to augment GPS for use during en route through Category I (CAT I) precision approach flight operations. WAAS has three components: (1) extra ranging sources using geostationary earth orbiting (GEO) communications satellites; (2) a vector of corrections to the GPS signal-in-space, including components for ionospheric delay estimations and clock and ephemeris errors; and (3) integrity monitoring to alert users of out-of-tolerance conditions. This paper describes real-time ionospheric algorithms that are part of the accuracy and integrity monitoring functions. A performance assessment is made with respect to the requirements specified in the WAAS procurement.*

\*This paper is based on system analysis studies performed by the Center for Advanced Aviation System Development (CAASD) of the MITRE Corporation and the Air Force Phillips Laboratory for the FAA Satellite Program Office. This paper reflects the views of the authors, who are responsible for the accuracy of the facts, analyses, and suggestions presented herein, and does not reflect the official views or policy of the FAA.

## INTRODUCTION

The Federal Aviation Administration (FAA) Satellite Program Office is developing a Wide-Area Augmentation System (WAAS) to augment GPS for use during en route through Category I (CAT I) precision approach flight operations. WAAS has three components: (1) extra ranging sources using geostationary earth orbiting (GEO) communications satellites; (2) a vector of corrections to the GPS signal-in-space, including components for ionospheric delay estimations and clock and ephemeris errors; and (3) an integrity monitoring function to alert users of out-of-tolerance operations. The WAAS will be implemented in three phases.

As part of the integrity monitoring function, the WAAS sends to the user a bound on the postcorrection ionospheric vertical error at each of the ionospheric grid points (IGPs) of an ionospheric delay correction grid covering the service area. The ionospheric error bound at each IGP is called the grid ionospheric vertical error (GIVE).

The ionospheric delay estimates are used by the user's receiver to correct the pseudorange measurements. Using the appropriate GIVE values, the user also calculates a vertical error bound on ionospheric delay after correction at each of his own ionospheric pierce points (IPPs). This error bound is called the user ionospheric vertical error (UIVE). Any UIVE calculated from the GIVEs must bound the user's postcorrection vertical ionospheric error with a probability of 0.999.

Finally, the user calculates a conservative bound of the vertical position error (VPE) using the calculated UIVEs, combined with other error bounds. The requirement for this bound is  $VPE \leq 19.2$  m. The WAAS Specification [1] was changed in the fall of 1995 to eliminate the initial and end-state GIVE bounds of 2.0 and 1.5 m, respectively. This allowed greater flexibility in meeting the VPE requirement. Nevertheless, some initial analysis has shown that to satisfy the VPE requirement, GIVE values of  $\leq 2.0$  m for Phase 1 and  $\leq 1.5$  m for Phase 3 are needed.

The GIVE and UIVE algorithms described in this paper have been developed and tested using P-code data measured from 5 mini-roque L1/L2 dual-frequency GPS receivers located at five sites on the east coast of the conterminous United States (CONUS) over a 9 month period. This period is characterized by a generally "quiet" ionosphere with periodic major and severe geomagnetic storm activity. L1/L2 receiver biases (measured by Stanford Telecommunication Inc. for the National Satellite Test Bed [NSTB]) are



included in the estimation. Also included are the L1/L2 satellite biases estimated and published in [2]. One of the sites is selectively employed as a user, and its dual-frequency measurements at each of its IPPs are used as truth for determining the effectiveness of the numerical estimates. The results are then extrapolated to the proposed WAAS architecture to determine whether the WAAS ionospheric function availability requirements can be met. Based on the availability of in-tolerance UIVE and GIVE values and assumptions regarding the proposed WAAS ground system topography and GPS/GEO constellation, a service volume related to the ionospheric function is defined and described in this paper for Phase 1 WAAS. The GIVE algorithm developed in this paper is being considered by the WAAS contractor for use in the WAAS master station (WMS).

## PURPOSE AND SCOPE

This paper describes real-time algorithms to (1) estimate the GIVE value to be included in the WAAS broadcast, and (2) determine the resultant UIVE magnitudes expected to be calculated at the user receiver, based on actual ionospheric data collected at key points in CONUS over a period of months. The GIVE and UIVE bounds and their methods of determination are important elements for assuring the integrity of the WAAS corrected position solution.

This paper describes the ionospheric function of WAAS as envisioned by the authors and as originally specified by the FAA, and does not necessarily represent the actual implementation of that function in WAAS. For example, since this work was done, certain changes have been made in the WAAS message format, such as changes in ionospheric correction quantization and the GIVE table. In addition, the WAAS implementation by the prime contractor differs from the architectural and algorithmic description contained in this paper.

## A SIMPLIFIED ARCHITECTURE FOR WAAS IONOSPHERIC FUNCTIONS

For Phase 1 WAAS there will be 24 wide-area reference stations (WRSs), 2 WMSs, 3 ground earth station (GES) sites, and 2 GEO satellites in addition to the 24 GPS satellites. Each WRS consists of three sets of wide-area receiver equipment (WRE). Each WRE can receive L1/L2 dual-frequency codeless GPS signals and an L1 GEO signal. The WRE may include weather sensors in addition to the communications equipment and computers.

Figure 1 shows a simplified diagram of the WAAS ionospheric functions and the minimum set of equipment needed to calculate these functions. In this figure, there are three groups of receivers with their associated antennas and weather stations, one WMS, one GES, and GPS and GEO satellites. (Phase I WAAS will have more redundancy than is shown in this figure.) The first group consists of  $n_1$  ( $= 24$  for Phase 1 WAAS) WREs. The main function of these receivers is to collect the pseudorange (PR) and carrier-phase data for each visible GPS satellite at L1 and L2 frequency bands, and send this data to the WMS. In addition, any weather data collected by the sensors is sent to the WMS. The WMS processes this data through a Kalman filter to calculate the carrier-smoothed vertical ionospheric delays for each GPS satellite IPP. Then the WMS uses the calculated vertical ionospheric delays at the WRS IPPs to calculate the vertical ionospheric delays for each IGP of the ionospheric grid. The weather information, if any, is used to calculate or verify the integrity of the tropospheric delay at each WRS location.

The measured slant ionospheric delay for each satellite is subtracted from the PR measurement for the same satellite. The residual PRs are used to calculate the satellite clock and ephemeris corrections. The latter two corrections are not discussed in this paper.

The second group of receivers consists of  $n_2$  WREs. For Phase 1 WAAS,  $n_2 = n_1 = 24$ , and this group of receivers is collocated with the first group. These receivers send their measurements to the WMS in a manner similar to that of the first group. The WMS uses this data and the vertical delays of the ionospheric grid, which were calculated using the data from the first group of WREs, to calculate the GIVE for each of the IGPs of the ionospheric grid. The methodology of the GIVE calculation is shown later in this paper.

The GIVEs are processed by the user receivers to calculate UIVEs, which are specified to bound vertical ionospheric errors (after WAAS corrections) with a probability of 0.999. WAAS is planning for a third group of receivers to be used as a hot standby for the other two groups. As shown in Figure 1, the authors are proposing an additional and smaller group of receivers ( $n_3 \leq n_1$ ) that are not collocated with the WRSs, but are deployed as wide-area monitors so they can monitor the success rate of this error bound. It is important that these monitors not be collocated with the WRSs, since if they were collocated, they would measure the bounding success rate at precisely those IPPs where the original data was collected and the error bounds formed. These monitors essentially act as users. Their

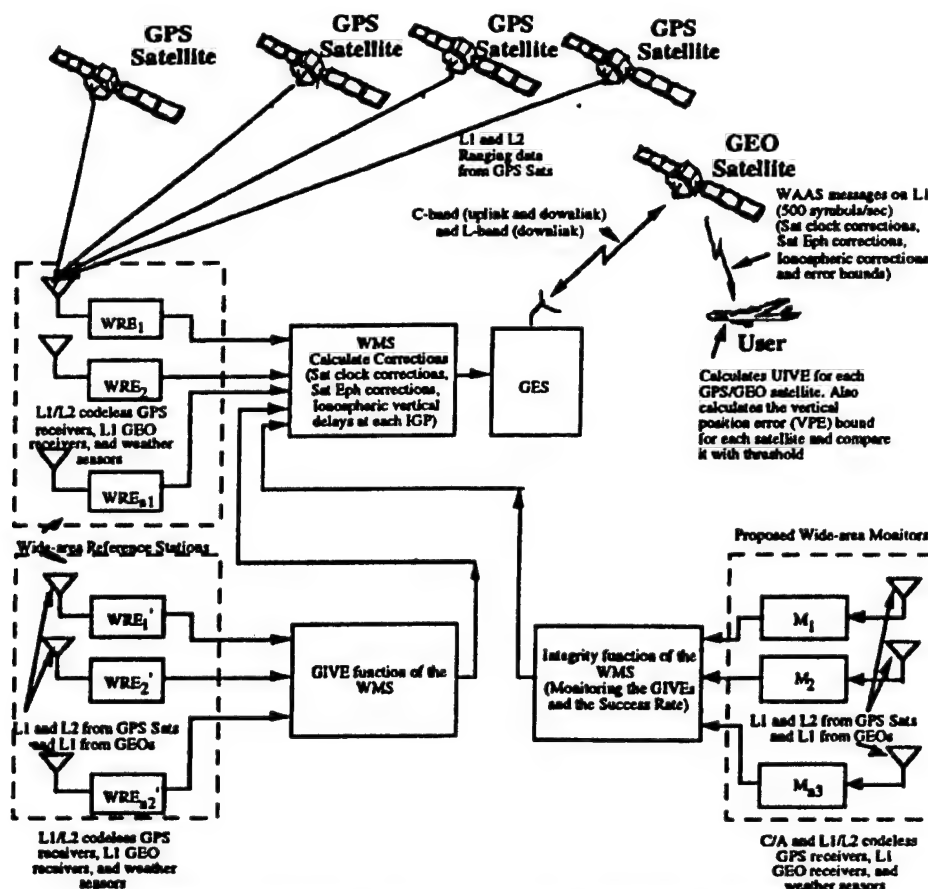


Fig. 1—A Simplified Diagram of the WAAS Ionospheric Functions Including Proposed Wide-Area Monitors

measurements are sent to the WMS. The WMS compares each monitor's vertical ionospheric errors (from measured data) with its corresponding calculated UIVEs. If the errors at any monitor exceed the UIVE, the maximum excess above UIVE is added to each GIVE. During the next update period, the WMS adds the maximum excess of monitor errors above UIVE to each GIVE of the region containing that monitor. This constitutes a closed-loop system. As will be seen from the results given in this paper, the success rate is increased by this closed-loop monitoring system. The GIVEs are expected to be increased only rarely, and then by a few centimeters. Just as the second group of receivers determines how well the grid is representing ionospheric delay, this third group of receivers determines the effectiveness of the error bounds.

## DEVELOPMENT CONSTRAINTS

The development of Phase 1 WAAS must take place within the limits of the physical resources available, as well as the performance and availability requirements that have been established.

## WAAS Physical Environment

The Phase 1 WAAS will employ a satellite constellation consisting of 24 GPS satellites and 2 GEO satellites. The ground station architecture will consist of 24 WRSs (21 in CONUS, and 1 each in Alaska, Hawaii, and Puerto Rico) and 2 WMSs. For Phases 2 and 3 WAAS, additional WRSs, WMSs, and GEOs may be required. Each WRS will have GPS dual-frequency receivers that periodically collect ionospheric data from the visible constellation. Currently, this period is 10 s. The raw data will be sent to the WMS, which will estimate ionospheric delays and error bounds at grid points and broadcast these to the users approximately every 5 min via geostationary communications satellites. The grid size has been fixed at 5 deg in CONUS, 10 deg beyond 55° latitude. These GIVE and UIVE algorithms were designed and tested for 5 deg grid squares (at midlatitudes), and they may require modification beyond 55° latitude.

## WAAS Ionospheric Requirements

For Phase 1 WAAS, the ionospheric function is defined as available if UIVEs calculated from

GIVEs bound the postcorrection user-interpolated ionospheric error with a probability of 0.999. Also, the user's vertical position error bound (VPE), which is calculated from the UIVEs combined with other user error bound components (e.g., user differential range error [UDRE], receiver noise, tropospheric error, multipath, and latency), should bound the user's vertical position error with probability  $\geq 0.999$ . This VPE should be  $\leq 19.2$  m at 200 ft decision height (DH). As mentioned before, there is no explicit requirement for GIVE, but a reasonable goal is to have  $GIVE \leq 2.0$  m for Phases 1 and 2 and  $\leq 1.5$  m for Phase 3. In Phase 1 WAAS, the system is required to be available 95 percent of the time over 50 percent of CONUS [1]. Because of WAAS message size restrictions, the grid-delay broadcast to the user must be quantized by  $q_u(0.0625$  m) such that  $\text{mod}(\text{IGP\_delay}, q_u) = 0$ . In addition, GIVE values on the grid must be given as an index to a table of maximum GIVE values, as shown in Table 1. Therefore, for each IGP, the WMS broadcasts the quantized vertical ionospheric delay and the GIVE indicator (GIVEI) corresponding to the GIVE values shown in Table 1, as required in the WAAS specification [1]. The user receiver will process these broadcast values to calculate the vertical ionospheric delay and UIVE for each of its IPPs. It should be noted that there is currently a proposal by RTCA to change both the quantization amount of ionospheric delay and the gradation of the GIVE table.

#### DESCRIPTION OF ALGORITHMS

Periodically (every 10 s), the WMS receives, for each satellite, PR and carrier-phase measured data on L1 and L2 from each WRS. A Kalman filter, similar to the filter described by [3, 4] and designed and implemented as described in [5] for

Table 1—GIVE Table

GIVEI	GIVE(m)
0	0.80
1	1.00
2	1.10
3	1.20
4	1.30
5	1.40
6	1.50
7	1.75
8	2.00
9	2.25
10	2.50
11	2.75
12	3.00
13	5.00
14	10.00
15	50.00

the FAA NSTB, processes this measured data to estimate (and smooth) the vertical ionospheric delays at the IPPs for each WRS. This information is used to estimate ionospheric delays at IGP on a  $5 \times 5$  deg imaginary grid located 350 km above the earth.

A slightly modified version of the ionospheric grid algorithm described in [6] uses equation (1) below to estimate the vertical ionospheric delays at each IGP. This ionospheric grid algorithm is a simple interpolation scheme that weights data directly according to the sine of the elevation angle and inversely according to distance. All IPPs farther than 600 nmi from the interpolated position are ignored in order to increase local fidelity while at the same time gathering enough points to produce a useful average. At the beginning of each data collection interval, the maximum gradient in the 16 grid squares surrounding each grid node is determined. If the gradient exceeds the equivalent of 1.6 m/5 deg of earth-centered angle, the distance limit is reduced from 600 to 425 nmi for averaging at that grid node. (The selection of the 600 nmi distance and the 1.6 m/5 deg gradient limit is based on extensive testing of the FAA ionospheric data.) This operation sacrifices pierce-point density in favor of locality when the ionospheric gradient is large. This latter distance restriction of 425 nmi was chosen since it is approximately the maximum diagonal distance of a grid square and ensures inclusion of all points in the 4 grid squares surrounding a grid node.

The general formula for interpolation that is used by the WMS to calculate the vertical ionospheric delay at each IGP (number  $p$ ) from the measurements at  $n$  IPPs is given in equation (1) below. The same interpolation equation also calculates the vertical ionospheric delay at the user's IPP (number  $p$ ) from the broadcast vertical ionospheric delays at  $n = 4$  IGP of the cell containing the user's IPP.

In general, for any set of  $n$  points ( $i = 1, 2, \dots, n$ ), the vertical ionospheric delay can be estimated at a point  $p$  through the following interpolation formula [6]:

$$\hat{D}_{vp} = \frac{\sum_{i=1}^n \left( \frac{\tau_p}{\tau_i} \right) \left( \frac{\sin(\theta_i)}{d_{ip}} \right) D_{vi}}{\sum_{i=1}^n \frac{\sin(\theta_i)}{d_{ip}}}, \quad d_{ip} \neq 0$$

$$= D_{vj} \quad d_{jp} = 0; j = 1, 2, \dots, n \quad (1)$$

where

$D_{vi}$  is vertical ionospheric delay at the  $i$ th point

$\hat{D}_{vp}$  is estimated vertical ionospheric delay at point  $p$

- $d_{ip}$  is distance between the  $i$ th given point and point  $p$
- $\tau_i$  is predicted vertical ionospheric delay at the  $i$ th point as estimated by an ionospheric model [7]
- $\tau_p$  is predicted vertical ionospheric delay at point  $p$  from the same ionospheric model
- $\theta_i$  is elevation angle from monitor station to satellite

At each IPP of the second group of receivers  $WRE'_1, WRE'_2, \dots, WRE'_n$  shown in Figure 1, the WMS estimates the value of vertical delay using equation (1), where the  $n$  given points refer to the values of vertical ionospheric delay at the 4 surrounding grid nodes. The truth values supplied by each receiver are used to determine the vertical errors at the  $i$ th IPP at time  $t$ :

$$e_{vi}(t) = \hat{D}_{vi}(t) - D_{vi}(t) \quad (2)$$

where  $\hat{D}_{vi}(t)$  is predicted delay at time  $t$  at the monitor's IPP based on the surrounding 4 grid nodes, and  $D_{vi}(t)$  is measured value of delay at time  $t$  at the monitor's IPP.

At the end of the update period (currently 5 min), the WMS will broadcast the latest delay values to users. These delay values are required to be quantized with a scale factor of  $q_u (= 0.0625 \text{ m})$  such that the value of delay at row  $r$  and column  $c$  of the grid ( $IGP_{rc}$ ) is:

$$\begin{aligned} \hat{D}_v(IGP_{rc}) &= \hat{D}_v(IGP_{rc}) - h + q_u, & h &\geq \frac{q_u}{2} \\ &= \hat{D}_v(IGP_{rc}) - h, & h < \frac{q_u}{2} \end{aligned} \quad (3)$$

where  $h = \text{mod}(\hat{D}_v(IGP_{rc}), q_u)$ .

Because of this requirement, the user receiver may receive a delay value that is up to  $q_u/2 (= 0.03125 \text{ m})$  removed from that of the WMS. This can be somewhat mitigated by adding the exact quantization error at each grid node to the GIVE at that grid node. Here the maximum quantization error  $q_u/2 \text{ m}$  has been added to the GIVE estimates at all IGPs.

#### Calculation of GIVEs

Since the broadcast of vertical delays/GIVEs to the user will occur approximately every 5 min, the data collection interval has been set to 5 min (although this is not required). Consequently, the WMS will collect  $m = 30$  error values (1 every 10 s) for each IPP sequence of the monitor. A GIVE will be calculated for every IGP on condition that there are at least 3 surrounding grid squares, each with at least 1 IPP sequence; otherwise, the GIVE is marked unavailable, which means it cannot be used in any subsequent UIVE

calculation for that period. This restrictive condition guarantees that GIVEs will be calculated only when the local pierce-point density is sufficiently high, and is related to a subsequent discussion on service volume availability. Where this condition is met, a conservative tolerance bound is constructed with error bound  $E_{vi}$  for every monitor IPP sequence in the 4 grid squares surrounding node  $IGP_{rc}$ . This bound is derived from a two-sided  $100\gamma\%$  statistical tolerance interval that contains at least a proportion  $p$  of a normally distributed population and is given by [8, 9]

$$E_{vi} = |\bar{e}_{vi}| + g_{(\gamma;p;m)} s_{vi} \quad (4)$$

with

$$\bar{e}_{vi} = \frac{1}{m} \sum_{k=1}^m e_{vi}(t_k) \quad (5)$$

$$s_{vi} = \sqrt{\frac{1}{m-1} \sum_{k=1}^m (\bar{e}_{vi} - e_{vi}(t_k))^2} \quad (6)$$

where  $g_{(\gamma;p;m)} = 5.43$  for confidence level  $\gamma = 0.999$ ,  $p = 0.999$ , and sample size  $m = 30$ . Of course,  $g_{(\gamma;p;m)}$  will have a different value if any of the three parameters  $\gamma$ ,  $p$ , or  $m$  is changed. The value  $g_{(\gamma;p;m)} = 5.43$  was calculated using the method described in [9].

The WMS then determines the grid vertical absolute error bias,  $\hat{e}_v$ , at node  $IGP_{rc}$  by using the interpolation scheme described earlier, but without the ionospheric model values:

$$\hat{e}_v(IGP_{rc}) = \frac{\sum_{i=1}^n \left( \frac{\sin(\theta_i)}{d_{ip}} \right) |e_{vi}(t_m)|}{\sum_{i=1}^n \frac{\sin(\theta_i)}{d_{ip}}} \quad (7)$$

This is an estimate of the magnitude of the underlying error biases in the grid at each grid node.

Finally, the GIVE is computed as the sum of the absolute error bias at the node, the maximum tolerance error bound in the 4 surrounding grid squares, and an allowance for the vertical ionospheric delay quantization requirement at the IGP:

$$\text{GIVE}(IGP_{rc}) = \hat{e}_v(IGP_{rc}) + \max_k \{E_{vk}\} + \frac{q_u}{2} \quad (8)$$

where  $E_{vk}$  is the tolerance bound for the  $k$ th monitor IPP sequence in one of the 4 surrounding squares.

This conservative formulation of GIVE is due to the problem of spatial decorrelation of data. Statistical tolerance bounds are of course determined at the places where data exists.

However, the required GIVE and UIVE bounds must be calculated at places where there is no data. A 0.999 tolerance bound can decay when moving significantly away from the location where it was calculated. Simple interpolation was generally found to be insufficient for bounding errors. Consequently, it was decided to use the maximum tolerance bound found in the neighborhood of each grid point. Because the GIVE sent to the user is required to come from a table value, the calculated GIVE is raised to the next highest value in Table 1.

#### Calculation of UIVEs

As mentioned previously, the GIVEs and vertical delay estimates at each IGP are broadcast to the user approximately every 5 min. With this information and the IPP location, the user receiver calculates the predicted vertical delay and the UIVE at that IPP. The UIVE is the maximum of the surrounding IGP GIVEs, with the condition that there be at least 3 GIVEs marked available:

$$\text{UIVE}_p = \max_{k=0,1}(\text{GIVE}(\text{IGP}_{r+k,c+k})) \quad (9)$$

where  $\text{IGP}_\pi$  indicates the grid node at the southwest corner of the square that contains the user's IPP. Again, the maximum was used instead of interpolation since it provided appreciably better results on the test set of data.

#### Closed-Loop Monitoring

To strike a balance between the often competing requirements of low GIVEs and high error bound probabilities, a system of independent regional monitors (Monitors  $M_1, M_2, \dots, M_n$  in Figure 1) at locations other than WRSs is proposed that would act as users in the sense of determining predicted delay and UIVEs for the monitor's IPPs from the grid. The monitor's truth values would be compared with the predicted delay from the grid to determine the actual error. A monitor would determine the maximum amount (if any) by which its actual vertical error exceeded any UIVE at any time in the 5 min data collection period. At the next grid update time, this amount would be used to increase the GIVEs in the region with the monitor that detected the excess. The excess error would be added to the newly calculated GIVEs sent to the user, but would not be added to the GIVEs sent to the monitor. This group of closed-loop monitors would have minor effects on the results, as will be seen in the next section. The concept itself may be important, however, in cases where the ionosphere changes more rapidly than normal (e.g., during severe geomagnetic storms).

## RESULTS

To determine whether the ionospheric requirements for an initial WAAS are met with these algorithms, it is necessary to:

- 1) Examine the numerical results of applying the algorithms to the 52-day set of ionospheric data that was available in order to assess whether the 2.0 m limit on GIVE can be attained while UIVEs bound the residual errors at a consistently high rate.
- 2) Examine the feasibility of bounding the ionospheric errors during a disturbed ionosphere (e.g., during a severe geomagnetic storm). Do the algorithms work during these severe storms? One would expect the GIVEs to be greater than 2.0 m in such cases, but can the errors be consistently bounded?
- 3) Examine what effect the real-time requirement for high data density has on the size of the service volume in order to assess whether this algorithm supports daily availability of 95 percent over 50 percent of CONUS.

#### Test Environment

It was not possible to test the complete environment that is proposed for the WAAS in Figure 1. The test data originated from five sites in the eastern CONUS. There was only one receiver at each site. One site was selected as a user and monitor site.

#### Numerical Results

To assess the effectiveness of these algorithms, actual user errors were compared with the calculated UIVEs at each user IPP where all previously mentioned conditions were met. In this way, the percentage of time the UIVE actually bounded the user's error was measured. The condition that there be at least 1 IPP in each of at least 3 surrounding grid squares at all times when GIVEs were calculated eliminated several data sets. The resulting data sets, which met this criterion at least some time during the day, consisted of 50 days of quiet ionosphere and 2 days of severe stormy geomagnetic conditions. (See Table 2.)

Table 2—Test Period

Quiet Ionospheric and Major Storms Data ( $A_p \leq 100$ )		Disturbed Ionospheric Data (Severe Geomagnetic Storm) ( $A_p > 100$ )	
November 1992:	6–7, 10–13, 16–21, 25–30	April 1993:	4*–5
December 1992:	8, 10–13		
April 1993:	4*, 7–18, 21		
June 1993:	21, 23		
July 1993:	2–5, 7–12, 14		

\*The morning of April 4 was quiet, and the afternoon was stormy.



Figures 2, 3, and 4 depict the results for all periods of geomagnetic activity. Figure 2 shows the mean, standard deviation (sigma), and 95th and 99th percentiles for GIVEs. On 4 April 1993, the 95th percentile derived from the calculated GIVEs before translation into table values was approximately 4 m. Since there was no 4 m table value, 5 m was chosen. Also, on 8 April 1993, the 99th percentile before translation into table values was approximately 3.6 m. Again, the next highest table value was 5. These two examples suggest that several more gradations in Table 1 above 3 m would lessen excessive overbounding of GIVEs. It is seen from this figure that the 95th percentiles of GIVEs are below 2.0 m most of the time.

Figure 3 shows the percentage of GIVEs below 2.0 m. This percentage is between 95 and 100 percent for all but 4 days. The percentages for these days are 90.2 percent on 19 November 1992, 91.9 percent on 8 December 1992, 93 percent on 2 July 1993, and 60.8 percent on 4 April 1993. On the first 2 days (19 November and 8 December

1992), the ionosphere was quiet ( $A_p \leq 50$ ). (The  $A_p$  index is a measure of geomagnetic activity published daily by the National Geophysical Data Center of the National Oceanic and Atmospheric Administration. It is a daily averaged planetary index based on data from a worldwide set of specific stations.) The 95th percentiles of GIVE for both days were 2.25 m. On the third day (2 July 1993), there was a major (not severe) geomagnetic storm ( $50 < A_p \leq 100$ ), which caused a large gradient in the ionosphere. The 95th percentile of the GIVE for that day was also 2.25 m. On the fourth day (4 April 1993), there was a severe geomagnetic storm ( $A_p > 100$ ), which caused a large ionospheric gradient. The 95th percentile of the GIVE for that day was 5.0 m.

Figure 4 shows the percentage of time that calculated errors (using truth values) were below the predicted UIVE value for the closed-loop monitor and for the user. The monitor and user results are almost identical for the majority of days. The monitor helps improve the success rate

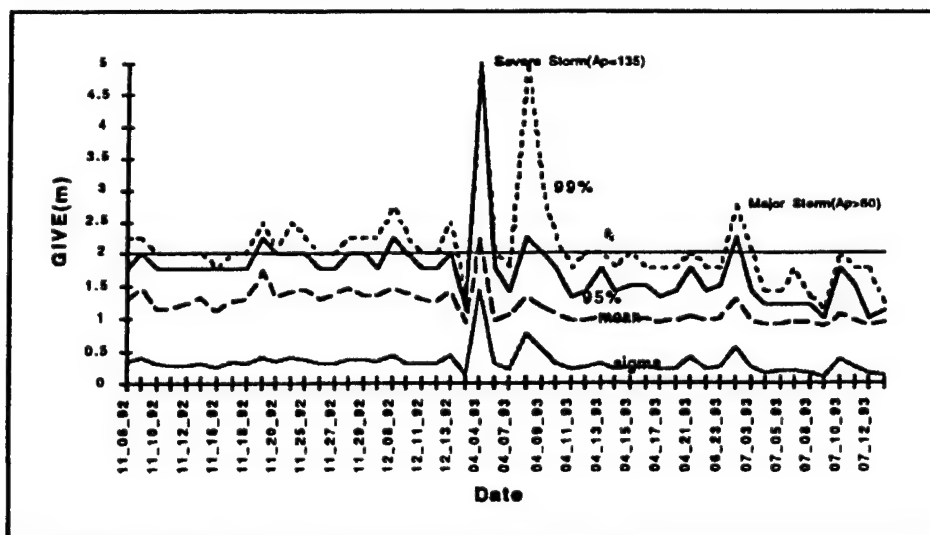


Fig. 2—Magnitude of GIVE

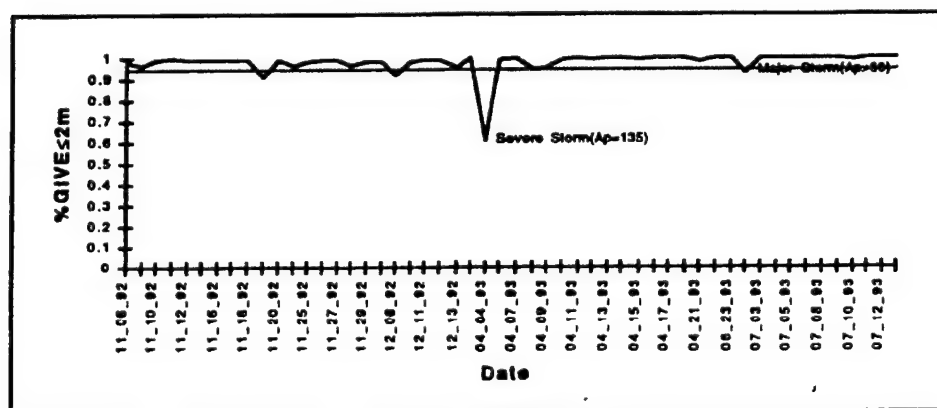


Fig. 3—Percentage GIVEs  $\leq 2.0m$



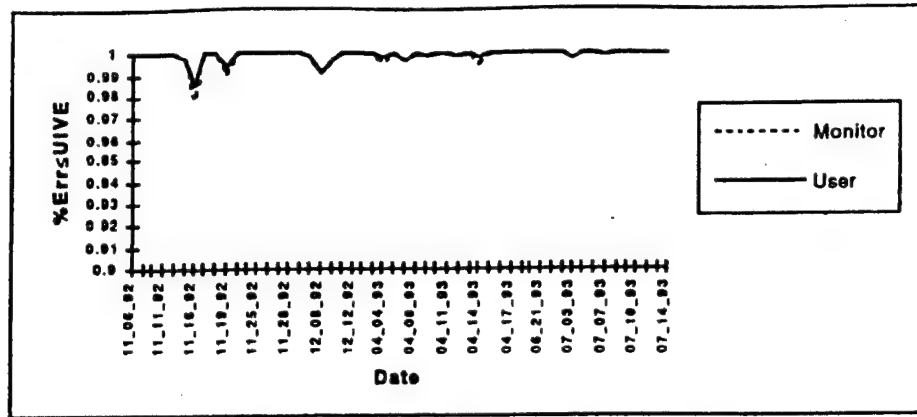


Fig. 4—Percentage Monitor and User Errors  $\leq$  UIVE

of the user when the rate is relatively low. For example, on 16 November 1992, the success rate for the user was increased from 97.8 to 98.6 percent, and on 19 November 1992, from 98.97 to 99.46 percent.

Table 3 depicts combined results for the several kinds of geomagnetic conditions. During a quiet ionosphere ( $A_p \leq 50$ ) and major (not severe) storms ( $50 < A_p \leq 100$ ), the 95th and 99th percentiles of GIVE are 1.75 and 2.25 m, respectively. The combined success rate in bounding GIVE for the user is 99.95 percent. During severe geomagnetic storms ( $A_p > 100$ ), the 95th and 99th percentiles of GIVE are both 5.0 m. The combined success rate for the user is 99.91 percent.

Table 4 shows statistical parameters, maximum, and minimum of the distribution of vertical error exceeding UIVE at the monitor (per 5 min update period). The table also shows the same parameters for user error after the maximum monitor error above UIVE for one grid update period has been added to the GIVEs for the next grid update period. It can be seen from this table that when the user error exceeds the UIVEs, the maximum value of the difference between the user error and UIVE is about 0.48 m, and the  $|\text{mean}| + 2 \text{ sigma} = 0.19 \text{ m}$ .

Figure 5 shows the 95th percentile of GIVEs mapped against the parameter F10.7, which is the solar flux density. The graph indicates the absence of a clear relationship or correlation between solar flux density and ionospheric grid error bounds. The results of [10] also show no correlation between short-term F10.7 and the total electron content (TEC), which is proportional to ionospheric delay. Typical values for F10.7 during solar maximum are between 300 and 350, and about 75 during solar minimum. The reader should be cautioned not to extrapolate the results of Figure 5 to the peak of the solar cycle. Extrapolation is not a substitute for examining data during the peak of the solar cycle.

#### Service Volume Implications

The results in the previous section are conditioned on the existence of at least 1 IPP in each of at least 3 grid squares surrounding the IGP in real time. Whenever this condition is not met, the IGP is marked "unavailable." This restriction maintains a high degree of pierce-point density, which favors the calculations in the algorithm. To determine whether this degree of pierce-point density could be maintained in the

Table 3—Combined Results

Conditions	$A_p$ Index	GIVE Mean (m)	GIVE Sigma (m)	GIVE 95% (m)	GIVE 99% (m)	% $\leq$ UIVE (monitor) (%)	% $\leq$ UIVE (user) (%)	% GIVE $\leq 2.0 \text{ m}$ (%)
Quiet Ionosphere and Major Storms	$\leq 100$	1.13	.36	1.75	2.25	99.92	99.95	98.80
Severe Storms	$> 100$	1.6	1.2	5.0	5.0	99.74	99.91	80.00

Table 4—Error Distribution Above UIVE for Monitor and User

Errors at:	Min (m)	Max (m)	Mean (m)	Sigma (m)
Monitor (max)	0.0011	0.4815	0.0728	0.0964
User	0.0001	0.4815	0.0511	0.0640

initial WAAS, a map of pierce-point density was constructed using the 24 known sites and the 24 GPS satellites projected to be in operation for the initial WAAS. A modified version of the NAVSTAR program [11] was used to determine how many pierce points would be available every

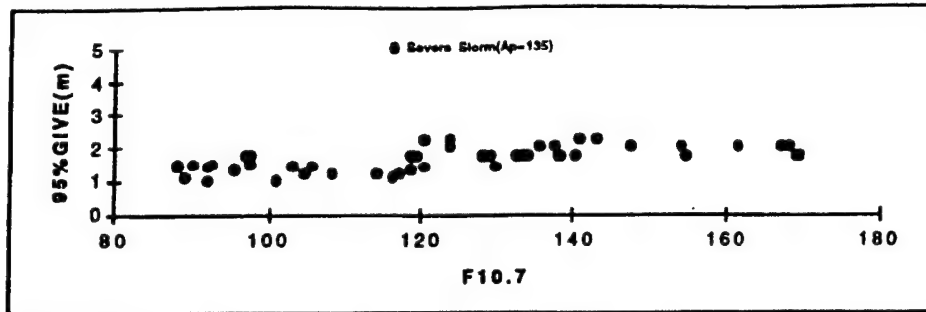


Fig. 5—Mapping of 95 Percent of GIVE to Solar Flux Density (F10.7)

minute in every grid square throughout the day. Next, for each grid node, the percentage of the day was determined for the occurrence of the condition of at least 1 IPP in each of at least 3 grid squares surrounding an IGP.

For the purposes of this analysis, the following conditional probability relationship was considered:

$$\begin{aligned} & \text{Pr}[\text{Ionospheric WAAS function available}] \\ &= \text{Pr}[\text{overall GIVE} \leq 2.0 \text{ m} \\ &| \text{IPP density requirement satisfied}] \\ &\times \text{Pr}[\text{IPP density requirement satisfied}] \\ &= 0.95 \end{aligned}$$

Since  $\text{Pr}[\text{overall GIVE} \leq 2.0 \text{ m} | \text{IPP density requirement satisfied}] = 0.988$  for nonsevere ionospheric conditions (from Table 3),  $\text{Pr}[\text{IPP density requirement satisfied}]$  must be at least 0.96 for a grid node to be marked as satisfying the density requirement.

Figure 6 depicts this condition over the defined service area. Dark circles indicate nodes where the IPP density requirement is satisfied at least

96 percent of the day. Figure 7 depicts the grid squares (dark) that would be operational based on this condition and the requirement that there be at least 3 surrounding grid nodes with GIVEs in order to calculate UIVEs.

## CONCLUSIONS AND RECOMMENDATIONS

The results of this paper are based on a 52 day set of data. However, the data was from midway through the solar cycle, and includes instances of quiet and disturbed ionospheric conditions. From this, the following conclusions are drawn:

- 1) Under nonsevere geomagnetic conditions ( $A_p \leq 100$ ), more than 50 percent of CONUS has a pierce-point density that can sustain GIVEs  $\leq 2.0 \text{ m}$  95 percent of the time, and the subsequent UIVEs calculated from these GIVEs bound the residual user errors an average of 99.95 percent of the time (and never fall below 97.84 percent for any day). This meets the initial WAAS availability requirement of the ionospheric function for precision approach.

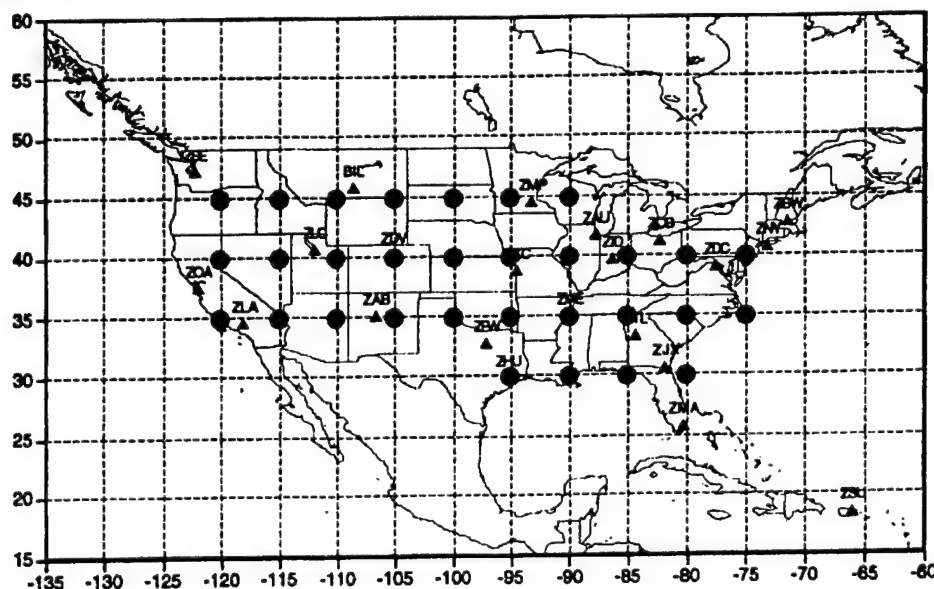
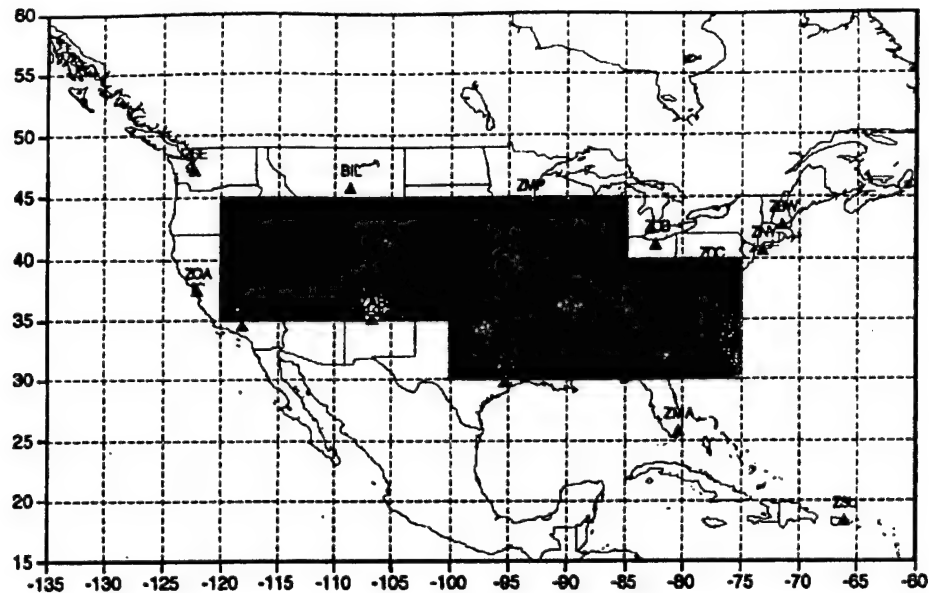


Fig. 6—Grid Nodes with Required Surrounding IPP Density



**Fig. 7—Grid Squares with at Least Three Surrounding Grid Nodes with Required IPP Density**

- 2) For one severe geomagnetic storm ( $A_p > 100$ ), the 95th percentile of the GIVEs is 5.0 m, and the user's success rate is 99.91 percent. This result means the algorithms were able to detect the change in ionospheric conditions and bound the ionospheric errors with a very high success rate. The impact of such large values of the ionospheric error bounds on the integrity and continuity of WAAS service must be further evaluated.
- 3) In the few cases where the user errors exceeded the UIVEs, the maximum value of the difference between the user error and UIVE was about 0.48 m, and the  $|\text{mean}| + 2\sigma$  was 0.19 m.
- 4) There is no apparent correlation between solar flux density (F10.7) and ionospheric grid error bounds. Typical values for F10.7 during solar maximum are between 300 and 350, and about 75 during solar minimum.
- 5) The percentage of the GIVEs below 2.0 m is 98.8 percent for quiet and major (not severe) geomagnetic storm conditions. During the one severe geomagnetic storm for which data was available, this percentage dropped to 80.0 percent.

- 3) In the few cases where the user errors exceeded the UIVEs, the maximum value of the difference between the user error and UIVE was about 0.48 m, and the  $|\text{mean}| + 2\sigma$  was 0.19 m.
- 4) There is no apparent correlation between solar flux density (F10.7) and ionospheric grid error bounds. Typical values for F10.7 during solar maximum are between 300 and 350, and about 75 during solar minimum.
- 5) The percentage of the GIVEs below 2.0 m is 98.8 percent for quiet and major (not severe) geomagnetic storm conditions. During the one severe geomagnetic storm for which data was available, this percentage dropped to 80.0 percent.

- 4) There is no apparent correlation between solar flux density (F10.7) and ionospheric grid error bounds. Typical values for F10.7 during solar maximum are between 300 and 350, and about 75 during solar minimum.
- 5) The percentage of the GIVEs below 2.0 m is 98.8 percent for quiet and major (not severe) geomagnetic storm conditions. During the one severe geomagnetic storm for which data was available, this percentage dropped to 80.0 percent.

- 5) The percentage of the GIVEs below 2.0 m is 98.8 percent for quiet and major (not severe) geomagnetic storm conditions. During the one severe geomagnetic storm for which data was available, this percentage dropped to 80.0 percent.

In developing these algorithms, the UIVE bounding requirement was considered to be paramount. The conservative nature of these algorithms, including the density requirement, was considered necessary in order to bound the errors in the test set of data. The density requirement was used to estimate availability in the service volume analysis, and while this meets Phase 1 requirements, availability requirements beyond Phase 1 would not be met without making some

**changes. There are several ways this problem could be mitigated:**

- 1) Adding more WRSs to increase the IPP density
- 2) Reducing the size of the grid (e.g., reducing the spacing between the IGPs) to increase accuracy and reduce errors
- 3) Allowing more frequent updates to users, especially when the ionosphere is very active

- 2) Reducing the size of the grid (e.g., reducing the spacing between the IGPs) to increase accuracy and reduce errors

- 3) Allowing more frequent updates to users, especially when the ionosphere is very active**

Since out-of-tolerance errors tend to persist for longer periods of time than the 10 s measurement update rate, a timely corrective broadcast to users could increase the bounding success rate. This in turn might allow for a slightly less conservative approach in the implementation of the algorithm.

## ACKNOWLEDGMENTS

The authors would like to acknowledge James K. Reagan and J. P. Fernow from The MITRE Corporation, Center for Advanced Aviation System Development (CAASD), for their review. The authors would also like to acknowledge J. C. Johns and Brian Mahoney of the FAA Satellite Program Office, who were the sponsors of this work.

## REFERENCES

1. *Specification for Wide Area Augmentation System (WAAS)*, U.S. Department of Transportation, Federal Aviation Administration, FAA-E-2892, May 9, 1994.
2. Wilson, B. D. and Mannucci, A. J., *Extracting Ionospheric Measurements from GPS in the Presence of Anti-Spoofing*, National Technical Meeting of The Institute of Navigation, September 23, 1994.

2. Wilson, B. D. and Mannucci, A. J., *Extracting Ionospheric Measurements from GPS in the Presence of Anti-Spoofing*, National Technical Meeting of The Institute of Navigation, September 23, 1994.

3. Goad, C. C., *Optimal Filtering of Pseudoranges and Phases from Single-Frequency GPS Receivers*, NAVIGATION, Journal of The Institute of Navigation, Vol. 37, No. 3, Fall 1990.
4. Eueler, H. and Goad, C. C., *On Optimal Filtering of GPS Dual Frequency Observations Without Using Orbit Information*, Bulletin Geodesique, Vol. 65, No. 2, 1991, pp. 130-43.
5. *NSTB Software Requirements Specification—Appendix A: Baseline Algorithms*, Report No. TR-92072, Stanford Telecommunication Inc., Reston, VA, August 1992.
6. El-Arini, M. B., O'Donnell, P. A., Kellam, P., Klobuchar, J. A., Wisser, T., and Doherty, P. H., *The FAA Wide Area Differential GPS (WADGPS) Static Ionospheric Experiment*, National Technical Meeting of The Institute of Navigation, January 20-22, 1993, San Francisco, CA.
7. Klobuchar, J. A., *Ionospheric Time-Delay Algorithm for Single-Frequency GPS Users*, IEEE Transactions on Aerospace and Electronic Systems, Vol. AES-23, No. 3, May 1987, pp. 325-31.
8. Hahn, G. J. and Meeker, W. Q., *Statistical Intervals: A Guide for Practitioners*, John Wiley & Sons, Inc., New York, 1991.
9. Odeh, R. E. and Owen, D. B., *Tables for Normal Tolerance Limit, Sampling Plans, and Screening*, Marcel Dekker, Inc., New York, 1980.
10. Klobuchar, J. A. and Doherty, P. H., *The Correlation of Daily Solar Flux Values with Total Electron*

*Content*, Proceedings of the International Beacon Satellite Symposium, MIT, Cambridge, MA, July 6-10, 1992, pp. 192-195.

11. Livingston, R., NAVSTAR program, Stanford Research Institute, February 1977.

#### ACRONYMS

CAT I	Category I
CONUS	Conterminous United States
DH	Decision Height
GEO	Geostationary Earth Orbiting
GIVE	Grid Ionospheric Vertical Error
GIVE I	Grid Ionospheric Vertical Error Indicator
IGP	Ionospheric Grid Point
IPP	Ionospheric Pierce Point
NSTB	National Satellite Test Bed
PR	Pseudorange
TEC	Total Electron Content
UDRE	User Differential Range Error
UIVE	User Ionospheric Vertical Error
VPE	Vertical Position Error
WAAS	Wide-Area Augmentation System
WMS	Wide-Area Master Station
WRE	Wide-Area Receiver Equipment
WRS	Wide-Area Reference Station

## Improving IRI-90 low-latitude electron density specification

Dwight T. Decker

Institute for Scientific Research, Boston College, Newton, Massachusetts

David N. Anderson

Air Force Research Laboratory, Hanscom Air Force Base, Massachusetts

Amanda J. Preble

Headquarters United States Air Force, Directorate of Weather, Pentagon, Washington, D. C.

**Abstract.** At low latitudes under moderate to high solar conditions, a number of comparisons between the international reference ionosphere (IRI-90) model of  $F$  region electron density profiles and observed profiles measured by the Jicamarca incoherent scatter radar indicate that during the daytime the observed profile shape can be much broader in altitude than that specified by IRI-90, while at night, just after sunset, observed  $F_2$  peak altitudes are significantly higher than what is specified by IRI-90. Theoretically derived ionospheric parameters such as  $F_2$  peak density ( $N_m F_2$ ),  $F_2$  peak altitude ( $h_m F_2$ ), and profile shape, which are contained in the parameterized ionospheric model (PIM), have been shown in some cases to be in better agreement with Jicamarca observations. This paper describes a new low-latitude option for IRI-90 that uses five ionospheric parameters derived from PIM: the bottomside profile half thickness,  $N_m F_2$ ,  $h_m F_2$ , and two parameters of a topside Chapman profile. The generation of electron density profiles using these five parameters is presented, as well as a description of how these parameters can be implemented into the IRI-90 model.

### 1. Introduction

The international reference ionosphere (IRI) is a global empirical model which specifies the monthly average of the electron density, electron temperature, ion temperature, and ion composition from 80 to 1000 km. It has been developed as a joint URSI/COSPAR project and first appeared as tables of profiles presented at the XVII General Assembly of URSI in 1972. However, the general philosophy was to develop a computer model based on critically evaluated ob-

servations, and so IRI quickly evolved from a set of tables to a computer program (IRI-78) available to the research community. Over the years, testing and modification of IRI has continued with extensive participation by the international research community. The result is that IRI has evolved and improved through several versions (IRI-80, IRI-86, IRI-90, IRI-95) and has become a valuable research tool [Bilitza *et al.*, 1993; Szuszczewicz *et al.*, 1996].

As a data-based model, the IRI is naturally only as good as the available observations. In the case of electron density, the data sources are ionosonde measurements, incoherent scatter measurements, rocket measurements, and a selection of satellite measurements [Bilitza,

Copyright 1997 by the American Geophysical Union.

Paper number 97RS01029.

0048-6604/97/97RS-01029\$11.00

1990]. Because the  $F_2$  peak parameters (peak density and height) are based on ground-based ionosonde measurements, which are for the most part located in the midlatitudes, there is a lack of observations from the low-latitude regions, the high latitudes/polar cap, and the ocean areas. Likewise, the thickness of the bottomside  $F$  region is based on ionosonde measurements and has similar problems in coverage. The topside  $F$  region is based on Alouette 1 and 2 topside sounder measurements from 1962 to 1966 [Llewellyn and Bent, 1973]; however, this period included only solar minimum and low solar moderate ( $F_{10.7} < 130$ ) conditions. Given this nonuniform coverage in both location and time of the various databases, it is not surprising that IRI does an excellent job of specifying the ionosphere's climatology for some regions and times while having problems with other regions and times.

In this paper, we focus on the low-latitude  $F_2$  region, a region where IRI has had some success reproducing the general climatology, especially for lower levels of solar flux, but where there are some persistent disagreements between model and observations [Abdu et al., 1996]. Early work based on total electron content (TEC) measurements found examples at low latitudes where IRI "severely underestimated" the observed TEC "during both day and night" [Bilitza, 1985, p. 15]. Analysis of these cases suggested that the problem was in the relative shape of IRI's  $F_2$  region at low latitudes. The topside of this layer comes from the Bent model [Llewellyn and Bent, 1973], and a correction to IRI's implementation of that model appeared in IRI-86. While this produced better agreement with satellite and incoherent scatter data, it was noted at the time that the new topside formula "only removed half of the difference between measured and predicted" TEC at the magnetic equator [Bilitza, 1985, p. 18]. Further, while IRI-86 appeared to do a reasonable job at low solar activity, comparisons with in situ satellite measurements during high solar activity indicated that IRI's topside profile still significantly underestimated the observations [Bilitza et al., 1987]. The other half

of the "shape of the  $F_2$  region" is the bottomside of the  $F_2$  layer, which is described by an analytic function parameterized in terms of a thickness parameter for which IRI offers two options. The recommended option in most cases comes from the Gulyaeva et al. [1987] model for the half-density height. However, this bottomside thickness has also had some problems at low latitudes. Mahajan et al. [1995] showed, using Arecibo incoherent scatter radar data, that IRI produced a bottomside that was too thick by differing amounts depending on season, and improvements to IRI have been suggested based on this work [Gulyaeva et al., 1996]. Comparisons to digisonde data from Jicamarca [Reinisch and Huang, 1996] have likewise shown some differences between data and IRI, with the most dramatic differences occurring in August 1993 when IRI's bottomside  $F_2$  layer was seen to be tens of kilometers thinner than observed. Finally, we turn to the  $F_2$  peak density ( $N_m F_2$ ) and height ( $h_m F_2$ ), which are used in IRI to complete the definition of the  $F_2$  region. For these two parameters, the most persistent problem at low latitudes has been with  $h_m F_2$  and in particular the inability of IRI in certain periods to reproduce the observed rising in altitude of the  $F_2$  layer just after sunset [Bilitza et al., 1993; Abdu et al., 1996].

As mentioned, the source of these problems is the nonuniform coverage of the available data. This is a particular problem at low latitudes because vertical  $\mathbf{E} \times \mathbf{B}$  drift leads to the formation of the equatorial anomaly and the development of a complex morphology quite different from that of the midlatitudes. However, the problems at low latitudes are also exacerbated by the large day-to-day variability of this region. In particular, it is problematic at best to attempt to model a feature such as the equatorial anomaly in terms of monthly medians when all the characteristics of the anomaly (intensity, location, extent, latitudinal shape) are known to vary greatly day to day. For example, owing to the changing position and extent of the anomaly, a single low-latitude ground station can day to day effectively be sampling different geophysi-



cal regions. Assembling data averages from several such stations can result in a smeared out anomaly that is not representative of an actual anomaly [Rawer, 1995]. While for some purposes such an average ionosphere is all that is needed, for other uses it is critical to have a representative, or "typical," ionosphere.

One effect of the issues described above is that theoretical modeling has begun to appear as a complementary approach to strict empirical modeling. Rush *et al.* [1983, 1984] used theoretical modeling to fill in the data gaps over the midlatitude oceans and, along with ground-based ionosonde observations, produced an improved set of maps of the  $F_2$  peak critical frequency ( $f_oF_2$ ). Such maps are the sources used by IRI for  $f_oF_2$  and hence  $N_mF_2$ . Further improvements to the  $f_oF_2$  maps were made using theory over the oceans, a larger database of ionosondes, and a harmonic analysis that was latitude dependent [Fox and McNamara, 1988]. At about the same time, efforts appeared that used first-principle theoretical models to produce parameterized models that would describe low-latitude theoretical morphology [Anderson *et al.*, 1987, 1989]. The purpose was to produce

a representative equatorial anomaly rather than a smeared out average anomaly [Daniell *et al.*, 1995]. In this paper, we propose a new option for IRI which would allow the results of low-latitude theoretical modeling of electron density to be incorporated directly into IRI. The purpose is to provide an improvement to IRI as well as to illustrate one way in which our theoretical understanding can be used to fill in the gaps of the observational databases used by IRI. In the next section, we present some observations compared with IRI-90 in order to quantitatively illustrate some of problems outlined above. This is followed by a description of the theoretical modeling of the low-latitude ionosphere, an example of a parameterized ionospheric model (PIM) option to IRI, and finally, a discussion and conclusion section.

## 2. Observations

Having qualitatively described some of the disagreements between IRI and observations at low latitudes, in this section we use comparisons between the Jicamarca incoherent scatter radar observations and IRI-90 to give quantitative examples of these disagreements. In Figure 1, we

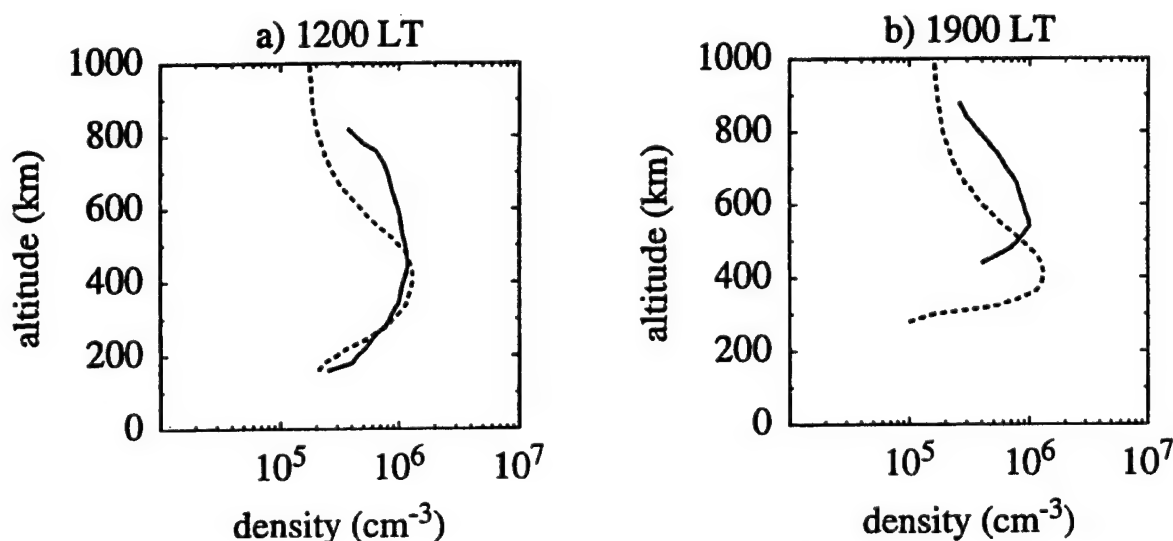


**Figure 1.** Comparison of Jicamarca observed profiles and IRI-90 (international reference ionosphere) profiles for October 1 and 2, 1970, at (a) 1200 LT and (b) 1900 LT. The solid curves are the observations, and the dashed curves are IRI-90.

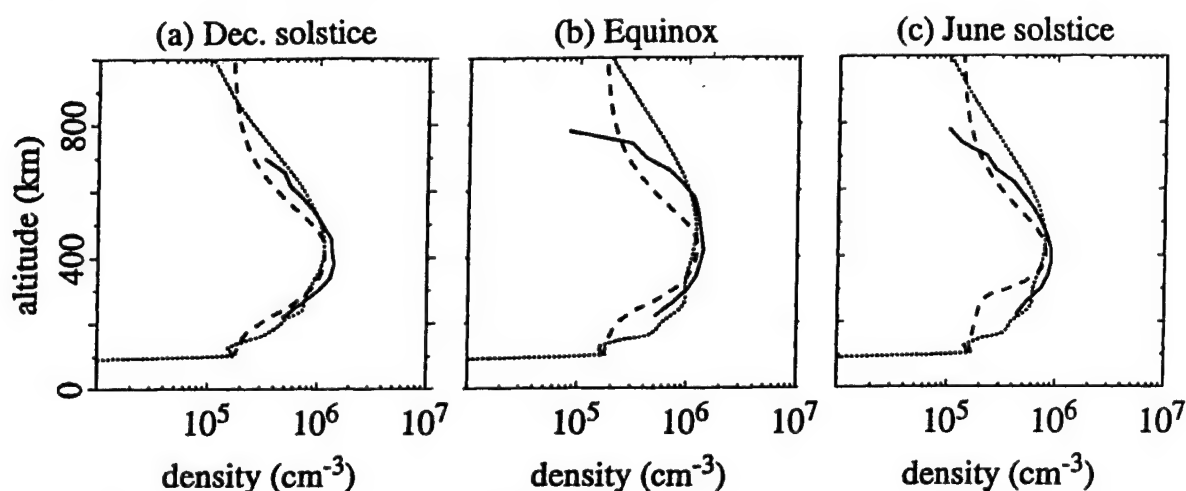


Figure 2. Seasonal comparison of IRI and parameterized ionospheric model (PIM) with Jicamarca average profile for 1200 LT, solar moderate conditions for (a) December solstice, (b) equinox, and (c) June solstice. The solid curves are observed average profiles ( $100 \leq F_{10.7} \leq 150$ ), the long dashed curves are IRI (sunspot = 80), and the dotted curves are PIM ( $F_{10.7} = 128$ ).

present an example of an electron density profile observed on October 1 and 2, 1970, during moderate solar conditions by the Jicamarca radar, which is located near the magnetic equator in Peru. Also included in the plot are IRI-90 profiles that were produced assuming a sunspot number of 80 ( $F_{10.7} = 130$ ). At 1200 LT the observed profile has a broad shape that is fairly typical of the daytime profile shape seen at Ji-

camarca during solar moderate and maximum conditions. On the other hand, IRI-90 has the thinner shape more characteristic of solar minimum, as well as an increased scale height above 700 km that suggests a transition from an  $O^+$  dominated  $F$  region to a  $H^+$  dominated topside. Later in the day, at 1900 LT the observed layer has been lifted to much higher altitudes due in most part to an observed enhanced postsunset E

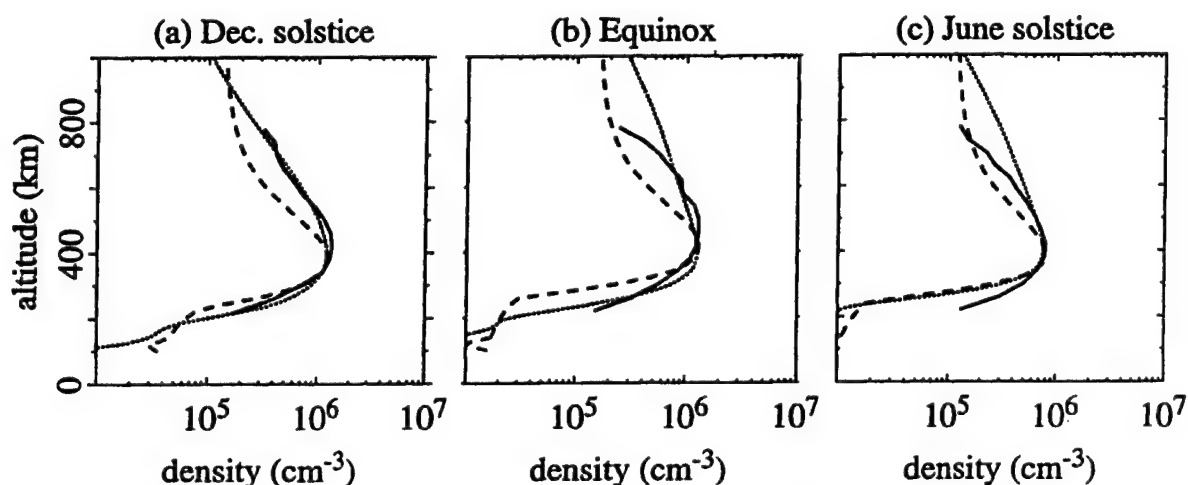


Figure 3. Same as Figure 2 but for 1800 LT.

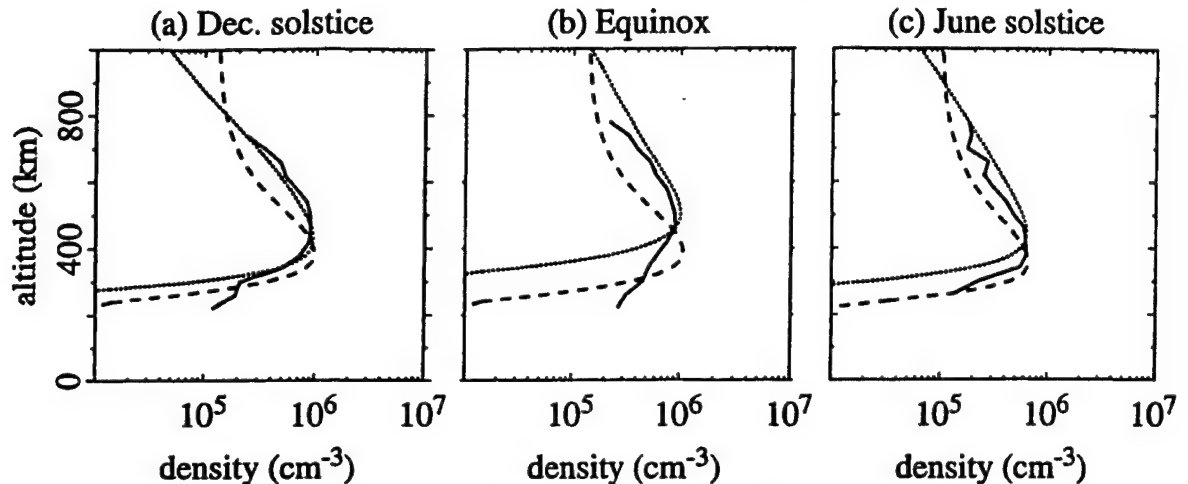


Figure 4. Same as Figure 2 but for 2000 LT.

$\times B$  upward drift. This again is a characteristic feature of the Jicamarca region, especially during solar moderate and maximum periods, and again is a feature not reproduced by IRI-90.

The point of the above comparison is to simply illustrate the type of problem that can be encountered at low latitudes when comparing IRI and actual observations. However, given that IRI is a model of monthly profiles, it should not be expected to necessarily reproduce the profiles on a given day. While the broad shape of the afternoon profiles and the postsunset lifting of the layer are not rare events and occur regularly, in order to validate that IRI has in fact a low-latitude problem, comparisons need to be made between some sort of averaged data and IRI. In Figures 2-4, which are adapted from Creamer [1992], we show the hourly averaged data from several years of Jicamarca observations for moderate solar flux conditions. December solstice refers to data taken during November through February, and June solstice refers to data from May to August. The equinox period was taken to be March and April along with September and October. These plots also include results from IRI-90 and the parameterized ionospheric model (PIM). In this section, we will focus on the data (solid curves) and IRI-90 (dashed curves) results. PIM results (dotted

curves) will be discussed in the following section. The IRI runs were made using a sunspot number of 80 and for days of the year 1, 100, and 182. The data are from days where the  $F_{10.7}$  ranged from 100 to 150.

We begin by noting that the observed profiles (solid curves) are generally broader than IRI-90 (dashed curves), though in several cases IRI-90 does a reasonable job. In Figure 2 (1200 LT) we see that for December solstice, the shape of IRI's profile compares quite well with the averaged data. At equinox, we begin to see some differences in both the topside and bottomside shapes between IRI and data. For June solstice, the differences in the bottomside shape are most apparent. In Figure 3 (1800 LT) we see similar trends, with clear differences between IRI-90 and data in topside shapes during December solstice and equinox and bottomside differences during June solstice and equinox. Finally, in Figure 4 (2000 LT), the postsunset lifting of the layer is evident (solid curves) during December solstice and equinox and is seen to be missed by IRI-90 (dashed curves). There is a smaller amount of lifting of the layer for June solstice, but it is difficult to see given that the data were placed into 40-km bins when producing these average profiles. If  $h_m F_2$  is taken from the unbinned data and then averaged, the June solstice

results then show a peak rise of just 16 km between 1700 and 2000 LT. In contrast, equinox shows a 55-km increase. Similar features are seen for maximum solar flux conditions but not for solar minimum conditions. IRI-90 also consistently shows an increased scale height above 700 km. While the data show some evidence that this is not the case (see equinox at 1200 and 1800 LT), in general, these observations are too low in altitude to clearly determine whether this increased scale height is appropriate.

While the observations shown thus far come from one location, similar features are also evident in other longitude sectors. Many of the works referenced in the introduction describe studies that included data from other longitude sectors. In Figure 5, we present profiles (R. Tsunoda, personal communication, 1995) observed by the Kwajalein incoherent scatter radar located near the equator in the Pacific sector. On the left is a profile from the early morning before upward drift  $\mathbf{E} \times \mathbf{B}$  drift has acted to broaden the peak, while on the right we see later in the day the characteristic broad layer of the low-latitude daytime that results from the upward  $\mathbf{E} \times \mathbf{B}$  drift. Further, it has been clearly established that the equatorial anomaly is global in nature [Walker, 1981; Su *et al.*, 1996] and that the  $\mathbf{E} \times \mathbf{B}$  drift, though different in detail,

is similar at all longitudes [Fejer *et al.*, 1995]. Given that the discrepancies described above are related to the effects of vertical  $\mathbf{E} \times \mathbf{B}$  drift and the equatorial anomaly, it is then consistent that IRI would have these low-latitude problems at other longitudes.

### 3. Theoretical Modeling

Over the last three decades, there have been many theoretical studies of the equatorial  $F_2$  region, and a number of computer models have been developed that reproduce the basic features of this region. Most recently, these models have evolved to the point that given realistic inputs for a particular day, they are capable of reproducing the ionosphere of that day [Preble *et al.*, 1994]. One such model is the global theoretical ionospheric model (GTIM), which calculates electron density profiles as a function of location and time by solving ion continuity and momentum equations. For the  $F$  region, the  $O^+$  ion density is determined by numerically solving the time dependent ion ( $O^+$ ) continuity equation. The needed velocity parallel to the magnetic field comes from combining the electron and ion momentum equations. The perpendicular velocity is taken as the  $\mathbf{E} \times \mathbf{B}$  drift where the electric field has to be provided as an input

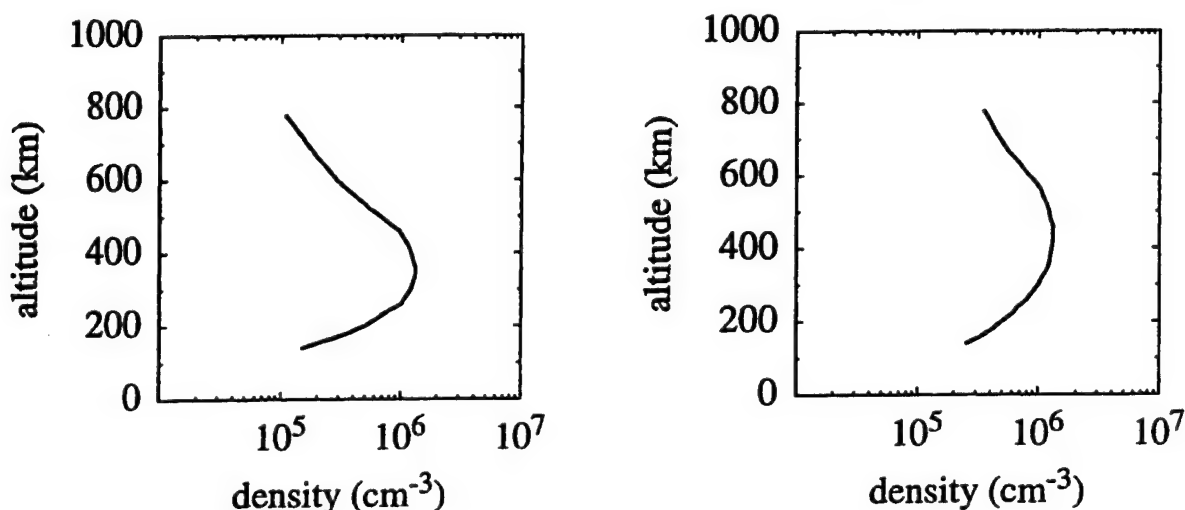


Figure 5. Electron density profiles observed by Kwajalein incoherent scatter radar.

to the model. A variety of other geophysical inputs are also required, including the neutral constituents, temperature, and winds; the electron and ion temperatures; the solar extreme ultraviolet (EUV) fluxes; and the geomagnetic field. For the lower altitudes, the molecular ions are determined by numerically solving the steady state local approximation of four coupled ion continuity equations [Anderson *et al.*, 1996]. In Figure 6, we present vertical profiles for 1200 and 1900 LT from GTIM simulations (dotted curves) that used the Jicamarca observed upward  $E \times B$  drift of October 1 and 2, 1970. We also include in the plot the electron density profiles (solid curves) observed by the Jicamarca radar at those times. We see that when the observed drift is used as an input to the model, the agreement between model and observation is excellent. Further, we see that the model reproduces both the broad profile shape of the daytime and the lifting of the  $F_2$  layer during the postsunset period. The additional curves (dashed curves) are GTIM results when zero vertical  $E \times B$  drift was used as input. These simulations illustrate the critical role that

the magnitude of the  $E \times B$  vertical drift has in determining both the shape of the daytime profile and the postsunset rising of the  $F_2$  layer.

Recently, a computationally fast parameterized ionospheric model (PIM) was developed at the Phillips Laboratory Geophysics Directorate as part of a global, real-time ionospheric specification model called PRISM (parameterized real-time ionospheric specification model) which is presently operational at the Air Force 55th Space Weather Squadron (55SWX) in Colorado Springs [Daniell *et al.*, 1995]. PIM is based on many runs of several theoretical ionospheric models and as such is a global ionospheric model based on theoretical climatology rather than empirical climatology. For the low latitudes, the theoretical model used was an early version of GTIM. It was run under three solar cycle conditions (low, middle, and high  $F_{10.7}$  cm flux values) and three seasons (fall-spring equinox, summer, and winter solstice periods) for four longitude sectors (American, Brazilian, European-Indian, and Pacific). Electron density profiles every  $2^\circ$  latitude and every hour local time were parameterized by nine empirical orthonormal func-

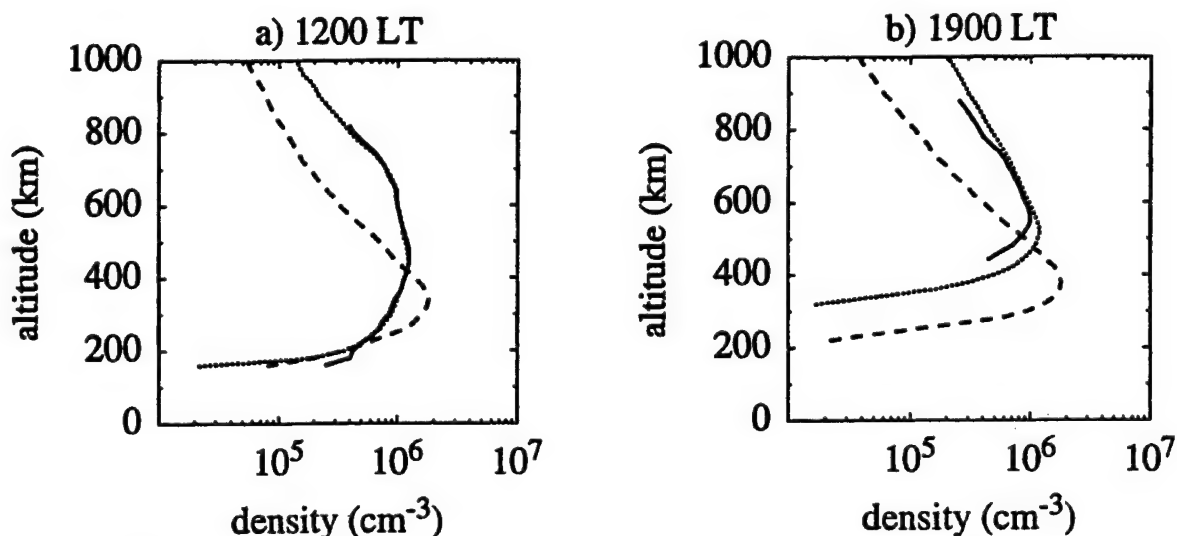


Figure 6. Comparisons of measured and calculated profiles on October 1 and 2, 1970, for (a) 1200 LT and (b) 1900 LT. The solid curves are the Jicamarca observations, the dots are calculations that used observed drifts, and the long dashes are the calculations using zero drifts.

tions (EOFs). At low and middle latitudes these EOFs were analytically fit in latitude and kept in tabular form over the 24-hour period. These tables and functions comprise the low-latitude portion of PIM and reproduce very accurately the electron density profiles generated by GTIM.

Given the success of theoretical models in reproducing the basic features of the low latitudes, we would expect that PIM should likewise reproduce those features. In Figures 2-4, we have included PIM results (dotted curves) along with the averaged Jicamarca data (solid curves) and the IRI-90 (dashed curves) results. In Figure 2 for December solstice, we see that PIM produces a profile that is broader than the data. Both PIM and IRI-90 underestimate  $N_m F_2$ , and to some extent the topside and bottomside data seem to split the difference between PIM and IRI-90. At equinox, PIM's (dotted curve) topside shape gives good agreement with data (solid curve) up to around 600 km. Above that height, both PIM and IRI miss the sharp falloff in the data. Again in the bottomside, the data split the difference between the models, though if we normalize IRI to the  $F_2$  peak of the observations, IRI (dashed curve) has the better bottomside shape. Finally, for June solstice, PIM produces a broader layer than IRI-90, with the data falling between the two models. However, this time it is PIM that has the better bottomside shape, with IRI-90 showing a much thinner bottomside than seen in the data. Turning to Figure 3 and 1800 LT, we again see a broader PIM (dotted curves) as compared with IRI-90 (dashed curves). For December, PIM's topside agrees quite nicely with the data, while IRI-90 shows a significantly different shape. Moving to equinox, up to around 600 km, PIM gives reasonable agreement with the observed topside, but as was the case at 1200 LT, both PIM and IRI-90 miss the sharp falloff seen in the data at higher altitudes. In the bottomside the observed layer appears to be a bit thicker than either model. June solstice again shows an observed topside shape that falls between the two models and an observed bottomside shape that

is thicker than either model. At 2000 LT (Figure 4), similar trends continue. PIM gives good agreement with observations over much of the  $F$  region. In particular, PIM captures the lifting of the layer that was missed by IRI-90. For equinox, PIM captures the topside shape and the lifting of the layer. However, both IRI-90 and PIM produce much thinner bottomsides than seen in the averaged data. Finally for June solstice, PIM shows a layer that has risen to a higher altitude ( $h_m F_2 \approx 440$  km) than that seen in the observations ( $h_m F_2 \approx 410$  km), while IRI-90 is down at a lower altitude ( $h_m F_2 \approx 355$  km).

Having seen how both IRI and PIM compare with data from Jicamarca for solar moderate conditions, let us now compare the two models over a larger region and for solar maximum conditions ( $F_{10.7} = 200$ ). In Figure 7, we directly compare PIM and IRI-90 profiles at 1700 UT in Jicamarca longitude meridian. The local time is around 1200, and we see that PIM produces a much broader  $F$  layer around the magnetic equator than does IRI-90. However, the PIM anomaly falls off much faster with latitude than does IRI-90 so that  $20^\circ$  north of the magnetic equator (around  $10^\circ$  north geographic) IRI-90 is producing a thicker layer. This illustrates how in regions of great variability, theoretical models can produce sharper features (in this case an anomaly that is narrower in latitude) than may be seen in models based on averaged data. In Figure 8, it is  $h_m F_2$  that is compared over the entire globe at 0000 UT, and we see that the largest differences between PIM and IRI-90 are confined to the postsunset period near the equator. The topside half thicknesses are compared in Figure 9, and here a sizable difference is seen near the magnetic equator but extended over  $180^\circ$  in longitude. This also points out how the differences in thickness between models are not confined to just one longitude sector. In Figure 7, a clear difference in layer thickness was seen in the American sector at 1700 UT. At 1200 UT, this difference is seen in the European-Indian sector.



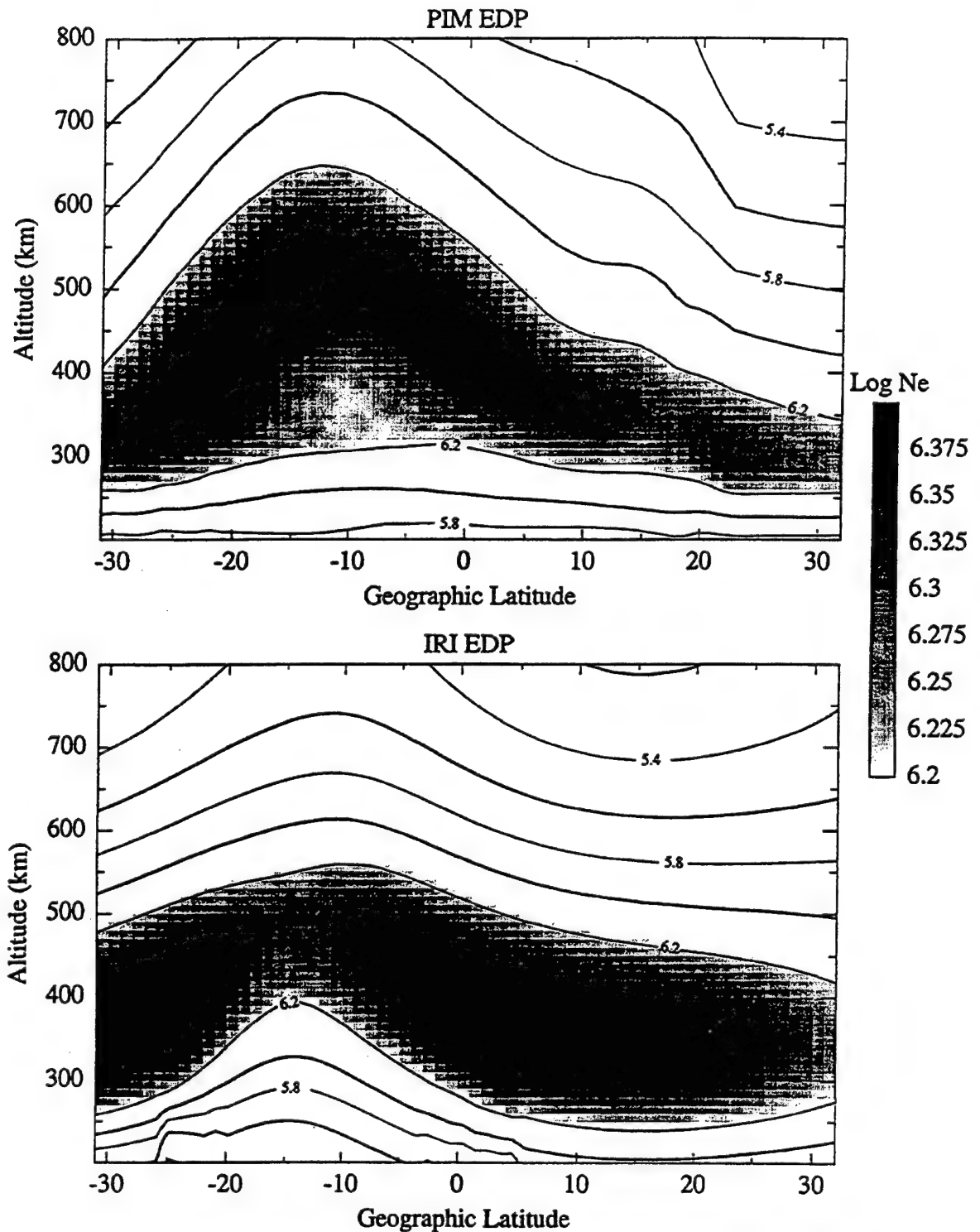
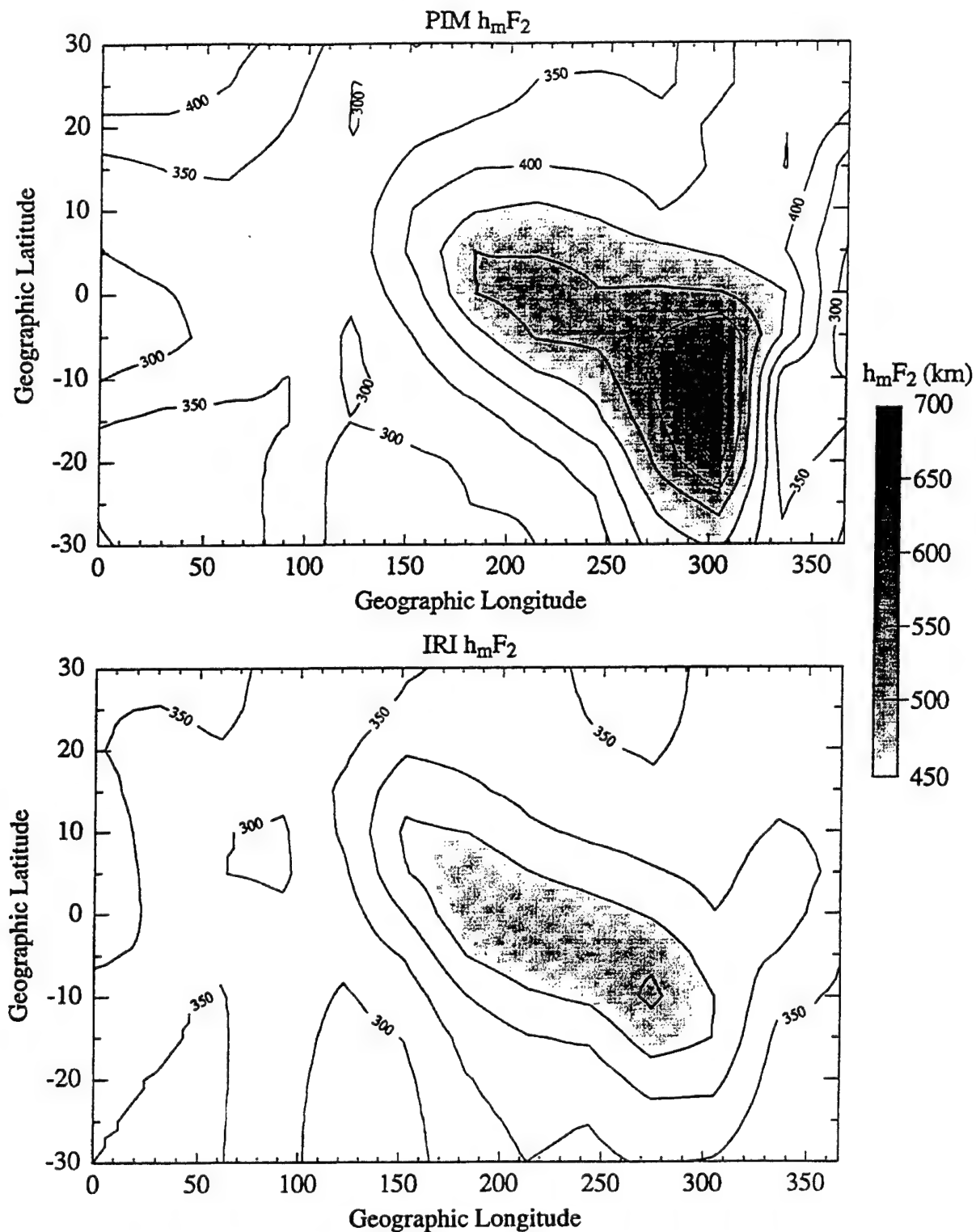
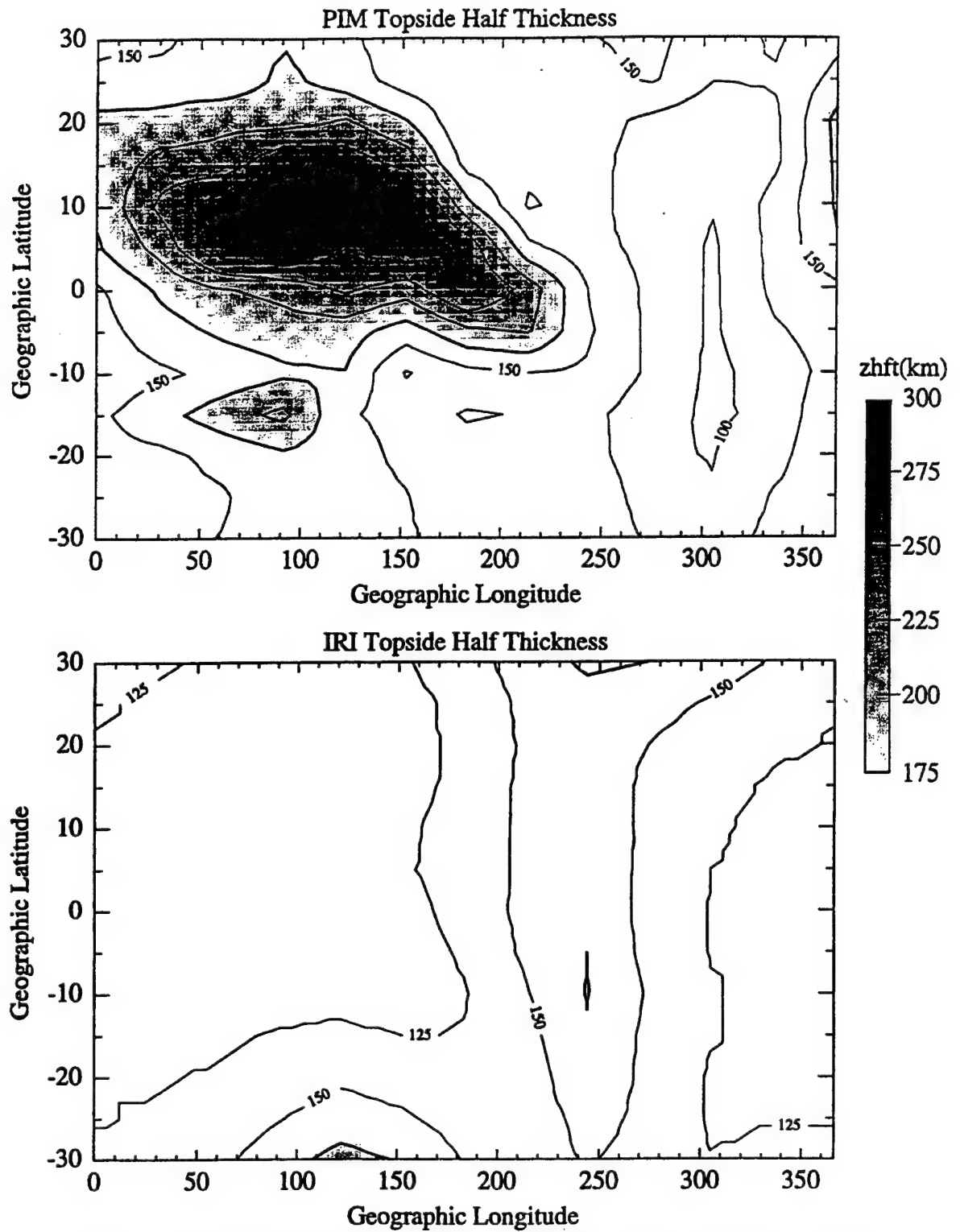


Figure 7. Electron density in the Jicamarca longitude meridian from PIM and IRI-90 for 1700 UT (1200 LT) under solar maximum conditions ( $F_{10.7} = 200$ ) on day 100.



**Figure 8.** Values of  $h_mF_2$  from PIM and IRI-90 for 0000 UT under solar maximum conditions ( $F_{10.7} = 200$ ) on day 100.



**Figure 9.** Topside half thickness from PIM and IRI-90 for 1200 UT under solar maximum conditions ( $F_{10.7} = 200$ ) on day 100.

#### 4. Proposed Improvement to IRI-90: PIM Option

In describing the electron density profile from 80 to 1000 km, IRI-90 uses six subregions: the topside, the  $F_2$  bottomside, the  $F_1$  layer, the intermediate regions, the  $E$  valley, the  $E$  bottomside, and the  $D$  region. The upper parts of this profile are in turn normalized to the  $F_2$  peak density ( $N_m F_2$ ) and altitude ( $h_m F_2$ ). The difficulties described in this paper have involved the topside and  $F_2$  bottomside regions as well as  $h_m F_2$ , and it is these quantities for which we propose an alternative source that we call a PIM option to IRI. In IRI,  $N_m F_2$  comes from either the CCIR or URSI coefficient sets that derive from Fourier and spherical harmonic expansions of ionosonde data. Likewise, there are CCIR coefficients of  $M(3000)$  which are used to infer  $h_m F_2$ . The topside profile shape comes from analytic fits of Bent's compilation of Alouette sounder data [Llewellyn and Bent, 1973]. The fits are done using Epstein functions which can be used to define a Booker function. The Booker function used in IRI-90 consists of three layers, and it uses eight parameters to define the profile. Five of the parameters are fixed, and the other

three are given as functions of geomagnetic latitude, solar flux, and  $f_o F_2$ . (This profile can be described in terms of a linear combination of LAY-functions [Bilitza and Rawer, 1990].) The bottomside is given by a fairly simple function which, as mentioned, uses a thickness parameter. The present IRI-90 either looks up this parameter or calculates from a half thickness from Gulyaeva *et al.* [1987]. The PIM option would involve using PIM values for  $N_m F_2$ ,  $h_m F_2$ , and bottomside half thickness directly in IRI. The difficulties discussed have not focused on  $N_m F_2$ , but we have included it as part of the PIM option so that it would include a complete independent  $F$  region. To use the topside from PIM in IRI will require either fitting Booker functions to PIM profiles or fitting with some other function that would then have to be incorporated into IRI.

Presently, IRI-90 allows inputting of a  $N_m F_2$  and  $h_m F_2$  chosen by the user. To input a bottomside half thickness chosen by the user requires modifications of the IRI driver routine such that a user-specified thickness can be accepted and substituted for the Gulyaeva *et al.* [1987] thickness. For the topside, we have ex-

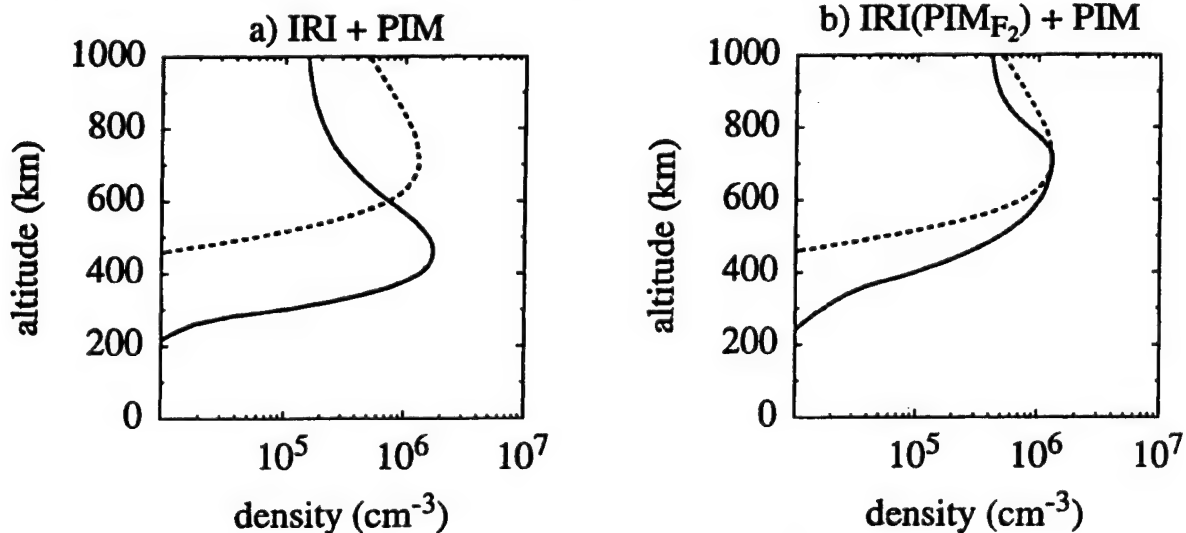


Figure 10. Comparisons under solar maximum conditions ( $F_{10.7} = 200$ ) at 2000 LT of IRI-90 and PIM profiles for (a) standard IRI and (b) IRI using PIM  $F_2$  peak parameters. Solid curves are IRI-90, and dashed curves are PIM.

plored one possibility by fitting topside PIM profiles with two-parameter Chapman profiles. The IRI driver was modified to accept these two parameters, and a routine was added to IRI to calculate the topside profile using a Chapman profile rather than a Booker function. Overall, the examples in this paper required only 20 lines of new code to IRI-90. An example of how this approach can allow IRI to reproduce PIM profiles using the five PIM parameters is given in Figures 10 and 11. In Figure 10a, we present the standard IRI-90 (solid curve) and PIM (dotted curve) profiles for 2000 LT at the magnetic equator for solar maximum conditions ( $F_{10.7} = 200$ ). We see a dramatic difference in both shape and  $h_m F_2$ . Figure 10b shows PIM compared with IRI-90 using  $N_m F_2$  and  $h_m F_2$  supplied by PIM. When the PIM bottomside half thickness is used by IRI-90, we see in Figure 11a that IRI-90 now reproduces well the lower  $F$  region of PIM. Finally, in Figure 11b, the PIM topside profile is also used by IRI-90, and we see that IRI using the full PIM option can do a reasonable job at reproducing the original PIM  $F$  region.

The next step in developing a global PIM option will be to determine the five PIM param-

eters over the globe under various geophysical conditions. It is expected that the resultant database of parameters will then have to be condensed to a convenient size. One possibility would be to fit the five PIM parameters to analytic functions in the same way as was done with the  $F_2$  peak parameters derived from ionosonde data (CCIR or URSI coefficients). Whether this is a feasible approach will require further work. Finally, while the focus in this paper is on low latitudes, we should note that at the 1994 COSPAR meeting in Hamburg, Germany, the IRI community endorsed developing a high-latitude PIM option to the IRI model. Given this fact, it would seem best to develop a global PIM option for IRI. This would avoid the problem of attempting to merge a PIM option in one region with standard IRI in other regions.

## 5. Discussion and Summary

At present, there are some clear shortcomings in IRI's description of the low-latitude ionosphere. On the other hand, theoretical models have been shown capable of reproducing some of the low-latitude features that are not repro-

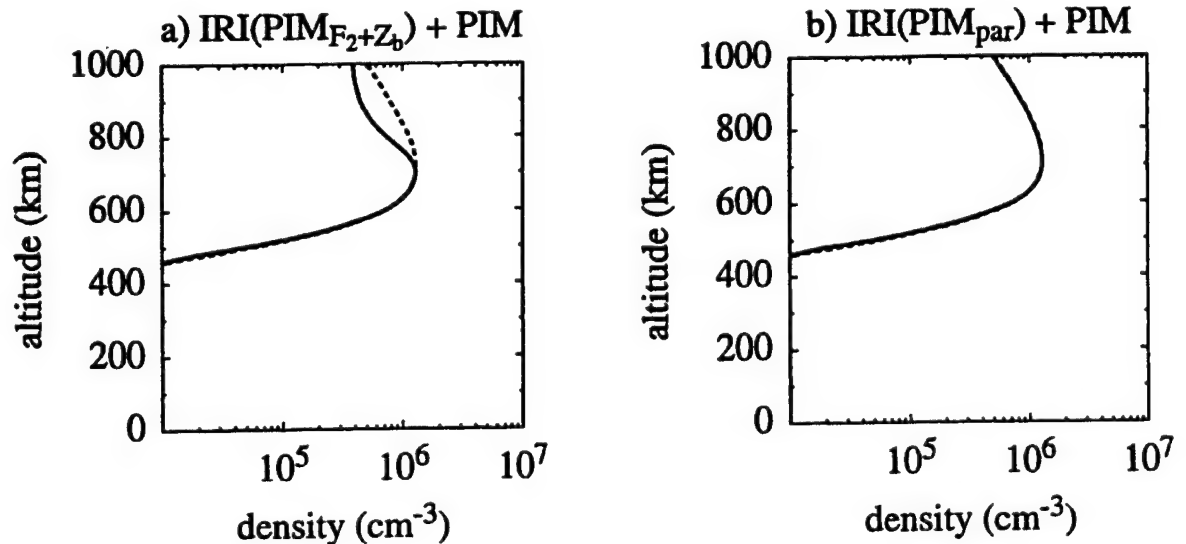


Figure 11. Comparisons at 2000 LT of IRI-90 and PIM profiles for (a) IRI using PIM  $F_2$  peak parameters and bottomside half thickness and (b) IRI using all five PIM parameters. Solid curves are IRI-90, and dashed curves are PIM.

duced by IRI-90. In particular, for periods of moderate to high solar activity, PIM has been shown to produce a broader  $F$  region than IRI and to capture the observed postsunset rising of the  $F_2$  layer. Given these facts, it has been suggested that it would be useful to develop a low-latitude PIM option to the IRI model. This suggestion was considered and endorsed by the IRI community at the 1995 IRI meeting in New Delhi, India. This low-latitude option will be part of a global PIM option being developed by Phillips Laboratory, and the global option will be delivered to the IRI community when completed.

The present version of IRI-90 is designed to accept  $N_m F_2$  and  $h_m F_2$  from outside sources. Thus it is straightforward to develop a PIM option for these parameters in IRI-90. Similarly, an external bottomside half thickness can easily be incorporated into IRI-90, given the manner in which IRI-90 presently defines its bottomside  $F$  region. Unfortunately, the parameter which is most in need of modification is the topside half thickness. Presently, there is no trivial way of incorporating such a thickness from another source such as PIM into the IRI. However, a fairly minor modification is possible that uses a two-parameter Chapman profile rather than the Booker functions. If use of the Booker functions is desired, then such functions would have to be fit to PIM profiles. Presently, we are most interested in pursuing the option that uses the Chapman profile and in developing representations of the five PIM parameters as functions of latitude, longitude, local time, solar cycle, season, and geomagnetic activity.

While we have demonstrated the possibility and potential of the PIM option, the same type of validation is needed for PIM as is necessary for any version of IRI. However, validating the PIM option faces the same problems that have hampered IRI validations, that is, the availability of suitable observations. To date, validation of the low-latitude portion of PIM has been confined to the American sector, primarily to comparisons with data from the Jicamarca incoherent scat-

ter radar. Further validation for the PIM option awaits other data sources. One near-term possibility is the TEC observations that are available from the dual-frequency, dispersive radar on the TOPEX/Poseidon satellite [Bilitza *et al.*, 1996]. These observations, which began around the beginning of 1993, would appear to offer an exciting opportunity for low-latitude testing of IRI, PIM and GTIM.

A key issue when considering the validation of models such as IRI or PIM is that of day-to-day variability. This is especially critical in a region, such as the low latitudes, where that variability can be quite large. This issue manifests itself in several ways. For example, the process by which one constructs an average from data becomes critical, especially if dealing with any type of variable structure. As mentioned in the introduction, the latitude extent of the anomaly can easily be smeared out if one takes routine averages of ground-based measurements. Another example is that of the shape of the altitude profile changing markedly from day to day even when the solar and magnetic conditions are not markedly different. In that case an "average profile" may represent only one of the possible profile shapes. In Figure 2 for December solstice, we see an average profile with a topside shape falling between IRI-90 and PIM. If one examines the scatterplots of the 18 profiles that went into making up this average [Creamer, 1992], one sees a range of profiles that go from very broad shapes, low peak densities ( $7.0 \times 10^5$ ), and high  $h_m F_2$  ( $>400$  km) to thin topsides (thinner than IRI), high peak densities ( $2.5 \times 10^6$ ), and lower  $h_m F_2$  ( $\sim 325$  km). In this case, both IRI and PIM fall within this range of profile shapes. We can speculate that the PIM profile's shape is representative of those days when the electric field was of a certain strength, while IRI being based on solar minimum data possibly represents those profiles from days with weaker electric fields. However, all the cases fall into the same category of magnetically quiet, moderate solar conditions. Of course, with such a range of shapes, it is difficult to determine what



is "typical," and there is little reason to expect that a theoretical model driven by an average  $E \times B$  drift based on one limited set of drift data will necessarily produce the "average" seen in a limited set of electron density profile data from a different period. In such regions with large variability, what is needed for IRI is an expanded capability that quantifies the variations about the "average profile." As for PIM, it is planned that the next version will be parameterized by an electric field strength parameter. In order to validate such a version of PIM and the above speculation, it would be useful to perform a GTIM model study where a database of simultaneous vertical drift and electron density profile measurements is available. In that case, one could verify whether the observed day-to-day variations in profile shape can be modeled as directly coming from the observed day-to-day variations in vertical drift.

The scale height differences above 700 km between the IRI-90 and PIM profiles are an obvious issue that needs to be addressed as we consider the issue of model validation. As mentioned in section 2, the increased scale height shown in IRI-90 suggests a transition from an  $O^+$  dominated  $F$  region to a  $H^+$  dominated topside. This suggestion comes from both theory and observations that have shown that this type of scale height change occurs when this transition of species occurs [Bilitza, 1990]. Further, the transition heights observed at solar minimum are generally consistent with the transition heights evident in the IRI-90 profiles. That this is so is, of course, reasonable, given that IRI's topside is based on solar minimum topside sounder data. However, observations have shown that the transition height moves up in altitude at higher levels of solar activity. This has been verified recently in a study of DMSP satellite data [West et al., 1997] that showed during low solar activity the transition height is well below 800 km and is well above 800 km during higher solar activity. Further, for the times of the DMSP data, it was seen that the  $H^+$  density at 800 km never gets much above  $1$  or  $2 \times 10^4$ .

In disagreement with this are the IRI-90 results which show for solar moderate conditions at 2148 LT (the time of DMSP data) a scale height change at around 700 km and  $H^+$  densities at 800 km of around  $9 \times 10^4$ . An observational solution to this problem should come from topside sounder data. However, only a small part of the Alouette-ISIS topside sounder database has been available for use [Bilitza, 1994]. It is expected that if and when more of this database becomes available, significant improvements can be made in IRI's topside morphology. On the theoretical side, we find that PIM does not include  $H^+$  and so obviously cannot describe the transition between species. Fortunately, the new version of GTIM under development includes  $H^+$  at low and middle latitudes. It is anticipated that the next version of PIM will be produced using this improved GTIM and thus should include the transition from  $O^+$  to  $H^+$  that occurs in the topside.

The two issues discussed above (daily profile shape changes and  $O^+/H^+$  transitions) are examples of the problems that arise in part from the lack of suitable databases. They are also examples of where theoretical models could be used to complement pure empirical modeling. That is, validated theory can serve to fill in the data gaps and provide a spatial and temporal framework when the databases are too sparse to do so. We expect that a next generation PIM that includes both  $H^+$  and an electric field parameterization can play such a role and serve to complement strict empirical modeling.

Finally, this work was done using IRI-90; however, during the writing of this paper, IRI-95 became available and could be run interactively via a World Wide Web site. We have rerun the cases shown in Figures 2-4 using IRI-95 and find essentially no differences in the topside and  $F_2$  peak parameters. However, for days 1 and 100, the bottomsides at 1200 LT coming from IRI-95 are somewhat thinner than the IRI-90 results. Given these results, it is evident that essentially all our conclusions based on IRI-90 remain true for IRI-95.

**Acknowledgments.** The work at Boston College was supported by Phillips Laboratory contracts F19628-93-K0001 and F19628-96-C0039.

## References

- Abdu, M. A., I. S. Batista, and J. R. de Souza, An overview of IRI-observational data comparison in American (Brazilian) sector low latitude ionosphere, *Adv. Space Res.*, **18**(6), 13-22, 1996.
- Anderson, D. N., M. Mendillo, and B. Herniter, A semi-empirical low-latitude ionospheric model, *Radio Sci.*, **22**, 292-306, 1987.
- Anderson, D. N., J. M. Forbes, and M. Codrescu, A fully analytical, low- and middle- latitude ionospheric model, *J. Geophys. Res.*, **94**, 1520-1524, 1989.
- Anderson, D. N., D. T. Decker, and C. E. Valladares, Global theoretical ionospheric model (GTIM), in *Solar-Terrestrial Energy Program: Handbook of Ionospheric Models*, edited by R. W. Schunk, pp. 133-152, Natl. Oceanic and Atmos. Admin., Boulder, Colo., August 1996.
- Bilitza, D., Electron density in the equatorial topside, *Adv. Space Res.*, **5**(10), 15-19, 1985.
- Bilitza, D., International reference ionosphere 1990, *NSSDC/WDC-A-R&S Rep. 90-22*, Goddard Space Flight Cent., Greenbelt, Md., 1990.
- Bilitza, D., Topside models: Status and future improvements, *Adv. Space Res.*, **14**(12), 17-26, 1994.
- Bilitza, D., and K. Rawer, New options for IRI electron density in the middle ionosphere, *Adv. Space Res.*, **10**(11), 7-16, 1990.
- Bilitza, D., K. Rawer, S. Pallaschke, C. M. Rush, N. Matuura, and W. R. Hoegy, Progress in modeling the ionospheric peak and topside electron density, *Adv. Space Res.*, **7**(6), 5-12, 1987.
- Bilitza, D., K. Rawer, L. Bossy, and T. Gulyaeva, International reference ionosphere - Past, present, and future, I, Electron density, *Adv. Space Res.*, **13**(3), 3-13, 1993.
- Bilitza, D., C. Koblinsky, S. Kia, R. Williamson, and B. Beckley, The equatorial anomaly region as seen by the TOPEX/POSEIDON satellite, *Adv. Space Res.*, **18**(6), 23-32, 1996.
- Creamer, A. P., Equatorial F-region electron densities over a solar cycle: Comparisons between observations and numerical models, M.S. thesis, 201 pp., Utah State Univ., Logan, 1992.
- Daniell, R. E., Jr., L. D. Brown, D. N. Anderson, M. W. Fox, P. H. Doherty, D. T. Decker, J. J. Sojka, and R. W. Schunk, Parameterized ionospheric model: A global ionospheric parameterization based on first principles models, *Radio Sci.*, **30**, 1499-1510, 1995.
- Fejer, B. G., E. R. de Paula, R. A. Heelis, and W. B. Hanson, Global equatorial ionospheric vertical plasma drifts measured by the AE-E satellite, *J. Geophys. Res.*, **100**, 5769-5776, 1995.
- Fox, M. W., and L. F. McNamara, Improved worldwide maps of monthly median foF2, *J. Atmos. Terr. Phys.*, **50**, 1077-1086, 1988.
- Gulyaeva, T. L., Progress in ionospheric informatics based on electron-density profile analysis of ionograms, *Adv. Space Res.*, **7**(6), 39-48, 1987.
- Gulyaeva, T. L., K. K. Mahajan, and N. K. Sethi, Modification of IRI half-density height option for low latitudes, *Adv. Space Res.*, **18**(6), 149-152, 1996.
- Llewellyn, S. K., and R. B. Bent, Documentation and description of the Bent ionospheric model, *Rep. AFCRL-TR-73-0657*, Air Force Geophys. Lab., Hanscom AFB, Mass., 1973.
- Mahajan, K. K., R. Kohli, N. K. Sethi, and V. K. Pandey, Variability of the F-region parameter h0.5, *Adv. Space Res.*, **15**(2), 51-60, 1995.
- Preble, A. J., D. N. Anderson, B. G. Fejer, and P. H. Doherty, Comparison between calculated and observed F region electron density profiles at Jicamarca, Peru, *Radio Sci.*, **29**, 857-866, 1994.
- Rawer, K., Ionospheric mapping in the polar and equatorial zones, *Adv. Space Res.*, **16** (1), 9-12, 1995.
- Reinisch, B. W., and X. Huang, Low latitude digisonde measurements and comparison with IRI, *Adv. Space Res.*, **18**(6), 5-12, 1996.
- Rush, C. M., M. PoKempner, D. Anderson, F. G. Stewart, and J. Perry, Improving ionospheric maps using theoretically derived values of  $f_oF_2$ , *Radio Sci.*, **18**, 95-107, 1983.
- Rush, C. M., M. PoKempner, D. Anderson, J. Perry, F. G. Stewart, and R. Reasoner, Maps of  $f_oF_2$  derived from observations and theoretical data, *Radio Sci.*, **19**, 1083-1097, 1984.
- Su, Y. Z., K.-I. Oyama, G. J. Bailey, S. Fukao, T. Takahashi, and H. Oya, Longitudinal variations of the topside ionosphere at low latitudes: Satellite measurements and mathematical modelings, *J. Geophys. Res.*, **101**, 17,191-17,205, 1996.
- Szuszcwicz, E. P., et al., F region climatology during the SUNDIAL/ATLAS 1 campaign of March

- 1992: Model-measurement comparisons and cause-effect relationships, *J. Geophys. Res.*, **101**, 26,741-26,758, 1996.
- Walker, G. O., Longitudinal structure of the F-region equatorial anomaly - A review, *J. Atmos. Terr. Phys.*, **43**, 763-774, 1981.
- West, K. H., R. A. Heelis, and F. J. Rich, Solar activity variations in the composition of the low-latitude topside ionosphere, *J. Geophys. Res.*, **102**, 295-305, 1997.
- Air Force Base, MA 01731-3010. (e-mail: danderson@plh.af.mil)
- D. T. Decker, Institute for Scientific Research, Boston College, 140 Commonwealth Avenue, St. Clement's Hall, Room 402, Chestnut Hill, MA 02167-3862. (e-mail: decker@plh.af.mil)
- A. J. Preble, Headquarters United States Air Force, Directorate of Weather, 1490 AF Pentagon, Washington, D. C. 20330. (email: ajpreble@aol.com)

---

D. N. Anderson, Air Force Research Laboratory, Geophysics Directorate, 29 Randolph Rd., Hanscom

(Received October 15, 1996; revised March 14, 1997; accepted April 8, 1997.)

## **Comparisons of TOPEX and Global Positioning System total electron content measurements at equatorial anomaly latitudes**

**J. A. Vladimer and M. C. Lee**

Department of Electrical and Computer Engineering, Boston University, Boston, Massachusetts

**P. H. Doherty and D. T. Decker**

Institute for Scientific Research, Boston College, Newton, Massachusetts

**D. N. Anderson**

Ionospheric Effects Division, Phillips Laboratory, Hanscom Air Force Base, Massachusetts

**Abstract.** Discrepancies exist between vertically measured ionospheric total electron content (TEC) and slant measurements of TEC that are converted to vertical with the use of a mapping function. Vertical measurements of TEC that are determined by the TOPEX altimeter are compared with equivalent vertical TEC values that are derived from the Global Positioning System (GPS) constellation at latitudes  $-40^\circ$  to  $+40^\circ$  and longitudes  $180^\circ$  to  $360^\circ$  during periods in 1993, 1994, and 1995. Also, comparisons are made with the Phillips Laboratory parameterized ionospheric model (PIM) predictions of vertical and equivalent vertical TEC from the same observation points. A trend of disagreement in maximum and minimum TEC values is observed between TOPEX and GPS passes that involve measurements within  $20^\circ$  to the south and to the north of the geomagnetic equator. PIM model predictions, although not exact in value, are consistent in configuration with these observations of overestimation as well as underestimation of TEC. It is shown that the errors are dependent on not only elevation angle but also azimuth of the line-of-sight direction. The elevation mapping function that relates the line-of-sight TEC to vertical TEC and other assumptions that are made in the application of the ionospheric shell model may be contributing factors to the slant-to-vertical conversion errors.

### **1. Introduction**

The TOPEX/Poseidon satellite was launched in 1992 by NASA and the French Space Agency, Centre National d'Etudes Spatiales (CNES) for the study of global ocean dynamics. The NASA dual-frequency altimeter provides accurate sea range measurements which require correction for the dispersive ionospheric radar signal delay. The resulting extensive over-ocean dataset for the total electron content (TEC) can be used as a supplement to land-based measurements such as those determined from the Global Positioning System (GPS) delay data. This worldwide network of satellites and ground receivers belongs to the International GPS Geodynamic Service (IGS). Among other technologies, GPS provides

continuous positioning and velocity determination which requires ionospheric TEC calibration.

It is difficult to provide accurate predictions of TEC at low latitudes due to the large temporal variations of the ionosphere near the magnetic equator. In this study, TOPEX and GPS TEC measurements are used in an attempt to determine the extent of disagreement in vertically obtained and slant-to-vertical converted TEC values at equatorial anomaly latitudes. The following GPS stations were used for this study: in South America, Santiago, Chile; Arequipa, Peru; Fortaleza, Brazil; and Kourou, French Guiana; and island locations Kokee Park, Pamatai, and Easter Island. TOPEX 10-day coverage, the GPS ground receivers, and their perspective to the geomagnetic equator are shown in Figure 1. Assumptions that are made in determining GPS line-of-sight TEC and other factors that may contribute to the disagreement with the TOPEX measurements will be discussed.

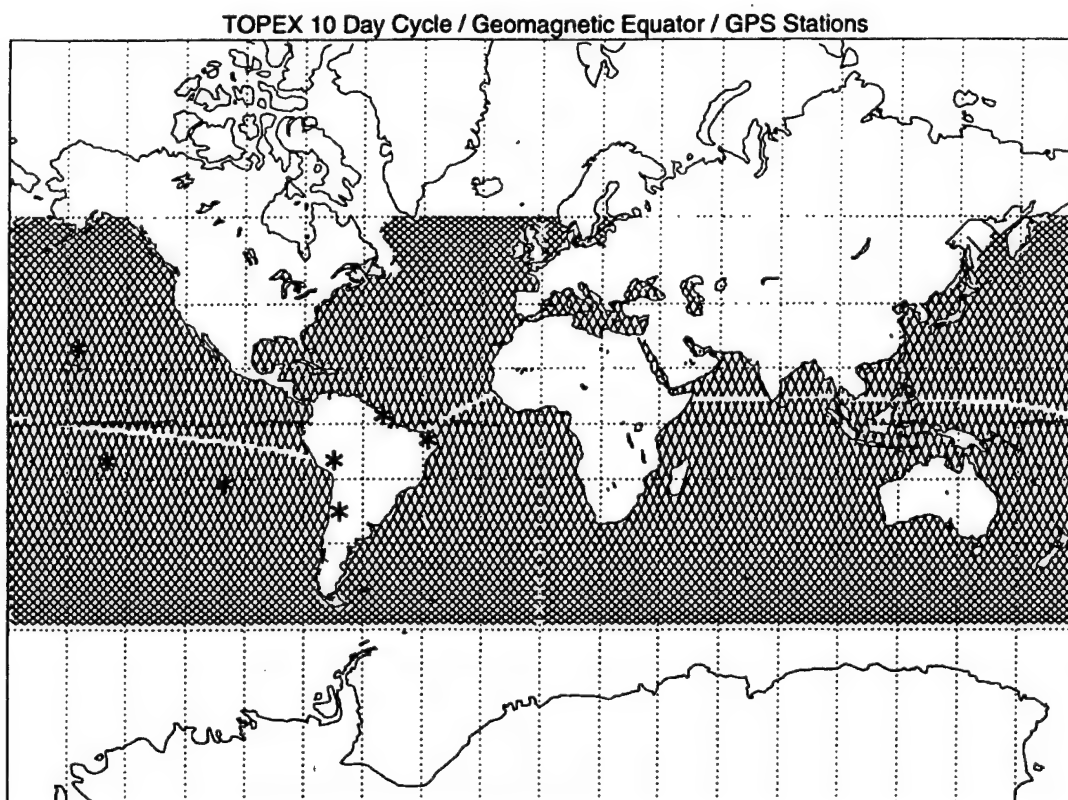


**Figure 1.** Geomagnetic equator is shown with TOPEX 10-day cycle and Global Positioning System (GPS) receivers. Locations are Kokee Park, Pamatai, Easter Island, Santiago, Arequipa, Fortaleza, and Kourou.

The TOPEX/GPS comparisons are focused on the TEC measurements near the magnetic equator during afternoon and evening hours. Large values of TEC are observed within  $30^\circ$  magnetic latitude on each side of the equator from approximately noon-time until 2200 LT as a result of the formation of the electromagnetic phenomenon known as the equatorial anomaly [Appleton, 1946]. These bilateral enhancements are formed by the perpendicular electrodynamic ( $\mathbf{E} \times \mathbf{B}$ ) uplifting of the  $F$  region plasma, in combination with the parallel plasma flow due to nonelectromagnetic forces of gravity and pressure gradients [Kelley, 1989; Balan and Bailey, 1995]. This so-called plasma fountain is illustrated in Figure 2.

The diurnal variation in electric field strength and ionospheric plasma density is believed to be caused by an increase in the thermospheric winds in the  $F$  region which create ion and electron separation. Currents develop, and in response, an electrostatic field is generated and interacts with the Earth's magnetic field, causing vertical plasma drifts [Ander-

son, 1981]. There is variability in the equatorial anomaly with respect to time of day, season, longitude, solar cycle, and other daily geophysical conditions indicated by magnetic and solar indices.

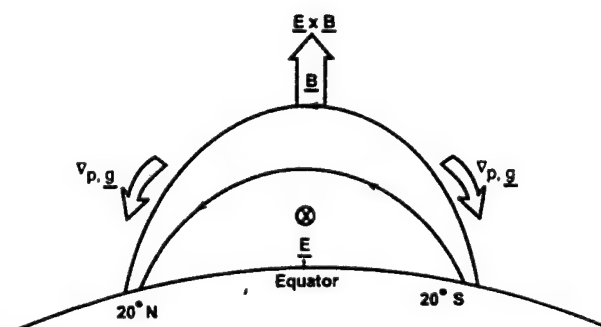


**Figure 2.** The "plasma fountain" produces ionization crests on both sides of the magnetic equator.

## 2. Total Electron Content Measurements

Each of the GPS satellites is in a 12-hour circular orbit at an inclination of 55° and an altitude of 20,000 km. GPS signals which are transmitted at dual-frequency ( $L_1$ , 1575.42 MHz, and  $L_2$ , 1227.60 MHz) experience a dispersive ionospheric delay. These GPS delay data provide line-of-sight TEC measurements. The measured pseudorange is given by

$$R_{\text{measured}} = R_{\text{true}} + \Delta R_{\text{ionosphere}} + \Delta R_{\text{other}} \quad (1)$$

where  $R_{\text{true}}$  is the true range,  $\Delta R_{\text{ionosphere}}$  is the ionospheric delay at the frequency  $L_1$  or  $L_2$ , and  $\Delta R_{\text{other}}$  are the range errors due to other frequency-dependent and non-frequency-dependent sources. The measured range is represented by the integral of the refractive index ( $n$ ) along the path of the signal, and the geometric range is the integral of ( $n = 1$ ) along the straight line between satellite and receiver.

Approximations are used to compute the ionospheric delay [Hofman-Wellenhof *et al.*, 1994].

1. Higher orders of frequency are ignored when considering the phase and group refractive indices:

$$n_{\text{phase}} = 1 + b_2/f_i^2 \quad n_{\text{group}} = 1 - b_2/f_i^2 \quad (2)$$

where  $b_2 = -40.3 N_e \text{ (Hz}^2 \text{ m}^3\text{)}$  and  $f_i$  is the frequency  $L_1$  or  $L_2$ . (TEC equals the integral of the electron density ( $N_e$ ) along the signal path.)

2. The geometric path (ray bending ignored) is used for the Fermat integrations, resulting in

$$\Delta R_{\text{ionosphere}} = (40.3/f_i^2) \text{ TEC} \quad (3)$$

where the TEC in this case is the vertical total electron content (elevation = 90°). To determine the slant TEC, a mapping function ( $M(E)$ ) is used to account for elevations that are less than the zenith angle:

$$M(E) = (1/\cos \phi) = [1 - (R \cos E/R + H)^2]^{-1/2} \quad (4)$$

where  $R$  is the radius of the earth and  $H$  is an average value of electron density peak positions which is approximated at 400 km.  $E$  is the elevation angle of the line-of-sight measurement, and  $\phi$  is the incident angle at the ionospheric shell intersect. Figure 3 shows the ionospheric shell geometry and the relationship between the slant and vertical paths. The ionospheric range delay is then given by

$$\Delta R_{\text{ionosphere}} = (1/\cos \phi)(40.3/f_i^2)(\text{vertical TEC}) \quad (5)$$

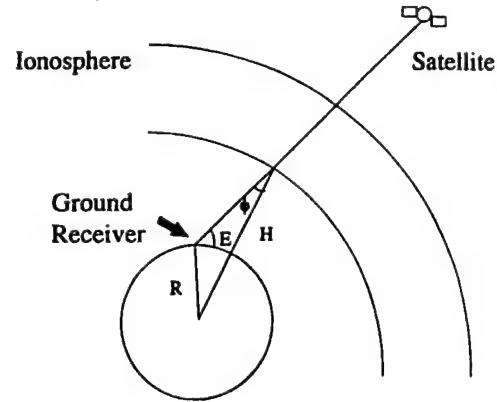


Figure 3. The ionospheric shell is shown with slant path at elevation (letter E). The incident angle ( $\phi$ ) is formed by the intersection of the slant and vertical paths at the subionospheric coordinates.

and the total electron content along an arbitrary line of sight is

$$\text{slant TEC} = (1/\cos \phi) \text{ vertical TEC} \quad (6)$$

The TOPEX satellite has an orbital altitude of 1336 km (equatorial reference) and an inclination of 66°. One full revolution, which is achieved in 112 min, consists of two passes, each of which spans 150° of longitude from west to east and 133° of latitude. (An ascending pass spans -66° to 66° latitude; a descending pass spans 66° to -66° latitude.) Consecutive revolutions are offset to the west by approximately 30°. This TOPEX coverage provides the ability to observe TEC variability across the world in 1 day at 30° intervals at approximately the same local time. There are 127 revolutions (254 passes) in a TOPEX cycle, which covers the same surface tracks every 10 days. The differential between UT and LT, in combination with the "overlap" required to accomplish ice-free ocean coverage, results in a 2 hour loss of local time for each consecutive 10-day cycle. Day-to-day TEC variability can be studied as well using TOPEX data, since the satellite's coverage during 1 day comes within 8° and 12 min of the previous day's position and local time. Figure 4a shows two consecutive days of TOPEX ascending passes. Figure 4b gives an example of TOPEX data which illustrates longitudinal and day-to-day variation in the equatorial anomaly.

The TOPEX orbital speed is 7.2 km s<sup>-1</sup>, and altimeter measurements are obtained at a rate of one per second. The ionospheric correction and vertical



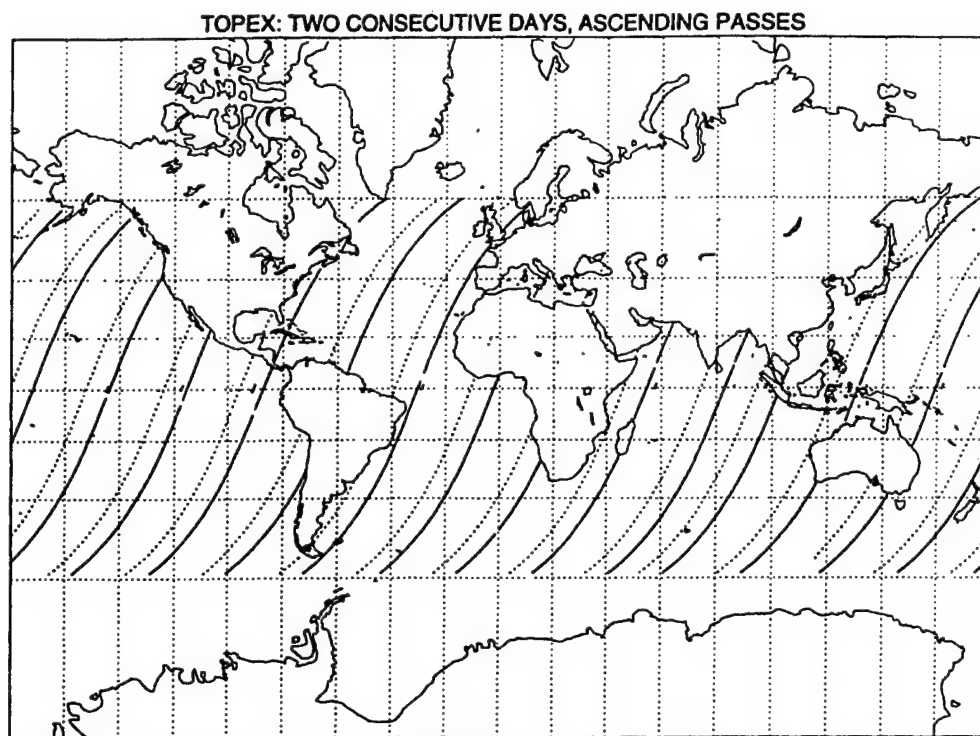


Figure 4a. Solid lines represent 1 day of TOPEX ascending passes. The dashed lines represent the next day's ascending passes.

TEC is computed from TOPEX dual-frequency range measurements. (5.3 GHz, C band, and 13.6 GHz, Ku band). Once again, we use (1) where  $R_{\text{measured}}$  is the  $R_C$  or  $R_{Ku}$  range measurement and  $\Delta R_{\text{ionosphere}}$  is the ionospheric range error which is assumed to have the form

$$b_C/f_C^2 \text{ or } b_{Ku}/f_{Ku}^2 \quad (7)$$

where  $b_i \approx 40.3$  TEC. The  $R_{\text{measured}}$  equations for C and Ku bands provide an expression for the ionospheric correction at Ku band:

$$\Delta R_{\text{ionosphere}} = [f_C^2/(f_{Ku}^2 - f_C^2)] [R_{Ku} - R_C] \quad (8)$$

and vertical TEC is given by

$$\text{vertical TEC} = \Delta R_{\text{ionosphere}} [f_C^2 f_{Ku}^2 / (f_{Ku}^2 - f_C^2) 40.3] \quad (9)$$

One TEC unit (TECU) ( $10^{16}$  el/m<sup>2</sup>) corresponds to 12.17 mm range error at the given TOPEX altimeter frequencies.

### 3. Assumptions and Considerations

Determination of arbitrary line-of-sight TEC with the use of a mapping function has been described previously [Lanyi and Roth, 1988]. This model assumes a thin-shell approximation of the ionosphere at a fixed height of 350 km (400 km is used for present measurements.) In addition, the ionosphere is assumed to be horizontally homogeneous and time independent over a period of 4–6 hours with respect to the Sun-Earth axis.

The comparisons between TOPEX and GPS also require the assumption of ionospheric time independence over several hours. For example, one window of comparison involves 20 min of TOPEX measurements to acquire maximum values of TEC over one anomaly hemisphere, while 1–2 hours of GPS measurements are needed to obtain the same peak values.

Another concern is instrument accuracy. The uncertainty in the TOPEX ionospheric correction has been evaluated to be approximately 0.5 cm [Imel, 1994]. The GPS measurements are affected by the

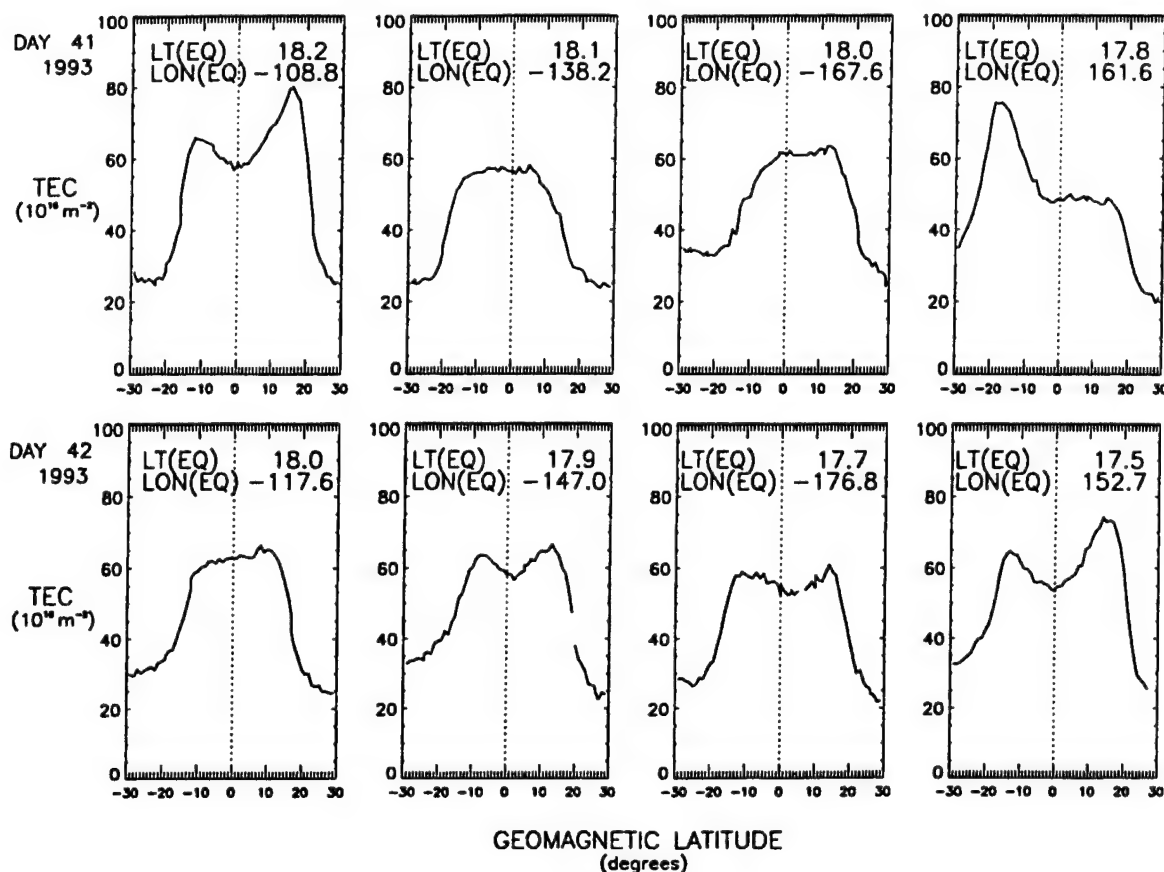


Figure 4b. The upper panels show four consecutive TOPEX passes on day 41 in the Pacific. The lower panels show four consecutive passes on day 42. Each of the lower passes is approximately  $8^\circ$  offset to the west and 12 min earlier (LT) than the corresponding upper pass.

satellite transmitter and ground receiver biases between the  $L_1$  and  $L_2$  signals. These biases are not elevation dependent and therefore are estimated independently with ionospheric TEC [Wilson *et al.*, 1995]. The GPS biases are taken as constant over the period of time of the TOPEX/GPS comparisons.

Finally, the protonosphere as a source of TEC is considered due to the altitude difference between TOPEX (1336 km) and GPS satellites (20,000 km). At night, the  $F_2$  layer of the ionosphere lowers, and possibly 50% of the total TEC is contributed by the protonosphere [Klobuchar *et al.*, 1994]. Since the TOPEX/GPS comparisons are limited to afternoon and evening local times (1400–2200), the protonosphere contribution is presumed to be insignificant.

#### 4. Observations and Modeling

The specific TOPEX/GPS passes that are used for comparison were chosen with consideration for time

(LT and UT) and longitudinal proximity, as well as directional agreement. For receivers located to the south of the equator, the ascending TOPEX passes are compared with GPS shell coverage that corresponds to lines of sight from approximately  $90^\circ$  elevation (over station) to  $15^\circ$  elevation,  $0^\circ$  azimuth (toward magnetic equator). For the same stations the descending TOPEX passes are compared with GPS passes with shell coverage corresponding to  $15^\circ$  elevation,  $0^\circ$  azimuth to  $90^\circ$  elevation.

Similarly, for stations located to the north of the magnetic equator, the TOPEX passes are compared with GPS coverage with ranges of line of sight from  $90^\circ$  elevation to ( $E = 15^\circ$ ,  $A = 180^\circ$ ) for descending passes and from ( $E = 15^\circ$ ,  $A = 180^\circ$ ) to  $90^\circ$  elevation for ascending passes. Figures 5a and 5b show an example of an ascending TOPEX/GPS pass comparison involving a southern GPS receiver and the plot of the respective TEC values.

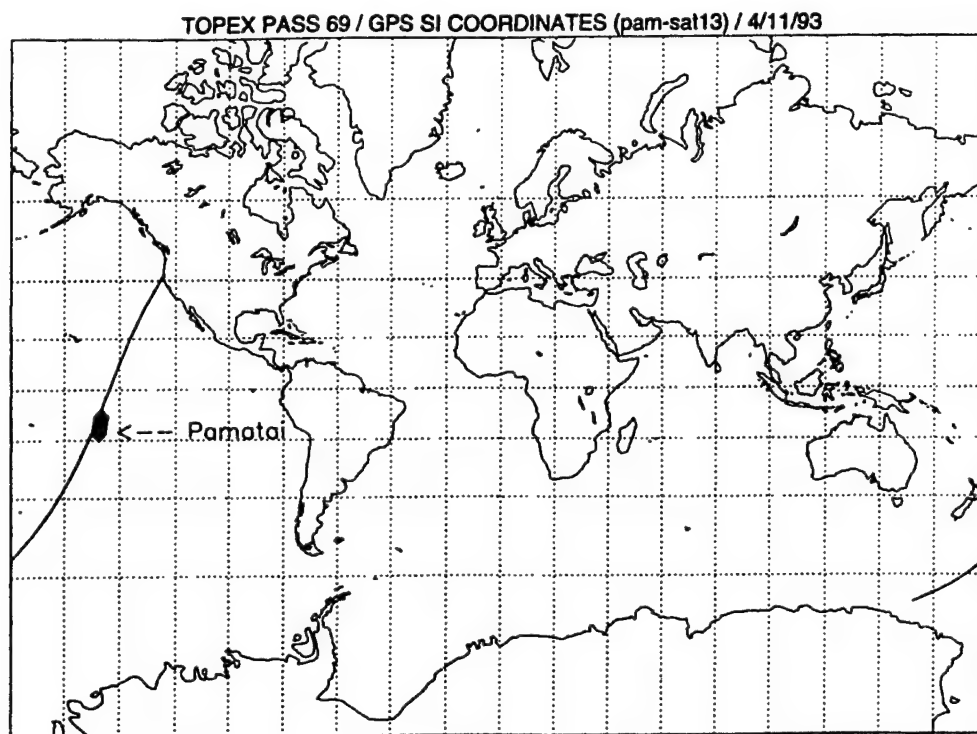


**Figure 5a.** A “window” of comparison between an ascending TOPEX pass and a portion of an ascending GPS pass with shell coverage over the southern hemisphere equatorial anomaly. The Pamatai station is indicated at the start of the GPS data.

Agreement in TEC is anticipated at high elevation and is seen consistently, although the separation or “coming away” from agreement begins to occur at elevation angles up to  $50^\circ$  and azimuth that is indicative of a line of sight toward the magnetic equator. This configuration of overestimation from Pamatai (Figure 5) is also illustrated in the results from Kokee Park, Easter Island, Santiago, and Kourou (Figure 6a), which are receivers that provide maximum TEC values at anomaly peaks. Receivers at Arequipa and Fortaleza, which provide TEC measurements of the anomaly minimum, reveal an underestimation of TEC that is seen at ranges of elevation as high as  $70^\circ$  (see Figure 6b). (Figure 7 indicates elevation angles that correspond to the Pamatai plot in Figure 5b and the Santiago and Arequipa plots in Figures 6a and 6b, respectively.)

GPS maximum values are in the range of 15–20 TECU higher than TOPEX maximum values, and GPS minimum values are approximately 5–10 TECU lower than the TOPEX measurements. Figure 7 shows another representation of the vertical TOPEX

TEC and the equivalent vertical GPS TEC in which the separation from agreement is clearly illustrated. The peak disagreement in overestimation and underestimation is seen at ranges of elevation from  $15^\circ$  to  $35^\circ$ . It should be noted that the results presented from these seven GPS receivers involve seven different GPS space vehicles.

The parameterized ionospheric model, which is the Phillips Laboratory’s theoretical climatological model [Daniell *et al.*, 1995], was used to evaluate differences in vertical TEC and slant-to-vertical TEC measurements from observation points of the GPS receivers that are listed above. Examples of PIM results are shown in Figure 8 for Pamatai and Kokee Park in the Pacific and Santiago and Arequipa in South America. The configurations are consistent with the observations with respect to the agreement in TEC at zenith and the separation from this agreement as the GPS pass excursion moves from  $90^\circ$  to low elevation with azimuth directed to the magnetic equator. The differences in the minimum TEC values are comparable to the observations at Arequipa and Fortaleza (5–10

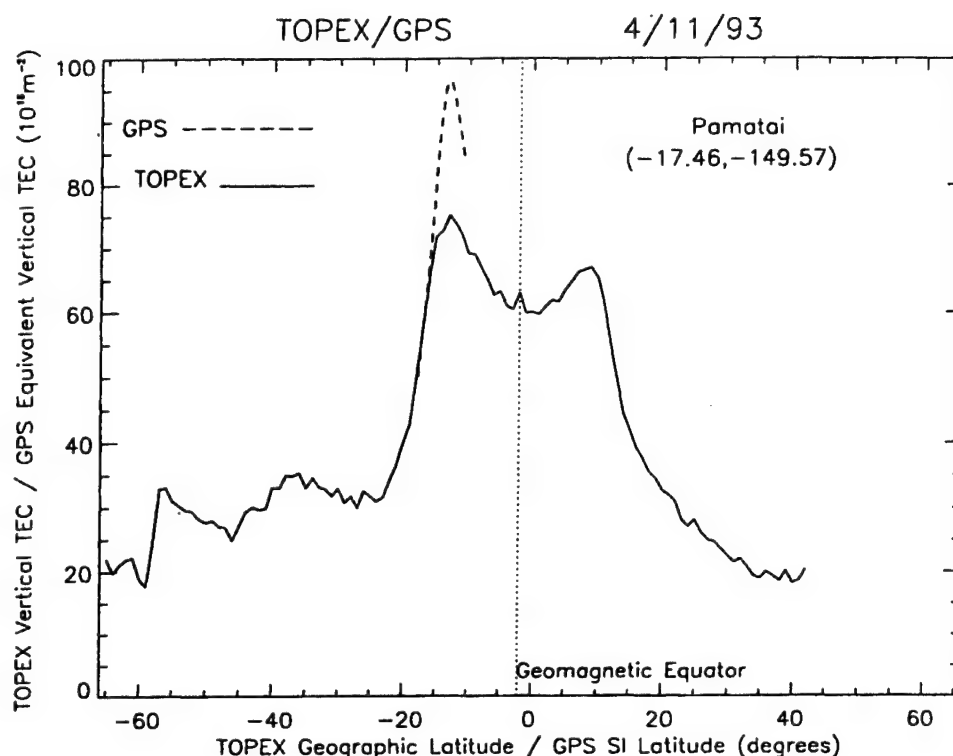


Figure 5b. TOPEX and GPS data for the Pamatai pass comparison.

TECU equivalent vertical less than vertical), but the overestimation values do not predict the extent of the discrepancies that were seen at Pamatai, Kokee Park, Easter Island, Santiago, and Kourou. While the PIM shows a difference of approximately 5–10 TECU of equivalent vertical over vertical, the data from these stations show a 15–30 TECU difference at the anomaly maximums.

## 5. Conclusions

Specific “windows” of comparison between TOPEX vertical TEC measurements and GPS slant measurements, which are mapped to vertical TEC values, reveal deviations from agreement at low latitude. The TOPEX and GPS TEC values are nearly equal when measurements are obtained at high elevation, but as the GPS line of sight moves from zenith to a slant line of sight with azimuth toward the magnetic equator, the comparisons show a separation from agreement. The variability in these TEC differences shows a dependence on the GPS pass and line of sight (elevation, azimuth) to ground receivers located at equatorial anomaly latitudes.

Problems in the application of the mapping function have been acknowledged [Lanyi and Roth, 1988; Wilson *et al.*, 1995] at low elevation (less than 20°), but the observations indicate that disagreement can begin to occur at elevations as high as 50°–70°. These results, in combination with the model (PIM) predictions of similar discrepancies, suggest that the ionospheric shell model with choice of constant shell height and the assumption of horizontal homogeneity may not be an accurate representation of the ionosphere near the magnetic equator. The need to modify the mapping function with adjustment to shell height ( $H$ ) was indicated by Lanyi and Roth [1988], but a constant value continues to be utilized. The errors in slant-to-vertical conversion of TEC require further evaluation of data from equatorial GPS stations and a more in-depth investigation of the source of the PIM prediction of these deviations at low latitude where the ionosphere is so highly variable.

Extending the TEC comparisons to include additional GPS equatorial stations, as well as other seasons and times of day, will be useful, specifically during periods when the ionosphere is not rapidly

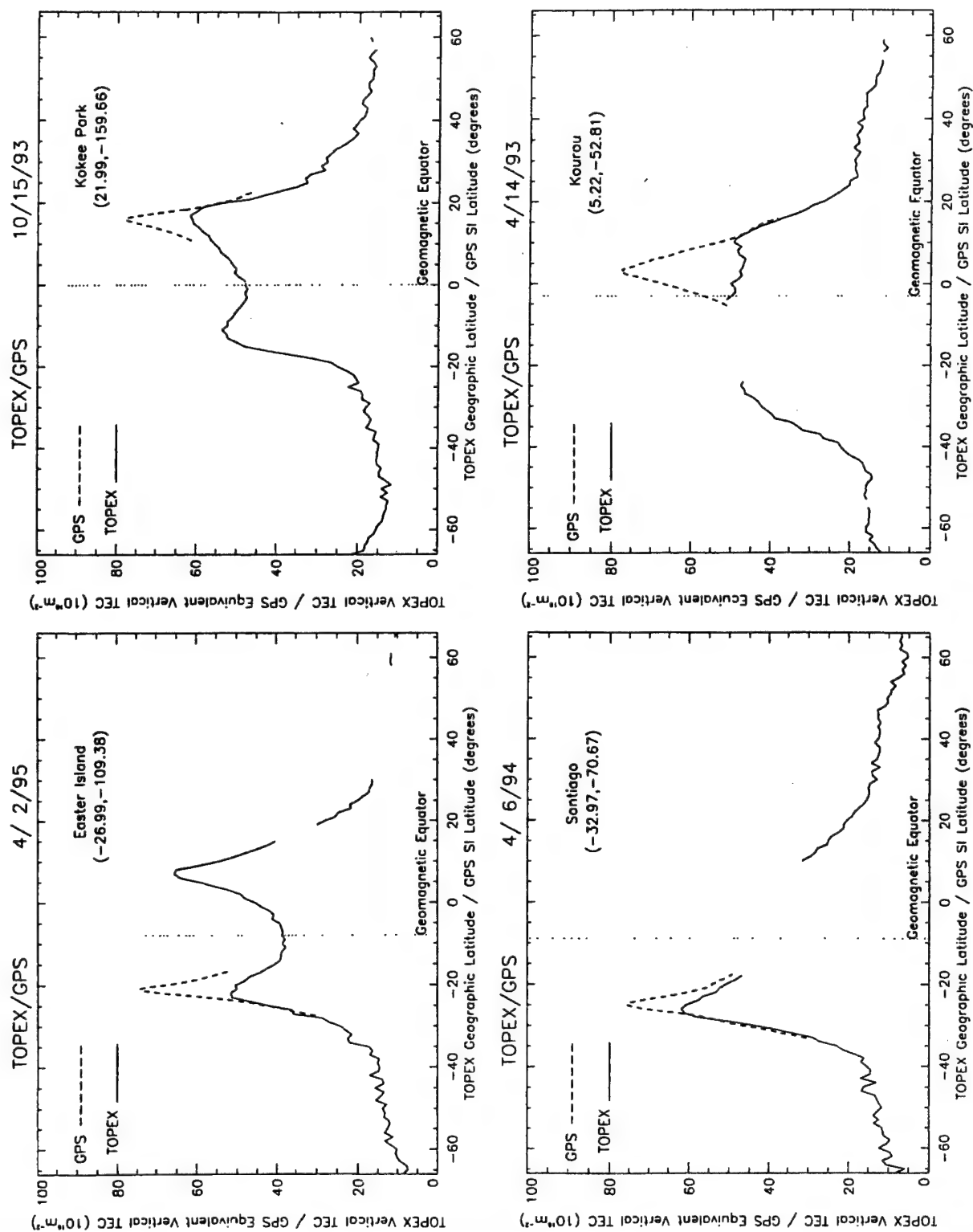


Figure 6a. Results are shown from GPS ground receivers at Easter Island, Kokee Park, Santiago, and Kourou.

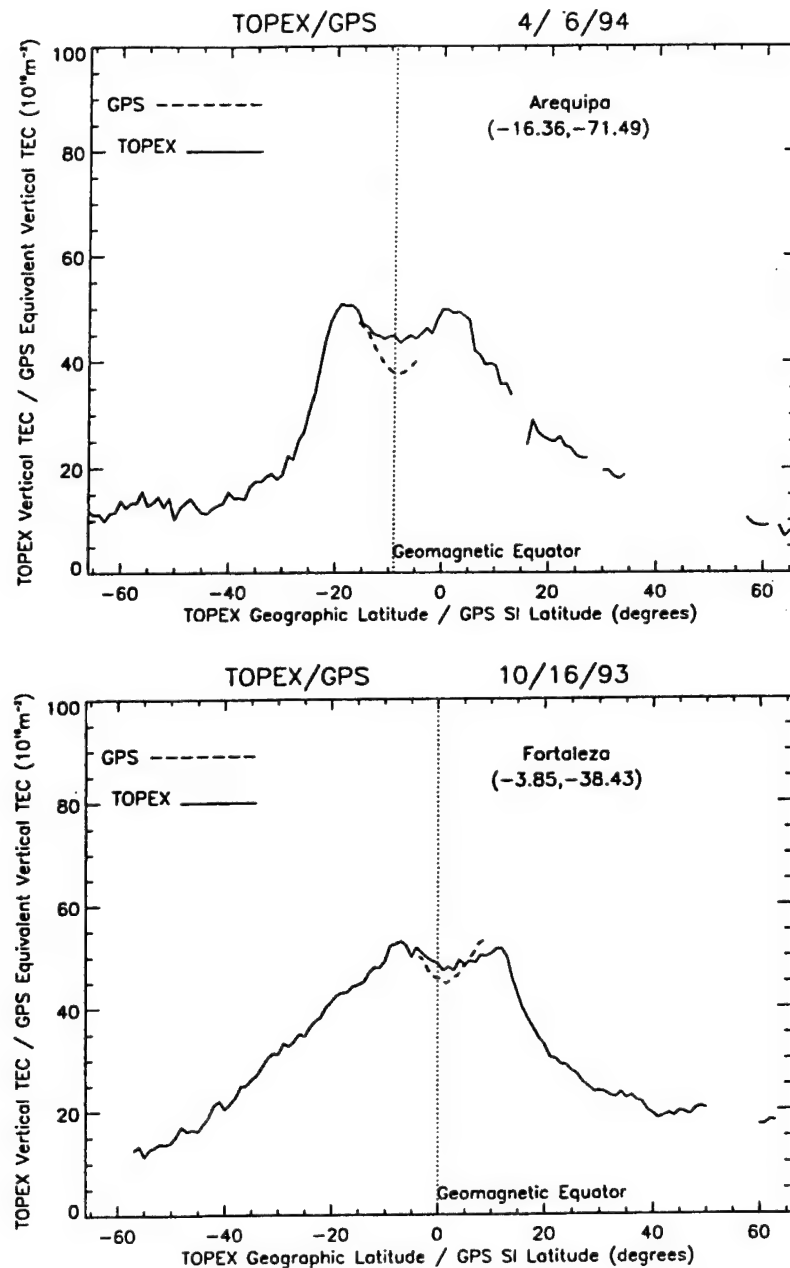


Figure 6b. Results are shown from GPS ground receivers at Arequipa and Fortaleza.

changing. The relative differences in TEC compared with the present results will provide important information with regard to the conversion errors. Improved accuracy in the prediction of TEC values near

the equator may result from not only the possible empirical modification to the mapping function but also the inclusion of low-latitude observations within the ionospheric model.



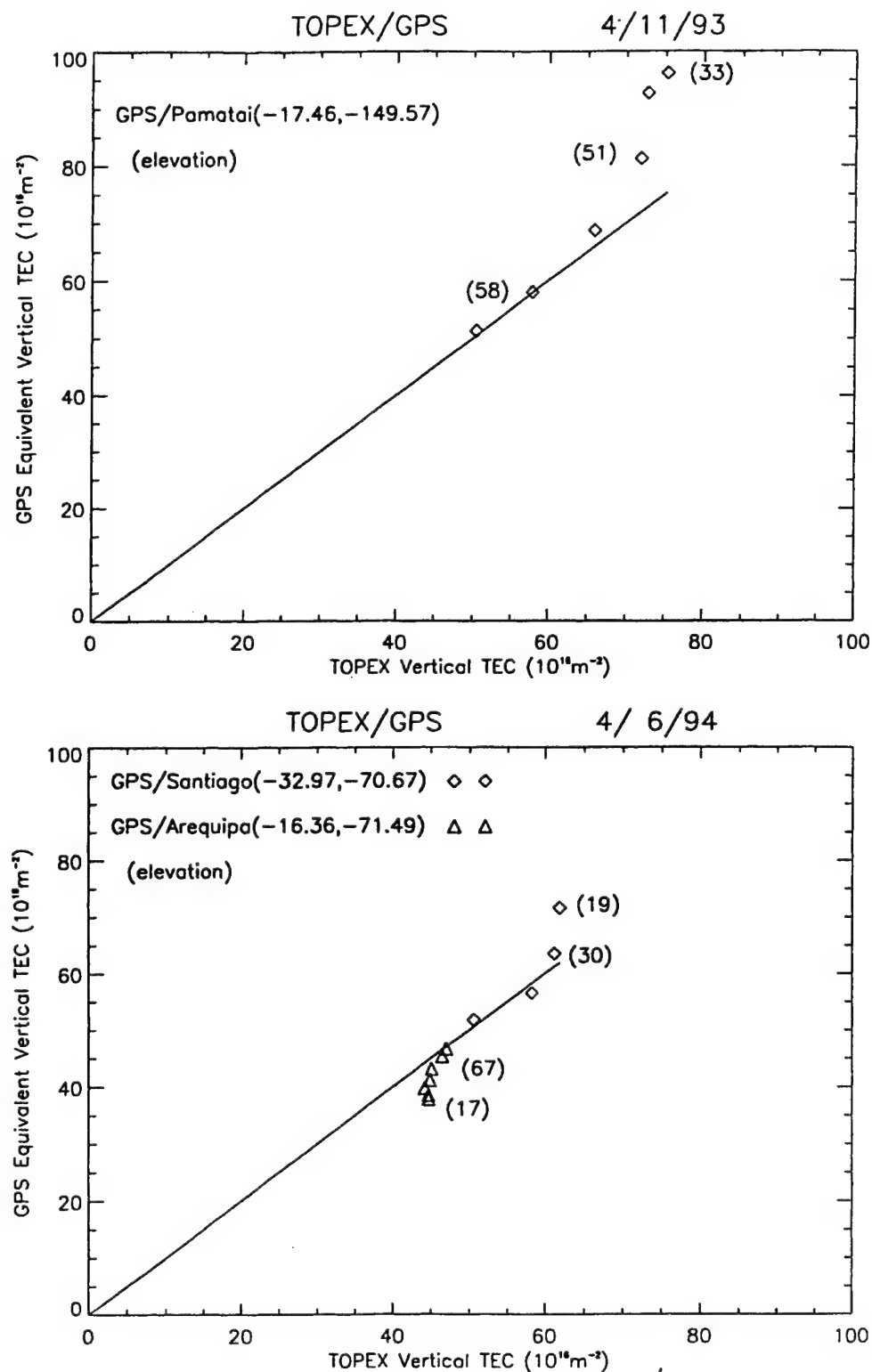
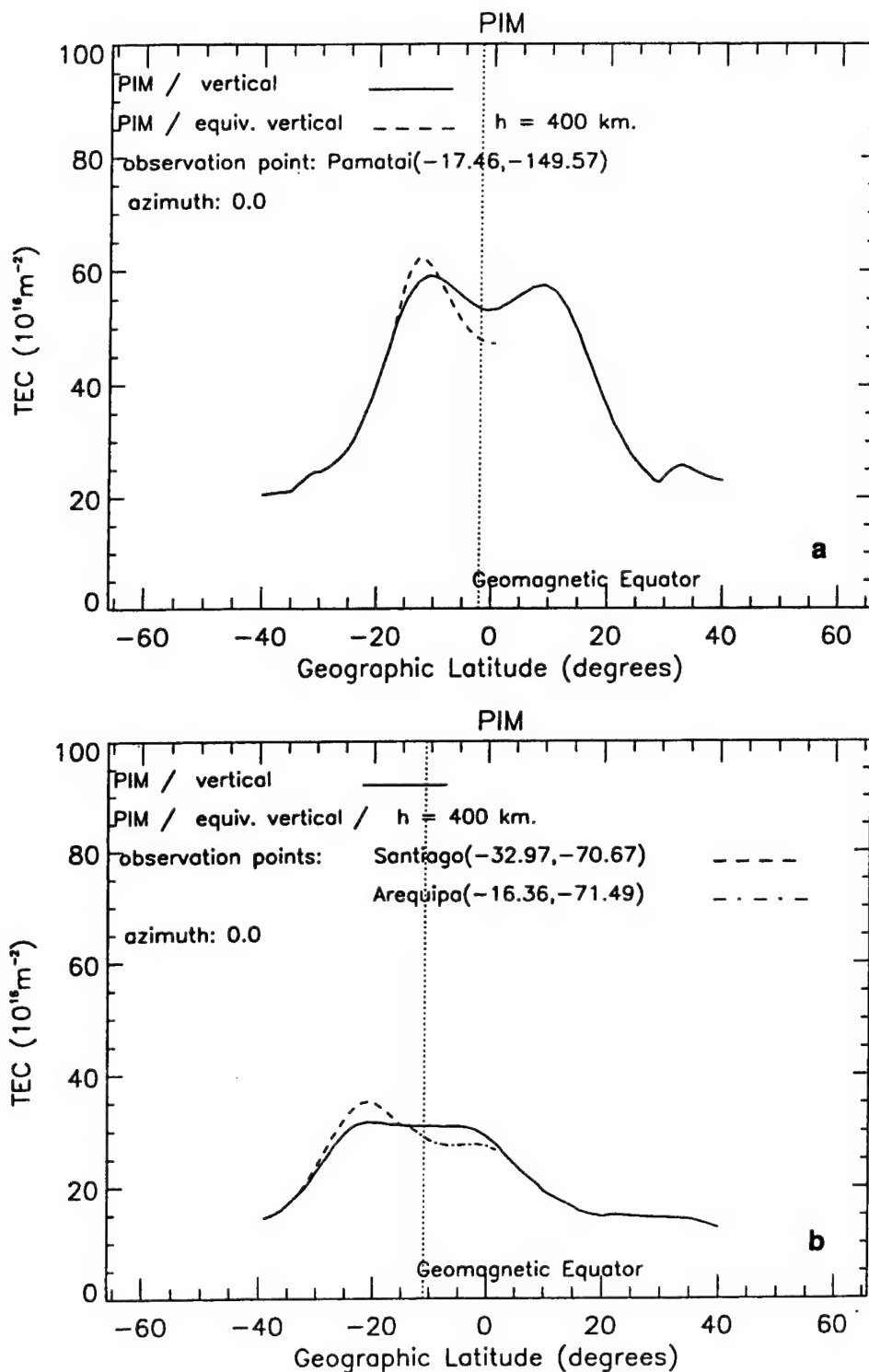


Figure 7. Another illustration of the separation from agreement at maximum and minimum total electron content.



**Figure 8.** Parameterized ionospheric model results are shown from (a) Pamatai and (c) Kokee Park; Figure 8b contains data from both Santiago and Arequipa.

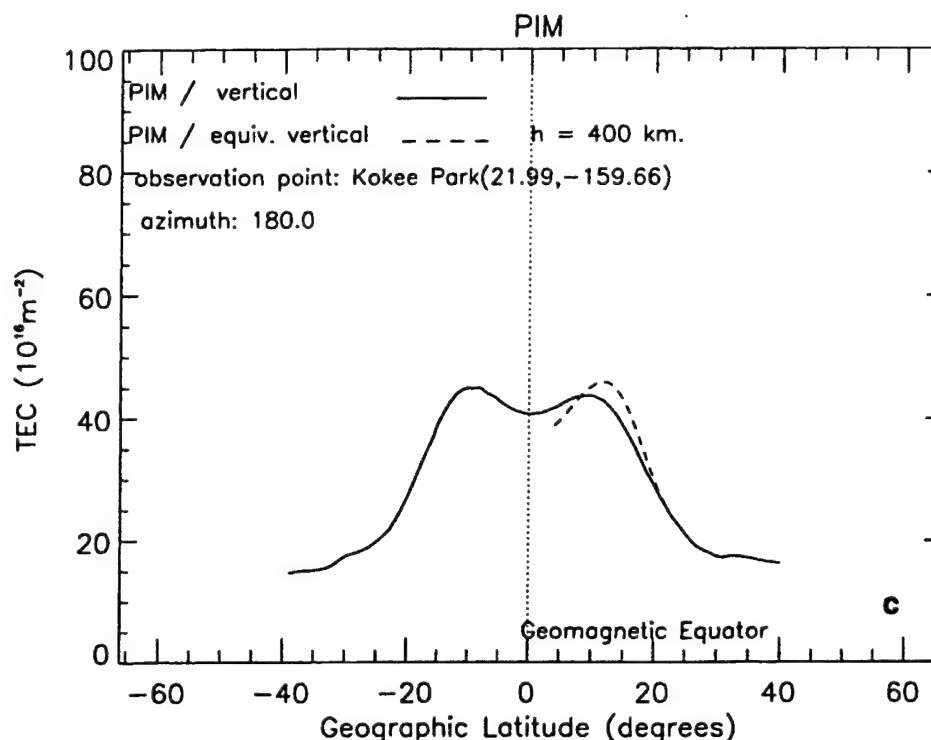


Figure 8. (continued)

**Acknowledgments.** This work was supported by Air Force Office of Scientific Research grant F49620-94-1-0365. The authors thank J. A. Klobuchar for useful discussions.

## References

- Anderson, D. N., Modelling the ambient, low latitude F-region ionosphere—A review, *J. Atmos. Terr. Phys.*, **43**, 753, 1981.
- Appleton, E. V., Two anomalies in the ionosphere, *Nature*, **157**, 691, 1946.
- Balan, N., and G. J. Bailey, Equatorial plasma fountain and its effects: Possibility of an additional layer, *J. Geophys. Res.*, **100**, 21,421, 1995.
- Daniell, R. E., L. D. Brown, D. N. Anderson, M. W. Fox, P. H. Doherty, D. T. Decker, J. J. Sojka, and R. W. Schunk, Parameterized ionospheric model: A global ionospheric parameterization based on first principles models, *Radio Sci.*, **30**, 1499, 1995.
- Hofmann-Wellenhof, B., H. Lichtenegger, and J. Collins, *GPS Theory and Practice*, 3rd ed., Springer-Verlag, New York, 1994.
- Imel, D. A., Evaluation of the TOPEX/Poseidon dual-frequency ionospheric correction, *J. Geophys. Res.*, **99**, 24,895, 1994.
- Kelley, M. C., *The Earth's Ionosphere*, Academic, San Diego, Calif., 1989.
- Klobuchar, J. A., P. H. Doherty, G. J. Bailey, and K. Davies, Limitations in determining absolute total electron content from dual-frequency GPS group delay measurements, in *Proceedings of the International Beacon Satellite Symposium*, pp. 1–4, Univ. of Wales, Aberystuyth, 1994.
- Lanyi, G. E., and T. Roth, A comparison of mapped and measured total ionospheric electron content using Global Positioning System and beacon satellite observations, *Radio Sci.*, **23**, 483, 1988.
- Wilson, B. D., A. J. Mannucci, and C. D. Edwards, Subdaily northern hemisphere maps using an extensive network of GPS receivers, *Radio Sci.*, **30**, 639, 1995.
- D. N. Anderson, Phillips Laboratory, Geophysics Directorate (GPSM), 29 Randolph Road, Hanscom Air Force Base, MA 01730-3010. (e-mail: danderson@plh.af.mil)
- D. T. Decker and P. H. Doherty, Institute for Scientific Research, Boston College, St. Clement's Hall, 140 Commonwealth Avenue, Chestnut Hill, MA 02167-3862. (e-mail: decker@plh.af.mil; doherty@plh.af.mil)
- M. C. Lee and J. A. Vladimer, Department of Electrical and Computer Engineering, Boston University, 8 St. Mary's Street, Boston, MA 02215. (e-mail: mclee@enga.bu.edu; vladi@acs.bu.edu)

(Received February 14, 1997; revised June 23, 1997; accepted August 12, 1997.)

## Intercomparison of physical models and observations of the ionosphere

D. N. Anderson,<sup>1</sup> M. J. Buonsanto,<sup>2</sup> M. Codrescu,<sup>3</sup> D. Decker,<sup>4</sup> C. G. Fesen,<sup>5</sup>  
T. J. Fuller-Rowell,<sup>3</sup> B. W. Reinisch,<sup>6</sup> P. G. Richards,<sup>7</sup> R. G. Roble,<sup>8</sup>  
R. W. Schunk,<sup>9</sup> and J. J. Sojka<sup>9</sup>

**Abstract.** Five physical models of the ionosphere were compared with each other and with data obtained at the Millstone Hill Observatory. Two of the models were self-consistent ionosphere-thermosphere models, while for the other ionospheric models the thermospheric parameters were provided by empirical inputs. The comparisons were restricted to midlatitudes and low geomagnetic activity, but four geophysical cases were considered that covered both the summer and winter solstices at solar maximum and minimum. The original motivation of the study was to determine why several physical models consistently underestimated the *F* region peak electron density, by up to a factor of 2, in the midlatitude, daytime ionosphere at solar maximum. This problem was resolved, but the resolution did not identify a lack of physics in any of the models. Instead, various chemical reaction rates, photoionization processes, and diffusion coefficients had to be adjusted, with the main one being the adoption of the Burnside factor of 1.7 for the diffusion coefficients. The subsequent comparisons of the models and data were for "standard" simulations in which uncertain inputs or processes were not adjusted to get better agreement with the data. For these comparisons, the five models displayed diurnal variations that, in general, agreed with the measurements. However, each one of the five models exhibited a clear deficiency in at least one of the four geophysical cases that was not common to the other models. Therefore, contrary to expectations, the coupled ionosphere-thermosphere models were not found to be superior to the uncoupled ionospheric models for the cases considered. The spread in  $N_m F_2$  calculated by the five models was typically less than a factor of 2 during the day but was as large as a factor of 10 at certain local times during the night. The latter problem was traced to insufficient nocturnal maintenance processes in two of the uncoupled ionospheric models. The general findings of this study have important implications for the National Space Weather Program.

### 1. Introduction

The physics of the terrestrial ionosphere is reasonably well understood and is described by a set of first principles equations [Schunk, 1988]. Efforts to simulate the ionosphere by solving the first principles equations have met with a high degree of success, as shown by comparisons of the model

predictions with observations. The shortcomings in the model/data comparisons are frequently attributed to inadequate constraints on the model inputs; hence it is difficult to establish the capabilities of an individual model by such comparisons. This study is based upon an intercomparison of five physical models that include the ionosphere. We use an alternative method to test the predictive capabilities of the models by carrying out an in-depth intercomparison of the models and an observational database. The test is based on standard model runs, with no allowance for adjusting uncertain input parameters. With this method, differences in how the physical formulations affect the model output can be evaluated, which may lead to identification of the strengths and weaknesses associated with each model.

The verification of the physical models, or at least the identification of relative merits of the models, is timely from another viewpoint. During the past solar maximum period, considerable interest focused on the detrimental effects of strong geomagnetic activity on communication systems, power grid operations, pipe line corrosion, and semiconductor manufacture [Allen *et al.*, 1989]. Although the ionospheric models in themselves do not predict the geomagnetic impact on these terrestrial systems, they do provide a measure of our understanding of storm effects. Accordingly, efforts to validate ionospheric models have been initiated both nationally and internationally. The international component

<sup>1</sup>Phillips Laboratory, Hanscom Air Force Base, Massachusetts.

<sup>2</sup>Atmospheric Sciences Group, Massachusetts Institute of Technology, Haystack Observatory, Westford.

<sup>3</sup>Environmental Research Laboratory/Space Environment Laboratory, NOAA, Boulder, Colorado.

<sup>4</sup>Institute for Space Research, Boston College, Chestnut Hill, Massachusetts.

<sup>5</sup>W. B. Hanson Center for Space Sciences, University of Texas, Dallas, Richardson.

<sup>6</sup>Center for Atmospheric Research, University of Massachusetts, Lowell.

<sup>7</sup>Computer Science Department, University of Alabama, Huntsville.

<sup>8</sup>National Center for Atmospheric Research, Boulder, Colorado.

<sup>9</sup>Center for Atmospheric and Space Sciences, Utah State University, Logan.

of this effort is the URSI commission working group on validation of ionospheric models (VIM) and the national component is the National Science Foundation coupling energetics and dynamics of atmospheric regions (NSF CEDAR) working group on problems related to ionospheric models and observations (PRIMO). The objectives of these two groups are complementary: PRIMO emphasizes the investigation of first-principal physical models, while VIM is interested in the validation of all ionospheric models, including empirical, semiempirical, hybrid, and physical models.

An initial objective of this study was to try to understand why there seemed to be a factor of 2 discrepancy between calculated and observed  $F$  region peak densities during the day at midlatitudes for solar maximum conditions. Electron density profiles derived from Digisonde ionograms [Reinisch and Huang, 1983] in the American and European sectors showed systematic differences from profiles calculated by data-driven or physical models [Reinisch et al., 1994]. It appeared that the model results consistently underestimated  $N_{\max}$  values for high levels of solar activity ( $F_{10.7}$  cm flux index values greater than 200), producing noontime values of  $\sim 1 \times 10^{12}$  el  $m^{-3}$  instead of the observed  $2 \times 10^{12}$  el  $m^{-3}$ . Since the models were incorporating climatological neutral parameters (densities, temperatures and winds), and established solar EUV production rates, charge exchange loss rates and ambipolar diffusion rates, it was unclear where the factor of two discrepancy originated from.

A study was initiated in 1991 to address this issue. Five ionospheric models were involved in the effort. Three of the models calculated ion and electron densities without self-consistent coupling to the neutral atmosphere, while two were fully coupled ionosphere-thermosphere models. The database of observations used in the study was to be from the extensive network of digital sounders [Reinisch, 1995] established by the U.S. Air Force and the University of Massachusetts-Lowell. These data were later augmented with Millstone Hill incoherent scatter radar measurements to cover low solar cycle conditions, for which no digital sounder data were yet available.

This paper presents the first intercomparison of the five physical ionospheric models. The models are the coupled thermosphere-ionosphere model (CTIM), the National Center for Atmospheric Research (NCAR) thermosphere-ionosphere general circulation model (TIGCM), the Utah State University time-dependent ionospheric model (TDIM), the University of Alabama at Huntsville field line interhemispheric plasma model (FLIP), and the Phillips Laboratory global theoretical ionospheric model (GTIM). It is important to bear in mind that the five models have different heritages, reflecting their development for different purposes. Since the models are not equivalent, it is not useful, or possible, to rank them by their capabilities in reproducing a selected subset of observations.

Section 2 presents details of the models and the observations used for verification. The extended descriptions of each model include identification of key caveats; these should be borne in mind in the later comparisons of the models with each other and with the observations. For simplicity we have carefully chosen the geophysical conditions and geographic location of the observations to minimize ambiguity and complications. Accordingly, the observational data set selected corresponds to quiet geomagnetic conditions at middle latitudes. Observations are taken from the extensive

Digisonde and incoherent scatter radar (ISR) databases at the Millstone Hill location (42.6° N, 288.5° E). The data selected for model validation cover the winter and summer solstices for solar cycle minimum and solar cycle maximum. The limitations of the observations are also discussed.

The intercomparisons of the models with each other and with the observations are presented in section 3. Section 4 discusses the degree of agreement and attempts to identify the limits of the physical models in the context of this study. The final section outlines possible extensions of the work for other locations and conditions.

## 2. Models and Observations

The five models used in this study were developed for different purposes over more than a decade. Each model has an extensive history of model development and validation that has appeared in the literature. In the following five sections each model is briefly described from the perspective of this study. To help the reader in contrasting the different attributes of these models, Table 1 summarizes the key features of each model. This summary of features emphasizes the differences in the models that are potentially relevant to this study.

### 2.1. NCAR TIGCM

The NCAR TIGCM represents an intermediate step in the development of a global thermospheric/ionospheric general circulation model by Roble and Dickinson and colleagues. The model was initially formulated in order to investigate the neutral composition and dynamics of the upper thermosphere [Dickinson et al., 1981, 1984; Roble et al., 1982]. The incorporation of ionized species in the model was a more recent development [Roble et al., 1988].

The model self-consistently solves the coupled nonlinear equations for momentum, energy, continuity, hydrostatics, and the equation of state for the neutrals and the ions. Densities of  $N_2$ ,  $O_2$ ,  $O$ ,  $N(^4S)$ ,  $N(^2D)$ ,  $NO$ ,  $N_2^+$ ,  $O_2^+$ ,  $O^+$ ,  $NO^+$  and  $N^+$  are calculated, as are the ion, electron, and neutral temperatures and the neutral winds. The latitude-longitude grid is  $5^\circ \times 5^\circ$ , with 24 levels in the vertical direction from 97 to about 500 km. Upward propagating tidal components are incorporated as perturbations to the lower boundary, as described by Fesen et al. [1991], and contributions from the semidiurnal modes (2,2) through (2,6) and the diurnal (1,1) mode are included [e.g., Forbes et al., 1993]. The semidiurnal tidal amplitudes and phases are provided by the lower atmosphere model of Forbes and Vial [1989]. In the simulations reported here, the diurnal (1,1) mode is specified by an amplitude of  $4.0 \times 10^4$  geopotential centimeters and a phase of 4.0 hours at the model lower boundary near 97 km.

The lower boundary conditions of the model for the neutral chemical constituents depend on the species, and can be either photochemical equilibrium or a specified mass mixing ratio or mass flux. The ionized species are assumed to be in photochemical equilibrium at the lower boundary. The neutral mean temperatures and winds at the lower boundary are prescribed by an annual tide consistent with the Cospas International Reference Atmosphere climatology; semidiurnal and diurnal tidal variations are imposed as described above. The ion temperature is assumed to be equal to the neutral temperature. The upper boundary conditions are diffusive

Table 1. Comparison Overview of the Five Physical Models

Model	TIGCM	TDIM	FLIP	GTIM	CTIM
Institution	NCAR-NSF	USU	UAH	PL-USAF	SEL-SHEFF/UCL
Method	3-D Eulerian	3-D Euler-Lagrange	1-D Lagrangian	3-D Euler-Lagrange	3-D Eulerian (semi-Lagrangian)
Resolution	(5° × 5° grid)	Single flux tube <sup>a</sup>	Single flux tube	Single flux tube <sup>a</sup>	(2° × 18° grid) <sup>b</sup>
Atmosphere	Self-consistent	MSIS86	MSIS86	MSIS86	Self-consistent
Winds	Self-consistent	HWM90	HWM90	HWM90	Self-consistent
Tides	(1,1), (2,2) to (2,6)	none	none	none	(2,2) and (2,4)
Low boundary	97 km	90 km	80 km	100 km	100 km
Upper boundary	~500 km	800 km	Complete field line	1000 km	10,000 km
EUV		Torr et al. [1979]	Richards 74113 <sup>c</sup>	Hinteregger et al. [1981]	Hinteregger et al. [1981]
Burnside factor included	yes	yes	yes	yes	yes

Abbreviations are 3-D, three-dimensional; 1-D, one-dimensional; USU, Utah State University; UAH, University of Alabama at Huntsville; PL-USAF, Phillips Laboratory-U.S. Air Force; SEL-SHEFF-UCL, Space Environment Lab-University of Sheffield-University College London.

<sup>a</sup> For this study.

<sup>b</sup> Latitude 2° and longitude 18°.

<sup>c</sup> Spectrum number.

equilibrium for the neutral and ionized constituents and zero vertical gradients for the temperatures. The O<sup>+</sup>-O collision frequency is multiplied by the Burnside factor of 1.7 [Salah, 1993].

The ion drifts in the model are obtained from the empirical model of Richmond et al. [1980] for low and middle latitudes and from the empirical model of Heelis et al. [1982] for high latitudes. The Richmond et al. [1980] model represents solar cycle minimum conditions; the drifts during solar cycle maximum are known to be substantially different, at least at low latitudes [e.g., Fejer, 1991].

The high-latitude processes included in the model are magnetospheric convection and particle precipitation, which result in momentum forcing and Joule heating. The auroral parameterizations used in the TIGCM are described by Roble and Ridley [1987]. The empirical convection model of Heelis et al. [1982] is used for calculations of ion drag and Joule heating, which are updated at each time step. The model representation of particle precipitation is based on satellite data for various levels of auroral activity. Geomagnetic disturbances produce increases in the auroral zone half width, mean particle energy, and particle flux, which are adjustable model parameters that vary with magnetic local time. The geographic and geomagnetic poles are offset in the model. The displacement of the auroral oval toward the nightside in geomagnetic coordinates results in its location at higher geographic latitudes on the dayside.

In terms of this study, the following facts are of particular interest. First, the model uses an Eulerian (fixed grid) approach. The upper boundary is determined by the radiation condition and may vary from approximately 300 to 600 km, depending on solar activity. Near solar maximum, the peak of the *F* layer may lie very near the top boundary of the model. In extreme cases, it may even fall outside the model grid. Also, interhemispheric plasma fluxes and, consequently, conjugate effects are not included. As noted earlier, the ion drifts are imposed in the present model version, and currently they represent solar minimum conditions. As a consequence, the postsunset reversal of the *E* × *B* drift in the model is very small. Finally, it is emphasized that this model couples the neutral and ionized atmospheres, including the winds and the ion and neutral densities. There is no opportunity, for example, to adjust the neutral winds to reproduce the observed *F* layer heights, as can be done with some of the purely ionospheric codes.

The TIGCM simulations presented here are for June 21 and December 21. The solar activity is represented by the *F*<sub>10.7</sub> cm index, which is taken to be 75 (195) for solar cycle minimum (maximum). All simulations are for quiet geomagnetic conditions: the cross-polar-cap potential is 30 kV and the total hemispheric power is 3 GW. This corresponds roughly to a *K<sub>p</sub>* level of 1. For each simulation the model is run to diurnally reproducible solutions; that is, the value of a modeled field at a given grid point and at a given universal time falls within a few percent of the value calculated on the previous day. Thus the results discussed here represent "steady state" conditions.

## 2.2. Utah State University TDIM

The TDIM model was developed over a two-decade period by Robert Schunk and coworkers. This model simulates a wide range of physical processes in the *E* and *F* regions of the



ionosphere and uses state-of-the-art input models to represent the neutral atmosphere, magnetosphere, and solar EUV. The physical model is based on the transport formulation, and in its present form solves the set of continuity, momentum, and energy equations. Coupled continuity and momentum equations are solved for  $O^+$ ,  $NO^+$ , and  $O_2^+$  as major ions, and then solutions are obtained for  $N_2^+$ ,  $N^+$ , and  $He^+$ , assuming they are minor ions; charge neutrality is assumed. Ion and electron energy equations are solved at each time step to obtain the  $O^+$  and electron temperatures. The coupled equations are solved as a function of altitude on a fixed grid, and a Lagrangian procedure is used to follow convecting plasma flux tubes. This facilitates the running of both global-scale and high-resolution, local-scale, simulations with the same formulation. An extensive effort has gone into midlatitude and high-latitude research, including auroral and polar cap magnetospheric dependencies. This work has also involved studying ionospheric weather features, such as polar cap patches, dayside troughs, Sun-aligned arcs, polar holes, etc.

The ionospheric model was initially developed as a midlatitude, multi-ion ( $NO^+$ ,  $O_2^+$ ,  $N_2^+$ , and  $O^+$ ) model by Schunk and Walker [1973]. The time-dependent ion continuity and momentum equations were solved as a function of altitude for a corotating plasma flux tube including diurnal variations and important *E* and *F* region processes. This model was extended to include high-latitude effects due to convection electric fields and particle precipitation by Schunk et al. [1975, 1976]. At that time, a simplified ion energy equation was also added, which was based on the assumption that local heating and cooling processes dominate (valid below 500 km). Flux tubes of plasma were followed as they moved in response to convection electric fields. A further extension of the model to include the minor ions  $N^+$  and  $He^+$ , an updated photochemical scheme, and the mass spectrometer/incoherent scatter (MSIS) atmospheric model was undertaken by Schunk and Raitt [1980].

The addition of plasma convection and particle precipitation models was undertaken by Sojka et al. [1981a, b], so that three-dimensional plasma distributions could be obtained. Schunk and Sojka [1982] expanded the model to include ion thermal conduction and diffusion thermal heat flow, with the result that the ion temperature is now rigorously calculated at all altitudes between 120 and 1000 km. The adopted ion energy equation and conductivities are those given by Conrad and Schunk [1979]. The electron energy equation was included by Schunk et al. [1986], and consequently, the electron temperature is now rigorously calculated at all altitudes. The electron energy equation and the heating and cooling rates were taken from Schunk and Nagy [1978], and the conductivities were taken from Schunk and Walker [1970]. The incorporation of the Sterling et al. [1969] equatorial ionospheric model and the various improvements to this model were undertaken by Sojka and Schunk [1985].

A detailed review of the TDIM theoretical development is given by Schunk [1988], while a review of observation model comparisons is given by Sojka [1989]. Sojka [1989] discusses the comparison of the TDIM with selected observations, and in most cases, favorable results were obtained. Often, however, this could be attributed to sparse observational data sets, which were inadequate to constrain the TDIM simulations. The PRIMO studies are attempting to constrain the TDIM and the other models through a uniform

procedure. The TDIM depends on empirical representations for the neutral atmosphere, MSIS-86 [Hedin, 1987], and the neutral wind, HWM90 [Hedin et al., 1991]. In addition, the Schunk and Nagy [1978]  $O-O^+$  collision frequency is scaled by the Burnside factor of 1.7 [Salah, 1993]. The magnetospheric inputs (convection electric field and auroral precipitation) are both assumed to be zero at the Millstone Hill latitude, where corotation dominates under quiet geomagnetic conditions.

## 2.3. University of Alabama at Huntsville FLIP

**2.3.1. FLIP model.** The FLIP model, which has been developed over a period of more than 10 years, has been described previously by Richards and Torr [1988] and, more recently, by Torr et al. [1990] and by Richards et al. [1994a, b]. The main component of this one-dimensional model calculates the plasma densities and temperatures along entire magnetic flux tubes from 80 km in the northern hemisphere through the plasmasphere to 80 km in the southern hemisphere. The model uses a tilted dipole approximation to the Earth's magnetic field. The equations solved are the continuity and momentum equations for  $O^+$ ,  $H^+$ , and  $He^+$ , as formulated for the topside ionosphere by St.-Maurice and Schunk [1977]. The  $He^+$  chemical and physical processes have been discussed by Newberry et al. [1989]. Collisions between ions and neutrals have been included in order to extend the equations into the *E* and *F* regions.

The FLIP model also solves the continuity and momentum equations for the first six vibrational levels of  $N_2$  in order to take into account the strong dependence of the  $O^+ + N_2 \rightarrow NO^+ + N$  reaction rate on vibrational excitation of  $N_2$  [Richards et al., 1986; Richards and Torr, 1986]. However, for this study involving the intercomparison of models, vibrationally excited  $N_2$  was not included.

The electron and ion temperatures are obtained by solving the energy equations [Schunk and Nagy, 1978]. Electron heating due to photoelectrons is provided by a solution of the two-stream photoelectron flux equations using the method of Nagy and Banks [1970]. The solutions have been extended to encompass the entire field line on the same spatial grid as the ion continuity and momentum equations.

**2.3.2. Model parameters.** In order to simulate the ionosphere, the FLIP model requires three key inputs: the neutral atmosphere, either  $h_m F_2$  or the meridional component of the neutral wind, and the solar EUV flux. The neutral densities and temperatures are taken from the mass spectrometer and incoherent scatter (MSIS-86) model [Hedin, 1987]. For winds, the FLIP model can input either modeled or measured winds. However, for purposes of this paper, FLIP employs winds from the IWM90 model [Hedin et al., 1991]. A better fit to the measured  $h_m F_2$  could have been obtained by using the algorithm of Richards [1991]. When using neutral winds from the HWM90 model, the  $O^+ - O$  collision frequency of Schunk and Nagy [1978] is scaled by the Burnside factor of 1.7, which has been adopted by the CEDAR community [Salah, 1993].

The EUV flux model has been described by Richards et al. [1994c]. It is based on the standard F74113 fluxes in the 37 wavelength intervals proposed by Torr et al. [1979], except that we have doubled the fluxes in the wavelength range below 250 Å. This modification is necessary so that the shape of the calculated photoelectron flux spectrum agrees with the shape of the measured photoelectron flux spectrum. Richards and

Torr [1988] have shown that the model photoelectron fluxes are in good agreement with the measured fluxes of Lee *et al.* [1980]. The F74113 flux spectrum has been chosen as our solar minimum standard because it was employed very successfully in the aeronautical calculations from the Atmosphere Explorer (AE) program. The solar activity scaling of the F74113 reference fluxes is achieved using both  $F_{10.7}$  and the 81 day average  $F_{10.7}$  as proxies. The solar cycle variation of the integrated solar EUV flux in the 50–575 Å wavelength range is in very good agreement with rocket measurements and the fluxes from the model of Tobiska [1991]. The photoionization rates from our EUV flux model are about 10% higher than those calculated from the Hinteregger *et al.* [1981] model.

An important consideration is the coupling flux of ions from the plasmasphere, which helps maintain the nighttime ionosphere. The particle and energy coupling between the ionosphere, plasmasphere, and conjugate ionosphere are handled self-consistently in the FLIP model. However, there is still some uncertainty for altitudes with  $L \geq 2$  due to the possibility that flux tubes may be in the process of refilling after being emptied by magnetic storms. For the calculations in this study, the flux tubes are assumed to be almost full, as they would be after several days free of storm activity. Thus the nighttime downward flux of ionization is close to the maximum possible.

#### 2.4. Phillips Laboratory GTIM

A global, time-dependent, first-principles  $F$  region ionospheric model, GTIM, has been developed at the Geophysics Directorate of Phillips Laboratory. GTIM is an  $F$  region model that calculates  $O^+$  ion densities as a function of altitude, latitude and local time. GTIM began as a low-latitude model [Anderson, 1971, 1973], evolved into a midlatitude model by assuming that the  $F$  region plasma corotates with the Earth, and finally became global by adding the high-latitude processes of  $E \times B$  convection drifts and energetic electron and ion particle precipitation [Decker *et al.*, 1994].

The model determines the  $O^+$  ion density by numerically solving the time-dependent ion continuity and momentum equations. The production rate includes production by photoionization, photoelectron impact ionization, particle precipitation and nocturnal photoionization. The loss occurs by charge exchange with  $N_2$  and  $O_2$ . It is within the momentum equations that the effects of gravity, pressure, the ambipolar electric field, and neutral wind are included in the model. To solve the final parabolic, partial differential equation, the finite differencing scheme of Crank and Nicholson [1947] is used to produce a set of linear algebraic equations, which are then solved using standard techniques for inverting a tridiagonal matrix. By applying this technique along a given magnetic field line, the  $O^+$  density is determined along that field line as a function of time. Solving such an equation naturally requires that both initial and boundary conditions be specified. For the initial condition we can specify any  $O^+$  profile along the field line that is desired. Normally, a generic profile appropriate for the initial time of the particular simulation is used. For the lower boundary condition at the foot of the field line (100 km), a local approximation is used to provide the  $O^+$  density. At the upper boundary, usually above 1000 km, either an  $O^+$  density or flux is specified. For low-latitude calculations, where the density is solved along the entire field line from one hemisphere to the other, the "upper"

boundary really becomes the other end of the field line at 100 km. Finally, by going through this procedure for many field lines, global  $O^+$  densities can be produced. A detailed description of the derivation and numerical solution of the appropriate equations can be found in the works by Anderson [1973] and Moffett [1979].

#### 2.5. CTIM

The CTIM has evolved from an integration of a neutral thermospheric code and a high-latitude and midlatitude ionosphere model. The neutral thermospheric model was originally developed by Fuller-Rowell and Rees [1980] at University College London (UCL); the ionospheric model originated from Sheffield University [Quegan *et al.*, 1982].

The original UCL version simulated the time-dependent structure of the vector wind, temperature and density of the neutral thermosphere by numerically solving the nonlinear primitive equations of momentum, energy and continuity. The global atmosphere was divided into a series of elements in geographic latitude, longitude and pressure. Each grid point rotates with the Earth to define a noninertial frame of reference in a spherical polar coordinate system. The latitude resolution is  $2^\circ$ , longitude resolution  $18^\circ$ , and each longitude slice swept through all local times with a 1-min time step. In the vertical the atmosphere is divided into 15 levels in logarithm of pressure from a lower boundary of 1 Pa at 80 km altitude.

The solution of a time-dependent mean mass equation was incorporated into the model by Fuller-Rowell and Rees [1983]. This formalism assumed the upper atmosphere could be approximated by two species, atomic oxygen and the sum of molecular nitrogen and oxygen. More recently, the major species composition was improved to include solution of the three major species ( $O$ ,  $O_2$ , and  $N_2$ ), including chemistry, transport and the mutual diffusion between the species.

The time dependent variables of southward and eastward wind, total energy density, and concentrations of  $O$ ,  $O_2$  and  $N_2$  are evaluated at each grid point by an explicit time-stepping numerical technique. After each iteration, the vertical wind is derived, together with temperature, density, and heights of pressure surfaces. The parameters can be interpolated to fixed heights for comparison with experimental data.

Fuller-Rowell *et al.* [1987] coupled the neutral thermosphere with the Sheffield University high-latitude and midlatitude ionospheric convection model [Quegan *et al.*, 1982]. Traditionally, ionospheric models are evaluated in a Lagrangian system, where the evolution of ion density and temperature of plasma parcels are computed along their convection paths. In the coupled model the ionospheric Lagrangian frame has been modified to be more compatible with the Eulerian frame by implementing a semi-Lagrangian technique [Fuller-Rowell *et al.*, 1988]. Adoption of a rotating frame of reference for the ionosphere eliminates the need for a "corotation potential."

Transport under the influence of the magnetospheric electric field is explicitly treated, assuming  $E \times B$  drifts and collisions with the neutral particles. The atomic ions  $H^+$  and  $O^+$  and ion temperature are evaluated over the height range from 100 to 10,000 km, including horizontal transport, vertical diffusion, and the ion-ion and ion-neutral chemical processes. Below 400 km, additional contributions from the molecular ion species  $N_2^+$ ,  $O_2^+$  and  $NO^+$ , and the atomic ion  $N^+$  are included.

The magnetospheric input to the model is based on the statistical models of auroral precipitation and electric field

described by Fuller-Rowell and Evans [1987] and Foster et al. [1986], respectively. Both inputs are keyed to a hemispheric power index (PI), based on the TIROS/NOAA auroral particle measurements, and are mutually consistent in this respect. The PI index runs from 1 to 10 to cover very quiet to storm levels of geomagnetic activity; the relationship between PI and  $K_p$  is given by Foster et al. [1986]. Equatorward of the auroral oval, a soft midlatitude background electron precipitation has been added to the TIROS/NOAA auroral model at all latitudes and local times. The spectrum of this additional particle source is assumed to be Maxwellian with an energy flux of  $0.05 \text{ mW m}^{-2}$  and a mean energy of 50 eV. The magnitude of the electric fields are increased by 30% above the original model values due to statistical smoothing.

The (2,2) and (2,4) tidal modes are imposed at 97 km altitude [Fuller-Rowell et al., 1991] with 300 m amplitude and a phase of 12 hours. The tides are imposed by adjusting the height of pressure level 4, near 97 km. Winds and temperatures respond through the physical processes included in the model and their influence propagates to higher altitudes. The EUV flux is calculated from the Hinteregger et al. [1981] reference spectra for high and low solar activity based on the Atmospheric Explorer (AE) measurements. The Schunk and Nagy [1978] O-O<sup>+</sup> collision frequency has been scaled by the Burnside factor of 1.7 [Salah, 1993].

To simulate the periods of interest for the present study, the day of year defines the solar declination angle, and the  $F_{10.7}$  cm index the solar EUV flux; both of these parameters are set in common with the other models; see section 3. The level of geomagnetic activity is the TIROS/NOAA power level 5, which defines a quiet to average level of magnetospheric input. The auroral power input to each hemisphere is 12 GW and the cross-polar-cap potential is 47 kV, conditions roughly equivalent to a  $K_p$  of 2. The model was run for several days at the prescribed levels of solar and geomagnetic activity until the results were diurnally reproducible.

As with the NCAR model, the neutral atmosphere is computed self-consistently with the ion density, so there is no opportunity to adjust the neutral wind or composition to "tune" the model. It is only possible to adjust the primary drivers of the thermosphere-ionosphere system.

## 2.6. Observations

The observations used for comparisons are all from Millstone Hill, Massachusetts; its location is 42.6°N latitude and 288.5°E longitude. This station was selected for the following reason. Observations of the middle latitude ionosphere are available from a latitude chain of Digisondes lying along the longitude of the east coast of North America. The Digisonde observations during solar maximum conditions were examined, and it was found that the observations from Millstone Hill were representative of the whole midlatitude ionosphere for the periods used in this study. Hence the data and model comparisons presented here are specifically for Millstone Hill, but the comparison is applicable to the entire midlatitude domain at this longitude.

Four periods were selected for model data comparisons: winter and summer during solar cycle minimum and maximum. These represent extremes in both seasonal and solar cycle conditions. Table 2 lists the solar and geophysical conditions during the four periods. For each period the average daily  $K_p$  sum is given for the preceding 3 days. These average values

Table 2. Solar Cycle and Seasonal Study Periods

Day	Year	$F_{10.7}^a$	$K_p$ Sum	Prior $K_p$ Sum <sup>b</sup>
June 19	1990	176	12 <sup>+</sup>	11
December 19	1990	198.5	4 <sup>-</sup>	13
June 25	1986	69.7	6 <sup>-</sup>	12
December 11	1986	70.4	15 <sup>+</sup>	13

<sup>a</sup> Monthly mean value.

<sup>b</sup> Daily average for the prior 3 days.

indicate that for all four periods the preceding days were also quiet and hence that the ionosphere was in a relatively quiescent state. This was a key factor in selecting these particular periods.

**2.6.1. Millstone Hill incoherent scatter radar (MHO) data.**  $N_m F_2$  and  $h_m F_2$  for June 23-25, 1986, and December 10-12, 1986, were obtained from incoherent scatter electron density profiles measured with the 68 m zenith-pointing antenna. Profiles of backscattered power versus height were obtained using a 0.32 ms pulse to give 48 km altitude resolution. These profiles were calibrated using  $f_o F_2$  measurements from the local ionosonde, and temperature corrected using the  $T_e / T_i$  ratio obtained from longer pulse (0.64 ms) data. The shorter pulses provide better altitude resolution, while the longer pulses are required for better spectral information needed to determine the temperatures. More details are provided by Buonsanto [1989].

The  $N_m F_2$  and  $h_m F_2$  derived from the Millstone Hill ISR data are shown in Figures 3 and 4 and are reasonably consistent with diurnal variations given by the IRI-90 model [Bilitza, 1990; Bilitza et al., 1993], which represents monthly averaged conditions. Mendillo et al. [1975] calculated standard deviations for each of 62 months of  $N_m F_2$  data at Wallops Island. The average value of these standard deviations varied from about 22% during the day to 28% at night. Hagan et al. [1992] compared  $N_m F_2$  at Wallops Island for quiet days in January 1985, 1986, and 1987, and found daytime values of  $N_m F_2$  that varied from approximately  $0.4 \times 10^{12} \text{ m}^{-3}$  on one day in 1987 to approximately  $0.65 \times 10^{12} \text{ m}^{-3}$  on one day in 1985. Less interannual variability was found for  $h_m F_2$ . The MHO  $N_m F_2$  and  $h_m F_2$  data presented here are within the range of these Wallops Island solar minimum results.

**2.6.2. Millstone Hill Digisonde data.** During the solar maximum summer and winter periods listed in Table 2 (June and December 1990), a chain of Digisondes was operating. These Digisondes [Reinisch, 1996] developed by the University of Massachusetts-Lowell, were automated such that its operation, data collection, and electron density profile analysis [Huang and Reinisch, 1996] would be carried out unattended. Doppler interferometry was applied to determine echo arrival directions [Reinisch et al., 1997]. This capability is particularly necessary in the selection of the vertical ionogram traces. For the applications of this study, this latter feature was crucial because both the critical frequency of the  $F$  layer and its true height were required.

Observations from five Digisondes (Bermuda 32.2°N, Wallops Island 37.9°N, Millstone Hill 42.6°N, Argentina 47.3°, and Goose Bay 53.2°) were obtained from the VIM database [Reinisch et al., 1994]. These data had all been manually inspected to ensure that the automated Digisonde analysis had been successful and to add data quality

information. This additional analysis had been carried out by Bodo Reinisch's group in the Center for Atmospheric Research at Lowell. As stated earlier, these observations from five stations were used to verify that the MHO observations were indeed representative of the midlatitude region at this longitude. Figures 1 and 2 show the Millstone Hill Digisonde observations.

### 3. Comparisons of Models and Observations

Comparison of the observed  $N_m F_2$  and  $h_m F_2$  with the five physical models are shown in the following figures. Some of the differences that will be seen are intrinsic to the specific model or associated with input functions that are based upon climatology trends from limited observations. Where appropriate, comments to this effect are provided. In each figure the thick gray lines represent the Millstone Hill observations. The other lines indicate the various model results. The model results were obtained for the particular day of the observations using the solar and geomagnetic conditions listed in Table 2, or as specified earlier for equivalent conditions.

#### 3.1. Solar Maximum: Winter

The thick gray line in Figure 1a shows the Millstone Hill Digisonde observations of  $N_m F_2$  for December 19, 1990, in a logarithm to the base 10 format. The observed values of  $h_m F_2$  are shown in Figure 1b, also as a thick gray line. Both  $h_m F_2$  and  $N_m F_2$  observations are 1 hour values. The uncertainty in  $N_m F_2$  derived from a measure of the  $F$  layer critical frequency is negligibly small in the context of the spread in model values shown in Figure 1a. Of more relevance is the question of how

well this  $N_m F_2$  diurnal variation is representative of ionospheric solar maximum, winter, low geomagnetic activity conditions at Millstone Hill? In part, this has been answered in section 2.6, where "similar days" show about a 20% standard deviation. This is not the same for the ISR and Digisonde  $h_m F_2$  values. The Digisonde  $h_m F_2$  are computed from path delays through the ionosphere to the peak [Chen *et al.*, 1994]. The variability from hour to hour in the observed  $h_m F_2$  is in fact a reasonable indication of the uncertainty in the analysis. A probable uncertainty of  $\pm 10$  km is consistent with the scatter for the Digisonde  $h_m F_2$ .

**3.1.1. TIGCM.** The dashed curves in Figure 1 represent the TIGCM calculated  $N_m F_2$  and  $h_m F_2$ . The model densities are larger than those observed at all times, except between 0000 and 0500 LT. Maximum differences are of the order of 50%. Bigger discrepancies are found in the comparison of  $h_m F_2$ . The model predicts a nearly flat diurnal variation, with the height varying from about 290 to 315 km. The observations, on the other hand, indicate the height changes by over 100 km, from 250 to over 350 km. The calculated layer is too high during the daytime and too low at night. An increase in the daytime neutral wind could improve the agreement. However, this is not a free parameter in the TIGCM, which self-consistently calculates both winds and composition.

**3.1.2. TDIM.** The lines with circles in Figure 1 represent the TDIM calculated  $N_m F_2$  and  $h_m F_2$ .  $N_m F_2$  is in very good agreement with the observations during the day, with values about 20% below those measured. At night the model  $N_m F_2$  values are about 40% too low. During the day the  $h_m F_2$  agreement with observations (Figure 1b) is good, but during the night the modeled  $h_m F_2$  occasionally exceeds the observations by up to 50 km. Note that the three uncoupled ionospheric models (TDIM, FLIP, and GTIM) use the same

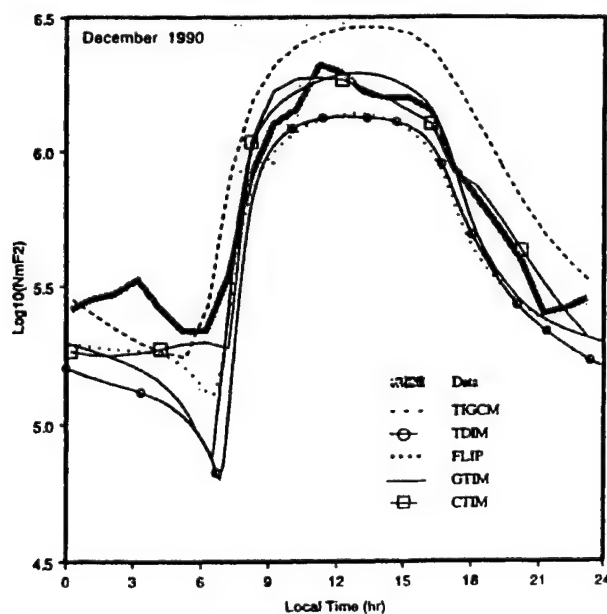


**Figure 1a.** A comparison of the observed  $N_m F_2$  diurnal variation at Millstone Hill (thick shaded line) with five physical ionospheric models for solar maximum, winter conditions. The model results are for the TIGCM (dashed line), TDIM (line with circles), FLIP (dotted line), GTIM (solid line), and CTIM (line with squares).

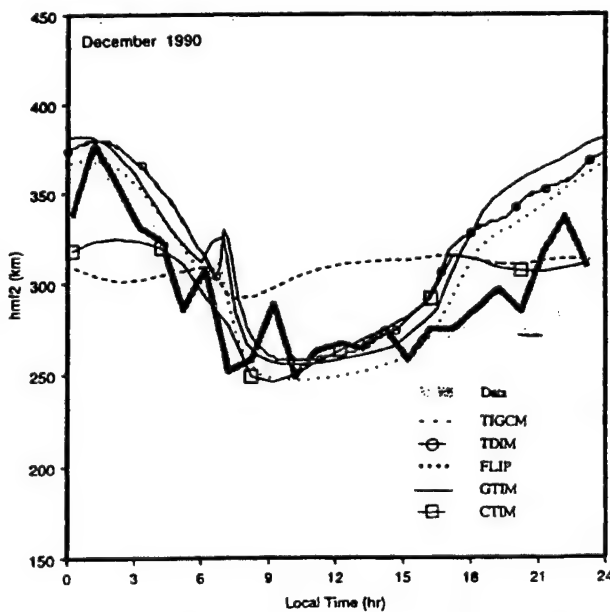


**Figure 1b.** A comparison of the observed  $h_m F_2$  diurnal variation at Millstone Hill (thick shaded line) with five physical ionospheric models for solar maximum, winter conditions. The model results are for the TIGCM (dashed line), TDIM (line with circles), FLIP (dotted line), GTIM (solid line), and CTIM (line with squares).



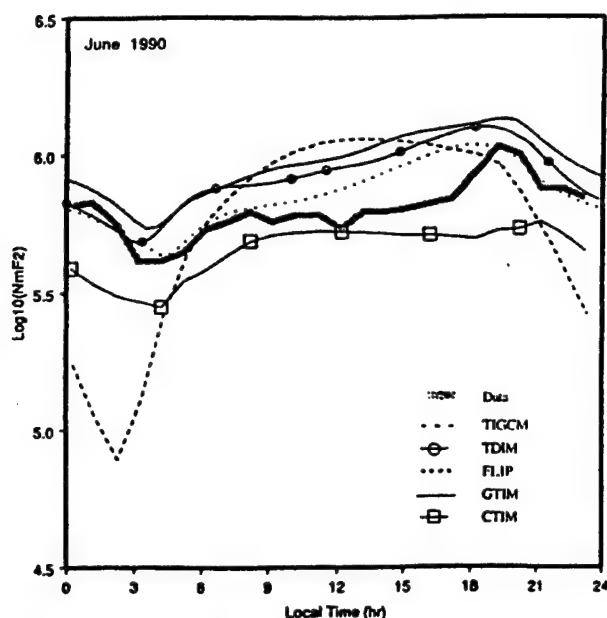


Figure 2a. A comparison of the observed  $N_m F_2$  diurnal variation at Millstone Hill with five physical ionospheric models for solar maximum, summer conditions.

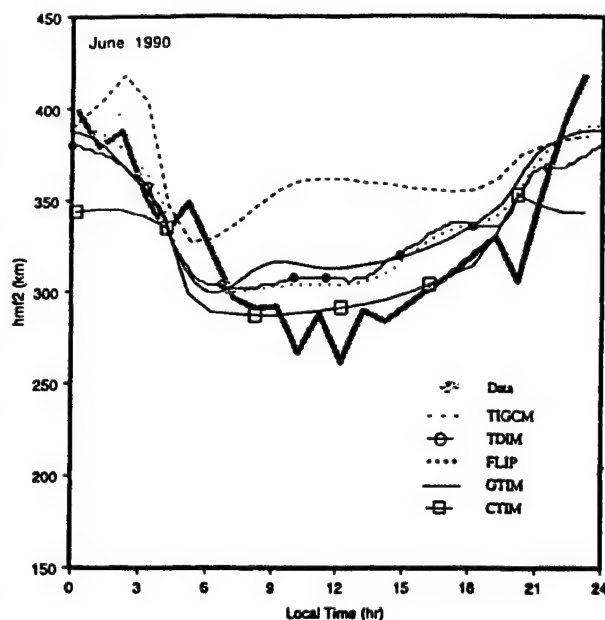


Figure 2b. A comparison of the observed  $h_m F_2$  diurnal variation at Millstone Hill with five physical ionospheric models for solar maximum, summer conditions.

neutral wind model (HWM90) in their calculations, and the three uncoupled models predict  $h_m F_2$  values that agree to within  $\pm 5$  km. This indicates that the discrepancies between the  $h_m F_2$  values calculated by these models and those measured are due to the adopted HWM90 model.

**3.1.3. FLIP.** The dotted line shows the FLIP model results. The FLIP model  $N_m F_2$  values are about 20% less than the observed densities during the day and about 50% less during the night. The agreement between the model and data would be improved during the day if the model were constrained to follow  $h_m F_2$  with the algorithm of Richards [1991] instead of using the HWM90 winds. On the other hand, the model  $N_m F_2$  would then be much too low at night because the HWM90 winds yield  $h_m F_2$  values that are more than 50 km higher than the observed  $h_m F_2$  at times during the night. The higher layer helps to preserve the ionospheric density. The  $h_m F_2$  from uncoupled ionospheric models, which use the standard HWM90 winds, indicate that the nighttime equatorward HWM90 winds may be too large on this occasion.

**3.1.4. GTIM.** The solid lines in Figure 1 represent GTIM calculated  $N_m F_2$  and  $h_m F_2$ . Throughout the daytime and to about midnight, the comparison with the observed  $N_m F_2$  is very good. From midnight to dawn, the modeled  $N_m F_2$  decays to lower values than observed in much the same way as the TDIM. The comparison between GTIM and observed  $h_m F_2$  values is also in excellent agreement throughout most of the daytime hours. However, between 1800 and 0800 LT, the calculated  $h_m F_2$  values exceed the measurements by about 25 to 50 km. This again indicates that the HWM90 winds at night need to be improved, which requires a more extensive neutral wind database.

**3.1.5. CTIM.** The CTIM  $N_m F_2$  and  $h_m F_2$  are plotted as lines with squares. Both parameters follow the observations very well. CTIM is the only model that achieves a slight night-early morning  $N_m F_2$  increase, which occurs at 0500 LT, in comparison to the observations that show a slight

maximum at 0300 LT. None of the models achieve a nighttime  $N_m F_2$  morphology that looks like that observed. In fact, the five models have relatively diverse nighttime morphologies.

### 3.2. Solar Maximum: Summer

Digisonde observations for June 19, 1990, are shown in Figure 2 by the thick gray lines. The five models runs for this day are for the conditions listed in Table 2. The calculated values of  $N_m F_2$  and  $h_m F_2$  are also shown in Figure 2 and are described below. In addition, a comparison of Figures 1a and 2a, in terms of the seasonal anomaly, is given.

**3.2.1. TIGCM.** The model predictions are shown in Figure 2 by the dashed curves. The observed  $N_m F_2$  shows little diurnal variation, while the model predicts a much larger variation. The TIGCM peak electron densities are too large during the day and too small at night. The largest discrepancy occurs from midnight to dawn, during which time the model predictions are nearly an order of magnitude too small. During the day, the model densities are, at most, about double those observed. The comparison of  $h_m F_2$  shows that the model layer height is typically higher than that observed. The differences are a maximum of 75 km during the day and 50 km at night. An increase in the daytime poleward winds would improve both  $N_m F_2$  and  $h_m F_2$  in the model.

The comparison of the summer/winter densities for the observations and the model illustrate the seasonal anomaly: daytime  $N_m F_2$  are observed to be larger in winter than in summer. Here we compare the model and measurement at 1200 LT. The observations indicate a winter/summer  $N_m F_2$  ratio of 2.91 and the model predicts a ratio of about 3.0.

**3.2.2. TDIM.** The model predictions are shown in Figure 2 by the lines with circles. During the day, the  $N_m F_2$  values are about 25% larger than observed, while in the night/predawn sector, the modeled densities are only slightly higher. The modeled  $h_m F_2$  are at higher altitudes during the day

and slightly lower altitudes at night relative to the observations. The fact that both the modeled  $N_m F_2$  and  $h_m F_2$  are larger than observed during the day indicates that the differences are likely to be due to the adopted neutral wind. The observed seasonal anomaly is 2.91 at 1200 LT and the ratio in the TDIM is 1.61. This difference is due to the model predicting larger summer densities than observed.

**3.2.3. FLIP.** The FLIP model (dotted line)  $N_m F_2$  values are in good agreement with the data both during the day and at night. The HWM90 winds also yield good agreement between the FLIP model and the measured  $h_m F_2$  for this day, with the model  $h_m F_2$  being about 25 km higher. Bringing the model  $h_m F_2$  into better agreement with the measurement by adjusting the wind would produce even closer agreement for the densities. Richards *et al.* [1994a] also found good agreement between the FLIP model and Digisonde data for summer 1990 at Millstone Hill. Summer solar maximum is the time when vibrationally excited  $N_2$  is expected to be most important [Richards and Torr, 1986; Ennis *et al.*, 1995]. Therefore such good agreement between the model and measurement without vibrationally excited  $N_2$  suggests that the aeronomy of vibrationally excited  $N_2$  may not yet be fully understood. On the other hand, if vibrationally excited  $N_2$  were included, it would act to further improve the agreement between the model and measurements during the day.

**3.2.4. GTIM.** The model results are depicted by the solid line in Figure 2. Throughout the entire 24-hour period, calculated  $N_m F_2$  values exceed observed values by about 20%. During the daytime, calculated  $h_m F_2$  values exceed observations by 20 km. The GTIM and TDIM results for both  $N_m F_2$  and  $h_m F_2$  are very similar, as expected since these two models have the most similar  $F$  region representation of all five models. Apparently, neutral winds can account for the discrepancy between GTIM and observed values, because, as in the TDIM comparison, GTIM calculated  $h_m F_2$  values are greater

than observed. A stronger poleward wind would lower the calculated  $h_m F_2$  values and would tend to decrease  $N_m F_2$  because of the larger loss rates at the lower altitudes.

**3.2.5. CTIM.** The daytime comparisons of  $N_m F_2$  and  $h_m F_2$  are very good, with the CTIM densities (lines with squares) being only 20% lower than observed. During the night (2000 to 0400 LT), the CTIM  $F$  layer is about 30 km too low and this is reflected in the lower  $N_m F_2$  values. However, overall the CTIM solar maximum results are in reasonable agreement with the observations.

### 3.3. Solar Minimum: Winter

MHO ISR observations for December 10–12, 1986, are shown in Figure 3 by the thick gray curves. The observed  $N_m F_2$  for 2 days is shown in Figure 3a. Both days show a minimum at midnight and then an increasing density toward dawn. This feature, a nighttime increase in density by a factor of 3 or more on a corotating plasma flux tube, usually implies a significant plasma source. The predictions from the five models are also shown in identical format to that in Figures 1 and 2.

**3.3.1. TIGCM.** The TIGCM predictions are shown in Figure 3 by the dashed curves. The agreement between the modeled and observed  $N_m F_2$  and  $h_m F_2$  is good to very good. The major discrepancies occur at night; the modeled peak densities are too large from about 0000 to 0400 LT, and the layer height is too low by about 25 km. Adjustments to the neutral wind cannot simultaneously resolve these two discrepancies.

**3.3.2. TDIM.** The agreement between the modeled (lines with circles) and observed  $N_m F_2$  and  $h_m F_2$  values is very good. The only discrepancy is in the predawn densities, which are too small in the TDIM. Such a decay of the nighttime  $F$  layer was not experienced to the same extent in earlier TDIM studies when simple meridional winds were used in place of the

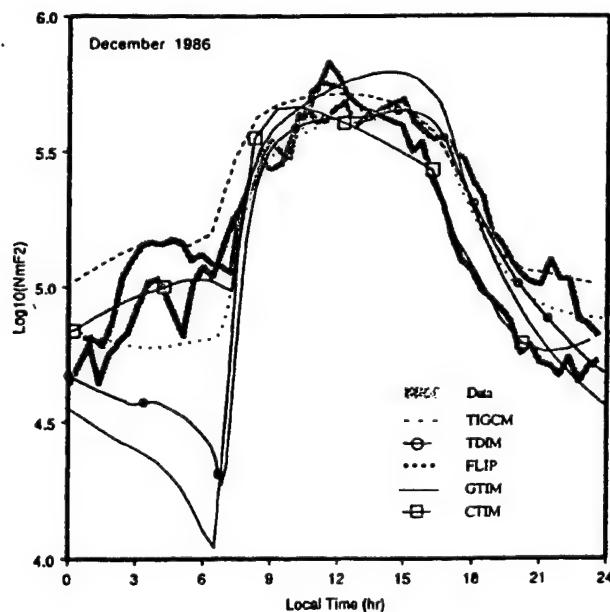


Figure 3a. A comparison of the observed  $N_m F_2$  diurnal variation at Millstone Hill with five physical ionospheric models for solar minimum, winter conditions.

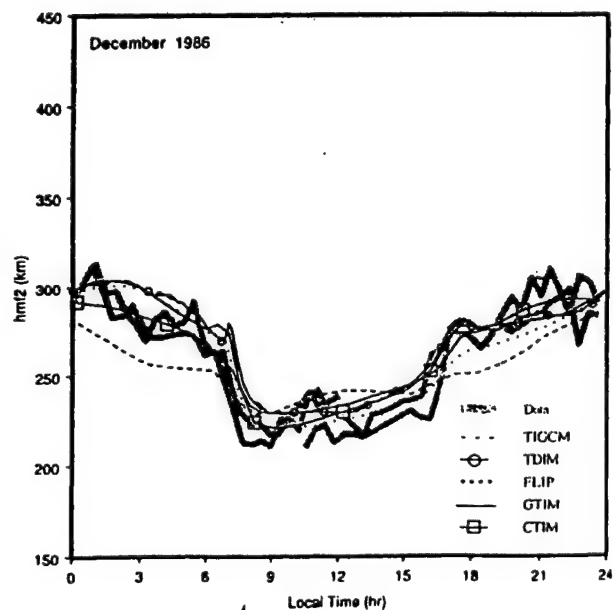


Figure 3b. A comparison of the observed  $h_m F_2$  diurnal variation at Millstone Hill with five physical ionospheric models for solar minimum, winter conditions.



HWM90 winds but was also present at solar maximum, winter with the HWM90 winds (Figure 1a.). However, this again points to the need for a resolution of the nighttime maintenance of the  $F$  layer, that is, what is the role of nighttime winds, topside plasma fluxes and in situ plasma sources? The discrepancy shown in the density can be reduced by a suitable choice of the topside flux or an adjustment to the wind [Sica *et al.*, 1990]. However, the observed factor of 3 enhancement in  $N_m F_2$  from 0000 LT to 0600 LT would be difficult to mimic with just a topside flux adjustment.

**3.3.3. FLIP.** For the solar minimum, winter comparison, there is generally good agreement between the FLIP model  $N_m F_2$  (dotted line) and the data, except between midnight and sunrise when the measured  $N_m F_2$  increases by a factor of 3. At these times the FLIP  $N_m F_2$  values merely stabilizes as a result of a downward plasmaspheric flux. The large increase in measured  $N_m F_2$  at night indicates that a substantial nocturnal ionization source is present and the plasmaspheric flux in the FLIP model is not adequate even though it is being supplied by a nearly full flux tube. There is generally good agreement between the modeled and measured  $h_m F_2$  for this day, indicating that the HWM90 winds are appropriate for most of the daytime and early evening, but the predawn enhancement issue needs to be studied further.

**3.3.4. GTIM.** The solid line depicts the calculated GTIM  $N_m F_2$  and  $h_m F_2$  values in Figure 3. The agreement in both  $N_m F_2$  and  $h_m F_2$  throughout the daytime and premidnight hours is very good and is again very similar to that for the TDIM. The greatest discrepancy between calculated and observed  $N_m F_2$  occurs between 0100 and 0600 LT, as was the case for the other two uncoupled models.

**3.3.5. CTIM.** The line with squares represents the CTIM  $N_m F_2$  and  $h_m F_2$  in Figure 3. During both day and night, the model follows the observations and very good agreement is found. As with the TIGCM, this model is able to generate an increase in the predawn  $N_m F_2$  values that follows the observations. However, between 0800 and 1600 LT, the daytime  $N_m F_2$  morphology is somewhat different from both the other models and the observations. CTIM has an  $N_m F_2$  maximum that occurs at 0830 LT and then continually decreases throughout the day, while the observed  $N_m F_2$  values peak between 1100 and 1400 LT. The other models also show differing daytime morphologies of  $N_m F_2$ , with GTIM, TDIM, and FLIP exhibiting  $N_m F_2$  peaks at about 1400 LT.

### 3.4. Solar Minimum: Summer

ISR observations from Millstone Hill for June 23-25, 1986, are shown in Figure 4 by the thick gray curves. The  $h_m F_2$  observations shown in Figure 4b have a very large variability during the daytime; for example, from 0800 to 0900 LT it increases by about 100 km and then it returns to its lower value by 1100 LT. During solar minimum, summer conditions, a well-known  $G$  condition exists in the dayside midlatitude ionosphere in which the  $h_m F_1$  layer electron density can be equal to or slightly greater than that of the  $h_m F_2$  layer [Buonsanto, 1990]. Hence the daytime  $h_m F_2$  data shown in Figure 4b is probably a mixture of  $h_m F_1$  and  $h_m F_2$ . In general, altitudes lower than 200 km are  $h_m F_1$  and are associated with a molecular ion peak, while those above 200 km are associated with the  $O^+$  peak ( $h_m F_2$ ). From this specific ISR data set it is not always possible to distinguish between these two layers. For this study, all the models display  $O^+$

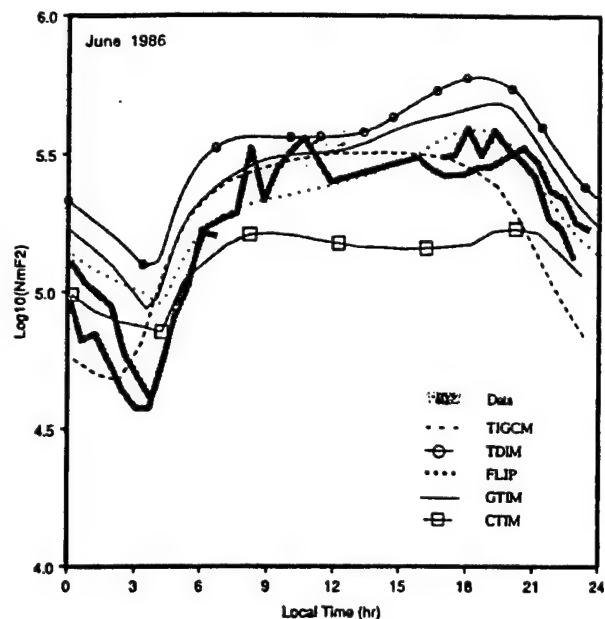


Figure 4a. A comparison of the observed  $N_m F_2$  diurnal variation at Millstone Hill with five physical ionospheric models for solar minimum, summer conditions.

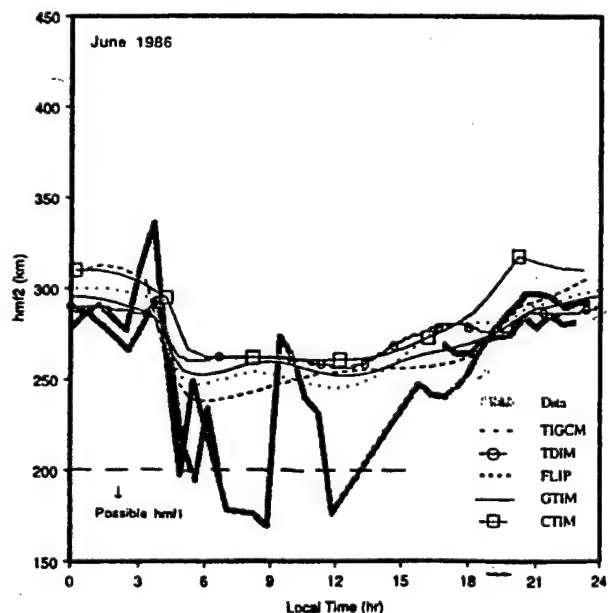


Figure 4b. A comparison of the observed  $h_m F_2$  diurnal variation at Millstone Hill with five physical ionospheric models for solar minimum, summer conditions.

layer results, which pertain to  $N_m F_2$  and  $h_m F_2$ . Hence the ISR observed altitudes greater than 200 km should be considered as  $h_m F_2$ , while those below 200 km are probably  $h_m F_1$ . Since the ISR only measures the electron density, and not the composition, it is not possible to unambiguously separate these two layers under  $G$  conditions. The predictions from the five models are also shown in Figure 4 in identical format to that in the three earlier figures.

**3.4.1. TIGCM.** The model predictions are shown in Figure 4 by the dashed curves. As with the winter comparison, the agreement between model and observations generally ranges from good to very good. The major discrepancies occur for the model densities from 1800–0200 LT, when the model values are too low. However, the predicted nighttime heights are fairly good, with a maximum difference of about 25 km from 0000 to 0300 LT. The observed seasonal anomaly during solar cycle minimum is 1.90 and the TIGCM predicts 1.6.

**3.4.2. TDIM.** The model daytime densities (line with circles) are about 50% higher than those observed, and the model  $F$  layer heights are also higher by about 50 km. The solar minimum seasonal anomaly is 1.90 in the observations and 1.30 in the simulations. As with solar maximum, the difference can be attributed to the modeled summer densities being too high as a result of  $h_m F_2$  being too high. An increased poleward wind would rectify this problem.

**3.4.3. FLIP.** In summer at solar minimum, the FLIP model  $N_m F_2$  (dotted line) is in excellent agreement with the data during the day, but it is too large between midnight and sunrise. In our experience, it is unusual for the FLIP model density to be too high at night. This could be partially explained by the model  $h_m F_2$  being about 25 km higher than the measured  $h_m F_2$  at night. The model  $h_m F_2$  also appears to be too high during the day, but there is a lot of scatter in the radar data.

**3.4.4. GTIM.** During solar minimum, summer conditions, good agreement between GTIM (solid curve) and observed  $N_m F_2$  values occurs from 0800 to 2100 LT, but the nighttime GTIM values exceed the measurements by a factor of 2 to 4. The apparent reason for the discrepancy can be traced to the neutral wind, which exhibits an increase in the equatorward component before sunset. This raises  $h_m F_2$  values significantly, from 250 to 300 km by 2100 LT, thereby causing a much slower decay of  $N_m F_2$  at night because of the slower loss rate at the higher altitudes.

**3.4.5. CTIM.** The CTIM (curve with squares) daytime  $F$  layer is low in density (about a factor of 2) and high in altitude (about 25 km). This particular combination of differences is not consistent with a problem in the neutral wind, not that the wind is an adjustable parameter in this model. In comparison with the other models, this low dayside  $N_m F_2$  is anomalous. All five models have very similar daytime  $h_m F_2$  values, and the other four have  $N_m F_2$  in agreement with observations or slightly higher. Hence a stronger dayside wind would lower  $h_m F_2$ , but it would also decrease the  $N_m F_2$  values further. Therefore, viewing the wind as the source of the error may not be the proper interpretation of the difference shown in the observed and modeled  $h_m F_2$  and  $N_m F_2$ . This issue is referred to again in the discussion section.

## 4. Discussion

In reviewing the preceding  $F$  region model-model and model-observation comparisons, the concern that one may be mixing oranges and apples is not substantiated. All the models exhibit diurnal morphologies consistent with observed seasonal and solar cycle trends. Each model, at some period of time and/or geophysical condition, has a deficiency, but it is not shared by the other models. Hence the identification of a common shortcoming in the physics, the inputs, or the boundary conditions is not possible. One is left with rather unspecified areas of concern. For example, in Figure 3, the

TDIM and GTIM densities in the presunrise hours are particularly low and the temporal variation is different from the observations. From earlier TDIM studies [Sica *et al.*, 1990], this problem was resolved by adjusting either the neutral wind and/or the topside flux within "reasonable" ranges. However, the specific values are ill determined by observation. In prior studies, the TDIM nighttime maintenance was achieved by stronger nighttime neutral winds than the HMW90 model provides. Hence, in this study, where the HMW90 is used without modification, adjustments in the topside plasma flux are needed. The effect of such a topside plasma flux can be seen by comparing the FLIP model results in Figure 3 with the TDIM and GTIM results. The FLIP results are also based on HMW90 winds but include a downward plasmaspheric flux for the case of a full flux tube. The effect of such a downward plasma flux is to maintain  $N_m F_2$  at a nearly constant level during the early morning hours. On the other hand, the measurements and coupled ionosphere-thermosphere models (CTIM and TIGCM) indicate that  $N_m F_2$  actually increases in the early morning (Figure 3). Hence for these geophysical conditions (solar minimum, winter) and local times (0000–0600 LT) the coupled ionosphere-thermosphere models are superior to the uncoupled models (TDIM, GTIM and FLIP). Unfortunately, this is not generally true, and at other times and/or geophysical conditions the coupled models are inferior to the uncoupled models.

A significant cause of the difference between the self-consistent thermosphere and ionosphere models (CTIM and TIGCM) and the stand-alone ionospheric models (GTIM, TDIM, and FLIP) is the dependence on neutral composition. Wells *et al.* [1997], in particular, showed that the CTIM tends to underestimate the  $O/N_2$  ratio in the summer hemisphere compared with MSIS. The cause of the low summer CTIM  $N_m F_2$  values in Figures 2a and 4a is probably related to this problem. In the winter hemisphere, the CTIM composition is closer to MSIS, and the resulting  $N_m F_2$  values are in closer agreement with the data. Similarly, the disagreement in  $N_m F_2$  between TIGCM (TIEGCM) and the data may be due to discrepancies in the neutral densities, particularly the molecular densities [Buonsanto *et al.*, 1997; Fesen *et al.*, 1997]. Fesen *et al.* [1997] presented comparisons of the  $O/(N_2 + O_2)$  ratio predicted by TIEGCM and MSIS for January near solar cycle minimum; the ratio ranged from 15 to 40 in the TIEGCM but was typically less than 10 in MSIS. The difference was due to the larger molecular densities in MSIS, which exceeded those in TIEGCM by factors of 2 to 4. The differences were especially pronounced at night. Changing the molecular densities would also affect the TIGCM (TIEGCM) representation of  $h_m F_2$ , since the altitude where chemical loss balances diffuse transport would be altered, as discussed by Fesen *et al.* [1997].

It is a puzzle why three of the models (TDIM, FLIP, and GTIM) use the HMW90, but they do not experience the same problems. In fact, in the FLIP model the topside flux is not a free parameter; it is computed self-consistently and, in general, the nightside  $F$  layer is maintained in a manner similar to that observed.

At midlatitudes during quiet conditions, the  $F$  layer dynamics and field-aligned transport is most dependent upon the neutral wind. Overall, the neutral wind is the primary source of the problem for the ionospheric models, but it is a self-consistent part of the coupled ionosphere-thermosphere models. A need exists to extend the observational databases of

the neutral wind models and to undertake careful investigation of the self-consistent winds generated in the coupled models, especially at other latitudes.

The fact that the results do not show the models having common deficiencies makes it particularly difficult to produce a profound conclusion. One is left arguing that each model uses dissimilar numerical techniques, spatial resolutions, even boundary conditions, which could account for the dissimilar behavior. Indeed, the models do not even share a common set of adjustable parameters. As already pointed out, for common processes (i.e.,  $O-O^+$  diffusion or  $O$  photochemistry), these have been made the same in each model.

Each of the models produced significantly more information than displayed in Figures 1 through 4. Several iterations and double checks on inputs and boundary conditions were made. In fact, a long list of other parameters that could be checked have been discussed in the PRIMO workshops. As a group, the decision to bring closure to the first PRIMO objective, that of resolving the factor of 2 deficiency in modeled noon  $N_m F_2$  at solar maximum, has been achieved. This was done by a set of adjustments to the diffusion coefficient, the photoionization chemistry, secondary electron production, and other model specific adjustments. Furthermore, the presentation of model results in Figures 1 through 4 represents a rather unique intercalibration of physical ionospheric models; one might even argue it is an exposé of how well (or poorly) the models perform.

## 5. Conclusion

The comparison of the five physical models has important implications for the National Space Weather Program. Specifically, plans are underway to use ionospheric models for specification and forecasting and for providing time delay corrections of Global Position System signals. It is therefore important to determine how reliable the model predictions are for different geophysical conditions.

In this study, five physical models containing ionospheres were compared with each other and with data obtained from the Millstone Hill Observatory. Two of the models were self-consistent ionosphere-thermosphere models, while for the other three models the thermospheric parameters were provided by empirical models. The comparisons were conducted for the easiest case (midlatitudes and quiet magnetic activity), and for four geophysical conditions covering both summer and winter at solar maximum and minimum. All of the simulations were based on standard model runs, with no allowance for adjusting uncertain input parameters or processes.

Perhaps the most important result obtained is that the self-consistent ionosphere-thermosphere models are not quantitatively or qualitatively superior to the uncoupled ionospheric models for the conditions studied. All of the models predicted diurnal variations that were consistent with the observed trends, and this was true for all four geophysical cases. However, each one of the models displayed a clear deficiency in at least one of the four geophysical cases that was not common to the other models. Quantitatively, the spread in  $N_m F_2$  calculated by the five models was the smallest during the day, typically less than a factor of 2, but at night the spread in the model results was as large as a factor of 10 at certain local times. The latter problem was traced to a lack of nighttime maintenance processes in some of the uncoupled ionospheric models. These results imply that reliable

quantitative predictions cannot be obtained from a "standard" model run, regardless of the model used. Data ingestion techniques will be required to obtain more reliable ionospheric predictions.

In the future, it would be useful to extend the comparison of the five models to the equatorial and high-latitude domains and to geomagnetically active conditions. It would also be useful to compare the five models when selected data sets are ingested into the models in order to determine what the improvement is and which of the models performs the best under these circumstances. Specifically, incoherent scatter radar and other data sets are available that can help constrain the models. For example, instead of using the HWM-93 empirical wind model to drive the uncoupled ionospheric models, one can use the observed winds. The observed winds can also be used to validate the winds calculated by the coupled ionosphere-thermosphere models. In addition, one can compare the observed and modeled ion and electron temperatures, vertical  $O^+$  fluxes, and electric fields.

**Acknowledgments.** B. W. Reinisch was supported by Phillips Laboratory contract F19628-90-K-0029. C. G. Fesen was supported by NSF/CEDAR grant ATM-9415977 and NASA grant NAGW-2656. P. G. Richards was supported by NSF grant ATM-9523786 and NASA grant NAGW-4455. R. W. Schunk and J. J. Sojka were supported by NASA grant NAGS-1484. The National Center for Atmospheric Research (NCAR) is supported by the NSF, and R. G. Roble was supported by NASA Space Physics Theory Program. The work at Boston College was supported by Phillips Laboratory contract F19628-93-K-0001. Millstone Hill radar data were acquired and analyzed under the support of NSF cooperative agreement ATM-94-08609 (and previous agreements) to the Massachusetts Institute of Technology.

The Editor thanks R. J. Moffett and H. Rishbeth for their assistance in evaluating this paper.

## References

- Allen, J., H. Sauer, L. Frank, and P. Reiff, Effects of the March 1989 solar activity, *Eos Trans. AGU*, **70**, 1486-1488, 1989.
- Anderson, D. N., Daily variation of the ionospheric  $F_2$  equatorial anomaly in the American and Asian sectors, *NCAR Coop. Thesis* 26, pp. 1-144, Natl. Cent. for Atmos. Res., Boulder, Colo., 1971.
- Anderson, D. N., A theoretical study of the ionosphere  $F$  region equatorial anomaly, I, Theory, *Planet. Space Sci.*, **21**, 409-419, 1973.
- Bilitza, D., International reference ionosphere 1990, *Nat. Space Sci. Data Cent.*, World Data Cent. A for Rockets and Satell., Greenbelt, Md., 1990.
- Bilitza, D., K. Rawer, L. Bosny, and T. Gulyaeva, International reference ionosphere: Past, present, and future, *Adv. Space Res.*, **13**, 3-13, 1993.
- Buonsanto, M. J., Comparison of incoherent scatter observations of electron density, and electron and ion temperature at Millstone Hill, with the International Reference Ionosphere, *J. Atmos. Terr. Phys.*, **51**, 441-468, 1989.
- Buonsanto, M. J., Observed and calculated  $F_2$  peaks heights and derived meridional winds at midlatitudes over a full solar cycle, *J. Atmos. Terr. Phys.*, **52**, 223-240, 1990.
- Buonsanto, M. J., M. Codrescu, B. A. Emery, C. G. Fesen, T. J. Fuller-Rowell, D. J. Melendez-Alvira, and D. P. Sipler, Comparison of the models and measurements at Millstone Hill during the January 24-26, 1993, minor storm interval, *J. Geophys. Res.*, **102**, 7267-7277, 1997.
- Chen, C. F., B. W. Reinisch, R. R. Gamache, M. J. Buonsanto, and B. D. Ward, The accuracy of ionogram-derived  $N(h)$  profiles, *Adv. Space Res.*, **14**, 43-46, 1994.
- Conrad, J. R., and R. W. Schunk, Diffusion and heat flow equations with allowance for large temperature differences between interacting species, *J. Geophys. Res.*, **84**, 811-822, 1979.
- Crank, J. and P. Nicholson, A practical method for numerical evaluation of solutions of partial differential equations of the heat-conduction type, *Proc. Camb. Phil. Soc.*, **43**, 50-67, 1947.
- Decker, D. T., C. E. Valladares, R. Sheehan, S. Basu, D. N. Anderson, and R. A. Heelis, Modeling daytime  $F$  layer patches over Sonderstrom, *Radio Sci.*, **29**, 249-268, 1994.

- Dickinson, R. E., E. C. Ridley, and R. G. Roble, A three-dimensional general circulation model of the thermosphere, *J. Geophys. Res.*, **86**, 1499-1512, 1981.
- Dickinson, R. E., E. C. Ridley, and R. G. Roble, Thermospheric general circulation with coupled dynamics and composition, *J. Atmos. Sci.*, **41**, 205-219, 1984.
- Ennis, A. E., G. J. Bailey, and R. J. Moffett, Vibrational nitrogen concentration in the ionosphere and its dependence on season and solar cycle, *Ann. Geophys.*, **13**, 1165-1171, 1995.
- Fejer, B. G., Low latitude electrodynamic plasma drifts, A review, *J. Atmos. Terr. Phys.*, **53**, 677-693, 1991.
- Fesen, C. G., R. G. Roble, and E. C. Ridley, Thermospheric tides at equinox: Simulations with coupled composition and auroral forcings, 2, Semidiurnal component, *J. Geophys. Res.*, **96**, 3662-3678, 1991.
- Fesen, C. G., B. A. Emery, M. J. Buonsanto, Q. H. Zhou, and M. P. Sulzer, Simulations of the F region during the January 1993 10 day campaign, *J. Geophys. Res.*, **102**, 7249-7265, 1997.
- Forbes, J. M., and F. Vial, Monthly simulations of the solar semidiurnal tide in the mesosphere and lower thermosphere, *J. Atmos. Terr. Phys.*, **51**, 649-661, 1989.
- Forbes, J. M., R. G. Roble, and C. G. Fesen, Acceleration, heating, and compositional mixing of the thermosphere due to upward propagating tides, *J. Geophys. Res.*, **98**, 311-321, 1993.
- Foster, J. C., J. M. Holt, R. G. Musgrave, and D. S. Evans, Ionospheric convection associated with discrete levels of particle precipitation, *Geophys. Res. Lett.*, **13**, 656-659, 1986.
- Fuller-Rowell, T. J., and D. S. Evans, Height integrated Pedersen and Hall conductivity patterns inferred from the TIROS-NOAA satellite data, *J. Geophys. Res.*, **92**, 7606-7618, 1987.
- Fuller-Rowell, T. J., and D. Rees, A three-dimensional, time dependent, global model of the thermosphere, *J. Atmos. Sci.*, **37**, 2545-2567, 1980.
- Fuller-Rowell, T. J., and D. Rees, Derivation of a conservative equation for mean molecular weight for a two constituent gas within a three-dimensional, time-dependent model of the thermosphere, *Planet. Space Sci.*, **31**, 1209-1222, 1983.
- Fuller-Rowell, T. J., D. Rees, S. Quegan, R. J. Moffett, and G. J. Bailey, Interactions between neutral thermospheric composition and the polar thermosphere using a coupled global model, *J. Geophys. Res.*, **92**, 7744-7748, 1987.
- Fuller-Rowell, T. J., D. Rees, S. Quegan, R. J. Moffett, and G. J. Bailey, Simulations of the seasonal and UT variations of the thermosphere and ionosphere using a coupled, three-dimensional, global model, *Pure Appl. Geophys.*, **127**, 189-217, 1988.
- Fuller-Rowell, T. J., D. Rees, H. Rishbeth, A. G. Burns, T. L. Killeen, and R. G. Roble, Modeling of composition changes during F-region storms: A reassessment, *J. Atmos. Terr. Phys.*, **53**, 541-550, 1991.
- Hagan, M. E., C. A. Barth, W. K. Tobiska, A. H. Manson, R. A. Vincent, M. J. Buonsanto, R. G. Burnside, and V. B. Wickwar, Observations of upper atmospheric weather during solar minimum winter, *J. Geophys. Res.*, **97**, 4163-4176, 1992.
- Hedin, A. E., MSIS-86 thermospheric model, *J. Geophys. Res.*, **92**, 4649-4662, 1987.
- Hedin, A. E., et al., Revised global model of thermosphere winds using satellite and ground-based observations, *J. Geophys. Res.*, **96**, 7657-7688, 1991.
- Heelis, R. A., J. K. Lowell, and R. W. Spiro, A model of the high-latitude ionospheric convection pattern, *J. Geophys. Res.*, **87**, 6339-6345, 1982.
- Hinteregger, H. E., K. Fukui, and B. R. Gilson, Observational, reference and model data on solar EUV, from measurements on AE-E, *Geophys. Res. Lett.*, **8**, 1147-1150, 1981.
- Huang, X. and B. W. Reinisch, Vertical electron density profiles from the Digisonde network, *Adv. Space Res.*, **18**(6), 121-219, 1996.
- Lee, J. S., J. P. Doering, T. A. Potemra, and L. H. Brace, Measurements of the ambient photoelectron spectrum from Atmosphere Explorer, 1, AE-E measurements below 300 km during solar minimum conditions, *Planet. Space Sci.*, **28**, 947-971, 1980.
- Mendillo, M., M. Buonsanto, and J. Klobuchar, The construction and use of storm-time corrections for ionospheric F region parameters, in *Effect of the Ionosphere on Space Systems and Communications*, edited by J. M. Goodman, pp. 361-371, Nav. Res. Lab., Washington, D. C., 1975.
- Moffett, R. J., The equatorial anomaly in the electron distribution of the terrestrial F region, *Fund. of Cosmic Phys.*, **4**, 313-318, 1979.
- Nagy, A. F., and P. M. Banks, Photoelectron fluxes in the ionosphere, *J. Geophys. Res.*, **75**, 6260-6270, 1970.
- Newberry, I. T., R. H. Comfort, P. G. Richards and C. R. Chappell, Thermal He<sup>+</sup> in the plasmasphere: Comparison of observations with numerical calculations, *J. Geophys. Res.*, **94**, 15,265-15,276, 1989.
- Quegan, S., G. J. Bailey, R. J. Moffett, R. A. Heelis, T. J. Fuller-Rowell, D. Rees, and R. W. Spiro, A theoretical study of the distribution of ionization in the high-latitude ionosphere and the plasmasphere: First results on the mid-latitude trough and the light-ion trough, *J. Atmos. Terr. Phys.*, **44**, 619-640, 1982.
- Reinisch, B. W., The Digisonde network and databasing, Rep. UAG-104, World Data Ctr. A for Sol.-Terr. Phys., Ionosonde Networks and Stn., pp. 8-15, Boulder, Colo., 1995.
- Reinisch, B. W., Modern ionosondes, in *Modern Ionospheric Science*, edited by H. Kohl, R. Ruester, and K. Schlegel, pp. 440-458, EGS Copernicus, 1996.
- Reinisch, B. W., and H. Xueqin, Automatic calculation of electron density profiles from digital ionograms, 3, Processing of bottomside ionograms, *Radio Sci.*, **18**, 477-492, 1983.
- Reinisch, B. W., D. Anderson, R. R. Gamache, X. Huang, C. F. Chen, and D. T. Decker, Validating ionospheric models with measured electron density profiles, *Adv. Space Res.*, **14**, (12)67-(12)70, 1994.
- Reinisch, B. W., D. M. Haines, K. Bibl, I. Galkin, X. Huang, D. F. Kitrosser, G. S. Sales, and J. L. Scali, Ionospheric sounding in support of over-the-horizon radar, *Radio Sci.*, **32**, 1681-1694, 1997.
- Richards, P. G., An improved algorithm for determining neutral winds from the height of the F<sub>2</sub> peak electron density, *J. Geophys. Res.*, **96**, 17,839-17,846, 1991.
- Richards, P. G., and D. G. Torr, A factor of 2 reduction in the theoretical F<sub>2</sub> peak electron density due to enhanced vibrational excitation of N<sub>2</sub> in summer at solar maximum, *J. Geophys. Res.*, **91**, 11,331-11,336, 1986.
- Richards, P. G., and D. G. Torr, Ratios of photoelectron to EUV ionization rates for aeronomic studies, *J. Geophys. Res.*, **93**, 4060-4066, 1988.
- Richards, P. G., D. G. Torr, and W. A. Abdu, Effects of vibrational enhancement of N<sub>2</sub> on the cooling rate of ionospheric thermal electrons, *J. Geophys. Res.*, **91**, 304-310, 1986.
- Richards, P. G., D. G. Torr, B. W. Reinisch, R. R. Gamache, and P. J. Wilkinson, F<sub>2</sub> peak electron density at Millstone Hill and Hobart: Comparison of theory and measurement at solar maximum, *J. Geophys. Res.*, **99**, 15,005-15,016, 1994a.
- Richards, P. G., D. G. Torr, M. J. Buonsanto, and D. P. Sipler, Ionospheric effects of the March 1990 magnetic storm: Comparison of theory and measurement, *J. Geophys. Res.*, **99**, 23,359-23,365, 1994b.
- Richards, P. G., J. A. Fennelly, and D. G. Torr, EUVAC: A solar EUV flux model for aeronomic calculations, *J. Geophys. Res.*, **99**, 8981-8992, 1994c.
- Richmond, A. D., et al., An empirical model of quiet-day ionospheric electric fields at middle and low latitudes, *J. Geophys. Res.*, **85**, 4658-4664, 1980.
- Roble, R. G., and E. C. Ridley, An auroral model for the NCAR thermospheric general circulation model, *Ann. Geophys.*, **5A**(6), 369-382, 1987.
- Roble, R. G., R. E. Dickinson, and E. C. Ridley, Global circulation and temperature structure of thermosphere with high-latitude plasma convection, *J. Geophys. Res.*, **87**, 1599-1614, 1982.
- Roble, R. G., E. C. Ridley, A. D. Richmond, and R. E. Dickinson, A coupled thermosphere/ionosphere general circulation model, *Geophys. Res. Lett.*, **15**, 1325-1328, 1988.
- Salah, J. E., Interim standard for the ion-neutral atomic oxygen collision frequency, *Geophys. Res. Lett.*, **20**, 1543-1546, 1993.
- Schunk, R. W., A mathematical model of the middle and high latitude ionosphere, *Pure Appl. Geophys.*, **127**, 255-303, 1988.
- Schunk, R. W., and A. F. Nagy, Electron temperatures in the F region of the ionosphere: Theory and observations, *Rev. Geophys.*, **16**, 355-399, 1978.
- Schunk, R. W., and W. J. Raitt, Atomic nitrogen and oxygen ions in the daytime high-latitude F region, *J. Geophys. Res.*, **85**, 1255-1272, 1980.
- Schunk, R. W., and J. J. Sojka, Ion temperature variations in the daytime high-latitude F region, *J. Geophys. Res.*, **87**, 5169-5183, 1982.
- Schunk, R. W., and J. C. G. Walker, Transport properties of the ionospheric electron gas, *Planet. Space Sci.*, **18**, 1535-1550, 1970.
- Schunk, R. W., and J. C. G. Walker, Theoretical ion densities in the lower ionosphere, *Planet. Space Sci.*, **21**, 1875-1896, 1973.
- Schunk, R. W., W. J. Raitt, and P. M. Banks, Effect of electric fields on

- the daytime high-latitude *E* and *F* regions, *J. Geophys. Res.*, **80**, 3121-3130, 1975.
- Schunk, R. W., P. M. Banks, and W. J. Raitt, Effects of electric fields and other processes upon the nighttime high latitude *F* layer, *J. Geophys. Res.*, **81**, 3271-3282, 1976.
- Schunk, R. W., J. J. Sojka, and M. D. Bowline, Theoretical study of the electron temperature in the high latitude ionosphere for solar maximum and winter conditions, *J. Geophys. Res.*, **91**, 12,041-12,054, 1986.
- Sica, R. J., R. W. Schunk, and P. J. Wilkinson, A study of the undisturbed mid-latitude ionosphere using simultaneous multiple site ionosonde measurements, *J. Geophys. Res.*, **95**, 8271-8279, 1990.
- Sojka, J. J., Global scale, physical models of the *F* region ionosphere, *Rev. Geophys.*, **27**, 371-403, 1989.
- Sojka, J. J., and R. W. Schunk, A theoretical study of the global *F* region for June solstice, solar maximum, and low magnetic activity, *J. Geophys. Res.*, **90**, 5285-5298, 1985.
- Sojka, J. J., W. J. Raitt, and R. W. Schunk, A theoretical study of the high-latitude winter *F* region at solar minimum for low magnetic activity, *J. Geophys. Res.*, **86**, 609-621, 1981a.
- Sojka, J. J., W. J. Raitt, and R. W. Schunk, Theoretical predictions for ion composition in the high-latitude winter *F* region for solar minimum and low magnetic activity, *J. Geophys. Res.*, **86**, 2206-2216, 1981b.
- Sterling, D. L., W. B. Hanson, R. J. Moffett, and R. G. Baxter, Influence of electromagnetic drifts and neutral air winds on some features of the *F*<sub>2</sub> region, *Radio Sci.*, **4**, 1005-1023, 1969.
- St.-Maurice, J.-P., and R. W. Schunk, Diffusion and heat flow equations for the mid-latitude topside ionosphere, *Planet. Space Sci.*, **25**, 907-920, 1977.
- Tobiska, W. K., Revised solar extreme ultraviolet flux model, *J. Atmos. Terr. Phys.*, **53**, 1005-1018, 1991.
- Torr, M. R., D. G. Torr, R. A. Ong, and H. E. Hinteregger, Ionization frequencies for major thermospheric constituents as a function of solar cycle 21, *Geophys. Res. Lett.*, **6**, 771-776, 1979.
- Torr, M. R., D. G. Torr, P. G. Richards, and S. P. Yung, Mid- and low-latitude model of thermospheric emissions, I, O<sup>+</sup> (<sup>4</sup>P) 7320 Å and N<sub>2</sub> (<sup>2</sup>P) 3371 Å, *J. Geophys. Res.*, **95**, 21,147-21,168, 1990.
- Wells, G. D., A. S. Rodger, R. J. Moffett, G. J. Bailey, and T. J. Fuller-Rowell, The effects of nitric oxide cooling and the photodissociation of molecular oxygen on the thermosphere/ionosphere system over Argentine Islands, *Ann. Geophys.*, **15**, 355-365, 1997.
- D. N. Anderson, Phillips Laboratory, PL/GPIM, Hanscom Air Force Base, MA 01731-5000.
- M. J. Buonsanto, Atmospheric Sciences Group, MIT, Haystack Observatory, Westford, MA 01886.
- M. Codrescu and T. J. Fuller-Rowell, ERL/SEL R/E/SEL, NOAA, 325 Broadway, Boulder, CO 80303.
- D. Decker, Institute for Space Research, Boston College, Chestnut Hill, MA 02167.
- C. G. Fesen, W. B. Hanson Center for Space Sciences, University of Texas, Dallas, Box 83068, MSFO2, Richardson, TX 75083-0688.
- B. W. Reinisch, Center for Atmospheric Research, University of Massachusetts, 600 Suffolk St., Lowell, MA 01854.
- P. G. Richards, Computer Science Department, University of Alabama in Huntsville, Huntsville, AL 35899.
- R. G. Roble, NCAR, 1850 Table Mesa Drive, Boulder, CO 80307-3000.
- R. W. Schunk and J. J. Sojka, Center for Atmospheric and Space Sciences, Utah State University, Logan, UT 84322-4405.

(Received January 7, 1997; revised September 9, 1997; accepted September 30, 1997.)



# Formation of polar cap patches associated with north-to-south transitions of the interplanetary magnetic field

C. E. Valladares, D. T. Decker, and R. Sheehan

Institute for Scientific Research, Boston College, Newton Center, Massachusetts

D. N. Anderson and T. Bullett

Geophysics Directorate, Phillips Laboratory, Hanscom Air Force Base, Bedford, Massachusetts

B. W. Reinisch

Center for Atmospheric Research, University of Massachusetts, Lowell

**Abstract.** On January 15, 1991, the Sondrestrom incoherent scatter radar probed the midday high-latitude ionosphere to gather evidence for the formation and entry of polar cap patches. During the experiment the interplanetary magnetic field (IMF)  $B_z$  was positive and steady for few hours until 1548 UT when a short negative excursion of  $B_z$  occurred. Prior to the  $B_z$  excursion, and when this parameter was directed northward, the Sondrestrom radar detected a quasi-stationary density feature situated near the poleward boundary of the oval. Convergent electric fields and slightly elevated  $T_e$  values were seen accompanying the  $F$  region density feature. A numerical model of the high-latitude ionosphere that uses a steady north  $B_z$  Heppner and Maynard convection pattern suggests that under these IMF conditions a tongue of ionization (TOI) can be formed near the midday sector, but it is confined to the poleward boundary of the auroral oval. It does not traverse into the polar cap. This simulated  $B_z$  northward TOI resembles the density feature seen in the radar data prior to the  $B_z$  negative excursion. When the  $B_z$  value was oriented southward, the radar detected the density feature moving poleward and then disappearing to the north of the radar field of view. At this time of  $B_z$  negative the radar data also displayed elevated  $T_i$  values and a new pattern of line-of-sight velocities. Nearly 34 min after the density feature departed from the field of view of the Sondrestrom radar, the Qaanaaq digisonde measured a factor of 2 increase in the  $f_oF_2$  values. Similar enhancements are typically attributed to the passage of a patch. We also conducted a numerical simulation of the transit of the density feature from its initial location near the polar cap boundary up to its passage through the Qaanaaq station. The time that the density feature reaches Qaanaaq in our simulations is in good agreement with the actual time that the enhanced patch-like number density was observed at Qaanaaq. The  $B_z$  switching mechanism does not dispute the validity of other patch formation mechanisms; it merely suggests that a  $B_z$  northward TOI can end up as a polar cap patch if a timely reversal of  $B_z$  occurs.

## 1. Introduction

Polar cap patches consist of discrete regions in the polar cap where the F-region number density is enhanced in comparison with its neighboring values. The plasma enhancement can be a factor of 10, as observed during solar maximum conditions [Buchau and Reinisch, 1991], or a factor of 3, as detected in solar minimum conditions [Buchau et al., 1985]. Incoherent scatter radars [Foster and Doupnik, 1984; Kelly and Vickrey, 1984], HF radars [Rodger et al., 1994; Pinnock et al., 1995], digisondes [Buchau et al., 1983], all-sky intensified photometers (ASIPs) [Weber et al., 1984,

1986], scintillation receivers [Basu et al., 1985, 1989], and ion drift meter (IDM) sensors on board satellites [Coley and Heelis, 1995] have all contributed to build a comprehensive morphological description of the polar cap patches. On the basis of these studies we presently know that polar cap patches occur under moderate and disturbed magnetic conditions, are almost uniquely correlated with a southward IMF  $B_z$  orientation, possess a size between 100 and 1000 km, and move in an antisunward fashion, a close replica in magnitude and direction of the background plasma velocity [Fukui et al., 1994]. During solar maximum conditions, patches have been observed to be associated with an intense level of scintillations [Buchau et al., 1985; Basu et al., 1985, 1989]. During solar minimum conditions, when the background and patch number densities are somewhat lower, the patch related scintillation level becomes much weaker.

Copyright 1998 by the American Geophysical Union.

Paper number 97JA03682.  
0148-0227/98/97JA-03682\$09.00



This fact points out the limitation that some techniques suffer when they are employed to detect patches. Other instrumentation, such as ASIPs, are also affected by the ambiguity in their measurements [Sojka *et al.*, 1997]. Nevertheless, if two or more different but complementary techniques are used simultaneously, or if an incoherent scatter radar suited with a fast scan capability is available, then an unambiguous detection of the location and the passage of a polar cap patch should be readily achieved.

Soon after the patch morphology was established, Buchau *et al.*, [1985], and de la Beaujardiere *et al.* [1985] postulated that the number density inside the patches was produced by solar EUV radiation in the sunlit ionosphere, probably at subcusp latitudes. Buchau *et al.* [1985] found a strong UT and seasonal control on the occurrence of patches. The patches were seen almost exclusively between 1200 and 0000 UT. Based on this fact, these authors argued that the dayside plasma convects through the throat under the influence of the high-latitude velocity pattern. The throat is defined as the region near midday at the separatrix between the convection cells in a typical two-cell  $B_z$  south convection pattern. It was also understood that in the northern hemisphere the offset of the geographic and magnetic poles [Sojka *et al.*, 1979] allows the convection pattern to reach and enclose plasma from lower geographic latitudes only at certain UT periods, explaining the strong UT dependence observed near the center of the northern polar cap. Another potential source of the patches is the local production of number density due to soft and intense cusp precipitation [Kelley *et al.*, 1982; Sojka and Schunk, 1986]. This mechanism may be more effective in the southern hemisphere where the offset of the geographic and magnetic poles is larger. The larger offset will place the cusp at higher geographic latitudes originating a larger contrast between the locally produced number densities and the number densities transported from the sunlit ionosphere. A different source for polar cap patches may occur during storm geomagnetic conditions. Foster [1993] pointed out that during disturbed times the afternoon cell expands to lower latitudes ( $63^\circ$  to  $46^\circ$   $\Lambda$ ), bringing high solar produced F-region plasma from a source region at midlatitudes. This author measured a factor of 5 increase in the storm-enhanced density (SED) in comparison with the quiet time number density.

While most of the mechanisms mentioned above envision a uniform and steady tongue of ionization (TOI) that enters the polar cap through the dayside throat, the nature of the patches being spatially localized, discrete, and completely detached from the auroral oval indicates the need to introduce a mechanism that could break the continuous TOI into smaller entities. Sojka *et al.* [1993, 1994] demonstrated that repetitive changes in the polarity of the IMF  $B_y$  component could lead to the production of large scale plasma structures by redirecting the TOI toward different locations in the polar cap. Rodger *et al.* [1994] and Valladares *et al.*, [1994] presented data from the Polar Anglo-American Conjugate Experiment and Sondrestrom radars, respectively, to indicate the presence of a large plasma flow near midday containing velocities above  $2 \text{ km s}^{-1}$ . It is known that a large plasma velocity can produce an increase in the ion temperature ( $T_i$ ) dependent  $\text{O}^+$  recombination rate, consequently depleting a region of the dayside F-region ionosphere. Modeling work conducted by Valladares *et al.* [1996] has demonstrated that in fact a section of the TOI can get eroded, therefore splitting

the TOI into smaller discrete entities. This chopped TOI will contain number densities much higher than non-TOI regions of the polar cap. This work indicated that transport is also important in bringing less dense plasma from earlier (or later) local times. Lockwood and Carlson [1992] have proposed that a transient burst of reconnection combined with an equatorward motion of the ionospheric projection of the X line could act accordingly to extract a region of the high number density subauroral plasma, detach it, and displace it poleward. They also proposed that a newly formed patch will be elongated or "cigar" shaped. Recent measurements at Qaanaaq have shown that the patches usually display well-elongated shapes with the major axis oriented along the dawn-dusk meridian [Fukui *et al.*, 1994]. While a number of mechanisms have been studied, it is becoming evident that in order to explain patch formation we need to know in detail how the convection process evolves [Crowley, 1996].

More recently, Coley and Heelis [1995] developed an adaptive algorithm to conduct an automated identification of patches using the entire DE 2 database. These authors found typical spatial scale size of the patches in the range 300 km to 400 km and the existence of density structures inside the polar cap even when the IMF was positive. However, Coley and Heelis [1995] used hourly values of the IMF, and their conclusions for the  $B_z$  north cases could be contaminated by cases when short negative excursions (20–30 min) of the IMF  $B_z$  occurred.

The need to study patch formation mechanisms stems from the disruptive effect that kilometer- and subkilometer-scale irregularities, which grow embedded inside the patches, produce on communication and navigation systems even in the gigahertz frequency window [Basu *et al.*, 1994]. The National Space Weather Program has indicated the importance of assessing the climatology of small-scale irregularities and understanding the formation of the larger scale structures. Obviously, the grand goal in the study of polar cap patches is to attain a forecasting capability of the appearance and development of these types of plasma structures.

A patch generation mechanism based on north-to-south IMF reversals has not received much attention. Tsunoda [1988] mentioned in a review paper that a north-to-south transition of the IMF could indeed lead to the formation of a discrete patch. However, neither experimental nor modeling verification has been forwarded. In this paper we present for the first time experimental data and corresponding computer modeling of a case study event that serves to introduce the  $B_z$  switching mechanism as another process for the formation and transport of large-scale plasma structures throughout the polar cap. We present data collected on January 15, 1991, by the Sondrestrom incoherent scatter (IS) radar and by two digisondes: one located at Sondrestrom and the other at Qaanaaq. This paper consists of five sections. Section 2 provides experimental evidence for the formation of a density feature near the poleward boundary of the oval during an interval when  $B_z$  is positive and steady. It also shows the initial poleward transport of this feature after the IMF turns southward. Section 3 describes two modeling efforts that were conducted. The first effort demonstrates that a density feature can exist near the poleward boundary of the oval if the convection pattern resembles the empirical north  $B_z$  Heppner and Maynard [1987] pattern and remains unchanged for tens of minutes. The second modeling work proves that a density

feature, such as the one measured by the Sondrestrom radar on January 15, 1991, will move toward the center of the polar cap when the high-latitude convection velocity changes to a typical  $B_z$  south convection pattern. Section 4 shows the results of a sensitivity study of the effect of the cross polar cap potential on the  $f_oF_2$  values of the density feature/patch. The paper ends with a discussion and conclusion section.

## 2. Experimental Observations

This section presents observations conducted with the Sondrestrom incoherent scatter radar (66.987°N, 50.949°W, 74° invariant latitude) and with two digisondes, one placed at Sondrestrom and the other at Qaanaaq (77.47°N, 69.23°W, 86° invariant latitude). It also introduces concurrent in situ measurements of the IMF by the IMP 8 satellite. The data sets under discussion were collected on January 15, 1991. This experiment was part of a 4 day High Latitude Plasma Structures (HLPS) campaign to observe the formation and entry of patches into the polar cap. The Sondrestrom radar operated only for 5 hours per day during the campaign window. The observation period was selected to be centered with magnetic local noon at Sondrestrom. During the observations the magnetic conditions were quiet ( $K_p = 2+$ ), and the  $F_{10.7}$  solar flux was  $184.6 \times 10^{-22} \text{ W m}^{-2} \text{ Hz}^{-1}$ .

### 2.1. IMP 8 Satellite Observations

At the time of the radar measurements the IMP 8 satellite was in the solar wind, well upstream from the Earth's bow shock. The X, Y, and Z coordinates, in the GSM system, were 35.0, 2.0, and -12.8 Earth radii, respectively. The IMF observations start at 1210 UT (Figure 1) during a sudden rise of the  $B_z$  values. The  $B_z$  component remains positive and near 5 nT until 1548 UT, when a sharp decrease and a reversal occurs. This component of the IMF remains near zero and

slightly negative between 1554:04 and 1608:54; after this period,  $B_z$  climbs back to the initial positive value. During the period of the radar observations,  $B_x$  and  $B_y$  are positive and negative, respectively. Using the expression given by Lockwood *et al.* [1989], we calculated that the propagation delay for the effect of the  $B_z$  IMF negative excursion to reach the Sondrestrom field of view (FOV) was  $\sim 16$  min. Consequently, to relate the IMF measurements of Figure 1 to the radar observations described later, it is necessary to add 16 min to the times of Figure 1. Our calculation of the delay time can be affected by an error of 2 min [Lockwood *et al.*, 1989].

### 2.2. Sondrestrom Radar Observations

On January 15, 1991, the Sondrestrom radar operated between 1145 and 1700 UT, using a transmitter pulse 320  $\mu\text{s}$  long and an antenna pattern consisting of rapid azimuth and elevation scans. The scan sequence started with a 360° azimuth scan (AZ) at a fixed 30° elevation angle, followed by an elevation scan (EL) in the plane of the magnetic meridian. While the AZ scan gives the largest spatial coverage, the EL scan provides a fine spatial resolution view in a latitudinal sectional cut of any structure aligned in the east-west direction. This antenna pattern permits an intuitive three-dimensional reconstruction of the number density profiles, within the volume probed by the radar, provided the ionosphere changes slowly during the 9 min of cycle time and the altitude of the F-region peak does not vary considerably in the east-west direction. While the EL scan gives the altitude and latitudinal dependence of the number density, the AZ scan hints at the east-west modulation of these profiles. The intuitive "reconstruction" is aided by the nature of the vertical profiles of each geophysical parameter at high latitudes. The plasma velocity profiles are constant along the field lines above 150 km altitude. The number density profiles peak at

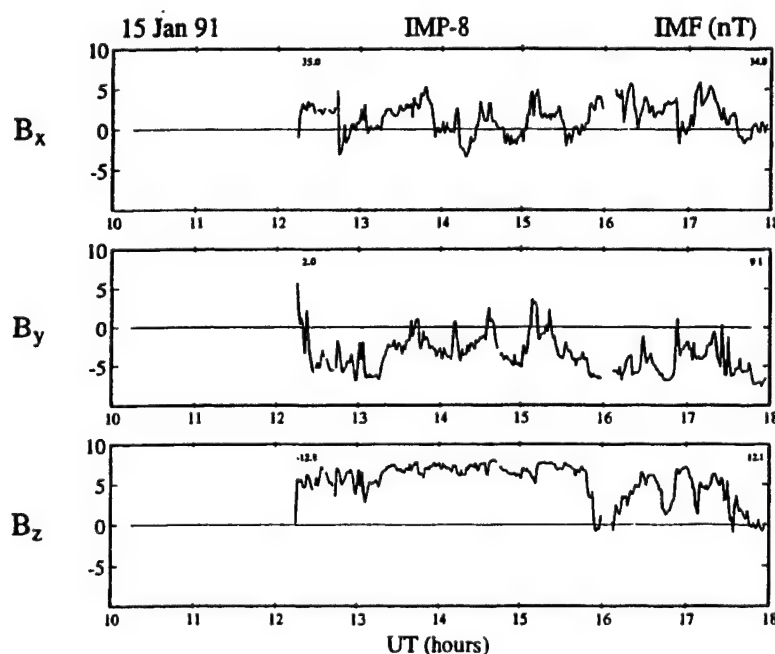


Figure 1. Interplanetary magnetic field data measured by IMP 8 on January 15, 1991. Shown from the top are the three IMF components in GSM coordinates. Units for all three quantities are nanoteslas.

the F-layer and then decay through the topside. The statistical uncertainties of the radar measurements are 3%, 50 m s<sup>-1</sup>, and 10% for the number density, line-of-sight velocity, and temperatures respectively.

Figure 2 displays the four geophysical parameters derived from the autocorrelation functions (ACFs) that were collected only during the elevation scans. The top panel shows the velocity vectors derived by using the line-of-sight ion drifts ( $V_{los}$ ) from the E and F-layers and the property of the field lines of being equipotential [de la Beaujardiere et al., 1985]. The three lower panels display the ion temperature ( $T_i$ ), the number density ( $N_e$ ), and the electron temperature ( $T_e$ ) at a fixed 320 km altitude. The resolved flow velocities are remarkably zonal, directed westward from 1230 UT until the end of the experiment. This measured flow is consistent with the convection patterns presented by Heppner and Maynard [1987] for  $B_z$  positive and  $B_z$  negative. The near-midday region of these statistical patterns shows zonal westward flows equatorward of the velocity reversal boundary.

The number density panel of Figure 2 shows a very sharp decline in its poleward extension. This abrupt latitudinal gradient is located 200 km northward of the station at 1243 UT and overhead at 1350 UT. We suggest that the formation of this abrupt  $N_e$  boundary is related not to the location of the terminator (heavy trace) but to the characteristics of the zonal flows. Another striking feature in the number density panel of Figure 2 is the presence of a density feature that seems to

grow and split from the dayside oval at 1300 UT. The density feature slowly moves poleward until 1500 UT, when it becomes quasi-stationary. At 1500 UT the  $N_e$  feature has a number density of  $10^6$  cm<sup>-3</sup>, is situated 400 km north of the station, and seems to be placed very close to the region of the convection reversal, as will be seen in the following figures. However, we are not calling this density feature a polar cap patch, at least between 1300 and 1620 UT, because it is not strictly either moving antisunward or transiting across the polar cap. The isolated region of high  $N_e$  constitutes a prominent feature in the gray scale plot and remains inside the radar field of view until 1619 UT, when it finally departs in the antisunward direction.

Figures 3-5 show a sequence of the geophysical parameters derived from several scans recorded by the Sondrestrom radar between 1549:05 and 1649:26 UT. Each column corresponds to a different scan, and only the most relevant parameters are shown. Data from the AZ scans are displayed by unfolding the conical surfaces of the antenna sweeps and projecting them onto 1600×1600 km ground surface with the radar at the center and geographic north directed toward the top of each plot. Because of the nature of the AZ scans, altitude and distance variations are intermixed. Nevertheless, it is possible to identify any localized density structure by examining the variations of the contour lines from an ideal uniform or circular pattern. The EL scans are displayed in the plane of the measurements, with magnetic north always placed in the

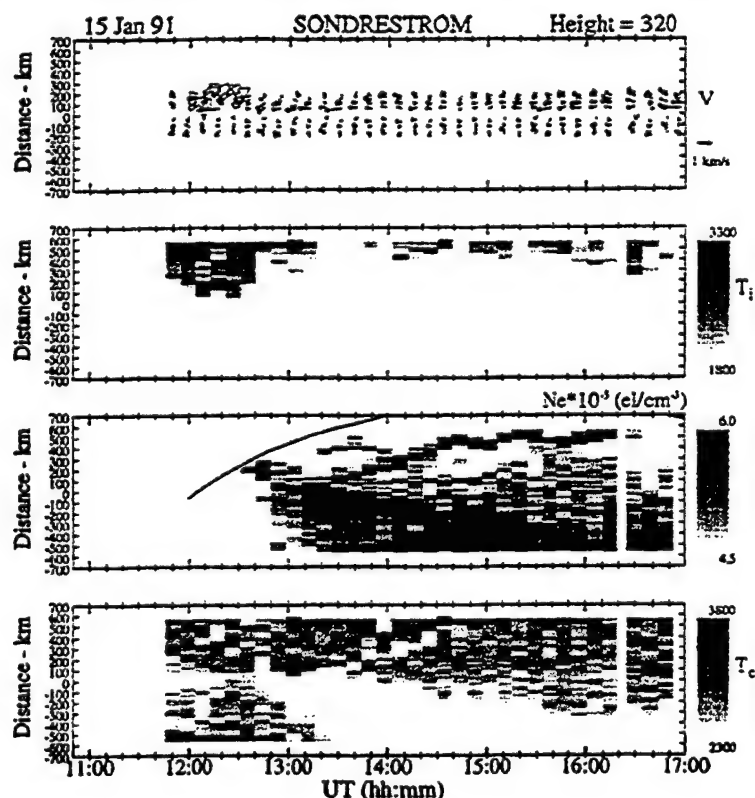
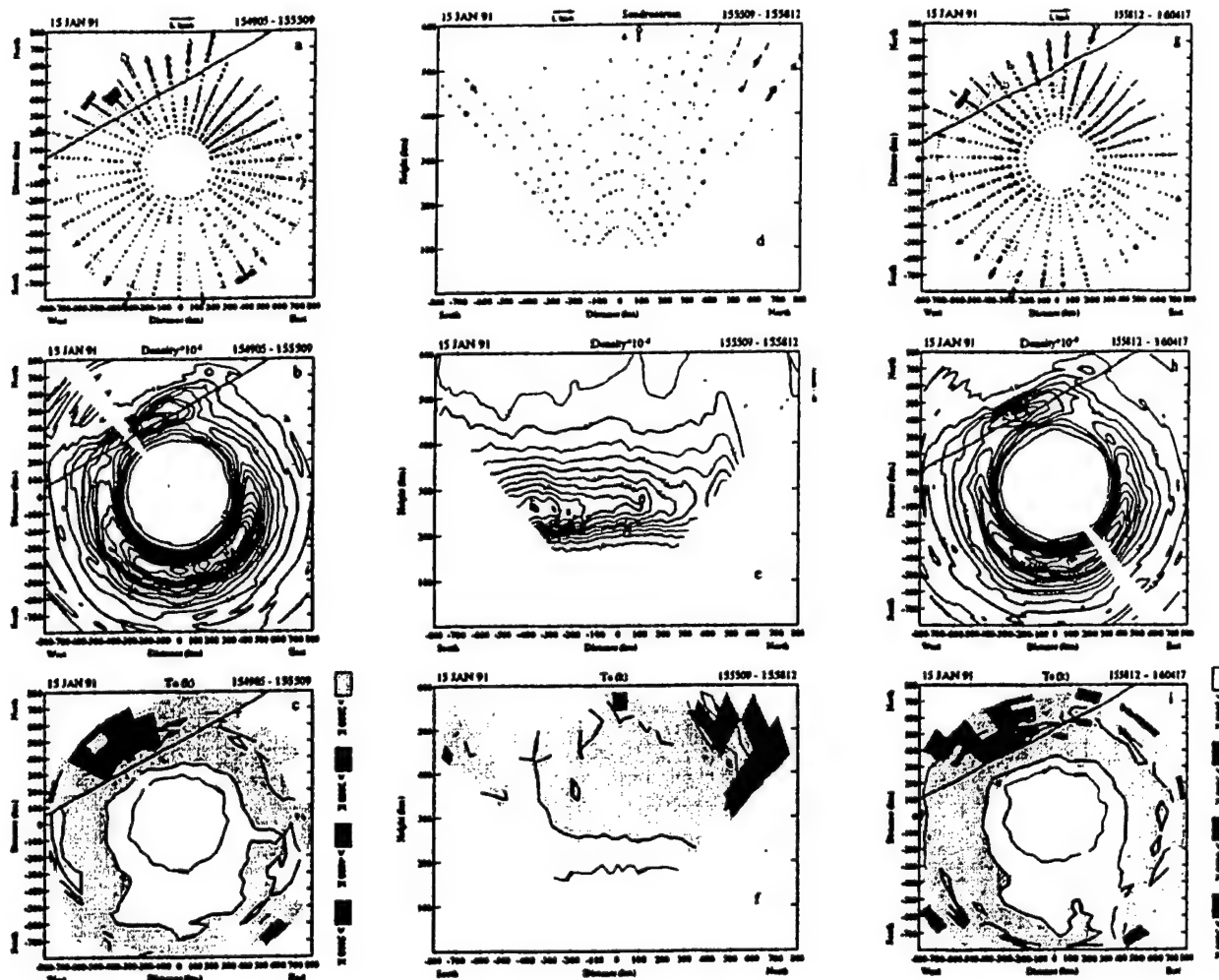


Figure 2. Low-resolution plot of the plasma parameters measured by the Sondrestrom ISR on January 15, 1991, between 1145 and 1655 UT. The  $T_i$ ,  $N_e$ , and  $T_e$  values were measured during the antenna EL scans during typical F region altitude of 320 km. The vector velocities presented in the top panel were derived using the  $V_{los}$  values measured in the E and F regions during the radar EL scans. The solid line in the  $N_e$  panel depicts the location of the solar terminator. The vertical axis of each panel corresponds to north-south horizontal distance from the radar site.



**Figure 3.** Plasma parameters measured by the Sondrestrom ISR on January 15, 1991 and during three consecutive scans. Only three of the four basic geophysical parameters ( $T_i$ ,  $V_{los}$ ,  $N_e$ , and  $T_e$ ) measured by the Sondrestrom ISR are presented here. The data were measured during two AZ scans and two EL scans interleaved between 1549:05 and 1604:17 UT. The values gathered during the AZ scans at  $30^\circ$  elevation are displayed in a projection to a plane tangent to the Earth at the radar site. Data from the EL scans are presented in the vertical plane of the radar measurements.

right side of the plot. The line-of-sight velocities are displayed by using arrows of different patterns and lengths according to the sign and magnitude of the plasma flow. Velocities directed toward the radar have also been lightly shaded. In a few cases the area probed by the radar has been darkly shaded to indicate that  $V_{los}$  exceeds  $1 \text{ km s}^{-1}$  (see Figure 4b). The number density contours are on a linear scale with the initial values and the interval between levels equal to  $10^5 \text{ cm}^{-3}$ . The  $T_i$  and  $T_e$  values are depicted in the form of gray-scaled contours varying in discrete steps of 1000 K.

Figure 3a shows a pattern of several reversals of the line-of-sight velocities. This can be explained by a sheared plasma flow containing eastward flows poleward of the line traced at 400 km north and westward flows equatorward of that line. The sign of the velocity reversal indicates also that the electric fields near the region marked by the solid line are convergent and consequently associated with an upward field-aligned current. We have also traced this line at the same

location in the other panels to indicate that the region containing convergent electric fields is situated very close to the density feature. Figure 3b reveals that the density feature (Figure 2) extends for at least 500 km in the east-west direction.  $T_e$  was also enhanced, reaching 3000 K poleward of the reversal line (Figure 3c). Because there are no significant number densities below 150 km altitude, as seen in the EL scans from earlier local times, we conclude that the precipitating particles that enhance  $T_e$  may be soft ( $<300 \text{ eV}$ ). This type of precipitation deposits most of its kinetic energy in the F-region, where the heat conductance along the field lines is large.

The elevation scans during the experiment were performed at  $-39^\circ$  azimuth angle, which is also the direction almost perpendicular to the ionospheric flows. This fact explains the small amplitude of the line-of-sight velocities and the mild shear seen during this scan. The EL scan that started at 1555:09 UT (Figures 3d-3f) shows the location of the density

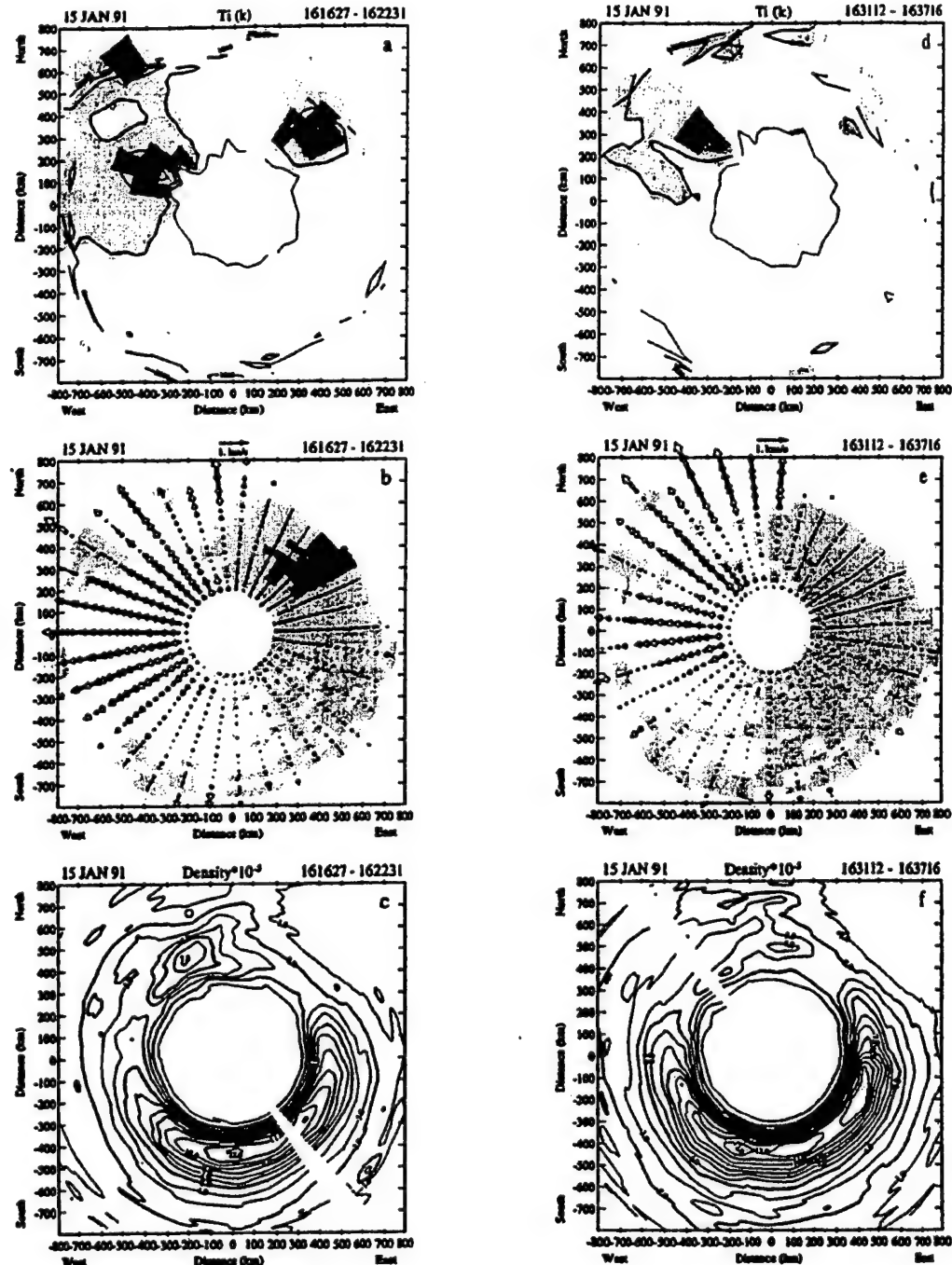
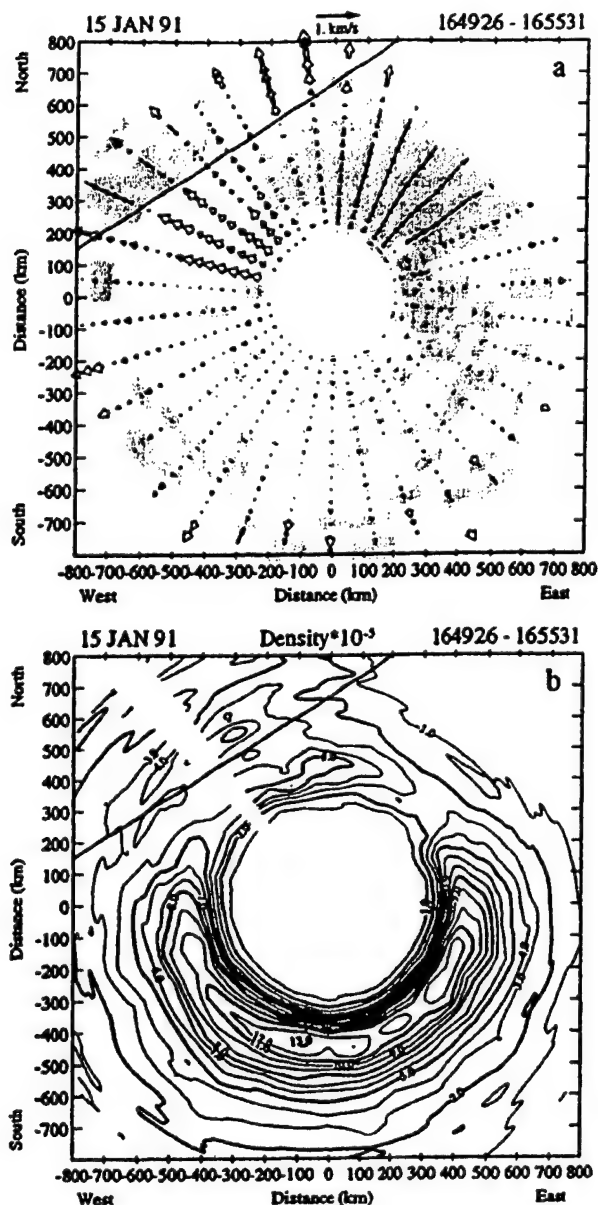


Figure 4. Same as Figure 3 but covering the period extending between 1616:27 and 1637:16 UT and measuring the  $T_i$ ,  $V_{los}$ , and  $N_e$  parameters.

feature to be 450 km north of the radar site. The  $T_e$  is also enhanced at this location but at altitudes above 450 km. EL scans conducted at earlier times measured the latitudinal width of the density feature to be 150 km. Note also that the highest number density is just poleward of the velocity shear and on the equatorward edge of the elevated  $T_e$ . While the presence of an isolated  $N_e$  structure accompanied with elevated  $T_e$  and convergent electric fields might suggest that particle precipitation is the source mechanism, we believe that

this density feature may be also formed from Sun-produced plasma entrapped in the  $B_z$  north type high-latitude convection. This hypothesis is based on (1) the fact that the density feature was initially part of the uniform auroral-subauroral number density, which seems to be sliced by the zonal flows, and (2) the modeling work presented in section 3. The AZ scan that started at 1558:12 UT (Figures 3g-3i) shows the location of the velocity reversal displaced 50 km poleward with respect to the previous AZ scan.





**Figure 5.** Same as Figure 3 but for the period extending between 1649:26 and 1655:31 UT.

The AZ scan that started at 1616:27 UT (Figures 4a-4c) shows a different distribution of velocities and number densities. The velocity frame displays a channel of large flows located just poleward of the station. This different pattern may represent the response of the high-latitude ionosphere to the reversal of the IMF  $B_z$ . The  $T_i$  panel (Figure 4a) displays two regions of intense Joule heating, one to the east and the other to the west of the station, and both of them are collocated with the region of large  $V_{los}$ .  $T_i$  is above 3000 K in these two regions. Figure 4c reveals that the antenna grazed the density feature for the last time at 1619:29 UT. We have used this time to mark the beginning of the transport of the  $N_e$  feature across the polar cap and its reconfiguration into a polar cap patch.

The AZ scan of Figures 4d-4f started with the radar pointing at  $-39^\circ$  from geographic north and proceeded counterclockwise. The large plasma jet and the corresponding enhanced Joule heating are observed only at the beginning of the scan (northwest region). The plasma jet had decayed or moved outside the radar FOV when the antenna reached the northeastern quadrant about 5 min later. The number density at the north is relatively depleted with peak  $N_e$  values near  $3 \times 10^5 \text{ cm}^{-3}$ . The following AZ scan (not shown here) displays an absence of density structures within the radar FOV. The AZ scan of Figures 5a and 5b shows the line-of-sight velocities and number densities resembling somewhat Figures 3a and 3b. There is a velocity reversal to the northwest and a region of enhanced number densities with values above  $5 \times 10^5 \text{ cm}^{-3}$  situated at 400 km north distance. We suggest that this "structure" constitutes a new density feature being formed after the  $B_z$  component switches back to positive.

### 2.3. Digisonde Observations

In Figure 6, we reproduce the  $f_oF_2$  values, and the equivalent peak number density (right scale) measured by two digisondes. One located at Qaanaaq (top panel) and the other at Sondrestrom (bottom panel). The Sondrestrom digisonde measured peak number densities near  $10^6 \text{ cm}^{-3}$  between 1300 and 1800 UT. This value is consistent with the number density values measured by the Sondrestrom incoherent scatter radar at the same time. During the same period (1300 to 1800 UT), the Qaanaaq digisonde detected a generally low

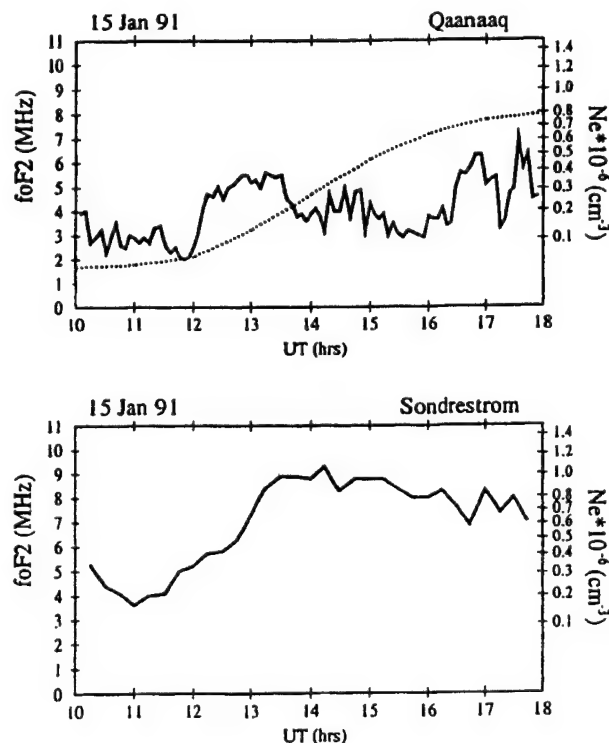


**Figure 6.** The  $f_oF_2$  values as a function of UT on January 15, 1991, recorded at two stations: (top) Qaanaq and (bottom) Sondrestrom. The dotted line in the top panel presents model results of  $f_oF_2$  values under ideal  $B_z$  south conditions.



number density ( $\sim 1 \times 10^5$  cm $^{-3}$  to  $5 \times 10^5$  cm $^{-3}$ ) but showed a bit more structure than was seen at Sondrestrom. In particular, around 1630 UT at Qaanaaq there was an abrupt increase from  $1.3 \times 10^5$  cm $^{-3}$  to  $4 \times 10^5$  cm $^{-3}$ . Fifteen minutes later, at 1645 UT, the number density at Qaanaaq reaches a value approximately equal to  $5 \times 10^5$  cm $^{-3}$ . The transit of the enhanced number density through Qaanaaq is abruptly terminated at 1715 UT. This behavior of the  $f_oF_2$  values is quite typical when patches are transiting through a polar cap station [Buchau *et al.*, 1983; Weber *et al.*, 1984; Buchau and Reinisch, 1991]. We have also included in the top panel the peak number density (see dotted line) that was obtained numerically by using the Global Theoretical Ionosphere Model (GTIM) [Anderson *et al.*, 1988]. This model run was conducted by using a steady  $B_z$  south convection pattern (Heelis-type,  $12^\circ$  radius, and 80 kV) as a fixed input. As we expected, the  $f_oF_2$  values measured at Qaanaaq are smaller than the modeled values when  $B_z$  is positive, no negative excursions of  $B_z$  exist, and no sun-aligned arcs are overhead the Qaanaaq digisonde, say between 1340 and 1630 UT. However, the digisonde data (solid curve) are higher than the model data (dotted line) between 1000 and 1340 UT when polar cap arcs populated the polar cap. An ASIP located at the Qaanaaq site, in fact, detected the passage of several polar cap arcs between 0930 and 1340 UT. After 1340 UT, when no polar cap arcs were observed, the Qaanaaq  $f_oF_2$  values are much less than the modeled values until 1630 UT when the density patch reached the Qaanaaq station. Note that the rise of the Qaanaaq  $f_oF_2$  values at 1630 UT occurs more rapidly than the increase of the modeled values (dotted line). This plot is also consistent with the fact that patches are not seen deep inside the polar cap when the IMF is steadily northward.

### 3. Numerical Modeling

We have used the GTIM developed by Phillips Laboratory and Boston College researchers [Anderson *et al.*, 1988; Decker *et al.*, 1994] to conduct two types of simulations. The first modeling task was to study whether convection during periods of positive  $B_z$  could create a quasi-stationary feature northward of Sondrestrom similar to what was observed prior

to 1616 UT. The second type of simulation was to provide a numerical confirmation that the  $N_e$  feature measured at Sondrestrom at 1616 UT transited across Qaanaaq and produced the plasma enhancements seen by the digisonde at 1650 UT. The idea is not to reproduce all the observed details, but to establish the feasibility that a brief period of negative  $B_z$  convection could take a density feature seen at Sondrestrom and convect it to Qaanaaq.

In general, GTIM calculates the  $O^+$  number density profile along a single flux tube by solving the coupled continuity and momentum equations for ions and electrons. Geophysical inputs to the GTIM are the solar flux, the neutral number density, the neutral wind, the neutral temperature, the ion and electron temperatures, the high latitude convection pattern, and the initial plasma number density. GTIM has proved to be well suited to conduct studies of the formation of polar cap patches, such as using variable convection patterns [Sojka *et al.*, 1993; Decker *et al.*, 1994], or using localized velocity vortices [Decker *et al.*, 1994; Valladares *et al.*, 1996]. The work presented here constitutes an initial examination of the  $B_z$  switching mechanism as a potential generator of patches. This work also studies the role of convection in patch formation by focusing for the first time on a period of essentially positive  $B_z$  that includes a brief switch to negative  $B_z$ . We are not modeling the formation of the Sondrestrom density feature *per se*; instead we start with number densities measured by the Sondrestrom IS radar and model the evolution of the density feature, its reconfiguration into a patch, and its transit across the Qaanaaq zenith location.

#### 3.1. $B_z$ North Simulation

Figure 7a shows the  $N_mF_2$  values as a function of magnetic latitude and local time obtained with the GTIM after following 12,800 flux tubes during 8 hours 16 min of simulation time. This first simulation used solar and magnetic conditions similar to the ones encountered during the experiment. It also employed a steady Heppner and Maynard [1987]  $B_z > 0$ ,  $B_y < 0$  convection pattern, which resulted in the best fit to the  $V_{los}$  measured by the radar AZ scans between 1549:05 and 1613:24 UT (see Figure 8a).

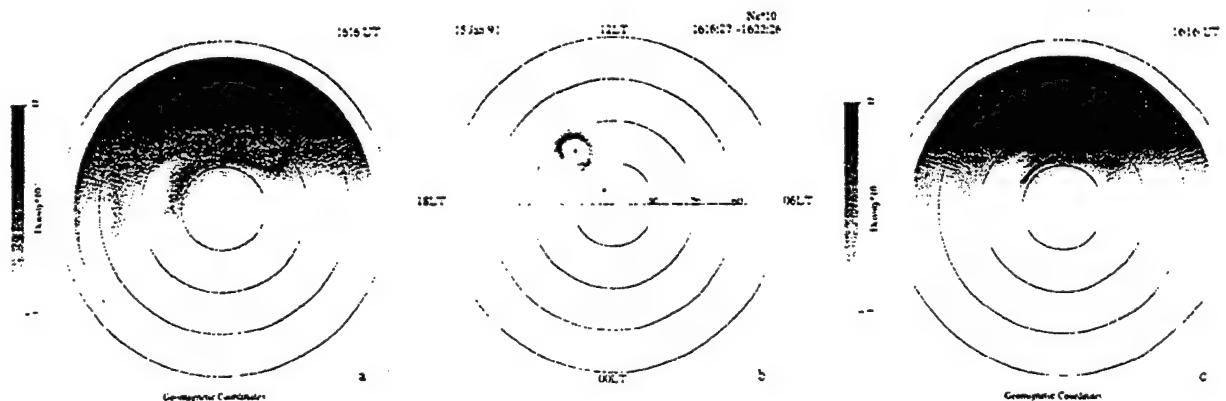


**Figure 7.** Series of polar plots. (a)  $N_mF_2$  (peak  $F$  region number density) values of the high-latitude ionosphere at 1616 UT, obtained by running the GTIM model for 8 hours 16 min and using steady  $B_z$  north convection pattern. (b) Number density values measure by the Sondrestrom ISR during the AZ scan that started at 1616:27 UT. Note the density structure in the poleward part of the scan. (c)  $N_mF_2$  used in the simulation of section 3. The latitudinal circles are in steps of  $10^\circ$ .

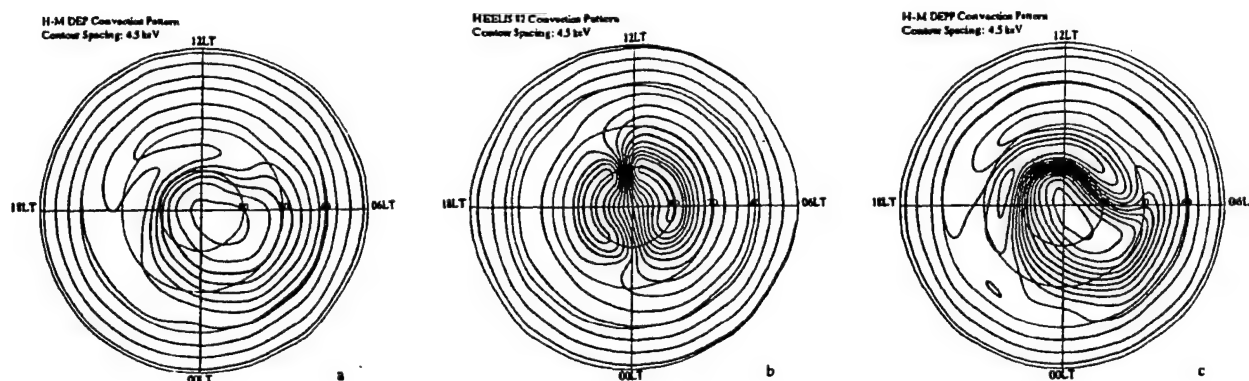


Figure 8. Series of polar plots of the high latitude convection patterns used in the simulations described in sections 3 and 4. Contour spacing is 4.5 keV. (a) Heppner and Maynard [1987] DEP pattern corresponding to  $B_z$  north and  $B_y$  negative conditions. (b) Heelis-type pattern for  $B_y = +6$  nT, cross polar cap potential of 90 kV, and  $10^\circ$  of polar cap radius. (c) H-M DEPP pattern for  $B_z$  north and  $B_y$  negative conditions and potential multiplied by a factor of 2.

Figure 7a shows a TOI, with characteristics different from those of the TOI calculated for  $B_z$  negative conditions (see Plate 1 of Valladares *et al.* [1996]). In the  $B_z$  positive case the TOI is displaced toward the duskside and does not reach the midnight side of the oval. The plasma simply circulates near the oval boundary. However, this structured plasma enhancement could be mistakenly identified as a polar cap patch by an orbiting satellite such as DMSP or DE 2. The TOI produced during  $B_z$  north conditions is not an isolated structure and is not moving antisunward. The white dot around 1400 LT and  $74^\circ$  shows the location of Sondrestrom. We see that the TOI is aligned east-west a few degrees north of Sondrestrom with number densities comparable to those observed in the density feature.

Figure 7b shows the number densities measured by the Sondrestrom radar during the conical AZ scan that started at 1616:27 (Figures 4a–4c). The locations of the Sondrestrom and the Qaanaaq sites are depicted in Figure 7b as black dots. The number densities have been projected to the same geomagnetic coordinates used in Figures 7a and 7c. In this plot we have included number densities measured at all ranges, consequently we are not presenting a display of  $N_m F_2$ , but instead show number density variations as a function of range from the radar site. The quasi-steady density feature is seen to be nearly aligned in the magnetic east-west direction and to lie poleward of Sondrestrom.

Comparison of Figures 7a and 7b reveals a close qualitative agreement between the  $B_z$  north TOI and the density feature. Both are located poleward of the polar cap boundary, have similar number densities, and appear to be stationary. There are clear differences in the details, the most obvious being that the TOI is much broader than the observed density feature. However, this feature is to be expected given the lack of time dependence in the convection input, the lack of small scale structure in the Heppner and Maynard pattern, and the lack of detailed particle inputs to the model.

### 3.2. Modeling of the January 15, 1991, Event

In the previous simulation our focus was on how the density feature observed at Sondrestrom might have been produced. In this second type of simulation we are concerned with the effect a period of  $B_z$  south convection could have on

that feature and whether that feature could be responsible for the number density increase seen over Qaanaaq at around 1650 UT. Given that the creation of the density feature is not the issue, we begin the simulation at 1616 UT and for the initial condition use an ionosphere adjusted to the number densities measured by the Sondrestrom ISR. Figure 7c shows the initial number density used in the numerical simulations of the patch transit across the polar cap. The number density distribution basically consists of the number densities shown in Figure 7b merged with the modeled number densities of Figure 7a. The peak number density within the feature was adjusted to equal  $9 \times 10^5 \text{ cm}^{-3}$ , as observed at 1549 UT. We also selected the convection pattern guided by the values of the IMF but in agreement with the line-of-sight velocities measured at Sondrestrom. Finally, to corroborate the validity of the mechanism under discussion, we compare the simulated number densities with the  $f_o F_2$  values measured by the Qaanaaq digisonde.

The convection pattern was selected after an iterative process of fitting several different  $B_z$  south patterns to the radar  $V_{105}$  values. We used the  $V_{105}$  data obtained during the AZ scans that started at 1616:27 and the one that started at 1631:12 UT, and we determined that the Heelis-type pattern [Heelis *et al.*, 1982] with a 90-kV cross polar cap potential, and a  $10^\circ$  polar cap radius reduced the standard deviation between the radar  $V_{105}$  and the velocity calculated from the convection pattern to less than  $90 \text{ m s}^{-1}$ . Twenty minutes into the simulation, at 1636 UT, the convection pattern was changed instantaneously, but in this case we used a Heppner-Maynard (H-M)  $B_z \gg 0$ ,  $B_y < 0$  pattern with potentials increased by a factor of 2. This pattern was found to give the best fit to the radar data of 1640 UT. Figure 8b shows the Heelis-type pattern used to implement the negative  $B_z$  excursion, and Figure 8c shows the H-M pattern used to simulate  $B_z$  northward conditions.

Figure 9 presents the results of this modeling effort in successive steps 4 min apart. In this format we reproduce the  $N_m F_2$  values for a limited region around the northern magnetic pole. The location of Qaanaaq is indicated by a white dot, and the coverage of the Sondrestrom ISR during elevation scans is shown by a white line. The magnetic pole is at the center of the bottom edge of each panel.

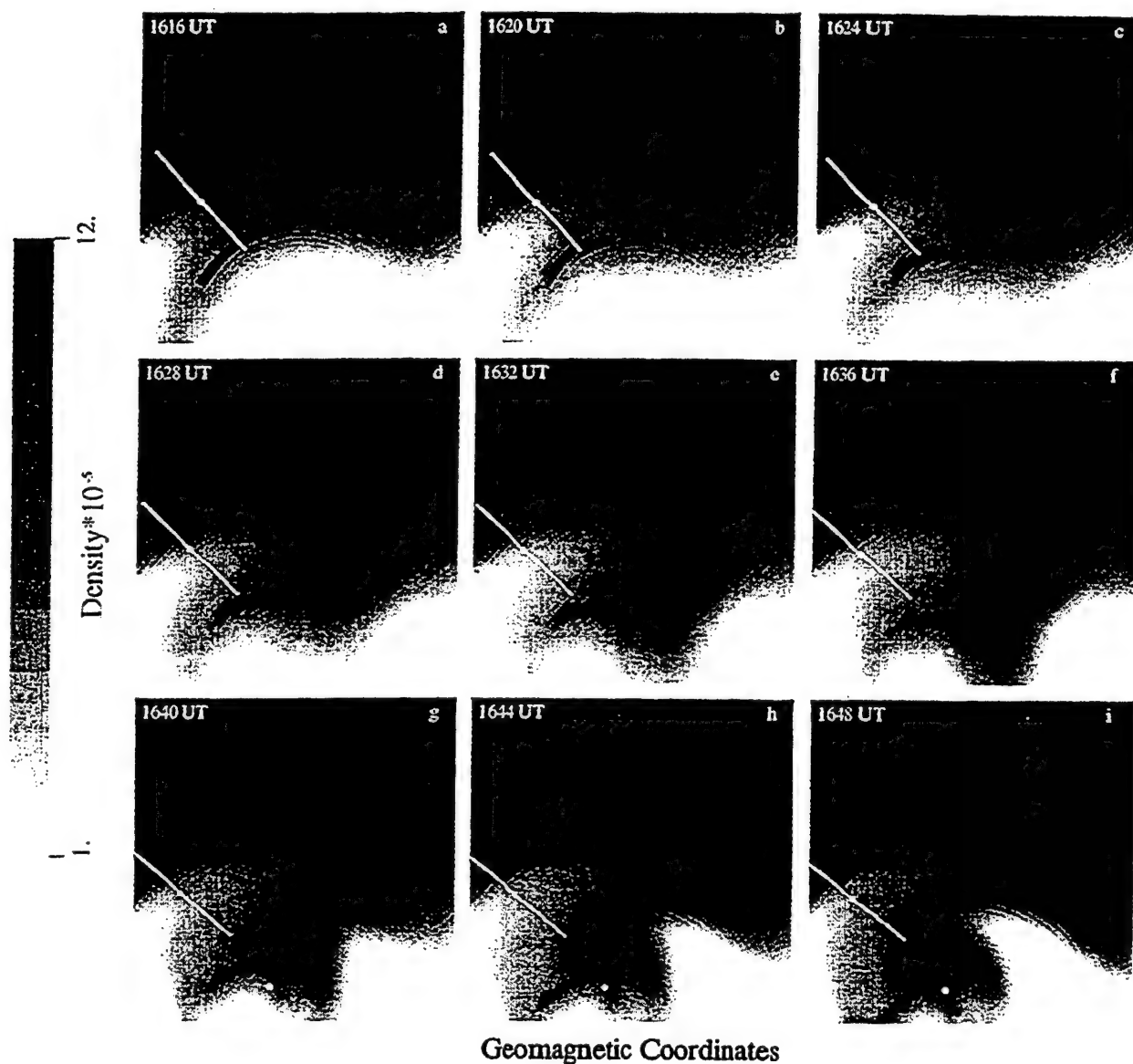


**Figure 9.** Each panel presents  $N_m F_2$  values of a section of the high-latitude ionosphere at times after the simulation of the patch initiation. The white dot near the bottom of each panel corresponds to the location of the Qaanaaq station. The white line near the left side of the panels indicates the extension of the elevation scans of Figure 3.

Figure 9a reproduces a part of the polar cap and auroral ionosphere near midday that was presented in Figure 7c. This corresponds also to the initial peak number density used in the simulation. No  $B_z$  negative TOI is seen in this panel. Figures 9b and 9c show a gentle poleward displacement of the boundary of the number density near midday. The following panels (Figures 9d-9f) display the formation of a new TOI with typical  $B_z$  south characteristics. This new structure is relatively narrow and does not intrude deep inside the polar cap even at 1636 UT (Figure 9f). However, a wider or more elongated TOI was obtained when a larger polar cap radius, a more intense cross polar cap potential, or a different day of the year was selected. Evidently, if we had allowed the  $B_z$  south Heelis-type pattern to prevail for a longer period,

say, one hour, then a fully developed  $B_z$  south TOI extending across the polar cap would have appeared. During the growth of the TOI the  $N_e$  feature (now with all the properties of a polar cap patch) is seen moving poleward (toward the bottom of the figure). The density feature moves antisunward, carried by the high-latitude convection, until 1636 UT, when it becomes more dawn-dusk aligned. At this point the  $N_e$  feature, like any polar cap patch, moves antisunward and consists of an isolated entity with number densities higher than the surroundings.

At 1636 UT we changed the convection pattern into a H-M  $B_z \gg 0$ ,  $B_y < 0$  convection pattern [Heppner and Maynard, 1987]. Four minutes later (Figure 9g) the flows associated with the new high-latitude convection start to erode and

significantly elongate part of the TOI that was formed during the  $B_z$  south excursion. This effect causes the new TOI to distort and lose its noon-midnight alignment; instead it becomes extended in the magnetic east-west direction. Figure 9h shows that the new  $B_z$  positive-type pattern brings low number density plasma from the afternoon and morning sides and erodes plasma both poleward, in the morning side, and equatorward in the afternoon section of the TOI. If the  $B_z$  north-related flow pattern remains unchanged for several minutes, as before 1616 UT, then an east-west elongated density structure will form near the velocity shear region and remain stationary in a corrected geomagnetic coordinate system. This new structure, created by the reconfiguration from a  $B_z$  south to a  $B_z$  north convection pattern, resembles the density structure that was seen in the radar data to remain stationary at the poleward boundary of the oval before 1616 UT. While this again illustrates how positive  $B_z$  convection may produce an east-west aligned feature, the differences between this TOI and that produced in our first simulation

illustrate the sensitivity of the modeled ionosphere to the recent time history of the ionospheric convection.

Figure 10 presents results from the simulation in a format more suitable for comparison with the experimental measurements. The inherent difference in the modeled and the experimental plots is the time resolution of both quantities. The radar AZ scans were gathered every 9 min, with a total sweeping time of 6 min employed to cover  $360^\circ$  of the sky. Conversely, the simulated AZ scans represent instantaneous snapshots of the ionosphere. Figure 10a has many features similar to the number density contours of Figure 4c; it illustrates the fact that the initial conditions reflect the experimental data. The peak number density at the southern part of the scan is  $1.1 \times 10^6 \text{ cm}^{-3}$ , equal to the maximum number density in the same part of the radar scan of Figure 4c. Figures 10f and 10g, corresponding to the simulated times of 1636 and 1640 UT, show low number densities near  $3 \times 10^5 \text{ cm}^{-3}$  at the northern end of the scan; this value is in good agreement with the number densities detected

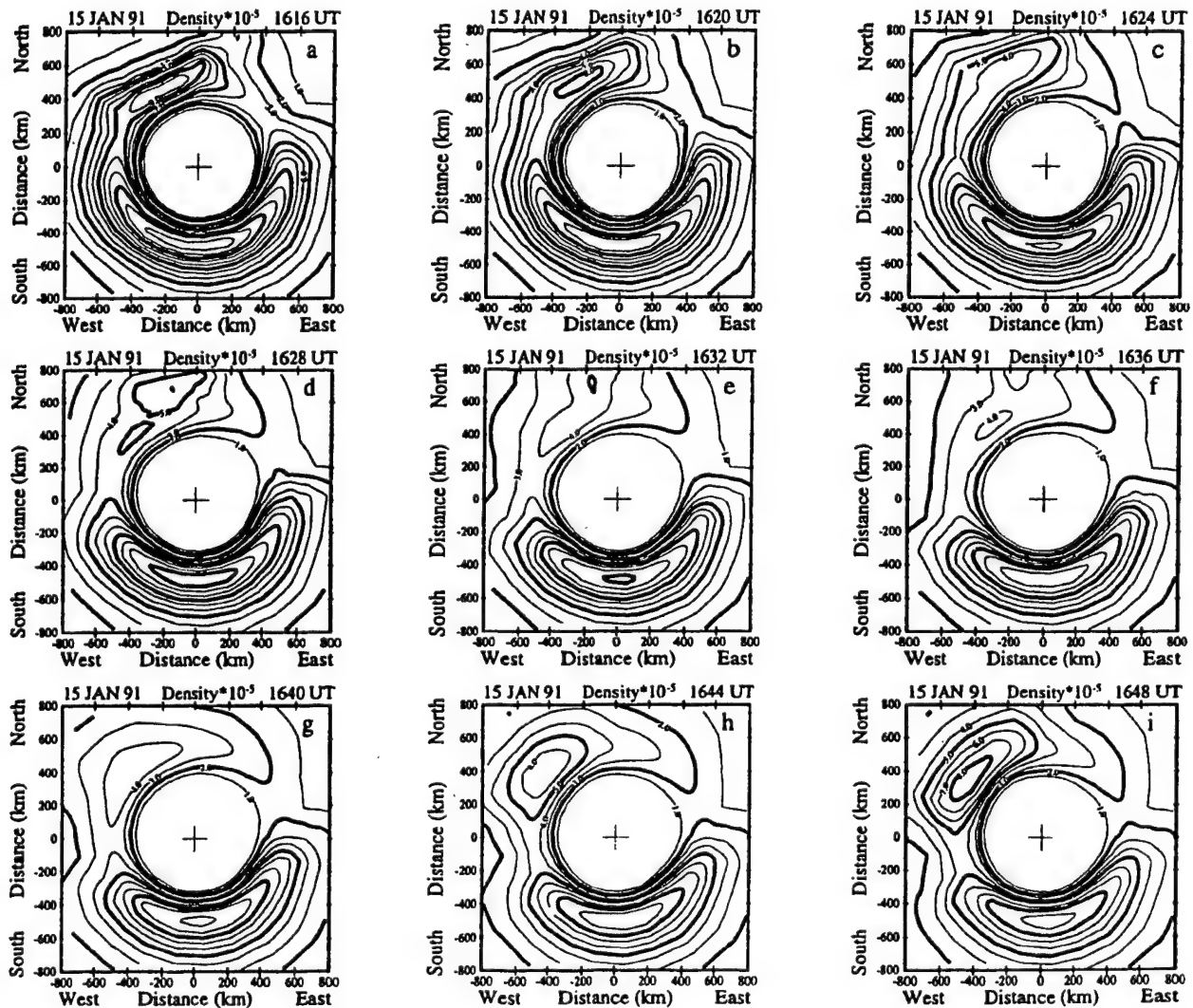


**Figure 10.** Simulated radar azimuth scans through the volumes displayed in Figure 9. Each panel shows an instantaneous scan of the number density around Sondrestrom at the UT indicated in the panels. Elevation is  $30^\circ$ .



by the Sondrestrom ISR during the scan between 1640:19 and 1646:23 UT (not shown). The number densities in the northern part of the simulated scan are below  $4 \times 10^5 \text{ cm}^{-3}$ , much less than  $10^6 \text{ cm}^{-3}$  seen 400 km south of the Sondrestrom station. The last two panels of the simulation correspond to times when the convection pattern was  $B_z$  north-like. Figures 10h and 10i show another density structure in the poleward part of the scan; this plasma intrusion of the distorted TOI reaches a number density near  $8 \times 10^5 \text{ cm}^{-3}$  in the scan at 1648 UT. In spite of being 400 km wide and located in the northwestern part of the scan, it resembles the density structure seen at the end of the scan of Figure 5b (1655 UT). The density structure measured by the ISR is much narrower, but this discrepancy may be caused again by the difference between the actual time-dependent convection and the statistical *Heppner and Maynard* [1987] patterns used in the present simulations.

#### 4. Sensitivity Study of $B_z$ South Parameters

Figure 11 shows the  $f_oF_2$  values collected by the Qaanaaq digisonde on January 15, 1991 (heavy trace), and the modeled  $f_oF_2$  obtained in four numerical simulations of the patch transit across the polar cap during the  $B_z$  south interval. The four thin traces of Figure 11 correspond to polar cap potential inputs of 80, 70, 60, and 50 kV. The size of the polar cap was kept fixed at  $10^\circ$ , and the length of the  $B_z$  south period remained at 20 min for all four cases.

To obtain the trace labeled 80 kV (well separated dots), we used the same input parameters as were used in the simulation discussed in section 3.2. The curves labeled 70, 60, and 50 kV were obtained after we changed the polar cap potential to those values. Although the 80-kV simulation revealed that the density structure passed overhead the Qaanaaq station, a quantitative comparison shows that the simulated  $f_oF_2$  values are much higher (maximum value is 8.6 MHz) than the values measured by the digisonde (6.4 MHz). The 80-kV trace provides only an envelope to both  $f_oF_2$  enhancements, seen between 1600 and 1800 UT. However, the simulated number

density value is almost a factor of 2 larger than the measured number density at Qaanaaq. The other three values of the cross polar cap potential provide smaller number density values, but the appearance of the density structure at Qaanaaq is delayed by the smaller velocity inside the polar cap. The 50-kV potential provides  $f_oF_2$  values closer to the measured values; however, the maximum amplitude occurs 5 min after the measured  $f_oF_2$  trace starts to decrease.

#### 5. Discussion and Conclusions

Figures 2-5 demonstrated the presence of an isolated region of enhanced number density located slightly poleward of the Sondrestrom site in the postnoon sector. This region was found to coincide with convergent electric fields, implying the existence of upward field-aligned currents. Elevated  $T_e$  values, at high altitudes, were also measured by the Sondrestrom ISR within the region called here a density feature. On the basis of these key elements, one possibility is that particle precipitation is the generation mechanism of the observed density structures. We do not dispute that in some cases, especially when they are located away from the noon sector, this is the correct interpretation. However, the simulations presented here point to solar-produced plasma and high-latitude velocity reconfiguration as a potential critical mechanism for producing the  $N_e$  feature observed on January 15, 1991. In addition, the model simulations discussed here did not consider any type of cusp-like precipitation. However, a well-defined density feature, quite similar to the observation, was well reproduced. We suggest that an east-west elongated density structure could be formed by zonal flows that seem to prevail near midday when the IMF  $B_z$  is positive. The zonal flows can also deform any newly formed TOI produced during  $B_z$  negative excursions. Any soft electron precipitation, accompanying the upward field-aligned currents, may simply augment the number density and increase  $T_e$  above 400 km. While soft precipitation, as encountered at the cusp, can increase the local number density, to be effective the particle flux (using typical cusp values) needs to remain stationary for several minutes in the frame of the moving plasma. However, it is possible that in some circumstances (e.g., cusp located at very high geographic latitudes) cusp precipitation may be the leading mechanism of patch formation. To more quantitatively assess the relative roles of convection and particle precipitation in producing polar cap patches, it will be necessary to perform simulations that include more realistic time-varying convection as well as spatially structured and time-varying precipitation.

Numerical simulations under steady IMF  $B_z$  northward conditions have revealed that a limited TOI can exist at very high latitudes. This TOI was found to be located in the early afternoon local time sector, displaced toward dusk, and extending into the noon-midnight direction barely  $10^\circ$  beyond the center of the polar cap. The TOI did not reach the midnight side of the auroral oval. We pointed out that this structured number density enhancement, which protruded well within the polar cap, could be mistakenly identified as a patch by an orbiting satellite. Ground-based measurements, such as those provided by combined use of a digisonde and an ASIP, or concurrent non local in situ velocity measurements could help to unequivocally identify a polar

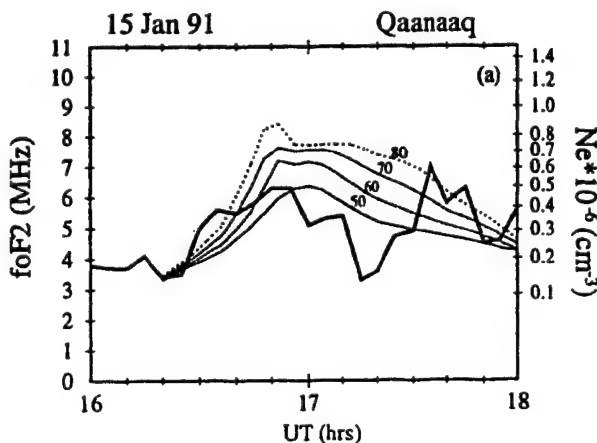


Figure 11. The solid line represents the critical frequency of the  $F$  region peak ( $f_oF_2$ ) as a function of universal time at Qaanaaq on January 15, 1991. The dotted lines correspond to modeled values of the  $f_oF_2$  index for different values of the polar cap potential.

cap patch [Basu *et al.*, 1990]. The  $B_z$  north TOI, or density feature was found to have a zonal flow; a transiting patch, or a  $B_z$  south TOI, usually has an antisunward flow. Thus the characteristics of the flow may help to exclude some of the cases that could be incorrectly catalogued as polar cap patches. Besides, a satellite pass near midday or an ASIP located near  $76^\circ$  invariant latitude will be able to identify auroral boundaries and point out the location of density structures with respect to these boundaries.

The IMP 8 satellite measured the three components of the IMF and indicated that between 1200 and 1800 UT the  $B_z$  component was predominantly positive, interrupted only by a short negative excursion at 1554 UT. The Qaanaaq all-sky imager observed typical polar cap arcs between 0930 and 1340 UT in agreement with the state of the IMF. Between 1200 and 1330 UT the Qaanaaq digisonde measured number density enhancements associated with dawn-dusk moving polar cap arcs and a variable pattern of drift velocities. At 1645 UT, when the density feature/patch reached Qaanaaq, we observed that the peak number density was at 335 km altitude and that the plasma drift was directed antisunwardly, without the variability seen previously at 1300 UT. Thus, we conclude that the factor of 3 number density enhancements detected by the Qaanaaq digisonde can be well explained by a patch transiting the polar cap.

The modeling work conducted for steady  $B_z$  positive conditions revealed that density structures can be readily created near the noon sector at latitudes near the poleward boundary of the auroral oval. The characteristics of the  $B_z$  north TOI are quite similar to the density feature observed between 1320 and 1619 UT. The difference in the width of the modeled and observed TOI may be attributed to the statistical nature of the H-M convection pattern, which may have smoothed out the fine latitudinal velocity features. We modeled the patch transit across the polar cap and its passage through the Qaanaaq FOV. This modeling run, discussed in section 3.2, produced number density values at the Qaanaaq station almost a factor of 2 larger than the measured number densities. When the cross polar cap potential was reduced to 50 kV, we obtained a good quantitative agreement between calculated and measured  $f_oF_2$  values.

Finally, it is clear that future progress will require obtaining more realistic inputs for both the convection and the precipitating particles. Convection models such as those of Weimer [1995, 1996] and observational sources such as the Super Dual Auroral Radar Network (SuperDARN) [Greenwald *et al.*, 1995] may provide the needed convection information. Presently, a weather model for precipitation is needed; however, in the future, UV imagers may be able to provide the needed weather inputs for particle precipitation.

This study leads to the following conclusions:

1. The Sondrestrom ISR detected a density feature that remained stationary within the poleward boundary of the auroral oval during a prolonged period of northward IMF  $B_z$  condition. This  $N_e$  feature was collocated with a region of sheared flows, elevated  $T_e$  values, and convergent electric fields.
2. After 1616 UT the Sondrestrom ISR measured a new pattern of velocities consisting of a poleward moving plasma, higher absolute values of the plasma flow, and the initiation of a poleward motion of the density feature. These changes

seem to be the manifestation of the high-latitude ionosphere in response to the negative IMF  $B_z$  excursion.

3. The modeling work has helped to verify that an elongated density feature residing near the poleward boundary of the oval can be produced during IMF  $B_z$  northward conditions and remain stationary in the frame of the convection pattern. We have demonstrated that a statistical convection pattern corresponding to  $B_z$  north, such as [e.g., Heppner and Maynard, 1987] can support the existence of a TOI protruding into the polar cap.

4. The modeling described here postulates that a density feature initiates a poleward motion right after  $B_z$  becomes negative. Good qualitative and quantitative agreement was obtained between the model results and the Qaanaaq digisonde  $f_oF_2$  values.

**Acknowledgments.** We would like to thank Santimay Basu and Herbert C. Carlson for careful reading of the manuscript. We thank Jan Sojka for providing numerical values of the number density at Qaanaaq under steady conditions, R. Lepping for making the IMF data available for this study, and J. Kelly for providing the Sondrestrom radar data in raw format. The work at Boston College was partially supported by Phillips Laboratory contracts F19628-97-C-0094 and F19628-96-C-0039 and by NSF grants ATM-9404088 and ATM-9613925. We thank the Danish Commission for Scientific Research in Greenland for permission to conduct ground experiments at Sondrestrom under continuing project A16-91.

The editor thanks A. S. Rodger, J. C. Foster, and another referee for their assistance in evaluating this paper.

## References

- Anderson, D.N., J. Buchau, and R.A. Heelis, Origin of density enhancements in the winter polar cap, *Radio Sci.*, **23**, 513, 1988.
- Basu, S., Su. Basu, C. E. Valladares, E. J. Weber, J. Buchau, G. J. Bishop, and B. W. Reinisch, Coordinated observations of high latitude ionospheric turbulence, in *Physics of Space Plasma (1988)*, SPI Conf. Proc. and Reprint Ser., vol. 8, p. 137, 1989.
- Basu, S., Su. Basu, P.K. Chaturvedi, and C.M. Bryant Jr., Irregularity structures in the cusp/cleft and polar cap regions *Radio Sci.*, **29**, 195, 1994.
- Basu, S., S. Basu, E. MacKenzie, and H.E. Whitney, Morphology of phase and intensity scintillations in the auroral oval and polar cap, *Radio Sci.*, **20**, 347, 1985.
- Basu, S., S. Basu, E. MacKenzie, W.R. Coley, J.R. Sharber, and W.R. Hoegy, Plasma structuring by the gradient drift instability at high latitudes and comparison with velocity shear driven processes, *J. Geophys. Res.*, **95**, 7799, 1990.
- Buchau, J., and B.W. Reinisch, Electron density structures in the polar F region, *Adv. Space Res.*, **11**(10), 29, 1991.
- Buchau, J., B.W. Reinisch, E.J. Weber, and J.G. Moore, Structure and dynamics of the winter polar cap F region, *Radio Sci.*, **18**, 995, 1983.
- Buchau, J., E.J. Weber, D.N. Anderson, H.C. Carlson Jr., J.G. Moore, B.W. Reinisch, and R.C. Livingston, Ionospheric structures in the polar cap: Their origin and relation to 250-MHz scintillation, *Radio Sci.*, **20**, 325, 1985.
- Coley, W.R., and R.A. Heelis, Adaptive identification and characterization of polar ionization patches, *J. Geophys. Res.*, **100**, 23,819, 1995.
- Crowley, G., Critical review on ionospheric patches and blobs, in *The Review of Radio Science 1992-1996* pp. 619-648, Oxford Univ. Press, New York, 1996.
- Decker, D.T., C.E. Valladares, R. Sheehan, Su. Basu, D.N. Anderson, and R.A. Heelis, Modeling daytime F layer patches over Sondrestrom, *Radio Sci.*, **29**, 249, 1994.
- de la Beaujardiere, O., J.D. Craven, V.B. Wickwar, G. Candal, J.M. Holt, L.A. Frank, L.H. Brace, D.S. Evans, and J.D. Winningham, Universal time dependence of nighttime F region densities at high latitudes, *J. Geophys. Res.*, **90**, 4319, 1985.
- Foster, J.C., Storm time plasma transport at middle and high latitudes, *J. Geophys. Res.*, **98**, 1675, 1993.



- Foster, J.C., and J.R. Doupnik, Plasma convection in the vicinity of the dayside cleft, *J. Geophys. Res.*, **89**, 9107, 1984.
- Fukui, K., J. Buchau, and C.E. Valladares, Convection of polar cap patches observed at Qaanaaq, Greenland during the winter of 1989-1990, *Radio Sci.*, **29**, 231, 1994.
- Greenwald, R.A., et al., DARN/SuperDARN: A global view of the dynamics of high-latitude convection, *Space Sci. Rev.*, **71**, 761, 1995.
- Heelis, R.A., J.K. Lowell, and R.W. Spiro, A model of the high-latitude ionospheric convection pattern, *J. Geophys. Res.*, **87**, 6339, 1982.
- Heppner, J.P., and N.C. Maynard, Empirical high-latitude electric field models, *J. Geophys. Res.*, **92**, 4467, 1987.
- Kelley, M.C., J.F. Vickrey, C.W. Carlson, and R. Torbert, On the origin and spatial extent of high-latitude F region irregularities, *J. Geophys. Res.*, **87**, 4469, 1982.
- Kelly, J.D., and J.F. Vickrey, F region ionospheric structure associated with antisunward flow near the dayside cusp, *Geophys. Res. Lett.*, **11**, 907, 1984.
- Lockwood, M., and H.C. Carlson, Production of polar cap density patches by transient magnetopause reconnection, *Geophys. Res. Lett.*, **19**, 1731, 1992.
- Lockwood, M., P.E. Sandholt, S.W.H. Cowley, and T. Oguti, Interplanetary magnetic field control of dayside auroral activity and the transfer of momentum across the dayside magnetopause, *Planet. Space Sci.*, **11**, 1347, 1989.
- Pinnock, M., A.S. Rodger, and F.T. Berkey, High-latitude F region electron concentration measurements near noon: A case study, *J. Geophys. Res.*, **100**, 7723, 1995.
- Rodger, A.S., M. Pinnock, J.R. Dudeney, K.B. Baker, and R.A. Greenwald, A new mechanism for polar patch formation, *J. Geophys. Res.*, **99**, 6425, 1994.
- Sojka, J.J., and R.W. Schunk, A theoretical study of the production and decay of localized electron density enhancements in the polar ionosphere, *J. Geophys. Res.*, **91**, 3245, 1986.
- Sojka, J.J., W.J. Raitt, and R.W. Schunk, Effect of displaced geomagnetic and geographic poles in high-latitude plasma convection and ionospheric depletions, *J. Geophys. Res.*, **84**, 5943, 1979.
- Sojka, J.J., M.D. Bowline, R.W. Schunk, D.T. Decker, C.E. Valladares, R. Sheehan, D.N. Anderson, and R.A. Heelis, Modeling polar cap F region patches using time varying convection, *Geophys. Res. Lett.*, **20**, 1783, 1993.
- Sojka, J.J., M.D. Bowline, and R.W. Schunk, Patches in the polar ionosphere: UT and seasonal dependence, *J. Geophys. Res.*, **99**, 14,959, 1994.
- Sojka, J.J., R.W. Schunk, M.D. Bowline, and D.J. Crain, Ambiguity in identification of polar cap F-region patches, *J. Atmos. Terr. Phys.*, **59**, 101, 1997.
- Tsunoda, R.T., High-latitude F region irregularities: A review and synthesis, *Rev. Geophys.*, **26**, 719, 1988.
- Valladares, C.E., Su. Basu, J. Buchau, and E. Friis-Christensen, Experimental evidence for the formation and entry of patches into the polar cap, *Radio Sci.*, **29**, 167, 1994.
- Valladares, C.E., D.T. Decker, R. Sheehan, and D.N. Anderson, Modeling the formation of polar cap patches using large plasma flows, *Radio Science*, **31**, 573, 1996.
- Weber, E.J., J. Buchau, J.G. Moore, J.R. Sharber, R.C. Livingston, J.D. Winningham, and B.W. Reinisch, F layer ionization patches in the polar cap, *J. Geophys. Res.*, **89**, 1683, 1984.
- Weber, E.J., J.A. Klobuchar, J. Buchau, H.C. Carlson Jr., R.C. Livingston O. de la Beaujardiere, M. McCready, J.G. Moore, and G.J. Bishop, Polar cap F layer patches: Structure and dynamics, *J. Geophys. Res.*, **91**, 121, 1986.
- Weimer, D.R., Models of high-latitude electric potentials derived with a least-error fit of spherical harmonic coefficients, *J. Geophys. Res.*, **100**, 19,595, 1995.
- Weimer, D.R., A flexible, IMF dependent model of high-latitude electric potential having "space weather" applications, *Geophys. Res. Lett.*, **23**, 2549, 1996.
- D. N. Anderson and T. Bullett, Phillips Laboratory, Geophysics Directorate, Hanscom Air Force Base, MA 01731.
- D.T. Decker, R. Sheehan, and C. E. Valladares, Institute for Scientific Research, Boston College, 885 Centre Street, Newton, MA 02159. (e-mail: cesar@dl5000.bc.edu)
- B.W. Reinisch, Center for Atmospheric Research, University of Massachusetts, Lowell, MA 01854.

(Received January 16, 1997; revised December 15, 1997; accepted December 16, 1997.)

## Characteristics of plasma structuring in the cusp/cleft region at Svalbard

S. Basu,<sup>1</sup> E. J. Weber,<sup>1</sup> T. W. Bullett,<sup>1</sup> M. J. Keskinen,<sup>2</sup> E. MacKenzie,<sup>3</sup>  
P. Doherty,<sup>3</sup> R. Sheehan,<sup>3</sup> H. Kuenzler,<sup>1</sup> P. Ning,<sup>4</sup> and J. Bongioliatti<sup>1</sup>

**Abstract.** Satellite scintillation, all-sky optical imager, and digisonde observations were coordinated during a cusp campaign conducted at Ny Alesund, Svalbard (78.9°N, 11.8°E; 75.7°N corrected geomagnetic latitude, over the period January 4–15, 1997. This paper is focused on a study of the distribution and dynamics of mesoscale (tens of kilometers to tens of meters) electron density irregularities in the dayside auroral region. This study has been performed at Ny Alesund, Svalbard, by measuring the effects of these irregularities on the amplitude scintillation of 250-MHz transmissions from a quasi-stationary polar satellite as well as the amplitude and phase scintillation of 1.6-GHz signals from Global Positioning System (GPS) satellites. These GPS scintillation measurements were augmented by the use of dual-frequency (1.2 and 1.6 GHz) GPS phase data acquired at the same station by the Jet Propulsion Laboratory for the International GPS Geodynamic Service (IGS). The continuous 250-MHz scintillation observations explored the daytime auroral ionosphere 2° poleward of Ny Alesund and showed that the scintillation spectra are often broad, as may be expected for irregularities in a turbulent flow region. Such irregularity dynamics were detected poleward of the nominal cusp region over the interval of 0600–1500 magnetic local time. The period of observations included the magnetic storm of January 10–11, 1997, when GPS observations of the IGS detected polar cap patches with total electron contents of  $3 \times 10^{16} \text{ m}^{-2}$  and large-scale (tens of kilometers) phase variations at the GPS frequency of 1.6 GHz that corresponded to temporal gradients of  $2 \times 10^{16} \text{ m}^{-2} \text{ min}^{-1}$ . However, amplitude scintillations at the GPS frequency of 1.6 GHz could not be detected in association with these large-scale phase variations, indicating that the irregularities with wavelengths less than the Fresnel dimension of 400 m were below the detectable limit. This is shown to be consistent in the context of enhanced ionospheric convection determined by digisonde and scintillation spectra.

### 1. Introduction

The cusp/cleft region [Newell and Meng, 1992] in the dayside auroral oval is recognized to be the seat of structured electric fields, soft particle precipitation, large plasma flows, and auroral break-up events [Sandholt et al., 1990; Smith and Lockwood, 1990]. These dayside auroral signatures are probed by multitechnique observations to investigate the coupling processes within the solar wind–magnetosphere–ion-

osphere system. From the standpoint of plasma structuring, the dayside auroral oval may be considered as the source region and gateway of major irregularity structures in the high-latitude ionosphere.

It is well established that the dayside auroral oval plays a major role in the formation of large-scale ionization structures, called patches, in the polar ionosphere [Buchau et al., 1983; Weber et al., 1984]. A great deal of research has revealed that under active magnetic conditions, the eastward electric field in the dayside auroral oval directs a “tongue of ionization” from the subauroral region into the polar cap which is sliced off into discrete structures by high plasma flows [Tsunoda, 1988; Valladares et al., 1994, and references therein]. The convecting patches develop intermediate scale (tens of kilometers to tens of meters) irregularities by the action of the gradient drift instability mechanism [Chaturvedi and Huba, 1987; Tsunoda, 1988, and references therein]. This was confirmed experimentally by showing that patches are

<sup>1</sup> Air Force Research Laboratory, Hanscom Air Force Base, Massachusetts.

<sup>2</sup> Plasma Physics Division, Naval Research Laboratory, Washington, D. C.

<sup>3</sup> Institute for Scientific Research, Boston College, Newton, Massachusetts.

<sup>4</sup> KEO Consultants, Brookline, Massachusetts.

associated with scintillations of satellite signals which arise from the scattering of radio waves from intermediate scale irregularities [Weber *et al.*, 1986]. Indeed, after weak scintillation events due to polar cap arcs are excluded, the statistics of the remaining strong scintillation events in the polar cap [Aarons *et al.*, 1981; Basu *et al.*, 1985; Kersley *et al.*, 1995] may be used as the statistics of polar cap patches.

In addition to patches which convect into the polar cap, the sheared electric field in the cusp/cleft region is a viable source of localized intermediate scale (tens of meters to tens of kilometers) irregularities. Basu *et al.* [1988] first identified irregularities in velocity shear regions associated with nightside auroral arcs and provided a comprehensive description of the density and electric field fluctuation spectra. This stimulated theoretical development of instabilities driven by velocity shears parallel and perpendicular to the magnetic field [Keskinen *et al.*, 1988; Basu and Coppi, 1990; Ganguli *et al.*, 1989]. Compared with convective instabilities at high latitudes, the irregularities generated in velocity shear regions exhibit strikingly enhanced electric field fluctuations for given relative density fluctuations. Scintillations of satellite signals due to irregularities in the velocity shear region are expected to be weaker than patch-induced scintillations since patches are associated with high plasma density. However, the enhanced electric field fluctuations are expected to broaden the frequency spectra of scintillations as well as the Doppler spectra of HF backscatter.

In this paper we present the results of 250-MHz scintillation observations made from Ny Alesund, Svalbard (78.9°N, 11.9°E; corrected geomagnetic latitude (CGMLAT) 75.7°N, 113.8°E), during the period January 5–15, 1997. The station latitude corresponds to the nominal cusp location, and the station crosses local magnetic noon at 0850 UT. We focus our attention on dayside auroral observations made during 0500–1300 UT. During these hours the propagation path to the satellite explored the ionospheric *F* region about 2° poleward of the station. Spectral studies of 250-MHz scintillation are performed to determine the dynamics of 1-km to 100-m scale irregularities. These scintillation observations are supported by all-sky imager and digisonde observations, as well as scintillation and total electron measurements by the use of Global Positioning System (GPS) satellites. This paper also discusses the plasma structures at various scales encountered during the major magnetic storm of January 10–11, 1997.

## 2. Experimental Observations

Scintillation measurements were performed at Ny Alesund by the use of 250-MHz transmissions from quasi-stationary beacon satellites. The receivers sample signal intensity at 50 Hz and process the signals on-line to determine the scintillation index ( $S_4$ ), defined as the normalized second moment of the signal intensity, the frequency spectra, and the distribution function. These parameters are obtained every 82 s and are then averaged to provide values at 5-min intervals. A GPS receiver at L1 (1.575 GHz), manufactured by Novatel, was deployed which acquires amplitude and phase at 50 Hz and obtains phase and amplitude scintillation at 82-s intervals. Dual-frequency GPS data were obtained from the Ny Alesund station of the International GPS Geodynamic Service (IGS), managed by the Jet Propulsion Laboratory. The IGS data provide 30-s values of carrier phase and group delay at both the GPS L1 (1.6 GHz) and L2 (1.2 GHz) frequencies. The data are processed to obtain the total electron content and the rate of change of the total electron content at 30-s intervals [Doherty *et al.*, 1994]. The all-sky imager mapped the dayside aurora at 630.0 nm and defined the optical auroral conditions at the subionospheric location which was probed by continuous 250-MHz scintillation measurements. The study is focused on daytime observations between 0800 and 1500 MLT, when the subionospheric location remained at about 78° CGMLAT, 2.3° poleward of Ny Alesund. Since Ny Alesund corresponds nominally to the dayside cusp region, this poleward position of scintillation observations during the daytime may be identified with the mantle region [Newell *et al.*, 1991].

## 3. Results and Discussions

Figure 1 shows the geometry of 250-MHz scintillation observations from Ny Alesund. The location of the station (75.7° CGMLAT) at magnetic noon (0850 UT) is indicated by a cross. The loci of the 350-km subionospheric position of scintillation observations with quasi-stationary satellites at different universal times (UT) are indicated at hourly intervals by asterisks and diamonds, which correspond to the two satellites. During this period the station will, of course, trace out a circular path, which is not shown in order to ensure clarity of the diagram; instead, its position at one particular time (0845 UT) corresponding to magnetic noon has been illustrated. Observations with each satellite are made for about 6

January 6, 1997

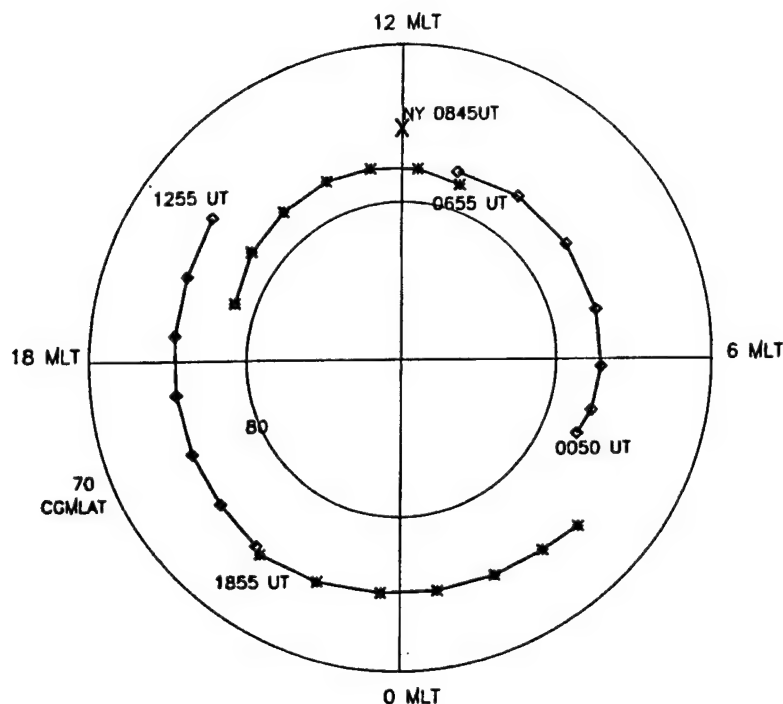


**Figure 1.** Shown is the geometry of 250-MHz scintillation observations in magnetic local time and the corrected geomagnetic latitude (CGMLAT) coordinate system. The measurements were made from Ny Alesund, Svalbard (CGMLAT 75.7°N) by using quasi-stationary beacon satellites. The position of the station is only shown at magnetic noon and is indicated by a cross. The 350-km subionospheric intersections of scintillation measurements at hourly universal time intervals are shown by crosses and diamonds.

hours, after which they are switched to the next available satellite. Although scintillation observations were performed around the clock, we shall focus in this paper on the results obtained during about 4 hours on either side of magnetic noon. Figure 1 shows that during this period, namely, 0500–1300 UT, scintillation observations probed the ionosphere at 78° CGMLAT, which, as mentioned above, is approximately 2° poleward of Ny Alesund.

We shall now discuss the characteristics of 250-MHz scintillation in the dayside auroral region with the typical example of January 6, 1997. It was a magnetically quiet day, as were most of the days during the campaign period. The Wind satellite data indicated that over the study period of 0500–1300 UT, the interplanetary magnetic field (IMF)  $B_z$  was southward, with  $B_z = -2$  nT for only 1 hour between 0900 and 1000 UT, and remained northward for the

rest of the period with values ranging between +2 and +3 nT. Figure 2 shows the 630.0-nm images obtained by the all-sky imager at Ny Alesund at 1-min intervals between 0954 and 0958 UT. The 180° field-of-view images are presented in all-sky lens coordinates, with a linear change in elevation angle from 90° at the center to 0° at the edge of the image. The top, bottom, right and left of each image represent the four cardinal directions, north, south, east and west, respectively. The images show the stable cusp aurora, which are characterized by a rather sharp equatorward edge and a markedly diffuse poleward edge [Maynard *et al.*, 1997]. The asterisks in these images represent the directions of the propagation path of satellite scintillation observations. These images indicate that the propagation path intersected the cusp plume poleward of the cusp [Newell *et al.*, 1991]. At this time, no optical emission at 427.8 nm was ob-

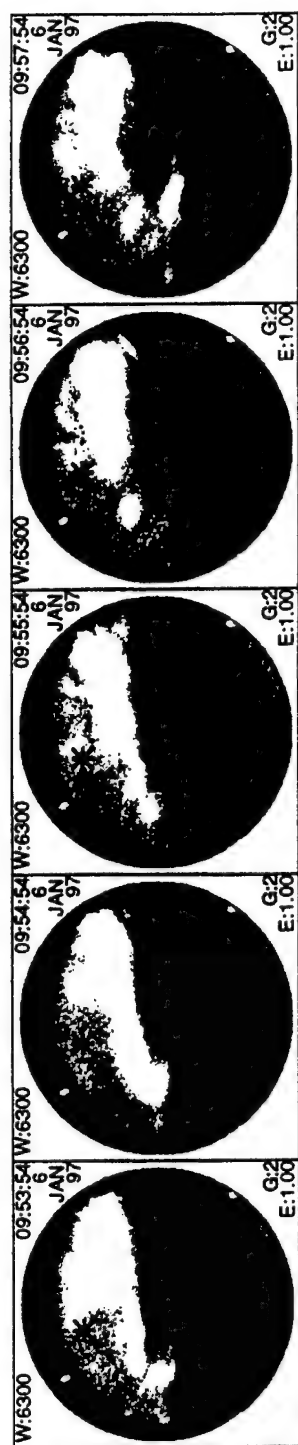
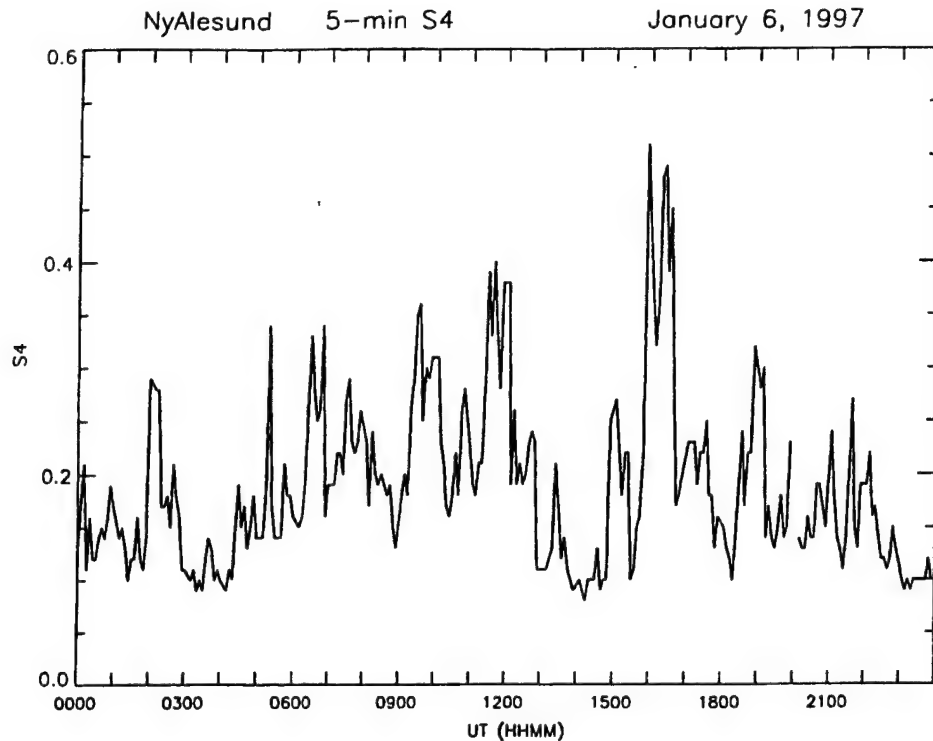


Figure 2. All-sky imager observations of the emissions at 630.0-nm wavelengths at each minute. The four cardinal directions, north, south, east, and west, correspond to the top, bottom, right, and left edges of the images. The observations are from Ny Alesund, Svalbard, on January 6, 1997. The elevation and azimuth of scintillation observations are indicated by asterisks in the images.

served, indicating that only soft particle precipitation was associated with the 630.0-nm images.

Figure 3 illustrates the variation of the  $S_4$  index of amplitude scintillation with UT as recorded on January 6, 1997. The  $S_4$  index, obtained from the ratio of the standard deviation of signal intensity fluctuation normalized to the average signal intensity, quantifies the strength of amplitude scintillation. In view of the prevailing solar minimum condition, scintillations were weak and did not exceed the weak scatter limit of  $S_4 = 0.5$ . Figure 3 clearly illustrates the daytime scintillation activity between 0500 and 1300 UT, with minimum  $S_4$  values increasing to 0.2 and individual events increasing to 0.4. It establishes the presence of subkilometer scale irregularities during daytime at 78° CGMLAT over an extended magnetic local time interval of 0845–1645 MLT. Considering the optical images shown in Figure 2, the narrow scintillation structure around 1000 UT in Figure 3 is to be associated with the cusp plume. Scintillations, however, are continuously observed over most of the daytime at locations poleward of the dayside auroral oval corresponding to the mantle region. Kersley *et al.* [1995] obtained the occurrence statistics of phase scintillation from Ny Alesund and showed that large-scale (>10 km) irregularities occur during much of the daytime and are distributed in a belt extending from the south to the north of the station.

We now illustrate that the frequency spectra of daytime amplitude scintillations observed slightly poleward of the cusp have very special characteristics. Figure 4 shows a set of four successive spectra at 5-min intervals. Each of these spectra is obtained by using the fast Fourier transform (FFT) algorithm averaged over four successive 82-s data segments. These samples were obtained near magnetic noon, and the spectra show the variation of the power spectral density (psd) in decibels with log frequency. Each spectrum is characterized by a flat low-frequency portion and then a linear roll-off at higher frequencies, indicating a power law variation of psd with frequency. It is to be noted that the scintillation index of all the samples conforms to weak scatter limit ( $S_4 < 0.5$ ). Under these conditions the power spectrum is expected to show a maximum at the Fresnel frequency ( $f_F$ ), above which the spectrum should roll off rapidly and below which the spectrum should again roll off but at a much shallower slope [Basu *et al.*, 1994]. The Fresnel frequency is given by  $f_F = \nu/(2\lambda z)^{1/2}$ , where  $\nu$  is the irregularity drift perpendicular to the propagation path,  $\lambda$  is the radio



**Figure 3.** Shown is the observed variation of the  $S_4$  index of scintillation at 250 MHz with universal time as observed on January 6, 1997. The  $S_4$  index of scintillation is defined as the normalized second moment of signal intensity. The measurements were performed from Ny Alesund, Svalbard. The observing period of 0400–1400 UT corresponds to dayside auroral measurements.

wavelength, and  $z$  is the slant range to the irregularity layer. The spectral set in Figure 4 does not conform to the weak scatter spectral specifications for uniform flow speed. Instead, the flat-topped low-frequency spectral form may be a result of the irregularities moving with a distributed velocity rather than a uniform flow speed [Lotova, 1981]. The corner frequencies of the spectra shown in Figure 4 vary from one spectra to another, indicating that the velocity dispersion is a function of space and time. Figure 5 illustrates two spectra from the early morning period that indicate the shape of a weak scintillation spectrum in a uniform flow region. In this case, the spectra have narrower bandwidths and exhibit spectral maximum, particularly noticeable in the left-hand (0204:54 UT) spectrum, and have steeper high-frequency roll-off, with power law spectral indices of about 3 as compared with power law indices of 2 in Figure 4. Finally, it is to be emphasized that the broadband spectra shown in Figure 4 are observed just poleward of the cusp, not only at magnetic noon

but over an extended period during the daytime. However, the signature of velocity dispersion is most enhanced around magnetic noon. In a recent comprehensive study of the cusp, Baker *et al.* [1995] have established that HF radar backscatter from the cusp exhibits wide and complex Doppler spectra. This result implies that the cusp is a region of high electric field turbulence which is in agreement with the DE 1 and DE 2 satellite data [Maynard *et al.*, 1991; Basinska *et al.*, 1992].

Another example of daytime scintillation at 250 MHz is shown in Figure 6. A clear commencement of a scintillation event at 0500 UT and the decay at 1200 UT may be noted. The campaign ended at 1200 UT, which caused the abrupt end of the data. The daytime scintillation event again corresponded to the poleward location of about  $78^\circ$  CGMLAT and covered the time interval of about 0900–1600 MLT. The magnitude of scintillation was weak and remained below the  $S_4$  level of 0.3. The scintillation spectra for this event are illustrated in Figure 7. As discussed earlier, the



SDRS Nyalesund

01/06/97 244 MHz

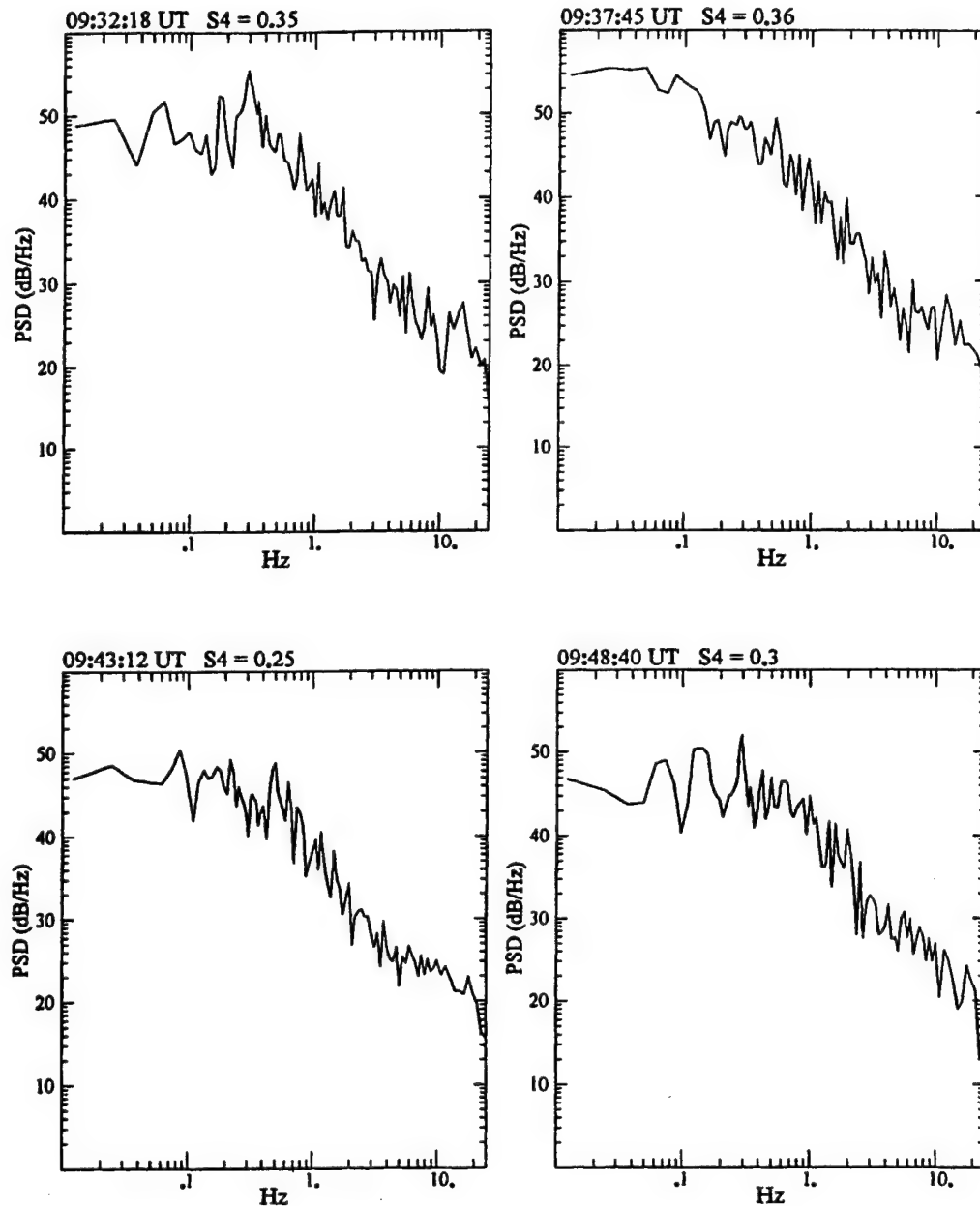


**Figure 4.** The frequency spectra of 250-MHz scintillations recorded on January 6, 1997, at Ny Alesund, Svalbard, are illustrated at 5-min intervals near magnetic noon. Broad spectra are illustrated.

flat-topped spectra indicate that the irregularities have turbulent velocities. The spectral width is considerably larger compared with the January 6, 1997, spectra, indicating larger velocity dispersion.

During the campaign period a major magnetic

storm occurred during January 9–11, 1997. To show the effect of the storm on amplitude scintillations at 250 MHz, the diurnal variations of  $S_4$  with UT during January 10–12, 1997, are shown in Figure 8. The quiet-day pattern of scintillations with enhanced ac-

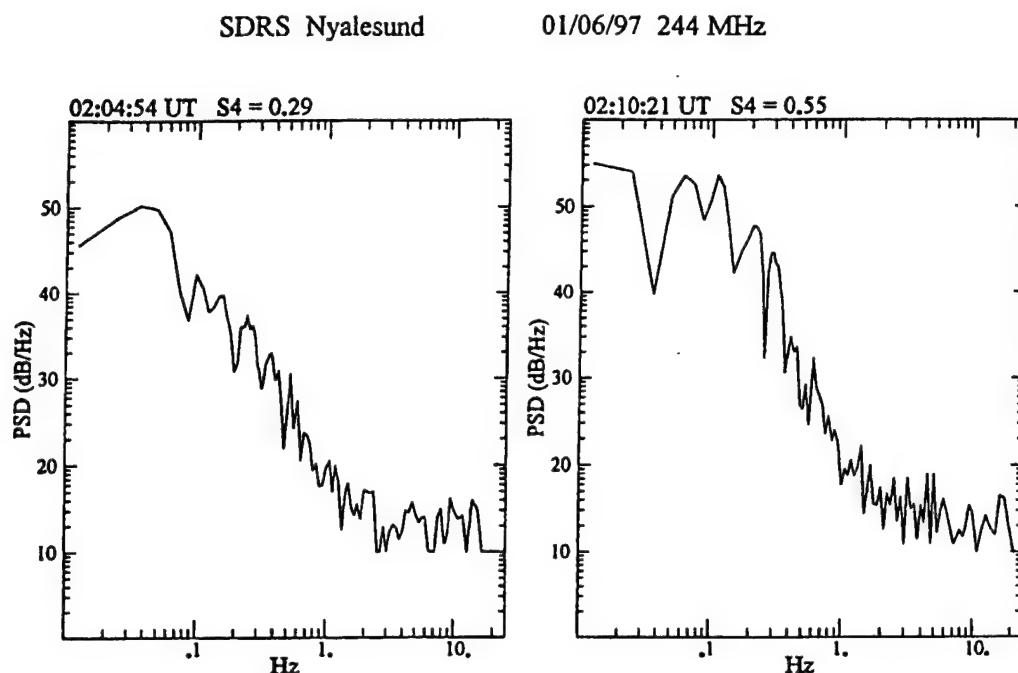


Figure 5. Same as in Figure 4 but obtained during early morning magnetic local time (MLT) hours. Narrowband spectra with Fresnel maximum are illustrated.

tivity around magnetic noon (0850 UT) was observed on January 10 and 12. The pattern changed drastically on January 11, however, when a long enduring prenoon scintillation event during 0000–1000 UT (0400–1400 MLT) was observed, as well as two additional events in the afternoon and early evening period during 1600–2200 MLT. During the prenoon period the Fresnel frequency of scintillation spectra were observed to be as high as 1 Hz. Using the expression given earlier that relates the irregularity drift velocity to the Fresnel frequency, we find that at this time, irregularity drift perpendicular to the propagation path was about 1 km/s. The digisonde at Ny Alesund detected polar cap patches and determined horizontal drifts that increased from 1 km/s at 0000 UT to 1.5 km/s around 0600 UT, which then decreased to about 600 m/s after 1200 UT. These results indicate that the station became a polar cap station due to the expansion of the auroral oval to lower latitudes under these magnetically active conditions, as confirmed by optical images that show no auroral emission within the entire field of view of the imager. This is probably the reason why the diurnal pattern of 250-MHz scintillation on January 11 was distinctly different from other days.

We used the GPS satellite data provided by the

IGS station at Ny Alesund to further investigate the patch characteristics. The IGS stations are equipped with dual-frequency (1.2 and 1.6 GHz) GPS receivers and provide differential carrier phase and differential group delay data at 30-s intervals. The GPS data were analyzed to estimate the total electron content (TEC) of the ionosphere and also the magnitudes of large-scale irregularity structures from the rate of change in differential carrier phase, which is equivalent to the rate of change of TEC. The rate of change of TEC is derived from the differential carrier phase data, which are provided at 30-s intervals. The data are filtered to remove variations with periods longer than 15 min, and then the rate of change of TEC is obtained at 1-min intervals from 30-s TEC values. This algorithm was first developed by J. A. Klobuchar and P. Doherty at Phillips Laboratory (now Air Force Research Laboratory) and has now been adapted by various groups for ionospheric studies at low and high latitudes by the use of the widely dispersed IGS network of stations [Doherty *et al.*, 1994]. In a recent paper, Pi *et al.* [1997] have indicated how measurements of the rate of change of TEC by the global IGS network may be exploited to monitor the instantaneous global distribution of ionospheric irregularities. Figure 9 shows the 350-km subionospheric position of

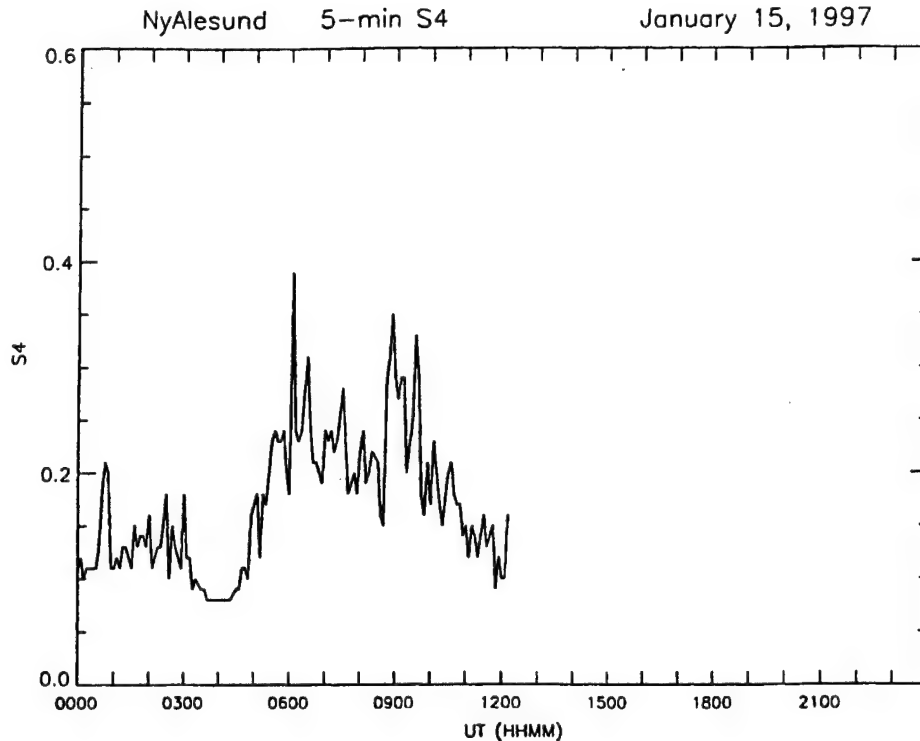


Figure 6. Same as in Figure 3 but performed on January 15, 1997.

GPS satellites, viewed from Ny Alesund, in the day sector between 0600 and 1800 MLT. The diamonds along the tracks signify locations where the rate of change of TEC exceeded  $1 \text{ TEC unit min}^{-1}$  (1 TEC unit =  $10^{16} \text{ electrons m}^{-2}$ ).

Figure 9 shows that the subionospheric track of satellite prn 26, viewed from Ny Alesund, crossed magnetic noon. The differential carrier phase and group delay data were combined to determine the total electron content. This result is illustrated in Figure 10, which shows the variation of equivalent vertical TEC as a function of universal time. The alternate increases and decreases of TEC signify the transit of polar cap patches across the GPS propagation path. It may be noted that, on average, the patches are associated with an increase of TEC by about 2 TEC units and the patch durations are about 30 min. The patches are very weak because of the prevailing solar minimum condition. The digisonde measurements at Ny Alesund indicated that at this time the horizontal drift is about  $600 \text{ m s}^{-1}$ . By combining the duration and the drift of the patches, we obtain the horizontal patch dimensions as 1080 km.

The convecting patches develop intermediate scale irregularities through the gradient drift instability mechanism [Chaturvedi and Huba, 1987; Tsunoda, 1988, and references therein]. With prevailing drift velocities as high as  $500\text{--}1000 \text{ m s}^{-1}$ , patches with relatively gentle spatial gradients of electron density of the order of 50 km, perpendicular to the magnetic field and in the direction of the drift, are expected to become unstable within about a minute and develop intermediate scale irregularities [Basu *et al.*, 1995]. In addition, since the patches may transit through all or part of the cusp enroute to the polar cap [Sojka *et al.*, 1994; Decker *et al.*, 1994], it is conceivable that the patches will be structured in density due to structured cusp electric fields [Maynard *et al.*, 1991; Basinska *et al.*, 1992] or structured particle precipitation from the magnetosheath. The association of density and electric field structures in velocity shear regions at auroral latitudes has been established from satellite in situ measurements [Basu *et al.*, 1988] and accounted for theoretically by several authors [Keskinen *et al.*, 1988; Basu and Coppi, 1990; Ganguli *et al.*, 1994]. We discussed earlier the presence of 250-MHz scintillation in the cusp region, which establishes the presence

SDRS Nyalesund

01/15/97 244 MHz

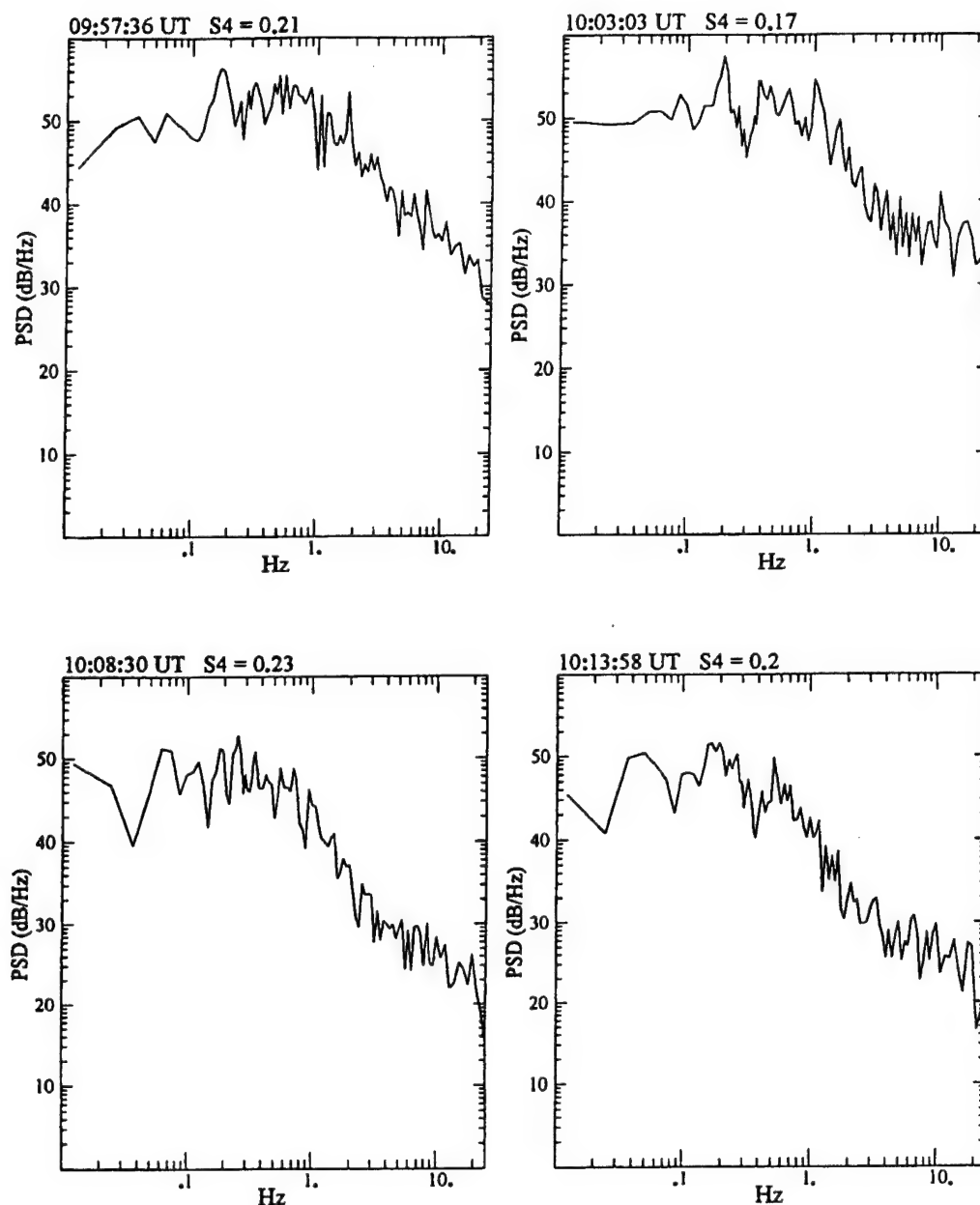
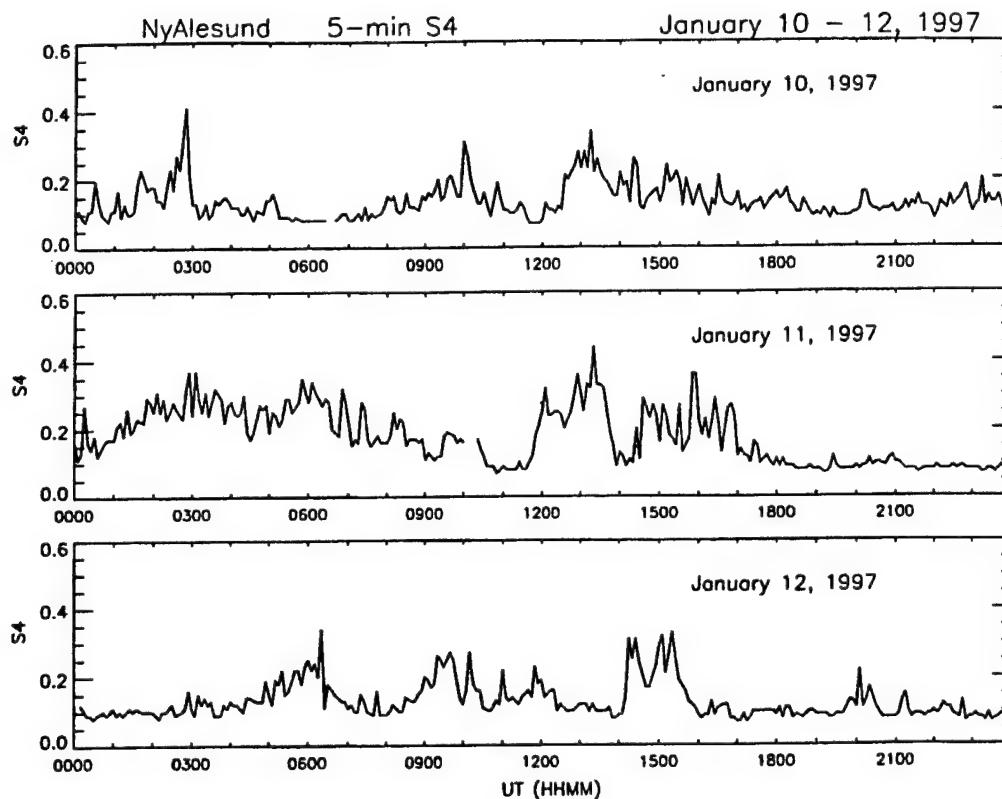


Figure 7. Same as in Figure 4 but on January 15, 1997.

of intermediate scale density irregularities in the range of about 1 km to 100 m. The patches may therefore enter the polar cap after being structured in the cusp at such subkilometer scales. However, since the cusp is localized, these irregularities will decay after the patches exit the source region. The approx-

imate lifetime of the intermediate scale density irregularities in the winter polar cap ionosphere is proportional to the square of irregularity scale size, perpendicular to the geomagnetic field, divided by the electron perpendicular diffusion coefficient. For an altitude of 350 km, 100-m and 1-km scale size density



**Figure 8.** Shown is the variation of  $S_4$  index of scintillation at 250 MHz with universal time observed during the magnetic storm period of January 10–12, 1997. The top and middle panels show the variations during the storm period of January 10 and 11, 1997, respectively, and the bottom panel shows the variation observed on January 12, 1997, immediately after the magnetic storm.

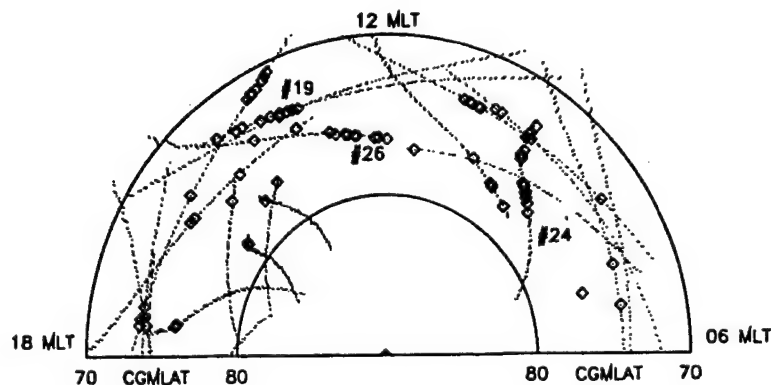


**Figure 9.** The 350-km subionospheric tracks of Global Positioning System (GPS) satellites as observed from Ny Alesund, Svalbard, on January 11, 1997. The tracks are illustrated in MLT-CGMLAT coordinates. The diamonds indicate that the rate of change of the total electron content (TEC) exceeded 1 TEC unit per minute (1 TEC unit =  $10^{16}$  electrons  $m^{-2}$ ). Some of these tracks are identified by the corresponding satellite prn's.

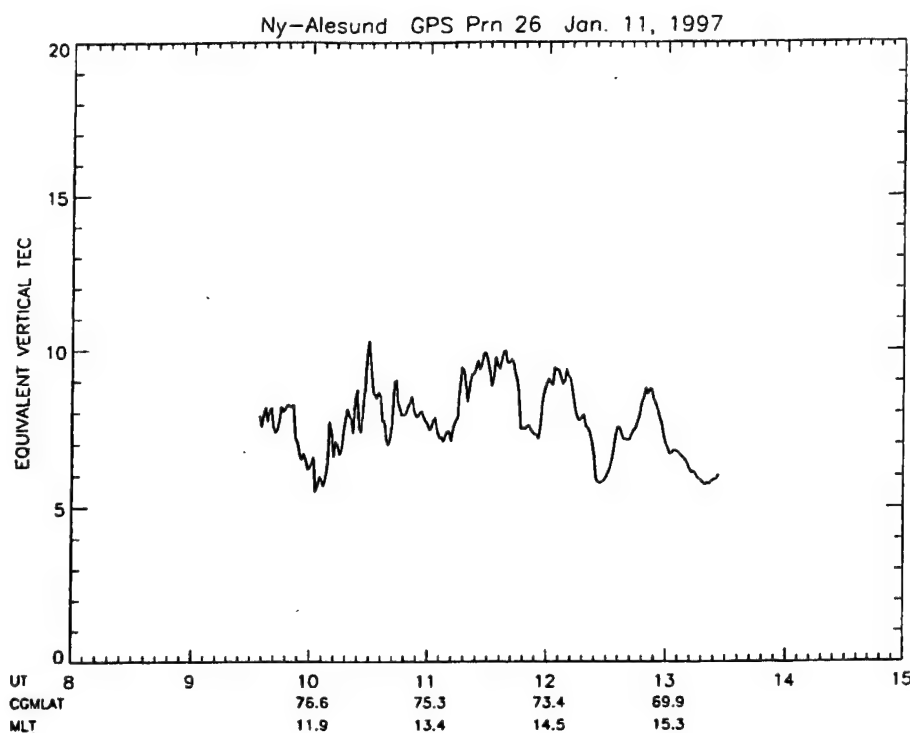


**Figure 10.** The equivalent vertical total electron content determined during the magnetic storm period of January 11, 1997, using the GPS observations of the International GPS Geodynamic Service (IGS) at Ny Alesund. Patches with about 2 TEC units were detected.

irregularities will decay with typical time constants of the order of minutes and hours, respectively. In view of such long lifetimes of subkilometer scale irregularities, the patches will already be structured when they enter the polar cap. This will contribute to a reduction of the growth time of irregularities in convecting patches by the gradient drift instability mechanism.

We shall now discuss the plasma structuring of patches by determining the rate of change of TEC from two frequencies (1.2 and 1.6 GHz) of GPS satellite observations as well as measuring amplitude scintillations of GPS signals at 1.6 GHz. Figure 11 shows the results of the rate of change of TEC per minute on January 11, 1997, which was determined from the IGS GPS data from Ny Alesund. Each horizontal line represents a GPS satellite with a specific prn and shows phase fluctuations expressed as fluctuations in changes of TEC per minute. The change of 1 TEC unit per minute corresponds to the spacing between the lines in the bottom right corner of the diagram. This representation has been effectively used by *Aarons et al.* [1996] and *Aarons* [1997]

for irregularity studies at both equatorial and high latitudes. Figure 11 shows that the satellite (prn 26) recorded changes mostly around  $\pm 1$  TEC  $\text{min}^{-1}$  around 1200 UT when it detected patches. If we recall that the digisonde recorded drifts of  $600 \text{ m s}^{-1}$  at this time, then the differential carrier phase data with a Nyquist period of 60 s correspond to irregularity wavelengths of 36 km. *Aarons* [1997] has recently performed a careful study of the rate of change of TEC at high latitudes by using the IGS data from 11 high-latitude stations. From this study he concluded that during solar minimum the rate of change of TEC (phase fluctuations) was lower at corrected geomagnetic latitudes  $>80^\circ$  as compared with that in the auroral oval. This observation depends on the fact that the phase fluctuations (or the rate of change of TEC) are a function of both change in TEC and the irregularity velocity. It is not clear if the lower values in the polar cap, compared with the auroral oval stations as reported by *Aarons* [1997], are a result of smaller irregularity amplitudes or smaller velocities. In the present study, with digisonde and spectral studies of scintillation, we could estimate the veloci-



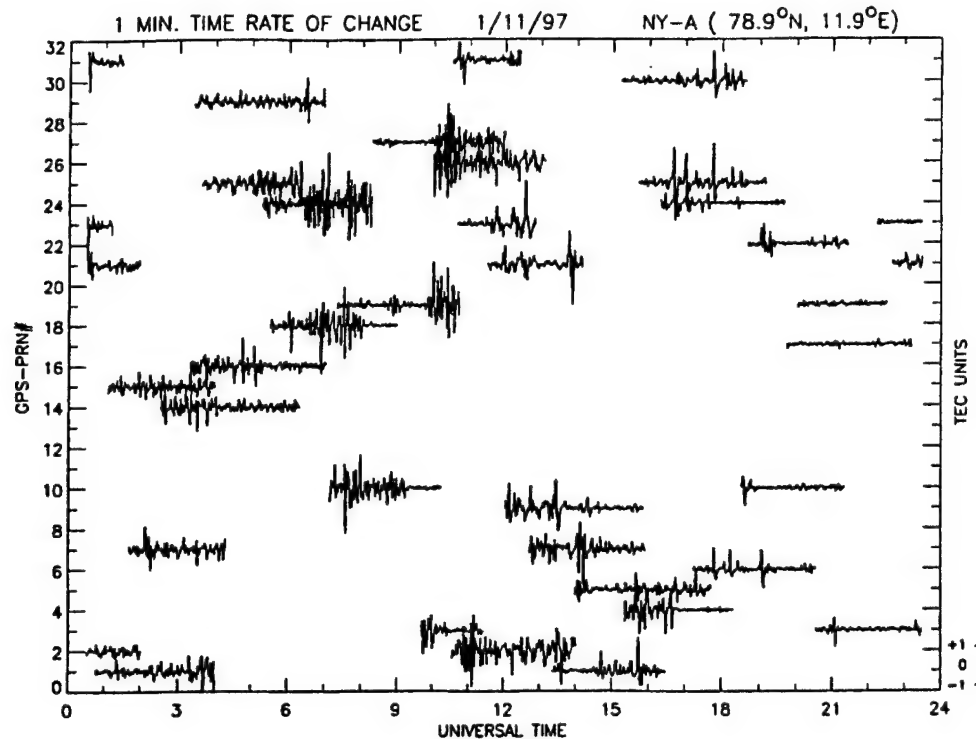


**Figure 11.** Shown are the rates of change of TEC as recorded by different satellites at Ny Alesund at different universal times during the magnetic storm period of January 11, 1997. The ordinate refers to prn of GPS satellites. The scale for the rate of change of TEC is indicated at the right bottom edge of the diagram.

ties and therefore determine the irregularity wavelengths with 30-s sampling of GPS carrier phase.

Amplitude scintillation measurements of GPS signals at 1.6 GHz were also conducted by using a receiver that recorded the signal amplitude at 50 Hz and processed on-line the  $S_4$  scintillation index every 82 s. The amplitude scintillation data are plotted in Figure 12 in the same format as Figure 11. In this case, however, the separation between the successive horizontal lines corresponds to  $S_4 = 0.25$ . It may be seen that the receiver failed to detect any amplitude scintillation from a GPS satellite (prn 26). Some of the satellites, such as prn 23, show scintillation-like activity a little before 0900 UT. The events are not scintillation but are caused by multipath effects at low elevation angles encountered during the rise and set of the satellite. Unlike phase scintillations, where the irregularity wavelength sampled in an experiment depends on the velocity of the irregularities, amplitude scintillations are caused by irregularities in the range of the Fresnel dimension to a dimension

smaller by about a decade. Thus, with irregularities at a range of 400 km, amplitude scintillations at the GPS frequency of 1.6 GHz are caused by irregularities in the wavelength range from 390 m, the Fresnel dimension, to about 30 m. These irregularity wavelengths (390–30 m) are 2–3 orders of magnitude smaller than those (36 km) detected by phase fluctuation measurements. Thus, in the presence of high ionospheric convection, the detection of large phase fluctuations may not signify the presence of smaller irregularities or be of sufficient strength to cause detectable levels of amplitude and phase scintillation.

#### 4. Conclusions

Under solar minimum conditions of January 1997, weak ( $S_4 < 0.4$ ) amplitude scintillations at 250 MHz were persistently observed during daytime at about  $2^\circ$  poleward of the nominal cusp region. Such scintillations, indicating the presence of subkilometer scale electron density irregularities, were observed not only

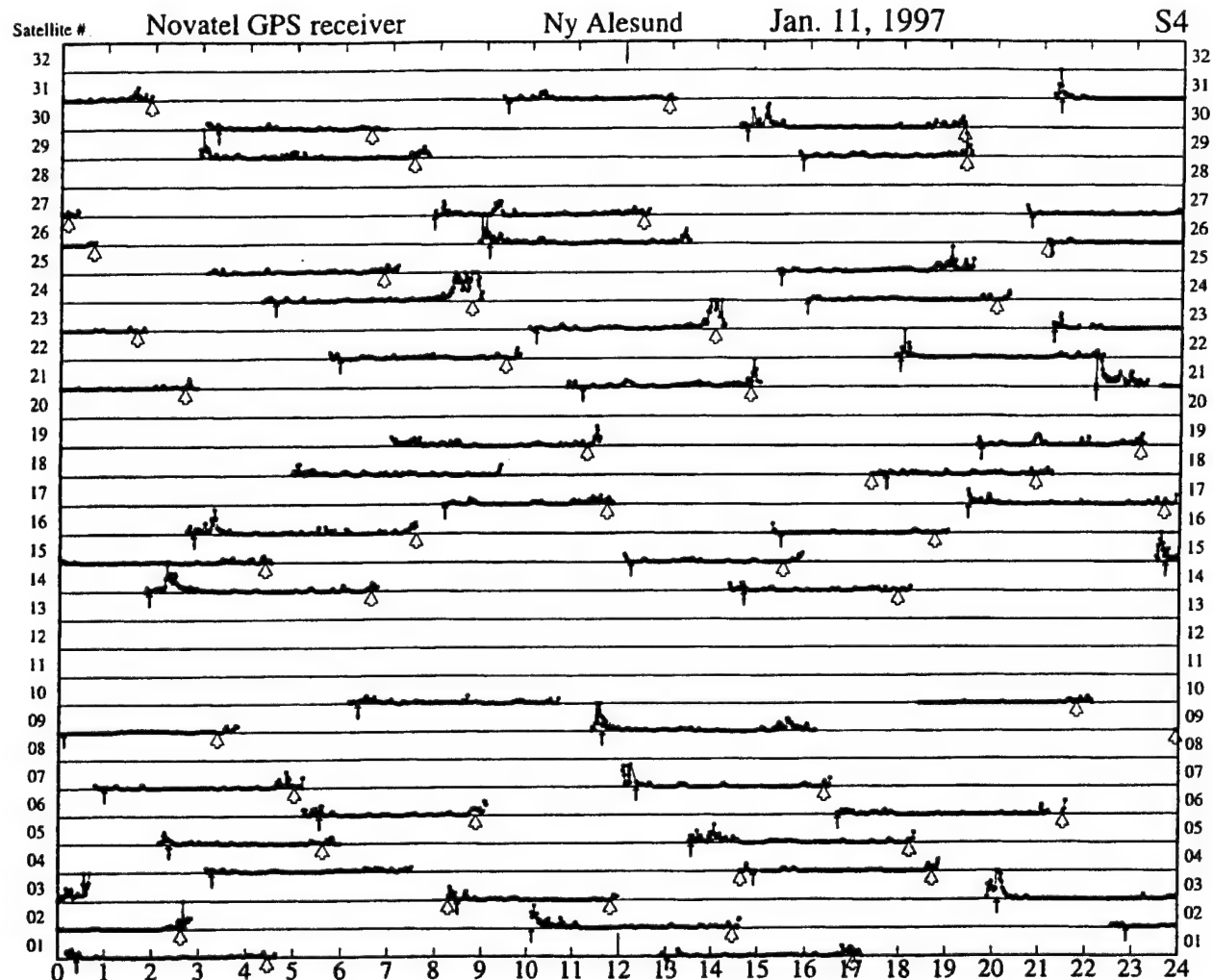


**Figure 12.** Shown is the amplitude scintillation at 1.6 GHz detected by different GPS satellites at different universal times during the magnetic storm period of January 11, 1997. The spacing between successive horizontal lines corresponds to an amplitude scintillation index of  $S_4 = 0.25$ . The figure shows that no amplitude scintillation was recorded. The scintillation-like variations are due to multipath effects which are encountered at low elevation angles.

near magnetic noon but also over much of the daytime, typically between 0900 MLT and 1500 MLT. The irregularities immediately poleward of the cusp may be convected from the proper cusp region or may be locally generated in the "cusp plume" region [Newell *et al.*, 1991]. The presence of irregularities in a longitudinally broad region slightly poleward of the cusp is probably related to the plasma mantle at low altitudes, which was first identified by Newell *et al.* [1991]. The discrete auroral features observed by these authors in this region and the associated field-

aligned currents may be the source of the observed irregularities.

The dayside scintillation is characterized by frequency spectra which are generally broad but are occasionally interspersed by narrowband spectra. In our previous study in the cusp region at Sondrestrom, Greenland, we detected velocity shear and also observed broad frequency spectra of scintillations, implying the presence of turbulent plasma flows [Basu *et al.*, 1994]. This result was explained in terms of shear instabilities. Baker *et al.* [1995] have recently used

high-latitude HF radar data and established that the important radar characteristic of the cusp are the wide and complex Doppler power spectra. They recognized that plasma instability processes may impact the Doppler spectra but favored the alternative in which the wide spectra resulted from a structure within the  $E \times B$  drift velocities. In this paper, we are reporting broad frequency spectra of scintillations poleward of the cusp region not only around magnetic noon but also away from noon. It is quite likely that in the presence of discrete auroral forms in the mantle [Newell *et al.*, 1991; Murphree *et al.*, 1990], shear instabilities may operate in this region and cause velocity turbulence in the nonlinear stage. This may also explain the observed broad frequency spectra of scintillation. Ganguli *et al.* [1994] have recently developed theories to show that a small amount of velocity shear in the transverse flow is sufficient to excite large-scale Kelvin-Helmholtz modes, which can nonlinearly steepen to excite microinstabilities that may energize ions.

We observed patches with small TEC enhancements only during the major magnetic storm. Modeling studies indicate that in view of the high geographic latitude of the cusp in the Ny Alesund sector, the corresponding polar cap patches and associated irregularities are weak and have low occurrence [Basu *et al.*, 1995]. We showed that at high latitudes in the presence of large convection speed, the IGS data sampled at 30-s intervals provide phase fluctuations at very large scales (40 km) and may not serve as an effective tracer of scintillation. With faster data sampling this IGS network may, however, be a very effective forecaster of scintillation.

**Acknowledgments.** We thank the staff of the Norsk Polarinstitut Research Station at Ny Alesund for their support during the January 1997 campaign and for continuous monitoring of the satellite receiving system. We gratefully acknowledge the help of JPL for supplying the GPS bias data. The work at Air Force Research Laboratory, Hanscom AFB, was partially supported by the Air Force Office of Scientific Research under task 2310G9.

## References

- Aarons, J., Global positioning system phase fluctuations at auroral latitudes, *J. Geophys. Res.*, **102**, 17,219, 1997.
- Aarons, J., J. P. Mullen, H. Whitney, A. Johnson, and E. Weber, UHF scintillation activity over polar latitudes, *Geophys. Res. Lett.*, **8**, 277, 1981.
- Aarons, J., M. Mendillo, R. Yantosca, and E. Kudeki, GPS phase fluctuations in the equatorial region during the MISETA campaign, *J. Geophys. Res.*, **101**, 26,851, 1996.
- Baker, K. B., J. R. Dudeney, R. A. Greenwald, M. Pinnock, P. T. Newell, A. S. Rodger, N. Mattin, and C.-I. Meng, HF radar signatures of the cusp and low-latitude boundary layer, *J. Geophys. Res.*, **100**, 7671, 1995.
- Basinska, E. M., W. J. Burke, N. C. Maynard, W. J. Hughes, J. D. Winningham, and W. B. Hanson, Small-scale electrodynamics of the cusp with northward interplanetary magnetic field, *J. Geophys. Res.*, **97**, 6369, 1992.
- Basu, B., and B. Coppi, Plasma collective modes driven by velocity gradients, *J. Geophys. Res.*, **95**, 21,213, 1990.
- Basu, S., Su. Basu, P. K. Chaturvedi, and C. M. Bryant Jr., Irregularity structures in the cusp/cleft and polar cap regions, *Radio Sci.*, **29**, 195, 1994.
- Basu, S., Su. Basu, J. J. Sojka, R. W. Schunk, and E. MacKenzie, Macroscale modeling and mesoscale observations of plasma density structures in the polar cap, *Geophys. Res. Lett.*, **22**, 881, 1995.
- Basu, Su., S. Basu, E. MacKenzie, and H. E. Whitney, Morphology of phase and intensity scintillations in the auroral oval and polar cap, *Radio Sci.*, **20**, 347, 1985.
- Basu, Su., S. Basu, E. MacKenzie, P. F. Fougere, W. R. Coley, N. C. Maynard, J. D. Winningham, M. Sugiura, W. B. Hanson, and W. R. Hoegy, Simultaneous density and electric field fluctuation spectra associated with velocity shears in the auroral oval, *J. Geophys. Res.*, **93**, 115, 1988.
- Buchau, J., B. W. Reinisch, E. J. Weber, and J. G. Moore, Structure and dynamics of the winter polar cap *F* region, *Radio Sci.*, **18**, 995, 1983.
- Chaturvedi, P. K., and J. D. Huba, The interchange instability in high-latitude plasma blobs, *J. Geophys. Res.*, **92**, 3357, 1987.
- Decker, D. T., C. E. Valladares, R. Sheehan, Su. Basu, D. N. Anderson, and R. A. Heelis, Modeling daytime *F* layer patches over Sondrestrom, *Radio Sci.*, **29**, 249, 1994.
- Doherty, P., E. Raffi, J. Klobuchar, and M. B. El-Arini, Statistics of time rate of change of ionospheric range delay, in *Proceedings ION GPS-94*, p. 1589, Inst. of Navig., Alexandria, Va., 1994.
- Ganguli, G., Y. C. Lee, P. J. Palmadesso, and S. L. Ossakow, Ion waves in a collisional magnetoplasma with a field-aligned current and a transverse velocity shear, in *Proceedings of the 1988 Cambridge Workshop in Theoretical Geoplasma Physics, Polar Cap Dynamics and High Latitude Ionospheric Turbulence*, pp. 231–242, Scientific, Cambridge, Mass., 1989.
- Ganguli, G., M. J. Keskinen, H. Romero, R. Heelis, T. Moore, and C. Pollock, Coupling of microprocesses and macroprocesses due to velocity shear: An application to the low-altitude ionosphere, *J. Geophys. Res.*, **99**, 8873, 1994.
- Kersley, L., C. D. Russell, and D. L. Rice, Phase scintilla-

- tion and irregularities in the northern polar ionosphere, *Radio Sci.*, 30, 619, 1995.
- Keskinen, M. J., H. G. Mitchell, J. A. Fedder, P. Satyanarayana, S. T. Zalesak, and J. D. Huba, Nonlinear evolution of the Kelvin-Helmholtz instability in the high-latitude ionosphere, *J. Geophys. Res.*, 93, 137, 1988.
- Lotova, N. A., Temporal scintillation spectra with allowance for the solar-wind velocity distribution: Theory, *Geomagn. Aeron.*, 21, 447, 1981.
- Maynard, N. C., T. L. Aggson, E. M. Basinska, W. J. Burke, P. Craven, W. K. Peterson, M. Sugiura, and D. R. Weimer, Magnetospheric boundary dynamics: DE 1 and DE 2 observations near the magnetopause and cusp, *J. Geophys. Res.*, 96, 3505, 1991.
- Maynard, N. C., E. J. Weber, D. R. Weimer, J. Moen, T. Onsager, R. A. Heelis, and A. Egeland, How wide in magnetic local time is the cusp? An event study, *J. Geophys. Res.*, 102, 4765, 1997.
- Murphree, J. S., R. D. Elphinstone, D. Hearn, and L. L. Cogger, Large-scale high-latitude dayside auroral emissions, *J. Geophys. Res.*, 95, 2345, 1990.
- Newell, P. T., and C.-I. Meng, Mapping of the dayside ionosphere to the magnetosphere according to particle precipitation characteristics, *Geophys. Res. Lett.*, 19, 609, 1992.
- Newell, P. T., W. J. Burke, C.-I. Meng, E. R. Sanchez, and M. E. Greenspan, Identification and observations of the plasma mantle at low altitude, *J. Geophys. Res.*, 96, 35, 1991.
- Pi, X., A. J. Mannucci, U. J. Lindqwister, and C. M. Ho, Monitoring of global ionospheric irregularities using the worldwide GPS network, *Geophys. Res. Lett.*, 24, 2283, 1997.
- Sandholt, P. E., M. Lockwood, T. Oguti, S. W. H. Cowley, K. S. C. Freeman, B. Lybekk, A. Egeland, and D. M. Willis, Midday auroral breakup events and related energy and momentum transfer from the magnetosheath, *J. Geophys. Res.*, 95, 1039, 1990.
- Smith, M. F., and M. Lockwood, The pulsating cusp, *Geophys. Res. Lett.*, 17, 1069, 1990.
- Sojka, J. J., M. D. Bowline, and R. W. Schunk, Patches in the polar ionosphere: UT and seasonal dependence, *J. Geophys. Res.*, 99, 14,959, 1994.
- Tsunoda, R. T., High-latitude *F* region irregularities: A review and synthesis, *Rev. Geophys.*, 26, 719, 1988.
- Valladares, C. E., S. Basu, J. Buchau, and E. Friis-Christensen, Experimental evidence for the formation and entry of patches into the polar cap, *Radio Sci.*, 29, 167, 1994.
- Weber, E. J., J. Buchau, J. G. Moore, J. R. Sharber, R. C. Livingston, J. D. Winningham, and B. W. Reinisch, *F* layer ionization patches in the polar cap, *J. Geophys. Res.*, 89, 1683, 1984.
- Weber, E. J., J. A. Klobuchar, J. Buchau, H. C. Carlson Jr., R. C. Livingston, O. de la Beaujardiere, M. McCready, J. G. Moore, and G. J. Bishop, Polar cap *F* layer patches: Structure and dynamics, *J. Geophys. Res.*, 91, 12,121, 1986.
- S. Basu, J. Bongiolatti, T. W. Bullett, H. Kuenzler, and E. J. Weber, Air Force Research Laboratory, AFRL/VSBI, 29 Randolph Road, Hanscom Air Force Base, MA 01731. (e-mail: santimay@aol.com; bullett@plh.af.mil; webere@plh.af.mil)
- P. Doherty, E. MacKenzie, and R. Sheehan, Institute for Scientific Research, Boston College, Newton, MA 02159.
- M. J. Keskinen, Plasma Physics Division, Naval Research Laboratory, 4555 Overlook Avenue, SW, Washington, D. C. 20375. (keskinen@ppd.nrl.navy.mil)
- P. Ning, KEO Consultants, 24 Brookline Avenue, Brookline, MA 02146.

(Received January 19, 1998; revised May 5, 1998; accepted May 8, 1998.)



## A comparison of TEC fluctuations and scintillations at Ascension Island

S. Basu<sup>a,\*</sup>, K.M. Groves<sup>a</sup>, J.M. Quinn<sup>a</sup>, P. Doherty<sup>b</sup>

<sup>a</sup>*Air Force Research Laboratory, VSBI, 29 Randolph Road, Hanscom AFB, MA, 01731, USA*

<sup>b</sup>*Institute for Scientific Research, Boston College, 140 Commonwealth Avenue, Chestnut Hill, MA, 02467, USA*

Received 11 March 1999; accepted 4 May 1999

### Abstract

With increasing reliance on space-based platforms for global navigation and communication, concerns about the impact of ionospheric scintillation on these systems have become a high priority. Recently, the Air Force Research Laboratory (AFRL) performed amplitude scintillation measurements of L1 (1.575 MHz) signals from GPS satellites at Ascension Island (14.45° W, 7.95° S; magnetic latitude 16° S) during February–April, 1998, to compare amplitude scintillations with fluctuations of the total electron content (TEC). Ascension Island is located in the South Atlantic under the southern crest of the equatorial anomaly of F2 ionization where scintillations will be much enhanced during the upcoming solar maximum period. Ascension Island is included in the global network of the International GPS Service (IGS) and the GPS receivers in this network report the carrier to noise ( $C/N$ ) ratio, the dual frequency carrier phase and pseudorange data at 30-s intervals. Such data with a sampling interval of 30 s were analyzed to determine TEC, the rate of change of TEC (ROT) and also ROTI, defined as the standard deviation of ROT. The spatial scale of ROTI, sampled at 30 s interval, will correspond to 6 km when the vector sum of the ionospheric projection of the satellite velocity and the irregularity drift orthogonal to the propagation path is of the order of 100 m/s. On the other hand, the scale-length of the amplitude scintillation index corresponds to the Fresnel dimension which is about 400 m for the GPS L1 frequency and an ionospheric height of 400 km. It is shown that, in view of the co-existence of large and small scale irregularities in equatorial irregularity structures, during the early evening hours, and small magnitude of irregularity drifts, ROTI measurements can be used to predict the presence of scintillation causing irregularities. The quantitative relationship between ROTI and S4, however, varies considerably due to variations of the ionospheric projection of the satellite velocity and the ionospheric irregularity drift. During the post-midnight period, due to the decay of small scale irregularities leading to a steepening of irregularity power spectrum, ROTI, on occasions, may not be associated with detectable levels of scintillation. In view of the power law type of irregularity power spectrum, ROTI will, in general, be larger than S4 and the ratio, ROTI/S4, in the present dataset is found to vary between 2 and 10. At high latitudes, where the ionospheric motion, driven by large electric fields of magnetospheric origin, is much enhanced during magnetically active periods, ROTI/S4 may be considerably larger than that in the equatorial region. © 2000 Elsevier Science Ltd. All rights reserved.

### 1. Introduction

During the post-sunset period, the F-region of the equatorial ionosphere often becomes unstable through a complex interaction between electric fields, neutral

\* Corresponding author. Tel.: +1-202-404-4384; fax: +1-202-767-0631.

E-mail address: santimay@aol.com (S. Basu).

winds and the earth's magnetic field (Rishbeth, 1981; Kelley, 1989). At this time, the eastward electric field is often enhanced to destabilize the ionosphere and the meridional neutral winds can exert a stabilizing force on the ionospheric plasma (Mendillo et al., 1992; Basu et al., 1996; Groves et al., 1997). In the presence of these competing forces, the ionosphere, on some evenings, becomes destabilized and causes plasma bubbles to form, which penetrate far into the topside ionosphere (McClure et al., 1977). While plasma bubbles have typical east–west dimensions of several hundred kilometers, these contain irregularities with scale-lengths ranging from tens of kilometers to tens of centimeters (Woodman and LaHoz, 1976; Tsunoda, 1980). Indeed, Basu et al. (1978) showed that between sunset and midnight, 3-m scale irregularities that cause radar backscatter at 50 MHz, co-exist with sub-kilometer scale irregularities that cause VHF and L-band scintillations. After midnight, however, the radar backscatter and L-band scintillations decay but VHF scintillations caused by km-scale irregularities persist for several hours.

As summarized in the previous paragraph, the overall nature of evolution of irregularities in the scale-length range of kilometers to tens of centimeters have been investigated. In this paper, we investigate the quantitative relationship between tens of kilometer and sub-kilometer scale irregularities in equatorial plasma bubbles. For this purpose, AFRL conducted an equatorial scintillation campaign at Ascension Island (14.41° W, 7.95° S; magnetic latitude 16° S) during February–April, 1998. Ascension Island (dip latitude: 16° S), is nominally located below the southern crest of the equatorial anomaly in the F-region and, as such, TEC and scintillations are enhanced during the post-sunset period, especially during the solar maximum period. Indeed, at this station, during the solar maximum period, scintillations at 1.5 GHz, exceeding 20 dB, are observed 20% of the time between sunset and midnight. During the present campaign at Ascension Island, AFRL acquired 1.575 GHz transmissions from GPS satellites and recorded amplitude scintillation data at a sampling frequency of 10 Hz. The amplitude scintillation index,  $S_4$ , defined as the second central moment of signal intensity, was computed every 60 s. These measurements probed ionospheric irregularities of about 400-m scale-length that corresponds to the Fresnel dimension. At this station, AFRL also monitors continuously 1.612 GHz and 250 MHz transmissions from geostationary satellites, Inmarsat and Fleetsat respectively, and obtains amplitude scintillation indices ( $S_4$ ) at these two frequencies.

The Ascension Island station is included in the ground-based global GPS network overseen by the International GPS Service (IGS) for Geodynamics. Each station in this network collects GPS data and

provides the carrier phase, pseudorange and carrier to noise ratio of the dual frequency signals. The carrier phase data is least square fit over 10-s intervals and the data is collected at 30-s intervals. Several researchers (Wanninger, 1993; Doherty et al., 1994; Aarons et al., 1996) have utilized the data at 30-s intervals to study ionospheric irregularities of electron density by computing the time rate of change of the differential carrier phase. This is equivalent to the rate of change of the total electron content (TEC), termed ROT, in units of TEC/min which can indeed provide information on the spatial variation of electron density deviation at large scale-lengths. Aarons et al. (1996; 1997) and Aarons (1997) have demonstrated the utility of such dataset for studying the irregularity characteristics in equatorial plasma bubbles and for investigating the evolution of large scale irregularities during magnetic storms at both low and high latitudes. Recently, Pi et al. (1997) have defined a rate of change of TEC index (ROTI) based on the standard deviation of ROT over a 5-min period. This index statistically quantifies the ROT measurements. It should be remembered, however, that such studies provide information on large scale irregularities of electron density. Since the data is sampled at 30-s intervals, the Nyquist period is 60 s. The scale length corresponding to this Nyquist period will be dictated by the components of the ionospheric projection of the satellite motion and the irregularities in a direction perpendicular to the propagation path. If the vector sum of these two velocities is, for example, 100 m/s then the irregularity scale-lengths sampled by ROT and ROTI will correspond to 6 km. On the other hand, amplitude scintillations of GPS satellites at 1.575 GHz measured by AFRL are caused by Fresnel scale irregularities (<400 m).

In this paper, we compare the  $S_4$  index of GPS scintillations with the ROTI values and, thereby investigate the evolution of large and small scale irregularities at scale-lengths of a few kilometers and 400 m, respectively. We shall illustrate the variation of this ratio and discuss it in the context of the GPS satellite trajectory, zonal plasma drift and irregularity spectral index. One of the motivations of this study was to determine if the global IGS network might be utilised for the specification of L-band scintillations.

## 2. Results and discussions

The scintillation measurements to be discussed in the paper were performed during February–April 1998. This period corresponded to the solar minimum period when the magnitude of scintillation of L-band signals from both GPS satellites and geostationary satellites varied between weak to moderate levels.



The dual frequency carrier phase and pseudorange data from the IGS receivers at 30-s intervals are combined to determine the total electron content (TEC) of the ionosphere. The differential carrier phase data alone are used to determine the rate of change of TEC (ROT) along the line of sight over each 30-s interval. The standard deviation of ROT, defined as the rate of change of TEC index (ROTI), is computed over 5-min intervals (Pi et al., 1997).

Fig. 1 shows the results of the analysis of Ascension Island data recorded on 25 February 1998. The top panel shows the UT variation of elevation angles of all GPS satellites above  $10^\circ$  elevation angle. By using the carrier phase and group delay measurements of GPS signals at L1 (1.575 GHz) and L2 (1.227 GHz) reported at 30-s intervals, the total electron content along the slant path from the receiver to the satellites are first determined. From a knowledge of ionospheric zenith angles, the slant TEC values are converted to

the equivalent vertical TEC values. The variation of the equivalent vertical TEC with universal time is shown in the second panel. The gap in the plot between 13:00 UT (12:00 local time) and 21:30 UT (20:30 local time) is caused by the signal loss due to receiver problems. The third and fourth panels illustrate respectively the variation of the rate of change of TEC/min (ROT) along the line of sight and the rate of TEC index (ROTI). From panel 2, the presence of some large scale depletions of TEC or plasma bubbles may be noted during the early evening hours between 21:30 UT (20:30 local time) and 24:00 UT (23:00 local time). A close comparison of panels 2, 3 and 4 indicate that TEC depletions in panel 2 correspond to increased fluctuations of ROT in panel 3 and larger values of ROTI in panel 4. This establishes that plasma bubbles are associated with large scale irregularities ( $\sim$  a few km scale-lengths).

Fig. 2 compares the temporal structures of ampli-

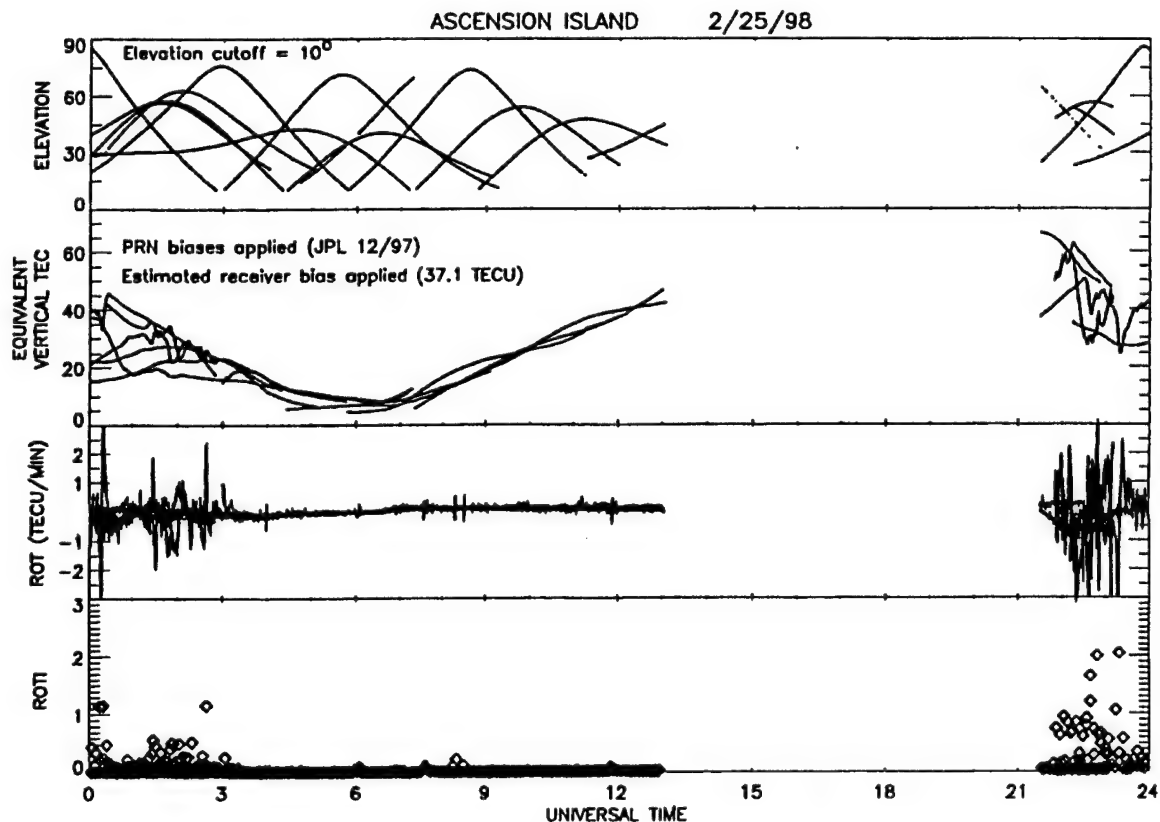


Fig. 1. Illustrates the results obtained from an analysis of observations made by the International GPS Service (IGS) receivers at Ascension Island on 25 February 1998. (a) The top panel shows the elevation angles of all GPS satellites, (b) the second panel shows the variation of the total electron content (TEC) with universal time, (c) the third panel shows the rate of change of TEC (ROT) in TEC units per min, where 1 TEC unit corresponds to  $10^{16}$  electrons  $m^{-2}$  and (d) the fourth panel shows ROTI, the standard deviation of ROT at 5-min intervals.

tude scintillation and ROTI obtained from the GPS satellite, PRN 18, during 16–17 February 1998. The time axis has been suitably adjusted so that pre- and post-midnight scintillation structures may be shown in the same diagram. The top panel illustrates the carrier-to-noise ( $C/N$ ) ratio recordings of GPS L1 (1.575 GHz) signals obtained by the AFRL scintillation receiver as a function of universal time. The sampling frequency of the  $C/N$  ratio was 10 Hz. The S4 index of amplitude scintillation, defined as the standard deviation of signal intensity fluctuations normalized by the average signal intensity, was obtained from the  $C/N$  ratio data at 1-min intervals. This is illustrated in panel 2. Comparing panel 2 with successive panels 3, 4 and 5, it may be concluded that the two enhanced scintillation (S4) structures, detected shortly after 22:00 UT and around 01:00 UT, correspond quite well with TEC depletions, ROT fluctuations and enhancements of ROTI. However, there are important differences

between the temporal structures of S4 and ROTI, which we shall address later in this section.

Fig. 3 shows the results for PRN 18 on 17–18 February 1998, in the same format as in Fig. 2. On this night, the TEC variations are very smooth and there is no detectable amplitude scintillation of GPS signals. However, there is small ROTI enhancement after 00:00 UT. It probably signifies the case of an eroded plasma depletion, which contains large-scale ROTI irregularities without the presence of any Fresnel scale irregularities.

A scatter plot of 15-min average values of S4 and ROTI is shown in Fig. 4. There is considerable scatter in the figure and the scatter increases if the data are not averaged. The GPS satellites with different trajectories have different values of the projected velocity in the ionosphere. The vector sum of the projected satellite velocity and the ionospheric drift in a direction perpendicular to the propagation path dictates the scale-length of ROTI. The scale-length variation of

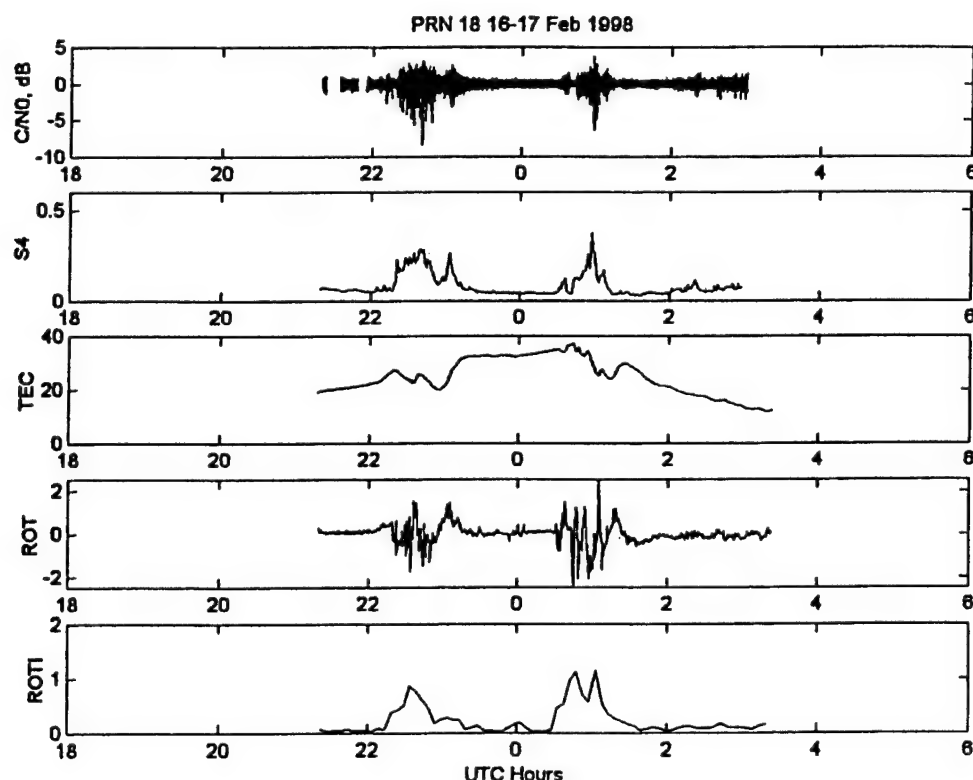


Fig. 2. Compares the amplitude scintillation index of GPS satellites with the total electron content (TEC) and its time derivatives from PRN 18 observations at Ascension Island on 16–17 February 1998. (a) The top panel shows the variation of the carrier to noise ratio of GPS L1 (1.575 GHz) signals, (b) the second panel shows the variation of the amplitude scintillation index at 1-min intervals, (c) the third panel shows the variation of TEC, (d) the fourth panel shows the rate of change of TEC (ROT) at 1-min interval and, (e) the fifth panel shows the standard deviation of ROT at 5-min intervals.

ROTI contributes primarily to the observed scatter. Overall, Fig. 4 indicates that when all satellites are considered, the ratio of ROTI/S4 varies between 2 and 10. We shall show that when satellites are considered individually, the range of variation of ROTI/S4 is much reduced.

Fig. 5 illustrates the relationship between ROTI and S4 individually for a set of satellites on particular days. Since ROTI values are obtained at 5-min intervals, the S4 values, derived at 1-min intervals, have been averaged over 5-min intervals. In these plots, ROTI/10 and S4 are plotted along the ordinate with the same scale. The top panel illustrates the results obtained from PRN 18 observations on 24 February 1998. The solid line plot shows the amplitude scintillation index (S4) and the rate of change of TEC index (ROTI) is shown in dotted lines. It may be noted both S4 and ROTI exhibit two structures, one in the pre-midnight hours and the other during the post-midnight period. For these structures, the ratio of the magnitudes of ROTI and S4 varies between 4 and 6. In the middle panel, the same two parameters are compared for PRN 13 observations on 23 March 1998. In this

case, the correspondence between two major S4 and ROTI structures and their sub-structures is striking, with the ratio of ROTI and S4 varying between 3 and 4. The bottom panel shows that on 27 March 1998, the same satellite (PRN 13) detected a S4 and ROTI structure early in the evening after 22:00 UT (21:00 local time). In the early phase, the overall correspondence between S4 and ROTI is good but there is a conspicuous time shift. At this time, the ratio ROTI/S4 approaches a value of 9; 1 h later, at about 23:00 UT, the ratio attains a value of 5, which approaches the value attained on 23 March 1998 between 23:30 and 01:00 local time. In the absence of reliable ionospheric drift measurements, it is not clear if the enhanced value of ROTI/S4 in the early phase is a result of enhanced irregularity drifts. As illustrated in Fig. 3, extreme values of ROTI/S4 may be encountered during the post-midnight period when S4 approaches zero for finite value of ROTI. This is a result of faster decay of Fresnel scale irregularities due to increased diffusion perpendicular to the magnetic field.

To a first approximation, the ratio of ROTI and S4 is dictated by the respective scale-lengths. The scale-

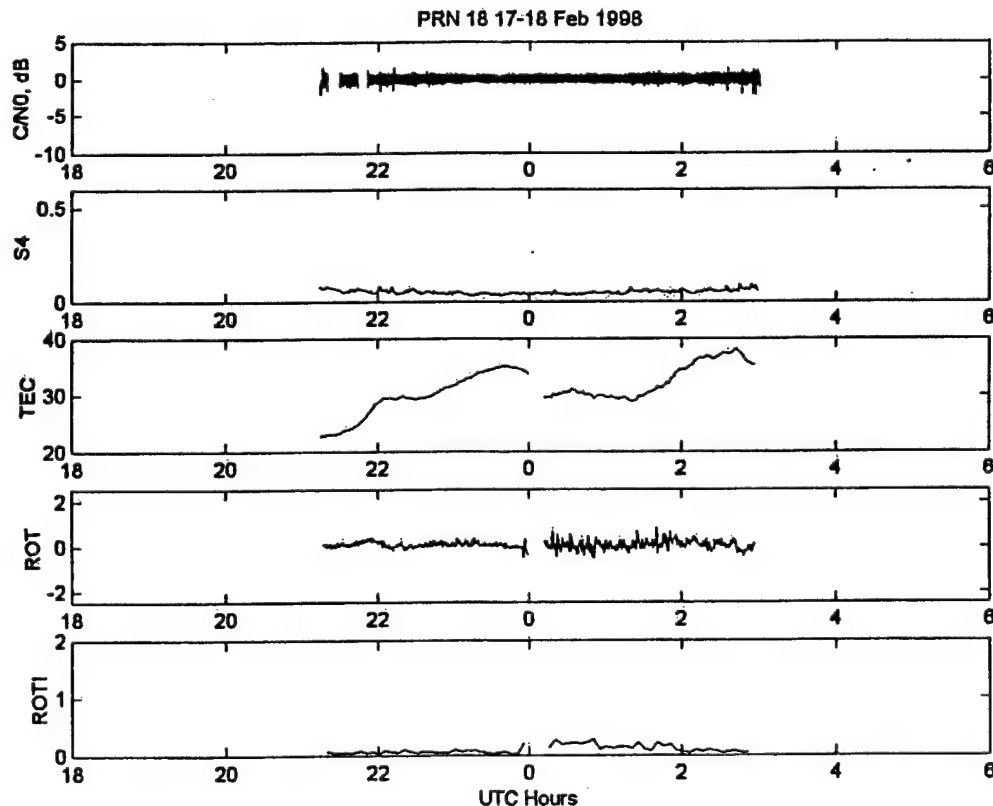


Fig. 3. Same as in Fig. 2 for PRN 18 on 17–18 February 1998

length of S4 corresponds to the Fresnel dimension,  $(2\lambda z)^{1/2}$ , where  $\lambda$  is the radio wavelength (0.39 m at the GPS L1 frequency of 1.575 GHz), and  $z$  is the slant range to the ionospheric point. For  $z = 400$  km, the Fresnel dimension is 390 m. With 30-s sampling interval, the Nyquist period of ROTI data is 60 s. The scale-length corresponding to ROTI is, therefore, the product of 60 s and the vector sum of the ionospheric projection of the satellite velocity and the drift of the ionospheric irregularities. The velocity component perpendicular to the propagation path to the GPS satellite which controls the temporal structure of ROT needs to be evaluated. For different GPS satellites with varying satellite trajectories, the ionospheric projection of the satellite velocity is different and, as such, even for the same irregularity drifts, the scale-length of ROTI for different satellites will be different. The effects of the ionospheric motion also need to be considered which, in the equatorial region, varies nominally from  $150 \text{ m s}^{-1}$  towards the east in the early evening hours to about  $30 \text{ m s}^{-1}$  to the east around midnight. Overall, the scale-length for ROTI will be larger for satellites with higher velocities and for higher ionospheric drifts.

The scale-length corresponding to S4 will not vary perceptibly for different satellites since the Fresnel dimension has weak dependence on the slant range to the ionospheric penetration point. Since the power spectral density is higher at larger scale-lengths due to the power law type of irregularity spectrum, the ratio of ROTI/S4 will be higher for satellites with higher projected velocities. Overall, the variations in the scale-length of ROTI, due to variations of the projected satellite velocity in the ionosphere and the irregularity drift, control in a major way the ratio of ROTI/S4.

### 3. Summary

The rate of change of TEC (ROT) and the rate of change of TEC index (ROTI) that can be obtained from widely dispersed IGS stations performing two-frequency GPS satellite observations can be used, especially in the equatorial region, as an indicator of the presence of scintillation causing small-scale ionospheric irregularities. This is a result of the small magnitude of zonal drifts in the equatorial ionosphere.

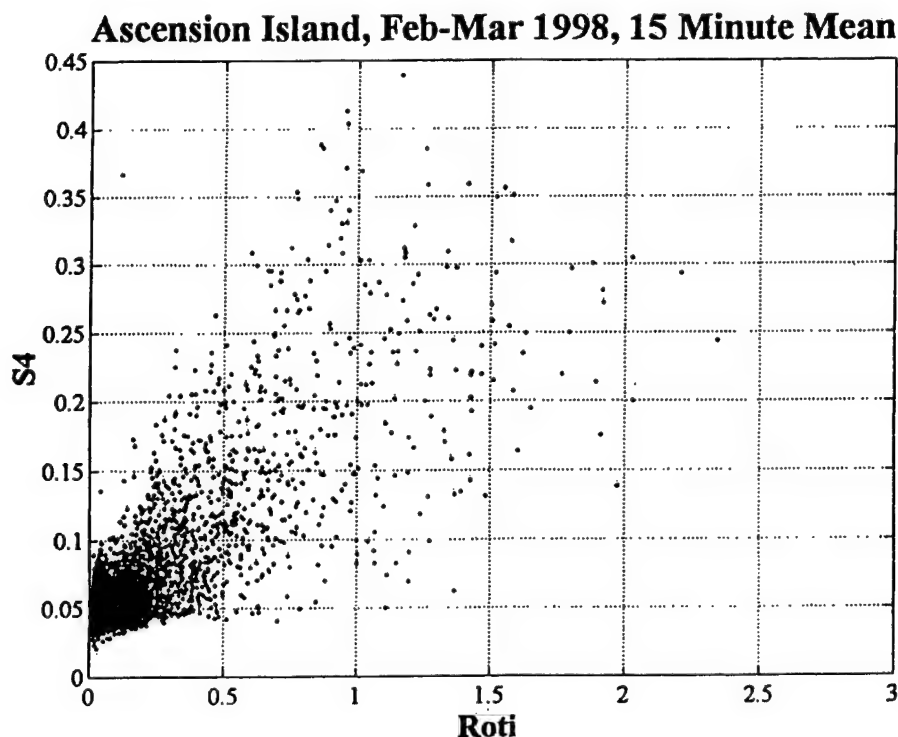


Fig. 4. Scatter plot of ROTI, the standard deviation of the rate of change of the total electron content and the amplitude scintillation index, S4, at GPS L1 (1.575 GHz) frequency.

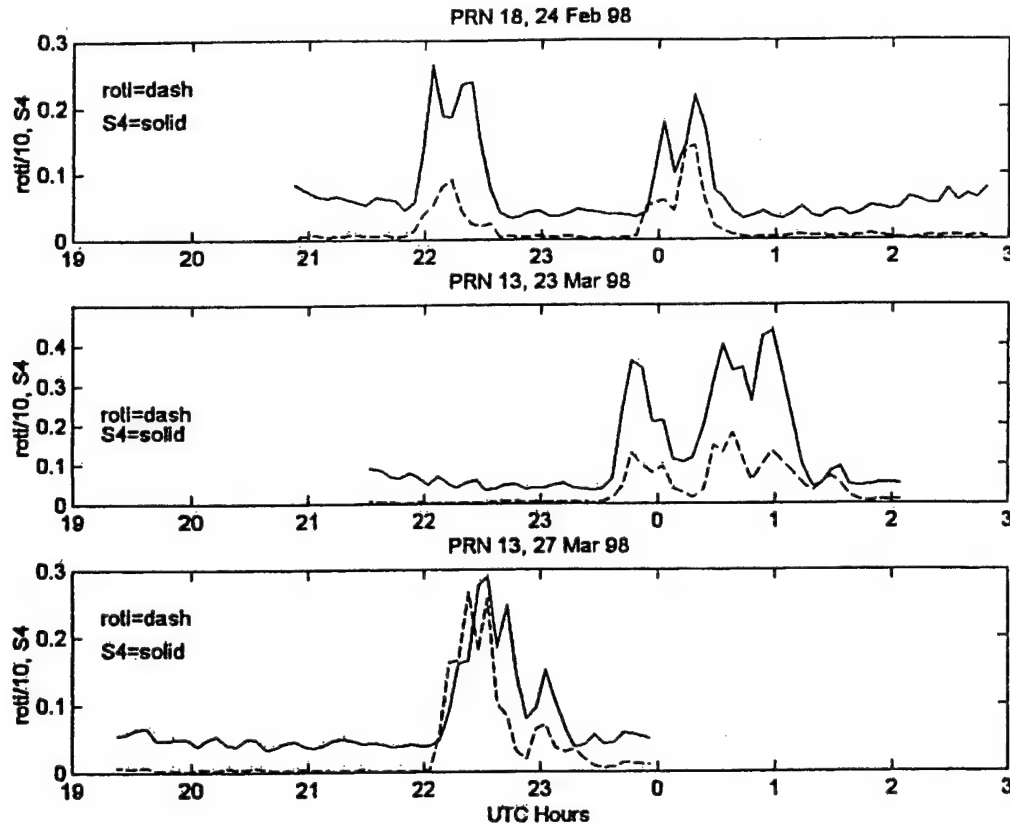


Fig. 5. Illustrates the universal time variations of ROTI, the standard deviation of the rate of change of TEC, and the amplitude scintillation index, S4, (a) in the top panel for PRN 18 on 24 February 1998, (b) in the second panel for PRN 13 on 23 March 1998, (c) in the third panel for PRN 13 on 27 March 1998.

sphere and the co-existence of large and small-scale irregularities in equatorial irregularity structures, at least during the pre-midnight period. In the post-midnight period, small Fresnel scale irregularities decay due to increased diffusion so that large scale (ROT and ROTI) irregularities may be detected without any associated amplitude scintillation.

It is difficult to obtain quantitative estimates of scintillation from an analysis of ROTI. The satellite velocity projected in the ionosphere and the velocity of the ionospheric irregularities control in a major way the ratio of ROTI/S4 since the variation of the Fresnel dimension is rather small. At high latitudes, the ionospheric motion during active conditions may approach speeds of a few  $\text{kms}^{-1}$ . As a result, the ratio of ROTI/S4 at high latitudes may be considerably larger than that in the equatorial region even though the small-scale irregularities are more intense at equatorial latitudes.

#### Acknowledgements

The authors wish to thank the Jet Propulsion Laboratory for providing the PRN biases. The work at the Air Force Research Laboratory was partially supported by the AFOSR Task 2310G9.

#### References

- Aarons, J., 1997. Global positioning system phase fluctuations at auroral latitudes. *J. Geophys. Res.* 102, 17,219.
- Aarons, J., Mendillo, M., Yantosca, R., 1996. GPS phase fluctuations in the equatorial region during the MISETA 1994 campaign. *J. Geophys. Res.* 101, 26,851.
- Aarons, J., Mendillo, M., Yantosca, R., 1997. GPS phase fluctuations in the equatorial region during sunspot minimum. *Radio Sci.* 32, 1535.
- Basu, S., Basu, S., Aarons, J., McClure, J.P., Cousins, M.D., 1978. On the co-existence of kilometer- and meter-scale

- irregularities in the nighttime equatorial F-region. *J. Geophys. Res.* 83, 4219.
- Basu, S., Kudeki, E., Basu, S., Valladares, C.E., Weber, E.J., Zengingonul, H.P., Bhattacharyya, S., Sheehan, R., Meriwether, J.W., Biondi, M.A., Kuenzler, H., Espinoza, J., 1996. Scintillations, plasma drifts, and neutral winds in the equatorial ionosphere after sunset. *J. Geophys. Res.* 101, 26,795.
- Doherty, P., Raffi, E., Klobuchar, J., El-Arini, M.B., 1994. Statistics of time rate of change of ionospheric range delay. In: *Proceedings of ION GPS-94, Part 2*, Salt Lake City 1589 pp.
- Groves, K.M., Basu, S., Weber, E.J., Smitham, M., Kuenzler, H., Valladares, C.E., Sheehan, R., Mackenzie, E., Secan, J.A., Ning, P., McNeill, W.J., Moonan, D.W., Kendra, M.J., 1997. Equatorial scintillation and systems support. *Radio Science* 32, 2047.
- Kelley, M.C., 1989. *The Earth's Ionosphere*. Academic Press, San Diego, California 71 pp.
- McClure, J.P., Hanson, W.B., Hoffman, J.H., 1977. Plasma bubbles and irregularities in the equatorial ionosphere. *J. Geophys. Res.* 82, 2650.
- Mendillo, M., Baumgardner, J., Pi, X., Sultan, P.J., 1992. Onset conditions for equatorial spread-F. *J. Geophys. Res.* 97, 13,865.
- Pi, X., Manucci, A.J., Lindqwister, U.J., Ho, C.M., 1997. Monitoring of global ionospheric irregularities using the worldwide GPS network. *Geophys. Res. Lett.* 24, 2283.
- Rishbeth, H., 1981. The F-region dynamo. *J. Atmos. Terr. Phys.* 43, 387.
- Tsunoda, R.T., 1980. Backscatter measurements of 11 cm equatorial spread F irregularities. *Geophys. Res. Lett.* 7, 848.
- Wanninger, L., 1993. Ionospheric monitoring using IGS data. In: *Proceedings of the 1993 Berne IGS Workshop, International GPS Service for Geodynamics, Berne, Switzerland, March 25–26*.
- Woodman, R.F., LaHoz, C., 1976. Radar observations of F-region equatorial irregularities. *J. Geophys. Res.* 81, 5447.



## Longitude structure of ionospheric total electron content at low latitudes measured by the TOPEX/Poseidon satellite

J. A. Vladimer, P. Jastrzebski, and M. C. Lee

Department of Electrical and Computer Engineering, Boston University, Boston, Massachusetts

P. H. Doherty and D. T. Decker

Institute for Scientific Research, Boston College, Newton, Massachusetts

D. N. Anderson

Space Vehicles Directorate, Air Force Research Laboratory, Hanscom Air Force Base, Massachusetts

**Abstract.** The longitude structure of ionospheric total electron content (TEC) at low latitudes has been evaluated using the NASA/Centre Nationale d'Etudes Spatiales TOPEX/Poseidon satellite. The TEC data set is given by the ionospheric range correction, which is computed from TOPEX dual-frequency altimeter measurements. The satellite's orbit allows analysis of vertically measured TEC values at approximately 30° intervals of longitude across the world at local time differences of only 6–12 min. Patterns of longitudinal dependence of the equatorial anomaly were observed during the equinoxes, summers, and winters of 1993, 1994, and 1995. TOPEX observations reveal occurrence of relative maximum anomaly TEC values in the Indian/Asian longitude sector. This dominance in TEC is seen most consistently in the Asian Southern Hemisphere. Also, a relative decrease in anomaly TEC values is evident in the western American region, which is observed primarily during equinox and winter. This configuration of the equatorial anomaly TEC is observed on a day-to-day basis at particular periods of local time. Global theoretical ionospheric model results are presented in an attempt to reproduce the distinctive longitude structure. Variability in  $E \times B$  vertical drift velocity within specific longitude sectors is shown to be a primary factor in the longitude dependence of equatorial anomaly TEC.

### 1. Introduction

The forecasting of ionospheric total electron content (TEC) is of significant importance to the consistent, precise operation of ground-based and space-based systems involving radio wave signal propagation. Satellite communication, aircraft and space vehicle positioning, and surveillance systems for both defense and commercial uses require ionospheric TEC calibration. It is difficult to provide accurate predictions of TEC at low latitude due to the large spatial and temporal variations of the ionosphere in equatorial regions. Large values of TEC are observed within 30° latitude to the north and south of the magnetic equator as a result of the formation of the electromagnetic phenomenon known as the equatorial anomaly [Appleton, 1946]. These bilateral en-

hancements are formed by the perpendicular electrodynamic ( $E \times B$ ) uplifting of the  $F$  region plasma in combination with the parallel plasma flow due to nonelectromagnetic forces of gravity and pressure gradients. The diurnal variation in electric field strength and ionospheric plasma density is believed to be caused by an increase in the thermospheric winds in the  $F$  region, which create ion and electron separation. Currents develop, and in response an electrostatic field is generated and interacts with the Earth's magnetic field, causing vertical plasma drifts [Anderson, 1981, and references therein]. Extreme day-to-day fluctuations in the equatorial anomaly have been observed, as well as variability with respect to time of day, season, longitude, solar cycle, and magnetic activity.

The NASA/Centre Nationale d'Etudes Spatiales (CNES) TOPEX/Poseidon satellite provides worldwide over-ocean values of vertical TEC within a longitude range of 0°–360° and a latitude range of

Copyright 1999 by the American Geophysical Union.

Paper number 1999RS900060.  
0048-6604/99/1999RS900060\$11.00

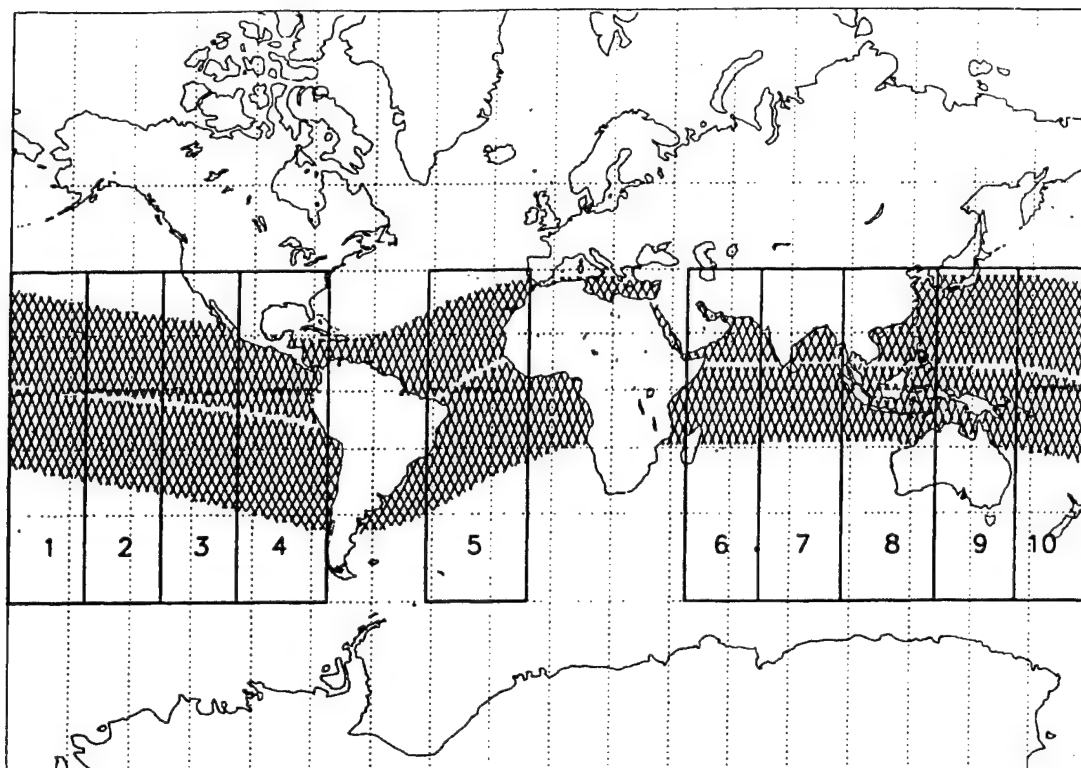


**Figure 1.** TOPEX coverage at low magnetic latitude is shown. Each of 10 defined bins contains the data from the same 10 days and local times.

$-66^{\circ}$ – $66^{\circ}$ . In this study the TOPEX data set was utilized to evaluate the low-latitude longitudinal structure of the ionosphere in terms of average values of TEC and repeated patterns of behavior of the equatorial anomaly. Ionospheric model simulations

were generated in an attempt to reproduce the observed consistent configurations of TEC within specific longitude sectors. Models employed were the Air Force Research Laboratory parameterized ionospheric model (PIM) and the global theoretical ion-

**Table 1.** Descriptions of Bins in Terms of Longitude, Latitude, and Declination Range at the Magnetic Equator

Longitude Sector	TOPEX Bin	Geographic Longitude Range (Magnetic Equator Crossing)	Geographic Latitude Range	Declination Range
Pacific	1	180°E–206°E	+1 to –1	11°E–12°E
	2	206°E–232°E	–1 to –5	10°E–12°E
American	3	232°E–255°E	–5 to –9	6°E–10°E
	4	255°E–285°E	–9 to –14	1°E–6°E
Brazilian	5	318°E–352°E	+4 to +11	8°W–10°W
Indian/Asian	6	45°E–70°E	+8 to +9	8°W–10°W
	7	70°E–97°E	+8 to +10	2°W–8°W
	8	97°E–128°E	+8 to +10	2°W–3°E
	9	128°E–155°E	+7 to +8	3°E–8°E
Pacific	10	155°E–180°E	+1 to +7	8°E–11°E

Bins are described in terms of longitude sector. The ranges of geographic longitude, geographic latitude and declination are referenced to the magnetic equator.

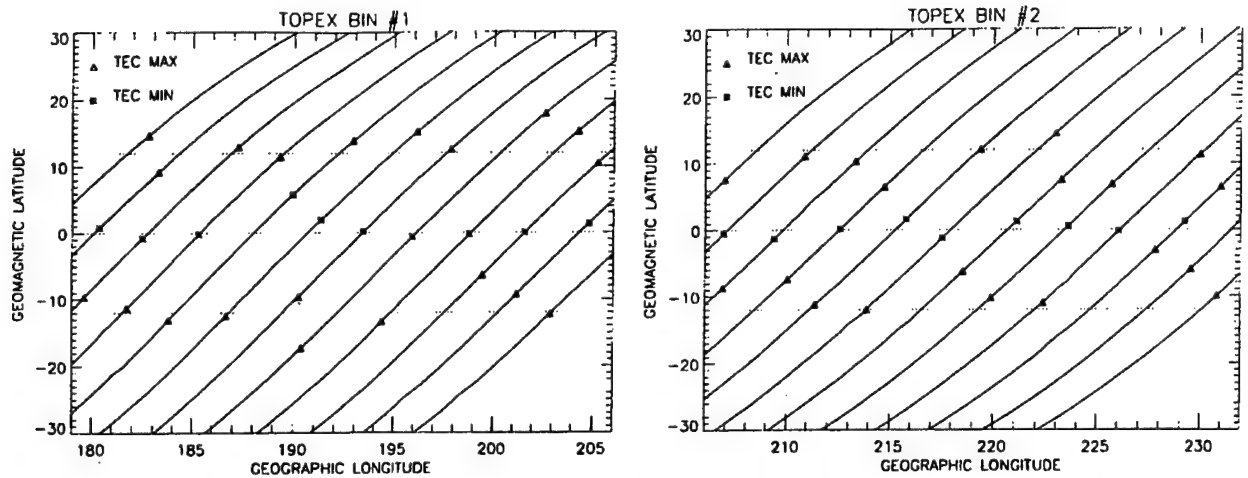


**Figure 2a.** TOPEX passes within adjacent bins 1 and 2 are shown. Equatorial anomaly crest and trough values are represented by triangles and stars, respectively.

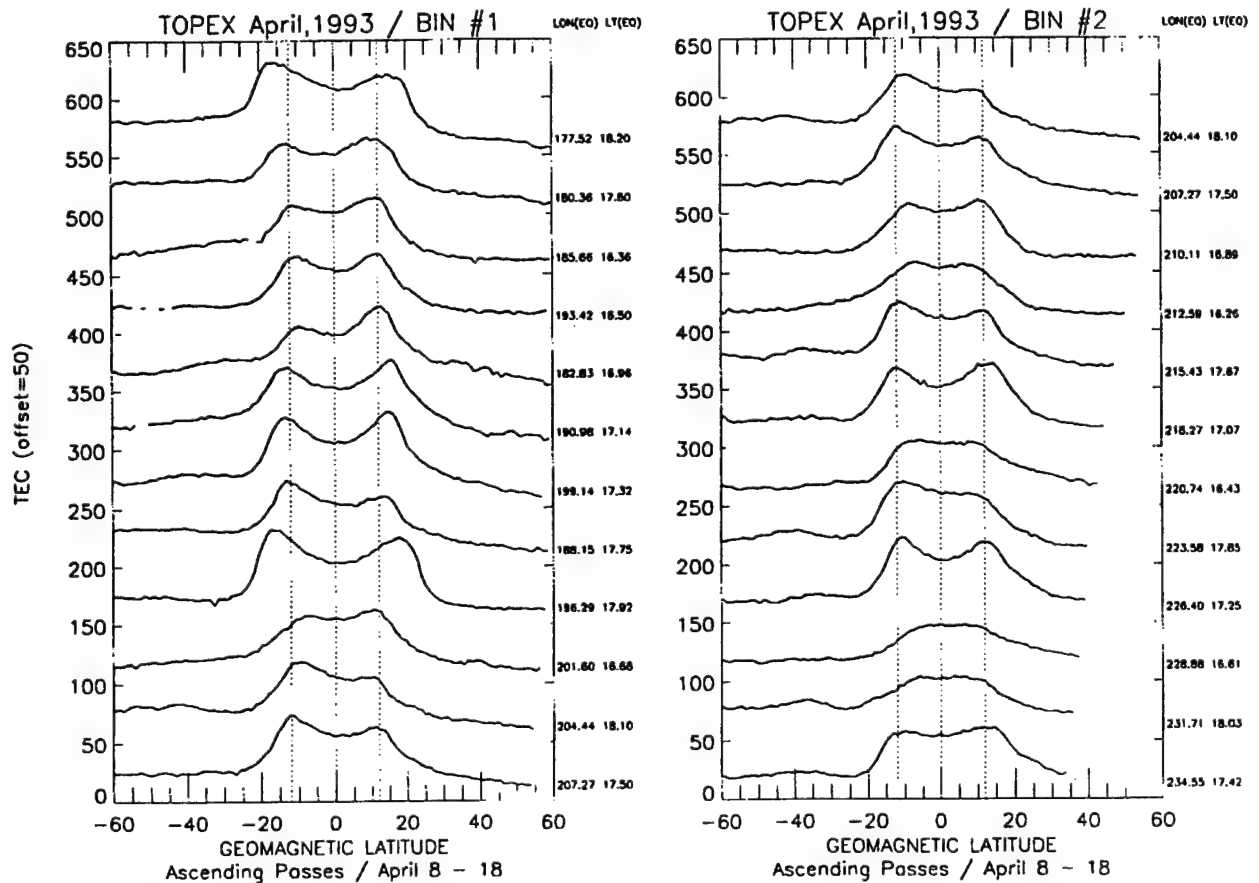


**Figure 2b.** Data from bins 1 and 2 illustrate the differences between anomaly shape and variability within bins of close proximity.

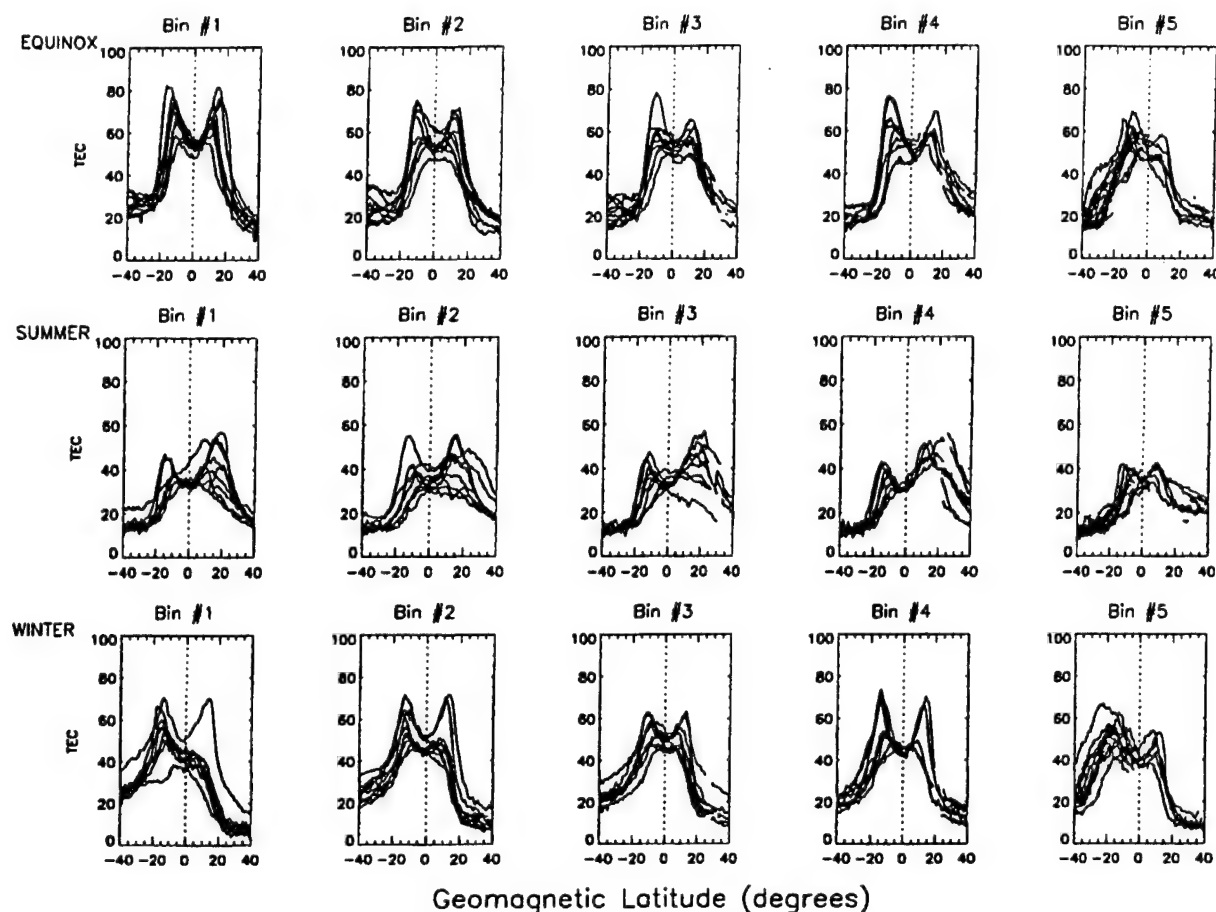


Figure 3a. Scatterplots from bins 1–5 show data during spring equinox, summer, and winter of 1993.

ospheric model (GTIM). These theoretical models were chosen for their ability to test the sensitivity of the ionosphere to variations in inputs such as  $\mathbf{E} \times \mathbf{B}$  vertical drift velocity, ion and electron temperatures, and other specific geophysical conditions which are described in section 3. The TOPEX coverage at equatorial anomaly latitudes and the defined longitude bins used for this work are shown in Figure 1. Table 1 describes each bin in terms of the longitude, latitude, and declination range at the magnetic equator. Specifically, the range of geographic longitude is given by the TOPEX pass crossings at the geomagnetic equator. The geographic latitude extent of the magnetic equator is indicative of the difference between the geographic and geomagnetic equators. Finally, the range of values and direction of declination at the magnetic equator within each bin are listed.

Previous studies have revealed discrepancies in TEC values within various longitude sectors using data collected at low-latitude ground stations [Walker, 1981; Su *et al.*, 1995]. Probable reasons for the longitudinal variability at these specific latitudes have been presented. Contributing factors include (1) the geomagnetic equator not being parallel to the geographic equator, (2) variations in magnetic declination, and (3) variations in electric and magnetic fields. The variability in range of the Earth's magnetic field over the magnetic dip equator has been described as the cause of the variation of equatorial ionospheric conductivity with longitude [Rastogi, 1962]. The resulting  $\mathbf{E} \times \mathbf{B}$  vertical drift and neutral wind velocities are described as the primary drivers that dictate the movement of ionization and directly influence the development of the equatorial anomaly. More recent studies have used TOPEX data to evaluate specific

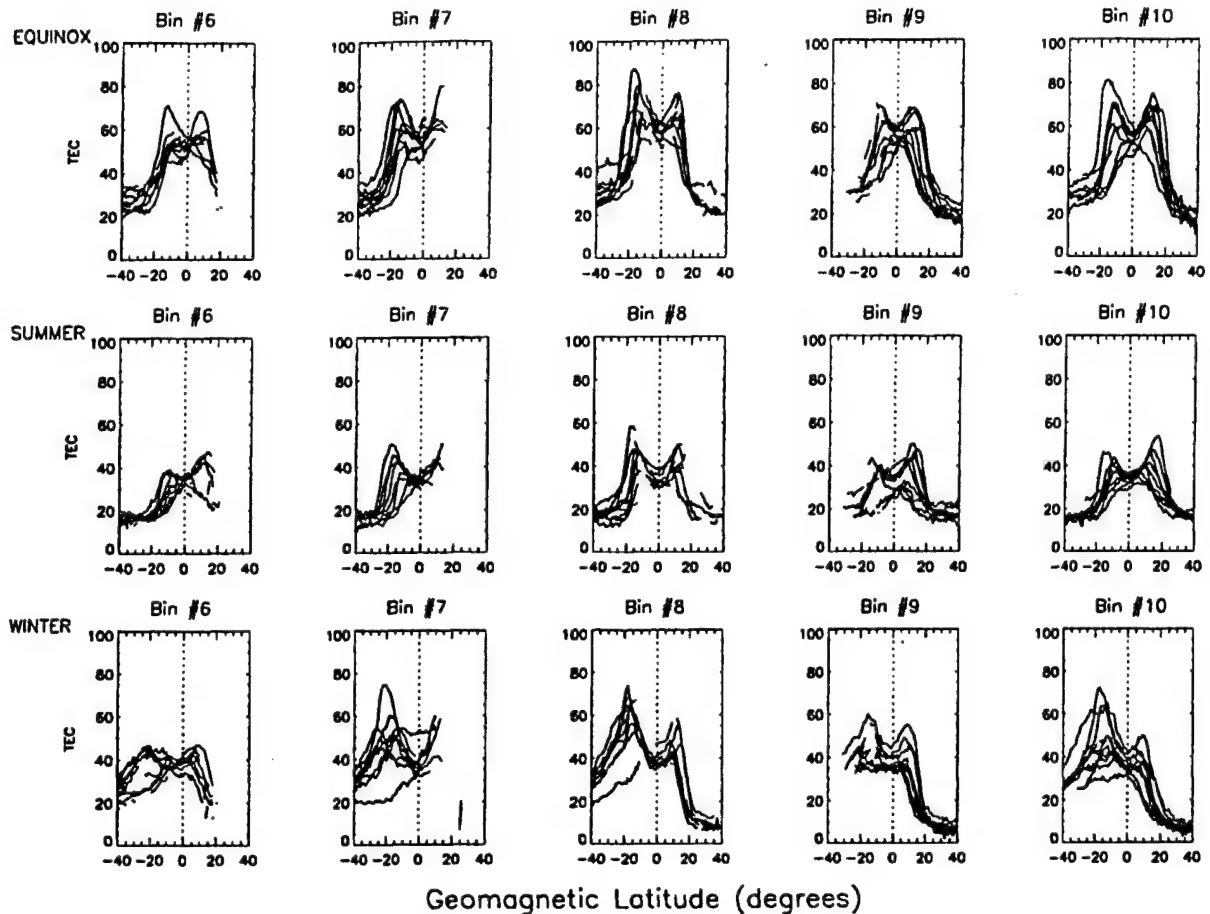


Figure 3b. Scatterplots from bins 6–10 show data during spring equinox, summer, and winter of 1993.

events and longitude structure during a particular seasonal period [Forbes *et al.*, 1997]. Additional works compare TOPEX to the International Reference Ionosphere (IRI) model results, with emphasis on interhemispheric asymmetry of the equatorial anomaly [Bilitza *et al.*, 1996]. The present study evaluates low-latitude TOPEX data during the periods of equinox, summer, and winter of 1993, 1994, and 1995. The seasonal focus of the model simulations is spring equinox 1993 at solar moderate conditions and relatively low magnetic activity ( $K_p \leq 4$ ). Simple modifications made to the vertical drift inputs of the GTIM provide low-latitude TEC values that approximate the TOPEX time-averaged longitude configuration. In section 2 the TOPEX orbit and dual-frequency altimeter measurements are reviewed, followed by a discussion of the limitations in the application of the TOPEX data to ionospheric research. Model calcu-

lations of TEC values and the comparison with the TOPEX data are presented in section 3. Discussion is given in section 4, and finally, conclusions are drawn in section 5.

## 2. Measurements and Observations

### 2.1. TOPEX TEC Measurements

The TOPEX/Poseidon satellite was launched in 1992 for the study of global ocean dynamics. The satellite has an orbital altitude of 1336 km (equatorial reference) and an inclination of  $66^\circ$ . One full revolution, which is achieved in 112 min, consists of two passes: An ascending pass spans  $-66^\circ$  to  $66^\circ$  latitude; a descending pass spans  $66^\circ$  to  $-66^\circ$  latitude. Consecutive revolutions are offset to the west by approximately  $30^\circ$ . This TOPEX coverage provides the ability to observe TEC variability across the world in 1 day at

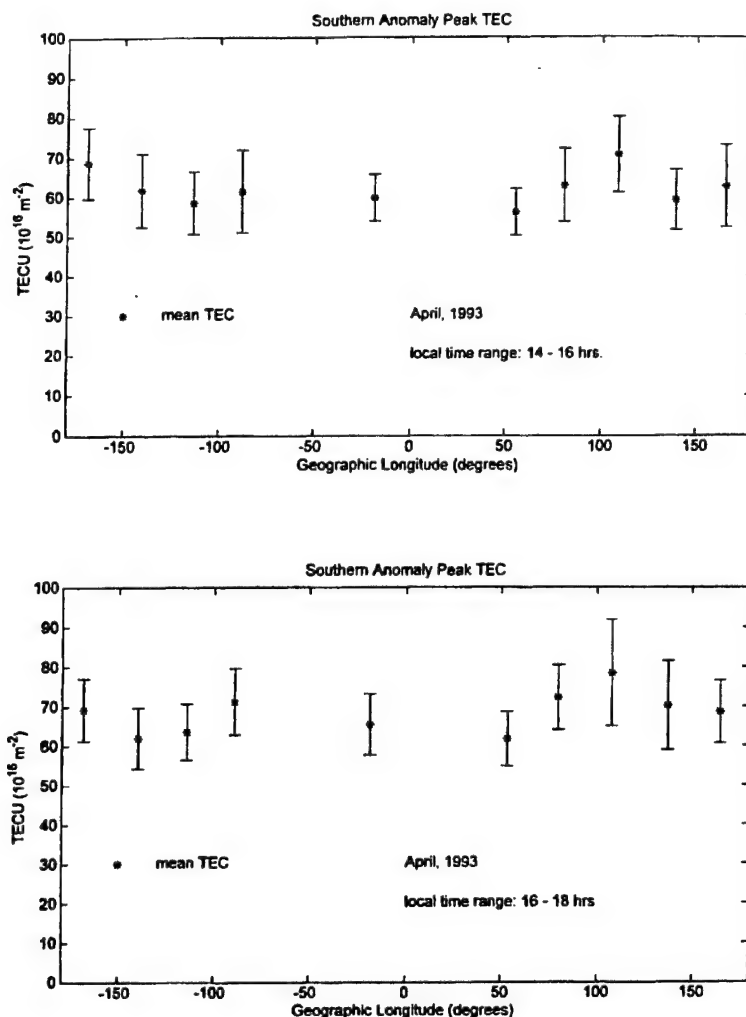


**Figure 3c.** Standard deviations are plotted with the mean total electron content (TEC) of the southern anomaly peaks. The bottom plot corresponds to Figures 3a and 3b (1600–1800 LT, April 1993). The top plot represents data from 1400–1600 LT.

30° intervals at approximately the same local time. There are 127 revolutions (254 passes) in a TOPEX cycle, which covers the same surface tracks every 10 days. The differential between UT and LT, in combination with the "overlap" required to accomplish ice-free ocean coverage, results in a 2-hour loss of local time for each consecutive 10 days of universal time.

TOPEX orbital speed is  $7.2 \text{ km s}^{-1}$ , and altimeter measurements are obtained at a rate of one per second. The ionospheric correction and vertical TEC are computed from TOPEX dual-frequency range

measurements (5.3 GHz, C band, and 13.6 GHz, Ku band). The measured range is given by

$$R_{\text{measured}} = R_{\text{true}} + \Delta R_{\text{ionosphere}} + \Delta R_{\text{other}} \quad (1)$$

where  $R_{\text{true}}$  is the true range,  $\Delta R_{\text{ionosphere}}$  is the ionospheric range error at the frequency, C or Ku and  $\Delta R_{\text{other}}$  are the range errors due to other frequency-dependent and non-frequency-dependent sources. The range error,  $\Delta R_{\text{ionosphere}}$  (centimeters), has the form  $b_C/f_C^2$  or  $b_{\text{Ku}}/f_{\text{Ku}}^2$ , where  $b_i$  equals  $40.3 \text{ TEC}_{\text{vertical}}$ , with  $f_i$  expressed in gigahertz. The measured range



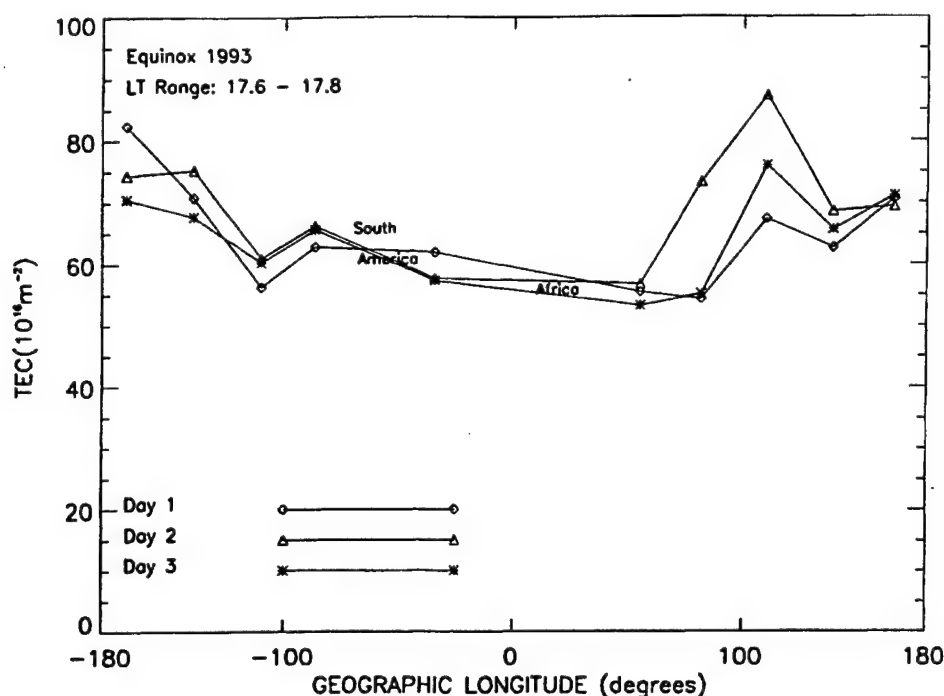


Figure 4. Data from 3 days at approximately the same local time are represented from each bin. Southern anomaly TEC values reveal a repeated longitude configuration.

equations for C and Ku bands provide an expression for the differential ionospheric correction:

$$\Delta R_{\text{ionosphere}} = [40.3 \text{ TEC}_{\text{vertical}}] [(f_{\text{Ku}}^2 - f_{\text{C}}^2) / f_{\text{C}}^2 f_{\text{Ku}}^2] \quad (2)$$

The vertical TEC follows as

$$\text{TEC}_{\text{vertical}} = \Delta R_{\text{ionosphere}} [f_{\text{C}}^2 f_{\text{Ku}}^2 / (f_{\text{Ku}}^2 - f_{\text{C}}^2) 40.3] \quad (3)$$

One TEC unit (TECU) ( $10^{16} \text{ el m}^{-2}$ ) corresponds to 12.17-mm range error at the given TOPEX altimeter frequencies. The uncertainty in the TOPEX ionospheric correction has been estimated to be approximately 0.5 cm, which corresponds to 0.41 TECU [Imel, 1994].

TOPEX satellite data present limitations in applications to studies involving TEC. Several constraining factors are described as follows:

1. The instruments do not obtain readings over land, resulting in discontinuities in the data set.
2. Because of the  $66^\circ$  inclination of the orbit, careful analysis of data from individual satellite passes is required. Differences in longitude (local time) exist between altimeter measurements of the two crests of the equatorial anomaly. The variations in longitude (local time) can range from  $10^\circ$ – to  $15^\circ$ +

( $40$ – min to  $60$ + min) depending on the latitudinal extent of the anomaly.

3. NASA TOPEX and CNES Poseidon share an antenna, which causes 10-day interruptions of the data set.

4. The use of data from a transiting satellite does not allow separation of diurnal from seasonal variability in TEC. For instance, equinox (March, April or September, October) represents 12 hours of local time, while summer (May–August) or winter (November–February) represents 24 hours of local time.

Observations are presented in the next section. Data comparisons which are extended across the 10 bins reveal a trend that is maintained over local time and season.

## 2.2. TOPEX TEC Observations

An example of TOPEX data from April 1993 is shown in Figures 2a and 2b. The data were processed by averaging over  $1^\circ$  of satellite orbit. (One degree corresponds to approximately 16 s of flight and 110 km of ground track.) Figure 2a shows a closer look at bins 1 and 2 in which  $30^\circ \times 30^\circ$  north and south subbins are created and averaged separately to compensate for the inclination of the orbit. The first two

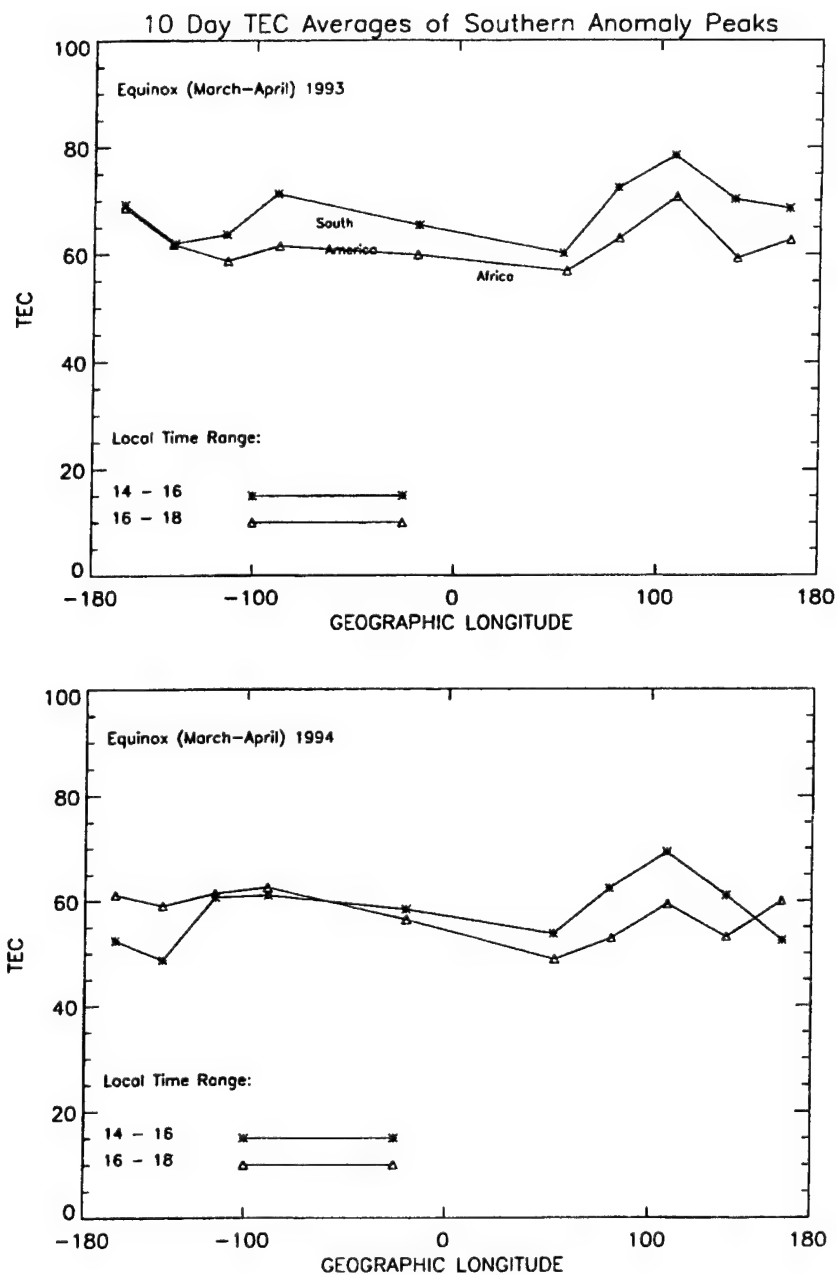


Figure 5. The longitude pattern is evident in the seasons of spring equinox, summer, and winter of 1993, 1994, and 1995.

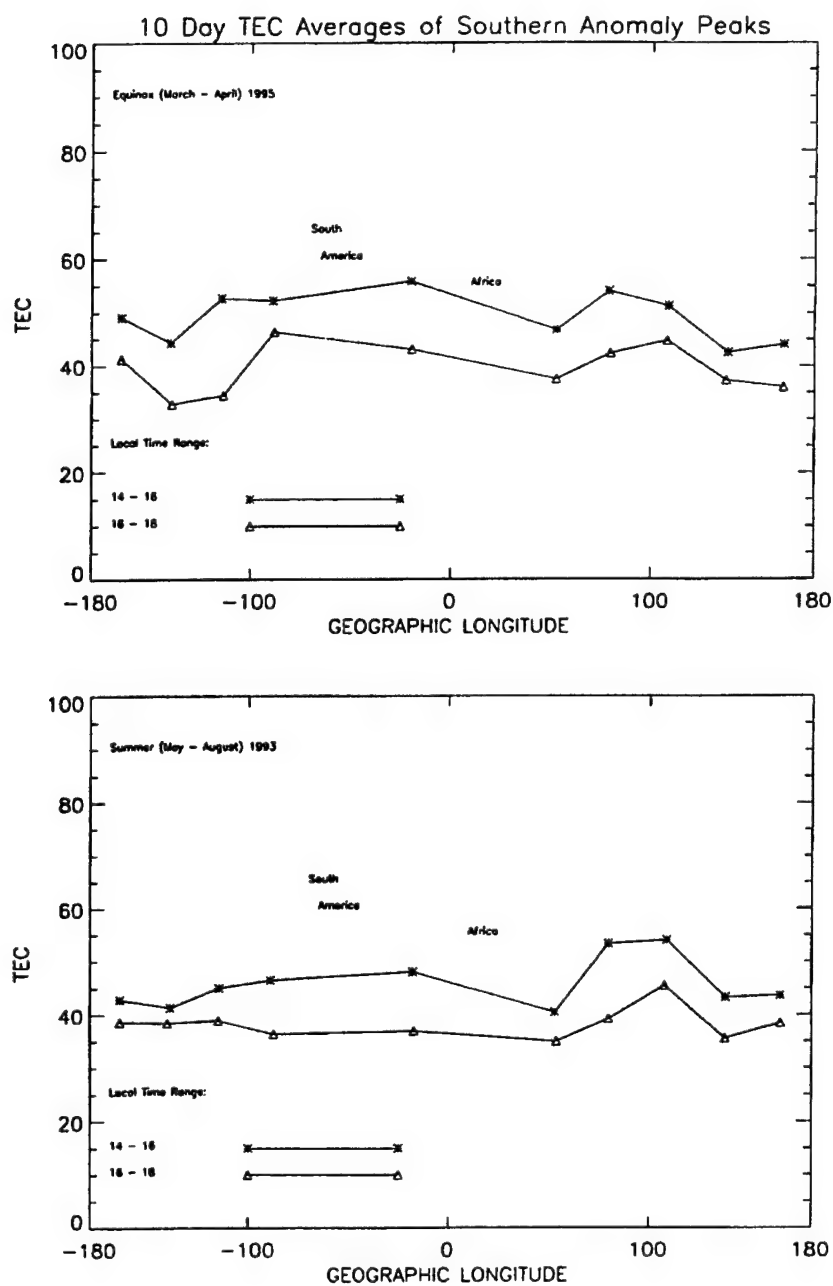


Figure 5. (continued)

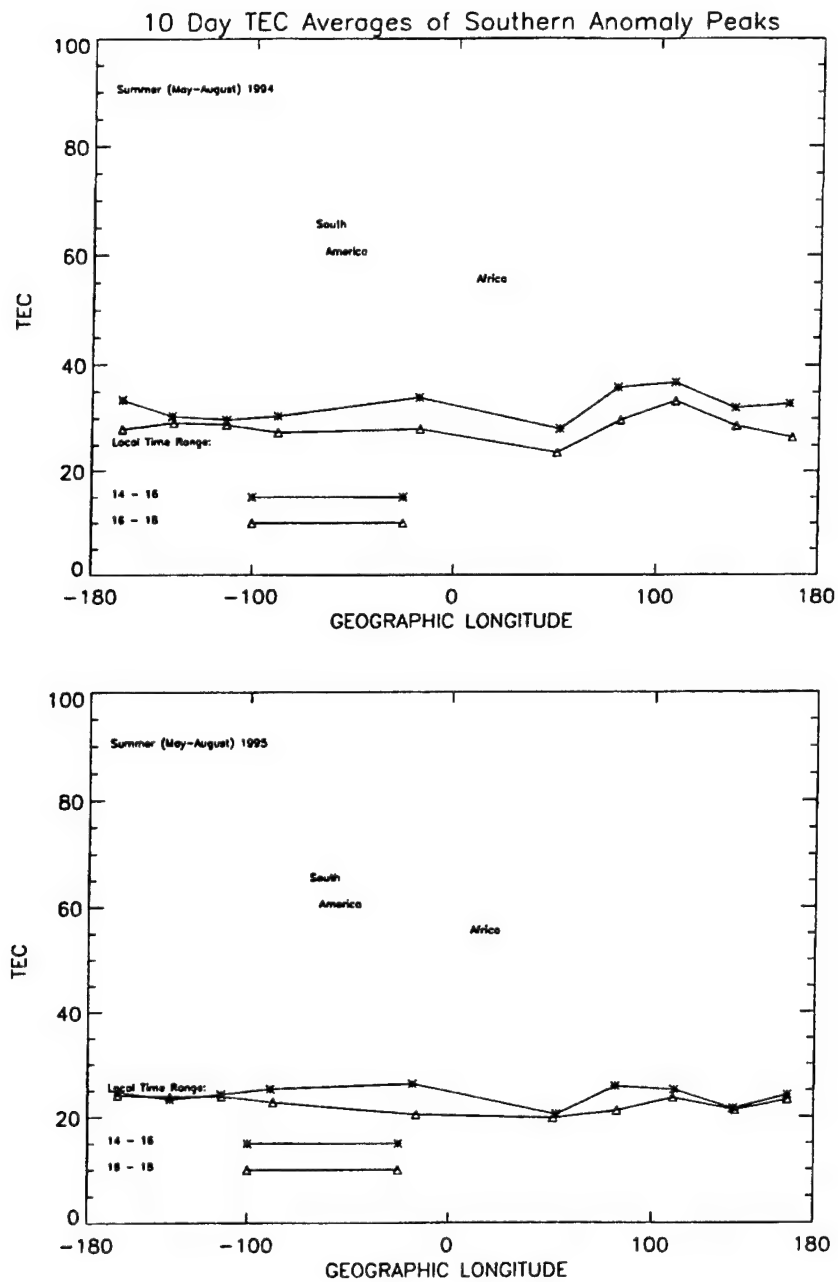


Figure 5. (continued)

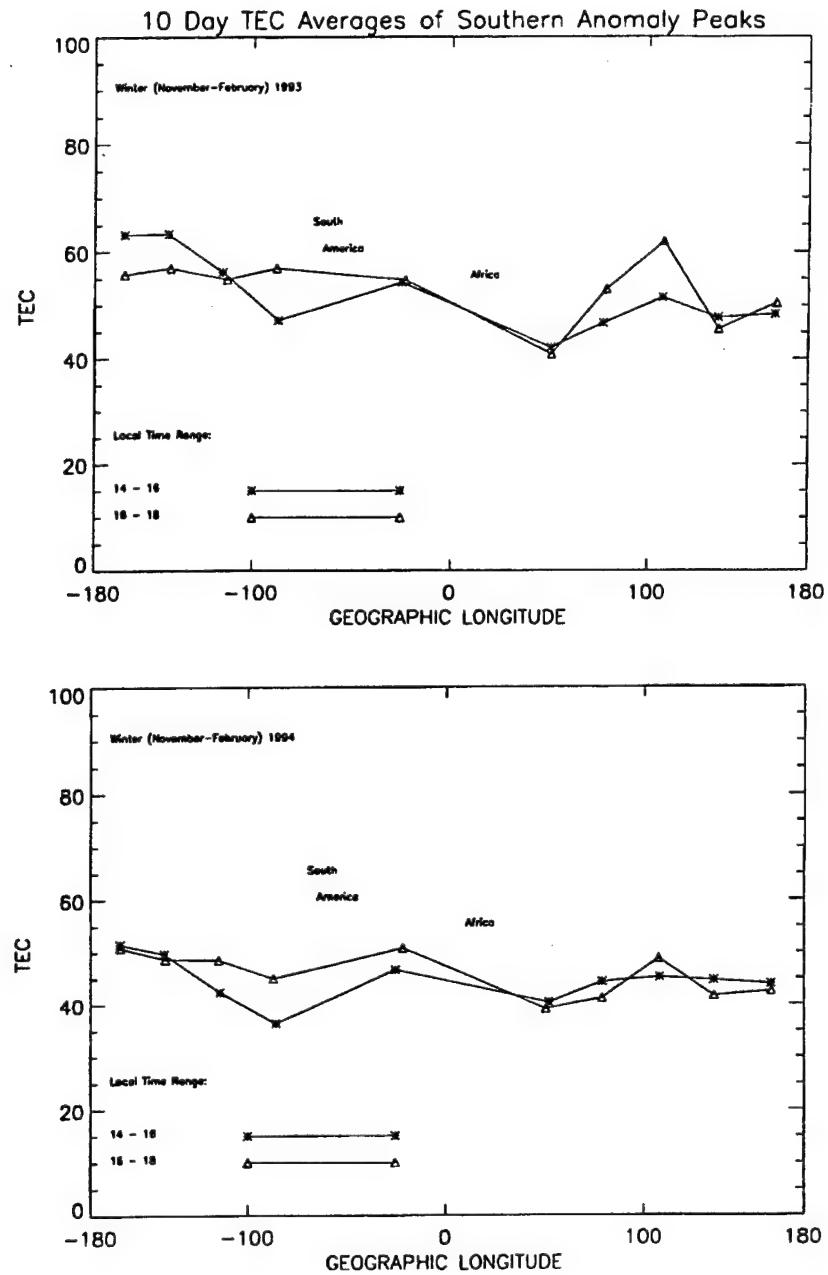


Figure 5. (continued)

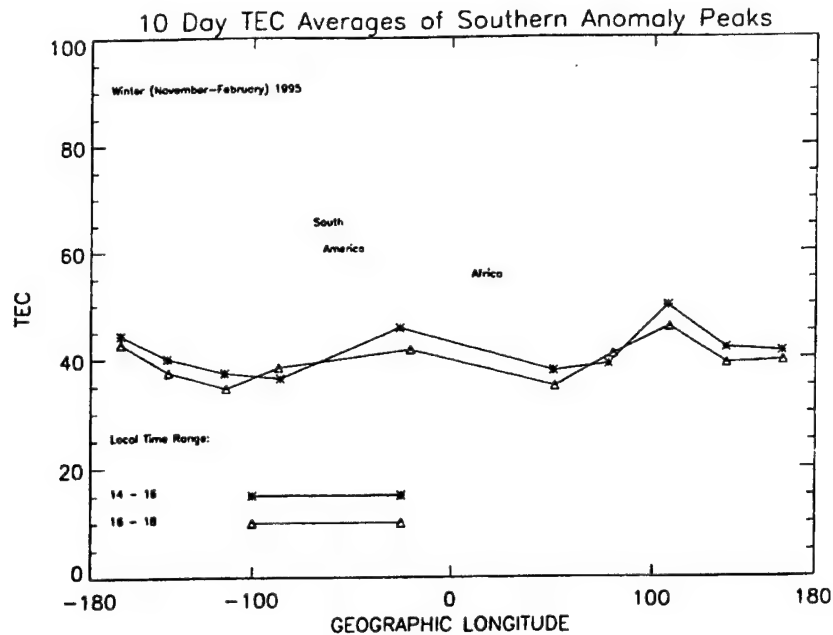


Figure 5. (continued)

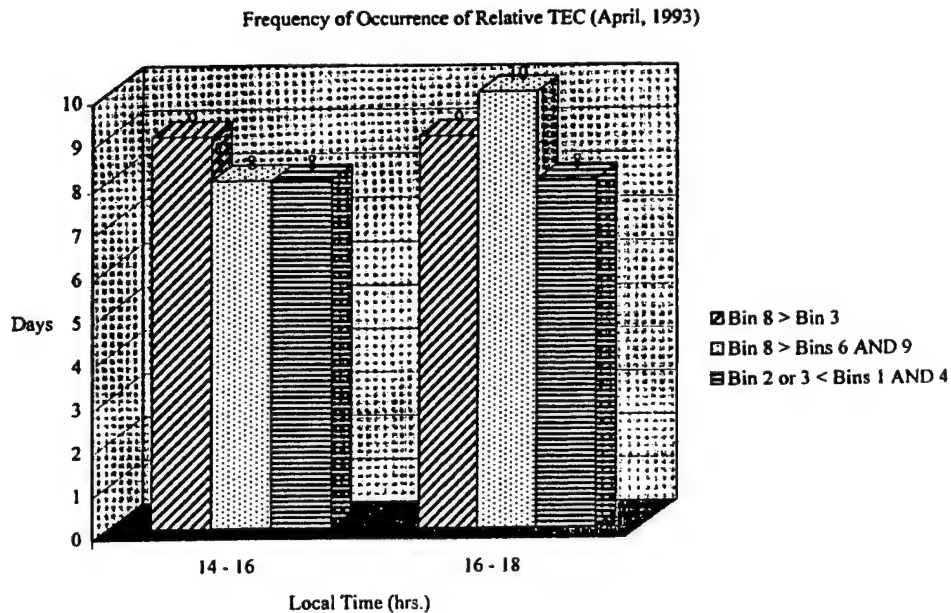
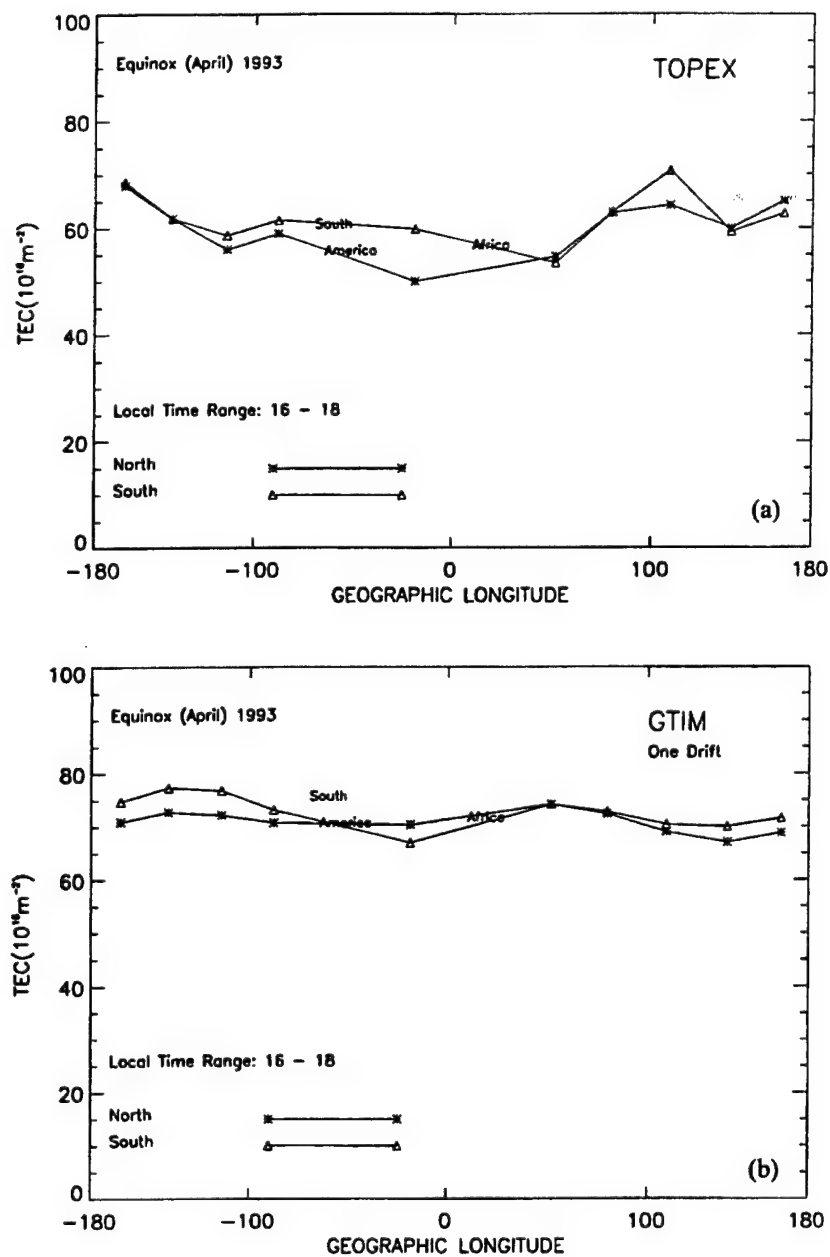


Figure 6. Each bar shows the number of days that one longitude bin's TEC value (southern anomaly peak) is greater or less than that of another bin. This consistent relative TEC pattern is representative of the TOPEX average longitude configuration.





**Figure 7.** TOPEX averages of north and south anomaly peaks during spring equinox at local times between 1600 and 1800 (Figure 7a) are compared with model results from the global theoretical ionospheric model (GTIM) with one drift input (Figure 7b) and GTIM with four drift inputs (Figure 7c).

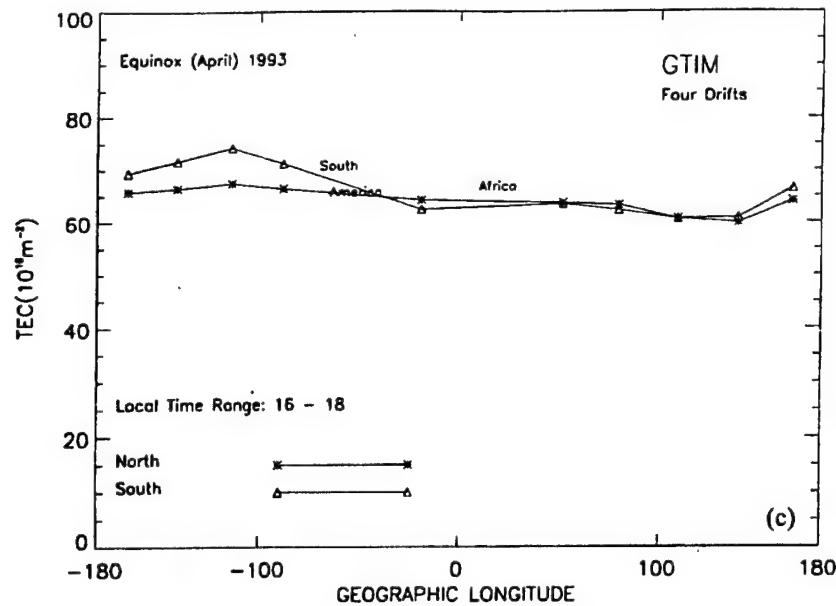


Figure 7. (continued)

passes and the last two passes are same-day passes and are shared with adjacent bins, thereby separating the TEC data (north from south) at bin boundaries. The maximum and minimum points of the equatorial anomaly are indicated symbolically. Lines are drawn at  $\pm 12^\circ$  magnetic latitude to accentuate the difference in latitudinal extent of the anomaly in the adjacent bins 1 and 2. This feature is also evident in Figure 2b, where the passes within each bin are plotted. Other characteristics to be observed are crest-to-trough ratios, hemisphere differences, and TEC gradients. Stronger anomaly formation with higher TEC values, larger gradients, and crest-to-trough ratios are seen in bin 1 compared with bin 2. Hemisphere differences are not significant or consistent in either bin.

Figures 3a and 3b illustrate the variability in TEC during spring equinox (April), summer (August), and winter (December) at 1600–1800 LT within bins 1–5 and bins 6–10, respectively. Several features of the equatorial anomaly can be examined in these scatter-plots. (A compromise in the data occurs in the Northern Hemisphere in bins 6 and 7 due to the presence of landmass.) Common to most longitude bins is the noticeable hemisphere asymmetry in summer and winter. Higher, more variable TEC is observed in the Northern Hemisphere in summer (reference to Northern Hemisphere summer and winter)

and in the Southern Hemisphere in winter, while the equinox period reveals more symmetric anomaly values. The hemisphere asymmetry in TEC is most likely due to changes in strength and direction of neutral wind. A trend of dominant TEC is seen in the Asian Southern Hemisphere (bin 8) during all seasons (see Figure 3b). In addition, a relative decrease in TEC is noticeable in bins 2–3, which is most evident in equinox and winter due to the larger Pacific TEC values observed during these seasons (see Figure 3a).

This longitude trend can be highlighted by focusing on peak TEC measurements within each bin. Data results shown in Figures 3c, 4, and 5 are concentrated in the south where there is the least land interruption of the TEC values. Both plots in Figure 3c show standard deviations of mean peak TEC values (southern anomaly crest) within the 10 longitude bins over two consecutive 10-day periods in April 1993. The bottom plot corresponds to the spring equinox data of Figures 3a and 3b for 1600–1800 LT. The top plot corresponds to April data for 1400–1600 LT. In spite of the expected variability in absolute TEC values, a distinct mean longitude pattern exists. Figure 4 shows TEC peak values of the southern anomaly crest on each of three consecutive days. The longitude pattern clearly is repeated on a day-to-day basis. Figure 6 illustrates the frequency of occurrence of the relative maximum TEC in the Indian/Asian region and the

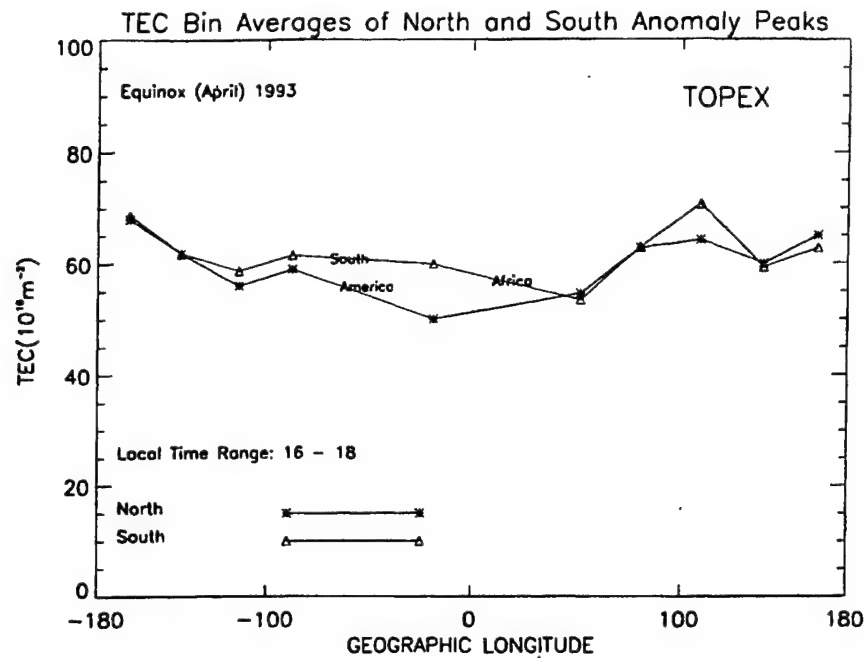


Figure 8a. TOPEX averages from Figure 7 are repeated for model comparison.

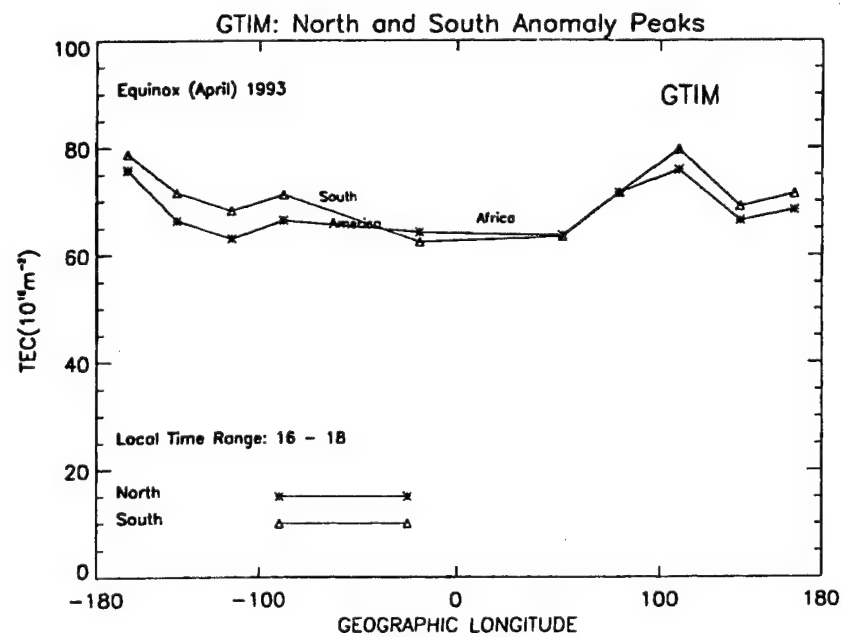
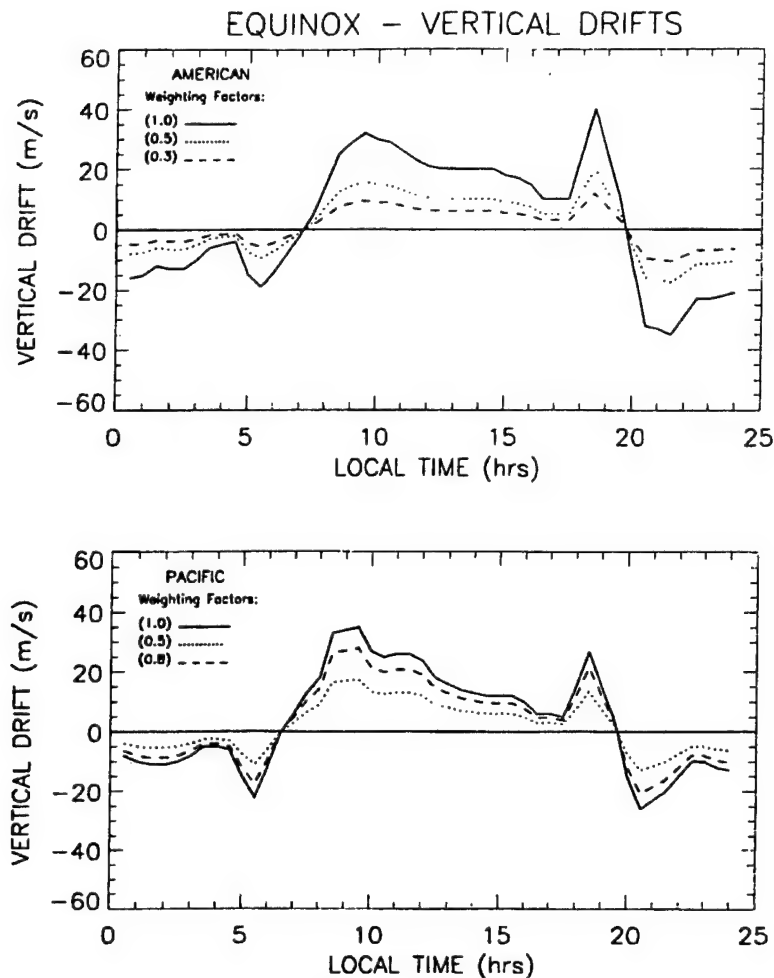


Figure 8b. GTIM results after drift weighting factor manipulation show a longitude pattern similar to TOPEX data.



**Figure 9.** The four empirical drifts from *Fejer et al.* [1995] are shown (solid lines). Half-weighting was required to acquire TEC values comparable to the parameterized ionospheric model (PIM) (dotted lines). Variable weighting achieves results closer to the TOPEX configuration (dashed lines).

relative diminishment of TEC in the western American region for the April periods. Each bar in the plot represents the number of days that one region's peak southern TEC value is greater or less than that of another region. Describing the plot from left to right, the first bar represents bin 8 greater than bin 3; the second bar represents bin 8 greater than both bins 6 and 9; and the third bar represents bin 2 or 3 less than both bins 1 and 4. Results are shown for time ranges of 1400–1600 and 1600–1800 LT. Figure 5 illustrates the longitude behavior of 10-day averaged maximum TEC values of the southern anomaly crest within 10 bins. The configuration of longitude dependence is maintained over a 4- to 6-hour local time range. The analysis is shown for spring equinoxes, summers, and

winters of 1993, 1994, and 1995. The data from 1400–1600 and 1600–1800 LT are shown separately to illustrate that although TEC values change, the overall configuration is similar during both time ranges. The most consistent occurrence of this pattern of TEC is seen during 1400–1800 LT and is altered when earlier and later local times are evaluated. The existence of a relative maximum in bins 7 and 8 and a relative minimum in bins 2 and 3 is evident to a certain extent in all seasons. The feature of stronger Indian/Asian peak values is seen consistently, although it diminishes with later local times and decreasing solar cycle. These results are in agreement with previous studies [*Su et al.*, 1995] which have evaluated summer data from stations near East Asia

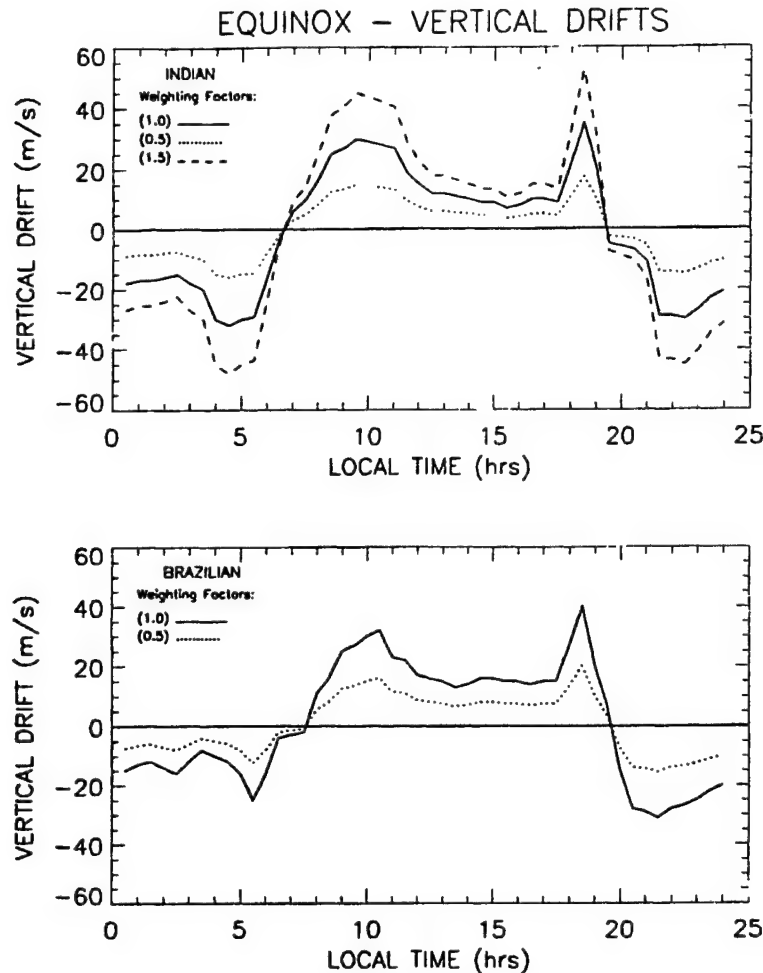
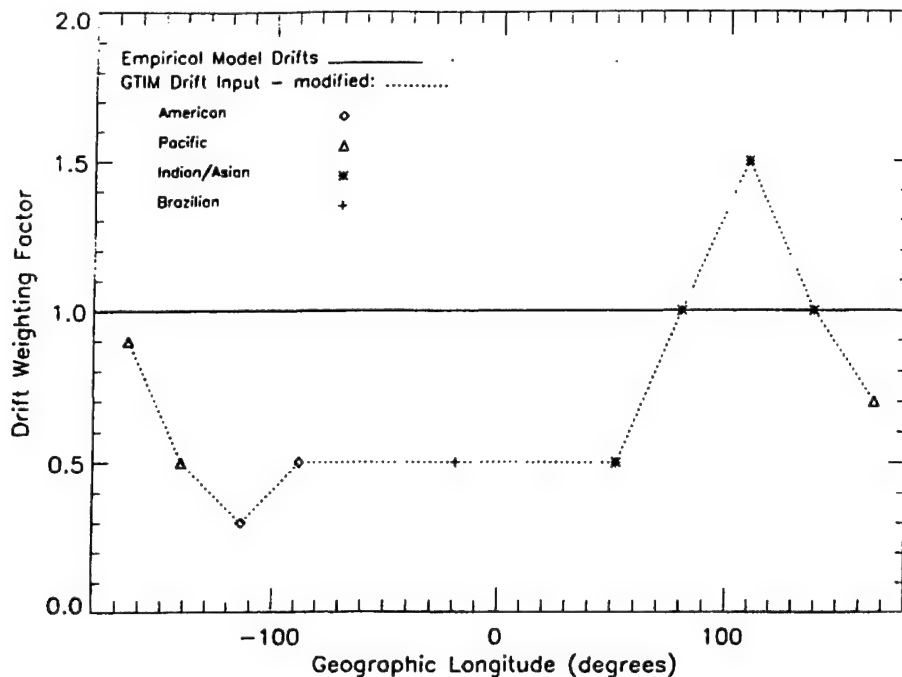


Figure 9. (continued)

and mid-Pacific longitudes. The enhanced TEC values in the Indian region are also consistent with previous findings of a maximum in the strength of the electric field over the magnetic equator in India during the equinox period [Rastogi, 1993]. In addition, Rastogi [1962] has described the intensity of the magnetic field ( $H$ ) as strongest in the Indian region and at a minimum in South America, while the range of  $H$  is greatest in the American region and least in India. The relative minimum trend in the western American/Pacific bins 2 and 3 is most obvious in equinox and, to a lesser extent, in summer due to decreasing TEC in bins 1 and 4. Also, in winter the relative minimum appears to shift toward bins 3 and 4, while bins 1 and 2 are maintained at values comparable to bin 8 in the Indian/Asian region.

### 3. Results of Model Calculations

The global theoretical ionospheric model (GTIM) is designed to generate the ionospheric conditions based on several parameters given for a specific day. This model uses ion continuity and momentum equations to calculate electron density profiles (EDPs) and total electron content (TEC) for a particular longitude and day of the year. Specifically, for the  $F$  region, the time-dependent ion ( $O^+$ ) continuity equation is utilized. The component parallel to the electric field velocity is derived from electron and ion equations; the perpendicular component is the  $\mathbf{E} \times \mathbf{B}$  drift. In addition to the electric field, the input parameters for the model include the neutral constituents, temperature, and winds. The ion and electron tempera-



**Figure 10.** Longitude sector vertical drifts and weighting factors are indicated for each of the 10 TOPEX bins. Required modification of weighting factors is shown. These factors were used for drift inputs to GTIM, giving results that approach TOPEX observations.

tures, solar EUV fluxes, and values of the magnetic field are also utilized [Decker *et al.*, 1997]. The parameterized ionospheric model (PIM) is a computationally efficient ionospheric and plasmaspheric model developed by the Air Force Research Laboratory to aid a global parameterized real-time ionospheric specification model (PRISM). The ionospheric part of the model consists of a database of results of several regional theoretical ionospheric models and a FORTRAN code designed to extract this data for particular geophysical conditions and spatial coordinates. While the ionospheric part of the model is based solely on theoretical climatology, the plasmaspheric portion of PIM is based on the Gallagher plasmaspheric ( $H^+$ ) empirical model. The geophysical parameters required are date and time, magnetic activity index ( $K_p$ ), orientation of the interplanetary magnetic field, solar activity indices ( $F_{10.7}$ ), and sunspot number (SSN). The model calculates the EDPs and TEC between the altitude of 90 and 25,000 km [Daniell *et al.*, 1995].

The results shown in Figure 7 are focused on 1993 spring TEC data. Averages of both the south and north maximum TEC values (i.e., the anomaly crests)

are presented for 1600–1800 LT. TOPEX (Figure 7a) shows hemisphere differences, which are most noticeable in bins 5 and 8, with small asymmetries in bins 3, 4, and 10. GTIM was run at approximately the average bin longitudes, first utilizing one drift input (Figure 7b) for all 10 longitude regions and then using four vertical drift inputs (Figure 7c). These average drifts were developed from AE-E satellite data which were collected at moderate to high solar flux conditions [Fejer *et al.*, 1995]. The weighting factor for these four longitude sector drifts was decreased by 0.5 in order to obtain GTIM results that were comparable to TOPEX TEC values, but longitude features were not reproduced. Most remarkable is the lack of TEC enhancement in the Pacific bin 1 and in the Indian/Asian bins 7 and 8. Overall, TEC values are higher than TOPEX, with indications of hemisphere asymmetry primarily in the Pacific and American sectors. PIM results (not shown) demonstrate a longitude pattern similar to GTIM, with a slight decrease in TEC and minimal hemisphere asymmetry. There is an insignificant difference in the GTIM outputs resulting from the use of one drift or four drifts. This outcome is expected due to the lack of longitude



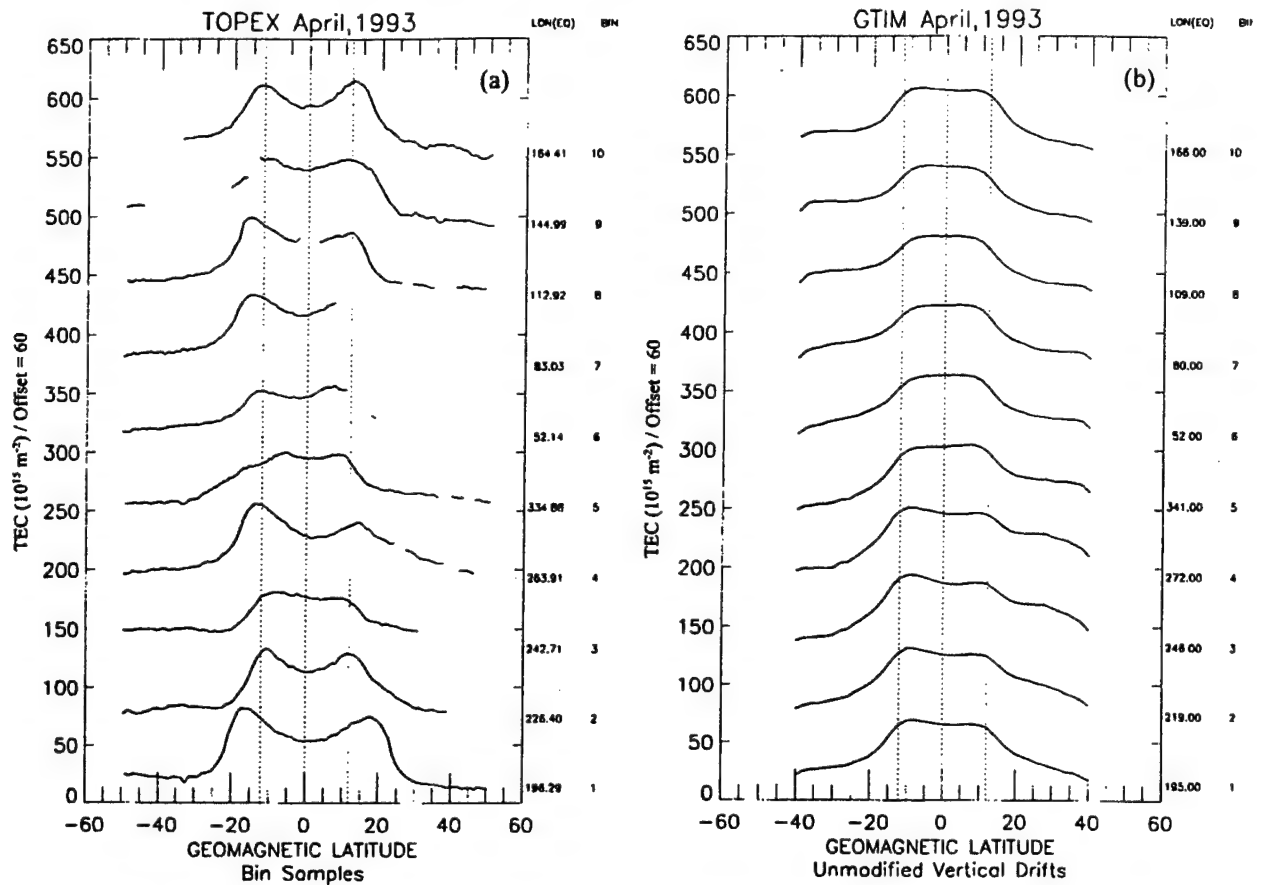


**Figure 11.** (a) TOPEX bin samples taken at approximately the average bin longitudes at 1630–1730 LT are shown. (b) GTIM results are shown from runs made at average bin longitudes. (Drift inputs are at half-weighting.) TOPEX longitude dependence is not observed. (c) GTIM results are shown from runs made at average bin longitudes. (Drift inputs are at variable weighting.) TOPEX peak TEC values are approximated.

dependence in the four empirical model average drifts during the equinox period.

Drifts were then altered again by a simple scaling manipulation which allowed GTIM to reproduce the TOPEX longitude shaping. Figures 8a and 8b illustrate the TOPEX and GTIM results, respectively. The TEC values are higher than TOPEX by 5–10 TECU, and hemisphere asymmetries are similar, with the exception of bins 5 and 10, which are reversed. The vertical drifts that have been modeled for four longitude sectors are shown in Figure 9. The solid lines represent the average drifts given by *Fejer et al.* [1995]. The dotted lines indicate the half-weighting that brought the GTIM results closer to the TOPEX values. The dashed lines are the input drifts that reproduced the TOPEX configuration. These manip-

ulated drifts appear to be within the scatter representation of the drift measurements [*Fejer et al.*, 1995]. Figure 10 indicates which of the four modeled drifts were used for the 10 longitude bins and the required changes in the drift weighting factors. Finally, Figure 11 shows specific anomaly shapes within bins 1–10. (Bin numbers are indicated to the right of the plots.) On the far left (Figure 11a), TOPEX passes chosen from each bin (at the GTIM run longitudes) are compared with the GTIM results with unmodified drifts (Figure 11b) and to the GTIM results with modified drifts (Figure 11c). The increase in drifts for the Indian/Asian and Pacific sectors caused not only higher TEC values but also an increase in the latitude spread of the crests and larger crest-to-trough ratios. A decrease in the drifts in the western American

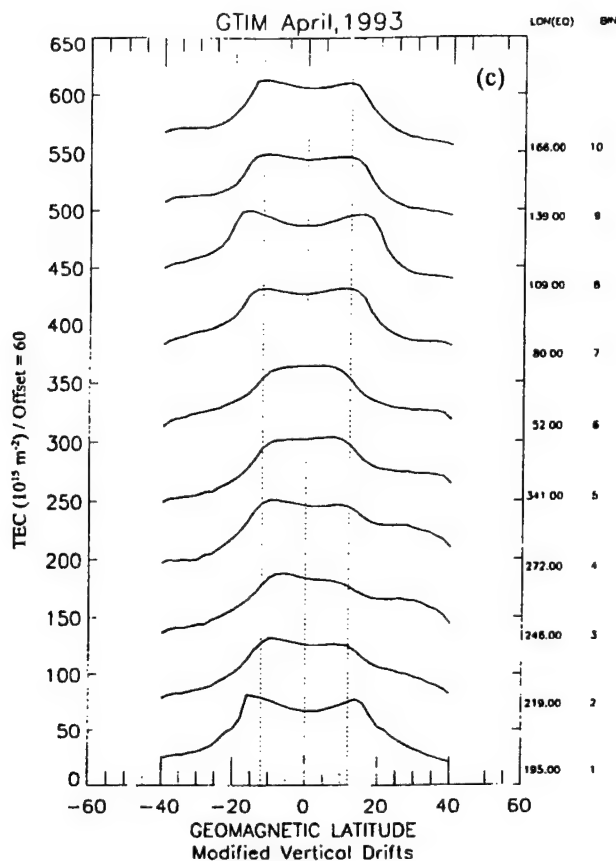


Figure 11. (continued)

region resulted in the opposite effect. There is some agreement in hemisphere asymmetry, but the magnitude of the crest-to-trough ratios and the TEC gradients are not well matched to the observations. Results at the Brazilian sector are inconclusive with respect to longitude dependency of adjacent bins due to the missing data over South America and Africa.

#### 4. Discussion

Results have shown that the ionosphere model (GTIM) responds to modifications of the  $\mathbf{E} \times \mathbf{B}$  vertical drift inputs and reproduces observed longitude dependence of TEC. More accurate shaping of the equatorial anomaly can be accomplished by additional adjustments to GTIM parameters and inputs. A change to a more appropriate low-latitude temperature model [Brace and Theis, 1981] was superimposed on the modified drift inputs. The GTIM output is shown in Figure 12b. An increase in the crest-to-trough ratios is a significant result. This improvement

in the crest-to-trough ratio is achieved by enhancement of the crest TEC values, but the anomaly trough values remain high compared with the observations. The increase in crest TEC is most noticeable at the longitudes where the drift weighting factors have been increased. TEC gradients have been improved as well. Results of an additional modification to the altitude gradient of the vertical drifts are shown in Figure 12c. It has been indicated previously [Pingree and Fejer, 1987] that the altitude variation of the vertical drift velocity is important in the development of the equatorial anomaly. Altitude dependence is not utilized in the initial GTIM runs. The modification of the altitude gradient involved a simple linear height variation in the vertical drift. The response is minimal, revealing an increase in crest-to-trough ratios in the Indian/Asian sector and a slight difference in TEC gradients. Previous work by one of the authors [Doherty *et al.*, 1997] yielded similar results. Improved anomaly TEC slopes and crest-to-trough ratios were demonstrated with changes to ion and electron temperatures and modification to the altitude gradient of the vertical drift velocity. These alterations to drifts and temperatures as well as variations to other model inputs such as neutral winds will provide the ability to investigate the factors that are responsible for the finer features of the equatorial anomaly.

#### 5. Conclusions

TOPEX over-ocean low-latitude TEC data have been averaged within 10 defined bins which, in total, span 360° of geographic longitude and 60° of geomagnetic latitude. The TOPEX satellite orbit allows evaluation of TEC for the same days at approximately the same local time within each bin. In spite of particular limitations of the TOPEX measurements, this extensive data set can be utilized in many applications to ionospheric research as a supplement to other space-based and ground-based sources of TEC data. In addition, validation of ionospheric models can be accomplished with TOPEX observations with the important goal of accurate space weather forecasting.

In this study, TOPEX has been used to demonstrate a trend of longitude dependence of the equatorial anomaly. Specifically, it is shown that a longitude configuration of the maximum values of the anomaly is maintained over a 4- to 6-hour period of time within three seasonal periods (spring equinox, summer, and winter) of 1993, 1994, and 1995. Other

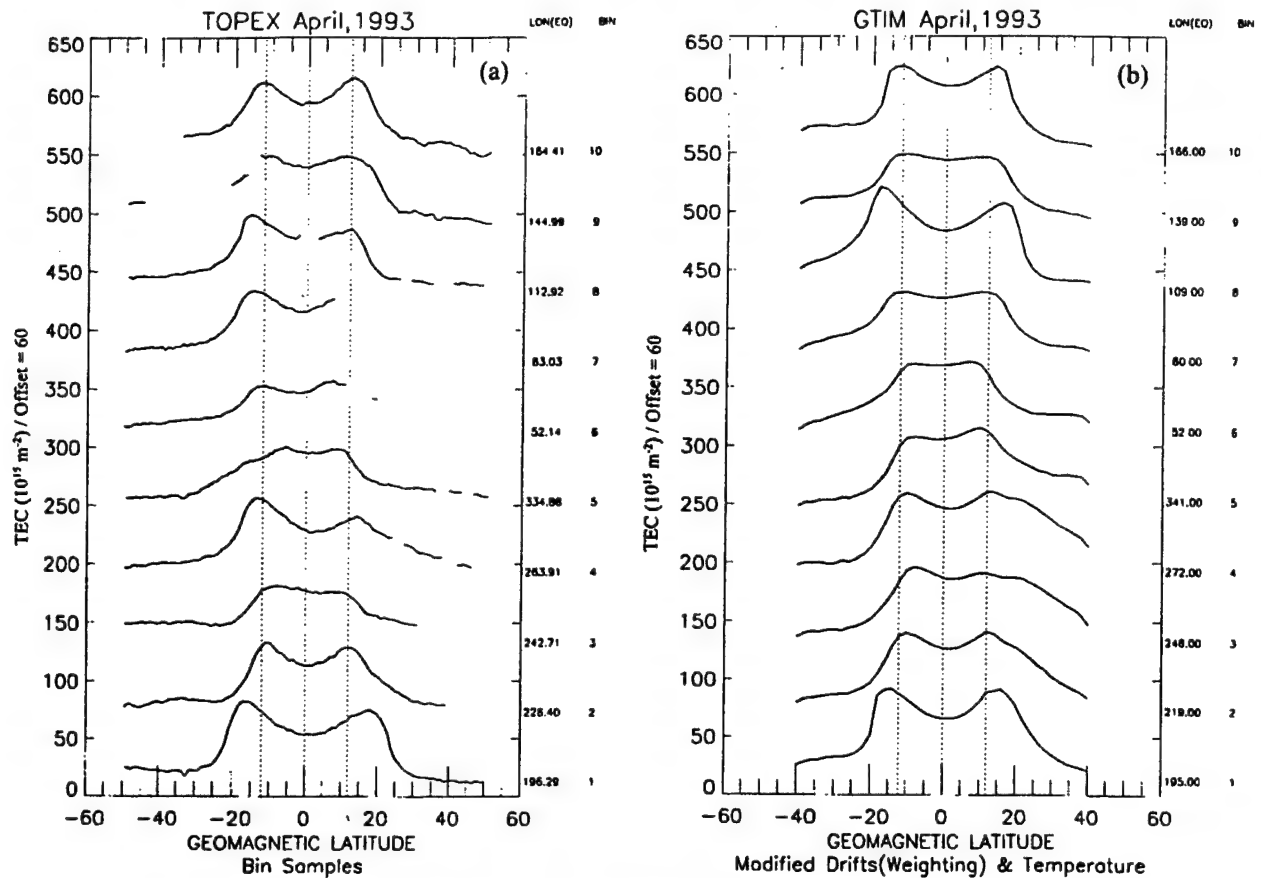


**Figure 12.** (a) Data are repeated from Figure 11a for comparison with model results. (b) GTIM results are shown. (Drift inputs are at variable weighting plus adjusted temperature model.) Significant improvement in crest-to-trough ratios and TEC gradients is seen. (c) GTIM results are shown. (Drift inputs are at variable weighting plus adjusted temperature model and modified drift altitude gradient.) Additional improvement in anomaly shaping is seen.

characteristics of the equatorial anomaly were observed and can be evaluated in terms of longitude dependence. These features include the latitude spread of the anomaly crests, the TEC gradients, the crest-to-trough ratios, and the hemisphere asymmetry. PIM results and GTIM runs with unmodified drift inputs do not reproduce the pattern of maximum TEC values provided by the TOPEX ionospheric correction during spring equinox of 1993. A straightforward manipulation of the vertical drift inputs to GTIM produced the TOPEX-observed longitude configuration. Although TEC values and latitude extent of the anomaly crests given by GTIM after drift input modification demonstrated improved agreement with TOPEX, other details of the anomaly shape were not well matched to the TOPEX obser-

vations. Additional alterations to the GTIM temperature model and vertical drift altitude gradient resulted in a significant improvement in the details of the shape of the equatorial anomaly including increased crest-to-trough ratios and TEC gradients.

Further evaluation of the TOPEX TEC data with respect to low-latitude longitude dependences combined with model simulations capable of reproducing these observations will lead to an improved understanding of the extreme variability in the equatorial anomaly and an increased capability of predicting the ionosphere at low latitudes. A global data set such as TOPEX can be utilized together with other sources of ionospheric measurements and observations to develop a data assimilative model which would be used as a tool for providing ionospheric "weather."

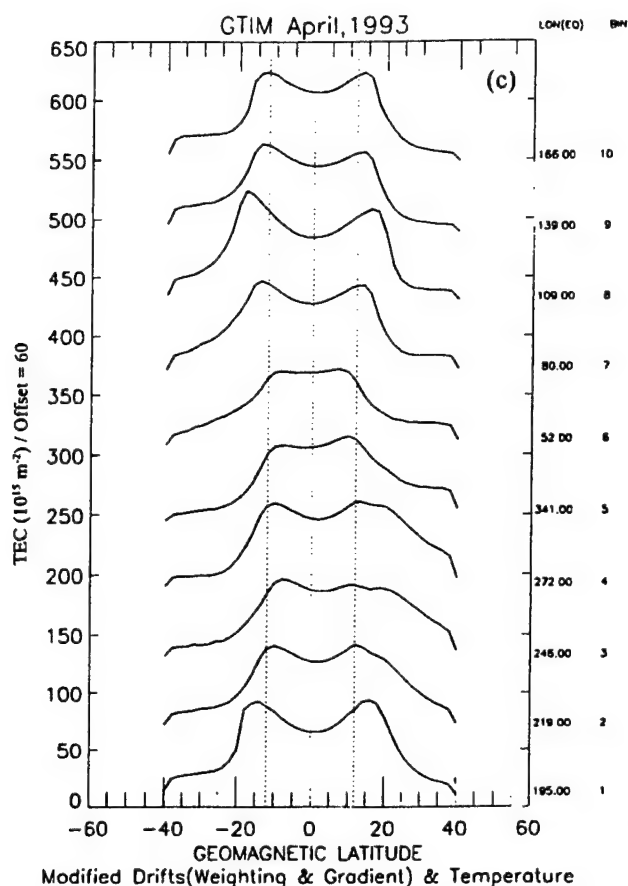


Figure 12. (continued)

**Acknowledgments.** This work was supported by Air Force Office of Scientific Research grant F49620-94-1-0365.

## References

- Anderson, D. N., Modeling the ambient, low latitude *F*-region ionosphere—A review, *J. Atmos. Terr. Phys.*, **43**, 753, 1981.
- Appleton, E. V., Two anomalies in the ionosphere, *Nature*, **157**, 691, 1946.
- Bilitza, D., C. Koblinsky, S. Zia, R. Williamson, and B. Beckley, The equatorial anomaly region as seen by the TOPEX/Poseidon satellite, *Adv. Space Res.*, **18**, 623, 1996.
- Brace, L. H., and R. F. Theis, Global empirical models of ionospheric electron temperatures in the upper *F*-region and plasmasphere based on in situ measurements for the Atmospheric Explorer C, ISIS 1, and ISIS 2 satellites, *J. Atmos. Terr. Phys.*, **43**, 1317, 1981.
- Daniell, R. E., L. D. Brown, D. N. Anderson, M. W. Fox, P. H. Doherty, D. T. Decker, J. J. Sojka, and R. W. Schunk, Parameterized ionospheric model: A global ionospheric parameterization based on first principles models, *Radio Sci.*, **30**, 1499, 1995.
- Decker, D. T., D. N. Anderson, and A. J. Preble, Improving IRI-90 low-latitude electron density specification, *Radio Sci.*, **32**, 2003, 1997.
- Doherty, P. H., D. N. Anderson, and J. A. Klobuchar, Total electron content over the Pan-American longitudes: March–April 1994, *Radio Sci.*, **32**, 1597, 1997.
- Fejer, B. G., E. R. dePaula, R. A. Heelis, and W. B. Hanson, Global equatorial ionospheric vertical plasma drifts measured by the AE-E satellite, *J. Geophys. Res.*, **100**, 5769, 1995.
- Forbes, J. M., D. Revelle, X. Zhang, and R. E. Markin, Longitude structure of the ionosphere *F* region from TOPEX/Poseidon and ground-based data during January 20–30, 1993, including the quasi 2-day oscillation, *J. Geophys. Res.*, **102**, 7293, 1997.
- Imel, D. A., Evaluation of the TOPEX/Poseidon dual-frequency ionosphere correction, *J. Geophys. Res.*, **99**, 24,895, 1994.
- Pingree, J. E., and B. J. Fejer, On the height variation of the equatorial *F* region vertical plasma drifts, *J. Geophys. Res.*, **92**, 4763, 1987.
- Rastogi, R. G., Longitudinal variation in the equatorial electrojet, *J. Atmos. Terr. Phys.*, **24**, 1031, 1962.
- Rastogi, R. G., Geomagnetic field variations at low latitudes and ionospheric electric fields, *J. Atmos. Terr. Phys.*, **55**, 1375, 1993.
- Su, Y. Z., G. J. Bailey, and N. Balan, Modelling studies of the longitudinal variations in TEC at equatorial anomaly latitudes, *J. Atmos. Terr. Phys.*, **57**, 433, 1995.
- Walker, G. O., Longitudinal structure of the *F*-region equatorial anomaly—A review, *J. Atmos. Terr. Phys.*, **43**, 763, 1981.
- D. N. Anderson, Space Vehicles Directorate, Air Force Research Laboratory, 29 Randolph Road, Hanscom AFB, MA 01731. (danderson@sec.noaa.gov)
- D. T. Decker and P. H. Doherty, Institute for Scientific Research, Boston College, St. Clement's Hall, 140 Commonwealth Avenue, Chestnut Hill, MA 02167-3862. (decker@plh.af.mil; doherty@plh.af.mil)
- P. Jastrzebski, M. C. Lee, and J. A. Vladimer, Department of Electrical and Computer Engineering, Boston University, 8 St. Mary's Street, Boston, MA 02215. (jane\_vladimer@res.raytheon.com; mclee@enga.bu.edu; piotr@acs.bu.edu)

(Received November 20, 1998; revised May 14, 1999; accepted May 20, 1999.)

# **The Alfvén-Fälthammar Formula for the Parallel $E$ -Field and its Analogue in Downward Auroral-Current Regions**

John R. Jasperse and Neil J. Grossbard, *Member, IEEE*

# The Alfvén–Fälthammar Formula for the Parallel $E$ -Field and its Analogue in Downward Auroral-Current Regions

John R. Jasperse and Neil J. Grossbard, *Member, IEEE*

**Abstract**—In this paper, we give an alternative derivation of the Alfvén–Fälthammar formula for a positive parallel  $E$ -field in upward auroral-current regions and its analogue for a negative parallel  $E$ -field in downward auroral-current regions. These formulas give new insight into the physics of the Birkeland current system. We find that for downward auroral-current regions, the velocity-space anisotropy in the ion distribution function is such that half the ion energy perpendicular to the magnetic field is greater than the ion energy parallel to the magnetic field. This is just opposite to the case for upward auroral-current regions. These results are compared to recent particle-in-cell simulations and FREJA satellite data.

**Index Terms**—Alfvén–Fälthammar formula, Birkeland current system, parallel  $E$ -fields in space plasmas.

## I. INTRODUCTION

THIS paper deals with the theory of the Birkeland current system which was discovered nearly 100 years ago and remains an active area of space physics research to this day. The Birkeland currents are a system of upward and downward magnetic field-aligned electrical currents in the auroral zone that flow between the magnetosphere and the ionosphere where particle number flux, momentum, and energy flux are exchanged. In our view, there is no problem more important to the understanding of space weather at high latitudes than to understand how the Birkeland current system works. For a study of the statistical properties of the Birkeland currents using TRIAD satellite data, see [1, Fig. 13]. For a recent case study using FAST satellite data, see [2, Fig. 3].

One of the purposes of this paper is to give an alternative derivation of the Alfvén–Fälthammar (A–F) formula for the parallel  $E$ -field ( $E_{\parallel}$ ) in upward auroral-current regions. There are several ways to derive this result [3]–[6]. The formulas for  $E_{\parallel}$  are the same but the derivations are not equivalent since different assumptions, closure approximations, and boundary conditions are used. Our derivation begins with the Vlasov equations and, as we will show, not only gives new insight into the physics of that problem, but may be generalized in a straightforward way to study downward auroral-current regions.

Manuscript received January 20, 2000; revised March 21, 2000.

J. R. Jasperse is with the Air Force Research Laboratory, Space Vehicles Directorate, Hanscom AFB, MA 01731 USA.

N. J. Grossbard is with Boston College, Institute for Scientific Research, Chestnut Hill, MA 02467 USA.

Publisher Item Identifier S 0093-3813(00)11345-1.

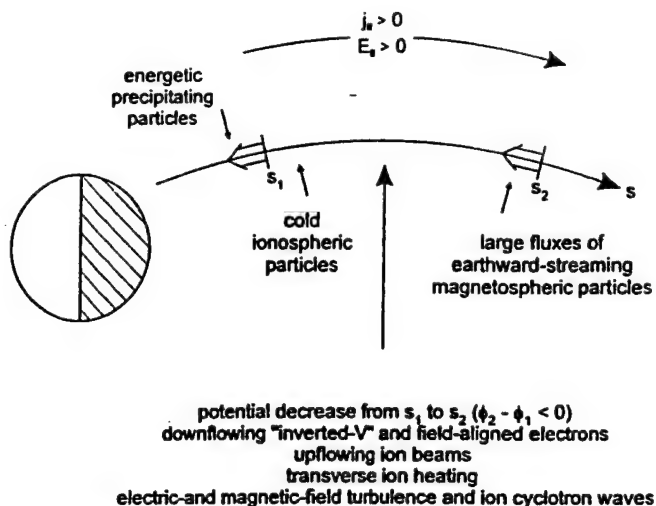


Fig. 1. Some properties of upward auroral-current regions.

The primary purpose of this paper, therefore, is to give the analogue of the A–F formula for  $E_{\parallel}$  for downward auroral-current regions. The derivation begins with a velocity-space diffusion model for the problem, and the formula that we give for  $E_{\parallel}$  also gives new insight into the physics of that problem.

There is a vast literature on upward auroral-current regions. For a review of rocket and satellite measurements before 1980, see [7]. For a sample of more recent satellite measurements, see [8] on FREJA results and FAST results in [9]. For example, the properties of upward auroral-current regions have been observed by the ISIS-1 [10], S3-3 [7], NOAA-6 [11], DE-1 [12], DE-2 [13], FREJA [14], POLAR [15], and FAST [16] satellites, to name a few. From these studies, we see that upward auroral-current regions are often characterized by

- 1) converging electrostatic shocks, upward pointing  $E_{\parallel}$ ;
- 2) downflowing “inverted-V” and field-aligned electrons;
- 3) large-scale density cavities;
- 4) upflowing ion beams and transverse ion heating;
- 5) electric- and magnetic-field turbulence and ion cyclotron waves;
- 6) large fluxes of earthward-streaming energetic ( $> \text{few kilovolts}$ ) magnetospheric particles.

Some of these properties are illustrated in Fig. 1 (not to scale). The theoretical literature, before 1993 is reviewed in [17]. For a more recent review, see [18, Introduction and Bibliography].

The properties of downward auroral-current regions are less explored. They have been observed by the ISIS-2 [19], DE-1



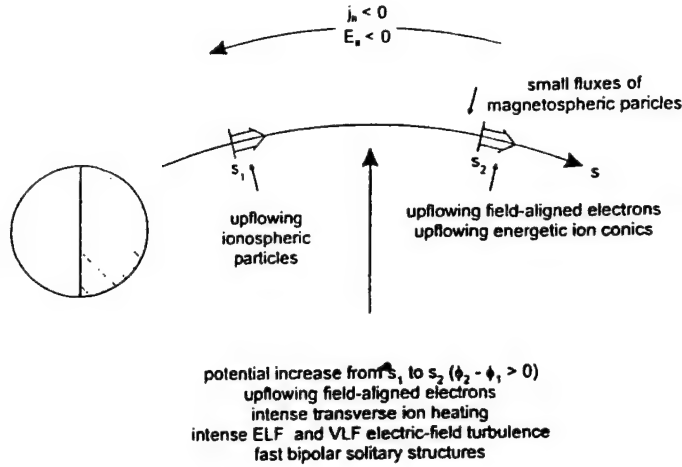


Fig. 2. Some properties of downward auroral-current regions.

[20], S3-3 [21], FREJA [22], FAST [23], [24], and other satellites. These downward currents often occur in the auroral zone adjacent to "inverted-V" structures [2], the dayside cusp-cleft region [21], and in association with the "black aurora" [25]. From these studies, we see that downward auroral-current regions are often characterized by

- 1) diverging electrostatic shocks, downward pointing  $E_{\parallel}$ ;
- 2) upflowing low energy (< few kilovolts) field-aligned electrons;
- 3) intense transverse ion heating;
- 4) small-scale density cavities;
- 5) intense ELF and VLF electric-field turbulence and fast bipolar solitary structures;
- 6) small fluxes of energetic (> few kilovolts) magnetospheric particles.

Some of these properties are illustrated in Fig. 2 (not to scale). Some theoretical work has been carried out for downward auroral-current regions using the multimoment fluid equations for the current-driven ion cyclotron instability [26]; particle-in-cell (PIC) simulations in the electrostatic approximation [27], [28]; and a velocity-space diffusion model for the problem [29], [30].

In Section II, we give the alternative derivation of the A-F formula for a positive  $E_{\parallel}$  in an upward auroral-current region, and, in Section III, its analogue for a negative  $E_{\parallel}$  in a downward auroral-current region. In Section IV, we discuss these results.

## II. PARALLEL $E$ -FIELD DUE TO INJECTED MAGNETOSPHERIC PARTICLES IN UPWARD AURORAL-CURRENT REGIONS

The purpose of this Section is to give an alternative derivation of the Alfvén-Fälthammar (A-F) formula for the parallel  $E$ -field ( $E_{\parallel}$ ) in upward auroral-current regions. The original derivation is given in [3]. Although we obtain the same formula for  $E_{\parallel}$ , the method we use is different. Our reason for presenting an alternative derivation here is that the method we use may be easily generalized and applied to downward auroral-current regions, as we will see in Section III.

### A. Vlasov Equations and the Quasi-Neutrality Condition

Upward auroral-current regions are often characterized by earthward-streaming energetic magnetospheric particles, the

presence of low-energy (or ambient) ionospheric particles, and wave-particle interactions. The simplest way to model an auroral arc that we can think of is to neglect the ambient ionospheric particles and wave-particle interactions, and to consider only the injected magnetospheric particles. In his review, Borovsky [17] discusses 12 mechanisms by which the auroral plasma can sustain an  $E_{\parallel}$ , thereby accelerating auroral particles, and also ten drivers (or generators) of the mechanisms. As we will see in this section, the A-F formula for a positive  $E_{\parallel}$  in upward auroral-current regions results from the following simple model for a quasi-stable auroral arc 1) the driver is the earthward-streaming energetic magnetospheric particles and 2) the mechanism that sustains  $E_{\parallel}$  is the differential velocity-space anisotropy between the ions and the electrons in the dipolar magnetic field.

In this paper, we assume that the gyrotropic approximation is valid and seek a steady-state solution. The Vlasov equations in one-spatial and two-velocity dimensions are

$$\left\{ v_{\parallel} \frac{\partial}{\partial s} + \left[ g_{\parallel} + \frac{q_{\alpha}}{m_{\alpha}} E_{\parallel} \right] \frac{\partial}{\partial v_{\parallel}} - \frac{1}{2B} \frac{dB}{ds} \left[ v_{\perp}^2 \frac{\partial}{\partial v_{\parallel}} - v_{\parallel} v_{\perp} \frac{\partial}{\partial v_{\perp}} \right] \right\} f_{\alpha} = 0 \quad (1)$$

and the quasi-neutrality (Q-N) condition is

$$n_e = \sum_{\beta} n_{\beta} \quad (2)$$

where  $\beta$  is summed over the ions. Here,  $g_{\parallel}$  and  $E_{\parallel}$  are the parallel components of the gravitational acceleration and the electrostatic field, respectively;  $B$  is the geomagnetic field;  $f_{\alpha} = f_{\alpha}(s, v_{\perp}, v_{\parallel})$  is the gyrotropically-averaged distribution function for each species  $\alpha$ ; and  $s$  is the distance from the earth along the geomagnetic flux tube. Also,  $f_{\alpha}$  is normalized to the particle density,  $n_{\alpha}$ , and the other quantities have their usual meanings.

In (2), we have replaced Poisson's equation with the Q-N condition. This greatly simplifies the problem. The standard argument for making this replacement is that for length scales which are long compared to the Debye length, the two are equivalent. However, this is not at all obvious since, in making this replacement, we have completely changed the nonlinear character and boundary conditions of the problem. Much has been written about this issue [4]–[6], [31]–[33].

### B. A-F Solution for $E_{\parallel}$ and Related Quantities from the Multimoment Fluid Equations

We now proceed to derive the multimoment fluid equations by multiplying (1) by  $v_{\perp}^n v_{\parallel}^{\ell}$  and integrating over all velocity space. We use the following notation:

$$\begin{aligned} \langle v_{\perp}^n, v_{\parallel}^{\ell} \rangle_{\alpha} &= \langle n, \ell \rangle_{\alpha} \\ &= 2\pi \int_{-\infty}^{\infty} dv_{\parallel} \int_0^{\infty} dv_{\perp} v_{\perp}^{1+n} v_{\parallel}^{\ell} f_{\alpha}(s, v_{\perp}, v_{\parallel}) \end{aligned} \quad (3)$$

$$\dot{A} = -B^{-1} dB/ds = A^{-1} dA/ds \quad (4)$$

where  $A$  is the cross sectional area of the flux tube. Here  $n$  and  $\ell$  are positive integers or zero. We obtain for all  $n$  and  $\ell = 0$

$$d/ds \langle n, 1 \rangle_{\alpha} + \dot{A} (1 + n/2) \langle n, 1 \rangle_{\alpha} = 0 \quad (5)$$

and for all  $n$  and  $\ell \geq 1$

$$\begin{aligned} d/ds \langle n, \ell + 1 \rangle_\alpha + \dot{A}(1 + n/2) \langle n, \ell + 1 \rangle_\alpha \\ + \ell \{ (q_\alpha/m_\alpha) (d/ds \Phi_{\alpha\parallel}) \langle n, \ell - 1 \rangle_\alpha \\ - (\dot{A}/2) \langle n + 2, \ell - 1 \rangle_\alpha \} = 0. \end{aligned} \quad (6)$$

Here,  $\Phi_{\alpha\parallel} = \phi_{\parallel} + (m_\alpha/q_\alpha)\phi_{G\parallel}$ , where  $\phi_{\parallel}$  is the electrostatic potential and  $\phi_{G\parallel}$  is the gravitational potential. The multimoment fluid equations for  $n = 0, \ell = 0$ ;  $n = 0, \ell = 1$ ;  $n = 0, \ell = 2$ ; and  $n = 2, \ell = 0$  are

$$d/ds n_\alpha u_\alpha + \dot{A} n_\alpha u_\alpha = 0 \quad (7)$$

$$\begin{aligned} d/ds n_\alpha w_{\alpha\parallel} + \dot{A} n_\alpha (w_{\alpha\parallel} - w_{\alpha\perp}/2) \\ + (q_\alpha/2) n_\alpha d/ds \Phi_{\alpha\parallel} = 0 \end{aligned} \quad (8)$$

$$\begin{aligned} d/ds n_\alpha Q_{\alpha\parallel} + \dot{A} n_\alpha (Q_{\alpha\parallel} - Q_{\alpha\perp}) \\ + q_\alpha n_\alpha u_\alpha d/ds \Phi_{\alpha\parallel} = 0 \end{aligned} \quad (9)$$

$$d/ds n_\alpha Q_{\alpha\perp} + 2\dot{A} n_\alpha Q_{\alpha\perp} = 0. \quad (10)$$

Here, we have introduced the standard definitions  $\langle 0, 0 \rangle_\alpha = n_\alpha$ ;  $\langle 0, 1 \rangle_\alpha = n_\alpha u_\alpha$ ;  $m_\alpha \langle 2, 0 \rangle_\alpha / 2 = n_\alpha w_{\alpha\perp}$ ;  $m_\alpha \langle 0, 2 \rangle_\alpha / 2 = n_\alpha w_{\alpha\parallel}$ ;  $m_\alpha \langle 2, 1 \rangle_\alpha / 2 = n_{\alpha\perp} Q_{\alpha\perp}$ ; and  $m_\alpha \langle 0, 3 \rangle_\alpha / 2 = n_\alpha Q_{\alpha\parallel}$ . The  $Q$ s denote the energy flux and should not be confused with the heat flux. Also, by definition,  $w_{\alpha\perp} = T_{\alpha\perp}$  and

$$w_{\alpha\parallel} = T_{\alpha\parallel}/2 + m_\alpha u_\alpha^2/2$$

where the temperatures are expressed in energy units. Adding (9) and (10) together and using (7), we may obtain an alternative equation for (9). Equations (7)–(10) may then be rewritten as

$$B d/ds (n_\alpha u_\alpha / B) = 0 \quad (11)$$

$$\begin{aligned} d/ds (n_\alpha w_{\alpha\parallel}) - B^{-1} dB/ds n_\alpha (w_{\alpha\parallel} - w_{\alpha\perp}/2) \\ + n_\alpha (q_\alpha/2) d/ds \Phi_{\alpha\parallel} = 0 \end{aligned} \quad (12)$$

$$B d/ds \{ [n_\alpha Q_{\alpha\parallel} + n_\alpha Q_{\alpha\perp} + q_\alpha n_\alpha u_\alpha \Phi_{\alpha\parallel}] / B \} = 0 \quad (13)$$

$$B^2 d/ds (n_\alpha Q_{\alpha\perp} / B^2) = 0. \quad (14)$$

Equations (11)–(14) are the standard conservation laws for the number flux, momentum, total energy flux, and perpendicular energy flux, respectively.

Formal expressions for  $E_{\parallel}$  may be found from (12) and (13) by simply rearranging the terms. Neglecting gravity, we see from momentum conservation (12) that

$$\begin{aligned} E_{\parallel} = (2/q_\alpha) \{ -B^{-1} dB/ds (w_{\alpha\parallel} - w_{\alpha\perp}/2) \\ + n_\alpha^{-1} d/ds n_\alpha w_{\alpha\parallel} \} \end{aligned} \quad (15)$$

and from total energy flux conservation (13) with the help of (11) that

$$E_{\parallel} = (B/q_\alpha n_\alpha u_\alpha) d/ds [(n_\alpha Q_{\alpha\parallel} + n_\alpha Q_{\alpha\perp}) / B]. \quad (16)$$

Equations (15) and (16) are  $2\alpha$  expressions for  $E_{\parallel}$  in terms of the moments of  $f_\alpha$ . We call them self-consistent formulas for  $E_{\parallel}$  since, once the explicit solution for the moments of  $f_\alpha$  are found, then (15) and (16) must be satisfied.

Equations (11)–(14) and (2) are  $4\alpha + 1$  equations for  $6\alpha + 1$  unknowns including the electrostatic potential  $\phi_{\parallel}$ . In order to solve them, we must introduce closure approximations. The standard procedure for closing the multimoment fluid equations is to use the gyrotropic limit of the Maxwellian-based 5-, 8-, 10-, 164

or 13-moment sets, or the bi-Maxwellian-based 6- or 16-moment sets. For a discussion of this procedure, see [34]. Specific solutions have also been worked out for a variety of plasma-flow conditions [35], [36]. Instead of using the standard procedure, we use a simpler closure approximation which, as we shall see later in this section, places a restriction on the type of flow conditions to which it may be applied. The closure we use is

$$Q_{\alpha\perp} \cong u_\alpha w_{\alpha\perp} \quad (17)$$

$$Q_{\alpha\parallel} \cong u_\alpha w_{\alpha\parallel}. \quad (18)$$

Using (11), (17), and (18), we find that the multimoment fluid equations become

$$d/ds (n_\alpha u_\alpha / B) = 0 \quad (19)$$

$$\begin{aligned} d/ds n_\alpha w_{\alpha\parallel} - B^{-1} dB/ds n_\alpha (w_{\alpha\parallel} - w_{\alpha\perp}/2) \\ + n_\alpha (q_\alpha/2) d/ds \Phi_{\alpha\parallel} = 0 \end{aligned} \quad (20)$$

$$d/ds (w_{\alpha\parallel} + w_{\alpha\perp} + q_\alpha \Phi_{\alpha\parallel}) = 0 \quad (21)$$

$$d/ds (w_{\alpha\perp} / B) = 0 \quad (22)$$

$$n_e = \sum_\beta n_\beta, \quad \beta = \text{ions}. \quad (23)$$

A few remarks about (19)–(23) are in order here. First, they are a set of  $4\alpha + 1$  nonlinear, first-order ordinary differential equations for  $4\alpha + 1$  unknowns subject to boundary conditions imposed at either end of the flux tube. Second, the closure approximation that we have used has, in effect, replaced the conservation of total energy flux (13) and the conservation of perpendicular energy flux (14), both of which are rigorous, by conservation relations for the total energy (21) and the perpendicular energy (22). These are just the conservation relations that we obtain from single-particle orbit theory. However, the concept of parallel and perpendicular temperature has been preserved in (19)–(23) as  $w_{\alpha\perp} = T_{\alpha\perp}$  and  $w_{\alpha\parallel} = T_{\alpha\parallel}/2 + m_\alpha u_\alpha^2/2$ . Third, when anomalous transport effects are neglected, (19) and (20) are identical to the steady-state versions of (1) and (2) in [37], where the authors have used the gyrotropic limit of the 16-moment set to study the polar wind. However, (21) and (22) differ from the higher order moment equations in [37], as the closure approximation is different.

Now, we proceed to solve (19)–(23) in closed form subject to appropriate boundary conditions. Consider  $s_1 \leq s \leq s_2$ , where  $s_1$  is in the ionosphere and  $s_2$  is in the magnetosphere. Equation (20) may be further simplified. We may eliminate  $\Phi_{\alpha\parallel}$  from (8) and (9) and use closure to obtain

$$d/ds n_\alpha u_\alpha w_{\alpha\parallel} - 2u_\alpha d/ds n_\alpha w_{\alpha\parallel} - \dot{A} n_\alpha u_\alpha w_{\alpha\parallel} = 0.$$

Using (7), we may further simplify to obtain

$$2w_{\alpha\parallel} dn_\alpha/ds + 2\dot{A} n_\alpha w_{\alpha\parallel} + n_\alpha dw_{\alpha\parallel}/ds = 0.$$

The left-hand side of this expression is proportional to  $d/ds (n_\alpha^2 w_{\alpha\parallel} / B^2)$  which is in turn proportional to  $d/ds (w_{\alpha\parallel} / u_\alpha^2)$ , so (20) may be replaced by

$$d/ds (w_{\alpha\parallel} / u_\alpha^2) = 0. \quad (24)$$

The hidden meaning of the closure approximation given by (18) is now revealed. If the ratio  $(T_{\alpha\parallel}/2 + m_\alpha u_\alpha^2/2)/(m_\alpha u_\alpha^2/2)$  does not change by very much on the flux tube, then (18) is a reasonable approximation. This requires that  $T_{\alpha\parallel}$  and  $m_\alpha u_\alpha^2$

change proportionally from  $s_1$  to  $s_2$  so that the above ratio is nearly constant. If we examine the experimental data and find that this approximation is valid, then (18) is a good closure approximation. However, we note that this closure may not apply to problems where the plasma flow evolves from subsonic to supersonic. We now integrate (22), (21), (24), and (19) from  $s$  to  $s_2$ , in that order, to find  $w_{\alpha\perp}$ ,  $w_{\alpha\parallel}$ ,  $u_\alpha$  and  $n_\alpha$  in terms of  $\phi_{\parallel}$  and the boundary values at  $s_2$ . We then specialize to an electron-ion plasma and impose the Q-N condition to solve for  $\phi_{\parallel}$ . Neglecting gravity, the solution is

$$w_{\alpha\perp}(s) = w_{\alpha\perp 2}[B(s)/B_2] \quad (25)$$

$$w_{\alpha\parallel}(s) = w_{\alpha\parallel 2} + w_{\alpha\perp 2}[1 - B(s)/B_2] + q_\alpha[\phi_{\parallel 2} - \phi_{\parallel}(s)] \quad (26)$$

$$u_\alpha(s) = u_{\alpha 2}[w_{\alpha\parallel}(s)/w_{\alpha\parallel 2}]^{1/2} \quad (27)$$

$$n_\alpha(s) = n_{\alpha 2}(B(s)/B_2)[w_{\alpha\parallel 2}/w_{\alpha\parallel}(s)]^{1/2} \quad (28)$$

$$\phi_{\parallel}(s) = \phi_{\parallel 2} + \left[ \frac{w_{i\parallel 2}w_{e\perp 2} - w_{e\parallel 2}w_{i\perp 2}}{e(w_{i\parallel 2} + w_{e\parallel 2})} \right] \left[ \frac{B(s)}{B_2} - 1 \right] \quad (29)$$

where the subscript 2 denotes the value of the quantity at  $s_2$  and  $e$  is the magnitude of the electronic charge. From (29), we see that  $E_{\parallel}$  is

$$E_{\parallel} = -d\phi_{\parallel}/ds = -K dB/ds \quad (30)$$

$$K = \left( \frac{1}{eB_2} \right) \left[ \frac{w_{i\parallel 2}w_{e\perp 2} - w_{e\parallel 2}w_{i\perp 2}}{w_{i\parallel 2} + w_{e\parallel 2}} \right]. \quad (31)$$

Equation (30) is the A-F formula for  $E_{\parallel}$  for upward auroral-current regions and is identical to (12) of [3, Sec. 5.1.3], except that  $w_{\alpha\parallel}$  has both a thermal part and a drift part, as  $w_{\alpha\parallel} = T_{\alpha\parallel}/2 + m_\alpha u_\alpha^2/2$ . It was derived in [3] by a different method, i.e., single-particle orbit theory, and applied for different boundary conditions. The boundary conditions used in [3] are that ionospheric ions are emitted at the lower boundary and magnetospheric electrons are injected at the upper boundary. For that problem,  $u_{i1}$  and hence  $u_{i2}$  are positive, and  $u_{e2}$  is negative. In this paper, we have applied the A-F formula to the problem where the ions and electrons are of magnetospheric origin and both are injected at the upper boundary, hence  $u_{i2}$  and  $u_{e2}$  are negative. Using (25), (26), and (29), we may also show that  $K$  is an invariant. Equation (30) is also equivalent to (28) obtained in [6] by using Persson's method of solution [4], [5]. As pointed out in [3], the differential particle anisotropy is such that  $[w_{i\parallel 2}w_{e\perp 2} - w_{e\parallel 2}w_{i\perp 2}]$  is positive and, since  $dB/ds$  is negative,  $E_{\parallel}$  is upward pointing.

A graph of the solution given by (25)–(30) is shown in Fig. 3, where  $s$  measures the distance along  $B$  from the surface of the earth. Remember that  $w_{\alpha\perp} = T_{\alpha\perp}$ . We have also plotted the current density,  $j_{\parallel}$ , which is defined as  $j_{\parallel} = en(u_i - u_e)$ . Here we have used the superscript  $M$  to denote the fact that the particles are of magnetospheric origin. In plotting the solution, we have imposed the following conditions. The physical conditions are  $s_1 - s_0 = 1000$  km,  $s_2 - s_0 = 6500$  km,  $m_i/m_e = 250$ ,  $B(s) = B_0(s_0/s)^3$ ,  $B_0 = 0.57$  Gauss, where  $s_0$ , the radius of the earth, is approximated by 6400 km. The boundary conditions at  $s_2$  are  $u_{i2} = u_{e2} = u_2 = 0.50$  cm/s,  $u_{i2} = -5.6 \times 10^3$  km/s,  $u_{e2} = -6.8 \times 10^3$  km/s,  $T_{i\parallel 2} = T_{e\parallel 2} = T_{\perp 2} = T_{\perp 2} = 1.0$  keV, and  $\phi_{\parallel 2} = -4.1 \times 10^3$

V. These parameters give  $j_{\parallel 2} = 0.10$   $\mu\text{A}/\text{m}^2$ ,  $w_{i\parallel 2} = 22.4$  keV, and  $w_{e\parallel 2} = 0.62$  keV. Since  $\phi_{\parallel}$  is arbitrary to a constant, we have adjusted  $\phi_{\parallel 2}$  so that  $\phi_{\parallel 1} = 0$  for convenience in plotting. The mass and temperature ratios are unrealistic and the current density is too small. However,  $w_{i\parallel 2} = 22.4$  keV is realistic for strong injection events [38]. We use these parameters in order to compare the A-F solution to Schriver's simulation [18] in Section II-D. In this example, since  $w_{e\perp 2}$  is comparable to  $w_{i\perp 2}$  and  $w_{i\parallel 2} \gg w_{e\parallel 2}$ , a good approximation for  $\phi_{\parallel}$  is

$$\phi_{\parallel}(s) \cong \phi_{\parallel 2} + e^{-1}w_{e\perp 2}[\gamma(s) - 1] \quad (32)$$

where  $\gamma(s) = B(s)/B_2$ . For these conditions, the potential drop from  $s_1$  to  $s_2$  ( $\phi_{\parallel 2} - \phi_{\parallel 1}$ ) scales as  $w_{e\perp 2}$ .

### C. Self-Consistent Formulas for $E_{\parallel}$

Equations (15) and (16) give four self-consistent formulas for  $E_{\parallel}$  in an electron-ion plasma. In order to verify the validity of these expressions, we use closure, substitute (25)–(29) into the right-hand sides of (15) and (16), and find that  $E_{\parallel}$  is indeed given by (30).

Consider (15) for the ions. It is

$$E_{\parallel} = (2/e)\{-B^{-1} dB/ds[w_{i\parallel} - w_{i\perp}/2] + n_i^{-1} d/ds n_i w_{i\parallel}\}. \quad (33)$$

We wish to demonstrate that  $E_{\parallel}$  is positive by using (33) and the results given in Fig. 3 instead of (30). To do this, we note that since  $-B^{-1} dB/ds$  is positive and  $w_{i\parallel} > w_{i\perp}/2$ , then the first term on the right-hand side of (33) is positive. The second term is negative, but  $|n_i^{-1} d/ds n_i w_{i\parallel}|$  is smaller than the first term inside the brackets, so  $E_{\parallel}$  is positive. This is shown in Fig. 4, where  $E_{\parallel}^{(1)}$  and  $E_{\parallel}^{(2)}$  denote the first and second terms on the right-hand side of (33), respectively, and  $E_{\parallel}^{(\text{total})}$  is the total  $E_{\parallel}$ . We see that once the solution is known, then the fact that  $E_{\parallel}$  is positive can be seen from the ion moments alone.

### D. Comparison to the Schriver Particle-in-Cell Simulation

In this section, we compare the A-F solution to the particle-in-cell (PIC) simulation in the electrostatic approximation given by Schriver [18]. The physical and boundary conditions that we chose in Section II-B are essentially identical to run number 3 in [18, Table 2], where  $u_i/v_{te}$  at  $s_2$  is 0.3. In both cases,  $u_{i2} = -5.6 \times 10^3$  km/s and  $w_{i\parallel 2} = 22.4$  keV. The fact that  $j_{\parallel 2}$  was 0.1  $\mu\text{A}/\text{m}^2$  in Section II-B and zero in the simulation makes little difference in the results.

As we saw in Section II-B, the A-F formula for  $E_{\parallel}$  was obtained when the ionospheric particles and wave-particle interactions were neglected, the Q-N condition was used in place of Poisson's equation, and only the injected energetic magnetospheric particles were included. From [18, Fig. 5], we see that the potential drop is  $-2.7$  kV compared to  $-4.1$  kV from the A-F formula shown in Fig. 3, and that the shape of  $\phi_{\parallel}(s)$  is concave downward ( $d^2\phi_{\parallel}/ds^2 < 0$ ) instead of convex upward ( $d^2\phi_{\parallel}/ds^2 > 0$ ) in the A-F formula. To find the polarization charge density, we may substitute  $\phi_{\parallel}$  into Poisson's equation. We find that the shape of  $\phi_{\parallel}$  in the simulation is consistent with the correct polarization charge density, whereas the A-F result is

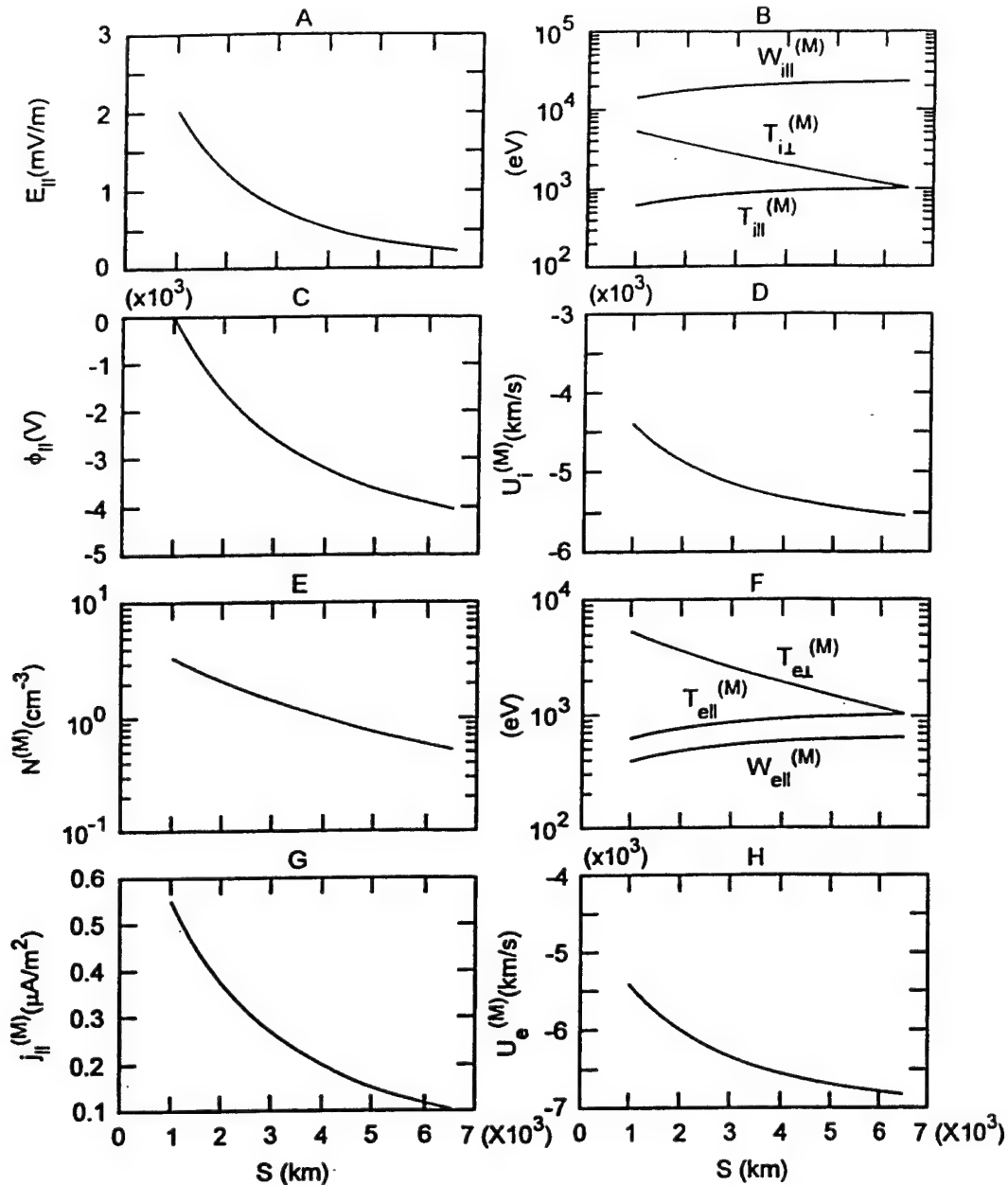


Fig. 3. The A-F solution for injected magnetospheric particles in an upward auroral-current region from (25)–(30). The symbols are defined in the text, and the superscript  $M$  denotes particles of magnetospheric origin.

not. Apparently, including ionospheric particles and wave-particle interactions, and using Poisson's equation instead of the Q-N condition, have modified the shape and magnitude of the potential drop.

However, it appears that the A-F formula gives the essential physics of the problem correctly, i.e., that for earthward-streaming energetic magnetospheric particles, it is the differential velocity-space anisotropy between the ions and the electrons that produces the potential drop and the upward pointing  $E_{||}$ .

### III. PARALLEL $E$ -FIELD CONSISTENT WITH THE TURBULENT HEATING OF IONOSPHERIC IONS IN DOWNWARD AURORAL-CURRENT REGIONS

The purpose of this section is to give the analogue of the A-F formula for  $E_{||}$  in downward auroral-current regions. For up-

ward currents,  $E_{||}$  is positive, as we saw in Section II; but for downward currents,  $E_{||}$  is negative, as we will see in this section. We obtain this result by generalizing the method presented in Section II.

#### A. Kinetic Diffusion Equations and the Quasi-Neutrality Condition

Downward auroral-current regions are often characterized by energetic ion conics and upflowing, field-aligned electrons of ionospheric origin; intense broadband ELF (BBELF) electric-field turbulence; and small fluxes of earthward-streaming magnetospheric particles. The simplest model for downward auroral-current regions that we can think of is neglecting the magnetospheric particles and considering only the ionospheric particles and the BBELF turbulence. In this paper, we also assume

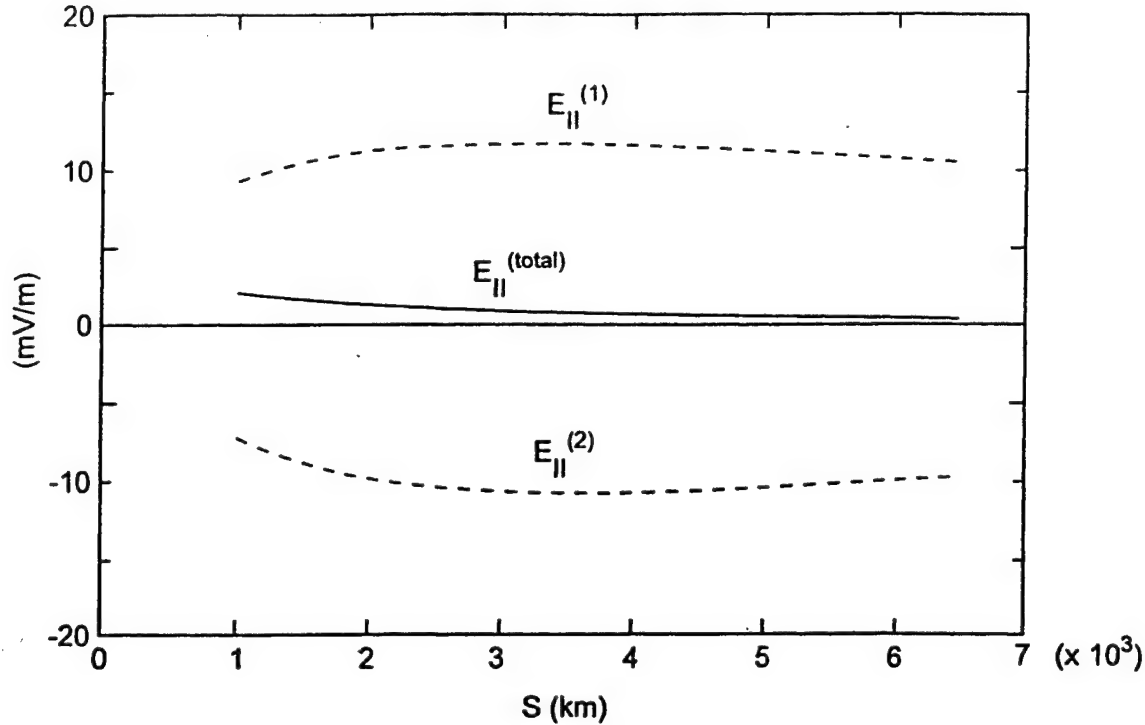


Fig. 4. The solution for  $E_{||}$  in an upward auroral-current region from the self-consistent A-F formula for  $E_{||}$  given by (33). Here,  $E_{||}^{(1)}$  is the positive contribution,  $E_{||}^{(2)}$  is the negative contribution, and  $E_{||}^{(total)}$  is the total.

that the spectrum of the BBELF turbulence is given experimentally. How the turbulence is driven (or generated) is an active area of research and beyond the scope of this paper. If an additional source of ion heating exists on the flux tube due, for example, to the presence of fast bipolar solitary structures as suggested in [23] and [24], then see Section IV for a brief discussion of how this effect may be incorporated into the method of solution presented in this paper.

In Section II-C, we showed that a positive  $E_{||}$  occurs when  $w_{i||} > w_{i\perp}/2$  for the ions, and the magnitude of the second term in (33) is smaller than the first term. In Section III-C, we will show that a negative  $E_{||}$  will occur when the reverse ion anisotropy is true, i.e., when  $w_{i\perp}/2 > w_{i||}$ , and certain other conditions are satisfied. Thus, in this section, we propose the following model for a negative  $E_{||}$  in a quasi-stable downward auroral-current region: 1) the driver of the BBELF turbulence is unspecified, but the spectrum of the turbulence is given experimentally and 2) the self-consistent  $E_{||}$  is sustained by a two-fold mechanism where the BBELF turbulence resonantly heats the ions perpendicular to  $B$  which, in a dipolar magnetic field, produces a velocity-space anisotropy in the ion distribution function where  $w_{i\perp}/2 > w_{i||}$ . Of course, the negative  $E_{||}$  must also be self-consistent with the upward acceleration of the electrons, and this relationship is also discussed in Sections III-B and III-D.

The steady-state kinetic diffusion equations in one-spatial and two-velocity dimensions are

$$\left\{ v_{||} \frac{\partial}{\partial s} + \left[ g_{||} + \frac{q_{\alpha}}{m_{\alpha}} E_{||} \right] \frac{\partial}{\partial v_{||}} - \frac{1}{2B} \frac{dB}{ds} \left[ v_{\perp}^2 \frac{\partial}{\partial v_{||}} - v_{||} v_{\perp} \frac{\partial}{\partial v_{\perp}} \right] \right\} f_{\alpha} = \left( \frac{\delta f}{\delta t} \right)_{\alpha} \quad (34)$$

$$\left( \frac{\delta f}{\delta t} \right)_{\alpha} = \frac{1}{v_{\perp}} \frac{\partial}{\partial v_{\perp}} v_{\perp} D_{\alpha\perp} \frac{\partial}{\partial v_{\perp}} f_{\alpha}, \quad (35)$$

and the quasi-neutrality (Q-N) condition is

$$n_e = \sum_{\beta} n_{\beta} \quad (36)$$

where  $\beta$  is summed over the ions. Equations (34)–(36) are identical to (1) and (2) except for the velocity-space diffusion term. Here,  $D_{\alpha\perp}$  is the perpendicular component of the gyrotropically averaged diffusion tensor, which is discussed below. Equation (34) has been used before to develop a kinetic theory of the “pressure cooker” effect in downward auroral-current regions [29], [30]. For the original reference on the “pressure cooker” effect, see [21].

As mentioned above, we assume that BBELF turbulence exists on the flux tube, is given experimentally, and that the waves heat the ions by cyclotron resonance near the ion gyrofrequency. Also, we do not specify the driver of the turbulence nor do we attempt a self-consistent treatment of the particles and the waves.

In general, the diffusion tensor for the problem contains both a perpendicular and a parallel part and is velocity dependent. It may be derived for electromagnetic modes from quasi-linear theory [39] or from Fokker-Planck theory by assuming that the particles undergo a random walk in velocity space [40]. If the dominant modes are electromagnetic and the ion energies are less than about 1 KeV, then  $k_{||} v_{||} \ll \Omega_i$  and  $D_{\perp} \gg D_{||}$ , where  $k_{||}$  is the parallel wave vector,  $\Omega_i$  is the ion gyrofrequency, and  $D_{||}$  is the parallel component of the diffusion tensor. For these conditions, the turbulent (anomalous), resonant perpendicular ion heating rate is

$$167 \quad \dot{w}_{i\perp} = 2\pi n_i D_{i\perp} = (q_i^2/2m_i) S_L(\omega = \Omega_i) \quad (37)$$



where  $S_L(\Omega_i)$  is the fraction of the total electric-field spectral density in the left-hand circular polarized (LHCP) electromagnetic ion cyclotron component and is velocity independent. This result may also be derived from simple arguments [41]. However, if the dominant modes are electrostatic, then the diffusion tensor for the problem contains velocity dependence, and (35) and (37) are approximate.

For the electrons,  $D_{e\perp} \cong 0$ , since there is no resonant heating at these low frequencies. However, preliminary studies show that under certain conditions, nonresonant wave-electron interactions are important. In this paper, we neglect all turbulent electron heating. Therefore, the approximation that we use is that the kinetic diffusion equation is used for the ion dynamics where only the perpendicular diffusion term is retained, and the Vlasov equation is used for the electron dynamics.

In (36), Poisson's equation has been replaced by the Q-N condition. The same remarks made in Section II-A about the validity of this replacement apply here.

### B. Numerical Solution for $E_{\parallel}$ and Related Quantities from the Multimoment Fluid Equations

We now proceed to derive the multimoment fluid equations by multiplying (34) by  $v_{\perp}^n v_{\parallel}^{\ell}$  and integrating over all velocity space. We use the same notation as in Section II-B. In addition, we need to evaluate the following integrals:

$$2\pi \int_{-\infty}^{\infty} dv_{\parallel} v_{\parallel}^{\ell} \int_0^{\infty} dv_{\perp} v_{\perp}^n \frac{\partial}{\partial v_{\perp}} v_{\perp} D_{\alpha\perp} \frac{\partial}{\partial v_{\perp}} f_{\alpha}.$$

Since  $D_{\alpha\perp}$  depends only on  $s$  in our model, the integrals are zero for  $n = 0$ , are

$$D_{\alpha\perp} 2\pi \int_{-\infty}^{\infty} dv_{\parallel} v_{\parallel}^{\ell} \int_0^{\infty} dv_{\perp} f_{\alpha} = D_{\alpha\perp} \langle -1, \ell \rangle_{\alpha}$$

for  $n = 1$  and  $n^2 D_{\alpha\perp} \langle n - 2, \ell \rangle_{\alpha}$  for  $n \geq 2$ . Using these definitions for the bracket symbols, the multimoment fluid equations for all  $n$  and  $\ell$  are

$$\begin{aligned} d/ds \langle n, \ell + 1 \rangle_{\alpha} + \dot{A} (1 + n/2) \langle n, \ell + 1 \rangle_{\alpha} \\ + \ell \{ (q_{\alpha}/m_{\alpha}) (d/ds \Phi_{\alpha\parallel}) \langle n, \ell - 1 \rangle_{\alpha} \\ - (\dot{A}/2) \langle n + 2, \ell - 1 \rangle_{\alpha} \} \\ = n^2 D_{\alpha\perp} \langle n - 2, \ell \rangle_{\alpha}. \end{aligned} \quad (38)$$

Using the same definitions and procedures as in Section II, we find that the multimoment fluid equations for  $n = 0, \ell = 0$ ;  $n = 0, \ell = 1$ ;  $n = 0, \ell = 2$ ; and  $n = 2, \ell = 0$  are

$$B d/ds (n_{\alpha} u_{\alpha}/B) = 0 \quad (39)$$

$$\begin{aligned} d/ds (n_{\alpha} w_{\alpha\parallel}) - B^{-1} dB/ds n_{\alpha} (w_{\alpha\parallel} - w_{\alpha\perp}/2) \\ + n_{\alpha} (q_{\alpha}/2) d/ds \Phi_{\alpha\parallel} = 0 \end{aligned} \quad (40)$$

$$\begin{aligned} B d/ds \{ [n_{\alpha} Q_{\alpha\parallel} + n_{\alpha} Q_{\alpha\perp} + q_{\alpha} n_{\alpha} u_{\alpha} \Phi_{\alpha\parallel}] / B \} \\ = \dot{w}_{\alpha\perp} n_{\alpha} \end{aligned} \quad (41)$$

$$B^2 d/ds (n_{\alpha} Q_{\alpha\perp} / B^2) = \dot{w}_{\alpha\perp} n_{\alpha}. \quad (42)$$

Equations (39)–(42) are the standard balance equations for the number flux, momentum, total energy flux, and perpendicular energy flux, respectively.

As in Section II, formal expressions for  $E_{\parallel}$  may be found from (40) and (41). Neglecting gravity, we have

$$\begin{aligned} E_{\parallel} = (2/q_{\alpha}) \{ B^{-1} dB/ds (w_{\alpha\perp}/2 - w_{\alpha\parallel}) \\ + n_{\alpha}^{-1} d/ds n_{\alpha} w_{\alpha\parallel} \} \end{aligned} \quad (43)$$

$$\begin{aligned} E_{\parallel} = -(q_{\alpha} u_{\alpha})^{-1} \dot{w}_{\alpha\perp} + (B/q_{\alpha} n_{\alpha} u_{\alpha}) d/ds \\ \cdot [(n_{\alpha} Q_{\alpha\parallel} + n_{\alpha} Q_{\alpha\perp})/B]. \end{aligned} \quad (44)$$

These are the self-consistent formulas for  $E_{\parallel}$  which must be satisfied once the solution for the problem is found.

In order to solve (39)–(42) and (36), we must introduce closure approximations. Instead of using the standard procedure, we introduce the same closure assumptions which we did in Section II-B by imposing (17) and (18). Using (17), (18), and (39), we see that the multimoment fluid equations become

$$d/ds (n_{\alpha} u_{\alpha}/B) = 0 \quad (45)$$

$$\begin{aligned} d/ds n_{\alpha} w_{\alpha\parallel} - B^{-1} dB/ds n_{\alpha} [w_{\alpha\parallel} - w_{\alpha\perp}/2] \\ + n_{\alpha} (q_{\alpha}/2) d/ds \Phi_{\alpha\parallel} = 0 \end{aligned} \quad (46)$$

$$d/ds (w_{\alpha\parallel} + w_{\alpha\perp} + q_{\alpha} \Phi_{\alpha\parallel}) = \dot{w}_{\alpha\perp}/u_{\alpha} \quad (47)$$

$$B d/ds (w_{\alpha\perp}/B) = \dot{w}_{\alpha\perp}/u_{\alpha} \quad (48)$$

$$n_e = \sum_{\beta} n_{\beta}, \quad \beta = \text{ions}. \quad (49)$$

Equations (45)–(49) are a set of  $4\alpha + 1$  nonlinear, first-order ordinary differential equations for  $4\alpha + 1$  unknowns subject to boundary conditions imposed at either end of the flux tube. With the aid of (45), we may show that as  $T_{i\parallel} \rightarrow 0$ , (47) and (48) for the ions reduce to the ion mean particle equations of motion given in [21] and [41].

The same remarks about this closure assumption made in Section II-B apply here. Basically, this closure amounts to the assumption that  $T_{\alpha\parallel}$  and  $m_{\alpha} u_{\alpha}^2$  change proportionately from  $s_1$  to  $s_2$ , so that the ratio  $(T_{\alpha\parallel}/2 + m_{\alpha} u_{\alpha}^2/2)/(m_{\alpha} u_{\alpha}^2/2)$  is nearly constant. We have examined some S3-3 [21], FREJA [22], and FAST [23] ion and electron particle data for downward auroral-current regions. We find that the ion conic data at the satellite altitude show distributions where both  $T_{i\parallel}$  and  $m_i u_i^2$  have increased more or less proportionately from their ionospheric boundary values. The satellite data also show "flat top" or "cigar shaped" electron distribution functions for downward auroral-current regions where a similar statement about  $T_{e\parallel}$  and  $m_e u_e^2$  is true. For these reasons, we argue that the closure we use is approximately valid for downward auroral-current regions.

Before we are able to solve the multimoment fluid equations, we must specify the turbulent, resonant perpendicular ion heating rate,  $\dot{w}_{i\perp}$ , and the boundary conditions. In this section, we impose conditions consistent with the FREJA experimental observations by Boehm *et al.* [22] for a downward auroral-current region. We do this so that we may compare the theoretical results to the experimental results in Section III-E. In that data set, the total electric-field spectral density,  $S(f)$ , was measured at the satellite altitude [22]. In the vicinity of the oxygen cyclotron frequency, we found that  $S(f) \sim f^{-\alpha}$ . Since  $S$  is evaluated at  $f = f_i$ , this leads to

$$S_L(f = f_i) = \eta_L S_o (s/s_o)^{3\alpha} \quad (50)$$

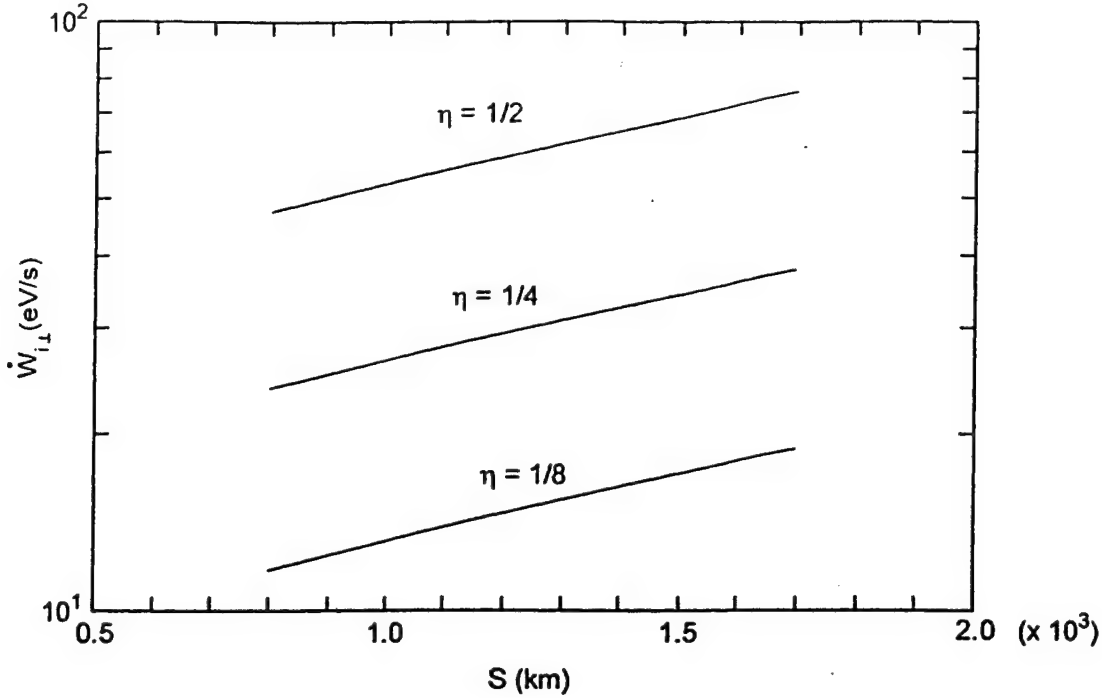


Fig. 5. The turbulent (anomalous), resonant perpendicular ion heating rate for  $\eta_L = 1/2, 1/4$ , and  $1/8$  from (37).

where

- $s_o$  the radius of the earth, is approximated by 6400 km;
- $\eta_L$  is the fraction of the total spectral power in the LHCP ion cyclotron component; and
- $\alpha$  is the spectral index.

For this data set, we found that  $S_o = 2 \times 10^{-5} \text{ (V/m)}^2 \text{ (Hz)}^{-1}$  and  $\alpha = 1.3$ . Since no information was available about the altitude dependence of  $S_o$ , we assumed it to be uniform. In Fig. 5, we show a graph of  $\dot{w}_{i\perp}$  versus  $s$  for  $\eta_L = 1/2, 1/4$ , and  $1/8$ . We see that as the ions are heated and move up the  $B$ -field line, the heating rate increases because the ions are in resonance with lower and lower frequencies. We also assume that the dominant ion was atomic oxygen and that  $s_1 - s_o = 800 \text{ km}$ ,  $s_2 - s_o = 1700 \text{ km}$  (the satellite altitude),  $B(s) = B_o(s_o/s)^3$ , and  $B_o = 0.57 \text{ Gauss}$ . The boundary conditions at  $s_1$  are  $n_{i1} = n_{e1} = n_1 = 10^3 \text{ cm}^{-3}$ ,  $u_{i1} = 0.5 \text{ km/s}$ ,  $u_{e1} = 15 \text{ km/s}$ ,  $T_{i\parallel 1} = T_{i\perp 1} = 0.1 \text{ eV}$ ,  $T_{e\parallel 1} = T_{e\perp 1} = 0.3 \text{ eV}$ , and  $\phi_{\parallel 1} = 0$ . These parameters give  $j_{\parallel 1} = -2.3 \text{ } \mu\text{A/m}^2$ ,  $w_{i\parallel 1} = 0.071 \text{ eV}$ , and  $w_{e\parallel 1} = 0.151 \text{ eV}$ , and are typical for the topside, high-latitude ionosphere [42].

We now proceed to solve (45)–(49) by a numerical method. The method finds the  $4\alpha + 1$  values of  $n_\alpha$ ,  $u_\alpha$ ,  $w_{\alpha\parallel}$ ,  $w_{\alpha\perp}$ , and  $\phi_{\parallel}$  as a function of  $s$  given their values at one boundary. In this case,  $s_1 \leq s \leq s_2$ , and the boundary is  $s_1$ . The procedure implements the semi-implicit discretization method of Bader and Deuffhard [43] and works for nonlinear systems of first-order differential equations that may be stiff. The method was tested by setting  $w_{i\perp}$  very small and thereby obtaining the analytical results given in Section II-B for those boundary conditions. A graph of the numerical solution is given in Fig. 6, where we have chosen  $\eta_L = 1/2$  and where  $s$  measures the distance along  $B$  from the surface of the earth. Remember that  $w_{\alpha\perp} = T_{\alpha\perp}$ . We

have also plotted the current density  $j_{\parallel}$ . Here, we have used the superscript  $I$  to denote the fact that the particles are of ionospheric origin. The dashed curve in the  $n^{(I)}$  graph gives the density of the background ionosphere when there is no turbulent perpendicular ion heating, i.e., when  $\dot{w}_{i\perp} = 0$ . We note here that there is a predicted potential increase of 610 V from 800 to 1700 km for the Boehm *et al.* data set.

In Sections III-C–III-E, we will discuss further aspects of the solution shown in Fig. 6. However, we wish to say here that the major point of this paper is that for downward auroral-current regions,  $E_{\parallel}$  is negative and there is a potential increase from the ionosphere to the magnetosphere. This is opposite to the result for upward auroral-current regions, where the A-F formula gives  $E_{\parallel}$  positive and a potential drop from the ionosphere to the magnetosphere. We also note here that  $\phi_{\parallel}$  is concave upward ( $d^2\phi_{\parallel}/ds^2 > 0$ ) and that the polarization charge density found from Poisson's equation has the correct sign for a negative  $E_{\parallel}$  region.

### C. Analogue for the A-F Formula for $E_{\parallel}$ in Downward Auroral-Current Regions

Equations (43) and (44) give four self-consistent formulas for  $E_{\parallel}$  in an electron-ion plasma. If we had an analytic solution of the problem, we could substitute it into any one of these expressions and get the correct formula for  $E_{\parallel}$ . Since we do not, we may substitute the numerical solution into these equations in order to understand how a negative  $E_{\parallel}$  is sustained in downward auroral-current regions.

For example, consider (43) for the ions. It is

$$E_{\parallel} = (2/e) \{ B^{-1} dB/ds (w_{i\perp}/2 - w_{i\parallel}) + n_i^{-1} d/ds n_i w_{i\parallel} \}. \quad (51)$$



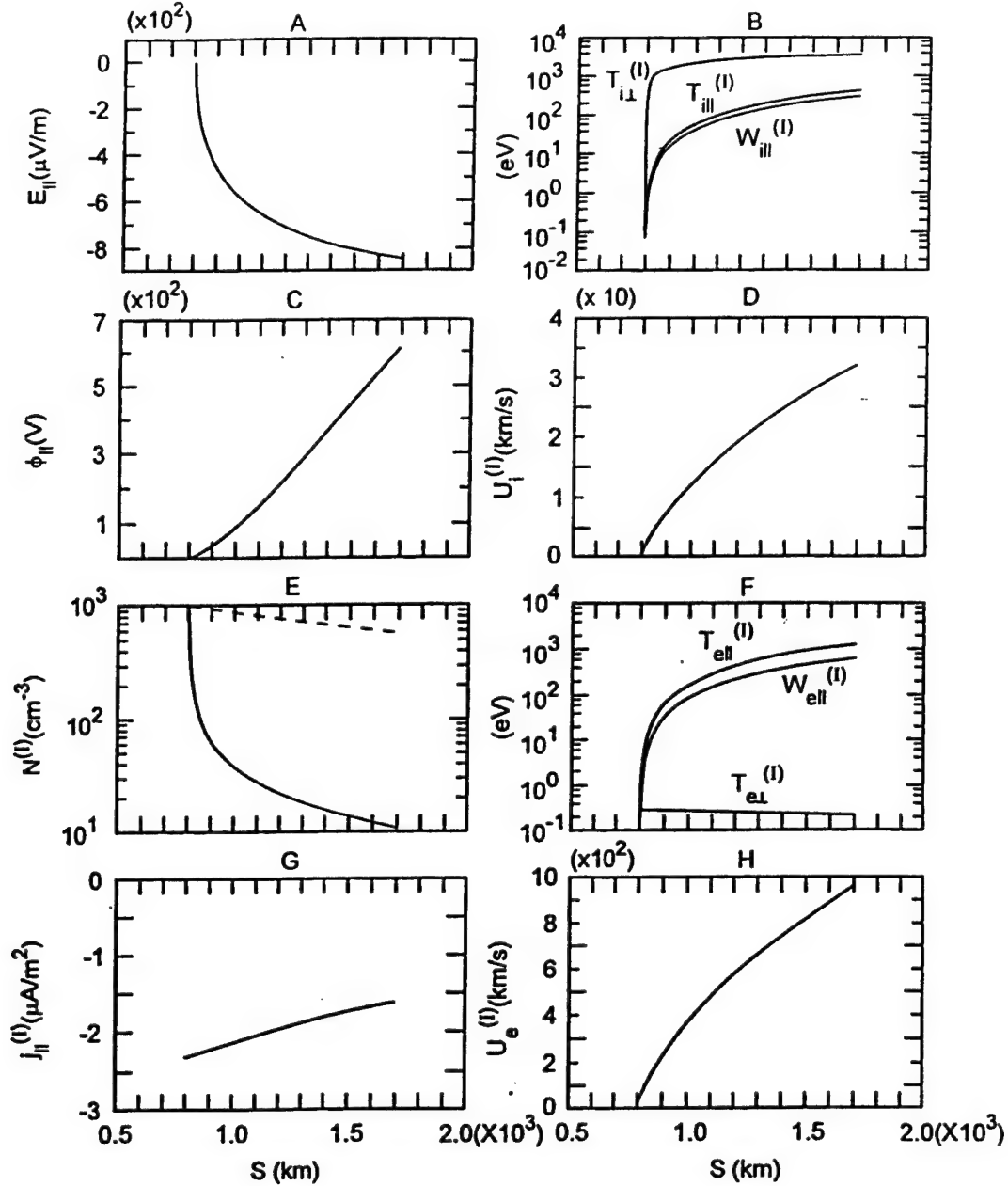


Fig. 6. The numerical solution for the turbulent (anomalous) heating of ionospheric ions in a downward auroral-current region observed by the FREJA satellite from (45)–(49). The symbols are defined in the text,  $\eta_L = 1/2$ , and the superscript  $I$  denotes particles of ionospheric origin.

We may integrate (48) from  $s_1$  to  $s$  to obtain a formal expression for  $w_{i\perp}$

$$w_{i\perp}(s) = \left[ \frac{B(s)}{B_1} \right] w_{i\perp 1} + B(s) \int_{s_1}^s ds' \left[ \frac{\dot{w}_{i\perp}(s')}{B(s') w_i(s')} \right]. \quad (52)$$

Now we can see what is happening in (51). If the turbulent perpendicular ion-heating rate is sufficiently large, then  $w_{i\perp}/2 - w_{i\parallel}$  is positive (see Fig. 6) and, since  $B^{-1} dB/ds$  is negative, the first term on the right-hand side of (51) is negative. From Fig. 6, we also see that  $n_i^{-1} d/ds n_i w_{i\parallel}$  is positive, but smaller than the magnitude of the first term of (51) inside the brackets. Therefore,  $E_{\parallel}$  is negative. This is shown in Fig. 7, where  $E_{\parallel}^{(1)}$

and  $E_{\parallel}^{(2)}$  denote the first and second terms on the right-hand side of (51), respectively, and  $E_{\parallel}^{(\text{total})}$  is the total  $E_{\parallel}$ . We see that once the numerical solution is known, then the fact that  $E_{\parallel}$  is negative can be understood from the ion moments alone.

For comparative purposes, we will refer to (51) and (52) as the analogue of the A–F formula for  $E_{\parallel}$  in downward auroral-current regions. Although (51) is formally the same as (33) in Section II-C, its physical content is different. For downward auroral-current regions, it is the turbulent, resonant perpendicular ion heating that produces the ion temperature anisotropy ( $w_{i\perp}/2 > w_{i\parallel}$ ) which is consistent with the negative  $E_{\parallel}$ . Since upward and downward auroral-current regions have opposite ion velocity-space anisotropies, their parallel  $E$ -fields have opposite signs.

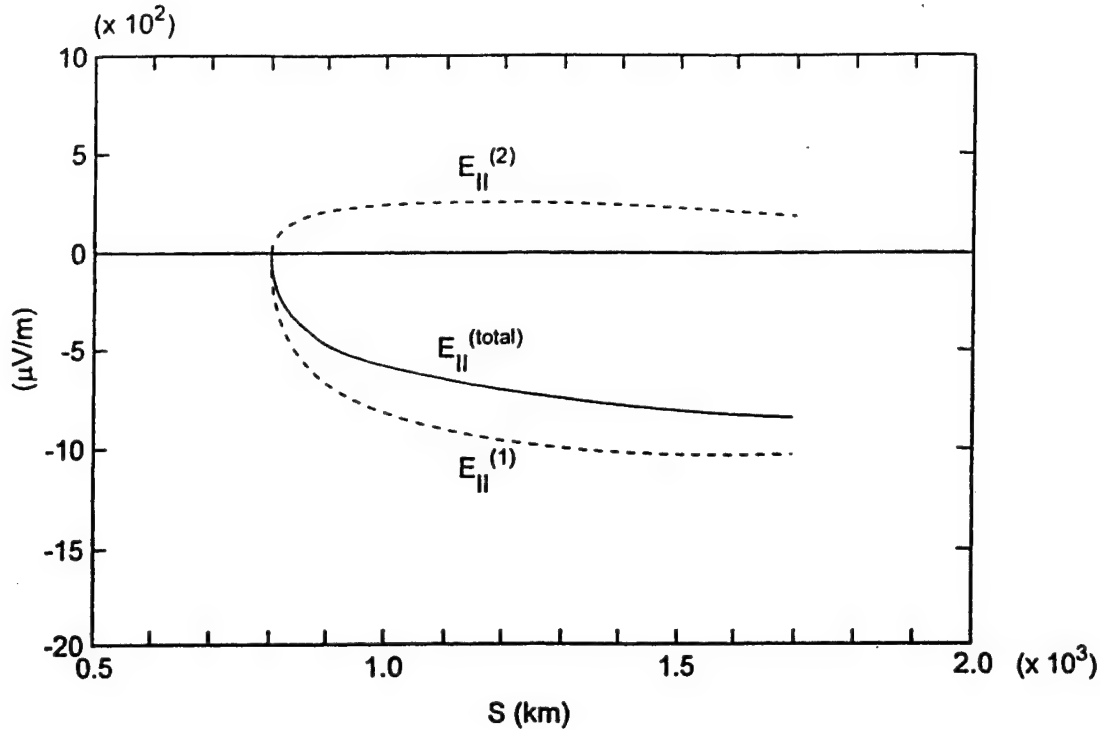


Fig. 7. The solution of the analogue of the A-F formula for  $E_{\parallel}$  in a downward auroral-current region given by (51). Here,  $E_{\parallel}^{(1)}$  is the negative contribution,  $E_{\parallel}^{(2)}$  is the positive contribution, and  $E_{\parallel}^{(total)}$  is the total.

#### D. Understanding the Behavior of the Solution

In Section III-C, we gave what we call an analogue of the A-F formula for  $E_{\parallel}$  in downward auroral-current regions and a condition on the moments of the ion distribution function which is self-consistent with the negative  $E_{\parallel}$ . Now, we wish to give a physical interpretation of the behavior of the ion and electron moments shown in Fig. 6, using the conservation relations.

In order to understand the behavior of  $T_{i\perp}$  and  $T_{e\perp}$ , we recall that  $w_{\alpha\perp} = T_{\alpha\perp}$  and use perpendicular energy balance (48). For the ions, we have

$$d/ds(T_{i\perp}/B) = \dot{w}_{i\perp}/u_i B. \quad (53)$$

Since  $\dot{w}_{i\perp}/u_i B$  is positive,  $T_{i\perp}/B$  increases with  $s$  in such a way that  $T_{i\perp}$  increases from its boundary value of 0.1 eV at 800 km to 3.4 keV at 1700 km. If other perpendicular ion heating processes operate on the flux tube due, for example, to the presence of fast bipolar solitary structures, then the heating rate for that process may be added to  $\dot{w}_{i\perp}$ . The amount of perpendicular ion heating would then be increased from that produced by the BBELF turbulence alone. For the electrons,  $\dot{w}_{e\perp}$  is zero, so

$$d/ds(T_{e\perp}/B) = 0 \quad (54)$$

and  $T_{e\perp}$  cools adiabatically from its boundary value of 0.3 eV at 800 km to 0.21 eV at 1700 km. If other electron heating processes operate on the flux tube, this result could be modified.

We saw in Section III-C that when  $\dot{w}_{i\perp}$  is sufficiently large, it dominates the particle dynamics and the gravitational potential can be neglected compared to the electrostatic potential. Under these conditions, consider total energy balance (47) for the elec-

trons. Since  $d/ds w_{e\perp}$  is small compared to  $d/ds w_{e\parallel}$ , we may neglect it to find that

$$d/ds w_{e\parallel} = d/ds [T_{e\parallel}/2 + m_e u_e^2/2] \cong -eE_{\parallel}. \quad (55)$$

Since  $E_{\parallel}$  is negative,  $w_{e\parallel}$  increases with  $s$  from its boundary value of 0.15 eV at 800 km to 610 eV at 1700 km. We see that it is the downward-pointing  $E_{\parallel}$  that is self-consistent with the upward acceleration of the electrons. Because of the closure assumption, which is consistent with the electron experimental data,  $w_{e\parallel}$  is partitioned proportionately between the thermal part and the drift part so that both increase with  $s$ . Equation (55) may be integrated from  $s_1$  to  $s$  to obtain an approximate conservation relation for  $\phi_{\parallel}$  and  $w_{e\parallel}$ .

$$e[\phi_{\parallel}(s) - \phi_{\parallel}(s_1)] \cong w_{e\parallel}(s) - w_{e\parallel}(s_1). \quad (56)$$

It is interesting to consider the more rigorous conservation of total energy flux for the electrons from (41) before any closure approximation is made. Since  $d/ds n_e Q_{e\perp}$  is small compared to  $d/ds n_e Q_{e\parallel}$  and the gravitational potential may be neglected compared to the electrostatic potential, we obtain

$$d/ds \{ (n_e u_e / B) [n_e Q_{e\parallel} / n_e u_e - e\phi_{\parallel}] \} \cong 0. \quad (57)$$

Using (39), we may simplify this expression and integrate from  $s_1$  to  $s$  to obtain

$$e[\phi_{\parallel}(s) - \phi_{\parallel}(s_1)] \cong E_0(s) - E_0(s_1) \quad (58)$$

where  $E_0$  is the characteristic energy and is defined as  $n_e Q_{e\parallel} / n_e u_e$ . This is just the conservation relation calculated from the experimental data for downward auroral-current regions discussed and illustrated in Fig. 2 of Carlson *et al.* [23]. When we compare (56) to (58), we see that our closure approximation is valid for electron distributions that are more

beam-like than thermal-like and therefore underestimates the value of  $\phi_{\parallel}$  compared to the more rigorous result given by (58).

Consider total energy balance (47) for the ions, where the gravitational potential may be neglected compared to the electrostatic potential

$$d/ds [T_{i\parallel}/2 + m_i u_i^2/2] + d/ds T_{i\perp} + e d/ds \phi_{\parallel} = \dot{w}_{i\perp}/u_i. \quad (59)$$

From Figs. 5 and 6, we find that  $\dot{w}_{i\perp}/u_i$  is larger than  $e d/ds \phi_{\parallel}$ , which is positive. Therefore, the perpendicular wave-ion heating rate supplies the energy to heat the ions perpendicular to  $B$  and causes the ions to be heated and accelerated parallel to  $B$ , as shown in (59). Because of the closure assumption, which is consistent with both the ion conic data and the kinetic solution for the ion "pressure cooker" effect [29],  $w_{i\parallel}$  is partitioned proportionately between the thermal part and the drift part so that both increase with  $s$ .

The rapid decrease of  $n$  can be understood from conservation of number flux (45)

$$d/ds(nu_{\alpha}/B) = 0. \quad (60)$$

Since  $u_i$  and  $u_e$  both increase with  $s$  and  $B$  decreases with  $s$ , then  $n$  decreases rapidly from  $10^3 \text{ cm}^{-3}$  at 800 km to  $11 \text{ cm}^{-3}$  at 1700 km. This produces a cavity in the downward auroral-current region. For comparative purposes, the dashed curve in Fig. 6 gives the background value of  $n$  when there is no turbulent ion heating.

The current density

$$j_{\parallel} = en(u_i - u_e) \cong -enu_e \quad (61)$$

is dominated by the electron drift and is therefore downward-pointing.

#### E. Comparison to a FREJA Satellite Observation of a Downward Auroral-Current Region

In this section, we compare the theoretical results given in Section III-B to the experimental results of Boehm *et al.* [22] for a FREJA satellite pass through a downward auroral-current region near 1700 km in the morning auroral zone. In the Boehm *et al.* data set, the total electric-field spectral density,  $S(f)$ , was determined experimentally at the satellite altitude and is given in Section III-B. In the theory we present, there is one adjustable parameter,  $\eta_L$ , which we have chosen as  $1/2$ . Also, we assume typical values [42] for the electron and ion moments at the lower boundary, which we chose to be 800 km. A comparison between the theoretical and experimental values for the quantities determined by the satellite at 1700 km is shown in Table I. The experimental values are taken from [22] where  $u_e$  was estimated using the formula  $j_{\parallel} \cong -enu_e$ , and  $\theta$  is the ion conic angle. The other theoretical quantities at 1700 km may be determined from Fig. 6. We see reasonable agreement for all values given in the table with the possible exception of  $T_{i\perp}$ . However, the estimated experimental value of 5 keV is probably too large, and a more realistic range is from 2 to 3 keV. It is important to note that using the experimental value for  $u_e$  of 940 km/s, we find that the drift part of  $w_{e\parallel}$  is 2.5 eV at 1700 km. From data shown in [22, Fig. 1], we also find that  $T_{e\parallel}/2 \gg m_e u_e^2/2$  at the satellite altitude. Apparently, the electrons do not run away in an  $E_{\parallel}$  field

as a beam, but appear as a field-aligned distribution with a large  $T_{e\parallel}/2$  compared to  $m_e u_e^2/2$ . This is also what is observed by the FAST satellite [23]. As pointed out in [22], this is probably due to strong wave-electron interactions. It is important to note here that wave-electron interactions are not taken into account in the present version of our theory, since we use the Vlasov equation for the electron dynamics. Instead, the experimental fact that  $T_{e\parallel}/2 \gg m_e u_e^2/2$  is modeled by the electron closure approximation that we use.

#### IV. DISCUSSION

In this paper, we give an alternative derivation of the A-F formula for a positive  $E_{\parallel}$  in upward auroral-current regions [see (30)], and propose an analogous formula for a negative  $E_{\parallel}$  in downward auroral-current regions [see (51) and (52)]. In addition, we derive a third result, i.e., an equivalent expression for the A-F formula for  $E_{\parallel}$  in terms of the ion moments alone [see (33)].

The A-F formula is a benchmark result not only for pedagogical reasons (it is a closed-form solution), but also because it clarifies the essential physics of a particular model for auroral arc formation. In that model, the driver is the earthward-streaming, energetic magnetospheric particles, and the mechanism for sustaining a positive  $E_{\parallel}$ , thereby accelerating the auroral particles, is the differential velocity-space anisotropy between the ions and the electrons in the dipolar magnetic field ( $w_{i\parallel} w_{e\perp} - w_{e\parallel} w_{i\perp} > 0$ ). Another way of looking at this result, in terms of the ion moments alone, reveals that  $E_{\parallel}$  is positive when  $w_{i\parallel} > w_{i\perp}/2$  and certain other conditions are met. According to the PIC simulation by Schriver, when ionospheric particles and wave-particle interactions in the electrostatic approximation are included in the model, the potential drop is reduced from its A-F value, and the shape of  $\phi_{\parallel}$  is modified. In his review, Borovsky [17] identifies ten drivers and 12 possible mechanisms, none of which appears to explain all aspects of auroral arc formation. It is clear that more analytical and simulation work on upward auroral-current regions is needed.

The primary result that we present in this paper is a model for a negative  $E_{\parallel}$  in downward auroral-current regions. The BBELF turbulence, which experiment shows is present, plays a central role. The driver of the turbulence is unspecified, but the spectrum of the turbulence is given experimentally. The self-consistent  $E_{\parallel}$  is sustained by a two-fold mechanism where the BBELF turbulence resonantly heats the ions transverse to  $B$  which, in a dipolar magnetic field, produces an ion velocity-space anisotropy where  $w_{i\perp}/2 > w_{i\parallel}$  [see (51) and (52)]. This is just the reverse anisotropy from that which occurs in the equivalent A-F formula for the ions [see (33)] and is consistent with an  $E_{\parallel}$  of the opposite sign. Of course,  $E_{\parallel}$  and hence  $\phi_{\parallel}$  must also be self-consistent with the upward acceleration of the electrons [see (56) and the more rigorous expression given by (58)]. In this paper, we do not attempt to resolve how the downward auroral-current region is driven. This subject is an active area of research and beyond the scope of the present work. For example, the BBELF could be driven by the electron beam, shear in the two-dimensional ion flow, or some other mechanism. Whatever the case may be, the conservation laws derived

TABLE I  
THEORY-DATA COMPARISON FOR A DOWNWARD AURORAL-CURRENT REGION

Quantity at 1700 km	Theory	FREJA Data
$n$ (cm <sup>-3</sup> )	11	~10
$u_e$ (km/s)	955	~940
$j_{\parallel}$ (μA/m <sup>2</sup> )	-1.6	~-1.5
$T_{e\parallel}$ (eV)	0.21	0.1 - 0.25
$T_{e\perp}$ (keV)	3.4	< 5
$\Delta\Phi_{\parallel}$ (Volts)	610	~700
$\theta$ (degrees)	106	100 - 110

from the appropriate kinetic model impose powerful constraints on the moments of the electron and ion distribution functions, the strength of the BBELF turbulence, and the magnitude and direction of  $E_{\parallel}$ . These conservation relations were discussed in Sections III-B and III-D. The central point of this paper is that both the velocity-space anisotropy of the particles and the turbulent heating of the ions play an important role in downward auroral-current regions.

When this model for downward auroral-current regions is applied to the FREJA data set by Boehm *et al.* [22] in the morning auroral zone, good agreement between theory and experiment is achieved (see Table I). For example, we find that  $j_{\parallel} \sim -1.6$  μA/m<sup>2</sup> at 1700 km, the average parallel  $E$ -field  $\langle E_{\parallel} \rangle \sim -680$  μV/m, and a potential increase of ~610 V from 800 to 1700 km are obtained. In [29] and [30], a kinetic theory of the "pressure cooker" effect was given for the S3-3 data set of Gorney *et al.* [21] using (34)–(36) for a downward auroral-current region in the dayside auroral zone. Again, good agreement between theory and experiment was achieved. Since the turbulence was weaker than that in the FREJA data, we found that  $j_{\parallel} \sim -0.4$  μA/m<sup>2</sup> at 6000 km,  $\langle E_{\parallel} \rangle \sim -12$  μV/m, and a potential increase of ~55 V from 1500 to 6000 km were obtained. In the anomalous transport calculation for the current-driven ion cyclotron instability reported in [26], they found that  $j_{\parallel} \sim -1.1$  μA/m<sup>2</sup> and  $\langle E_{\parallel} \rangle \sim -0.1$  μV/m for a 1 V potential increase in 10<sup>4</sup> km. This result for  $\langle E_{\parallel} \rangle$  appears to be too small to be of significance in downward auroral-current regions.

The model presented here for downward auroral-current regions needs to be generalized. There is the obvious need to identify the driver of the BBELF turbulence and to treat the wave-particle interactions self-consistently. Aside from this, there are other, more straightforward generalizations that can be carried out. Recently, we have generalized this work in two ways. In addition to the presence of the heated and accelerated ionospheric particles, we have included a magnetospheric population of earthward-streaming ions and electrons. We find that as the flux of the magnetospheric particles is increased, a positive contribution to  $E_{\parallel}$  is produced, and the total  $E_{\parallel}$  is less negative. In fact, if the flux of magnetospheric particles is large enough, the two effects combine to produce a positive  $E_{\parallel}$  and an upward

auroral-current situation. A second way in which we have generalized the model is to include wave-particle interactions in the equation for the electrons. The BBELF waves cannot heat the electrons perpendicular to  $B$  by a cyclotron resonant interaction because the frequencies are too low, but there is a nonresonant diffusion process which acts parallel to  $B$ . Preliminary results indicate that this diffusion process spreads out the electron distribution function in velocity space parallel to  $B$ , prevents the formation of a runaway electron beam, and maintains a parallel electron energy,  $w_{e\parallel}$ , where  $T_{e\parallel}/2 > m_e u_e^2/2$ .

It should be mentioned here that there are processes other than ion cyclotron resonance with broadband waves by which ions can be heated in space plasmas. For a discussion of these processes, see [44]. Recently, a new process has been proposed based on an analysis of FAST data. The data show that within a broad region of downward auroral current, there are narrow subregions where intense bursts of fast bipolar solitary structures occur. These subregions coincide with enhanced ion heating (see [24, Fig. 1]). It has been pointed out [23] that the random pulses in the perpendicular  $E$ -field of the solitary structures as they propagate past the nearly stationary ions, could lead to a significant amount of stochastic ion heating. If a perpendicular ion heating rate can be calculated for this process, then it may be added to  $\dot{w}_{i\perp}$  in (41) and (42). The resulting multimoment fluid equations may then be solved using the same method as presented in Section III-B. This would lead to an enhanced amount of perpendicular ion heating, as indicated in [24, Fig. 1].

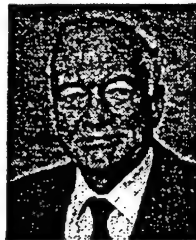
#### ACKNOWLEDGMENT

The authors are indebted to M. Boehm for supplying details on the FREJA data set discussed in Section III. They also acknowledge important conversations with M. Boehm, T. Chang, J. Lemaire, W. Lennartsson, D. Schriver, and M. Schulz.

#### REFERENCES

- [1] T. Iijima and T. A. Potemra, "Large-scale characteristics of field-aligned currents associated with substorms," *J. Geophys. Res.*, vol. 83, no. A2, pp. 599–615, 1978.
- [2] R. C. Elphic *et al.*, "The auroral current circuit and field-aligned currents," *Geophys. Res. Lett.*, vol. 25, no. 12, pp. 2033–2036, 1998.
- [3] H. Alfvén and C. G. Fälthammar, *Cosmical Electrodynamics*. Oxford, U.K.: Oxford Univ. Press, 1963, ch. 5.
- [4] H. Persson, "Electric field along a magnetic field line of force in a low-density plasma," *Phys. Fluids*, vol. 6, no. 12, pp. 1756–1759, 1963.
- [5] —, "Electric field parallel to the magnetic field in a low-density plasma," *Phys. Fluids*, vol. 9, no. 6, pp. 1090–1098, 1966.
- [6] D. P. Stern, "One-dimensional models of quasi-neutral parallel electric fields," *J. Geophys. Res.*, vol. 86, no. A7, pp. 5839–5860, 1981.
- [7] F. S. Mozer, C. A. Cattell, M. K. Hudson, R. L. Lysak, M. Temerin, and R. B. Torbert, "Satellite measurements and theories of low altitude auroral particle acceleration," *Space Sci. Rev.*, vol. 27, pp. 155–213, 1980.
- [8] R. Lundin, G. Haerendel, and S. Grahn, "The FREJA project," *Geophys. Res. Lett.*, vol. 21, no. 17, pp. 1823–1826, 1994.
- [9] C. W. Carlson, R. F. Pfaff, and J. G. Watzin, "The fast auroral snapshot (FAST) mission," *Geophys. Res. Lett.*, vol. 25, no. 12, pp. 2013–2016, 1998.
- [10] R. F. Benson and W. Calvert, "ISIS 1 observations at the source of auroral kilometric radiation," *Geophys. Res. Lett.*, vol. 6, no. 6, pp. 479–482, 1979.
- [11] L. R. Lyons and D. S. Evans, "An association between discrete aurora and energetic particle boundaries," *J. Geophys. Res.*, vol. 89, no. A4, pp. 2395–2400, 1984.

- [12] D. A. Gurnett, R. L. Huff, J. D. Menietti, J. L. Burch, J. D. Winningham, and S. D. Shawhan, "Correlated low-frequency electric and magnetic noise along the auroral field lines," *J. Geophys. Res.*, vol. 89, no. A10, pp. 8971-8985, 1984.
- [13] C. S. Lin, J. N. Barfield, J. L. Burch, and J. D. Winningham, "Near-conjugate observations of inverted-V electron precipitation using DE-1 and DE-2," *J. Geophys. Res.*, vol. 90, no. A2, pp. 1669-1681, 1985.
- [14] R. E. Erlandson, L. J. Zanetti, M. H. Acuna, A. I. Eriksson, L. Eliasson, M. H. Boehm, and L. G. Blomberg, "FREJA observations of electromagnetic ion cyclotron ELF waves and transverse oxygen ion acceleration on auroral field lines," *Geophys. Res. Lett.*, vol. 21, no. 17, pp. 1855-1858, 1994.
- [15] F. S. Mozer, R. Ergun, M. Temerin, C. Cattell, J. Dornbeck, and J. Wygant, "New features of time domain electric-field structures in the auroral acceleration region," *Phys. Rev. Lett.*, vol. 79, no. 7, pp. 1281-1284, 1997.
- [16] J. P. McFadden *et al.*, "Spatial structure and gradients of ion beams observed by FAST," *Geophys. Res. Lett.*, vol. 25, no. 12, 1998.
- [17] J. E. Borovsky, "Auroral arc thickness as predicted by various theories," *J. Geophys. Res.*, vol. 98, no. A4, pp. 6101-6138, 1993.
- [18] D. Schriver, "Particle simulation of the auroral zone showing parallel electric fields, waves, and plasma acceleration," *J. Geophys. Res.*, vol. 104, no. A7, pp. 14655-14670, 1999.
- [19] D. M. Klumpar and W. J. Heikkilä, "Electrons in the ionospheric source cone: Evidence for runaway electrons as carriers of downward Birkeland currents," *Geophys. Res. Lett.*, vol. 9, no. 8, pp. 873-876, 1982.
- [20] J. L. Burch, P. H. Reiff, and M. Sugiura, "Upward electron beams measured by DE-1: A primary source of dayside region-1 Birkeland currents," *Geophys. Res. Lett.*, vol. 10, no. 8, pp. 753-756, 1983.
- [21] D. J. Gorney, Y. T. Chiu, and D. R. Croley, "Trapping of ion conics by downward parallel electric fields," *J. Geophys. Res.*, vol. 90, no. A5, pp. 4205-4210, 1985.
- [22] M. H. Boehm *et al.*, "Observations of an upward-directed electron beam with the perpendicular temperature of the cold ionosphere," *Geophys. Res. Lett.*, vol. 22, no. 16, pp. 2103-2106, 1995.
- [23] C. W. Carlson *et al.*, "FAST observations in the downward auroral current region: Energetic upgoing electron beams, parallel potential drops, and ion heating," *Geophys. Res. Lett.*, vol. 25, no. 12, pp. 2017-2020, 1998.
- [24] R. E. Ergun *et al.*, "FAST satellite observations of large-amplitude solitary structures," *Geophys. Res. Lett.*, vol. 25, no. 12, pp. 2041-2044, 1998.
- [25] G. Marklund, L. Blomberg, C. G. Fälthammar, and P. A. Lindqvist, "On intense diverging electric fields associated with the black aurora," *Geophys. Res. Lett.*, vol. 21, no. 17, pp. 1859-1862, 1994.
- [26] S. B. Ganguli and P. J. Palmadesso, "Plasma transport in the auroral return current region," *J. Geophys. Res.*, vol. 92, no. A8, pp. 8673-8690, 1987.
- [27] N. Singh, H. Thiemann, and R. W. Schunk, "Simulations of auroral plasma processes: Electric fields, waves and particles," *Planet. Space Sci.*, vol. 35, no. 3, pp. 353-395, 1987.
- [28] R. M. Winglee *et al.*, "Particle acceleration and wave emissions associated with the formation of auroral cavities and enhancements," *J. Geophys. Res.*, vol. 93, no. A12, pp. 14567-14590, 1988.
- [29] J. R. Jasperse, "Ion heating, electron acceleration, and the self-consistent parallel  $E$  field in downward auroral current regions," *Geophys. Res. Lett.*, vol. 25, no. 18, pp. 3485-3488, 1998.
- [30] J. R. Jasperse and N. J. Grossbard, "Ion heating, electron acceleration, and the self-consistent parallel  $E$  field in downward auroral current regions," in *Physics of Space Plasmas*, T. Chang and J. R. Jasperse, Eds., 1998, pp. 181-186.
- [31] Y. T. Chiu and J. M. Cornwall, "Electrostatic model of a quiet auroral arc," *J. Geophys. Res.*, vol. 85, no. A2, pp. 543-556, 1980.
- [32] W. Lennartsson, "Some aspects of double layer formation in a plasma constrained by a magnetic mirror," *Laser Particle Beams*, vol. 5, pp. 315-324, 1987.
- [33] J. Lemaire, A. Barakat, J. M. Lescaux, and B. Shizgal, "A method for solving Poisson's equation in geophysical and astrophysical plasmas," *Rarefield Gas Dynam.*, vol. 28, pp. 417-423, 1991.
- [34] A. R. Barakat and R. W. Schunk, "Transport equations for multicomponent anisotropic space plasmas: A review," *Plasma Physics*, vol. 24, no. 4, pp. 389-418, 1982.
- [35] S. B. Ganguli and P. J. Palmadesso, "Plasma transport in the auroral return current region," *J. Geophys. Res.*, vol. 92, no. A8, pp. 8673-8690, 1987.
- [36] T. I. Gombosi and C. E. Rasmussen, "Transport of gyration-dominated space plasmas of thermal origin. I. Generalized transport equations," *J. Geophys. Res.*, vol. 96, no. A5, pp. 7759-7778, 1991.
- [37] S. B. Ganguli, H. G. Mitchell, and P. J. Palmadesso, "Behavior of ionized plasma in the high latitude topside ionosphere: The polar wind," *Planet. Space Sci.*, vol. 35, no. 6, pp. 703-713, 1987.
- [38] E. Möbius, F. M. Ipavick, M. Scholer, G. Gloeckler, D. Hovestadt, and B. Klecker, "Observations of a nonthermal ion layer at the plasma sheet boundary during substorm recovery," *J. Geophys. Res.*, vol. 85, no. A10, pp. 5143-5148, 1980.
- [39] R. Z. Sagdeev and A. A. Galeev, *Nonlinear Plasma Theory*. New York: W. A. Benjamin, 1969, ch. 2.
- [40] S. Ichimaru, *Basic Principles of Plasma Physics*. New York: W. A. Benjamin, 1973, ch. 10.
- [41] T. Chang, G. B. Crew, N. Hershkowitz, J. R. Jasperse, J. M. Retterer, and J. D. Winningham, "Transverse acceleration of oxygen ions by electromagnetic ion cyclotron resonance with broad band left-hand polarized waves," *Geophys. Res. Lett.*, vol. 13, no. 7, pp. 636-639, 1986.
- [42] R. W. Schunk and A. F. Nagy, "Ionospheres of the terrestrial planets," *Rev. Geophys. Space Phys.*, vol. 18, no. 4, pp. 813-852, 1980.
- [43] G. Bader and P. Deuflhard, "A semi-implicit mid-point rule for stiff systems of ordinary differential equations," *Numerische Mathematik*, vol. 41, pp. 373-398, 1983.
- [44] M. Andre *et al.*, "Ion energization mechanisms at 1700 kilometers in the auroral region," *J. Geophys. Res.*, vol. 103, pp. 4199-4222, 1998.



John R. Jasperse was educated at Harvard University, Cambridge, MA and Northeastern University, Boston, MA, where he received the Ph.D. in physics in 1967.

From 1968 to 1970, he was a Lecturer in the Physics Department at Northeastern University where he taught electromagnetic theory and plasma physics. In 1965, he joined the Air Force Research Laboratory (formerly called the Air Force Cambridge Research Laboratory) located at Hanscom AFB, MA, where he is currently a Group Leader in the Space Physics Models Branch. He has served as a Visiting Scientist at the Massachusetts Institute of Technology Center for Space Research since 1979. His current research interests are in the area of ionospheric and magnetospheric physics and plasma physics.

Dr. Jasperse has received a number of awards, honors, and achievements, including the Marcus O'Day and Guenter Loeser Awards. He is listed in American Men of Science and is a co-convenor of the Cambridge Workshop Series in Theoretical Geoplasma Physics. Since 1964, he has authored 87 journal articles, 12 book chapters and conference proceedings, has given numerous lectures at major institutions, and has been a requested consultant for several Department of Defense agencies.



Neil J. Grossbard (M'76) received the B.S. degree in physics from the Massachusetts Institute of Technology in 1959 and the M.S. degrees from Northeastern University in physics in 1962, mathematics in 1971, and electrical engineering in 1981.

He is a Senior Research Physicist at Boston College. His expertise in numerical analysis and modeling methods has enabled him to solve numerous problems in the fields of signal processing and differential, partial differential, and integral equations. Mr. Grossbard has many scientific publications in *Physical Review*, *Journal of Applied Physics*, *Geophysical Research Letters* and other journals.



# Ionospheric effects of major magnetic storms during the International Space Weather Period of September and October 1999: GPS observations, VHF/UHF scintillations, and in situ density structures at middle and equatorial latitudes

Sunanda Basu,<sup>1</sup> Santimay Basu,<sup>2</sup> C. E. Valladares,<sup>3</sup> H.-C. Yeh,<sup>4</sup> S.-Y. Su,<sup>4</sup>  
E. MacKenzie,<sup>3</sup> P. J. Sultan,<sup>2</sup> J. Aarons,<sup>5</sup> F. J. Rich,<sup>2</sup> P. Doherty,<sup>3</sup>  
K. M. Groves,<sup>2</sup> and T. W. Bullett<sup>2</sup>

**Abstract.** In this paper we present a study of the ionospheric effects of a halo coronal mass ejection (CME) initiated on the Sun on September 20, 1999, and causing the largest magnetic storm during this month on September 22–23, 1999, with the hourly *Dst* index being  $-167$  nT at  $\sim 2400$  UT on September 22. The recurrent CME on October 18 caused an even larger magnetic storm on October 22, 1999, with *Dst* of  $-231$  nT at  $\sim 0700$  UT. The ionospheric effects of these two major magnetic storms are studied through their effects on a prototype of a Global Positioning System (GPS)-based navigation system called Wide Area Augmentation System (WAAS) being developed by the Federal Aviation Administration for use in the continental United States and their impact on global VHF/UHF communication systems. It is shown that the penetration of transient magnetospheric electric fields equatorward of the shielding region at midlatitudes, which have been well-correlated in the past with rapid changes in the well-known *Dst* index (or through its recently available high resolution 1-min counterpart the SYM-H index), can cause large increases of total electron content (TEC), TEC fluctuations, and saturated 250-MHz scintillation, and these, in turn, may have significant impacts on WAAS. The local time of *Dst* changes (and not just *Dst* magnitude) was found to be very important for WAAS, since the largest effects on TEC are seen near dusk. The prompt penetration of these magnetospheric electric fields all the way to the magnetic equator causes augmentation or inhibition of equatorial spread *F*. The global ionospheric response to these storms has been obtained from ground-based TEC observations with a GPS network and space-based in situ density and electric field measurements using the Republic of China Satellite-1 (ROCSAT-1) and several Defense Meteorological Satellite Program satellites. These prompt penetration electric fields cause VHF/UHF scintillations and GPS TEC variations at low latitudes in the specific longitude sector for which the early evening period corresponds to the time of rapid *Dst* variations and maximum *Dst* phase. The effects of the delayed ionospheric disturbance dynamo and those of decreased magnetospheric convection on postmidnight irregularity generation are shown to be confined to a part of the same longitude range that actively responded to the prompt penetration of electric fields in the early evening sector.

## 1. Introduction

The Solar Terrestrial Energy Program–Research, Applications and Modeling Phase (S-RAMP) Group of the Scientific Committee for Solar Terrestrial Physics (SCSTEP) con-

ceived and coordinated a month-long campaign interval during September 1999 as an International Space Weather Period (ISWP) to follow the progress of space weather events from their initiation on the Sun to their impacts at the Earth, including their effects on space-based and ground-based technological systems and for assessment of the accuracy of specification and forecasting techniques. A great deal of material on the geoeffective solar wind events during this month has been compiled in a special Web page for which the URL is [http://aoss.engin.umich.edu/intl\\_space\\_weather/sramp/](http://aoss.engin.umich.edu/intl_space_weather/sramp/) to which the reader is referred for additional information (J. U. Kozyra, private communication, 1999). Here we provide some basic information on the interplanetary shocks and southward interplanetary magnetic fields (IMF) that triggered the largest magnetic storm during the core campaign period.

This large magnetic storm was triggered by an interplanetary magnetic cloud (IMC) event extending from 2000 UT on September 22 to 0700 UT on September 23 with maximum IMF >

<sup>1</sup>Atmospheric Sciences Division, National Science Foundation, Arlington, Virginia, USA.

<sup>2</sup>Space Vehicles Directorate, Air Force Research Laboratory, Hanscom Air Force Base, Massachusetts, USA.

<sup>3</sup>Institute for Scientific Research, Boston College, Chestnut Hill, Massachusetts, USA.

<sup>4</sup>Institute of Space Science, National Central University, Chung-Li, Taiwan.

<sup>5</sup>Center for Space Physics, Boston University, Boston, Massachusetts, USA.

Copyright 2001 by the American Geophysical Union.

Paper number 2001JA001116.

0148-0227/01/2001JA001116\$09.00



25 nT. This IMC was able to drive a major magnetic storm with minimum  $Dst$  of  $-167$  nT at  $\sim 2400$  UT on September 22. The most likely solar source was a faint but complete halo coronal mass ejection (CME) event seen at 0606 UT on September 20 which had a travel time of 63 hours (or a speed of  $660 \text{ km s}^{-1}$ ) to reach Earth. The following month a CME recurrent with the September 20 event was observed at 0006 UT on October 18. This resulted in another major magnetic storm with minimum  $Dst$  of  $-231$  nT, which occurred at 0700 UT on October 22, 1999. This latter CME was a partial  $210^\circ$  wide halo type which took 77 hours (or a speed of  $540 \text{ km s}^{-1}$ ) to reach Earth. This storm has also been made part of the ISWP study. We will utilize both storms in this paper, to emphasize that ionospheric effects on specific communication or navigation systems are greatly dependent on the local time of maximum magnetic perturbations and not just on the magnitude of the perturbations. Thus we shall show that the September 1999 storm had a more severe effect on such systems in the United States than the October 1999 storm even though the latter was classified as a much bigger magnetic storm.

Since one of the major objectives of this enterprise was to provide as complete as possible space-based and ground-based observations of these space weather events, we tried to use several global databases to follow the effects of these storms on the total electron content (TEC) and plasma density irregularity structure of the middle- and low-latitude ionosphere. In particular, we chose to cover the middle-latitude ionosphere as an important Global Positioning System (GPS)-based navigation system is being developed for this region in the continental United States. Earlier morphological studies by *Aarons et al.* [1972] and *Aarons and Allen* [1971] have shown that the middle-latitude ionosphere is quite benign, its characteristics being generally determined by the diurnal, seasonal, and solar cycle variations in solar production. It is only during major magnetic storms that this predictable variability can be dramatically overturned as the high-latitude convection pattern expands equatorward. Numerous studies made over the last three decades using the Millstone Hill incoherent scatter radar and the TEC and scintillation network of the Air Force Research Laboratory have delineated the major features of ionospheric storms which result from large energy inputs to the upper atmosphere associated with major magnetic storms. *Foster* [1993] presents a good review of the results obtained starting from 1970. For instance, the enhancement of TEC during local dusk at 1800 LT is well known [*Mendillo et al.*, 1970]. *Rishbeth and Hanson* [1974] suggested that this increase was caused by advection of relatively dense plasma into the observing volume, a fact that was confirmed by observations made at Millstone Hill [*Evans*, 1973; *Buonsanto et al.*, 1979]. *Buonsanto* [1999] in his comprehensive review on ionospheric storms points out that this dusk effect of TEC increase should be distinguished from a more long-lived positive storm effect which is due to large-scale changes in the thermospheric circulation caused by heating in the auroral zone. After the TEC increase at dusk, particularly at high midlatitudes, there is a sharp transition to a negative phase, which can generally be attributed to the equatorward motion of the midlatitude trough [*Mendillo and Klobuchar*, 1975; *Buonsanto et al.*, 1979]. Geostationary satellite observations at 137 MHz made from Hanscom Field, Massachusetts, for which the subionospheric (350 km) location is  $L = 2.8$  showed abrupt onset of scintillations during such major magnetic storms which were coincident with sharp TEC decreases and the appearance of stable auroral red (SAR) arcs

[*Basu*, 1974]. At that time, Basu hypothesized that perhaps the same processes that give rise to SAR arcs at the equatorward edge of the plasmopause are also responsible for generating field-aligned plasma density irregularities of approximately kilometers to hundreds of meters scales that give rise to VHF scintillations.

In the intervening two decades many studies have provided evidence for the presence of intense convection electric fields in the expanded auroral oval [*Foster and Aarons*, 1988; *Yeh et al.*, 1991, and references therein] while transient fields penetrate equatorward of the shielding region at midlatitudes [*Gonzales et al.*, 1983; *Burke et al.*, 1998]. *Foster and Rich* [1998] provide a good summary of such results. Unfortunately, the Millstone Hill incoherent scatter radar (ISR) was not operating during these particular September and October storms, the ISR World Days being scheduled near the middle of the month in both cases. Thus, for these two storms we utilize the scintillation data from Hanscom Air Force Base (AFB), Massachusetts, the Digisonde data from Millstone Hill, and the TEC fluctuation data from the nearby station in Westford, Massachusetts, to monitor the small (approximately kilometers to hundreds of meters) and large (approximately tens of kilometers) scale irregularity behavior in conjunction with Defense Meteorological Satellite Program (DMSP) F12, F13, and F14 overflights to monitor the particles and fields and thermal density structure in the topside ionosphere. In addition, we utilize GPS TEC data from a latitudinal chain of International GPS Service for Geodynamics (IGS) stations to monitor TEC across the continental United States.

Since a major objective of the ISWP is to monitor the effects on technological systems, we chose to study the possible impact of these storms on the Wide Area Augmentation System (WAAS) of the Federal Aviation Administration (FAA). The WAAS is a system which provides corrections to enable aviation users of the Standard Positioning Service (SPS) GPS capabilities to achieve accuracy, integrity, and availability in all phases of flight from enroute through precision approach to airports [*Dehel et al.*, 1999]. One of the corrections provided by the WAAS to enable accuracy improvements is the correction for the signal delay due to the ionosphere. Users of the SPS GPS system are currently limited to the  $L_1$  frequency (1.575 GHz) and are not directly able to measure the delay of the signal due to the ionosphere. The WAAS provides this delay information in the form of a grid of data, which is transmitted to the user as part of the corrections. One of the questions confronting the users of the WAAS system is the effect of ionospheric storms, with its associated steep TEC gradients particularly during the current sunspot maximum phase. It is thus important to establish their effects on system operation and to explore the possibility of impact mitigation through predictions.

While studying the midlatitude impacts, it became apparent that penetration electric fields during magnetic storms would also affect WAAS-like systems currently under development in countries such as Japan, India, and the Latin American region. We thus utilized a latitudinal chain of TEC stations operating from Bogota, Colombia, to Santiago, Chile [*Valladares et al.*, 2001], in conjunction with TEC fluctuation data at numerous low-latitude stations from the IGS network to provide a global description of such perturbations. The effect of amplitude scintillation on the GPS and VHF/UHF communication systems was studied by utilizing the Air Force Research Laboratory (AFRL) scintillation network in the South American and

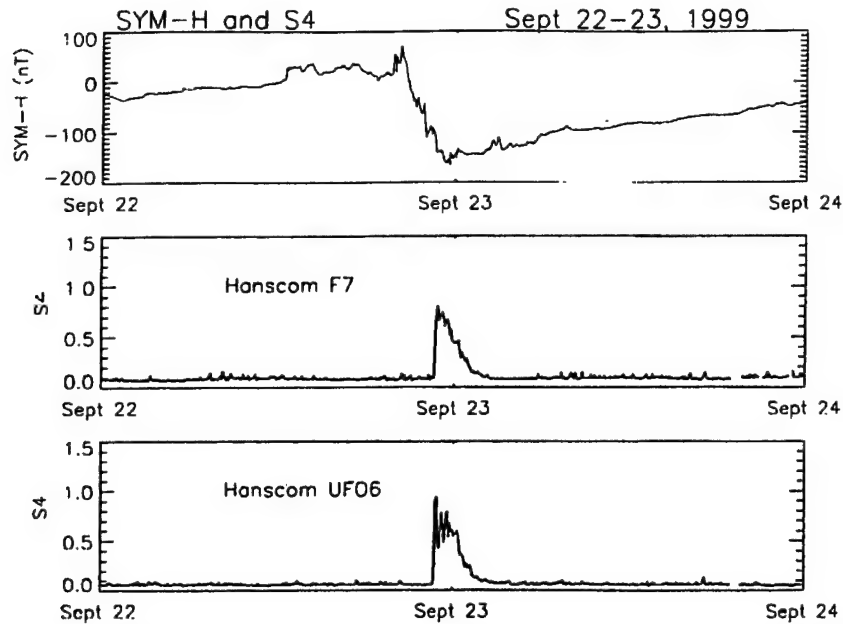


**Figure 1.** Scintillation index  $S_4$  at 250 MHz from two geostationary satellites Fleetsat 7 (F7) and UFO6 (U6) received at Hanscom Air Force Base (AFB), Massachusetts, plotted against SYM-H index for September 22–24, 1999.

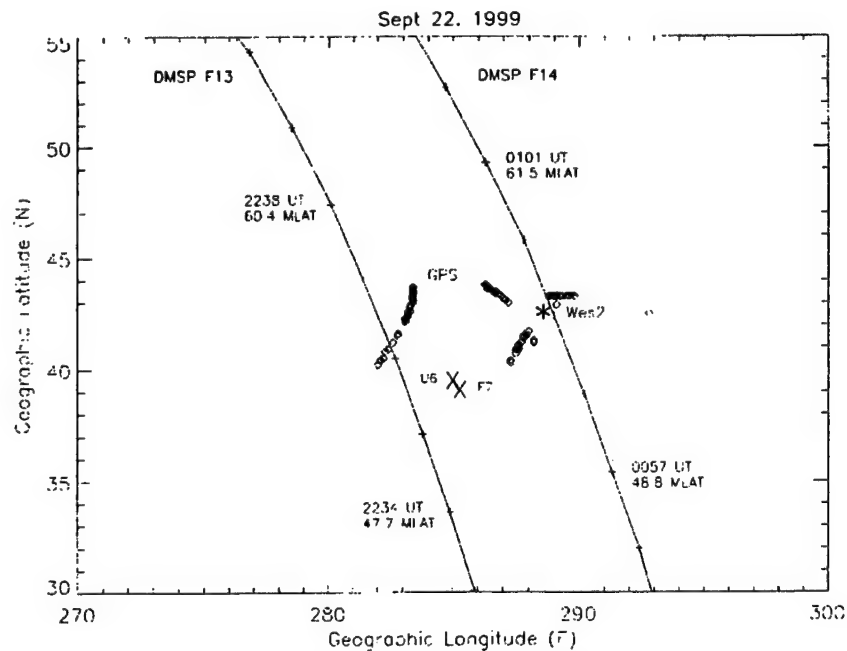


**Figure 2.** The 350-km intersection points for F7 and U6 for scintillation data from Hanscom AFB, Massachusetts, shown in Figure 1. Several subionospheric (350 km) tracks of GPS satellites from Westford (Wes2 indicated by a star) obtained between 2200 and 2400 UT on September 22 are also shown. The diamonds on the tracks indicate total electron content (TEC) fluctuations  $>1 \text{ TEC U min}^{-1}$ . Two Defense Meteorological Satellite Program (DMSP) subsatellite tracks (indicated by solid lines) close to Hanscom are also shown; the F13 track is for 2233–2240 UT on September 22, and the F14 track is for 0056–0102 UT on September 23. The corrected magnetic latitudes (MLATs) of the 110-km field line mapped positions of the DMSP satellites are indicated along the tracks at two specific UTs.

F13

22 Sept 1999

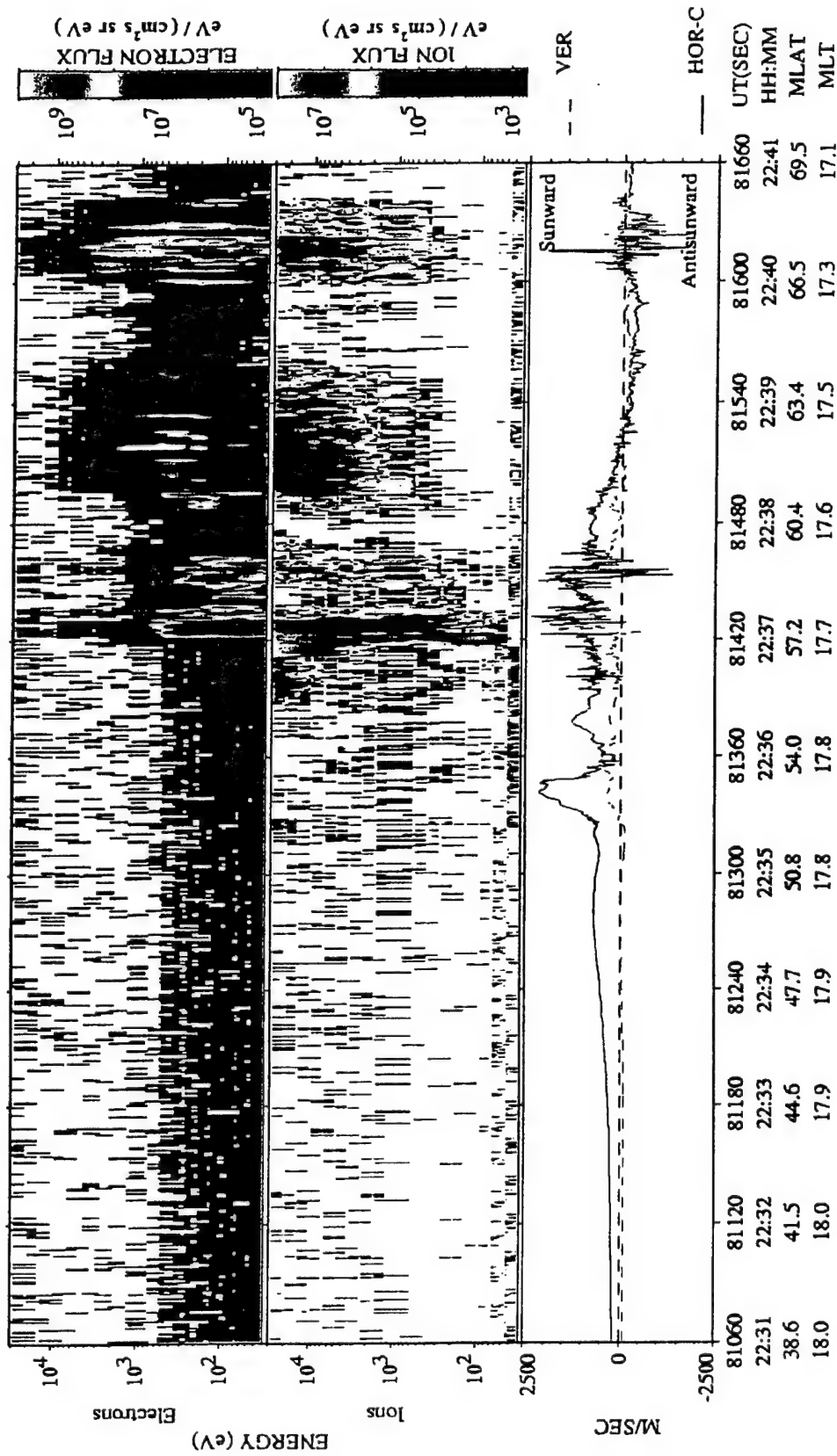


Plate 1. DMSP F13 measurements for the satellite track shown in Figure 2. The top and middle plots contain energy versus time spectrograms for downcoming electron and ion fluxes. Color codes for directional differential fluxes, particles  $(\text{cm}^2 \text{ s sr eV})^{-1}$  are given to the right of the spectrograms. All parameters are plotted as functions of UT, MLAT, and the magnetic local time. The bottom plot gives the horizontal (solid line) and vertical (dashed line) components of plasma drift. A large horizontal and sunward drift structure of  $2000 \text{ m s}^{-1}$  is seen between 2235:20 and 2236:00 UT.

South Atlantic sectors. A novel feature is the extensive LT coverage provided by the high-resolution (1024 Hz) in situ measurements at 600 km from the Republic of China Satellite-1 (ROCSAT-1) with an inclination of 35° in addition to the coverage at 840 km provided by the Sun-synchronous DMSP satellites at specific LT.

## 2. September 22–24, 1999, Magnetic Storm

We will first present the perturbations in the middle-latitude ionosphere as a result of this magnetic storm and eventually follow the perturbations all the way to the equatorial ionosphere. Along the way, we will point out the possible impacts on WAAS and similar systems that may be operating under similar storm conditions.

### 2.1. Midlatitude Effects

The top panel of Figure 1 shows the high-resolution (1-min) values of the SYM-H index [Iyemori et al., 2000], which closely follows the hourly *Dst* index developed by Sugiura and Poros [1971]. During this storm a fairly strong ring current developed with the SYM-H index reaching below  $-160$  nT just prior to 2400 UT on September 22. The middle and bottom panels show the scintillation index *S*<sub>4</sub> (defined by Briggs and Parkin [1963]) at 250 MHz from two geostationary satellites F7 and UFO6 plotted as a function of UT from Hanscom AFB, Massachusetts. The sudden onset of scintillations at 2240 UT on both ray paths as SYM-H (*Dst*) index drops precipitously is very evident. The geographic coordinates of the subionosphere (350 km) intersection are shown in Figure 2. The intersection points in the ionosphere are extremely close for the two geostationary satellites giving rise to simultaneous onsets of the scintillations. The orbits of two DMSP satellites and the subionospheric intersections of several GPS satellites obtained between 2200 and 2400 UT from the nearby station of Westford, Massachusetts, are also shown for subsequent use.

Earlier measurements by Wygant et al. [1998] on the CRRES spacecraft during the March 24, 1991, geomagnetic storm had shown that the large-scale magnetospheric electric field repeatedly penetrated into the inner magnetosphere between  $L = 2$  and  $L = 4$  when the rate of change of *Dst* was of the order of  $-50$  nT h<sup>-1</sup>. In this instance that rate of change was  $-75$  nT h<sup>-1</sup> between 2200 and 2300 UT on September 22, 1999. Thus the impulsive onset of scintillations at  $L = 2.8$  (53° magnetic latitude (MLAT) in this longitude sector) for the Hanscom intersection points is in all likelihood linked to the appearance of electric fields and plasma density gradients in that vicinity. (For a discussion of the relationship between different magnetic coordinate systems in this longitude sector and the representation of DMSP positions in geographic and magnetic coordinates to be discussed below, see Basu et al. [1983a].) The scintillation event lasts for ~2 hours. The Millstone Hill radar has documented many instances of such fields and gradients at ionospheric heights [Yeh et al., 1991; Foster, 1993; Foster and Rich, 1998]. Unfortunately, as mentioned earlier, the radar was not operating on that day, but the two DMSP orbits shown in Figure 2, particularly the F13, provides unmistakable evidence for a large penetration electric field in the vicinity of Hanscom at 1748 MLT, i.e., at dusk. Plate 1 shows DMSP F13 measurements taken at northern high latitudes on September 22, 1999, just west of the ionospheric intersection points for the F7 and UFO6 satellites in the early evening magnetic local time (MLT) sector between 2231 and

2241 UT. The top and middle plots contain directional differential fluxes of downcoming electrons and ions with energies between 30 eV and 30 keV in energy versus time color spectrogram format [Hardy et al., 1984]. The bottom panel shows the horizontal and vertical components of the plasma drift obtained from the ion drift meter (IDM) on board the satellite [Rich and Hairston, 1994]. The most important point for our purpose is the large horizontal sunward drift of  $\sim 2000$  m s<sup>-1</sup> and a small generally upward drift seen between 52°–54° MLAT (2235:20–2236 UT) and straddling the two satellite intersection points equatorward of the energetic electron and ion precipitation boundaries. The sunward or westward drift is caused by a northward electric field of magnitude  $\sim 100$  mV m<sup>-1</sup> consistent with measurements at the Millstone Hill radar under similar conditions quoted above. Such westward and small upward drifts were also evident in the DMSP F14 data, the orbital track for which was shown in Figure 2.

Two other measurements, namely, those using the GPS receivers [Doherty et al., 1994] and the Digisonde [Reinisch and Xueqin, 1983] provide evidence for an abrupt *F* region height rise and increase in the TEC. The TEC data from Westford, Massachusetts (42.6°N, 288.5°E), are shown in Figure 3 for September 22, 1999. These data are obtained by using the carrier phase and group delay measurements of GPS signals at *L*<sub>1</sub> (1.575 GHz) and *L*<sub>2</sub> (1.227 GHz) reported at 30-s intervals along the slant path from the receiver to the satellites. Using the ionospheric zenith angles, we convert the slant TEC to equivalent vertical TEC shown. The plot is obtained by combining TEC observations from the entire constellation of GPS satellites above 30° elevation over the 24-hour UT period and taking care of satellite and receiver biases in an appropriate manner [Doherty et al., 1994]. Although the TEC variation is not as smooth as that seen on quiet days (quiet day behavior is shown in Figure 5), the most significant aspects of the data are the increase in TEC of  $\sim 10$  TEC units ( $10^{16}$  el m<sup>-2</sup>) around 2130 UT followed after 2200 UT by the precipitous drop of 35 TEC units at the very fast rate of  $\sim 1$  TEC unit min<sup>-1</sup>. Similarly, the Digisonde data (not shown) operating at this station also exhibit a sudden increase in the height of the ionosphere starting after 2135 UT followed by a large decrease in the critical frequency *f*<sub>o</sub>*F*<sub>2</sub> (consistent with the approach of a trough) from 9.5 MHz at 2135 UT to 4.5 MHz at 2250 UT, and the ionograms show evidence of spread *F* throughout this time period. This afternoon height rise and TEC increase in the storm initial phase have been widely reported in the literature. They are considered to be a combined effect of an eastward electric field in the presence of sunlight and advection of plasma from lower latitudes [Foster, 1993, and references therein].

The precipitous drop in *f*<sub>o</sub>*F*<sub>2</sub> and TEC is accompanied by large fluctuations in TEC starting at 2210 UT as shown in Figure 4. This diagram was obtained by considering the differential carrier phase data alone along the line of sight over each 30-s interval [Pi et al., 1997; Basu et al., 1999; Bhattacharyya et al., 2000]. Figure 4 shows that TEC fluctuations were very small throughout the day until 2200 UT. Shortly thereafter, very large fluctuations, some as large  $\pm 5$  TEC units min<sup>-1</sup>, are seen for several tens of minutes on almost all the satellite ray paths visible from Westford at that time. The subionospheric tracks for these satellites were shown in Figure 2. The small diamonds along the GPS satellite tracks show the locations for which the TEC fluctuations were greater than 1 TEC unit min<sup>-1</sup>. Large-magnitude fluctuations on the order of  $\pm 5$  TEC

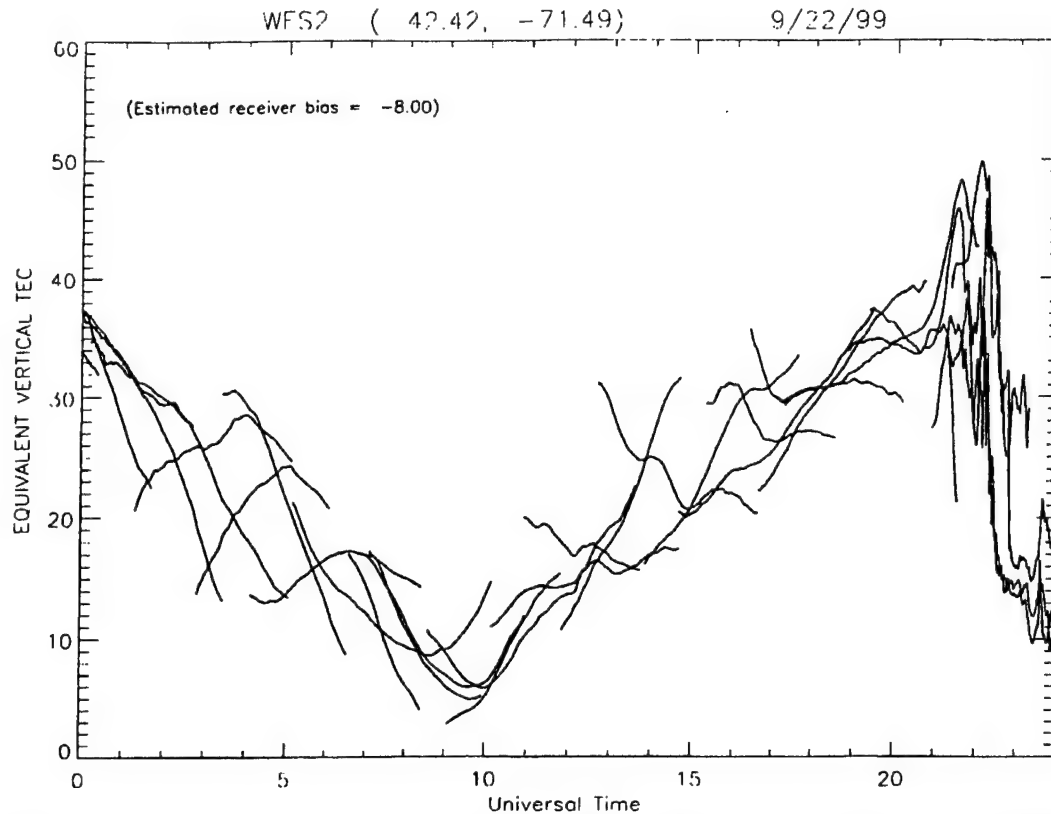


Figure 3. The equivalent vertical TEC measured using GPS satellites at Westford, Massachusetts (WES2), on September 22, 1999.

units  $\text{min}^{-1}$  are expected to be a problem for the WAAS system (A. J. Mannucci, private communication, 2000). If we consider the TEC fluctuations at Westford and the scintillations at Hanscom AFB to be two different manifestations of the irregular structure of the ionosphere, then it is possible to estimate the rate of equatorward motion of this irregularity front by considering the subionospheric separation between the TEC and scintillation ray paths and the delay in onset times. Using this separation to be 425 km and the delay to be 30 min, we obtain an average equatorward motion of  $\sim 230 \text{ m s}^{-1}$  for the disturbance. Thus the 30-s sampling interval of the TEC fluctuations corresponds to a spatial scale of  $\sim 7 \text{ km}$  or minimum resolvable north-south irregularity wavelengths of 14 km. In other words, the TEC fluctuations are caused by tens of kilometers scales as compared to the intensity scintillations at 250 MHz, which are caused by irregularities on the order of a kilometer or smaller (determined by the Fresnel dimension). Possible causes of these large- and small-scale irregularities will be discussed in section 4.

To determine the behavior of this large-scale gradient across the continental United States, where the WAAS system is to operate, we investigated the TEC behavior at the NE-SW chain of stations of the IGS network. The GPS TEC data from Westford, Massachusetts (WES2), North Liberty, Iowa (NLIB), Colorado Springs, Colorado (AMC2), and Pietown, New Mexico (PIE1), over a 4-day period covering the storm are shown in Figure 5. Their locations together with those of other IGS sites including stations in the equatorial region are shown in Figure 6. This diagram was kindly provided by X. Pi

and shows a small subset of the total number of IGS stations [Pi *et al.*, 1997]. The TEC scale in Figure 5 is shown in terms of range delay to make this diagram more useful to the WAAS users. To compare Figures 3 and 5 one should recall that 6.15 TEC units is equivalent to 1 m of range delay at the GPS  $L_1$  (1.575 GHz) frequency. The storm time TEC increase causes a range delay of 8 m at Westford rising to 12 m at lower latitudes. This is followed by a much more dramatic TEC decrease from 12 to 2 TEC units in the course of an hour at some stations, owing to the equatorward motion of the midlatitude trough. The motion of these large-scale features from N-S across the United States is very evident. An unexpected and sharp range delay change of this magnitude is expected to be of concern to WAAS users. The TEC behavior on September 21 is introduced as the normal quiet day behavior for comparison to the storm time behavior on September 22. While at Westford the storm time TEC curve shows mostly a change of shape (an abrupt increase followed by a fast decrease) with both the quiet day and storm TEC causing 6–8 m range delay, the TEC behavior at lower latitudes shows an increase from 8 to 12 m in the delay introduced by the ionosphere.

The TEC increase is followed by a severe decrease on September 23, first in the existence of very low nighttime TEC values in the trough followed by a significant decrease in TEC during the daytime. This is the well-known storm negative phase caused by a composition change of the ambient ionosphere [cf. Buonsanto, 1999, and references therein]. From the point of view of the WAAS users, a decrease of 4 m in the range delay is expected at most stations during the daytime due to the storm negative phase.

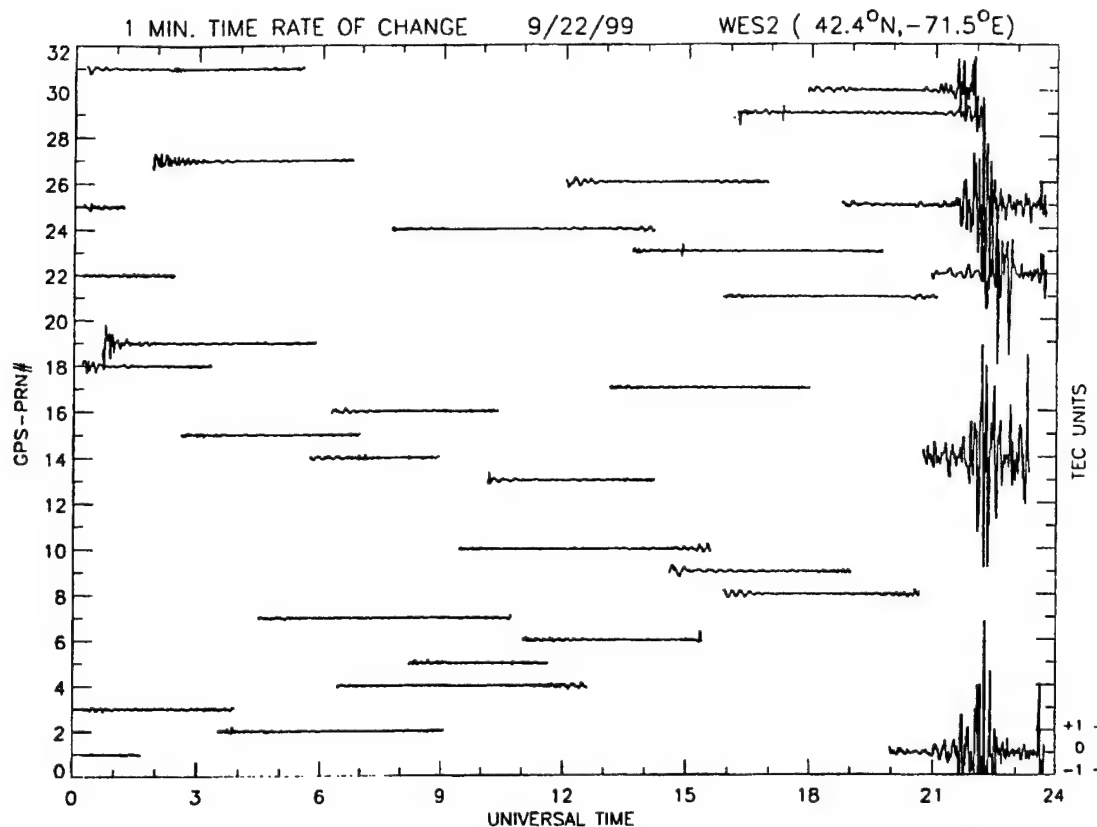


Figure 4. The time rate of change of TEC in TEC units ( $10^{16} \text{ el m}^{-2}$ )  $\text{min}^{-1}$  measured using data shown in Figure 3 at Westford, Massachusetts (WES2), on September 22, 1999.

However, since this is a gradual change, it is much easier to accommodate than the TEC increase and decrease at the storm onset. Normal TEC values giving rise to expected range delays are finally approached on September 24. Thus the ionospheric storm caused as a result of the magnetic storm has a large measurable impact on a navigation system operating in what was expected to be a relatively benign midlatitude ionosphere.

## 2.2. Equatorial Effects

The effect of the magnetic storm seemed to create enhanced effects at lower mid-latitudes as evidenced by the TEC behavior shown in Figure 5. This was interpreted as a combined effect of the prompt penetration of the eastward electric field into the ionosphere and the storm-enhanced plasma density and consequent TEC increase seen in the dusk sector by Foster [1993]. A natural extension of this midlatitude study seemed to be the investigation of the effect of this prompt penetration on equatorial scintillations and TEC gradients and their consequent impacts on WAAS-like systems being developed for low latitudes.

An important feature of the low-latitude *F* region is the presence of the equatorial anomaly, with peaks in the plasma density at  $\pm 15^\circ$  dip latitude and minima at the magnetic equator. They are the result of the upward motion of the plasma at the magnetic equator and its consequent diffusion along the magnetic field lines [Hanson and Moffett, 1966]. The TEC anomaly starts to develop as early as 1100 LT. The crests move away from the equator with increasing local time, as the *F*

region at the equator moves to higher altitudes and reaches a maximum development around the afternoon hours [Basu and Das Gupta, 1968]. On some evenings a strong resurgence of the anomaly takes place; this is probably due to the well-known prereversal enhancement (PRE) of the vertical drift, which generally occurs around 1900 LT [Woodman, 1970; Tanaka, 1981]. A well-developed PRE has been found to be one of the most important indicators associated with the onset of equatorial spread *F* (ESF) by Basu *et al.* [1996] and Fejer *et al.* [1999]. In a very recent paper, Valladares *et al.* [2001] have shown the existence of a close relationship between the temporal evolution of the TEC profiles as a function of latitude near sunset and the onset of ESF. Their data came from the year 1998. We utilize that array of TEC stations in South America extending from Bogota, Colombia, to Santiago, Chile, in conjunction with ground scintillation observations from Ancon, Peru, and Antofagasta, Chile, shown in Figure 7, to study the effect of this magnetic storm on the equatorial ionosphere.

The scintillation data from Ancon, Peru, using the F8 satellite are shown in Figure 8. It starts rather abruptly at 2308 UT (1808 LT), as is generally the case at equatorial stations [Basu *et al.*, 1978]. However, there are two surprising aspects to these measurements. One is the start of the scintillations at 1808 LT, which is actually 15 min before *E* region (100 km) sunset at the satellite intersection point, and the other is the total absence of scintillations throughout the night at the F7 intersection point to the west of Ancon, which is separated from the F8 intersection point by 630 km. Thus it seems that the scintillation onset



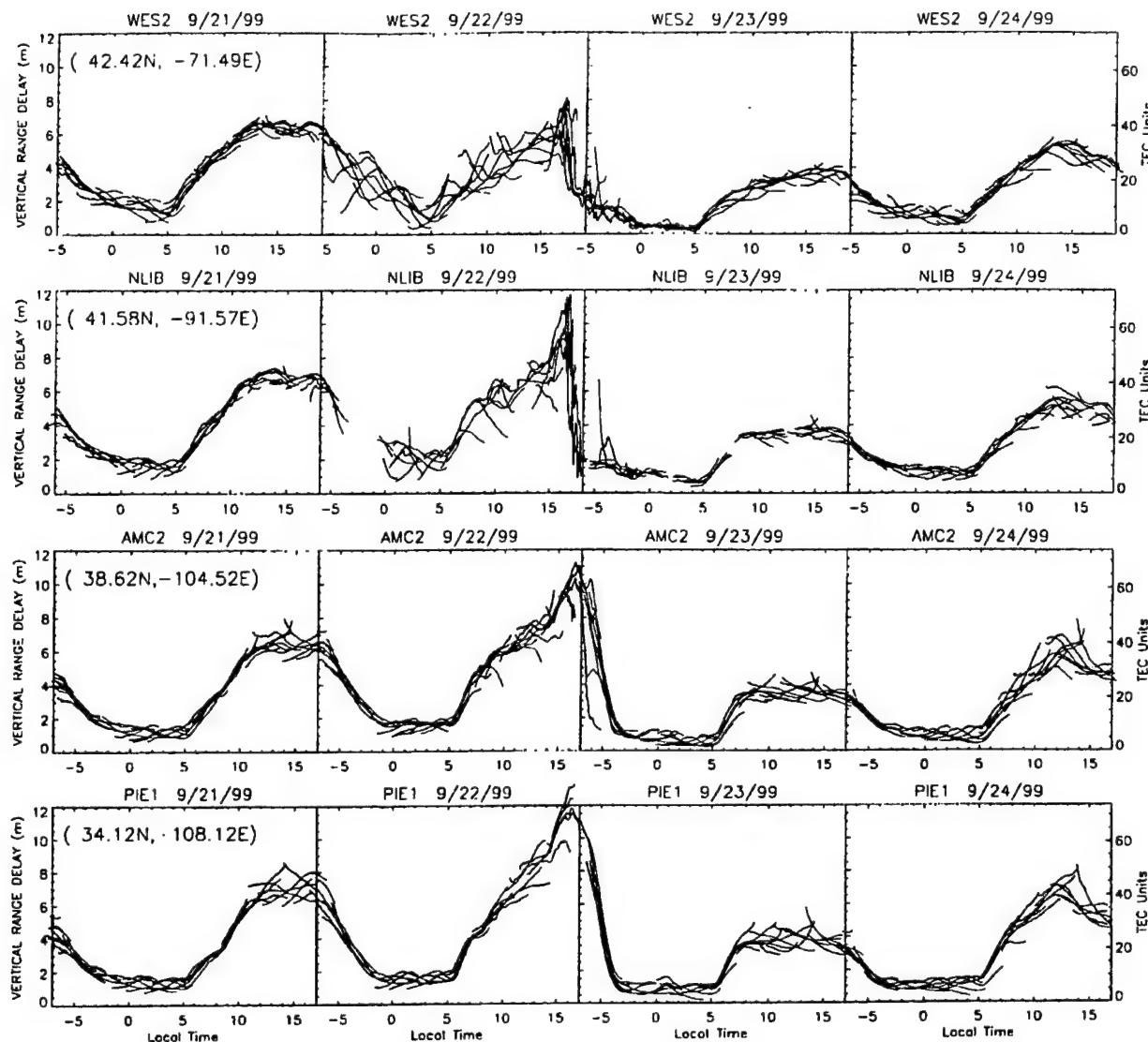


**Figure 5.** Range delays recorded at four stations in the International GPS Service for Geodynamics (IGS) network, namely, Westford, Massachusetts (WES2), North Liberty, Iowa (NLIB), Colorado Springs, Colorado (AMC2), and Pietown, New Mexico (PIE1), during September 21–24, 1999. Range delay can be related to TEC at 1.575 GHz by noting that a 6.15 TEC units change causes a 1-m range delay.

is related to the prompt penetration of eastward electric field made possible by the conductivity gradients near sunset. Further, the equatorial prompt penetration at dusk was very localized in longitude. There was no scintillation at 1.7 GHz for the Antofagasta G8 ray path which was within the irregularity zone, thereby indicating that the integrated strength of turbulence caused by the disturbance was not large enough to create perturbations at such a high frequency. The scintillations on both F7 and F8 ray paths during the evening of September 21–22 from Ancon are most likely due to the expected occurrence of ESF on normal quiet days at equinox during solar maximum in the Peruvian sector [Aarons, 1993].

In the absence of Jicamarca radar data we utilized the array of GPS TEC stations shown in Figure 7 to study the latitudinal behavior of TEC in the hope of getting some clues to the vertical plasma drift behavior which may have some bearing on

the scintillation asymmetry to the west and east of Ancon. The latitude variation of TEC was computed by utilizing GPS data as was done by Valladares *et al.* [2001] the only difference being that the latitude variation was computed separately for data obtained to the west and east of 72°W longitude. Further, only the data from the southern half were utilized, because of the gaps in the chain to the north. Our scintillation ray paths also intersect close to the magnetic equator and to the south of it. The data in Figure 9 show a fairly remarkable difference between the east and west cuts with the former showing evening anomaly peak development at 1800 UT (2300 LT) and 1900 LT (0000 UT) whereas the latter shows TEC peaks at the equator, thereby indicating that the evening anomaly had not formed in the west. While this does not provide a cause for the difference, this asymmetric behavior provides evidence for the enormous importance of the PRE of the vertical drift in the generation of ESF.

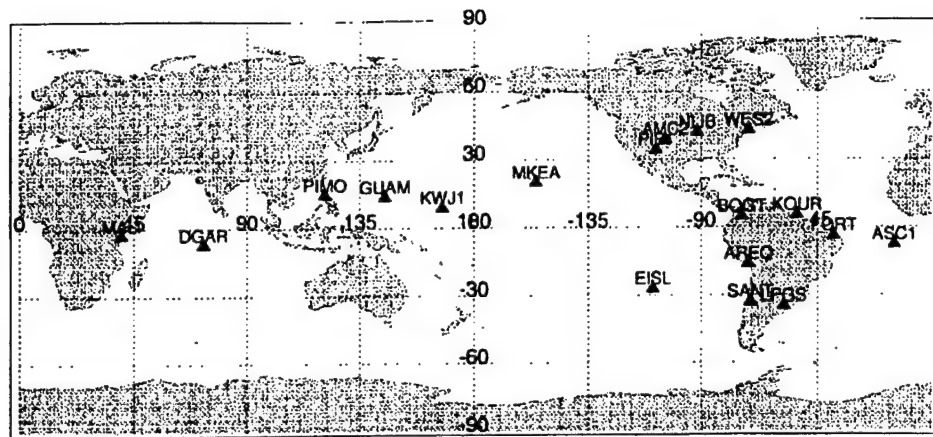


**Figure 6.** Global map showing IGS stations that provided data for this study. MALI, Malindi; DGAR, Diego Garcia; PIMO, Manila; KWJ1, Kwajalein; MKEA, Hawaii; EISL, Easter Island; BOGT, Bogota; KOUR, Kourou; AREQ, Arequipa; SANT, Santiago; LPGA, LaPlata; FORT, Fortaleza; ASC1, Ascension Island.

The TEC and scintillation data taken together provide indirect proof that the westward boundary of the penetration electric field in the equatorial region is probably close to 73°W (287°E). To provide an eastward boundary, we checked several global databases, both space- and ground-based. The DMSP F12 and F14 data of topside densities at 840 km, which crossed the magnetic equator at 321°E at 2318 UT and 324°E at 2306 UT, respectively (near the eastern edge of Brazil), were the only ones to show perturbations in the form of density depletions in the equatorial region. These passes are at 2100 LT, and one expects irregularities to show up in the topside by this time. No other passes in the vicinity showed any signatures of topside disturbances. Unfortunately, the ROCSAT-1 data were not available during the night of September 22–23. This is because the severe Taiwan earthquake of September 21 knocked out power to the mission operation centers for a couple of days.

In terms of ground-based data sources from the IGS network, the TEC fluctuation data of the type shown in Figure 4 for Westford were checked for many equatorial stations at different longitudes shown on the global map in Figure 6. There was an absence of fluctuations at Hawaii (MKEA), Easter Island (EISL), Bogota (BOGT), Arequipa (AREQ), and Santiago (SANT), i.e., stations on islands in the Pacific Ocean and along the west coast of South America. However, TEC fluctuations were observed at Kourou (KOUR), Fortaleza (FORT), and LaPlata (LPGA) on the east coast of South America. The TEC fluctuations started at 2110 UT in Fortaleza, Brazil (*E* region sunset is 2107 UT), and continued intermittently up to 0800 UT on September 23; the magnitude, however, never exceeded  $\pm 2$  TEC units  $\text{min}^{-1}$ . The Fortaleza ground-based data are thus consistent with the DMSP F12 and F14 orbits presented earlier. Both scintillations and IGS data are available from Ascension Island (ASC1). The Ascension Island 250-MHz scintillation data had an abrupt onset at 2127 UT (2027 LT), i.e., a fairly late start for a station where *E* region sunset is at 1930 UT with no gigahertz scintillation observed that night. This probably indicates that the scintillation was caused by structures that drifted in from the west. The Ascension Island IGS data showed significant TEC fluctuations after 2100 UT and continued intermittently up to 0400 UT.

Unfortunately, no IGS stations are available on the west coast of Africa, the closest one being on the east coast at Malindi (MALI), which showed no storm-related TEC perturbations. For completeness, we checked the station at Diego Garcia (DGAR) and those in the Far East such as Manila (PIMO) and Kwajalein (KWJ1). However, since the time of storm onset corresponds to the postmidnight to morning hours at these stations, no perturbations in TEC were detected. No late time disturbances, such as that attributed to the prompt penetration due to a northward turning of the IMF (see the overshielding concept discussed by Kelley [1989]) or that due to the ionospheric disturbance dynamo [Blanc and Richmond, 1980; Fejer *et al.*, 1999], were detected on the western side of South America for this particular storm. However, the TEC fluctuation data for Fortaleza and the 250-MHz scintillation data from Ascension provide evidence for a postmidnight event in the 0300–0500 LT time frame. Using ACE data, we found that the northward turning of the IMF for this storm had taken place at 0048 UT, if the expected propagation delay is included (J. Fedder, private communication, 2001). This is pre-midnight LT for both Ascension Island and Fortaleza, such that the prompt penetration due to overshielding is not expected to lead to fresh irregularity generation. Thus it seems that the postmidnight event is probably due to the effect of the disturbance dynamo alone. Unfortunately, no postmidnight zonal drift data were available that could have put this hypothesis on a firmer footing.

Given the various caveats we have mentioned, this storm in its development phase seemed to have had a positive effect on irregularity formation rather than an inhibition on the generation of equatorial irregularities in a very limited range of longitudes between 73°W and 15°W. In other words, the prompt penetration of the electric field in the eastward direction due to increased magnetospheric convection seemed to be confined to the longitude region which was close to the *E* region sunset for the UT range over which SYM-H (*Dst*) showed maximum variation including the time period when it remained at its most minimum level. Any positive late time effect also seemed to be confined to a part of this longitude range. We will return to a discussion of this point vis-à-vis the findings of storm time electric field models [Spiro *et al.*, 1988;

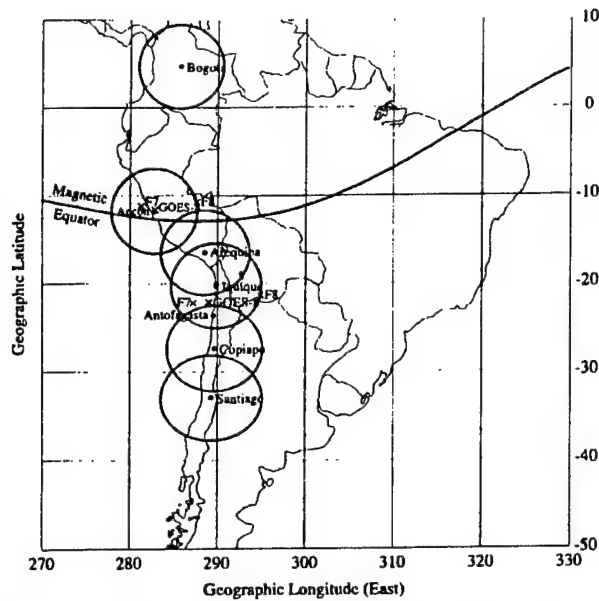


**Figure 7.** Equatorial array of GPS stations on the west coast of South America providing latitude variation of TEC data. The circles around the stations indicate 30° elevation coverage. Also shown are 350-km ionosphere intersection points to Fleetsat 7 (F7), Fleetsat 8 (F8), and GOES 8 from Ancon, Peru, and Antofagasta, Chile.

*Fejer and Scherliess, 1997; Scherliess and Fejer, 1997]* in section 4.

### 3. October 21–23, 1999, Magnetic Storm

We will follow the scenario used for the September 22–24 storm to describe this major October storm.

#### 3.1. Midlatitude Effects

In Figure 10 we show the VHF scintillation data from two geostationary satellites observed at Hanscom AFB plotted against the high-resolution SYM-H index. The onset of scintillation at 0120 UT and 0440 UT on both ray paths is well correlated with the two times of fast reductions in the SYM-H (or *Dst* index) between 0000–0200 UT and 0400–0600 UT, each of  $\sim 45 \text{ nT h}^{-1}$ . The minimum value of  $-230 \text{ nT}$  for SYM-H was reached around 0700 UT on October 22. While the first scintillation region is  $\sim 100 \text{ min}$  wide, the second interval of high scintillation is 4 hours long, which includes 2 hours of moderate scintillation.

In the absence of the Millstone ISR data, we utilize the Digisonde located there and are benefited by the 5-min sounding interval specially used for the ISWP as shown in Figure 11. The fall in  $f_oF_2$ , from a flat peak of 12 MHz starts from 2100 UT on October 21 (not shown) and is part of a gradual sunset decay. It is greatly accelerated beyond 0050 UT on October 22 when  $f_oF_2$  falls from 7.5 to 3.1 MHz (a factor of almost 6 decrease in  $N_m F_2$ ) at 0235 UT with high values of  $hmF_2$ , the height of the peak of the  $F_2$  layer (both characteristics of the trough). It is interesting to note that even though it is close to local midnight,  $f_oF_2$  starts increasing to a value of  $\sim 6.0 \text{ MHz}$  at 0545 UT (0045 LT), and an *E* region makes its appearance between 0400 and 0650 UT. Between 0650 and 0745 UT there is a gap in the data. These effects are generally thought to be due to a varying spectrum of particle-induced ionization. Soft particles can cause *F* region ionization, with some *E* region contribution, and then with a hardening of the precipitating particles affecting the *D* region, we eventually reach a point at which the *F* region cannot be seen at all because of increased radio-wave absorption (J. W. Wright, private communication, 2001). During the entire time period between 0100 and 1100 UT (except the gap region mentioned above), the ionograms

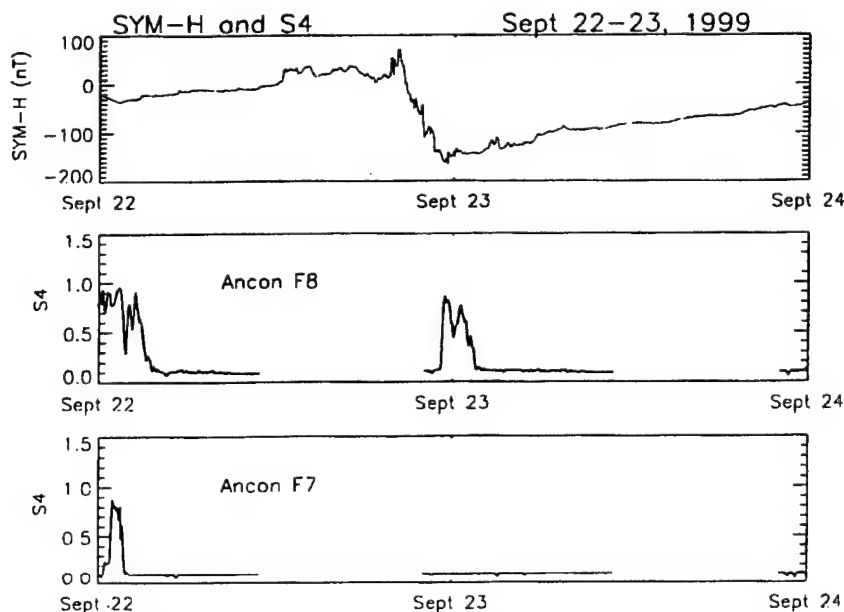


**Figure 8.** Scintillation at 250 MHz from two geostationary satellites Fleetsat 7 (F7) and Fleetsat 8 (F8) recorded at Ancon, Peru, plotted against the SYM-H index for September 22–24, 1999. Note the complete absence of scintillations on F7 during the evening of September 22–24, 1999. Note the complete absence of scintillations on F7 during the evening of September 22–23, 1999.

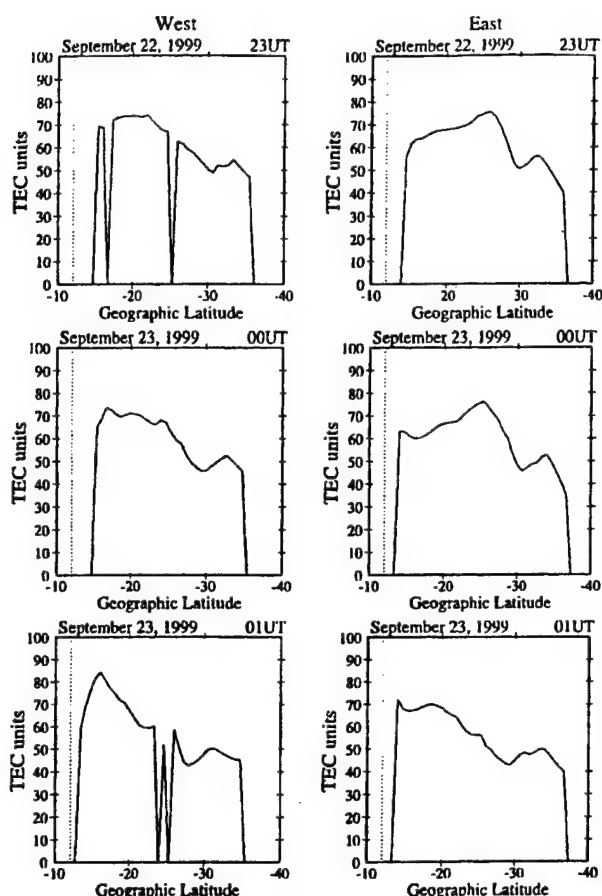


**Figure 9.** The latitude variation of TEC using the southern half (in magnetic latitudes) of the array computed to the west and east of longitude 72°W. While the data from the eastern half show a clear formation of the equatorial anomaly at 2300 UT (1800 LT) on September 22 and 0000 UT (1900 LT) on September 23 at 25°S (15° magnetic latitude), the western half does not show any evidence for anomaly development with the TEC peak being close to the magnetic equator. The abrupt discontinuities in the plots are the result of data dropouts.

show evidence of spread  $F$  with the magnitude of  $df/f$ , where  $df$  is the frequency spread around the critical frequency, being on the order of 10%.

The equivalent vertical TEC data for October 22, 1999, from Westford, Massachusetts, are shown in Figure 12 and are obtained exactly as detailed in the description for Figure 3. The quick fall in TEC beyond 0000 UT (1900 LT) to below 10 TEC units is very evident. Also very prominent is an increase in TEC to ~20 TEC units between 0400 and 0800 UT. This is followed by another decrease until sunrise the next morning at 1100 UT (0600 LT) when TEC gradually increases in value but reaches a maximum which is only half that seen on the previous day (compare Plate 2). This is quite consistent with the extended negative phase following major magnetic storms due to composition changes in the ionosphere [cf. Buonsanto, 1999].

The TEC fluctuations for October 22 on each GPS satellite are shown in Figure 13. Again, this is obtained in a manner similar to Figure 4. It is rather interesting to note that the TEC fluctuations in the vicinity of 0100 UT associated with the quick TEC fall brought about by the equatorward motion of the

trough are rather moderate ( $\pm 1$ –2 TEC units) compared to the September 22 case. The large TEC fluctuations in this case (some as large as  $\pm 4$  TEC units) are primarily confined to the period between 0630 and 0800 UT, which covers the time when the Digisonde was unable to record the background ionospheric parameters due to increased absorption. It is rather important to note from Figure 12 that these large TEC fluctuations are confined to the trailing edge of the TEC enhancement near local midnight. Since  $AE$  ( $>1000$  nT) and  $Sym-H$  or  $Dst$  ( $>-200$  nT) were both at extreme levels at this time, and the ionograms showed evidence of auroral particle precipitation, it is a very reasonable assumption that this TEC increase is due to an auroral blob generated locally and/or convected into this region whose trailing edge has been structured by the gradient drift instability [Basu et al., 1990]. We will return to a discussion of this point in section 4.

This October 1999 storm was very important from the point of view of the WAAS prototype testing. This was the first major magnetic storm, which could be used to observe the robustness and accuracy of early WAAS algorithms in operation. Plate 2 displays TEC from four stations in the IGS network going from NE to SW (clockwise starting from lower right), as was done in Figure 5 for the September 22 storm. In the October case, however, each station TEC (expressed in terms of vertical range delay) has a vertical range delay overplotted in red. These vertical range delays were obtained from the estimated ionospheric vertical delays provided by the WAAS Ionospheric Grid Points (IGPs). In the panels directly below the TEC data we show the WAAS parameter called Grid Ionospheric Vertical Error (GIVE). The GIVE values are the estimated errors in the IGP values. Plate 2 illustrates that GIVE values increased to 6 m or more when short-term fluctuations were seen in TEC between 0000 and 1000 UT on October 22 (1900 LT on October 21 to 0500 LT on October 22 for Westford). At other times, GIVE values rarely exceeded 1.5 m. As in the case of Figure 5, Plate 2 also shows larger storm effects at the lower-latitude stations in Colorado and New Mexico. In an operational WAAS an aircraft user will interpolate the grid of IGPs for a local vertical range delay, apply that vertical delay to all satellites in view, and then use the GIVE values as an input to a function which estimates overall position error [Dehel et al., 1999]. The impact of ionospheric storm activity on WAAS is currently under intense investigation by a WAAS Ionospheric Working Group (WIWG) (P. Doherty, private communication, 2000). The results shown in Plate 2 are representative of early attempts to observe WAAS behavior during magnetic activity. In general, the September 1999 storm had a much larger effect on the midlatitude ionosphere in the continental United States as compared to the October storm, because the storm's main phase came at an earlier local time even though the October storm had a large negative  $Sym-H$  ( $Dst$ ) per se.

### 3.2. Equatorial Effects

Following the same logic of studying the effect of the penetrating electric fields on the equatorial ionosphere as in section 2.2, we turn our attention to the equatorial region. The plasma density irregularities associated with this storm produced a widespread effect, in terms of longitude coverage, and long-lived effects, in terms of time coverage. The ROCSAT-1 measurements allowed us to track both these variabilities in a meaningful way. This satellite with the Ionospheric Plasma and Electrodynamics Instrument (IPEI) on board was launched on

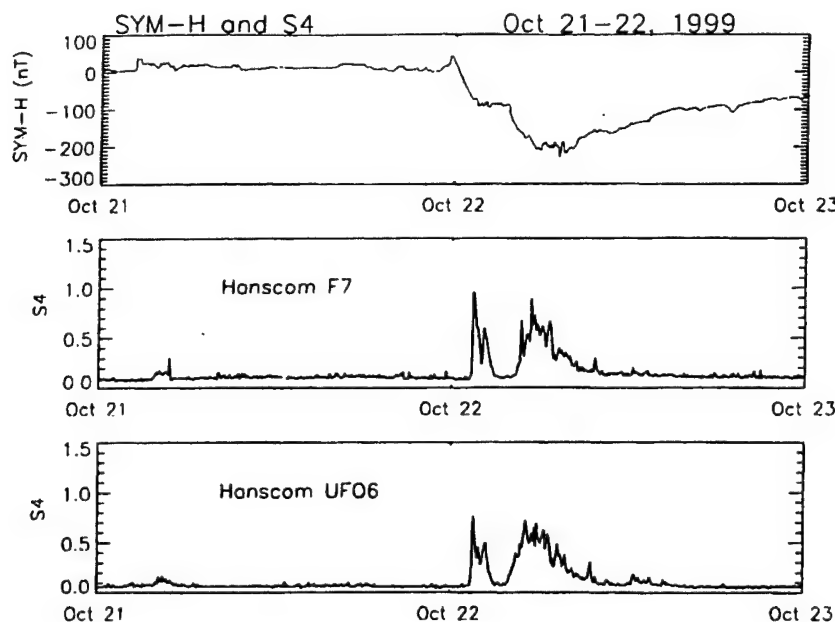


Figure 10. Same as in Figure 1 but for October 22–23, 1999.

January 27, 1999, into an almost circular orbit near 600 km with inclination of  $35^\circ$  [Yeh *et al.*, 1999]. Supporting information was obtained from DMSP F12, F13, and F14, the ground scintillation data, and the TEC data from the IGS network.

One of the more interesting aspects of the scintillation data for this storm is the nearly simultaneous onset at all three Ancon and Antofagasta (F7, F8, and G8) ray paths whose positions were shown in Figure 7. One set of such measurements for the Ancon F7 (at 250 MHz) and G8 (at  $L$  band) satellites is shown in Plate 3 for October 22 (Plates 3a and 3d) together with the spaced receiver drift measurements [Basu *et al.*, 1986; Valladares *et al.*, 1996] and power spectral densities (psds) at three specific irregularity scale lengths in Plates 3b and 3c (the drifts and psds are discussed later in the section). The scintillation, particularly at 250 MHz, continued for a long period of time. The simultaneous scintillation onset at these different ray paths and the persistence of scintillations for a long period through the night can be better understood by considering the coordinated density and velocity data from ROCSAT-1.

In Figure 14 we present the data from ROCSAT-1 which were taken at 1024 Hz (but plotted at 1 Hz) for the first two successive orbits on October 22. The data in the top panel shows a snapshot of a series of depletions in density, also known as plasma bubbles [McClure *et al.*, 1977], seen between 0011:30 and 0021:20 UT covering a longitude range within which most of the ray paths from Ancon and Antofagasta intersect except the western fringe (when presumably the satellite moved out of the equatorial irregularity belt). This orbit obtained immediately after storm onset (IMF  $B_z$  south) shows the presence of enhanced eastward electric field of  $1\text{--}2\text{ mV m}^{-1}$  in the evening period compared to the quiet day pattern on October 20, 1999 (H.-C. Yeh, private communication, 2001). This indicates that the effect of the prompt penetration of the electric field has reached equatorial latitudes. The presence of plasma bubbles and scintillations associated with an eastward electric field indicates that the Rayleigh-Taylor insta-

bility mechanism is operative over a wide swath of longitudes [Ossakow, 1981].

The next ROCSAT orbit at 0145 UT (bottom panel of Figure 14) shows a further development of bubbles with a series of depletions extending from  $267^\circ$  to  $300^\circ\text{E}$  longitude straddling the magnetic equator with the deepest depletion containing only  $10^2\text{ cm}^{-3}$  located close by. The velocity measurement for this orbit shows a continued presence of an enhanced eastward electric field in the evening period. What is more interesting is the gradual development from westward in orbit 1 to an eastward electric field in orbit 2 over the postmidnight time frame (H.-C. Yeh, private communication, 2001). The latter probably indicates a development of the disturbance dynamo after the storm has continued for a couple of hours. The highest density exceeding  $10^6\text{ cm}^{-3}$  is seen at the northern crest of the equatorial anomaly in both the top and bottom panels that constitute orbits 1 and 2 for October 22. Presumably, ROCSAT was sampling the irregularities in the immediate topside, as the  $F$  peak tends to be high during sunspot maximum at equinox. It is the irregularities on the high-density walls of such depletions or bubbles that give rise to intense VHF and gigahertz scintillations [Basu *et al.*, 1983b]. It should be noted from the scintillation data on the top and bottom panels of Plate 3 that while the amplitude scintillation at VHF is intense ( $S4 \sim 1$ ) for several hours, the  $L$  band G8 scintillation is weak with  $S4 < 0.2$ . On this night the simultaneous G8 data from Antofagasta (not shown) showed  $S4 > 0.5$  up to 0530 UT. It is the greater background density near anomaly peak stations that gives rise to the larger magnitude of scintillations even when bubble structures are seen throughout the equatorial belt. On this night, severe scintillations were observed particularly in a southerly direction, i.e., toward the southern anomaly crest on the GPS  $L1$  frequency at Antofagasta with the scintillation maximizing at  $S4$  of 1.2 between 0100 and 0200 UT as shown in Figure 15. Such high levels of  $S4$  on so many different ray paths may pose a problem for WAAS-like systems in the equatorial region.

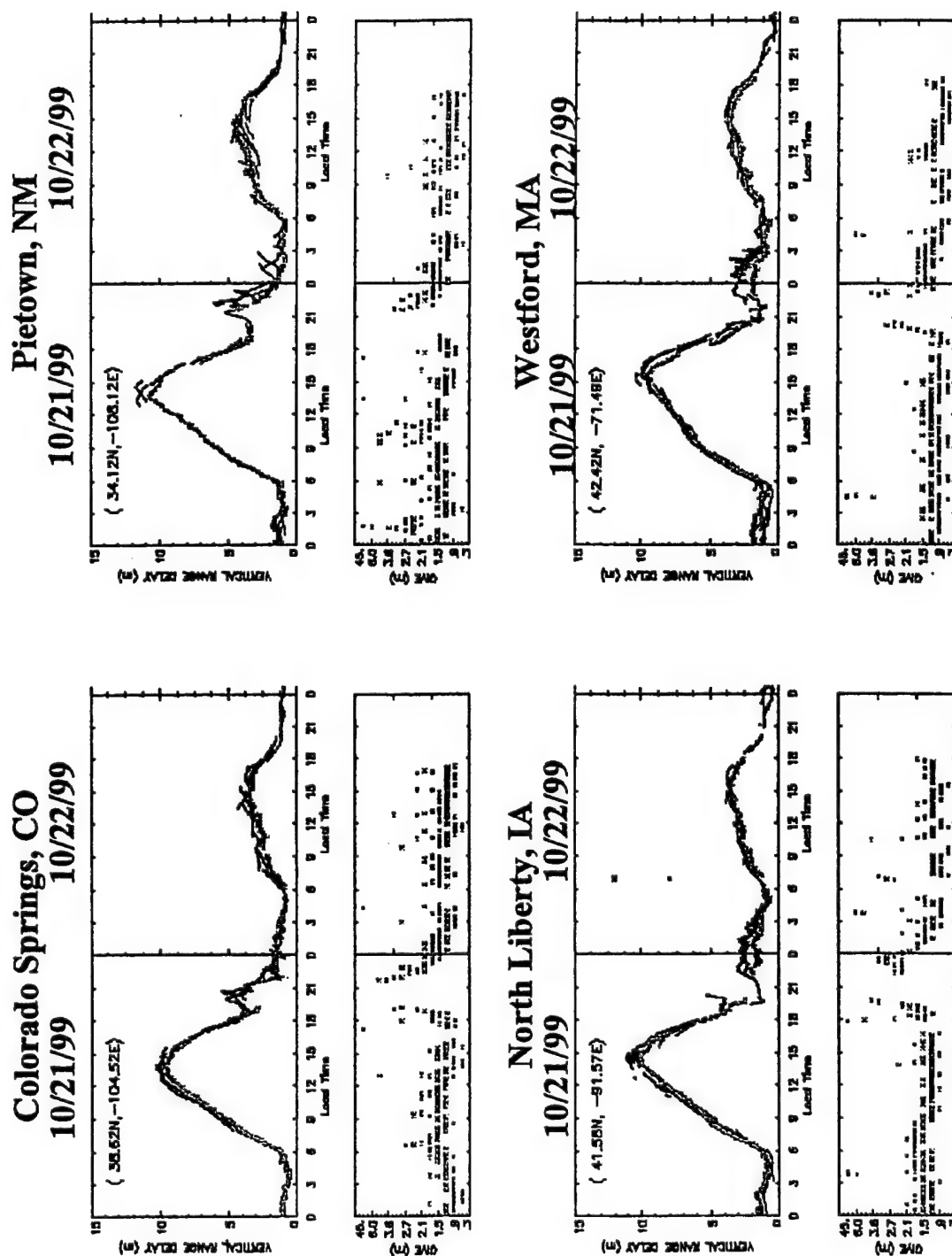
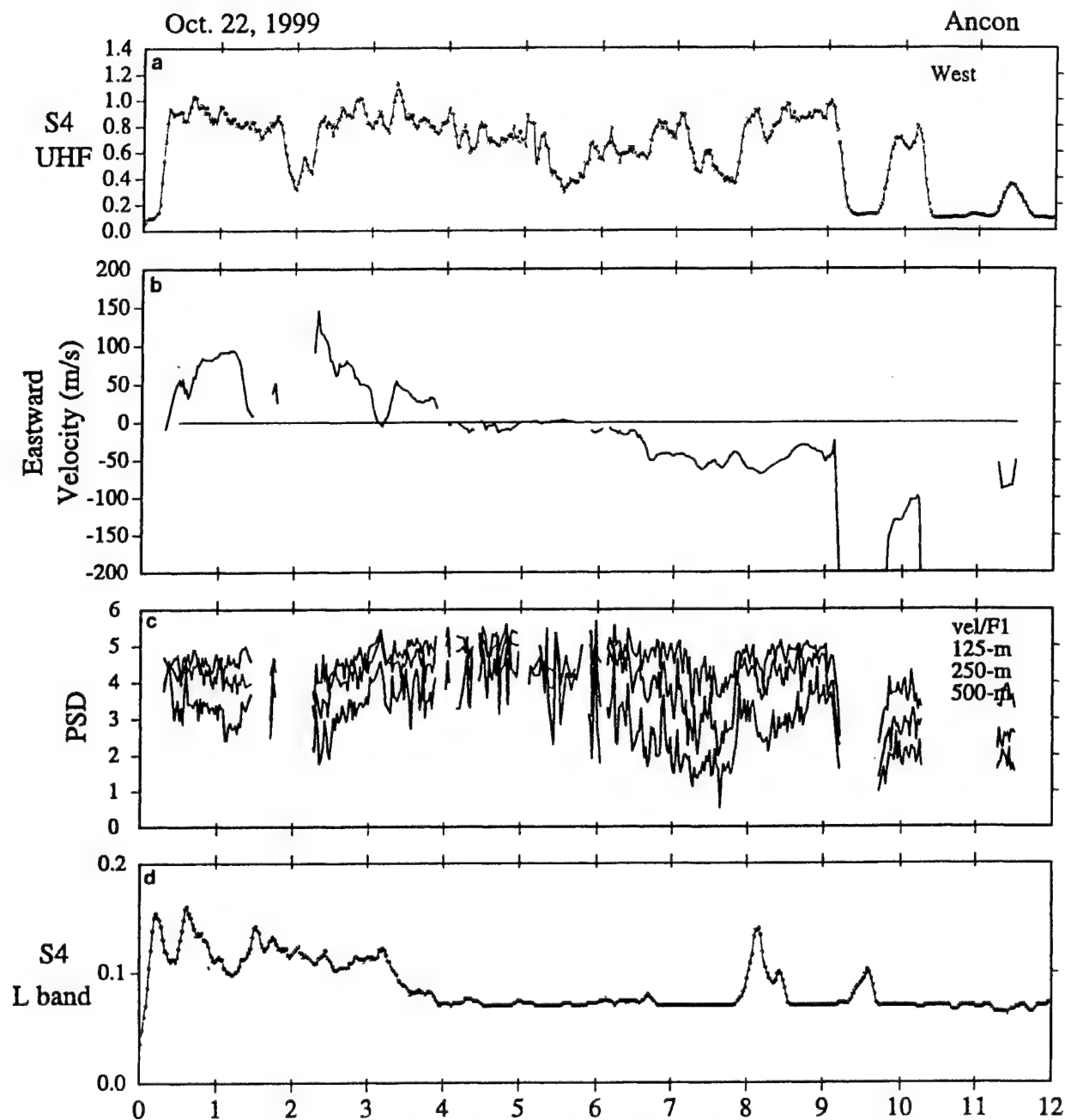
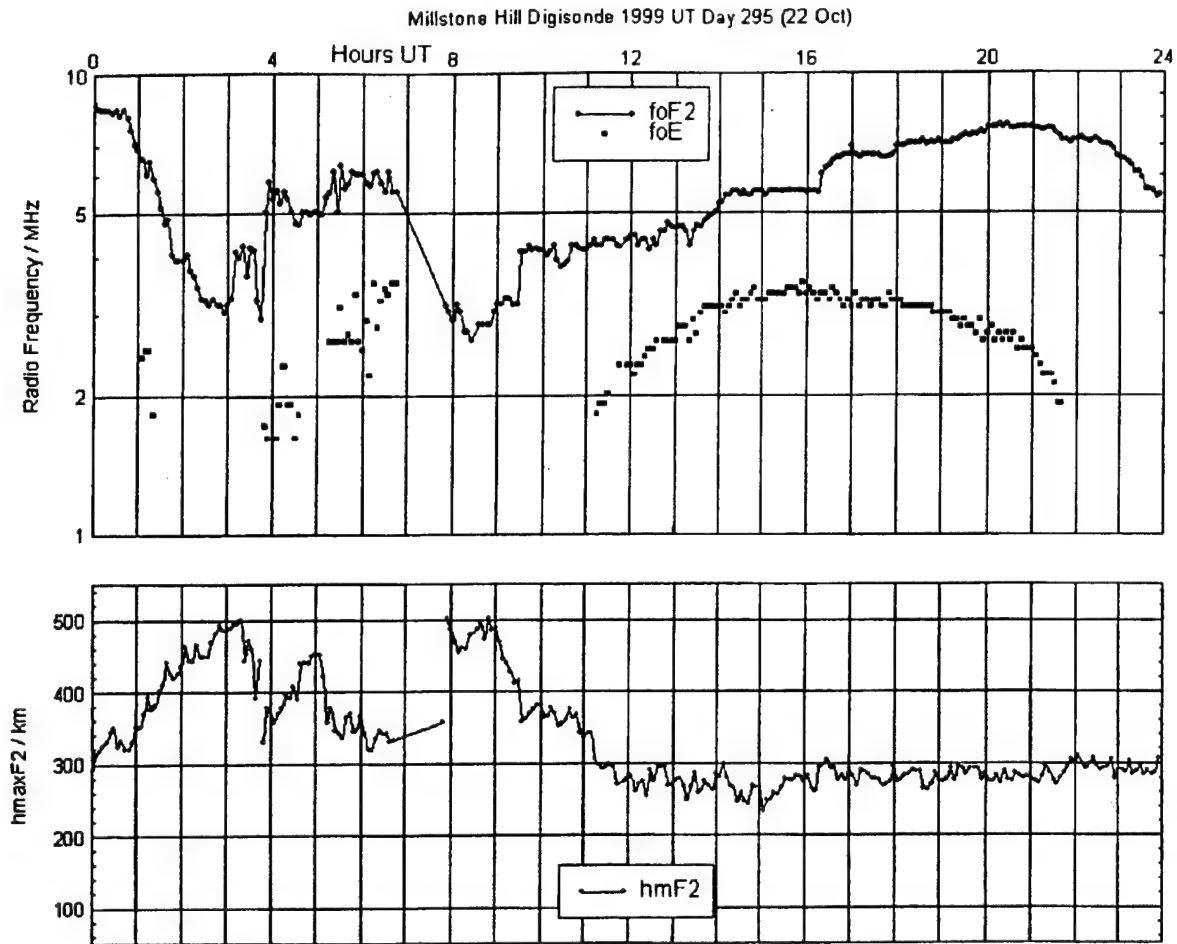


Plate 2. Similar to Figure 5 but for October 21–22, 1999, which has an estimated Wide Area Augmentation System (WAAS) range delay overplotted in red. The output of the WAAS error-bound algorithm called Grid Ionospheric Vertical Error (GIVE) is plotted in meters (m) on the lower panel, and also in red, for each station.





**Plate 3.** Scintillation data obtained at Ancon, Peru, on October 22, 1999. (a) The 250-MHz (UHF) data from F7 (to the west). (b) The E-W irregularity drift from spaced receiver measurements using the F7 satellite. (c) Power spectral densities in  $\text{dB Hz}^{-1}$  at 500, 250, and 125 m on a logarithmic scale obtained by combining the fast Fourier transform spectra and the E-W irregularity drift shown in Plate 3b. (d) The 1694-MHz (L band) data from G8.



**Figure 11.** Digisonde data showing the  $F$  layer critical frequency  $f_oF_2$ , the  $E$  layer critical frequency  $f_oE$ , and the maximum height of the  $F$  layer  $hmF_2$  observed at Westford, Massachusetts, on October 22, 1999. Note that the appearance of  $f_oE$  between 0400 and 0700 UT (2300–0200 LT) implies the presence of auroral particle precipitation. The break in the data from 0700 to 0800 UT is caused by increased absorption.

While the ROCSAT-1 gives a good idea of the E-W extent of the irregularities in the early evening hours, the DMSP F12 and F14 satellites provide a N-S cut through the equatorial irregularities that percolate to the topside and moreover provide a good coverage through the middle latitudes as well. Figure 16 shows the density at 840 km observed by F14 with an equatorial crossing near 0120 UT and one from F12 at 0140 UT both providing an approximate N-S cut through ROCSAT orbit 2 between 0155 and 0200 UT. Both the F14 and F12 orbits provide evidence for a wide belt of equatorial irregularities covering  $\pm 20^\circ$  of magnetic latitude. They also provide evidence for deep depletions ( $10^3 \text{ cm}^{-3}$ ) reaching the topside. Within the depletions the drifts (not shown) are upward and westward with the background vertical and horizontal drifts being quite small.

In addition to the equatorial density (there is a break in the data for F14) the midlatitude density behavior seen in both DMSP orbits is very consistent with the Digisonde and TEC data from Westford presented in section 3.1. Both types of data show a deep trough at  $52^\circ$  magnetic latitude followed by a density increase or blob poleward of the trough. The DMSP orbits pass just to the west of the Westford (W) station as

shown in the top panel of Figure 16. It is quite conceivable that the auroral blob may be convected equatorward to  $\sim 50^\circ$  magnetic latitude at later UT as a result of the continued intensification of the magnetic storm up to 0700 UT. As a matter of fact, the DMSP orbits show that there is very little of the entire nighttime global topside ionosphere that is not disturbed.

To return to the equatorial ionosphere, we consider the zonal irregularity drifts shown in Plate 3b. The drifts are mostly eastward in the range of  $50\text{--}100 \text{ m s}^{-1}$  between 0100 and 0300 UT and then decrease gradually to very small values between 0400 and 0600 UT, turn actually westward at 0630 UT, and continue in that direction with a magnitude of  $50 \text{ m s}^{-1}$  (with some larger values) until  $\sim 1200 \text{ UT}$  (0700 LT) when the data ends. (There was a small-magnitude scintillation event between 1300 and 1400 UT that is not shown.) Drifts usually turn westward at sunrise [Woodman, 1972]. Thus the reversal past local midnight during this magnetically disturbed period is, in general, considered to be the effects of an ionospheric disturbance dynamo setting up a neutral wind system driven by joule heating at high latitudes [Blanc and Richmond, 1980]. There was some indication from orbit 2 of the ROCSAT data that a

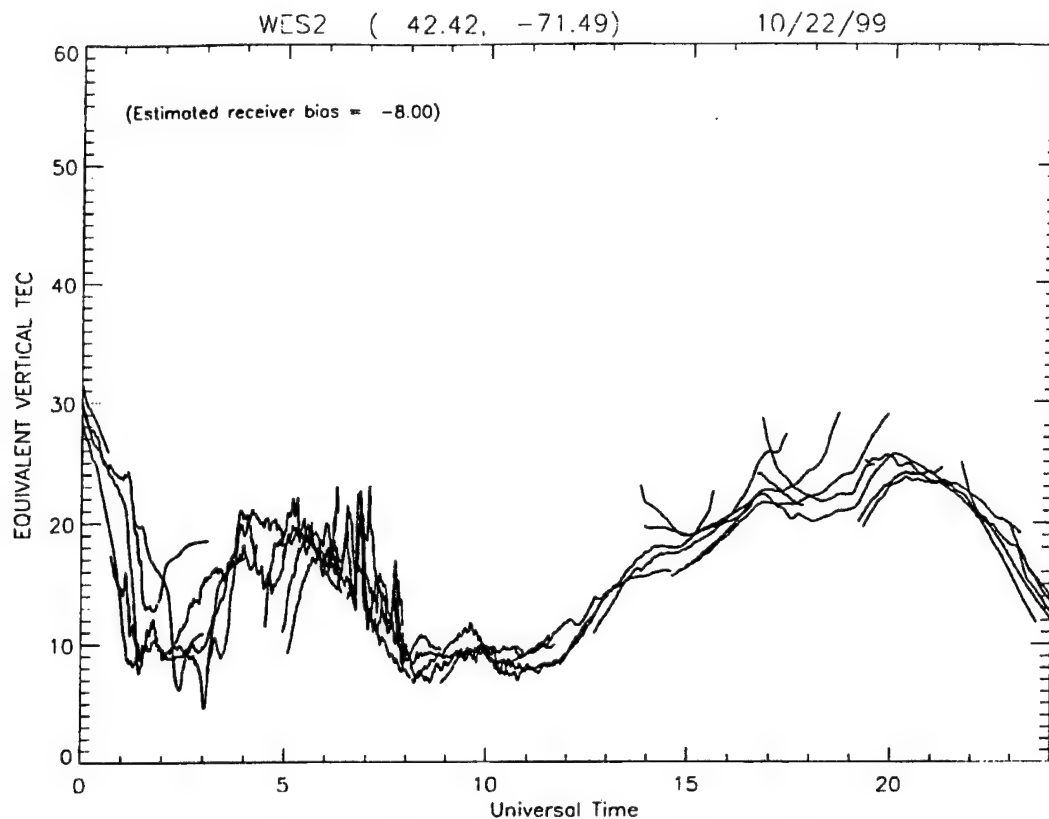


Figure 12. Same as in Figure 3 but for October 22, 1999.

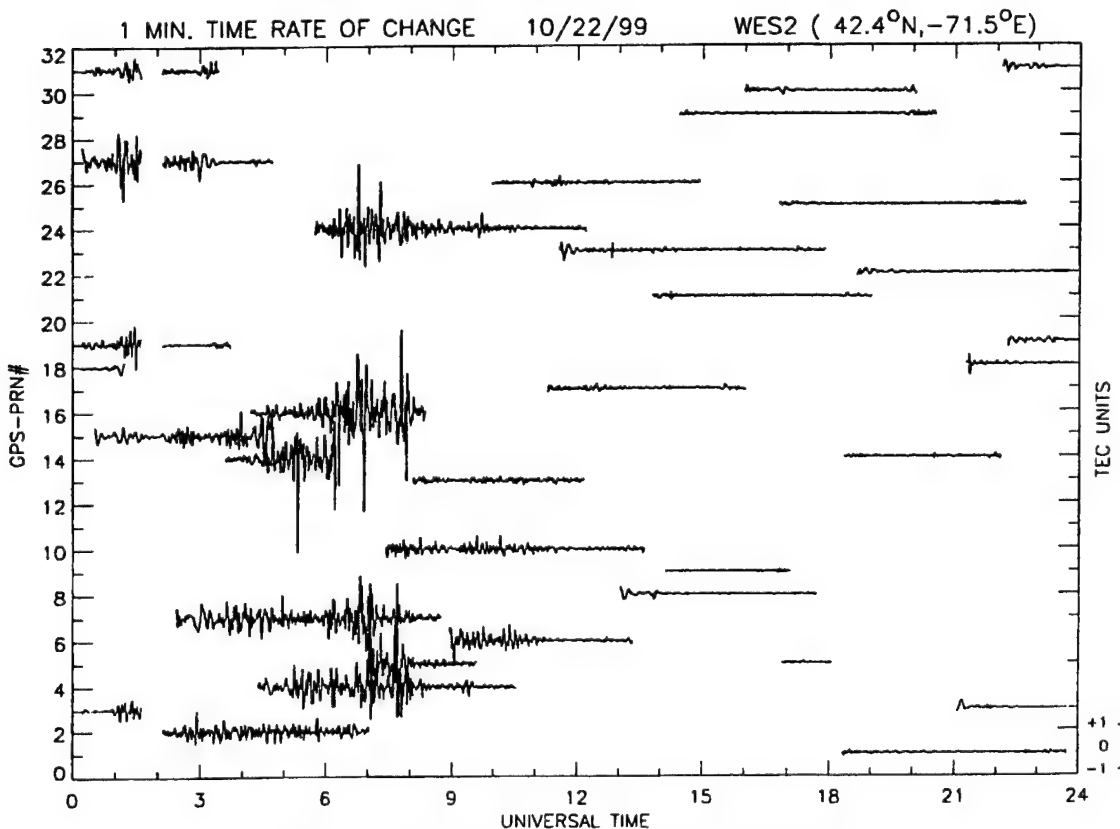


Figure 13. Same as in Figure 4 but for October 22, 1999.

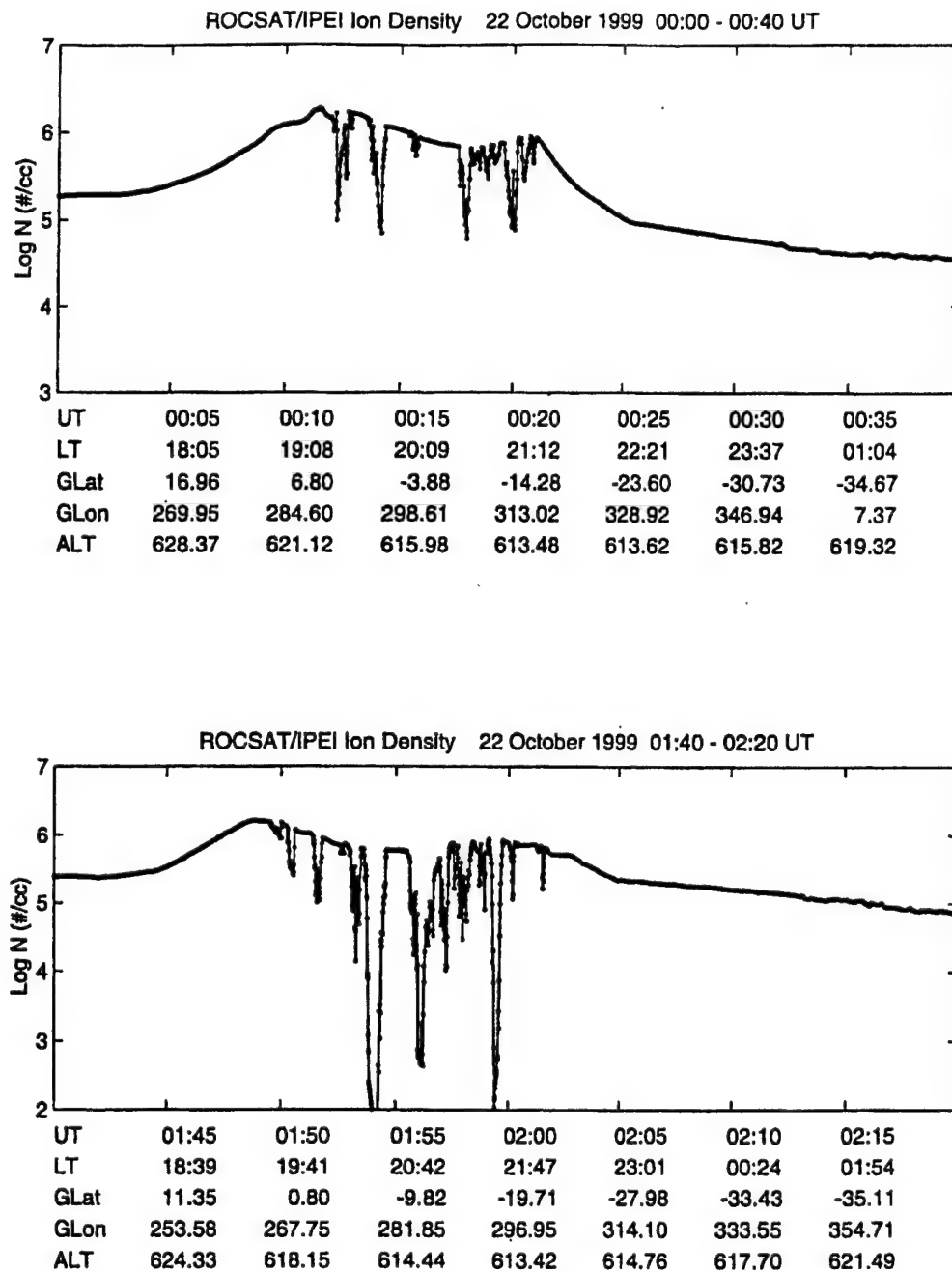
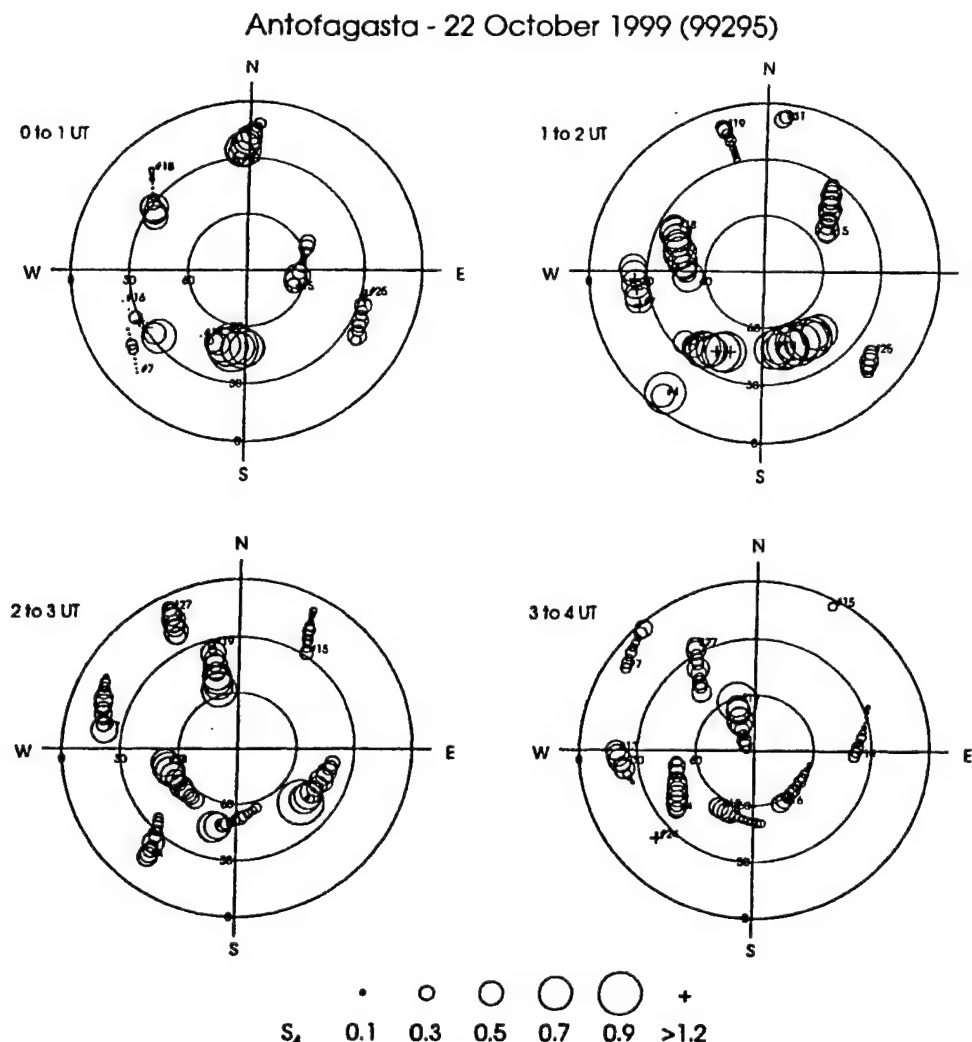


Figure 14. The total ion density measured by the ROCSAT-1 satellite between 0000–0040 and 0140–0220 UT on October 22, 1999. Wide regions of equatorial irregularity structures extending over 30° of longitude range are seen on both orbits at 600-km altitude.

disturbance dynamo process was gradually getting set up. The disturbance dynamo usually requires a few hours [Scherliess and Fejer, 1997] to be established as opposed to the prompt penetration effects both for increasing and decreasing high-latitude convection which occur within tens of minutes of storm intensification [Spiro *et al.*, 1988; Fejer and Scherliess, 1995, 1997]. The scintillation structure starting just prior to 0800 UT (0300 LT) in Plate 3a seems to be due to the fresh generation of equatorial irregularities in the postmidnight hours. We base our hypothesis on several aspects of the scin-

tillation data analysis and the simultaneous ROCSAT data shown in Figure 17. The scintillation data provide two reasons for considering the 0800–0900 UT structure to be freshly generated: (1) Scintillations at gigahertz, though small, are definitely observable after many hours of no gigahertz scintillation, and (2) the psds at specific scale lengths, obtained from a combination of the frequency scale of the fast Fourier transform (FFT) spectra and the irregularity drift shown in Plate 3b and depicted in Plate 3c (plotted on log scale), show large amplitudes. In particular, the psds at 500, 250, and 125 m



**Figure 15.** Hourly polar plots of the position and scintillation levels, plotted at 5-min intervals, of all GPS links tracked by the station at Antofagasta, Chile, on October 22, 1999, between 0000 and 0400 UT. Circle size corresponds to  $S_4$  level as shown in the legend. Pseudorandom noise (PRN) numbers are plotted at the initial satellite position. The large concentric circles denote elevation angles of 60°, 30°, and 0°. Between 0100 and 0200 UT, intense levels of scintillation are seen on four satellites simultaneously to the south and west of the station.

become suddenly enhanced. This psd behavior is similar to the scintillation characteristics early in the evening when only freshly generated irregularities are observed.

The corresponding ROCSAT data are shown in Figure 17. The irregularity structures between 0820 and 0830 UT are in the Hawaiian sector, and we will discuss that aspect later when trying to determine a westward boundary for the equatorial irregularities. The other structure near 0850 UT (corresponding to 0335 LT) embraces the field line connected to the scintillation ray path from South America and actually passes to the south of Antofagasta. Yeh *et al.* [2001], on the basis of positive correlation of density depletion and enhanced eastward electric field of 1–2 mV m<sup>-1</sup> resulting from the in-phase contributions of the prompt penetration magnetospheric (due to a sudden northward turning of the IMF) and the long-lasting ionospheric disturbance dynamo electric fields, argue for fresh generation for this large irregularity structure, and we

concur on the basis of scintillation characteristics. We shall also discuss these findings in section 4 in more global terms.

As we did for the September 22–23, 1999, magnetic storm, we would like to provide some eastern and western boundaries for equatorial irregularities observed during the October 22 storm. In this case the ROCSAT-1 data are extremely helpful in establishing both eastward and westward boundaries. Plate 4 depicts eight successive orbits on ROCSAT-1, at least five of which showed equatorial irregularities in the early evening generation phase. The portion of the orbits, which are in bold, both yellow and blue show the regions of irregularities. The actual density data showing the presence of irregularities for orbits 1, 2, and 6 have been shown in Figures 14 and 17. It is interesting to note from the LT attached to the first six orbits at irregularity onset that the ROCSAT-1 satellite detected irregularities between 1852 and 1936 LT except for orbit 3. This indicates that, by and large, the satellite must have inter-

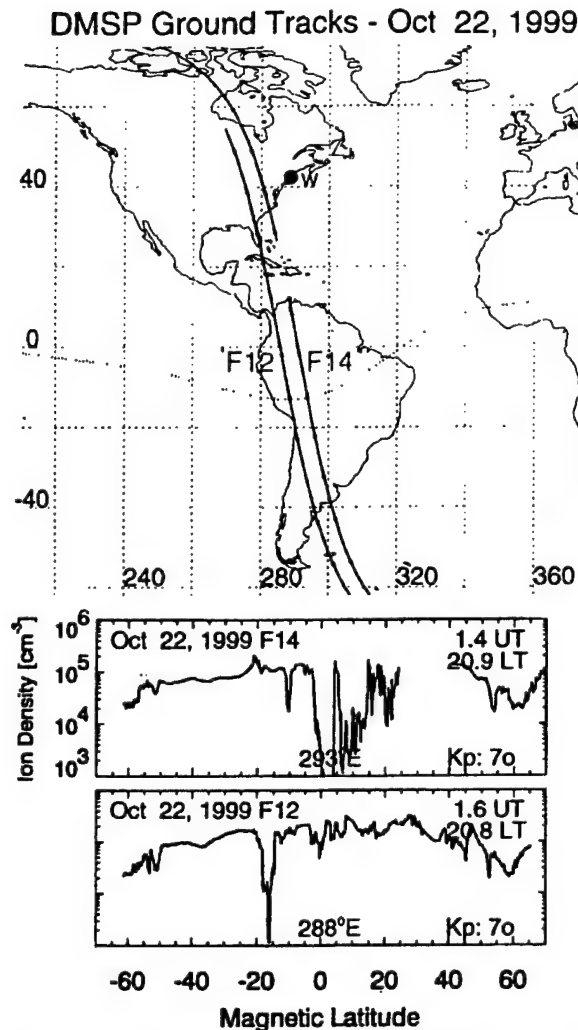


**Figure 16.** The ion density data at 840 km for the DMSP F12 and F14 orbits (middle and bottom panels) on October 22, 1999, and their orbital tracks (top panel). Wide regions of equatorial irregularities and the existence of the midlatitude trough at  $\sim 50^\circ$  with density enhancement poleward of the trough are clearly visible on both satellites particularly in the Northern Hemisphere.

cepted freshly generated irregularities. While orbits 1 and 2 occurred during the 0000–0200 UT period of intensifying SYM-H (or  $Dst$ ), orbits 4–6 occurred during the second intensification between 0400 and 0600 UT and continued into the time when SYM-H  $< -200$  nT up to  $\sim 0900$  UT. Thus, on the basis of Plate 4, we find that the equatorial irregularities for this magnetic storm were generated over longitudes ranging between  $\sim 170^\circ\text{E}$  and  $315^\circ\text{E}$ . It is extremely tempting, as in the case of the September 22–23, 1999, storm, to associate the belt of longitudes where  $E$  region sunset occurred during times of rapidly increasing negative  $Dst$  and  $Dst$  minimum phase as the ones affected by a prompt penetration of magnetospheric electric field into equatorial latitudes. In addition, we found at least one region of probable fresh generation of irregularities at 0300 LT in the South American sector (between  $235^\circ$  and  $300^\circ\text{E}$ ) that was a good candidate for being caused by the

effects of the ionospheric disturbance dynamo perhaps in conjunction with prompt penetration effects due to the northward turning of the IMF as shown in Figure 1 of Yeh *et al.* [2001].

It is very encouraging to note that other ground- and space-based data sets are all consistent with the findings based on ROCSAT-1. For instance, the IGS data for Ascension Island, Malindi, Diego Garcia, Manila, Guam, and Kwajalein showed no activity; that is, no TEC fluctuations were seen, while significant activity was observed at Arequipa, Santiago, and Easter Island. The DMSP F12, F13, and F14 satellite overflights were also consistent with the ROCSAT-1 data presented in Plate 4. Later orbits of ROCSAT-1, namely, orbits 7–12 between 1030 and 1725 UT (orbits 7 and 8 were plotted in Plate 4), all showed smaller-amplitude density irregularities at later local times (0400–0900 LT) but all within the range of longitudes between  $\sim 170^\circ$  and  $315^\circ\text{E}$ . Many of these orbits passed through the South American sector and are consistent with the scintillation observations which showed continued activity between 0010 and 0910 UT and thereafter with breaks up to 1400 UT.

#### 4. Summary and Discussion

We have studied the ionospheric effects of two major equinoctial magnetic storms ( $Dst < -150$  nT) near solar maximum (smoothed sunspot number  $\sim 150$ ) by considering the scintillation and TEC data from some middle-latitude stations which form part of the IGS network within the United States. We found that the prompt penetration of magnetospheric electric fields caused TEC increases, followed by rapid TEC decreases related to the equatorward motion of the midlatitude trough. These effects were enhanced if the rapid  $Dst$  intensifications took place in the afternoon sector near dusk. The equatorward motion of the trough was accompanied by TEC fluctuations, some as large as  $\pm 5$  TEC units  $\text{min}^{-1}$ , and saturated 250-MHz scintillations which may impact the GPS-based navigation system called WAAS and UHF communication links. In its simplest form, the effects of the prompt penetration of electric fields could be traced all the way to the magnetic equator and seemed to be confined to the range of longitudes for which the sunset times (probably at  $E$  region heights) coincided with the times of storm intensifications and its maximum phase. Thus, with the study of these two storms, one (in September 1999) for which the storm development and recovery was short and in the 2200–0100 UT time frame, a narrow swath of  $\sim 60^\circ$  in the South American and South Atlantic longitudes was affected. The other one (in October 1999) had a much longer development and recovery in the 0000–0900 UT hours and affected a much wider region extending over almost  $145^\circ$  of longitude in the South American and Pacific sectors. Thus extreme variability in irregularity occurrence at particular sites is often encountered during magnetic storms as has been reported by many authors [Aarons *et al.*, 1997; Abdu *et al.*, 1995, and references therein]. Because of the great variety of data types and sites used and different types of effects observed on communication and navigation systems, we provide a summary of our findings and references to the relevant diagrams in Tables 1a and 1b to help the reader.

It should be emphasized that equinox solar maximum conditions are conducive to equatorial irregularity generation at all longitudes during magnetically quiet times (see the review by Basu and Basu [1985, and references therein]). Further, general morphological studies based on  $Kp$  also indicate that



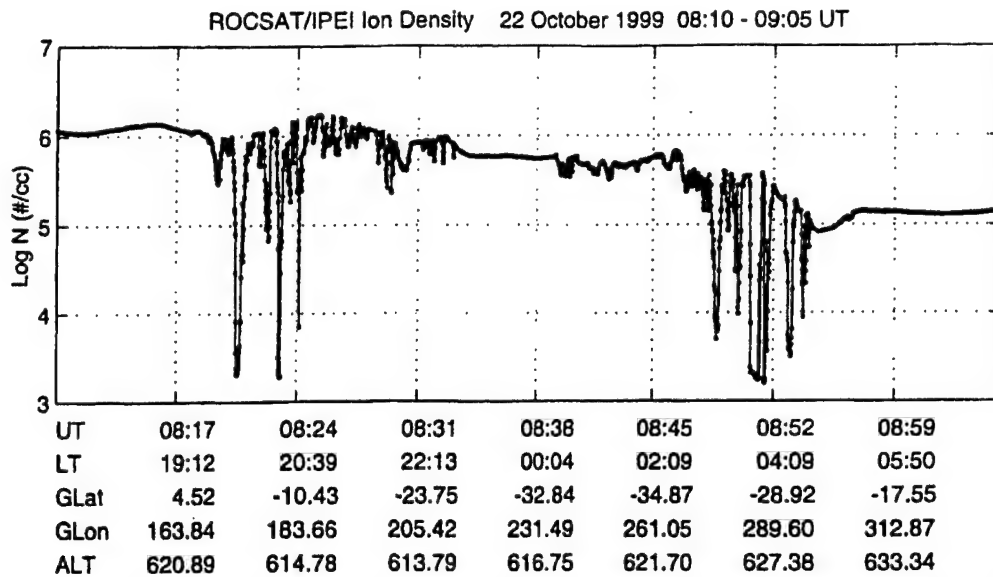


**Figure 17.** ROCSAT-1 total ion density data at 600 km between 0810 and 0905 UT on October 22, 1999. The irregularity structure near 0820 UT is in the Hawaiian sector whereas that near 0850 UT intersects the magnetic field lines going through the Ancon and Antofagasta stations.

scintillations tend to decrease with high  $Kp$  in the early evening hours [Groves *et al.*, 1997]. There is evidence from Jicamarca radar measurements for postmidnight irregularity generation during enhanced geomagnetic activity [Fejer *et al.*, 1999]. However, these times have much lower  $F$  region density so that irregularities, even if they are present, cannot cause intense scintillations in the gigahertz range. Our results, albeit limited to only two equinox storms, show that the equatorial irregularities may be enhanced or inhibited depending on the UT of storm intensification and length of the main phase. A recent paper by Huang *et al.* [2000] has pointed out the presence of equatorial bubbles during the initial and main phase of magnetic storms. In our discussion, in the interest of clarity, we have mainly considered the effect of the prompt penetration of electric fields of magnetospheric origin into low latitudes primarily during the increasing phase of the cross polar cap potential associated with the southward turning of the IMF and the intensification of the ring current. We have briefly mentioned the later time effects, due to the northward turning of the IMF and the more gradual onset of the ionospheric disturbance dynamo. In these two particular cases even the post-midnight events occurred within the region affected by the prompt penetration in the early evening hours. In a study of the May 23–24, 1998, great storm event, Aarons *et al.* [1999] had found a very longitude limited equatorial disturbance in the postmidnight phase that the authors attributed to the disturbance dynamo.

Our experimental findings at equatorial latitudes are generally consistent with the model predictions of the short-lived prompt penetration of electric fields both for increased and decreased magnetospheric convection [Fejer and Scherliess, 1997] and the more long-lived disturbance dynamo fields [Scherliess and Fejer, 1997] developed on the basis of Jicamarca radar measurements. These authors have used a linear relationship between the cross polar cap potential and  $AE$ , the auroral electrojet index [Ahn *et al.*, 1992], for the development of their empirical models. We have used the variation in the

1-min SYM-H index (which closely approximates the hourly  $Dst$  index) as the indicator for the prompt penetration of electric fields. Our results show that for the case of well-identified major magnetic storms during the initial phase, the time variation of the SYM-H index can effectively track the effects due to this type of prompt penetration of electric fields on communication and navigation systems operating at middle and equatorial latitudes. For the disturbance dynamo effects, however, the  $AE$  index during such large magnetic storms is probably a more appropriate measure of the energy input into high latitudes. For the September and October storms discussed in this paper the  $AE$  index increase and SYM-H decrease occurred in concert, making it difficult to distinguish between the efficacy of the two indices as a proxy for the cross polar cap potential. However, for the case of the July 15, 2000, superstorm, the  $AE$  increase occurred several hours prior to the SYM-H decrease due to ring current development. In that case the midlatitude and equatorial impacts due to prompt penetration of the magnetospheric electric field in the initial phase were still better ordered by variations in the SYM-H index which seemed to be taking place in an environment affected by the disturbance dynamo [Foster *et al.*, 2000; Basu *et al.*, 2001]. The effects on systems of these prompt penetration fields in the dusk sector, particularly during solar maximum, are large enough to merit a serious modeling effort for this magnetosphere-ionosphere coupled phenomenon. Indeed, such modeling efforts are underway to calculate the prompt penetration electric field from model results of the stormtime ring current [Ridley and Liemohn, 2001]. It is encouraging to note that in this modeling effort the magnitude of the penetration electric field is related to  $Dst^*$ , a solar wind pressure corrected  $Dst$  index [Kozyra *et al.*, 1998].

The prompt penetration of magnetospheric electric fields into the midlatitude ionosphere induces variations in TEC that may adversely affect the performance of navigation systems. Garcia *et al.* [2000] have documented a similar case at Arecibo, Puerto Rico, where GPS TEC perturbations were observed in

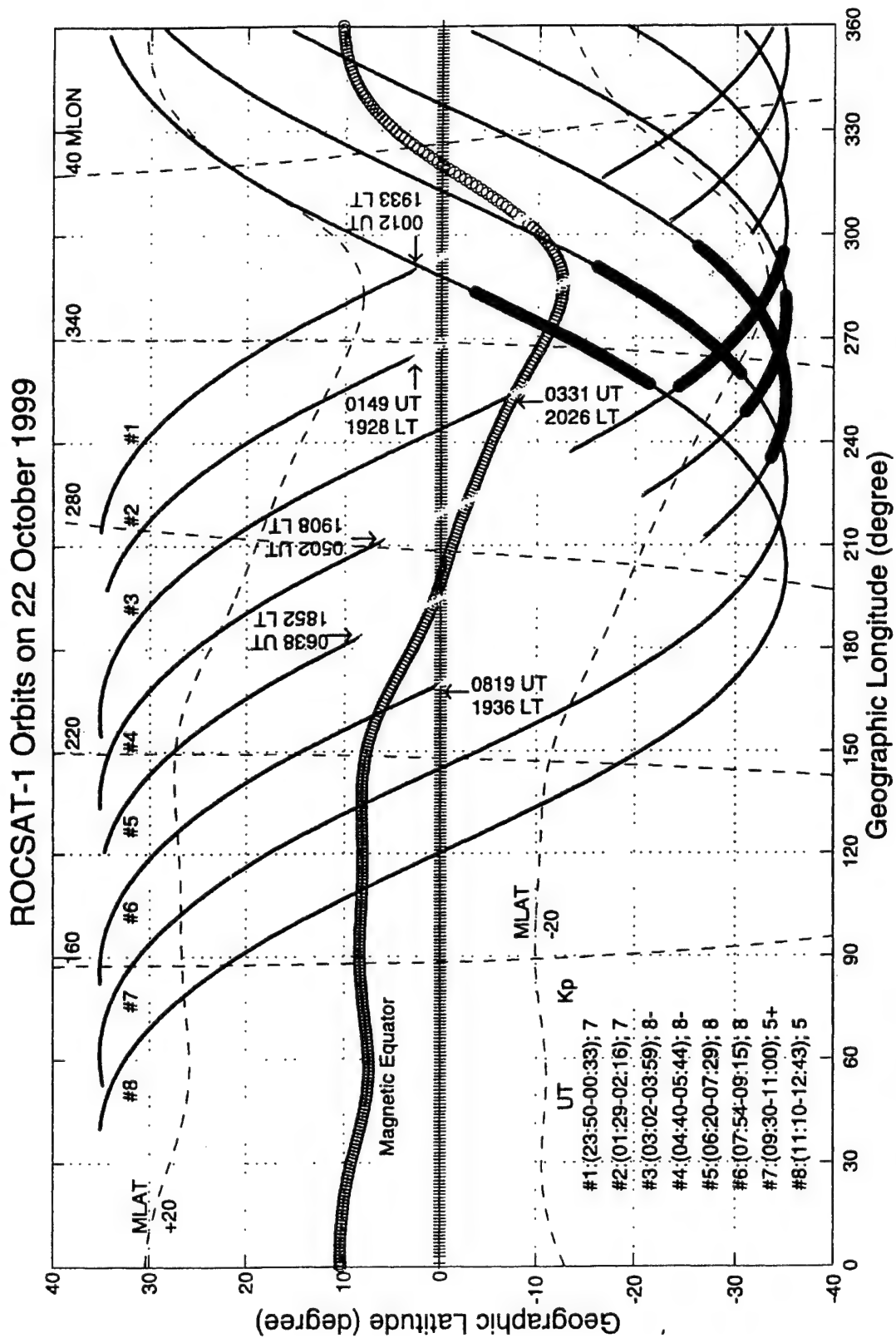


**Plate 4.** Equatorial portions of the first eight orbits of ROCSAT-1 between 0000 and 1200 UT on October 22, 1999. The thick yellow and blue lines on the orbits indicate the presence of density irregularities at 600 km. The LT at the onset of irregularities for the first six orbits is indicated on the diagram. These six orbits covered the range of longitudes where a fresh generation of equatorial irregularities was seen during the early and main phase of the October 22, 1999, magnetic storm. The thick blue lines show irregularities in the postmidnight phase.

**Table 1a.** September 22, 1999,  $Dst_{min} \sim -167$  nT at 2400 UT,  $(dDst/dt)_{max} \sim 75$  nT h<sup>-1</sup> Between 2200 and 2300 UT\*

Ionospheric Effects	Observation	Remarks
Prompt effect at midlatitudes		
Large ( $\sim$ km s <sup>-1</sup> ) westward (sunward) convection velocity and increase of $hmF_2$ and TEC between 2100 and 2200 UT (1600–1700 LT)	DMSP F13 and F14; Millstone Digisonde; IGS GPS RX	magnetospheric $E$ field penetration before sunset with northward and eastward components (Figure 2, Plate 1, and Figures 3 and 5)
Increase of $hmF_2$ ; and precipitous decrease of $NmF_2$ and TEC between 2210 and 2245 UT (1710–1745 LT)	Digisonde; IGS GPS RX	trough moves equatorward (Figures 3 and 5)
Impulsive 250-MHz scintillation and GPS phase fluctuation onset between 2210 and 2240 UT (1710–1740 LT)	Hanscom scintillation RX; IGS GPS RX	plasma instabilities associated with trough gradient cause electron density irregularities with scale lengths of tens of kilometers to tens of meters (Figures 1 and 4)
Prompt effect at equatorial latitudes		
Scintillation at 250 MHz, plasma bubbles, and GPS phase fluctuation; all between 15°W and 73°W	Ancon scintillation RX; South American GPS network; DMSP F12 and F14; global IGS GPS RX	prompt penetration of eastward $E$ field over longitude sector for which early evening period corresponds to the time of rapid $Dst$ (SYM-H) variations; equatorial anomaly development and plasma instability induced topside irregularities (Figures 6–9)
Postmidnight effects at equatorial latitudes		
Postmidnight scintillation in South Atlantic	Ancon and Ascension scintillation RX	possible disturbance dynamo-induced irregularity formation over longitude sector affected by prompt penetration $E$ field

\*TEC, total electron content; IGS, International GPS Service for Geodynamics; GPS, Global Positioning System; RX, Receiver.

conjunction with airglow enhancements during a high geomagnetic activity period. Our study has shown that the LT of penetration of the electric field dictates the magnitude of the system impacts. A specific occurrence at local dusk is the equatorward motion of the midlatitude trough that, in turn, creates plasma instabilities driven by the gradient. If one assumes that in addition to the large sunward (or westward) flow seen in Plate 1, the plasma is moving equatorward in the neutral frame of reference, then this geometry is consistent with the requirements of the gradient drift instability (see the review by Tsunoda [1988]). Sometimes these equatorward and westward motions bring auroral blobs into the erstwhile midlatitude ionosphere, the trailing edges of which are also seen to cause intense 250-MHz amplitude scintillations and TEC fluctuations at GPS frequencies. This unexpected TEC increase and its fluctuations in the midnight time frame caused the largest errors in the WAAS algorithms in the continental United States. Needless to say, the morphology of such trough-wall gradients and auroral blob structures has to be studied using a large data-base such as the one existing at Millstone Hill [Vo and Foster, 2001] so that predictive schemes may be developed for use during magnetic storms.

Finally, we come to a consideration of the effects of penetrating electric fields on the equatorial ionosphere. At the recent Equatorial Aeronomy Symposium in Antalya, Turkey, in May 2000, there was consensus among the participants that the topic is still one of the major unknowns in the field. Most of our information to date has come from the modeling efforts undertaken by B. G. Fejer and L. Scherliess (see references quoted earlier) based on vertical drift measurements by the Jicamarca radar. These single-point measurements have been skillfully interpreted by these authors to provide LT and storm time coverage at all longitudes for both the prompt penetration (for convection increase and decrease) fields and the disturbance dynamo. We took a more global approach in an

attempt to link a UT-driven phenomenon (namely, ring current development) with one dependent on LT, namely,  $E$  region sunset, creating conductivity gradients at specific locations. For the two storms discussed here and the July 15, 2000, storm [Basu et al., 2001], we find that equatorial irregularities are generated in the prompt penetration of the development phase at longitudes for which  $E$  region sunset is observed during a fast change in the SYM-H index on the order of 50 nT h<sup>-1</sup>, and SYM-H achieves values in the range of about  $-150$  nT or smaller. Obviously, many more magnetic storms have to be studied under different seasonal and sunspot cycle conditions to test this hypothesis. If it holds, then it could be introduced as a nowcasting tool in equatorial scintillation prediction.

Both these storms provided evidence for the fresh generation of irregularities in the post-midnight time frame. This can be attributed to the disturbance dynamo generated eastward electric field. Both storms also showed a prompt northward turning of the IMF indicating storm recovery, which could have provided a short-lived in-phase contribution to the disturbance dynamo effects. However, for the September 1999 storm the northward turning was not at the appropriate time whereas for the October storm the two effects seemed to have provided an in-phase contribution in the postmidnight irregularity generation. What is quite interesting is that the postmidnight event for both storms occurred within a part of the longitude range affected by prompt penetration in the early evening (generation) period. The same was found to be true for the July 15, 2000, storm [Basu et al., 2001]. If this holds up for more storm studies, it may indicate that the background ionosphere which turned unstable earlier in the evening had a greater likelihood of becoming unstable again in the postmidnight hours. However, since the most favorable time for this joint effect is near 0300 LT [Scherliess and Fejer, 1997], the impacts on commu-

**Table 1b.** October 22, 1999,  $Dst_{min} \sim -231$  nT at 0700 UT,  $(dDst/dt)_{max} \sim 45$  nT h<sup>-1</sup> During 0000–0200 and 0400–0600 UT

Ionospheric Effects	Observation	Remarks
Prompt effect at midlatitudes		
250-MHz scintillation onset at 0120 and 0440 UT	Hanscom scintillation RX	scintillation structures due to two periods of penetration $E$ fields; monitored by two periods of fast $Dst$ (SYM-H) decreases (Figure 10)
$NmF_2$ and TEC fast decrease at 0000–0300 UT (1900–2200 LT)	Millstone Digisonde; IGS GPS RX	trough moves equatorward causes first scintillation structure (Figures 10–12)
$NmF_2$ and TEC increase during 0400–0700 UT (2300–0200 LT)	Digisonde; IGS GPS RX; DMSP F-12 and F-14	auroral blob causes TEC increase; second scintillation event observed (Figures 10–12 and 16)
GPS phase fluctuation between 0500 and 0800 UT	IGS GPS RX	trailing edge of blob structured; WAAS parameter GIVE exceeds 6 m during TEC fluctuation (Figures 12 and 13 and Plate 2)
Prompt effect at equatorial latitudes		
250-MHz and $L$ band scintillation onset at 0010 UT (1910 LT)	Ancon scintillation RX; ROCSAT-1	near-simultaneous plasma bubble generation over 30° longitude interval (Figure 7, Plate 3, and Figure 14)
Strong GPS amplitude scintillation near crest of equatorial anomaly	Antofagasta GPS RX; ROCSAT-1	plasma bubbles extend to equatorial anomaly crest (Figures 14 and 15)
Irregularities in the topside detected over a longitude interval of 170°E–315°E in the local evening hours	ROCSAT-1 satellite	prompt penetration of eastward $E$ field over longitude sector for which early evening period corresponds to the time of rapid $Dst$ (SYM-H) variations (Plate 4)
Topside plasma bubbles cover $\pm 20^\circ$ MLAT	DMSP F12 and F14	plasma bubbles attain high altitudes (>840 km) over the magnetic equator (Figure 16)
Postmidnight effects at equatorial latitudes		
Fresh generation of irregularities and scintillation at 0800 UT (0300 LT) with westward drift	Ancon scintillation RX; ROCSAT-1	IMF $B_z$ northward turning and ionospheric disturbance dynamo induced irregularity generation and westward drift (Plate 3 and Figure 17)

nication and navigation systems may be rather limited as the background densities are much lower at that local time.

**Acknowledgments.** Sunanda Basu gratefully acknowledges a six-month professional development leave from the National Science Foundation that made this study possible. She thanks the Air Force Research Laboratory at Hanscom AFB, MA, and the National Central University (NCU) at Chung-Li, Taiwan, for hosting her during this period. Santimay Basu also thanks the NCU for its hospitality. The efforts of J. U. Kozyra and D. Webb in providing space weather information through the International Space Weather Clearinghouse Web page are much appreciated. We thank J. W. Wright for his assistance with the Digisonde data analysis. The work at AFRL was supported by AFOSR task 2311AS. The work at Boston College was supported by NSF grant ATM-9819912 and AFRL contract F19628-97-C-0094. The work at NCU was supported by NSC (ROC) grant NSC 89-NSPO (A)-PDD-008-STP01.

Janet G. Luhmann thanks the referees for their assistance in evaluating this paper.

## References

- Aarons, J., The longitudinal morphology of equatorial  $F$ -layer irregularities relevant to their occurrence, *Space Sci. Rev.*, **63**, 209, 1993.
- Aarons, J., and R. S. Allen, Scintillation boundary during quiet and disturbed magnetic conditions, *J. Geophys. Res.*, **76**, 170, 1971.
- Aarons, J., R. S. Allen, and H. E. Whitney, Observations of scintillations of two satellite beacons near the boundary of the irregularity region, *Planet. Space Sci.*, **20**, 965, 1972.
- Aarons, J., M. Mendillo, and R. Yantosca, GPS phase fluctuations in the equatorial region during sunspot minimum, *Radio Sci.*, **32**, 1535, 1997.
- Aarons, J., M. Mendillo, and B. Lin, The great magnetic storm of May 1998 and its effect on phase fluctuations in the auroral and equatorial regions, paper presented at Ionospheric Effects Symposium, Off. of Nav. Res., Arlington, Va., 1999.
- Abdu, M. A., I. S. Batista, G. O. Walker, J. H. A. Sobral, N. B. Trivedi, and E. R. de Paula, Equatorial ionospheric electric fields during magnetospheric disturbances: Local time/longitudinal dependencies from recent EITS campaign, *J. Atmos. Terr. Phys.*, **57**, 1065, 1995.
- Ahn, B.-H., Y. Kamide, H. W. Kroehl, and D. J. Gorney, Cross polar potential difference, auroral electrojet indices, and solar wind parameters, *J. Geophys. Res.*, **97**, 1345, 1992.
- Basu, S., and A. Das Gupta, Latitude variation of electron content in the equatorial region under magnetically quiet and active conditions, *J. Geophys. Res.*, **73**, 5599, 1968.
- Basu, S., Su. Basu, J. Aarons, J. P. McClure, and M. C. Cousins, On the co-existence of km- and m-scale irregularities in the nighttime equatorial  $F$ -region, *J. Geophys. Res.*, **83**, 4219, 1978.
- Basu, S., Su. Basu, J. LaBelle, E. Kudeki, B. J. Fejer, M. C. Kelley, H. E. Whitney, and A. Bushby, Gigahertz scintillations and spaced receiver drift measurements during Project Condor equatorial  $F$ -region rocket campaign in Peru, *J. Geophys. Res.*, **91**, 5526, 1986.
- Basu, S., et al., Scintillations, plasma drifts, and neutral winds in the equatorial ionosphere after sunset, *J. Geophys. Res.*, **101**, 26,795, 1996.
- Basu, S., K. M. Groves, J. M. Quinn, and P. Doherty, A comparison of TEC fluctuations and scintillations at Ascension Island, *J. Atmos. Terr. Phys.*, **61**, 1219, 1999.
- Basu, S., Su. Basu, K. M. Groves, H.-C. Yeh, S.-Y. Su, F. J. Rich, and P. J. Sultan, Response of the equatorial ionosphere in the South Atlantic region to the great magnetic storm of July 15, 2000, *Geophys. Res. Lett.*, **28**, 3577, 2001.
- Basu, Su., VHF ionospheric scintillations at  $L = 2.8$  and formation of stable auroral red arcs by magnetospheric heat conduction, *J. Geophys. Res.*, **79**, 3155, 1974.
- Basu, Su., and S. Basu, Equatorial scintillations: Advances since ISEA-6, *J. Atmos. Terr. Phys.*, **47**, 753, 1985.
- Basu, Su., E. MacKenzie, S. Basu, H. C. Carlson, D. A. Hardy, F. J. Rich, and R. C. Livingston, Coordinated measurements of low-energy electron precipitation and scintillations/TEC in the auroral oval, *Radio Sci.*, **18**, 1151, 1983a.

- Basu, Su., S. Basu, J. P. McClure, W. B. Hanson, and H. E. Whitney, High resolution in situ data of electron densities and VHF/GHz scintillations in the equatorial region, *J. Geophys. Res.*, **88**, 403, 1983b.
- Basu, Su., S. Basu, E. MacKenzie, W. R. Coley, J. R. Sharber, and W. R. Hoegy, Plasma structuring by the gradient-drift instability at high latitudes and comparison with velocity-shear driven processes, *J. Geophys. Res.*, **95**, 7799, 1990.
- Bhattacharyya, A., T. L. Beach, S. Basu, and P. M. Kintner, Nighttime equatorial ionosphere: GPS scintillations and differential carrier phase fluctuations, *Radio Sci.*, **35**, 209, 2000.
- Blanc, M., and A. D. Richmond, The ionospheric disturbance dynamo, *J. Geophys. Res.*, **85**, 1669, 1980.
- Briggs, B. H., and I. A. Parkin, On the variation of radio star and satellite scintillation with zenith angle, *J. Atmos. Terr. Phys.*, **25**, 339, 1963.
- Buonsanto, M., Ionospheric storms: A review, *Space Sci. Rev.*, **61**, 193, 1999.
- Buonsanto, M. J., M. Mendillo, and J. A. Klobuchar, The ionosphere at  $L = 4$ : Average behavior and response to geomagnetic storms, *Ann. Geophys.*, **35**, 15, 1979.
- Burke, W. J., et al., Electrodynamics of the inner magnetosphere observed in the dusk sector by CRRES and DMSP during the magnetic storm of June 4–6, 1991, *J. Geophys. Res.*, **103**, 29,399, 1998.
- Dehel, T., K. Pham, and J. Sheftic, National Satellite Test Bed (NSTB) observations of the effects of ionospheric storms on a prototype wide area augmentation system, paper presented at National Technical Meeting, Inst. of Navig., San Diego, Calif., 1999.
- Doherty, P., E. Raffi, J. A. Klobuchar, and M. B. El-Arini, Statistics of time rate of change of ionospheric range delay, paper presented at 7th International Technical Meeting, Inst. of Navig., Salt Lake City, Utah, 1994.
- Evans, J. V., The causes of storm-time increases of the  $F$ -layer at midlatitudes, *J. Atmos. Terr. Phys.*, **35**, 593, 1973.
- Fejer, B. G., and L. Scherliess, Time dependent response of equatorial ionospheric electric fields to magnetospheric disturbances, *Geophys. Res. Lett.*, **22**, 851, 1995.
- Fejer, B. G., and L. Scherliess, Empirical models of storm time equatorial zonal electric fields, *J. Geophys. Res.*, **102**, 24,047, 1997.
- Fejer, B. G., L. Scherliess, and E. R. dePaula, Effects of the vertical plasma drift velocity on the generation and evolution of equatorial spread  $F$ , *J. Geophys. Res.*, **104**, 19,859, 1999.
- Foster, J. C., Storm time plasma transport at middle and high latitudes, *J. Geophys. Res.*, **98**, 1675, 1993.
- Foster, J. C., and J. Aarons, Enhanced antisunward convection and  $F$  region scintillations at mid-latitudes during storm onset, *J. Geophys. Res.*, **93**, 11,537, 1988.
- Foster, J. C., and F. J. Rich, Prompt midlatitude electric field effects during severe geomagnetic storms, *J. Geophys. Res.*, **103**, 26,367, 1998.
- Foster, J. C., S. Basu, Su. Basu, A. J. Coster, and F. J. Rich, Subauroral ionospheric disturbance and space weather effects during the July 15–16, 2000 geomagnetic storm, *Eos Trans. AGU*, **81**(48), Fall Meet. Suppl., SH62A-10, 2000.
- Garcia, F. J., M. C. Kelley, J. J. Makela, P. J. Sultan, X. Pi, and S. Musman, Mesoscale structure of the midlatitude ionosphere during high geomagnetic activity: Airglow and GPS observations, *J. Geophys. Res.*, **105**, 18,417, 2000.
- Gonzales, C. A., M. C. Kelley, R. A. Behnke, J. F. Vickrey, R. Wand, and J. Holt, On the latitudinal variations of the ionospheric electric field during magnetospheric disturbances, *J. Geophys. Res.*, **88**, 9135, 1983.
- Groves, K. M., et al., Equatorial scintillation and systems support, *Radio Sci.*, **32**, 2047, 1997.
- Hanson, W. B., and R. J. Moffett, Ionization transport effects in the equatorial  $F$  region, *J. Geophys. Res.*, **71**, 5559, 1966.
- Hardy, D. A., L. K. Schmidt, M. S. Gussenhoven, F. J. Marshall, H. C. Yeh, T. L. Shumaker, A. Huber, and J. Pantazis, Precipitating electron and ion detectors (SSJ/4) for the Block 5D/Flights 4-10 DMSP satellites: Calibration and data presentation, *Tech. Rep. AFGL-TR-84-0317*, Air Force Geophys. Lab., Hanscom Air Force Base, Mass., 1984.
- Huang, C. Y., W. J. Burke, J. S. Machuzak, L. C. Gentile, and P. J. Sultan, DMSP observations of equatorial plasma bubbles in the topside ionosphere near solar maximum, *Eos Trans. AGU*, **81**(48), Fall Meet. Suppl., SA21A-10, 2000.
- Iyemori, T., T. Araki, T. Kamci, and M. Takeda, Mid-latitude geomagnetic indices "ASY" and "SYM" for 1999 (provisional), <http://swdcdh.kugi.kyoto-u.ac.jp/acasy/asy.pdf>, World Data Cent. C2 for Geomagn., Kyoto, Japan, 2000.
- Kelley, M. C., *The Earth's Ionosphere*, pp. 95–104, Academic, San Diego, Calif., 1989.
- Kozyra, J. U., et al., The role of precipitation losses in producing the rapid early recovery phase of the great magnetic storm of February 1986, *J. Geophys. Res.*, **103**, 6801, 1998.
- McClure, J. P., W. B. Hanson, and J. F. Hoffman, Plasma bubbles and irregularities in the equatorial ionosphere, *J. Geophys. Res.*, **82**, 2650, 1977.
- Mendillo, M., and J. A. Klobuchar, Investigations of the ionospheric  $F$ -region using multistation total electron content observations, *J. Geophys. Res.*, **80**, 643, 1975.
- Mendillo, M., M. D. Papagiannis, and J. A. Klobuchar, Ionospheric storms at midlatitudes, *Radio Sci.*, **5**, 895, 1970.
- Ossakow, S. L., Spread- $F$  theories: A review, *J. Atmos. Terr. Phys.*, **43**, 437, 1981.
- Pi, X., A. J. Mannucci, U. J. Lindqwister, and C. M. Ho, Monitoring of global ionospheric irregularities using worldwide GPS network, *Geophys. Res. Lett.*, **24**, 2283, 1997.
- Reinisch, B. W., and H. Xueqin, Automatic calculation of electron density profiles from digital ionograms, 3, Processing of bottomside ionograms, *Radio Sci.*, **18**, 477, 1983.
- Rich, F. J., and M. Hairston, Large-scale convection patterns observed by DMSP, *J. Geophys. Res.*, **99**, 3827, 1994.
- Ridley, A. J., and M. W. Liemohn, A model-derived storm time asymmetric ring current driven electric field description, *J. Geophys. Res.*, in press, 2001.
- Rishbeth, H., and W. B. Hanson, A comment on plasma "pile up" in the  $F$  region, *J. Atmos. Terr. Phys.*, **36**, 703, 1974.
- Scherliess, L., and B. G. Fejer, Storm time dependence of equatorial disturbance dynamo zonal electric fields, *J. Geophys. Res.*, **102**, 24,037, 1997.
- Spiro, R. W., R. A. Wolf, and B. G. Fejer, Penetration of high-latitude electric field effects to low latitudes during SUNDIAL 1984, *Ann. Geophys.*, **6**, 39, 1988.
- Sugiura, M., and D. J. Poros, Hourly values of equatorial  $Dst$  for years 1957–1970, *NASA-GSFC Doc. X-645-71-278*, Goddard Space Flight Cent., Greenbelt, Md., 1971.
- Tanaka, T., Severe ionospheric disturbances caused by the sudden response of evening subequatorial ionospheres to geomagnetic storms, *J. Geophys. Res.*, **86**, 11,335, 1981.
- Tsunoda, R., High-latitude  $F$ -region irregularities: A review and synthesis, *Rev. Geophys.*, **26**, 719, 1988.
- Valladares, C. E., R. Sheehan, S. Basu, H. Kuenzler, and J. Espinoza, The multi-instrumented studies of equatorial thermosphere aeronomy scintillation system: Climatology of zonal drifts, *J. Geophys. Res.*, **101**, 26,839, 1996.
- Valladares, C., S. Basu, K. Groves, M. P. Hagan, D. Hysell, A. J. Mazzella Jr., and R. E. Sheehan, Measurement of the latitudinal distributions of total electron content during equatorial spread  $F$  events, *J. Geophys. Res.*, in press, 2001.
- Vo, H. B., and J. C. Foster, A quantitative study of ionospheric density gradients at mid-latitudes, *J. Geophys. Res.*, in press, 2001.
- Woodman, R. F., Vertical drift velocities and east-west electric fields at the magnetic equator, *J. Geophys. Res.*, **75**, 6249, 1970.
- Woodman, R. F., East-west ionospheric drifts at the magnetic equator, *Space Res.*, **12**, 968, 1972.
- Wygant, J., D. Rowland, H. J. Singer, M. Temerin, F. Mozzer, and M. K. Hudson, Experimental evidence on the role of the large spatial scale electric field in creating the ring current, *J. Geophys. Res.*, **103**, 29,527, 1998.
- Yeh, H.-C., J. C. Foster, F. J. Rich, and W. Swider, Storm-time electric field penetration observed at mid-latitude, *J. Geophys. Res.*, **96**, 5707, 1991.
- Yeh, H. C., S. Y. Su, Y. C. Yeh, J. M. Wu, R. A. Heelis, and B. T. Holt, Scientific mission of the IPEI payload on board ROCSAT-1, *Terr. Atmos. Ocean Sci.*, suppl., p. 19, March 1999.
- Yeh, H. C., S. Y. Su, and R. A. Heelis, Storm time plasma irregularities in the pre-dawn hours observed by the low-latitude ROCSAT-1 satellite at 600 km altitude, *Geophys. Res. Lett.*, **28**, 685, 2001.

J. Aarons, Center for Space Physics, Boston University, Boston, MA 02215, USA.

S. Basu, T. W. Bullett, K. M. Groves, F. J. Rich, and P. J. Sultan, Space Vehicles Directorate, Air Force Research Laboratory, Hanscom AFB, MA 01731-3010, USA.

Su. Basu, Atmospheric Sciences Division, National Science Foundation, 4201 Wilson Boulevard, Rm. 775, Arlington, VA 22230, USA. (sbasu@nsf.gov)

P. Doherty, E. MacKenzie, and C. E. Valladares, Institute for Scientific Research, Boston College, Chestnut Hill, MA 02467, USA.

S.-Y. Su and H.-C. Yeh, Institute of Space Science, National Central University, Chung-Li, 32054 Taiwan.

(Received February 28, 2001; revised June 15, 2001; accepted June 18, 2001.)



### 3. OTHER PUBLICATIONS

This list includes papers that were presented at various scientific meetings and included in the Proceedings of those meetings.

Basu, B., Decker, D.T. and Jasperse J.R., "Incident Proton Spectra: Ionospheric Effects of High Energy Power Law Tails", *Proceedings of the Ionospheric Effects Symposium 1996*, 340-345, 1996.

Doherty, P.H., Anderson, D.N., Eicher, J. and Klobuchar, J.A., "Total Electron Content Over the Pan American Longitudes: March-April 1994", *Proceedings of the Ionospheric Effects Symposium 1996*, 441-449, 1996.

Preble, A.J., Decker, D. T. and Anderson, D. N., "Improving IRI90 Low Latitude Ionospheric Specification", *Proceedings of the Ionospheric Effects Symposium 1996*, 243-251, 1996.

Sultan, P.J., "Satellite Signatures of the Global Occurrence Morphology of Equatorial Spread-F", *Proceedings of the Ionospheric Effects Symposium 1996*, 287-292, 1996.

Gendron, P.J., Doherty, P.H. and Klobuchar, J.A., "Absolute Real-Time Ionospheric Measurements from GPS Satellites in the Presence of Anti-Spoofing", *Proceedings of the ION 52nd Annual Meeting*, 547-556, 1996.

Doherty, P.H., Decker, D.T., Anderson, D.N. and Wilson, B.D., "Observed Ionospheric Dependence on Solar Activity: Implications for a New Single Frequency GPS User Algorithm", *Proceedings of The 9th International Technical Meeting of The Satellite Division of the Institute of Navigation*, 565-574, 1996.

Doherty, P.H., Loh, R. and Anderson, D.N., "The Spatial and Temporal Variations in Ionospheric Range Delay", *Proceedings of the Institute of Navigation 53<sup>rd</sup> Annual Meeting*, 231, 1997.

Decker, D.T., Wise, J.O., Borer, W.S., Daniell, R.E., and Doherty, P.H., "Validation of PRISM: Real Time Specification", *Proceedings of the Ionospheric Effects Symposium 1999*, 340-347, September 1999.

Doherty, P.H., Decker, D.T., Sultan, P.J., Rich, F.J., Borer, W.S., and Daniell, R.E., "Validation of PRISM: The Climatology", *Proceedings of the Ionospheric Effects Symposium 1999*, 330-339, September 1999.

Smitham, M.C., Doherty, P.H., Delay, S.H., and Bishop, G.J., "Determination of Position Errors for Single-Frequency GPS Receivers", *Proceedings of the Ionospheric Effects Symposium 1999*, 647-654, September 1999.

Klobuchar, J.A., Doherty, P.H., Das Gupta, A., Sivaraman, M. R., Sarma, A.,  
"Equatorial Anomaly Gradient Effects on a Space-Based Augmentation System",  
*Proceedings of the International Beacon Satellite Symposium*, 216-221, 2001.

McNamara, L.F., VHF Transequatorial Propagation and Equatorial Bubbles",  
*Proceedings of the Ionospheric Effects Symposium 2002*, 667-671, September 2002.

Bishop, G., Bullett, T., Groves, K., Quigley, S., Doherty, P., Sexton, E., Scro, K.,  
Wilkes, R. and Citrone, P., "Operational Space Environment Network Display  
(OpSEND)", *Proceedings of the Ionospheric Effects Symposium 2002*, 25-32,  
September 2002.

Bishop, G., Decker, D., Sexton, E., Doherty, P., de la Braujardiere, O., Bullett, T.,  
Quigley, S. and Groves, K., "Space Weather Model and Product Validation",  
*Proceedings of the Ionospheric Effects Symposium 2002*, 33-39, September 2002.

#### 4. PRESENTATIONS

This list includes the presentations made under the context of this contract.

Basu, B., Decker, D.T. and Jasperse, J.R., "Incident Proton Spectra: Ionospheric Effects of High Energy Power Law Tails", presented at the Ionospheric Effects Symposium held in Alexandria, VA in May, 1996.

Doherty, P.H., Anderson, D.N., Eicher, J. and Klobuchar, J.A., "Total Electron Content Over the Pan American Longitudes: March-April 1994", presented at the Ionospheric Effects Symposium held in Alexandria, VA in May, 1996.

Preble, A.J., Decker, D.T. and Anderson, D.N., "Improving IRI90 Low Latitude Ionospheric Specification", presented at the Ionospheric Effects Symposium held in Alexandria, VA in May, 1996.

Sultan, P.J., "Satellite Signatures of the Global Occurrence Morphology of Equatorial Spread-F", presented at the Ionospheric Effects Symposium held in Alexandria, VA in May, 1996.

Gendron, P.J., Doherty, P.H. and Klobuchar, J.A., "Absolute Real-Time Ionospheric Measurements from GPS Satellites in the Presence of Anti-Spoofing", presented at the ION-GPS 52nd Annual Meeting held in Cambridge, MA in June 1996.

Vladimer, J.A., Ewell, V.R., Lee, M.C., Doherty, P.H., Decker, D.T. and Anderson, D.N., "Ionospheric TEC Observations from the TOPEX Satellite", presented at the 23<sup>rd</sup> IEEE International Conference of Plasma Science in Boston, MA in June 1996 and the PRIMO session at the Cedar Workshop in Boulder, CO in June 1996.

Sultan, P.J., "DMSP-Based Prediction of Equatorial Scintillation", presented at the Cedar Workshop held in Boulder, CO in June, 1996.

Doherty, P.H., Decker, D.T., Anderson, D.N. and Wilson, B.D., "Observed Ionospheric Dependence on Solar Activity: Implications for a New Single Frequency GPS User Algorithm", presented at the ION-GPS 96 Meeting held in Kansas City, MO in September, 1996.

Stergis, C.G., "Instrumentation for UV and Visible Measurements Above Thunderstorms", presented at the annual meeting of the International Society for Optical Engineering held in Denver, CO in August, 1996.

Decker, D.T., Valladares, C.E. and Anderson, D.N., "Modeling F-Region Polar Cap Patches and Boundary Blobs", presented at the 31<sup>st</sup> COSPAR Scientific Assembly held in Birmingham, United Kingdom in July, 1996.

Anderson, D.N., Decker, D.T. and Doherty, P.H., "Global Ionospheric Modeling of Geomagnetic Storms", presented at the 31<sup>st</sup> COSPAR Scientific Assembly held in Birmingham, United Kingdom in July, 1996.

Anderson, D.N., Decker, D.T. and Valladares, C.E., "Modeling High Latitude F-region Mesoscale Structures", presented at the 25<sup>th</sup> General Assembly of URSI held in Lille, France from August 28 to September 5, 1996.

Decker, D.T. and Anderson, D.N., "Simulations of GPS/MET Ionospheric Observations", presented at the 25<sup>th</sup> General Assembly of URSI held in Lille, France from August 28 to September 5, 1996. Also presented at the 1996 Fall AGU meeting held in San Francisco, CA in December, 1996.

Decker, D.T., Doherty, P.H. and Anderson, D.N., "Modeling the Low Latitude F Region Weather" presented at the SWIFT workshop, CEDAR meeting, held in Boulder, Colorado in June 1997

Decker, D.T., Valladares, C.E., MacKenzie, E., Anderson, D.N., Basu, S., and Basu, Su, "Modeling the Climatology and Weather of Large-Scale Plasma Structures in the High Latitude F Region", presented at the Third Joint Workshop for CEDAR HLPS/GAPS held at in Peaceful Valley, Colorado, June 15-17, 1997.

Decker, D.T., Valladares, C.E. and Anderson, D.N., "Specifying the High Latitude F Region Weather" presented at the IAGA meeting held in Uppsala, Sweden in August 1997.

Anderson, D.N., Decker, D.T., Doherty, P.H. and Fox, M.W., "Modeling the Low Latitude F Region Weather" presented at the 1997 IAGA meeting held in Uppsala, Sweden in August, 1997.

Decker, D.T., Valladares, C.E., MacKenzie, E., Anderson, D.N., Basu, S. and Basu, Su, "Modeling the Climatology and Weather of Blobs", presented at the 1997 IAGA meeting held in Uppsala, Sweden in August, 1997.

Doherty, P.H., Loh, R. and Anderson, D.N., "Statistics of the Spatial and Temporal Variations in Ionospheric Range Delay", presented at ION-GPS 97 held in Kansas City, Missouri in September 1997.

Anderson, D.N., Decker, D.T. and Doherty, P.H., "Simulations of GPS/MET Ionospheric Observations", presented at the Workshop on Ionospheric Determination and Specification for Ocean Altimetry and GPS Surface Reflections held in Pasadena, California, December 1997.

Anderson, D.N., Decker, D.T., Doherty, P.H. and Fox, M.W., " Modeling the Low Latitude F Region Weather", presented at the Fall AGU meeting held in San Francisco, California in December 1997.

Decker, D.T., Valladares, C.E., MacKenzie, E., Anderson, D.N., Basu, S. and Basu, Su, "Modeling the Climatology and Weather of Large-Scale Plasma Structures in the High Latitude F Region", presented at the Fall AGU meeting held in San Francisco, California in December 1997.

Decker, D.T., "The Status of F-Region Weather Modeling", presented at the 1998 National Radio Science Meeting held in Boulder, Colorado in January 1998.

Doherty, P.H., Klobuchar, J.A. and Aarons, J., "An Overview of Ionospheric Effects on GPS Signals", presented at the 1998 National Radio Science Meeting held in Boulder, Colorado in January 1998.

Doherty, P.H., Sultan, P.J., Decker, D.T., Borer, W.S., Daniell, R.E. and Brown, L.D., "Validation of Ionospheric Models", presented at AGU Fall Meeting held in San Francisco, CA in December 1998.

Anderson, D.N., Decker D.T., Rich, F.J., Doherty, P.H. and Rocken, C., "GPS/MET Occultations: Validation of Ionospheric Inversion Techniques Through Comparisons with Ground-Based and Satellite Sensor Observations", presented at the Jet Propulsion Laboratory (JPL) Altimetry Workshop held in Pasadena, CA in December 1998.

Decker, D.T., Doherty, P.H., Anderson, D.N., Rich, F.J. and Rocken, C., "GPS Occultation: A New Remote Sensing Technique for the Ionospheric Topside?", presented at the 1998 Spring AGU Meeting, Boston, MA, May 1998.

Groves, K.M., Basu, S., Quinn, J., Kuenzler, H., Bishop, G., Doherty, P. and Ning, P., "A Comparison of TEC Fluctuations and Scintillations at Ascension Island", presented at the National Radio Science Meeting, Boulder, CO, January 1999.

Decker, D.T., Wise, J.O., Borer, W.S., Daniell, R.E. and Doherty, P.H., "Validation of PRISM: Real Time Specification", presented at the 1999 Ionospheric Effects Symposium, Alexandria, VA, May 1999.

Doherty, P.H., Decker, D.T., Sultan, P.J., Rich, F.J., Borer, W.S. and Daniell, R.E., "Validation of PRISM: The Climatology", presented at 1999 Ionospheric Effects Symposium, Alexandria, VA, May 1999.

Smitham, M.C., Doherty, P.H., Delay, S.H. and Bishop, G.J., "Determination of Position Errors for Single-Frequency GPS Receivers", presented at the 1999 Ionospheric Effects Symposium, Alexandria, VA, May 1999.

Doherty, P.H., Smitham, M.C., Delay, S.H. and Bishop, G.J., "Determination of Position Errors for Single-Frequency GPS Receivers", presented at the Institute of Navigation Annual Meeting, Cambridge, MA, June 1999.

Decker, D.T., Doherty, P.H., Sultan, P.J., Rich, F.J., Borer, W.S. and Daniell, R.E., "Validation of Ionospheric Models: The Climatology", presented at the GIFT workshop at the CEDAR Meeting, Boulder, CO, June 1999.

Decker, D.T., Wise, J.O., Borer, W.S., Doherty, P.H. and Daniell, R.E., "Assessment of Ionospheric Models: Weather Specification", presented to the IUGG 99 Meeting, Birmingham, UK, July 1999 and to the URSI General Meeting, Toronto, CA, August 1999.

Doherty, P.H., "Predicting Single-Frequency GPS Positioning Errors", seminar series presentation at the Air Force Geophysics Laboratory, August 1999.

Doherty, P.H., Decker, D.T., Sultan, P.J., Borer, W.S. and Daniell, R.E., "Assessment of Ionospheric Models: The Climatology", presented to the IUGG 99 Meeting, Birmingham, UK, July 1999 and to the URSI General Meeting, Toronto, CA, August 1999.

Decker, D.T., Wise, J.O., Daniell, R.E., Doherty, P.H. and Borer, W.S., "Validation of an Ionospheric Specification Model", presented at the Fall AGU Meeting, San Francisco, CA, December 1999.

Doherty, P.H., Decker, D.T., Sultan, P.J., Rich, F.J., Borer, W.S. and Daneill, R.E., "Comparisons Between Ionospheric Models and Observed Climatology", presented at the Fall AGU Meeting, San Francisco, CA, December 1999.

Hilmer, R.V., Ginet, G.P., Kadinsky-Cole, K., Quigley, S., Decker, D.T. and Doherty, P.H., "Space Environment Models Addressing Operational Hazards: An AF-GEOSPACE Perspective on Current Capabilities", presented to the 38<sup>th</sup> Aerospace Sciences Meeting of the American Institute of Aeronautics and Astronautics, Reno, NV, January 2000.

Decker, D.T., Borer, W.S., Doherty, P.H., Wise, J.O. and Daniell, R.E., "Comprehensive Evaluation of Ionospheric Models", presented to the Chapman Conference on Space Weather, Clearwater, FL, March 2000.

Bishop, G., Quigley, S., Groves, K., Bullett, T., Doherty, P., Cook, C., Citrone, P., Scro, K. and Wilkes, R., "OpSend: Mission-Tailored Graphical Products for DoD Warfighters", presented to the AGU Fall Meeting held in San Francisco, CA in December, 2000.

Pulliam, R., Borer, W.S., Decker, D.T. and Doherty, P.H., "Operational Ionosphere Model Validations Study", presented at the AIAA Space 2000 Conference held in Long Beach, CA in September 2000.



Pulliam, R., Borer, W.S., Decker, D.T. and Doherty, P.H., "Evaluation of Metrics for Ambient Ionospheric Specification", presented to the AGU Fall Meeting held in San Francisco, CA in December 2000.

Basu, S., Basu, Su., Valladares, C.E., Aarons, J., Doherty, P. and Groves, K., "Ionospheric Effects of Major Magnetic Storms During the International Space Weather Period of September and October 1999: GPS Observations and VHF/UHF Scintillations at Middle and Equatorial Latitudes", presented to the International Workshop on Space Weather Effects held in Boston, MA in June 2001.

Beaujardiere, O. D., Decker, D.T., Borer, W., Retterer, J., Bullett, T., Bishop, G., Groves, K., Jeong, L. and Doherty, P., "Future Directions in Ionospheric Space Weather Application", presented as an invited talk to the Fall AGU 2001 Meeting, held in San Francisco, CA in December 2001.

Bishop, G., Quigley, S., Groves, K., Bullet, T., Doherty, P., Sexton, E., Citrone, P., Scro, K. and Wilkes, K., "Operational Space Weather Impact Maps for RF Systems", presented to the International Workshop on Space Weather Effects held in Boston, MA in June 2001.

Doherty, P.H., Klobuchar, J.A. and Delay, S.H., "The Great Ionospheric Storm of July 2000: GPS Measurements and System Effects", presented at the Space Weather Workshop held in Boulder, CO in May 2001.

Doherty, P.H., Klobuchar, J.A. and Delay, S.H., "Ionospheric Response to the Great Storm of July 2000", presented at the International Workshop on Space Weather Effects held in Boston, MA in June 2001.

Doherty, P.H., Klobuchar, J.A., Delay, S.H. and Valladares, C.E., "Ionospheric Scintillation Effects on WAAS Receivers in the Auroral and Near-Equatorial Regions", presented at the International Beacon Satellite Symposium held in Boston, MA in June 2001.

Pulliam, R., Borer, W., Decker, D.T. and Doherty, P.H., "PRISM Validation Study", presented to the International Workshop on Space Weather Effects held in Boston, MA in June 2001.

Bishop, G., Bullett, T., Groves, K., Quigley, S., Doherty, P., Sexton, E., Scro, K., Wilkes, R. and Citrone, P., "Operational Space Environment Network Display (OpSEND)", presented to the Ionospheric Effects Symposium 2002, Alexandria, VA, May 2002.

Bishop, G., Decker, D., Sexton, E., Doherty, P., de la Braujardiere, O., Bullett, T., S. Quigley, S. and Groves, K., "Space Weather Model and Product Validation", presented to the Ionospheric Effects Symposium 2002, Alexandria, VA, May 2002.

McNamara, L.F., VHF Transequatorial Propagation and Equatorial Bubbles", presented to the Ionospheric Effects Symposium 2002, Alexandria, VA, May 2002.

de la Beaujardiere, O., Decker, D., Rich, F., Retterer, J., Burke, W., Basu, B., Bullett, T., Crowley, G., Kelley, M., Makela, J., McNamara, L., Huang, C. and Doherty, P., "The global ionosphere during the April 17 to 20, 2002 Magnetic Storm", presented as an invited talk to Fall AGU, San Francisco, CA, December 2002.